UNIVERSITY OF LEEDS

The development of structural mass spectrometry based techniques for the study of aggregation-prone proteins.

Owen Cornwell

School of Molecular and Cellular Biology

Astbury Centre for Structural Molecular Biology

University of Leeds

Submitted in accordance with the requirements for the degree of Doctor of Philosophy

December 2019

Declaration

The candidate confirms that the submitted work is his own and that appropriate credit has been given within the thesis where reference has been made to the work of others.

Jointly Authored Publications

Chapters 4 and 5 contain work from the following published manuscript:

Cornwell, O., et al., Comparing Hydrogen Deuterium Exchange and Fast Photochemical Oxidation of Proteins: a Structural Characterisation of Wild-Type and ΔN6 β2-Microglobulin. Journal of The American Society for Mass Spectrometry, 2018. **29**(12): p. 2413-2426.

In this work, all experimental work and data analysis was performed by OC. Optimisation of the HDX workflow and associated method development was performed by OC and JRA. Initial development and coding of the novel processing algorithm was performed by OC. Final development and coding of the PAVED software available for download was performed by JRA.

Chapter 6 contains work from the following published manuscript:

Cornwell, O., et al., Long-Range Conformational Changes in Monoclonal Antibodies Revealed Using FPOP-LC-MS/MS. Analytical Chemistry, 2019. **91**(23): p. 15163-15170.

In this work, all experimental work and data analysis was performed by OC. Data acquisition was performed at AstraZeneca (Granta Park, Cambridge) by OC under the supervision of NJB.

Acknowledgements

Firstly, I'd like to thank my two academic supervisors, **Alison and Sheena**, not just for taking me on as a student when I had nowhere else to go, but for their continued support and encouragement throughout the four years of my PhD at Leeds. I'd like to recognise **James Ault**, our MS facility manager, for his significant contribution to the work in this thesis, and for not yelling at me when I text him on Sundays in a panic because the HDX robot has squashed the syringe again. **Rachel George**, for keeping the lab running smoothly and doing all the jobs that I really should know how to do but don't, and all past and present members of the lab that helped me out along the way (particularly Anton, Hugh, Tom, Patrick, Emma, Leon and Nasir!).

I'd also like to thank my industrial supervisor **Nick Bond**, as well as **Dan Higazi**, and **Jim Scrivens**, my two original supervisors. Similarly, an honourable mention is thoroughly deserved by **Sue Slade**, for looking after me at several conferences, as well as stocking my formerly deficient kitchen full of a variety of cooking utensils - and a garlic crusher.

I'd also like to thank my family, and the doctors and nurses at Royal Papworth Hospital. Their hard work, which makes writing a PhD thesis look *unbelievably* easy, has given my family and I more time with my dad, for which I will be forever grateful. With recent events I've come to appreciate the true significance of my family's guidance in my life, and just how far away I'd be from getting a PhD, without them. I love you all.

Well…most of you.

Lastly, I'd like to recognise the essential, if less obvious, contributions made from a number of other people, entities and institutions. I realise I'm running out of space on the page so I'll be brief. I'd like to thank Mr Clark (my A-level chemistry teacher), Dr Brandon Reeder (my undergraduate project supervisor), the quality control department for KP's dry roasted peanuts, Dr Malcolm Finney and his wife Kathy, Spam, laser pointers, the 'Find and Replace' function in Microsoft Excel, John Cleese, Lemsip Cold & Flu, Chinese takeaway restaurants (especially the one on Town Street), scientific calculators, the complaints department at British Telecom, Robert Palmer, large USB sticks, most small and medium sized USB sticks, the cast and crew of Stargate: SG1, Oxo cubes, VAX essentials vacuum cleaners, pot noodle sandwiches, and last, but by no means least, my dragon tree houseplant - Steve.

Oh and my girlfriend Sophie.

She was great too…

Un-acknowledgements

I would also like to ***not*** gratefully thank my former landlord, and the staff at the Wakefield branch of Linely & Simpson letting agents, for refusing to fix my leaky bedroom window for two years until I got fed up with it and moved out, somewhere about a third of the way through Chapter 5.

Table of Contents

JOINTLY AUTHORED PUBLICATIONS III

ACKNOWLEDGEMENTS V

TABLE OF CONTENTS IX

LIST OF FIGURES XIV

LIST OF TABLES XIX

LIST OF EQUATIONS XX

LIST OF ABBREVIATIONS XXI

ABSTRACT XXV

1 INTRODUCTION I: MASS SPECTROMETRY THEORY 2

1.1 Overview and history of mass spectrometry 2

1.2 Ionisation 3

1.2.1 Electrospray ionisation 4

1.3 Mass analysers 7

1.3.1 Quadrupole analysers 8

1.3.2 Linear ion traps 13

1.3.3 Time-of-flight (ToF) analysers 16

1.3.4 Orbital trapping analysers 20

1.4 Ion Detectors 25

1.4.1 Electron multipliers 25

1.4.2 Image current detection 26

1.5 Analysis of mass spectrometry data 27

1.5.1 Mass error and mass accuracy 29

1.6 Tandem mass spectrometry (MS/MS) 29

1.7 Liquid chromatography – mass spectrometry (LC-MS) 31
1.8 LC-MS/MS data acquisition methods 33
1.8.1 Data dependent acquisition (DDA) 33
1.8.2 Data independent acquisition (DIA) 35
1.9 Ion mobility spectrometry – mass spectrometry (IMS-MS) 36
1.9.1 Drift tube IMS (DTIMS) 37
1.9.2 Travelling wave IMS (TWIMS) 38
1.10 Commercial instruments used in this thesis 40
1.10.1 Waters Synapt high definition mass spectrometer 40
1.10.2 Thermo Q Exactive hybrid quadrupole – orbitrap mass spectrometer 41
1.10.3 Thermo orbitrap fusion tribrid mass spectrometer 42
2 INTRODUCTION II: PROTEIN AGGREGATION, STRUCTURE AND DYNAMICS STUDIED BY MASS SPECTROMETRY 46
2.1 Protein folding, misfolding and aggregation 49
2.1.1 Protein folding 49
2.1.2 Misfolding, aggregation and disease 52
2.1.3 Structure and formation of amyloid 53
2.2 Beta-2 microglobulin (β_2m) 56
2.2.1 Normal function and dialysis related amyloidosis 56
2.2.2 β_2m aggregation *in vitro* 59
2.2.3 β_2m folding pathway and the I_T state 60
2.2.4 ΔN6 β_2-microglobulin 62
2.2.5 D76N β_2-microglobulin 63
2.3 Protein aggregation in biopharmaceuticals 65

2.3.1 MEDI1912 and MEDI1912_STT 68
2.4 Mass spectrometry in structural biology 69
2.4.1 Accurate mass determination, native MS and ion mobility 70
2.4.2 Fragmentation and peptide sequencing 72
2.4.3 Hydrogen deuterium exchange (HDX) 74
2.4.4 Fast photochemical oxidation of proteins (FPOP) 79
2.5 Aim of the thesis 83
3 MATERIALS AND METHODS 86
3.1 Protein preparation and purification 86
3.1.1 Wild-type, D76N and ΔN6 86
3.1.2 WFL and STT 90
3.2 Native MS 90
3.2.1 Sample preparation 90
3.2.2 Waters Synapt G1 HDMS 90
3.2.3 Calculation of *in silico* CCS 93
3.3 Intact mass analysis 94
3.4 Hydrogen Deuterium Exchange 94
3.4.1 Experimental 94
3.4.2 Data processing and analysis 95
3.5 Fast Photochemical Oxidation of Proteins 96
3.5.1 Experimental procedures for the analysis of β_2m 96
3.5.2 Experimental procedures for the analysis of WFL and STT 97
3.5.3 Data processing and analysis 97
3.5.4 Calculation of solvent accessible surface area 98

3.6 Homology modelling of mAbs 98

4 IMS-MS AND HDX-LC-IMS-MS/MS COMPARING B_2M VARIANTS 100

4.1 Protein preparation and initial characterisation 101

4.2 Native IMS-MS 104

4.3 HDX-LC-IMS-MS 113

4.4 Development of a new HDX-MS processing algorithm 117

4.5 Evaluating the PAVED algorithm 123

4.6 Deuterium uptake behaviour of the D76N variant of β_2m 129

4.7 Discussion 132

4.7.1 The PAVED algorithm 132

4.7.2 HDX behaviour of the D76N variant 134

4.7.3 Insights on the aggregation propensity of the D76N variant 135

4.7.4 Attempted HDX-ETD single residue experiments 136

5 FPOP-LC-MS/MS COMPARING B_2M VARIANTS 144

5.1 FPOP method validation 144

5.2 FPOP LC-MS/MS of wild-type, D76N and ΔN6 β_2m 154

5.2.1 Wild-type Vs ΔN6 160

5.2.2 Positional isomers in FPOP experiments 165

5.2.3 FPOP behaviour of the D76N variant of β_2m 176

5.3 Discussion 178

5.3.1 Interpretation of FPOP data 178

5.3.2 FPOP method development 180

5.3.3 FPOP of the ΔN6 truncation variant of β_2m 183

5.3.4 FPOP of the D76N variant of β_2m 184

6 FPOP-LC-MS/MS OF WFL AND STT 186

6.1 Initial characterisation and overview 186

6.2 Regions surrounding the W30S and F31T mutations 190

6.3 Constant domains and the C_L-C_H1 interface 195

6.4 Analysis of retention time data 200

6.5 Discussion 205

6.5.1 Retention time analysis 206

7 CONCLUDING REMARKS 208

7.1 A new understanding of FPOP 208

7.1.1 How do HDX and FPOP compare? 209

7.2 The D76N variant 210

7.3 What did we learn from studying biopharmaceuticals? 212

7.4 Final thoughts 215

8 APPENDICES 218

8.1 Related information for Chapter 4 218

8.2 Related information for Chapter 5 241

8.3 Related information for Chapter 6 246

9 REFERENCES 260

List of Figures

Figure 1.1 Overview of a mass spectrometer. *3*

Figure 1.2 Overview of the Electrospray ionisation (ESI) source. *5*

Figure 1.3 ESI ionisation mechanisms. *6*

Figure 1.4 Different definitions of m/z resolution. *8*

Figure 1.5 Schematic diagram of a quadrupole mass analyser. *9*

Figure 1.6 The m/z separation of ions in the two lateral planes of a quadrupole. *11*

Figure 1.7 Stability diagrams for ions in a quadrupole. *12*

Figure 1.8 Basic design of the linear ion trap. *13*

Figure 1.9 Dipolar resonance ejection in linear ion traps. *15*

Figure 1.10 The relationship between dipolar resonance ejection frequency and applied AC amplitude. *16*

Figure 1.11 m/z separation by time-of-flight mass spectrometry (ToF-MS). *18*

Figure 1.12 Schematic diagram of an orthogonal acceleration time-of-flight mass spectrometer (oa-ToF). *19*

Figure 1.13 Schematic diagram of an electrostatic reflector. *20*

Figure 1.14 The Kingdon trap and the Knight trap: early orbital ion traps. *21*

Figure 1.15 The orbitrap mass analyser: an 'ideal' Kingdon trap. *23*

Figure 1.16 Excitation by injection, and radial de-phasing of ions in an orbitrap. *24*

Figure 1.17 Schematic diagram of a microchannel plate continuous dynode electron multiplier. *26*

Figure 1.18 Image current detection in orbitrap mass analysers. *27*

Figure 1.19 Determination of charge states in a mass spectrum. *28*

Figure 1.20 The workflow of a product ion scan. *30*

Figure 1.21 Separating and analysing complex mixtures by liquid chromatography-mass spectrometry (LC-MS). *32*

Figure 1.22 Operating procedure of data dependent acquisition (DDA) in LC-MS experiments. *34*

Figure 1.23 Operating procedure for data independent acquisition (DIA) in LC-MS experiments. *35*

Figure 1.24 Data analysis in DIA-MS^E. *36*

Figure 1.25 The principle of drift cell ion mobility spectrometry. *37*

Figure 1.26 Schematic diagram of a stacked ring ion guide *38*

Figure 1.27 Separation of ions by travelling wave ion mobility spectrometry (TWIMS). *39*

Figure 1.28 Schematic diagram of a Waters Synapt G2Si HDMS. *41*

Figure 1.29 Schematic diagram of a Thermo Q Exactive mass spectrometer. *42*

Figure 1.30 Schematic diagram of a Thermo orbitrap fusion tribrid mass spectrometer. *43*
Figure 2.1 Transcribing, translating and folding polypeptide chains. *47*
Figure 2.2 Idealised folding funnel/energy landscape for protein folding. *51*
Figure 2.3 Generalised mechanism of protein aggregation. *53*
Figure 2.4 Structure of an amyloid fibril. *54*
Figure 2.5 Energy landscape for protein folding, misfolding and aggregation. *55*
Figure 2.6 The structures of β_2m and the class 1 major histocompatibility protein complex. *57*
Figure 2.7 β_2m amyloid deposits in dialysis related amyloidosis (DRA). *58*
Figure 2.8 The folding pathway of β_2m. *61*
Figure 2.9 Wild-type, and aggregation-prone variants of β_2m. *65*
Figure 2.10 The structure of an IgG1 antibody. *66*
Figure 2.11 A summary of structural MS methods. *69*
Figure 2.12 Idealised native and non-native charge state distributions. *71*
Figure 2.13 Peptide sequencing by product ion scan MS/MS. *73*
Figure 2.14 Fragment ions generated from peptide ion dissociation. *73*
Figure 2.15 General HDX-MS experimental workflow. *75*
Figure 2.16 Mechanisms of acid and base catalysed deuterium exchange. *78*
Figure 2.17 General theory of FPOP labelling. *81*
Figure 2.18 Aims of this thesis. *84*
Figure 3.1 The pINK plasmid containing the gene of one of three variants of β_2m. *86*
Figure 4.1 Size exclusion purification of wild-type β_2m. *102*
Figure 4.2 CD spectra for three variants of β_2m. *103*
Figure 4.3 Denatured ESI-MS analysis of three variants of β_2m. *104*
Figure 4.4 Native ESI-MS analysis of three variants of β_2m. *106*
Figure 4.5 3D IMS-MS plots of three variants of β_2m. *107*
Figure 4.6 Arrival time distributions from ESI-IMS-MS analysis of the 6^+ charge state of three variants of β_2m. *108*
Figure 4.7 Linear calibration plot for native ESI-IMS-MS CCS values. *109*
Figure 4.8 Gas-phase molecular dynamics and CCS values for three variants of β_2m. *112*
Figure 4.9 Automated HDX-LC-IMS-MS/MS workflow using a Synapt G2Si. *113*
Figure 4.10 Sequence coverage of wild-type, D76N and ΔN6 β_2m from online pepsin digestion. *114*
Figure 4.11 Generating deuterium uptake plots for peptides of β_2m variants. *115*
Figure 4.12 Example deuterium uptake plots highlighting increases in uptake in the ΔN6 truncation variant. *117*
Figure 4.13 PAVED graphical user interface. *123*

Figure 4.14 Consolidation of HDX-MS data using positional averaging.....125
Figure 4.15 Comparing HDX-MS between three β_2m variants data after 30 seconds deuteration.....126
Figure 4.16 PAVED difference plots of HDX-MS data for wild-type, D76N and ΔN6 β_2m.....127
Figure 4.17 Visualising differences in deuterium uptake relative to wild-type β_2m.....128
Figure 4.18 Deuterium uptake plots for peptides covering the D76N substitution.....130
Figure 4.19 Back exchange correction for peptides covering the D76N substitution. 131
Figure 4.20 A-B loop hydrogen exchange uptake plots. 132
Figure 4.21 Hydrogen bonding in the E-F loop of wild-type β_2m. 135
Figure 4.22 ETD fragmentation of peptide P1.....137
Figure 4.23 Deuterium scrambling analysis on peptide P1. 138
Figure 4.24 Online HDX-LC-ETD-MS of the N-terminal peptide of β_2m.....139
Figure 4.25 ETD fragmentation of the E-F loop of wild-type β_2m.....140
Figure 4.26 Alternative acid protease digests of wild-type β_2m. 141
Figure 5.1 Schematic diagram of a typical FPOP experimental setup. 146
Figure 5.2 Visualising laminar flow in capillaries. 148
Figure 5.3 Velocities and time spent in the irradiation zone calculated for different flow regimes in the FPOP capillary.....149
Figure 5.4 Exposure events per protein in the current FPOP experimental arrangement. 151
Figure 5.5 Native MS of FPOP oxidised wild-type β_2m.....152
Figure 5.6 The effect of FPOP oxidation on native IMS ATDs and sequence coverage in proteolytic digests of wild-type β_2m. 153
Figure 5.7 Denatured ESI-MS of three β_2m variants following FPOP. 155
Figure 5.8 Peptide coverage of three variants of β_2m following chymotrpyptic digest. 156
Figure 5.9 Residues modified by FPOP in wild-type, D76N and ΔN6 β_2m mapped onto the β_2m structure. 157
Figure 5.10 Analysis workflow for FPOP-LC-MS/MS experiments. 158
Figure 5.11 Residue level quantification of FPOP oxidations in three variants of β_2m. 159
Figure 5.12 Differences in FPOP oxidation between wild-type and ΔN6 β_2m.....160
Figure 5.13 Minor side chain rearrangements detected by FPOP between wild-type and ΔN6 β_2m..161
Figure 5.14 FPOP oxidation compared with SASA calculated from NMR structures. 162
Figure 5.15 The rotation of the Phe 30 side chain in the ΔN6 truncation variant of β_2m. 164
Figure 5.16 Identification of positional isomers in FPOP modified peptides. 166
Figure 5.17 Positional isomers of +16 Da hydroxyl radical-mediated phenylalanine oxidation. 168
Figure 5.18 Quantification of positional isomers identified from Phe30.....170
Figure 5.19 Quantification of positional isomers identified from Trp 60. 171

Figure 5.20 Overlaid states in the NMR structures of wild-type and ΔN6 β_2m. *172*
Figure 5.21 Common oxidation products of the hydroxyl radical-mediated oxidation of tryptophan. *174*
Figure 5.22 Full and tandem MS scans of the 2-hydroxytryptophan oxidation product of Trp 60. ... *175*
Figure 5.23 Structural differences between wild-type and D76N β_2m observed by FPOP. *176*
Figure 5.24 Positional isomers of oxidised Tyr 78 in three variants of β_2m. *177*
Figure 5.25 Proximity of the Trp 60 side chain to nearby Phe side chains. *178*
Figure 5.26 Chimeric MS/MS data from co-isolation of overlapping oxidised peptides. *182*
Figure 5.27 A schematic representation of DDA vs DIA MS/MS workflows for FPOP data acquisition. *183*
Figure 6.1 Example peptide coverage map of mAbs WFL and STT following FPOP and tryptic digestion. *188*
Figure 6.2 Modified residues identified following FPOP-LC-MS/MS of WFL and STT. *190*
Figure 6.3 XICs for modified and unmodified peptides covering the W30S and F31T mutations. *191*
Figure 6.4 Representative MS/MS for peptide 24-38 of WFL. *193*
Figure 6.5 Quantification of FPOP modifications identified in WFL and STT. *194*
Figure 6.6 Differences in FPOP oxidation between WFL and STT. *197*
Figure 6.7 Identifying and quantifying positional isomers of oxidised Trp 152. ..... *198*
Figure 6.8 Analysis of the effect of FPOP oxidations on peptide retention time in RP-LC. *201*
Figure 6.9 Chemical structures of histidine and 2-oxo histidine. *202*
Figure 6.10 Histidine oxidations in peptides show charge state biases towards lower charge states. . *203*
Figure 6.11 Possible in-source oxidations observed during FPOP-LC-MS/MS experiments. *204*
Figure 8.1 R code for the original PAVED algorithm. *235*
Figure 8.2 XIC of peptide 79-87. ..... *241*
Figure 8.3 XIC of peptide 88-95. ..... *242*
Figure 8.4 XIC of peptide 53-67 from the heavy chain of STT. *246*
Figure 8.5 XIC of peptide 53-67 from the heavy chain of WFL. *246*
Figure 8.6 XIC of peptide 68-87 from the heavy chain. *247*
Figure 8.7 XIC of peptide 117-132 from the heavy chain. *247*
Figure 8.8 XIC of peptide 133-144 from the heavy chain. *248*
Figure 8.9 XIC of peptide 145-158 from the heavy chain. *248*
Figure 8.10 XIC of peptide 286-289 from the heavy chain. *249*
Figure 8.11 XIC of peptide 313-328 from the heavy chain. *249*
Figure 8.12 XIC of peptide 367-381 from the heavy chain. *250*
Figure 8.13 XIC of peptide 372-381 from the heavy chain. *250*

Figure 8.14 XIC of peptide 404-420 from the heavy chain. 251
Figure 8.15 XIC of peptide 428-450 from the heavy chain. 251
Figure 8.16 XIC of peptide 18-46 from the light chain.....252
Figure 8.17 XIC of peptide 68-106 from the light chain.....252
Figure 8.18 XIC for peptide 107-114 from the light chain. 253
Figure 8.19 XIC for peptide 154-170 from the light chain. 253
Figure 8.20 XIC for peptide 176-190 from the light chain. 254
Figure 8.21 XIC for peptide 194-208 from the light chain. 254

List of Tables

Table 2.1 Summary of the twenty different naturally occurring amino acid structures, masses and abbreviations. 48

Table 2.2 Reactivities and common mass additions in hydroxyl radical oxidation of amino acid side chains. 80

Table 3.1 Solution components of Tris-tricine buffered SDS-PAGE gels used for analysis of β_2m. 89

Table 3.2 Summary of instrument source and IMS conditions used in native IMS-MS experiments. . 91

Table 4.1 Calculated CCS values for wild-type, D76N, and ΔN6 β_2m. 110

Table 5.1 Determining the number of irradiation events under different flow regimes of a laminar flow model in FPOP experiments. 150

Table 5.2 Residues modified by FPOP in wild-type, D76N and ΔN6 β_2m. 157

Table 5.3 A summary of residues to which multiple mono-oxidised XIC peaks could be assigned. .. 167

Table 5.4 A summary of Phenylalanine positional isomer ratios calculated from FPOP quantification data for Phe 22, Phe 30 and Phe 70 in the β_2m protein sequence. 169

Table 6.1 A summary of modifications observed following FPOP of the mAbs WFL and STT. 189

Table 8.1 Raw state data (as exported from DynamX) for HDX-MS experiments. 218

Table 8.2 PAVED processed data for D76N β_2m. 229

Table 8.3 Paved processed data for wild-type β_2m. 231

Table 8.4 Paved processed data for ΔN6 β_2m. 233

Table 8.5 Quantification and assignment data for FPOP of wild-type, D76N and ΔN6 β_2m. 243

Table 8.6 Raw data table for WFL and STT FPOP data. 255

List of Equations

Equation 1.1 Definition of resolution. *7*

Equation 1.2 Dynamic potential on quadrupolar rods generated by superimposed AC and DC potentials. *9*

Equation 1.3 The relationship between potential and kinetic energy for ions accelerated in ToF-MS. *17*

Equation 1.4 The relationship between flight time and m/z for ions accelerated in ToF-MS. *17*

Equation 1.5 The relationship between z axis oscillation frequency and m/z in an orbitrap mass analyser. *24*

Equation 1.6 Calculating mass from a mass spectrum. *27*

Equation 1.7 Determination of charge states in non-isotopically resolved mass spectra. *29*

Equation 1.8 The definition of mass accuracy. *29*

Equation 1.9 The Mason-Schamp equation. *38*

Equation 3.1 Conversion of measured ellipticity to mean residue ellipticity. *89*

Equation 3.2 Correcting literature CCS for mass, charge and buffer gas mass. *92*

Equation 3.3 Correcting drift time for m/z dependent flight time. *92*

Equation 3.4 Linear calibration curve used to determine unknown CCS values from analyte proteins. *92*

Equation 3.5 Calculation of CCS values for analyte proteins based on a linear calibration plot. *93*

Equation 3.6 Quantifying FPOP oxidations at residue level resolution. *98*

Equation 4.1 Simplified Rayleigh equation to model charges on the surface of globular, natively folded proteins. *105*

Equation 4.2 Previously published HDX-MS peptide level data consolidation approaches. *120*

Equation 4.3 PAVED algorithm: calculating combined mean relative fractional uptake per residue. *121*

Equation 4.4 PAVED algorithm: calculating combined standard deviation per residue. *121*

Equation 4.5 Proposed modelling of HDX data based on PAVED processing. *133*

Equation 5.1 Calculating irradiation volumes in FPOP capillary experimental setups assuming a plug flow model. *147*

Equation 5.2 Calculating the velocity of solvent at different radii from the capillary centre in laminar flow. *147*

Equation 5.3 Simultaneous equations calculating the maximum and minimum number of irradiation events for different flow regimes in FPOP. *150*

List of Abbreviations

AC = Alternating current

ATD = Arrival time distribution

BEH = Ethylene bridged hybrid

BSA = Bovine serum albumin

BSE = Bovine spongiform encephalopathy

CCS = Collision cross section

CD = Circular dichroism

CDR = Complementarity determining region

CEM = Chain ejection model

CI = Chemical ionisation

CID = Collision induced dissociation

CRM = Charge residue model

DC = Direct current

DTIMS = Drift tube ion mobility spectrometry

DDA = Data dependent acquisition

DIA = Data independent acquisition

DNA = Deoxyribonucleic acid

DRA = Dialysis related amyloidosis

DTT = Dithiothreitol

ECD = Electron capture dissociation

EDC = Enhanced duty cycle

EDTA = Ethylenediaminetetraacetic

EI = Electron ionisation

ESI = Electrospray ionisation

ETD = Electron transfer dissociation

FPOP = Fast photochemical oxidation of proteins

FWHM = Full width half maximum

GAG = Glycosaminoglycan

HCD = High energy collision induced dissociation

HDMS = High definition mass spectrometer

HDX = Hydrogen deuterium exchange

HNSB = Dimethyl(2-hydroxy-5-nitrobenzyl)sulfonium bromide

HPLC = High performance liquid chromatography

IEM = Ion ejection model

Ig = Immunoglobulin

IMS = Ion mobility spectrometry

IPTG = Isopropyl β- d-1-thiogalactopyranoside

IRM = Ion routing multipole

LB = Lysogeny broth

LC = Liquid chromatography

LIT = Linear ion trap

m/z = Mass to charge ratio

mAb = Monoclonal antibody

MCP = Micro channel plate

MD = Molecular dynamics

MeCN = Acetonitrile

MHC1 = Class 1 major histocompatibility complex

MS = Mass spectrometry

MWCO = Molecular weight cut off

nESI = Nano electrospray ionisation

NGF = Nerve growth factor

NMR = Nuclear magnetic resonance

oa-ToF = Orthogonal acceleration time-of-flight

PAVED = Positional averaging for visualising exchange data

PDB = Protein data bank

PLGS = ProteinLynx global server

PMSF = Phenylmethylsulfonyl fluoride

Ppm = Parts per million

RF = Radio frequency

RP-LC = Reverse phase liquid chromatography

RT = Retention time

SAP =Serum amyloid P

SASA = Solvent accessible surface area

SDS-PAGE = Sodium dodecyl sulphate polyacrylamide gel electrophoresis

SEC = Size exclusion chromatography

SRIG = Stacked ring ion guide

ssNMR = Solid state nuclear magnetic resonance

TEMED = Tetramethylethylenediamine

ToF = Time-of-flight

TWIMS = Travelling wave ion mobility spectrometry

UPLC = Ultra performance liquid chromatography

XIC = Extracted ion chromatogram

B_2m = β_2 – microglobulin

Abstract

The structural characterisation of aggregation-prone proteins, and the development of methods which allow such investigations, is of paramount importance to the prevention and treatment of illnesses such as Alzheimer's disease, and to the development of the next generation of biotherapeutic medicines.

This thesis outlines the development of several structural mass spectrometry based techniques, including hydrogen deuterium exchange (HDX) and fast photochemical oxidation of proteins (FPOP) to study the structure and dynamics of two protein systems: β_2 – microglobulin (β_2m), along with two of its variants (ΔN6 and D76N), as well as WFL and STT, two biotherapeutic antibody variants.

The first aggregation-prone variant of β_2m studied, missing the six N-terminal residues (ΔN6), showed significant structural changes compared with the wild-type protein close to the truncation site when examined by FPOP-LC-MS/MS, consistent with experiments performed using more well-established structural MS methods, such as HDX. A thorough examination of the data revealed the presence of positional isomers, generated from the oxidation of aromatic amino acids within peptides, which showed oxidation patterns consistent with known structural changes observed by NMR, indicating sub-amino acid level resolution may be achievable using FPOP. The second aggregation-prone variant, D76N, showed significant structural changes proximal to the site of the amino acid substitution when using HDX, but only minimal changes when analysed by FPOP-LC-MS/MS. We hypothesise that these changes may be due to a disruption of hydrogen bonding networks within the loop containing the amino acid substitution, and that these differences may lead, or contribute, to the increased aggregation propensity of the D76N variant, relative to the wild-type protein.

FPOP-LC-MS/MS analysis of the antibody variants WFL and STT, so called due to their different amino acid sequences in the heavy chain complementarity determining regions (CDRs), revealed long-range conformational changes at the interface between the two constant domains of the Fab arm, a considerable distance from the site of the

amino acid substitutions. Although the relationship between these observed changes and the propensity of WFL to undergo reversible self-association cannot be determined from these data, these experiments strongly indicate that conformational changes can be transmitted between the antigen binding region and the constant domains of the Fab arm – two regions often considered to be functionally independent. The large data set obtained from these experiments allowed further development of the FPOP experimental technique, where trends in the altered hydrophobicity of modified peptides, probed by relative retention time shifts of peptides following separation by reverse-phase chromatography, highlight the possibility of using such analyses to aid in the assignment of modified species, when coupled to tandem MS analysis.

Overall, the data presented in this thesis shed new light on the changes in protein structure and dynamics associated with the two aggregation-prone variants of β_2m, as well as the aggregation-prone mAb, WFL which may provide key insights into the causes of aggregation or reversible self-association in these proteins. Similarly, the work presented here contributes significantly to a greater understanding of FPOP, the application of both FPOP and HDX towards the study of aggregation-prone proteins, and provides a foundation for the further advancement of these methods in future research.

Chapter 1:

Introduction I: Mass spectrometry theory

1 Introduction I: Mass Spectrometry Theory

"I feel sure that there are many problems in chemistry which could be solved with far greater ease by this than any other method."

- J.J Thomson, from the Preface of "Rays of positive electricity and their application to chemical analysis", 1913, [1].

1.1 Overview and history of mass spectrometry

Mass spectrometry (MS) is an analytical technique used to determine molecular mass by measuring the mass to charge ratio (*m/z*) of ions in the gas phase. The earliest work in the field of mass spectrometry was done by J.J Thomson in 1897, where he observed that cathode rays under vacuum could be deflected by electromagnetic fields [2]. This lead to the discovery of the electron, and determination of its mass to charge ratio, winning Thomson the Nobel Prize in physics in 1906. Later, in April 1912, Thomson, along with his assistant F.W. Aston, constructed the first mass spectrometer, called a parabola ion spectrograph at the time, using the same principle of deflecting ion beams with electromagnetic fields to study ions of neon. They discovered that the neon ion beam generated two different parabolas when deflected by the magnetic field, suggesting the presence of two different atomic masses, ^{20}Ne and ^{22}Ne – the first evidence of isotopes in a stable element [3]. Aston would later go on to study isotopes of other stable elements using a refined version of the spectrograph instrument, an early version of what would later be called a magnetic sector mass spectrometer, winning his own Nobel Prize in chemistry in 1922.

Since then, MS has advanced from the electromagnets and photographic detector plates used by Thomson and Aston, to a diverse range of intricate mass analysers and detector systems. New ionisation methods, as well as advances in MS instrument technology and chemical labelling techniques, have allowed MS to evolve from the

study of elementary particles, to the investigation of complex biological systems such as proteins - the structure, dynamics and aggregation of which will be the main focus of this thesis.

Although many of today's modern mass spectrometers, and the analysis methods used, would be unrecognisable to Thomson and Aston, the essential principle of determining the *m/z* of a gas phase ion, by manipulating electric or magnetic fields has remained the same. As such, MS can be broken down into three fundamental components: ionisation, *m/z* separation, and detection (Figure 1.1).

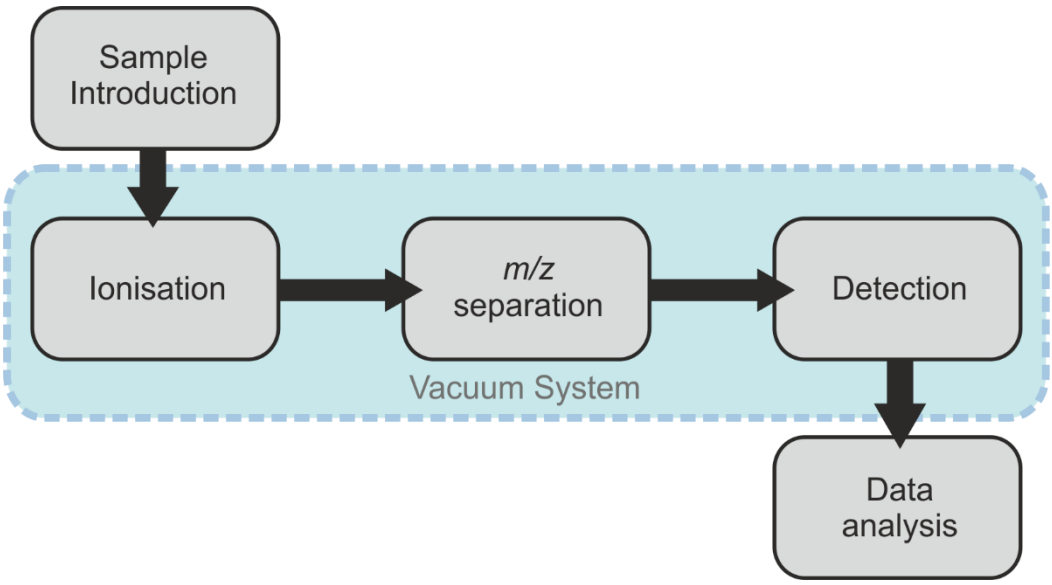

Figure 1.1 Overview of a mass spectrometer. Samples are ionised and introduced into the gas phase before *m/z* separation by a mass analyser. This is followed by detection of the ions and data analysis.

1.2 Ionisation

For a molecule to be analysed by MS, it must first be ionised. Although dozens of ionisation methods have been developed to suit specific experiments or types of analyte, historically, one of the most practical, and thus widely used, ionisation methods was electron ionisation (EI) [4]. In an EI source, a heated filament is used to generate electrons which are then accelerated towards an orthogonal path of gaseous molecules. With the appropriate wavelength and kinetic energy, these electrons can

ionise the nearby gaseous sample, before the product ions are directed towards a mass analyser. However, EI frequently induces fragmentation of the analyte, a property not always experimentally useful, so complementary ionisation methods, such as chemical ionisation (CI) were developed to reduce fragmentation and study intact molecular ions [5]. Chemical ionisation uses EI to ionise gas reagents in the source region, such as methane or isobutane, which in turn undergo ion-molecule collisions with the gaseous analyte, ionising the sample by proton transfer.

These, and other similar ionisation methods are, however, limiting in the sense that they require the analyte to be in the gas phase prior to ionisation. For years, this made MS analysis of large biomolecules, such as proteins, problematic, effectively limiting MS to the analysis of thermally stable, volatile compounds that could be introduced into the gas phase by heating.

1.2.1 Electrospray ionisation

The development of electrospray ionisation-MS (ESI-MS) in 1984 by John Fenn revolutionised the study of large biomolecules by mass spectrometry [6, 7]. During ESI, an atmospheric pressure ionisation technique, a voltage is applied across a thin, metal coated glass capillary containing a low μM concentration of analyte in a volatile buffer solution. The applied voltage forms a unique solvent formation at the capillary tip know as a Taylor cone, which generates a fine spray of charged droplets containing the analyte of interest [8] (Figure 1.2). Gradual desolvation of these droplets reduces their size until Coulombic repulsion from charges on the droplet surface overcomes the force of surface tension – a point known as the Rayleigh limit [9, 10]. When the Rayleigh limit is reached, droplet fission creates smaller progeny droplets, and the desolvation process continues.

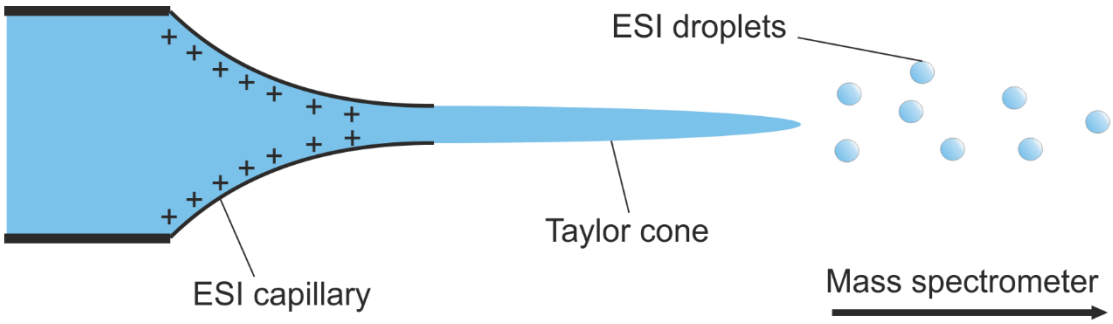

Figure 1.2 Overview of the Electrospray ionisation (ESI) source. A voltage is applied across a capillary containing the analyte in a solution of volatile buffer. The applied voltage causes the solution to form a Taylor cone at the end of the capillary, where charged droplets containing the analyte are ejected.

Three main models exist to explain the formation of ions from this point forward: the charge residue model [11], the ion evaporation model [12] and the chain ejection model [13] (Figure 1.3). The charge residue model (CRM) suggests that continued droplet desolvation and Coulombic fission of progeny droplets eventually results in completely desolvated ions. The ion evaporation model (IEM) differs slightly in that ions are proposed to be ejected from the droplet surface once the droplet radii have been sufficiently reduced. It has been suggested, however, that both models may occur, depending on the size of the sample being ionised [13]. Larger, globular species are proposed to ionise via the CRM, whereas the IEM has been suggested as the most likely ionisation mechanism for small, inorganic ions [13, 14]. The chain ejection model (CEM) was proposed recently as a possible ionisation mechanism, primarily for unfolded proteins, where the extended hydrophobic nature of the unfolded chain leads to rapid migration to the droplet surface, followed by stepwise ejection starting at the chain terminus [13].

While small, volatile molecules could still be ionised by ESI, usually accepting a single charge forming $[MH]^+$ ions, this newly developed 'soft' ionisation technique allowed far larger, non-volatile biomolecules such as peptides and proteins to be ionised without fragmentation, typically adopting multiple charges such that $[M+nH]^{n+}$, where M is the molecular weight and n is an integer.

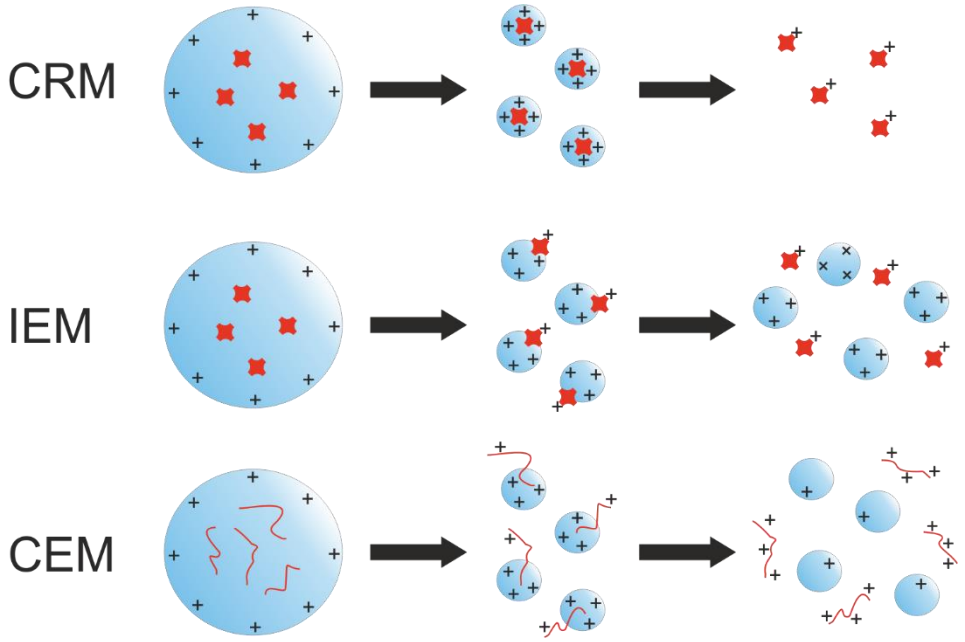

Figure 1.3 ESI ionisation mechanisms. Desolvation of ESI droplets decreases their size until reaching the Rayleigh limit, where Coulombic fission generates smaller progeny droplets. Three models explain how ions are generated from the ESI droplets: the charge residue model (CRM), the ion evaporation model (IEM) and the chain ejection model (CEM).

In the years since its development, ESI-MS technology has advanced significantly. With the development of nano-ESI (nESI), smaller capillaries (1-2 μm orifice) with lower flow rates (20 nl min^{-1}), allowed for lower sample consumption and decreased initial droplet size, aiding the desolvation process [15]. Several different variations of the ESI/nESI source have since been developed to suit a variety of specific applications including 3D imaging MS of tissue samples [16], real time analysis of human breath [17], ionisation of electrosurgical aerosols [18] and numerous others [19-22].

As a result of this unparalleled versatility, and the unique capability of ESI to maintain non-covalent interactions during ionisation - a feature particularly useful in the study of protein complexes [23] - ESI, today, is one of the most widely used ionisation sources in biological MS. Along with Koichi Tanaka for the development of soft laser desorption ionisation techniques, for his efforts in developing ESI, and providing "electrospray wings for molecular elephants", Fenn was awarded the Nobel Prize in chemistry in 2002.

1.3 Mass analysers

After ionisation, ions are separated according to their *m/z* using a mass analyser. Like most other regions of the mass spectrometer, mass analysers are kept at a constant high vacuum (low pressure) to prevent unwanted ion-molecule collisions and increase ion transmission and resolution. While all mass analysers use some combination of static or dynamic electric fields to achieve *m/z* separation, the basic difference between different analysers is the manner in which these fields are applied. There are three main features by which different mass analysers are often characterised: mass range limit (the *m/z* range over which an analyser can measure ions), scan speed (the rate at which mass spectra can be acquired) and resolution. Although different definitions have been proposed [24, 25] resolution is typically defined using Equation 1.1, where $\Delta m/z$ is either the peak width at half height for a given *m/z*, also known as its full width half maximum (FWHM) (Figure 1.4a), or the difference in *m/z*, between two peaks of equal intensity, with an overlap of <10% relative intensity between them (Figure 1.4b). It is useful to note, however, that for some mass analysers, resolution is dependent on *m/z* and thus changes across the *m/z* range.

$$R = \frac{m/z}{\Delta m/z} \tag{1.1}$$

Equation 1.1 Definition of resolution. Resolution (R) is equal to the mass to charge ratio of the ion (m/z) divided by $\Delta m/z$, which is defined as either the peak width at half height (Figure 1.4a), or the distance between two peaks of equal intensity, with 10% relative overlap (Figure 1.4b).

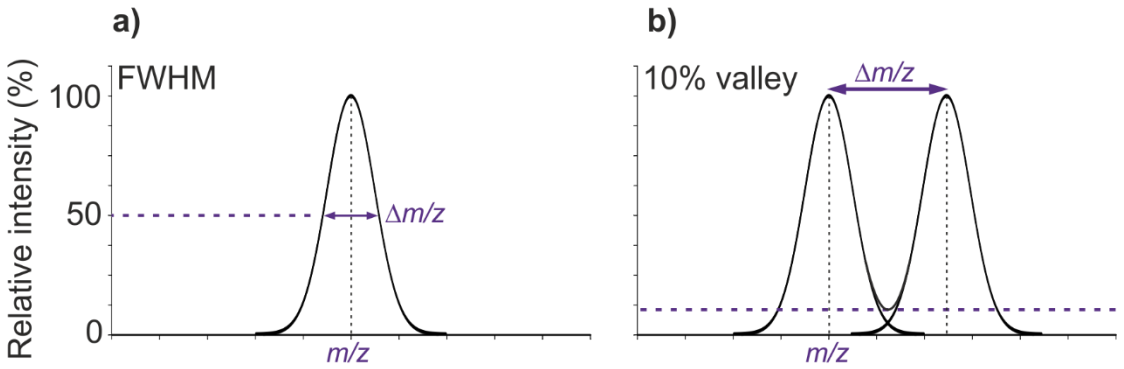

Figure 1.4 Different definitions of *m/z* resolution. **a)** Resolution defined by the peak width at half height (FWHM) and **b)** the difference in *m/z* between two peaks that overlap at 10% relative intensity.

Although an extensive review of mass analysers is beyond the scope of this thesis, certain types of mass analyser have been shown to be particularly useful in the field of biological mass spectrometry.

1.3.1 Quadrupole analysers

First described by Wolfgang Paul and co-workers in 1953 [26], a quadrupole mass analyser is a tuneable *m/z* filter, frequently used in combination with other mass analysers, where ions of different *m/z* are separated by the differential stability of their trajectories as they pass through the instrument. Ions with a stable trajectory are able to pass through the length of the quadrupole and reach the detector, where ions with unstable trajectories are filtered out. The quadrupole itself is made from two pairs of parallel metal rods arranged perpendicular to one another, where opposite direct current (DC) polarities are applied to each rod pair, such that opposite rods have the same charge, and adjacent rods have opposite charge (Figure 1.5).

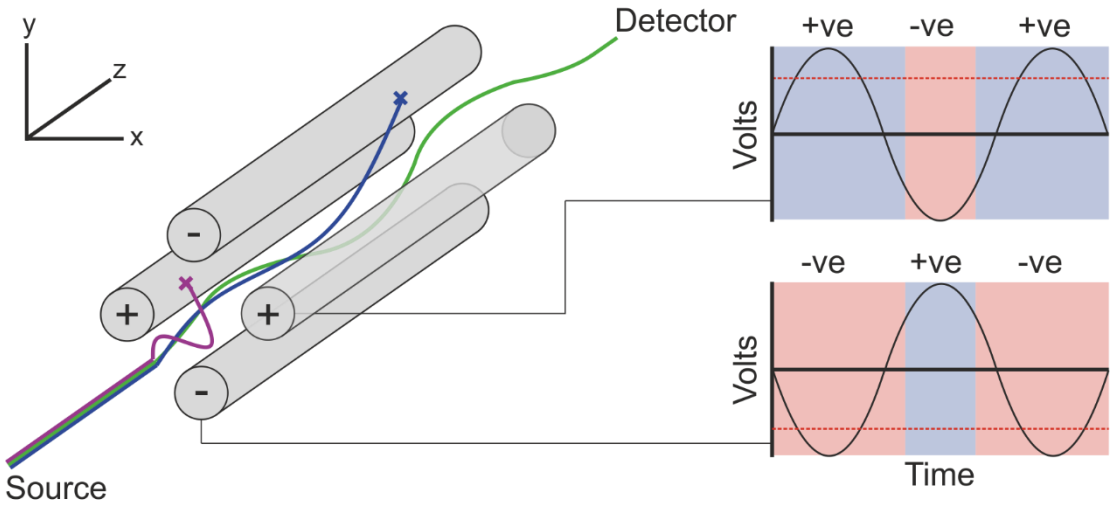

Figure 1.5 Schematic diagram of a quadrupole mass analyser. Voltages applied to each rod pair are seen on the right where DC (dashed red line) and RF-AC (solid black line) potentials are superimposed, resulting in changing rod polarities which generate spiral-like trajectories for ions passing through the analyser. Separation occurs by differential stability of these ion trajectories for a given AC and DC potential.

A radio frequency (RF) alternating current (AC), with a zero-to-peak amplitude greater than that of the applied DC voltage is also applied to the rods, such that the waveforms of adjacent rods are 180° out of phase, resulting in a dynamic potential on each rod defined by:

$$\Phi_0 = U - V\cos(2\pi v)t \qquad (1.2)$$

Equation 1.2 Dynamic potential on quadrupolar rods generated by superimposed AC and DC potentials. The potential applied to the rod (Φ_0) is a combination of the DC potential (U), and the AC potential where V is the 0-to-peak amplitude, v is the frequency and t is time.

The combined effect of these potentials is to periodically change the polarity on each rod pair simultaneously, where ions are attracted to, and then repelled by, each of the four rods, resulting in a spiral-like trajectory for ions passing through the quadrupole. It is convenient to conceptualise the quadrupole as filtering ions separately in the two lateral planes of the analyser: X-Z (left to right, and along) and Y-Z (up and down, and along). In the X-Z axis, the average polarity on the rods is positive, hence

positively charged ions will be repelled by the rods and focused into the centre of the analyser. The brief change to negative polarity in the X-Z plane will have a negligible effect on the trajectory of higher *m/z* ions, as they respond less significantly to the polarity change than to the average polarity on the rod, allowing these ions to pass through to the detector unhindered. Conversely, the trajectories of lower *m/z* ions, which respond more significantly to the polarity change, are more likely to be destabilised, and therefore less likely to reach the detector. Thus the X-Z plane of the quadrupole acts as a 'high pass *m/z* filter' allowing only high *m/z* ions to pass through to the analyser (Figure 1.6) [27, 28]. In the Y-Z axis, the average polarity on the electrodes is negative, hence positively charged ions are pulled from a stable trajectory in the centre of the analyser, towards the rods. Lower *m/z* ions, responding more significantly to the temporary change to positive polarity, are repelled back towards the centre of the analyser and are able to pass through to the detector with stable trajectories. Higher *m/z* ions, being more affected by the average polarity on the rod, have unstable trajectories in this plane, and depolarise on the rods before exiting the quadrupole. The Y-Z plane, then, acts as a 'low pass *m/z* filter' (Figure 1.6).

For an ion to be able to pass through the quadrupole and reach the detector, it must lie in the overlapped stability region between the two planes of the quadrupole, where the *m/z* of the ion is high enough to be stable in the X-Z plane, but low enough to be stable in the Y-Z plane. The main determinants of an ion's stability through the quadrupole are the frequency of the polarity changes (i.e. AC frequency – typically maintained constant) and the magnitude of the applied DC and AC voltages (U and V as per Equation 1.2) [29]. While a fixed value of U and V can be maintained to allow consistently only ions of a particular *m/z* to have stable trajectories through the analyser, maintaining a fixed *ratio* of U and V while changing their absolute values, allows the quadrupole to sequentially stabilise the trajectory of different *m/z* ions. Thus, a quadrupole can behave as a scanning mass analyser, building up a mass spectrum by rapidly ramping up the AC and DC voltages, sequentially allowing ions of different *m/z* through to the detector (Figure 1.6).

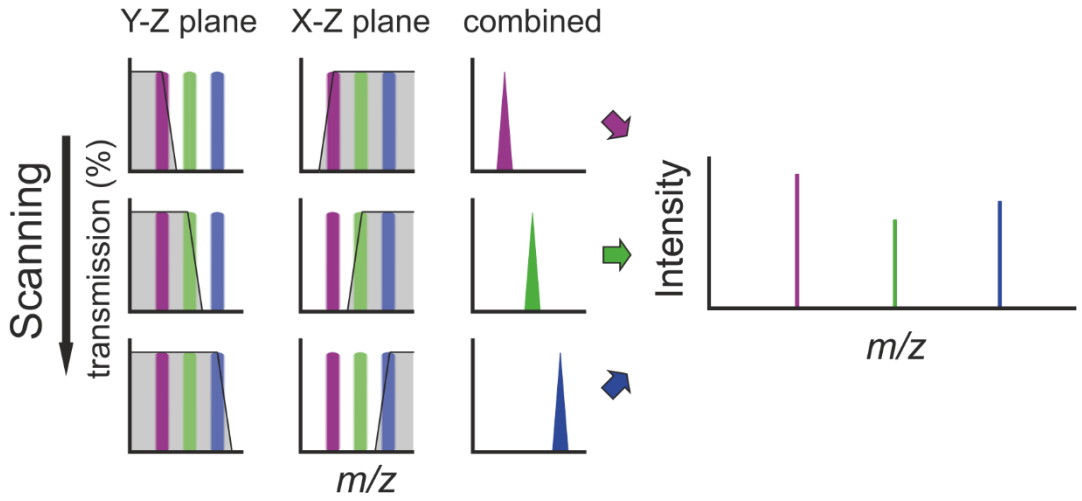

Figure 1.6 The *m/z* separation of ions in the two lateral planes of a quadrupole. The low pass *m/z* filter (Y-Z) and the high pass *m/z* filter (X-Z) work together to stabilise the trajectory of ions in the quadrupole (*m/z* values with stable trajectories in each plane are in the grey shaded area of each plot). A mass spectrum is acquired by sequentially stabilising the trajectories of different *m/z* ions by increasing U and V.

The effect of U and V on the stability of different *m/z* ions in the quadrupole can be readily visualised using stability areas calculated from a complex series of equations known as the Mathieu and Paul equations [26, 30] (Figure 1.7). The increase in DC and AC voltage necessary for scanning *m/z* analysis is visualised as the scan line in Figure 1.7, where an intersection between this line and a stability area highlights conditions at which an ion will have a stable trajectory in both planes of the quadrupole, and successfully reach the detector. The green *m/z* value in Figure 1.7, for example, at position 1 on the scan line has an *m/z* too *high* for the applied voltages to have a stable trajectory, so is stable in the X-Z plane (high pass) but unstable in the Y-Z plane (low pass). The reverse is true for this ion at position 3 on the scan line. Only at position 2, where the scan line intersects the stability region, will the green *m/z* ion have a stable trajectory through the quadrupole.

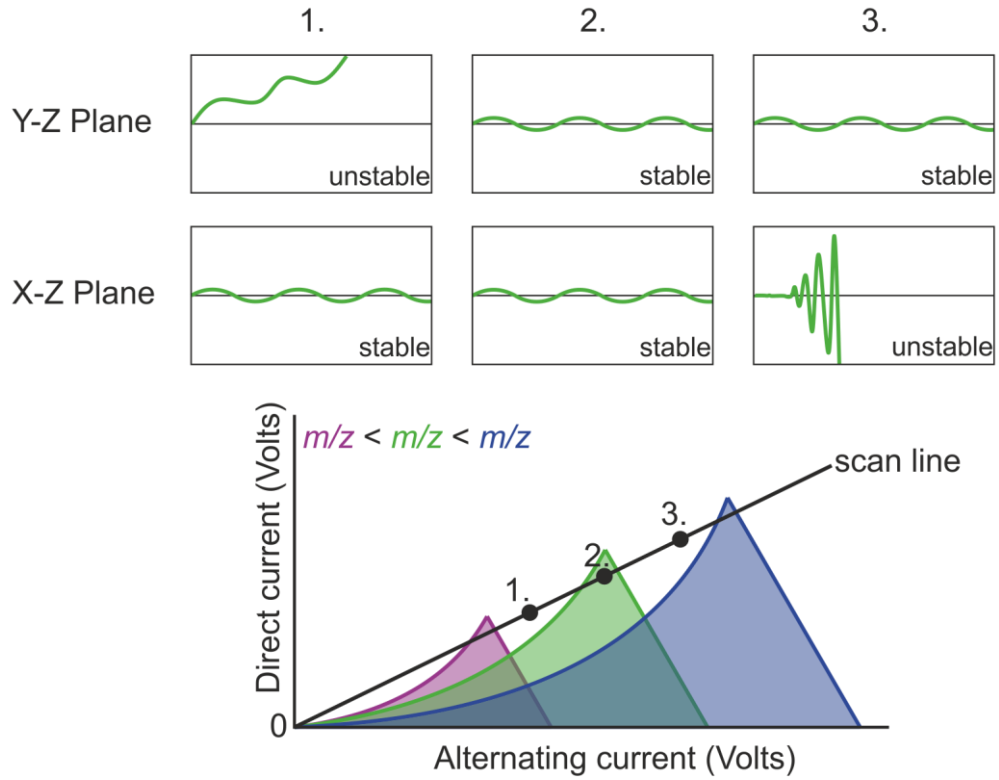

Figure 1.7 Stability diagrams for ions in a quadrupole. Each lateral plane of the quadrupole acts as an *m/z* filter, allowing either low *m/z* ions (Y-Z), or high *m/z* ions (X-Z) to pass through to the detector. The combined stability area for both lateral planes as a function of DC and AC voltage for high (blue), low (purple) and intermediate (green) *m/z* values is shown, where an ion will have a stable trajectory in the quadrupole at voltages where the scan line intersects the stability area. The stability of the green ion is shown, in each plane of the quadrupole, at U:V ratios at positions 1,2 and 3 on the scan line.

The gradient of the scan line (i.e. the ratio of U and V) determines the *m/z* resolution of the quadrupole, visually represented in Figure 1.7 as the stability area above the scan line (the smaller this area, the higher the resolution). Although the resolution can be increased by adjusting to a higher U/V ratio (steeper scan line gradient), quadrupoles are inherently low resolution mass analysers, and are usually operated at unit resolution (two peaks one *m/z* unit apart) [29]. Similarly, quadrupoles are limited in their detectable *m/z* range, which is typically no more than 3000-4000 *m/z* [29, 31], although this can be increased by lowering the frequency of the AC potential, typically at the cost of sensitivity and resolution [31]. Their advantage, however, is their fast scan speed, and the independence of ion kinetic energy and initial lateral ion

positioning on *m/z* separation, allowing ions to be continually infused into the analyser – a characteristic ideal for coupling to continuous ionisation sources such as ESI. Additionally, by removing the DC potential entirely, a quadrupole can function in RF-only mode (Y=0 in Figure 1.7), allowing a very wide range of *m/z* ions to be transmitted through the analyser simultaneously, effectively acting solely as an ion guide – a characteristic ideal for using quadrupoles in conjunction with other mass analysers.

1.3.2 Linear ion traps

Conceptually very similar to a quadrupole mass analyser, the most common variant of the linear ion trap (LIT), sometimes referred to as the 2D ion trap or Paul trap, after Wolfgang Paul, consists of four parallel rods, each of which is cut into three separate sections, usually referred to as a segmented quadrupole. A quadrupolar RF field is applied (i.e. waveforms of adjacent rods are 180° out of phase) to the centre section, confining ions in the X and Y dimensions, and DC potentials are applied to the two end sections, repelling ions back and forth axially along the trap, thus confining ions to the centre of the device in all three dimensions (Figure 1.8) [32].

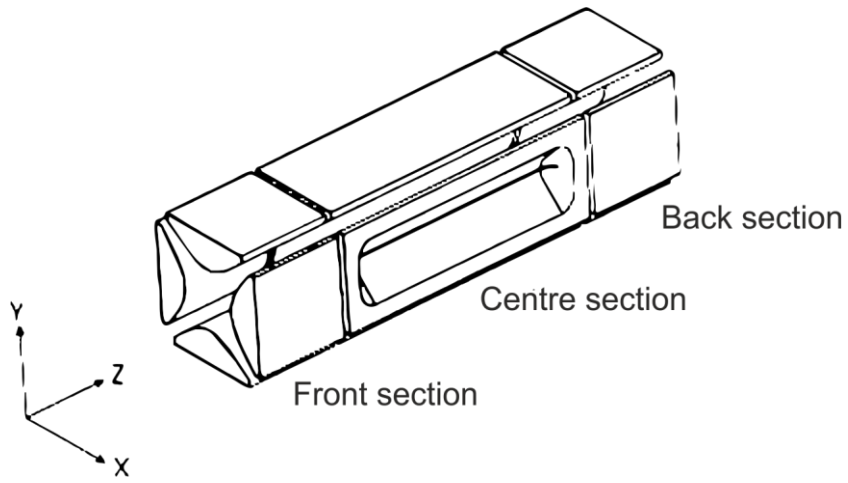

Figure 1.8 Basic design of the linear ion trap. DC confinement potentials are applied to the front and back sections of the segmented quadrupole. RF-AC quadrupolar potentials are applied to the centre section to radially confine ions. Slots are cut into the x axis centre rods for radial ion ejection.

Although, in principle, LITs can operate in a similar fashion to quadrupole mass analysers, manipulating DC and RF amplitudes in the centre section to select or scan through different *m/z* ions to generate a mass spectrum [33], the most common mode of operation for separating ions according to their *m/z* in LITs involves dipolar resonance ejection [32]. In this mode of operation, supplemental AC potentials are applied to both x axis rods, such that the waveform on each rod is out of phase by 180° [32]. When the oscillation of an ion in the trap resonates with the waveform of the AC field, it is pushed and pulled further away from the centre of the trap, with each oscillation, linearly increasing the amplitude of its oscillation until it is ejected through slots in the x axis rods, and analysed by one of two detectors – either side of the trap (Figure 1.9).

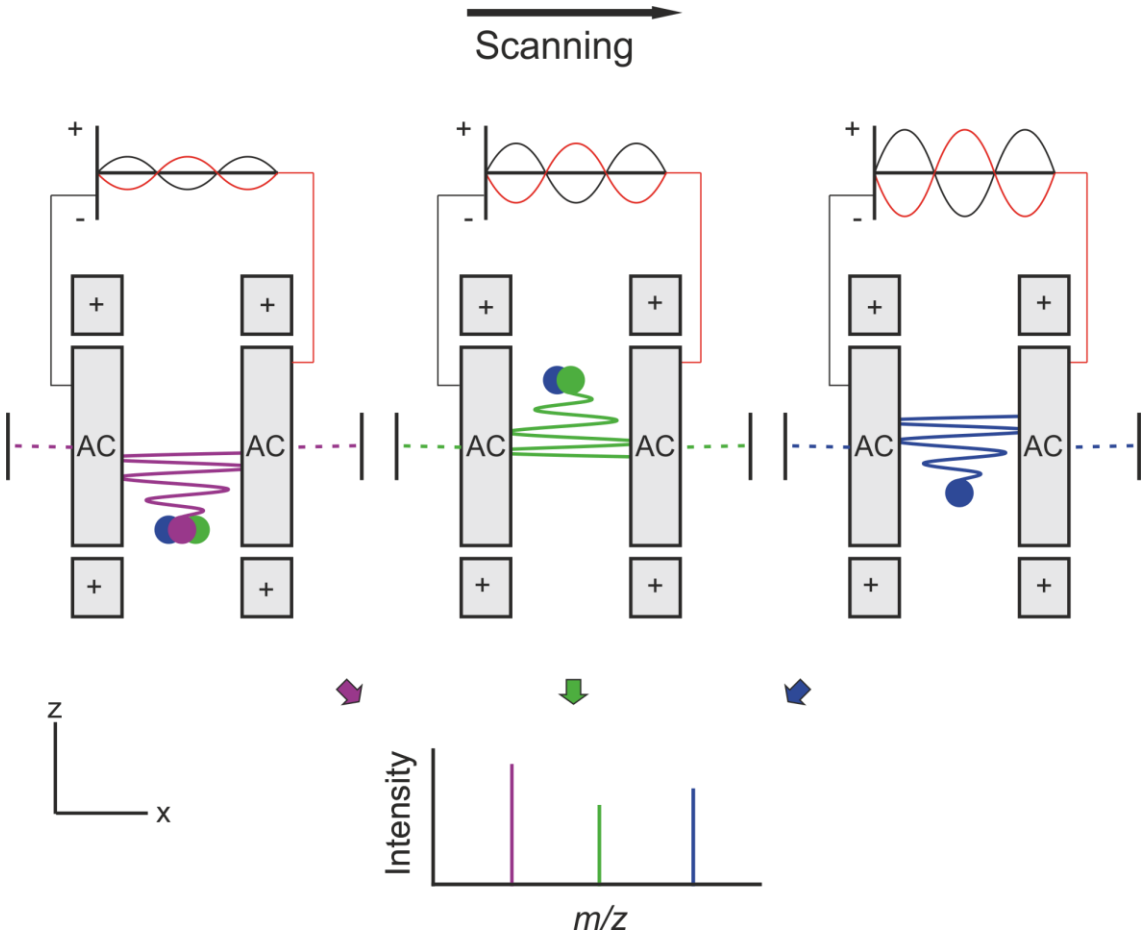

Figure 1.9 Dipolar resonance ejection in linear ion traps. Ions trapped in the centre section of the ion trap are subjected to supplemental AC fields, the amplitude of which is ramped to sequentially eject ions of increasing *m/z*. Ions are ejected through slots in the x axis rods to detectors either side of the trap.

The resonance frequency of an ion is positively correlated with *m/z*, but is similarly correlated with the applied AC amplitude. Thus, by maintaining a high, fixed AC frequency and ramping the AC amplitude, the resonance frequency for all ions in the trap is increased, until ions of increasing *m/z* sequentially reach a resonance frequency matching the AC waveform and are ejected from the trap, thus achieving *m/z* separation (Figure 1.10) [29, 33].

While LITs are often used as standalone mass analysers, with scan speeds and resolutions similar to quadrupole mass analysers [33], in many commercial mass spectrometers, LITs are also used as ion storage devices and collision cells, before *m/z* separation is achieved by other means [34]. Indeed, fragmentation of trapped ions can

be readily achieved by filling the device with a collision gas, and exciting ions to elevated energies, below the energy required for resonance ejection [33]. This versatility, coupled with the ability to eject ions both axially, and laterally after storage or fragmentation, makes the 2D ion trap a valuable multi-use component in many commercial instruments [34]. Indeed, the RF ion confinement technology that underpins both the quadrupole and the LIT, as well as other mass analysers such as the 3D ion trap, is now widely considered to be an essential tool in MS instruments for a wide variety of applications. For his work in the development of the ion trap technique, Paul was awarded the Nobel Prize in physics in 1989.

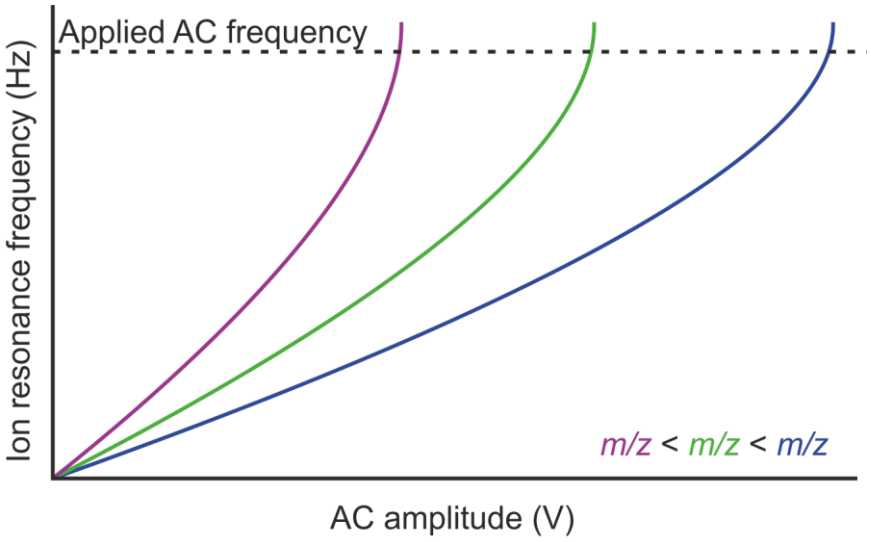

Figure 1.10 The relationship between dipolar resonance ejection frequency and applied AC amplitude. Increasing AC amplitude increases the resonance frequency for ions in the trap, until the resonance frequency of increasing *m/z* ions approaches the AC waveform frequency, and ions are ejected from the trap.

1.3.3 Time-of-flight (ToF) analysers

Initially proposed by Stephens in 1946 [35], then later developed by Cameron and Eggers in 1948 [36], a time-of-flight (ToF) mass spectrometer, or 'Velocitron' as Cameron and Eggers called it, separates ions of different *m/z* according to their flight time through a high vacuum, field free region of the instrument called a flight tube

(Figure 1.11). The aptly named "pusher" voltage provides the initial kinetic energy needed to accelerate ions through the flight tube towards the detector, where the relationship between the applied pusher voltage and ion kinetic energy is defined as:

$$\frac{1}{2}m\left(\frac{L}{t}\right)^2 = zeV \tag{1.3}$$

Equation 1.3 The relationship between potential and kinetic energy for ions accelerated in ToF-MS. Potential energy, given by zeV (where z is the number of charges on the ion, e is the elementary charge on an electron and V is the pusher voltage), is converted into kinetic energy, where m is the ion mass, L is the length of the flight tube, and t is the flight time.

Rearranging this formula, we can show that the time taken for an ion to traverse the flight tube, for a given acceleration voltage, is proportional to the square root of its *m/z*.

$$t^2 = \frac{m}{z}\left(\frac{L}{2eV}^2\right) \xrightarrow{yields} t \propto \sqrt{\frac{m}{z}} \tag{1.4}$$

Equation 1.4 The relationship between flight time and *m/z* for ions accelerated in ToF-MS. All terms inside the brackets are constant, therefore, flight time is shown to be proportional to the square root of the *m/z*.

Thus, ions of different *m/z* have different flight times within the instrument, and reach the detector at different times. This also demonstrates a positive correlation between *m/z* and flight time, where higher *m/z* ions take longer to traverse the flight tube. As there is, *in principle*, no limit to how long an ion can take to reach the detector, ToF-MS has a particularly high detectable mass range, making this type of mass analyser ideally suited to the study of large biomolecules. Indeed, conventional ToF-MS instruments have been used to study intact bacteriophage capsids up to 18 MDa [37]. Similarly, as flight tubes are classically no more than 1-2 m in length (to maintain sensitivity), flight times are typically on the order of μs, meaning ToF-MS

instruments are also capable of fast scanning speeds, usually acquiring multiple scans in order to build up a mass spectrum.

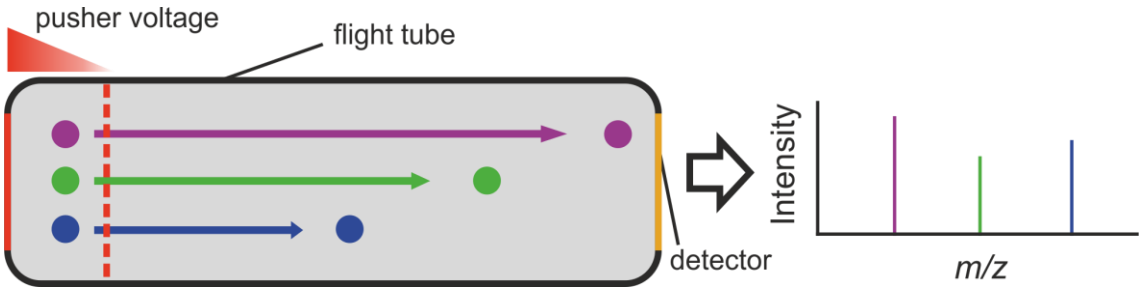

Figure 1.11 *m/z* separation by time-of-flight mass spectrometry (ToF-MS). An acceleration voltage pushes ions through a field free flight tube under high vacuum. Ions of different *m/z* are accelerated to different velocities such that ions of lower *m/z* reach the detector first.

However, unlike quadrupole or LIT mass analysers, ToF-MS is a pulsed analysis technique, requiring ions to start from approximately the same position relative to the pusher voltage, in order to ensure a minimal kinetic energy distribution is delivered to ions of the same *m/z*. Spatial distribution of ions in the pusher region results in uneven exposure to the acceleration voltage, where some ions of the same *m/z* receive a greater accelerative force towards the detector than others. The result is that ions with the same *m/z* reach the detector at slightly different times, broadening the resulting *m/z* peaks and lowering instrument resolution. This complicates the effective coupling of ToF-MS to continuous ionisation sources, such as ESI, as a continuous stream of ions directed towards the detector would generate a large spatial distribution of ions in the ToF direction. This problem was addressed by Dawson and Guilhaus in 1989, with the development of orthogonal acceleration ToF-MS [38].

1.3.3.1 Orthogonal acceleration Time-of-flight (oa-ToF)

In orthogonally accelerated ToF instruments, the ion beam from the ionisation source is orientated orthogonally to the direction of the ToF *m/z* separation. Ions generated

in the source are allowed to accumulate in the pusher region before the acceleration voltage is applied to direct ions towards the detector (Figure 1.12). Successive 'pushes' from the acceleration voltage allow a continuous stream of ions to be effectively analysed by pulsed ToF separation, and permits continuous ionisation sources, such as ESI, to be effectively coupled to ToF mass analysers. With this orientation, ions are not initially travelling in the direction of the detector, minimising their spatial and velocity distributions in the ToF direction, thus also minimising kinetic energy dispersion of ions of the same *m/z*. While this has a favourable effect on instrument resolution, *some* variations in kinetic energy will remain. It is therefore useful to minimise this distribution further by other methods.

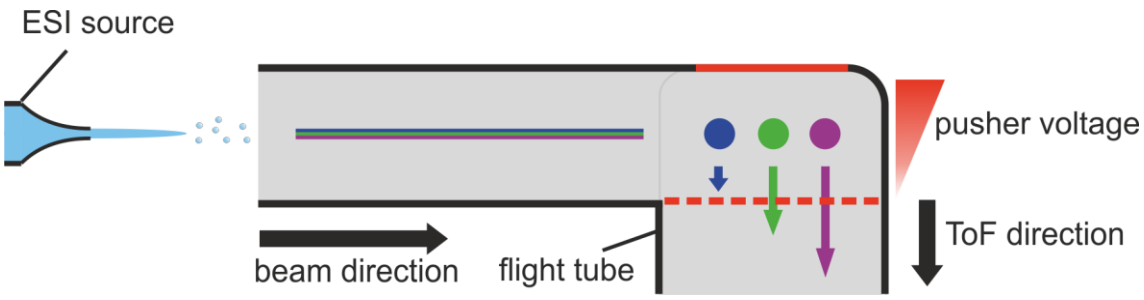

Figure 1.12 Schematic diagram of an orthogonal acceleration time-of-flight mass spectrometer (oa-ToF). The beam of ions from the source region is accelerated orthogonally towards the detector, allowing effective coupling to continuous ionisation sources.

1.3.3.2 Reflectrons

A reflectron, or electrostatic reflector, is an ion mirror device developed by Mamyrin and colleagues in the 1970's, used to further minimise differences in the flight time of ions of the same *m/z* in ToF mass analysers [39]. Ions directed into the reflectron by the pusher acceleration voltage are reflected ~180° back towards the detector by the increasing electric field gradient of the device. Ions with higher kinetic energy penetrate more deeply into the reflectron before changing trajectory, effectively lengthening their flight path relative to those of lower kinetic energy. This has the effect of normalising the overall flight time of ions of the same *m/z* with different

velocities, increasing the resolution of the instrument (typical commercial ToF-MS instruments equipped with reflectrons can attain resolutions of ~20,000 at *m/z* 400 [40]). Usually, ToF mass analysers with reflectrons are operated in 'V-mode' where ions are passed through a single reflectron device before reaching the detector (Figure 1.13). However, many modern ToF instruments are equipped with multiple reflectron devices and can operate in 'W-mode', where ions are passed through two reflectrons, further increasing resolution at the cost of sensitivity.

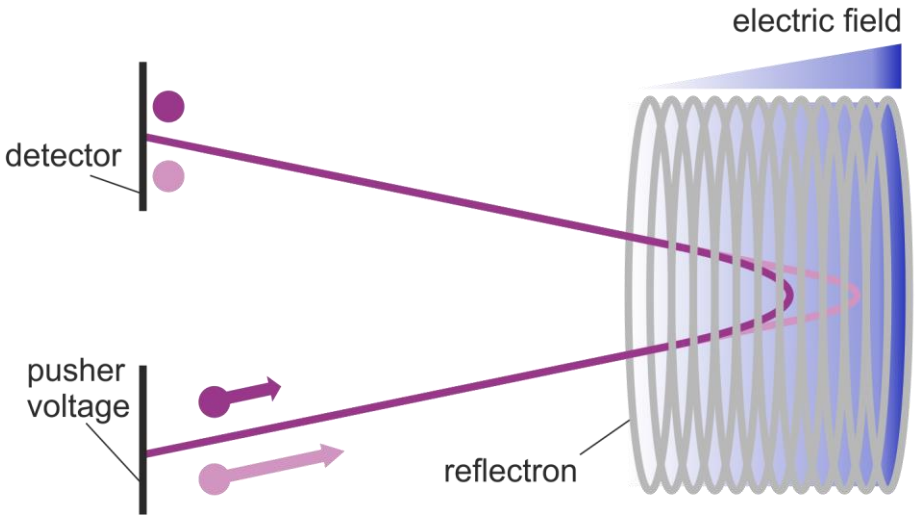

Figure 1.13 Schematic diagram of an electrostatic reflector. Ions of the same *m/z* with higher kinetic energies (pink) penetrate further into the reflectron than those with lower kinetic energy (purple). The resulting longer flight path for higher kinetic energy ions normalises their flight time with lower energy ions allowing them to reach the detector simultaneously.

1.3.4 Orbital trapping analysers

Orbitral ion traps work by holding ions in stable orbits around a central electrode. The simplest and earliest example of an orbital ion trap is the Kingdon trap, developed by K.H Kingdon in 1923 (Figure 1.14) [41]. In a Kingdon trap, a DC voltage is applied to a length of wire running lengthwise at the centre of an outer cylindrical electrode. When injected orthogonally into the trap, the logarithmic electric field generated by the DC voltage on the wire is able to trap ions with appropriate initial conditions (i.e. kinetic energy, starting position) in stable orbits around the central electrode, until

collisions with residual gas molecules in the trap cause ions to collide with the wire. DC voltages are applied to flat, end cap electrodes at either end of the cylinder to trap ions laterally. However, as ions in a Kingdon trap are free to move both around, and along the central electrode, no *m/z* separation of ions can occur. As such, Kingdon traps can only function as orbital trapping devices, rather than mass analysers.

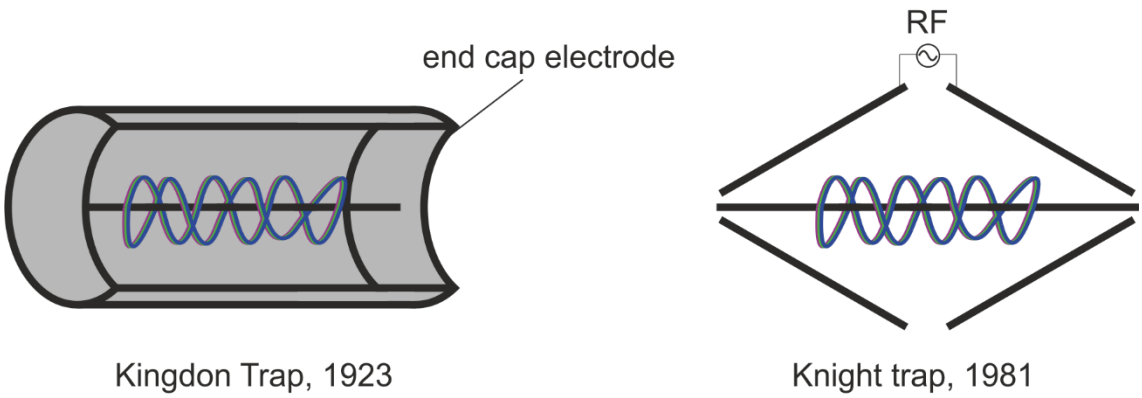

Figure 1.14 The Kingdon trap and the Knight trap: early orbital ion traps. Ions are kept in stable orbits around a central electrode and are contained axially by either end cap electrodes (Kingdon trap) or by a quadrupolar field (Knight trap).

An important step forward in the use of orbital ion traps for *m/z* separation of ions was the development of the Knight trap in 1981 (Figure 1.14) [42]. Like Kingdon's device, ions in a Knight trap form stable orbits around a central wire from which an applied DC potential generates a logarithmic electric field. However, this configuration differs from the Kingdon trap in that the outer cylinder is replaced by a split electrode, where an RF-AC potential is applied to generate a quadrupolar electric field. Together, the inner and outer electrodes produce a combined quadrupolar and logarithmic field, or quadro-logarithmic field, directing ions to oscillate back and forth along the axis of the central wire, whilst maintaining stable orbits around the wire. In *principle*, the effect of this field should induce harmonic oscillations of ions, such that ions of different *m/z* oscillate along the central electrode at different frequencies, thus achieving *m/z* separation. In *practice*, Knight noted that

the resonance frequencies observed for ions trapped in this manner were broad, shifted and weak when compared to what theory would suggest [42]. He proposed that interference between the DC potential on the central wire, and the RF potential on the outer electrodes, creates a non-ideal quadro-logarithmic field, disturbing the harmonic oscillation of ions and detrimentally effecting *m/z* separation [42]. His suspicions were confirmed in 1996, where calculations by Gillig, Bluhm and Russell showed that in order to achieve purely harmonic oscillations of ions along the central electrode, and thus achieve useful *m/z* separation in an orbital ion trap, the central electrode and trapping volume must have spindle-like geometries [43].

1.3.4.1 Orbitrap mass analysers

The orbitrap, developed in 2000 by Alexander Makarov [44], is an orbital ion trap device approximating the 'ideal Kingdon trap', where a DC potential applied to a central, spindle-shaped electrode, provides the quadro-logarithmic field necessary for *m/z* separation [44] (Figure 1.15). Unlike the Knight trap, where ions are 'pushed' back and forth along the central electrode by the quadrupolar field applied to the outer electrodes, the unique field generated by the central electrode of the orbitrap is such that ions are 'pulled' towards the equator of the spindle (r in Figure 1.15) and can undergo harmonic oscillations along the z axis without the need for an applied field on the outer electrodes - typically held at virtual ground potential in orbitrap mass analysers [44].

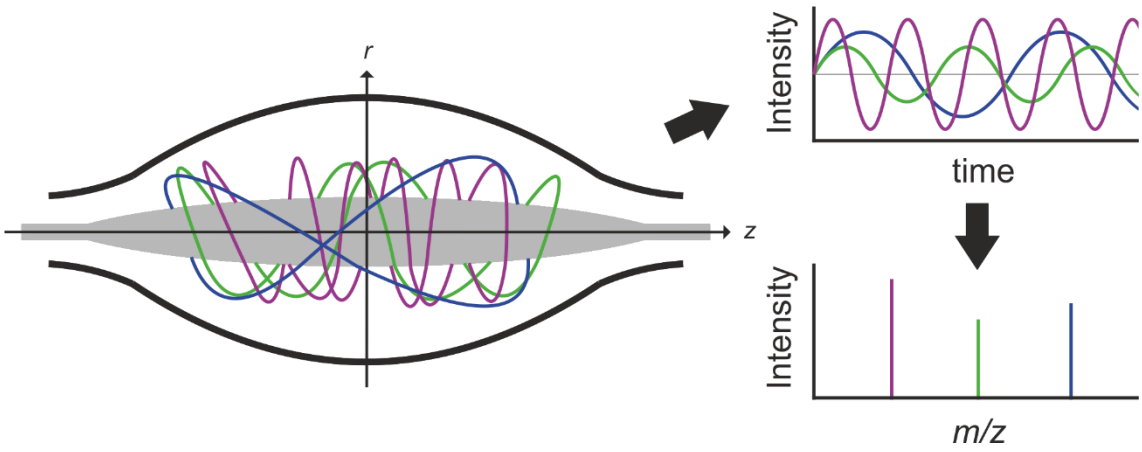

Figure 1.15 The orbitrap mass analyser: an 'ideal' Kingdon trap. Ions injected into the trap undergo harmonic oscillations in the z axis, where the oscillation frequency is proportional to the *m/z* of the ion. Analysis of the different frequencies and intensities produced by each different *m/z* ion is used to generate a mass spectrum.

Upon injection into the orbitrap, as with both Knight and Kingdon's devices, ions rapidly form stable orbits around the centre electrode. The frequency of these radial orbits is dependent on the kinetic energy of the ion, as well as other factors such as initial ion position [44]. As such, upon injection of an ion packet into the orbitrap, ion orbits in the radial dimension rapidly go out of phase, as ions with more initial kinetic energy orbit with a higher frequency than those with lower initial kinetic energies. Typically, ions are injected into the orbitrap tangentially at one end of the central electrode, a so called 'excitation by injection' method [44], to ensure ions are drawn immediately towards the equator of the spindle, and begin to oscillate along the z axis without any additional energy input (Figure 1.16) [44]. If the dimensions of the injected ion packet are small enough, radial de-phasing, coupled with the tangential off-equator ion injection, causes ions of the same *m/z* to form 'rings' around the centre electrode, where each ring oscillates back and forth along the spindle with a frequency inversely proportional to its *m/z* (Figure 1.16, Equation 1.5). The different oscillation frequencies observed can then be used to generate a mass spectrum.

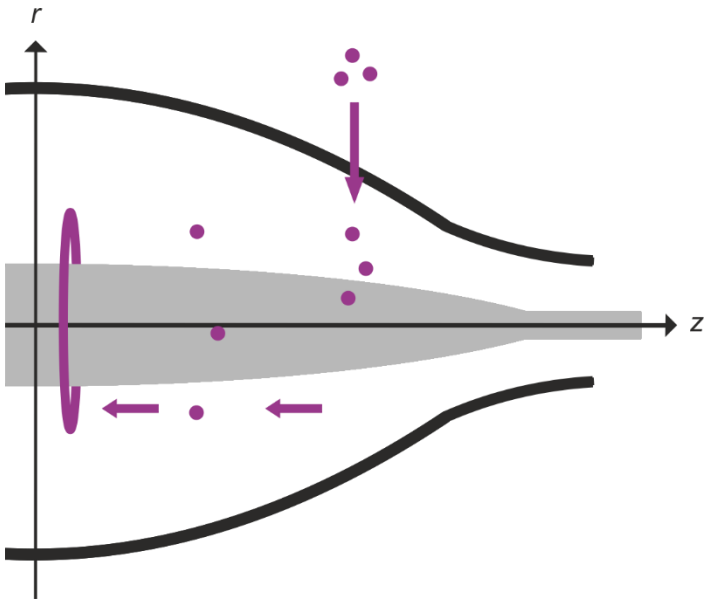

Figure 1.16 Excitation by injection, and radial de-phasing of ions in an orbitrap. Ions are injected tangentially at one end of the electrode, to initiate z axis oscillations. Differences in the initial kinetic energy and position of ions cause rapid de-phasing of ion orbits in the radial dimension. Together, these properties cause ions of the same *m/z* to form a 'ring' of ions orbiting the centre electrode, which oscillates back and forth at a frequency proportional to *m/z*.

Crucially, the relationship between oscillation frequency and *m/z* shown in Equation 1.5 also demonstrates that, unlike the frequency of the radial ion orbits, z axis oscillation frequency is independent of ion kinetic energy, and only dependent on the *m/z* of the ion and the properties of the static electric field in the trapping volume.

$$2\pi v = \sqrt{\frac{k}{m/z}} \tag{1.5}$$

Equation 1.5 The relationship between z axis oscillation frequency and *m/z* in an orbitrap mass analyser. Where *v* is the oscillation frequency, *m/z* is the mass to charge ratio of an ion and *k* is the field curvature.

As a reliable measurement of oscillation frequency, and thus the *m/z* of an ion, requires multiple oscillations along the centre electrode to occur, the scanning speed of orbitraps is significantly slower than quadrupole, LIT, or ToF mass analysers, typically on the order of 10 Hz [45], where scan times are longer if higher resolution

measurements are required. Similarly, unlike quadrupoles where resolution is largely independent of *m/z*, the resolution of orbitrap mass analysers decreases as a function of $(m/z)^{0.5}$ [46]. Nevertheless, orbitrap mass analysers are, due to the unique ion motions around the central electrode, inherently high resolution instruments, where continued development has thus far enabled orbitraps to achieve up to 1,000,000 resolution (FWHM) at *m/z* 200 [47]. Similar to ToF instruments, orbitrap mass analysers require pulses of ion packets for analysis, and as such are often coupled to continuous ionisation sources via a curved linear ion trap, usually called the C-trap. The purpose of this is twofold: to accumulate and store ions from the ionisation source, cooling them with collisions with gas molecules, and to rapidly (100-200 ns) inject ion packets into the orbitrap with minimal spatial and temporal spread [48], crucial for maintaining the coherence of the harmonic oscillations of ions. This linear ion trap, rather than the orbitrap itself, is often the limiting factor in the detectable mass range limit [29]. However, recent advances in instrument technology upstream of the mass analyser, have enabled orbitrap instruments to study high molecular weight intact protein complexes up to several MDa [49].

1.4 Ion Detectors

Ion detection is the final fundamental component in a mass spectrometer. Far from the photographic plates used as detectors by Thomson and Aston in the early 20th century, today, the purpose of an ion detector in mass spectrometry is to produce a signal from the separated ions, which can interpreted by a computer in order to generate a mass spectrum.

1.4.1 Electron multipliers

One of the most commonly used detector systems in modern mass spectrometers is the electron multiplier. In this type of detector, ions collide with a conversion dynode, causing the emission of secondary particles, including electrons. This sets off a cascade

effect, where electrons are further amplified, generating a current which can then be detected by a computer. For ToF instruments, the microchannel plate detector (Figure 1.17), a type of continuous dynode electron multiplier, is the favoured detector system due its fast response time – a characteristic useful for a mass analyser where narrow pulse width and precise time measurements are critical.

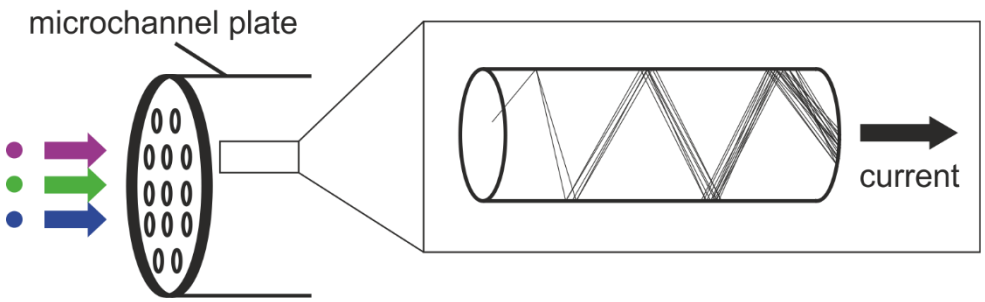

Figure 1.17 Schematic diagram of a microchannel plate continuous dynode electron multiplier. Ions striking the detector set off a cascade of electrons which generate a current detected by a computer.

1.4.2 Image current detection

Clearly, for some mass analysers such as orbitraps, the path of the ion must remain undisturbed in order to measure its *m/z*. For this type of separation, a non-destructive method of ion detection is required. In image current detection, the presence of ions is detected by the induced current produced on metal surfaces as the ions approach. The magnitude of the induced current is proportional to distance, so as ions move closer to the surface, the induced current increases. In orbitrap mass analysers, the outer electrodes function as the image current detector surfaces, where the detected waveform of induced current is used to determine the *m/z* of the ion (Figure 1.18). Typically for orbitrap mass analysers, a short delay after ion injection into the trap is allowed before image current detection begins. This allows time for ions to radially de-phase and form orbital rings around the electrode, reducing the presence of interfering harmonic signals from in-phase radial oscillations [44]. Overlapping and interfering image current signals generated from multiple different *m/z* ions in the

trap are then processed by fast Fourier transform algorithms to generate a mass spectrum [50].

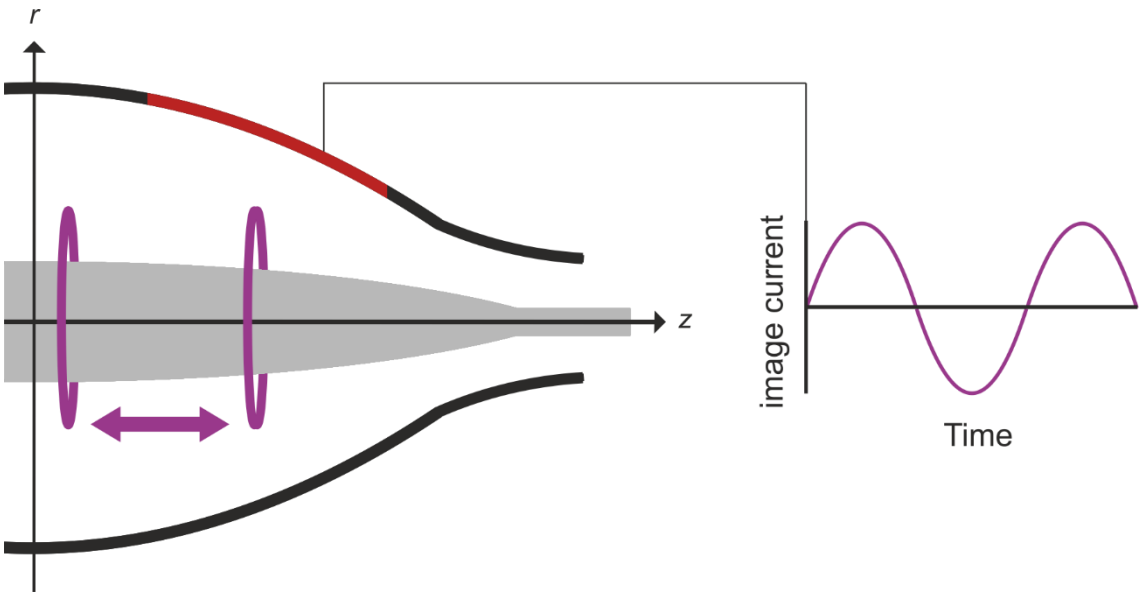

Figure 1.18 Image current detection in orbitrap mass analysers. The induced current on the outer electrodes of the orbitrap oscillates with the z axis oscillation of ions along the spindle electrode. The oscillation of this signal is then used to determine the *m/z* of the detected ion.

1.5 Analysis of mass spectrometry data

Once a mass spectrum (i.e. *m/z* vs intensity) has been generated, the mass can then be determined, for positively charged ions, using Equation 1.6. However, this equation demonstrates that, before the mass can be calculated, the number of charges on the analyte (n), also known as the charge state, must be determined.

$$Mass = {}^{m}/_{z} - 1.0072n \qquad (1.6)$$

Equation 1.6 Calculating mass from a mass spectrum. The mass, for positively charged ions, is equal to *m/z* multiplied by the charge state (n), where the mass of the additional protons is subtracted. Mass of a proton = 1.0072 Da.

For analysis of biomolecules ionised by ESI, where a distribution of different charge states is often observed, n for a given charge state is typically determined in one of two ways. If the resolution is sufficient to observe the naturally abundant isotopes of ^{13}C, then the mass difference between two adjacent isotopic peaks will be approximately 1 Da, due to the additional neutron in the atomic nuclei of carbon. The charge state, then, is equal to the reciprocal of the difference in *m/z* between two adjacent peaks in the isotope distribution (Figure 1.19a).

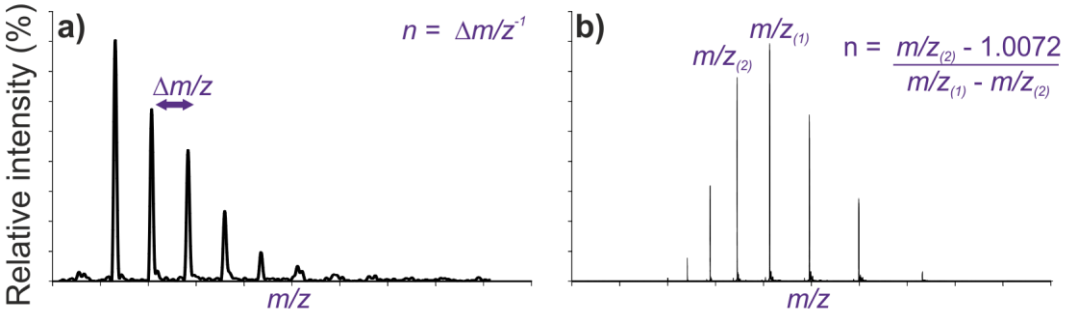

Figure 1.19 Determination of charge states in a mass spectrum. **a)** Example peptide isotope distribution. With isotopic resolution, the charge state can be determined from the natural abundance of ^{13}C, where the mass difference between two adjacent peaks is known. **b)** Example protein charge state distribution. Without isotopic resolution, the charge state of a peak can be determined from the charge state distribution using a set of simultaneous equations (Equation 1.7).

For larger species, where ^{13}C isotopes are less easily resolved, the charge state can be determined using adjacent peaks in the charge state distribution. Knowing that n must be an integer, and that adjacent peaks in the charge state distribution must be either n+1 (lower *m/z*) or n-1 (higher *m/z*), n can be calculated for a given *m/z* peak using a set of simultaneous equations (Equation 1.7, Figure 1.19b). As isotopes are typically not resolved in these spectra, the mass calculated is the average mass, rather than the monoisotopic mass.

$$Mass = {}^{m}/_{z_{(1)}}\, n - 1.0072n = {}^{m}/_{z_{(2)}}\, (n+1) - 1.0072(n+1) \qquad (1.7)$$

Equation 1.7 Determination of charge states in non-isotopically resolved mass spectra. Adjacent peaks in a charge state distribution have a different number of charges but are ionised from the same molecule, and have the same mass, after correcting for the different number of additional protons. This can be used to calculate n for a given peak and, subsequently, to calculate mass.

1.5.1 Mass error and mass accuracy

Mass accuracy is typically quoted in parts per million (ppm) and is a measure of how close the calculated mass is to the theoretical mass of the molecule (Equation 1.8) [51].

$$Mass\ accuracy = \frac{Theoretical\ mass - Observed\ mass}{Theoretical\ mass} \times 10^6 \qquad (1.8)$$

Equation 1.8 The definition of mass accuracy. Measured in ppm, mass accuracy is a measure of how close the calculated mass is to the theoretical mass of the molecule being studied.

1.6 Tandem mass spectrometry (MS/MS)

For many applications in mass spectrometry, such as experiments where fragmentation of specific ions is required, one stage of mass analysis is not enough. For this reason, many modern mass spectrometers are equipped with multiple mass analysers, frequently separated by collision cells for ion fragmentation, enabling *m/z* separation to be performed in tandem, usually referred to as MS/MS. While the use of multiple mass analysers allows a variety of different MS/MS workflows, a commonly used workflow in biological mass spectrometry, particularly for the structural analysis of proteins, is the product ion scan (Figure 1.20).

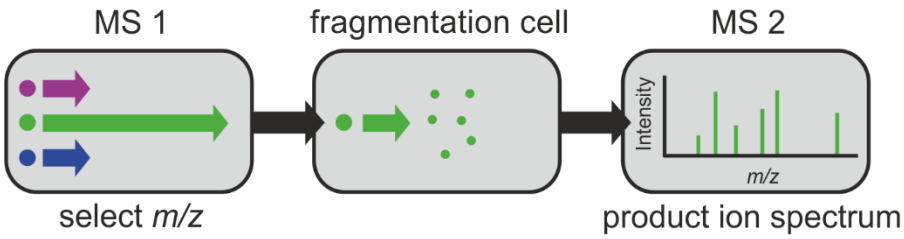

Figure 1.20 The workflow of a product ion scan. Ions are selected in the first mass analyser (usually a quadrupole) which are then fragmented in the collision cell. A second mass analyser separates the product ions produced from the fragmented precursor ion.

In a product ion scan, the first mass analyser, usually a quadrupole, selects ions of a particular *m/z* to pass through to the fragmentation cell. The selected ion is then fragmented, and the product ions resulting from the fragmentation are then examined by the second mass analyser.

1.6.1.1 Fragmentation methods

A variety of different fragmentation methods are available for MS/MS experiments, each of which causes different fragmentation properties of biological molecules, discussed later in Section 2.4.2. One of the most commonly used methods of ion fragmentation in biological mass spectrometry is collision induced dissociation (CID) [52]. In CID, a collision gas, typically argon, nitrogen or helium, is introduced into the fragmentation cell, where ions suffer collisions with the gas molecules effectively 'heating' the ions by transferring kinetic energy into internal energy. CID is a slow, or ergodic, fragmentation technique where the added internal energy is redistributed throughout the molecule and breaks the weakest bonds first, usually non-covalent interactions, before breaking the weakest covalent bonds. An alternative, but similar, method of fragmentation is higher energy C-trap dissociation (HCD), characterised by the rapid injection of ions into a gas filled region of the instrument where, similar to CID, collisions with the buffer gas cause the ions to fragment. However, HCD typically generates fragment ions faster than CID which often uses a slower resonance excitation method to initiate buffer gas collisions and fragmentation [53]. The

terminology behind these two fragmentation techniques, however, is often confusing, where HCD on some instrument geometries is often more similar to CID in others (i.e. HCD on the Thermo Q Exactive is more similar to CID on the Waters Synapt instruments, discussed later in section 1.10).

Alternatively, fast acting fragmentation techniques such as electron capture dissociation and electron transfer dissociation (ECD and ETD respectively), use the addition of low energy electrons, either by use of electron emitters (ECD) or anionic gas phase reagents (ETD) to fragment ions. Although less common than either CID or HCD, fragmentation techniques such as ETD or ECD are useful for applications where the maintenance of non-covalent interactions is prioritised, or to get complementary or additional fragmentation data. The utility of various fragmentation methods for experiments in structural mass spectrometry is discussed later in Section 2.4.2.

1.7 Liquid chromatography – mass spectrometry (LC-MS)

The analysis of biological samples by mass spectrometry is often complicated by the complexity of the sample, where many different species occupying a single mass spectrum can make data analysis significantly more challenging. Liquid chromatography (LC) is a separation technique often used prior to ionisation and MS analysis, where the aqueous sample is passed through an analytical column which separates the components of the solution by certain physical properties (size/charge etc…) depending on the type of LC employed (Figure 1.21).

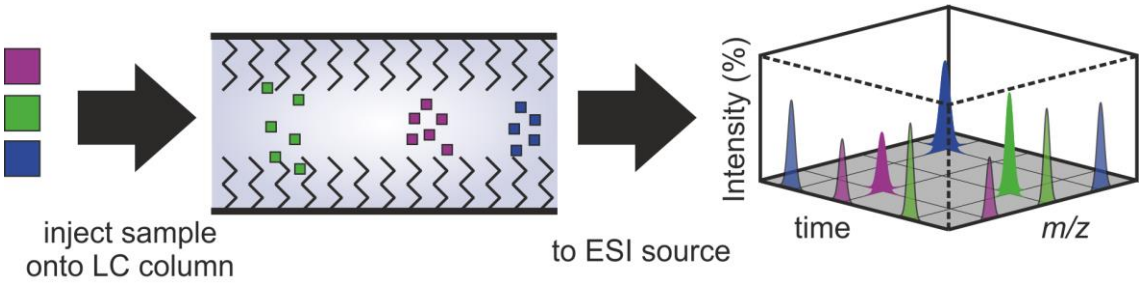

Figure 1.21 Separating and analysing complex mixtures by liquid chromatography-mass spectrometry (LC-MS). The sample is injected into an analytical column, which separates components of the solution by a set a physical properties such as size, charge or polarity. Following separation and elution from the column, the separated components are ionised by ESI and analysed by MS.

The most common form of liquid chromatography employed in biological mass spectrometry is reverse-phase LC (RP-LC), which separates molecules according to their polarity [54]. Generally, the inner surface of the analytical column is coated with silica bound alkyl chains of varying lengths, although for analysis of biological samples, an 18 carbon length alkyl chain, frequently short-handed to "C18", is the most commonly used. As alkyl chains are highly non-polar (hydrophobic), any non-polar (or hydrophobic) components of the injected sample will interact with the inner surface of the column to a greater extent than the more polar, or hydrophilic, molecules in the solution. Thus, the most polar compounds in the sample have the shortest retention time on the column and elute first, where the least polar compounds have the longest retention time and elute later. Typically, the least polar molecules are eluted from the column by gradually making the solvent less polar, weakening their interaction with the column surface. This is usually achieved by increasing the concentration of non-polar solvents in the solution, such as acetonitrile (MeCN) [54]. Advances in LC separation technology led to the development of high-performance LC (HPLC) and later ultra-performance LC (UPLC) – systems that operate at higher pressure and offer increased speed and resolution [55]. Usefully, many of these LC systems have been developed to operate using solution conditions and flow rates compatible with ESI sources, so they can be effectively coupled directly to a mass spectrometer [55].

1.8 LC-MS/MS data acquisition methods

As discussed earlier in Section 1.6, tandem mass spectrometry experiments are useful for acquiring fragment ion spectra of the ion of interest which, for biomolecules, is typically used for peptide sequencing, discussed later in Section 2.4.2. When continually infusing a pure analyte into the mass spectrometer, the intact and fragment ion spectra can be easily acquired separately by activating and deactivating fragmentation in the collision cell, to obtain both the intact mass measurement, and the fragment ion spectra necessary to analyse the sample. However, when LC is used to separate complex mixtures prior to MS analysis, the ion is only introduced into the mass spectrometer for the brief period that it elutes off the LC column, making rapid acquisition of both the intact, and the fragment ion spectra for each molecule challenging. To tackle this issue, instrument methods have been developed to allow rapid automated switching between high and low energies in the collision cell, allowing acquisition of both MS, and tandem MS data of ions as they are introduced into the mass spectrometer from online LC separation. Generally, there are two main acquisition modes that achieve this: data dependent, and data independent, acquisition.

1.8.1 Data dependent acquisition (DDA)

In data dependent acquisition modes (DDA), the spectra for intact molecular ions are first acquired by deactivating the fragmentation, and allowing a full *m/z* scan of all ions eluting from the LC column at that time. A user-defined number of the most intense *m/z* ions from the initial scan, sometimes called the MS1 or precursor ion scan, are then sequentially selected by the first mass analyser for fragmentation and spectral analysis by the second mass analyser. When complete, another full *m/z* scan is acquired at the new, now longer, LC retention time, and the cycle is repeated for as long as the LC elution takes place (Figure 1.22). Typically, a dynamic exclusion time

is applied such that the same *m/z* value is not repeatedly selected if it remains at high intensity after the DDA cycle finishes. This is to prevent continual fragmentation of the same ions, and to more effectively utilise the available MS/MS time to fragment ions of different *m/z*.

However, DDA modes for LC-MS/MS present a trade-off between the speed, and depth of the analysis. Whilst sequentially selecting and fragmenting ions, full scan intact MS data cannot usually be acquired, thus some ions eluting from the LC column may be missed if the DDA cycle takes too long. Conversely, making the cycle shorter by reducing the number of different *m/z* ions to select and fragment, allows the DDA cycle to repeat more frequently, but at the cost of narrowing the analysis to only a few of the most intense ions. That said, the use of product ion scans and *m/z* selection in DDA make it a very popular MS/MS method, as only ions fragmented from the precursor are present in the tandem MS spectra, drastically simplifying data analysis.

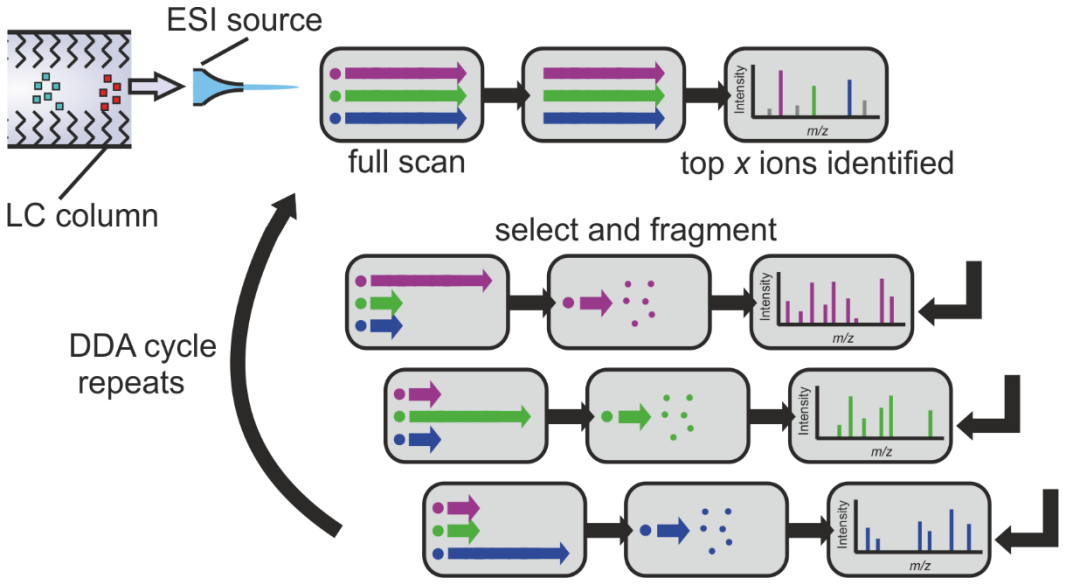

Figure 1.22 Operating procedure of data dependent acquisition (DDA) in LC-MS experiments. A full MS scan is first performed to determine the most abundant ions in the spectra at the current LC retention time. The top x most intense ions, x being a parameter tuneable by the operator, are then sequentially selected by the first mass analyser (usually a quadrupole) where product ion scans are used to obtain tandem MS spectra for each ion selected. When x is reached, a full scan is performed again. This process is repeated across the entire LC gradient elution.

1.8.2 Data independent acquisition (DIA)

Data independent acquisitions (DIA) involve rapid switching between high and low energy modes without any *m/z* selection (Figure 1.23). The result is that co-eluting precursor ions are fragmented together, generating complex tandem MS spectra with fragment ions present from multiple precursors. Whilst this method allows both deep and rapid analysis of the sample, acquiring MS1 and MS2 spectra quickly for ions as they elute from the LC column, the data analysis is far more complicated, as assigning which fragment ions in the high energy spectra belong to which precursor ions in the MS1 spectra can be challenging.

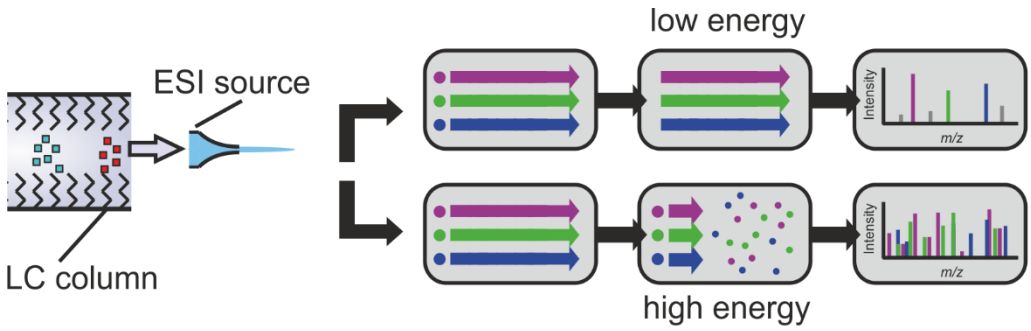

Figure 1.23 Operating procedure for data independent acquisition (DIA) in LC-MS experiments. The instrument switches rapidly between high and low energy modes without any precursor *m/z* selection. Co-eluting precursors are fragmented together generating highly complex MS/MS data.

One common method of DIA data analysis, termed MS^E, matches precursor ions to their respective fragment ions by retention time alignment [56]. In this method, shown in Figure 1.24, the change in intensity of the precursor and fragment ions over the course of the LC separation is used to determine their respective retention times. Fragment ions will have the same retention time as the precursor ion from which they are produced, so these data can be used to reconstruct MS/MS data and assign fragment ions to their corresponding intact molecular ions.

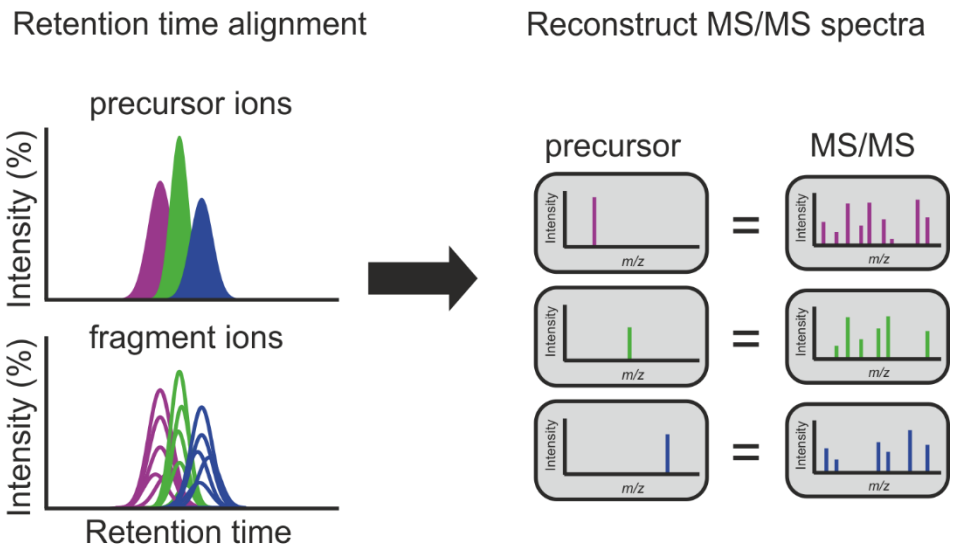

Figure 1.24 Data analysis in DIA-MS[E]. The retention times of precursor ions are matched to the retention times of the fragment ions. These data are then used to reconstruct the tandem MS spectra which correspond to particular precursor ions.

1.9 Ion mobility spectrometry – mass spectrometry (IMS-MS)

Although liquid phase separation techniques, such as LC, used prior to ionisation, are useful for separating complex biological mixtures, additional separation of the sample after ionisation is often helpful to further simplify the data analysis. Originally known as plasma chromatography [57] and conceptually very similar to LC separation, ion mobility spectrometry (IMS) separates gas phase ions based on the physical properties of size and charge [58]. Although commonly used independently in airport security for detecting nitro-organic explosives [59], IMS has been shown to be a useful research tool, when used in conjunction with MS analysis, for the separation and analysis of large biomolecules. For example, owing to the speed at which IMS can separate ions (typically on the order of milliseconds) IMS can be used in conjunction with LC as an orthogonal separation technique for further partitioning of complex biological samples, prior to MS analysis (LC-IMS-MS). Similarly, with appropriate instrument geometry, precursor, or fragment ions in MS/MS experiments can be separated by IMS by fragmenting the molecular ion before, or after, IMS separation. Although a variety

of different types of IMS are now available, two of the most commonly available IMS methods are summarised below.

1.9.1 Drift tube IMS (DTIMS)

The simplest form of IMS is drift tube IMS (DTIMS) where ions are drawn by a weak electric field through a drift tube filled with a neutral buffer gas, typically He or N_2 [58, 60]. Larger ions suffer more collisions with the buffer gas and are slowed down, eluting from the drift tube later than smaller ions, which suffer fewer buffer gas collisions (Figure 1.25). However, more highly charged ions are affected more by the electric field and are drawn through the drift tube faster than ions with fewer charges. Thus, IMS separation is dependent on both the size and the charge of an ion, as well as the properties of the buffer gas (i.e. polarizability) which is usually kept constant. By using IMS-MS in tandem to determine the mass and charge of an ion, and with precise knowledge of the experimental conditions in the drift tube, the drift time of an ion through the IMS device can be used to calculate the rotationally averaged collision cross section, or CCS (Ω), a measurement of an ions' size in a given buffer gas, using the Mason-Schamp equation (Equation 1.9) [61].

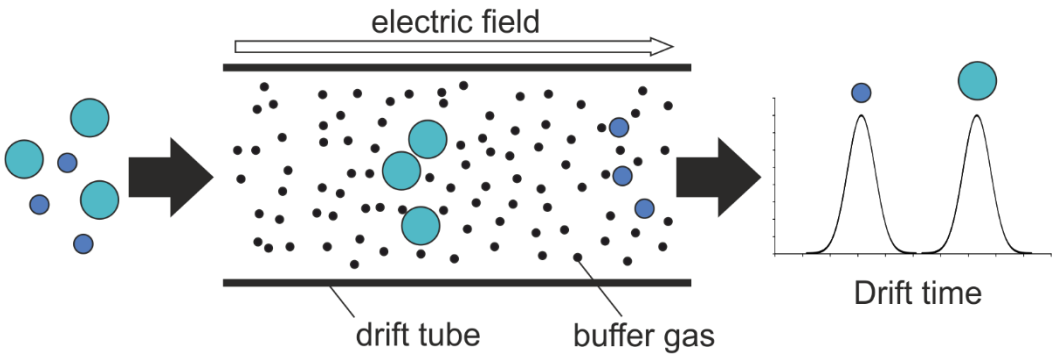

Figure 1.25 The principle of drift cell ion mobility spectrometry. Ions are drawn by a weak electric field through a drift tube filled with a neutral buffer gas. Larger ions suffer more collisions with the buffer gas and have longer drift times, separating them from smaller, more mobile ions which suffer fewer buffer gas collisions.

$$\Omega = \frac{(18\pi)^{1/2}}{16} \cdot \frac{ze}{(k_B.T)^{1/2}} \cdot \left(\frac{1}{\mu}\right)^{1/2} \cdot \frac{760}{P} \cdot \frac{T}{273.2} \cdot \frac{1}{N} \cdot \frac{t_D.E}{L} \quad (1.9)$$

Equation 1.9 The Mason-Schamp equation. The relationship between rotationally averaged collision cross section (Ω) and drift time (t_D). Where E is electric field, L is the length of the drift region, T is temperature, P is pressure, z is the charge on the analyte, e is the elementary charge of an electron, k_B is the Boltzmann constant, N is the buffer gas density and μ is the reduced mass of the ion-neutral pair.

Although recent commercial developments have improved DTIMS technology [62], historically, many conventional drift tube IMS instruments were plagued by sensitivity issues, sampling only a small proportion of the total ion current [63]. As a result, many commercial instruments use an alternative form of IMS known as travelling wave IMS or TWIMS.

1.9.2 Travelling wave IMS (TWIMS)

First incorporated into a commercial instrument in 2006 by the Waters Corporation [64], TWIMS consists of a stacked ring ion guide (SRIG) of ringed electrodes where an applied RF voltage, operating such that adjacent electrodes are 180° out of phase with each other, serves to radially confine the ions during transit through the device (Figure 1.26) [65].

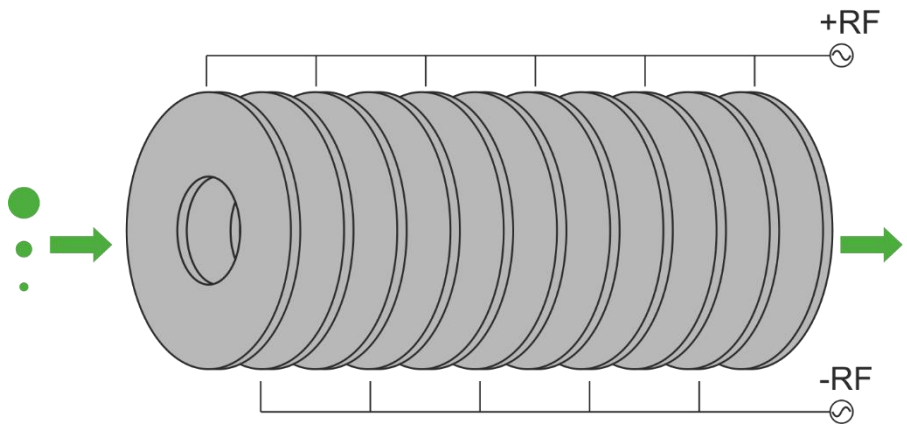

Figure 1.26 Schematic diagram of a stacked ring ion guide. RF voltages are applied to ringed electrodes, such that adjacent rings are 180° out of phase with each other. The electric field generated serves to radially confine ions during their transit through the device.

A DC potential is superimposed over the RF-AC potential on adjacent pairs of electrodes and, after a short time, is switched off and moved to the next pair of electrodes. This generates a travelling DC potential or 'wave' which pushes ions through the IMS device. Ions with higher mobility are able to 'surf' this wave for longer as they suffer fewer buffer gas collisions, whereas lower mobility ions 'roll over' the wave and remain in the TWIMS cell until pushed by the next wave (Figure 1.27). Separation parameters in TWIMS can be easily changed and optimised by voltage manipulation of the wave height and velocity, or buffer gas pressure [66]. However, the complex nature of the dynamic electric field in TWIMS complicates the relationship between drift time and CCS. As such, despite several attempts to resolve and understand this issue [67, 68], TWIMS is currently unable to directly measure the CCS of separated ions, and instead must rely on a calibration approach, based on known CCS values from DTIMS measurements [69].

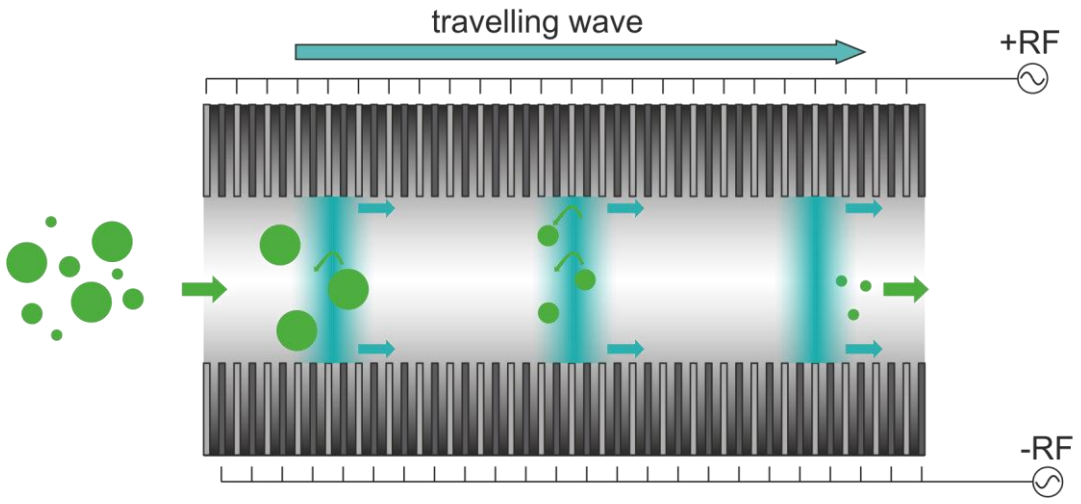

Figure 1.27 Separation of ions by travelling wave ion mobility spectrometry (TWIMS). A travelling DC potential pushes ions through the SRIG towards the detector. High mobility ions that suffer fewer buffer gas collisions keep up with the wave for longer and have shorter drift times. Lower mobility ions are overtaken by the wave and undergo more 'roll over' events, having longer drift times.

1.10 Commercial instruments used in this thesis

1.10.1 Waters Synapt high definition mass spectrometer

The Synapt series of instruments from the Waters Corporation, follow standard Q-ToF instrument geometry, where a quadrupole mass analyser is followed by an orthogonal acceleration, reflectron ToF mass analyser. Between these two mass analysers, is the 'Tri-wave' region, where three separate SRIG cells are situated. The first cell, typically filled with argon gas, can act as a collision cell, and serves to trap and accumulate ions before they pass into the next SRIG, equipped with TWIMS separation in a nitrogen buffer gas. The third and final SRIG in this region, known as the transfer cell, is typically used to maintain IMS separation prior to mass analysis, but can also be used as a second collision cell, allowing for post-IMS CID if necessary. For each ion packet released by the trap cell and subjected to TWIMS separation, 200 acceleration pushes, or bins, in the ToF are initiated before the trap cell releases the next ion packet. By knowing when each ion packet was released and by which push the ions were accelerated for ToF separation, the drift time of each ion can be calculated. This drift time can be corrected for *m/z* independent flight time in the transfer cell, as well as *m/z* dependent flight time between the transfer exit lens and the pusher region [66]. In practice, however, these corrections only minimally change the drift time (typically ~0.2 ms) and, given that other sources of error, such as precisely determining the drift time apex, are usually much larger, these corrections are not routinely applied [63].

The Z-spray source region, so called for its distinctive Z shape, is designed to remove neutral molecules in the electrospray, as the path of these molecules will not be directed by the voltages controlling the ion path. While this is present on the earlier version of this instrument (Syanpt G1), later versions of this instrument, such as the Synapt G2Si, were also equipped with a stepwave device, to further remove neutral molecules and increase ion transmission, as well as a short, helium filled SRIG immediately prior to the TWIMS cell, to cool ions and increase IMS resolution.

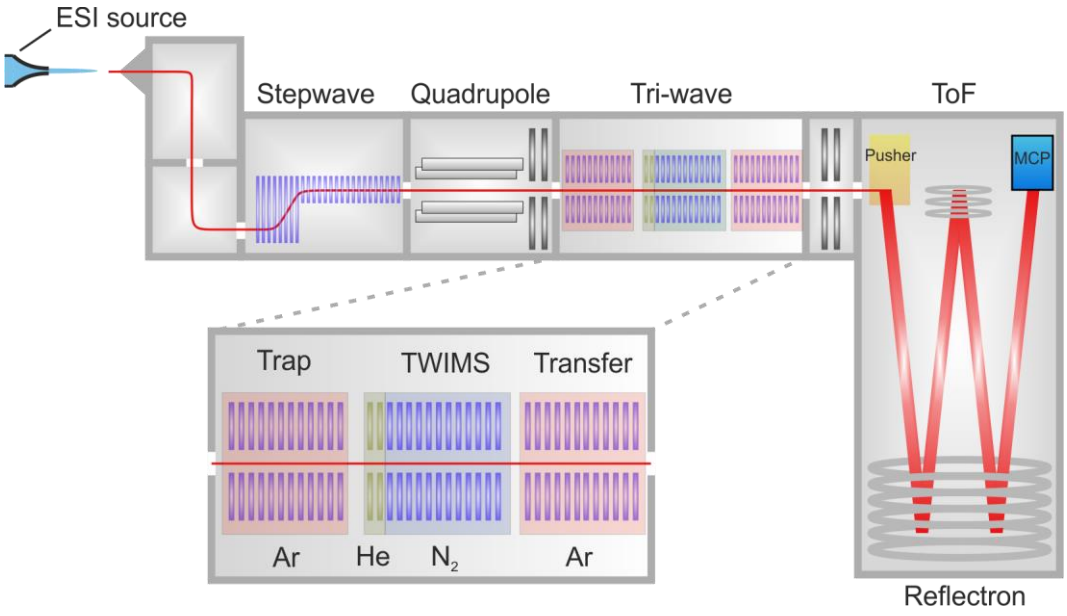

Figure 1.28 Schematic diagram of a Waters Synapt G2Si HDMS. A typical Q-ToF design, ions pass through a stepwave ion guide device to remove neutral molecules before entering the quadrupole. Ions then enter the tri-wave region, where they pass through three SRIG cells: Trap, IMS and transfer. Finally ions enter a high vacuum ToF region equipped with a dual stage reflectron and an MCP detector.

1.10.2 Thermo Q Exactive hybrid quadrupole – orbitrap mass spectrometer

Following ionisation, ions in a Q-Exactive orbitrap MS, developed by Thermo Fisher Scientific, traverse a bent flatpole ion guide, before passing through a quadrupole mass filter, where *m/z* selection can be applied if necessary, and finally into a curved linear ion trap called the C-trap. Here, ions are accumulated before either being injected laterally into the orbitrap for *m/z* analysis, or axially into the nitrogen filled HCD cell, if MS/MS fragmentation is required. Following fragmentation, fragment ions can be injected back into the C-trap and, subsequently, the orbitrap for fragment ion analysis.

The scan time of the orbitrap mass analyser can be adjusted, allowing control of resolution and MS acquisition speed, and, although in principle ToF mass analysers have a faster scan speed than orbitraps, the DDA cycle of the Q-Exactive is considerably faster than the current commercially available ToF instruments, capable of acquiring tandem MS spectra at 12 Hz [70]. Similarly, the accumulation time of

quadrupole selected ions in the C trap can be adjusted based on their intensities as measured by MS1 scans in the orbitrap, a process known as predictive automatic gain control, allowing lower intensity ions to be accumulated for longer before fragmentation, generating better quality MS/MS data [70]. Although, with the default instrument setup, this instrument geometry cannot separate ions by IMS, and is not well suited to high mass ions, such as those generate by native MS (discussed later in Section 2.4.1), the above characteristics make this instrument ideally suited to biological mass spectrometry in proteomics workflows and peptide fragmentation.

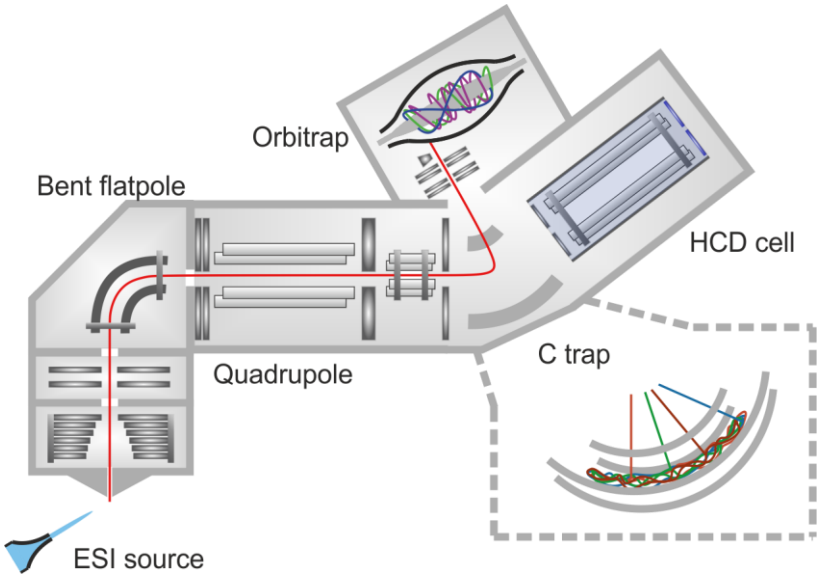

Figure 1.29 Schematic diagram of a Thermo Q Exactive mass spectrometer. Ions pass through a series of focusing lenses in the source region, before traversing a bent flatpole ion guide, the quadrupole mass filter and into the C-trap, a curved linear ion trap. Ions are then injected, laterally out of the C-trap, into the orbitrap, where *m/z* is measured by image current detection, or axially into the HCD cell, a nitrogen filled collision cell, if MS/MS fragmentation is required. Adapted from [70].

1.10.3 Thermo orbitrap fusion tribrid mass spectrometer

With a similar architecture to the Q Exactive instrument, ions in the orbitrap fusion tribrid MS are first accumulated in the nitrogen filled ion routing multipole (IRM). If a single MS analysis is required, these ions are typically passed back into the C-trap for *m/z* analysis in the orbitrap. However, if MS/MS experiments are required, this

instrument architecture lends itself to a diverse range of options for fragmentation and analysis. For example, quadrupole selected ions can be fragmented in either the high pressure cell of the linear ion trap, by CID with the helium collision gas, or fragmented more quickly (by ~10-30 ms) by HCD fragmentation simply by injection of ions into the IRM at elevated energies [71]. Fragment ions can then be analysed by the linear ion trap, by injecting ions into the low pressure cell, or by the orbitrap, via the C-trap and the IRM (Figure 1.30).

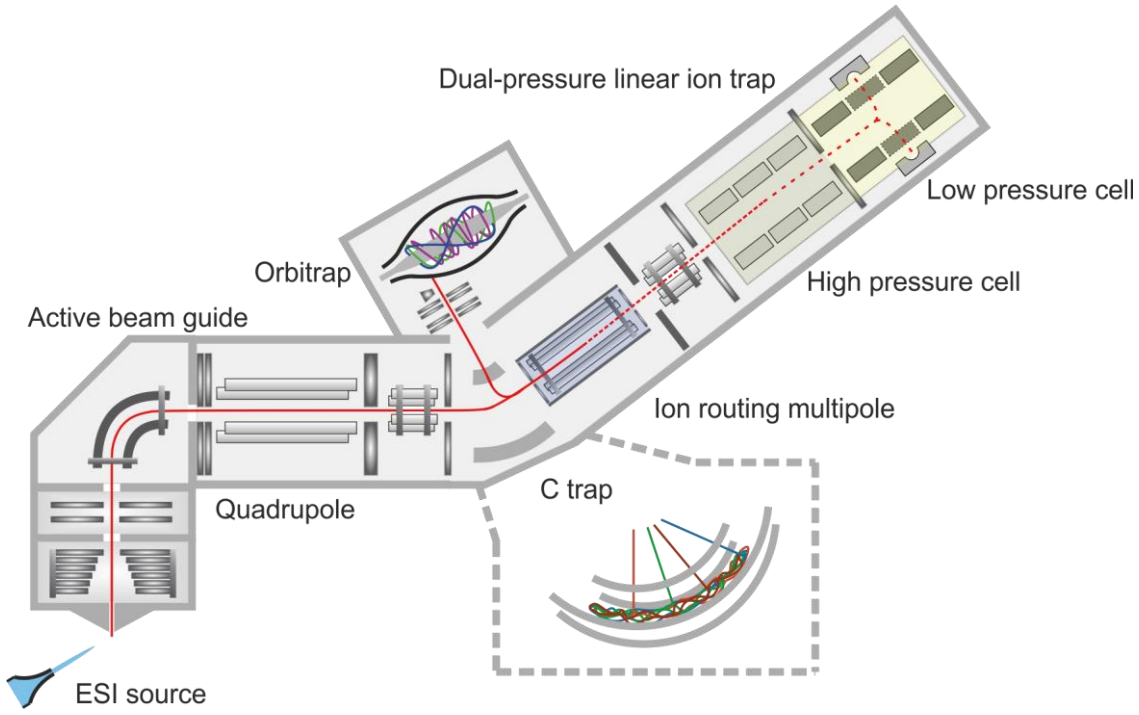

Figure 1.30 Schematic diagram of a Thermo orbitrap fusion tribrid mass spectrometer. Similar to the architecture of the Q Exactive instrument, ions are accumulated in the ion routing multipole before being passed, either back into the C-trap for injection into the orbitrap, or into the dual pressure linear ion trap mass analyser for an alternative route for mass analysis or MS/MS experiments. Adapted from [71].

Although *m/z* analysis for the precursor, and fragment ions, for a typical DDA workflow, can both be performed in the orbitrap (a workflow unimaginatively named orbitrap-orbitrap), the unique 'T' shaped geometry of the instrument is such that precursor and fragment ion analysis can be performed simultaneously by precursor

analysis in the orbitrap, and fragment ion analysis in the linear ion trap (orbitrap-iontrap workflow). This parallelisation streamlines MS/MS acquisition, taking advantage of both the high resolution of the orbitrap and fast scan speeds of the linear ion trap, drastically increasing the DDA cycle speed, and allowing the orbitrap fusion instrument to achieve MS/MS fragmentation frequencies of up to 22 Hz [71].

Chapter 2:

Introduction II: Protein aggregation, structure and dynamics studied by mass spectrometry

2 Introduction II: Protein aggregation, structure and dynamics studied by mass spectrometry

"…the most remarkable thing about proteins is that they can do almost anything."

-Francis Crick, Co-discoverer of the Structure of DNA, 1958 [72].

Essential for nearly all biochemical processes, proteins can be thought of as the molecular machines that maintain life, where almost everything inside a cell is itself, or is synthesised by, a protein. Some of the more well-known roles proteins adopt are enzymes, biological catalysts for a cells' metabolism, and antibodies, a vital component of the adaptive immune system. However, proteins have an almost uncountable number of other functions. Opsin proteins in the retina mediate the conversion of photons into electrochemical signals to enable sight [73]. Motor proteins like kinesins 'walk' through cells moving cellular cargo from one place to another [74]. Even the air we breathe is transported around our bodies using the oxygen binding protein haemoglobin.

The remarkable ability of these molecules to function in such a wide variety of roles, for most proteins, relies on adopting a specific three-dimensional shape, or conformation. These 3D shapes are formed by the folding of one or more polypeptide chains - long strings of peptide bond linked amino acids - the main structural components of proteins (Figure 2.1). In 1961, after demonstrating for the first time that protein folding could be reversible, work for which he would later be awarded the Nobel Prize in chemistry, C.B Anfinsen famously concluded that the specific sequence of amino acids in a polypeptide chain, contains all the information necessary for the protein to adopt its native fold [75]. Although varying significantly in length from just ~50 or so amino acids, up to several thousand for larger proteins, polypeptides are composed of only twenty different types of amino acids, sometimes

known as residues, each of which differ by the structural and chemical components of their side chain, varying in size, shape, hydrophobicity and charge (Table 2.1). Additionally, many proteins adopt post-translational modifications, such as acetylation or phosphorylation, altering the chemistries of the modified amino acids and allowing the protein to correctly fold and perform its biological function [76].

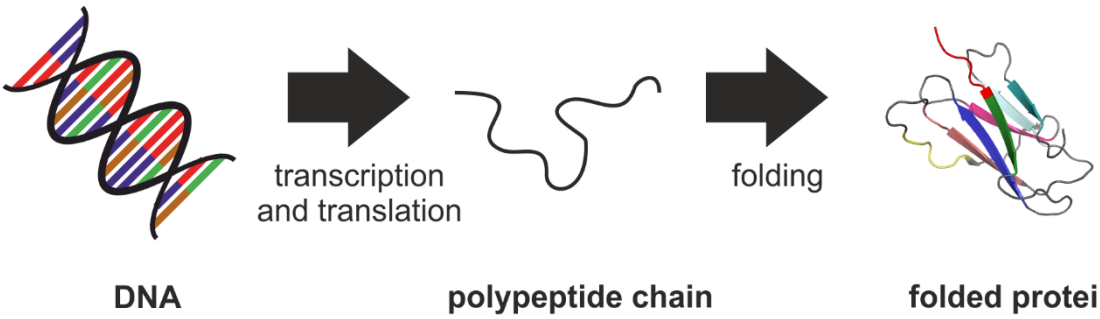

Figure 2.1 Transcribing, translating and folding polypeptide chains. DNA is transcribed and translated into a chain of amino acids called a polypeptide. The sequence of those amino acids in the chain determines how the polypeptide folds, to generate the three-dimensional structure, or conformation, of a fully folded protein.

Techniques such as X-ray crystallography [77], nuclear magnetic resonance spectroscopy (NMR) [78] and, more recently, cryo-electron microscopy [79] allow us to study the final folded structure of proteins, and observe some of the interactions which stabilise them: the hydrophobic effect, where hydrophobic side chains are buried in the protein core, away from solvent, disulphide bonds between cysteine residues, and hydrogen bonds formed between side chains, or the polypeptide backbone. Despite this, understanding the protein folding problem; exactly *how* proteins adopt their native fold from the sequence of a largely unstructured polypeptide, persists as one of the greatest challenges in modern structural biology [80, 81].

Table 2.1 Summary of the twenty different naturally occurring amino acid structures, masses and abbreviations.

Name	Abbreviations	monoisotopic mass (Da)	R group (side chain)
glycine	gly, G	57.021	
alanine	ala, A	71.037	
threonine	thr, T	101.047	
valine	val, V	99.068	
serine	ser, S	87.032	
leucine	leu, L	113.084	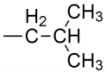
tryptophan	trp, W	186.079	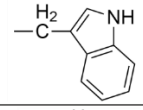
isoleucine	ile, I	113.084	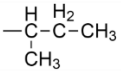
phenylalanine	phe, F	147.068	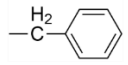
tyrosine	tyr, Y	163.063	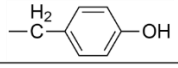
asparagine	asn, N	114.042	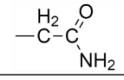
methionine	met, M	131.040	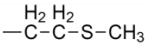
glutamine	gln, Q	128.058	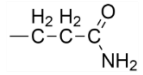
cysteine	cys, C	103.009	
arginine	arg, R	156.101	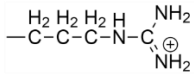
histidine	his, H	137.058	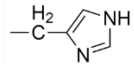
lysine	lys, K	128.094	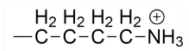
proline	pro, P	97.052	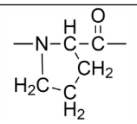
aspartic acid	asp, D	115.026	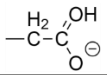
glutamate	glu, E	129.042	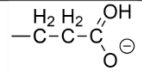

2.1 Protein folding, misfolding and aggregation

In 1968, Cyrus Levinthal famously summarised the protein folding problem by demonstrating that even a relatively small polypeptide of 100 or so residues has such a large number of possible conformations physically available to it, that an exhaustive search of all of them, even when sampling at 10 trillion conformations per second, would take longer than the current lifetime of the universe to complete [82]. Knowing that proteins can find and adopt their native fold in as little as a few microseconds [80], this problem, now known as Levinthal's paradox, effectively illustrated that the native state of a polypeptide could not possibly be found simply by searching conformations at random [83].

2.1.1 Protein folding

In the face of Levinthal's paradox, many models have been proposed to explain how polypeptides fold into proteins on a biological timescale. The framework model proposed that smaller secondary structural elements, such as α-helices, folded first before these pre-formed structural elements dock together to create the overall native fold [84-87]. Conversely, the hydrophobic collapse model proposed that the need for hydrophobic side chains in the polypeptide to be free from solvent interaction, leads to a collapsed molten globule state with hydrophobic side chains at its core. This collapsed globule was proposed to aid protein folding by compacting the polypeptide into a confined volume, narrowing the conformational search necessary to find the native state [88, 89]. The nucleation-condensation model combines these two processes, suggesting that protein folding occurs by the formation of a small nucleus, that may involve weak secondary structure, followed by collapse of the polypeptide around it [90].

Today, protein folding is thought of in the context of energy landscapes or 'folding funnels' [81], where the internal free energy of the polypeptide (y axis) is plotted against entropy (x axis), a measure of the conformational freedom of the molecule (Figure

2.2). Native-like interactions formed by folding polypeptides, perhaps driven by hydrophobic interactions or partially folded secondary structure, are, on average, more stable than non-native interactions. These favourable contacts are therefore more persistent, forming partially folded intermediate structures with lower internal energy and restricted conformational freedom (i.e. reduced entropy). This further directs the polypeptide towards ever more stable, lower energy species, eventually adopting the fully folded native state, usually considered to be the lowest energy, most thermodynamically stable structure that is kinetically accessible under physiological conditions [91].

A thought experiment proposed by Dawkins [92] and discussed elsewhere [82] is useful for understanding this concept. Consider the, now infamous, infinite monkey theorem: a monkey randomly hitting keys on a typewriter will, given an infinite amount of time, produce the complete works of Shakespeare. To make it easier for the monkey, we reduce the number of typewriter keys to just 27, the 26 letters and a space key, and instead of having to produce the complete works of Shakespeare, the monkey only has to correctly type a single phrase from Hamlet: 'Methinks it is like a weasel'. Randomly typing letters, it would take approximately 10^{40} key strokes for the monkey to correctly type out this statement [82]. However, if, with each attempt, the monkey cannot change those letters already in the correct positions, analogous to the polypeptide finding a stable native-like interaction, he need only attempt the statement a few thousand times before correctly reproducing Hamlet's comment.

This analogy simplifies the problem somewhat. In actuality, protein conformations are in constant dynamic equilibrium, where changing environmental or solution conditions (temperature, pH etc…) shifts the equilibrium to populate more unfolded or native forms of the molecule. Depending on their relative stabilities, partially folded states can often revert to more unfolded conformations rather than move towards the native state, analogous to the monkey merely finding it *difficult* to change correctly placed letters rather than *impossible*. Similarly, there is some debate as to whether folding intermediates are useful, on-pathway structures towards the native

state, or kinetically trapped stable conformers that result in less efficient folding [93]. Nevertheless, this simplification does effectively demonstrate that there can be several different ways of attaining the correct native fold and that a biased search, rather than a random search, is what solves Levinthal's paradox, where the sequence of amino acids in a polypeptide chain, are selected by evolution to not only allow the protein to effectively perform its biological function, but to fold quickly and effectively into the native structural conformation.

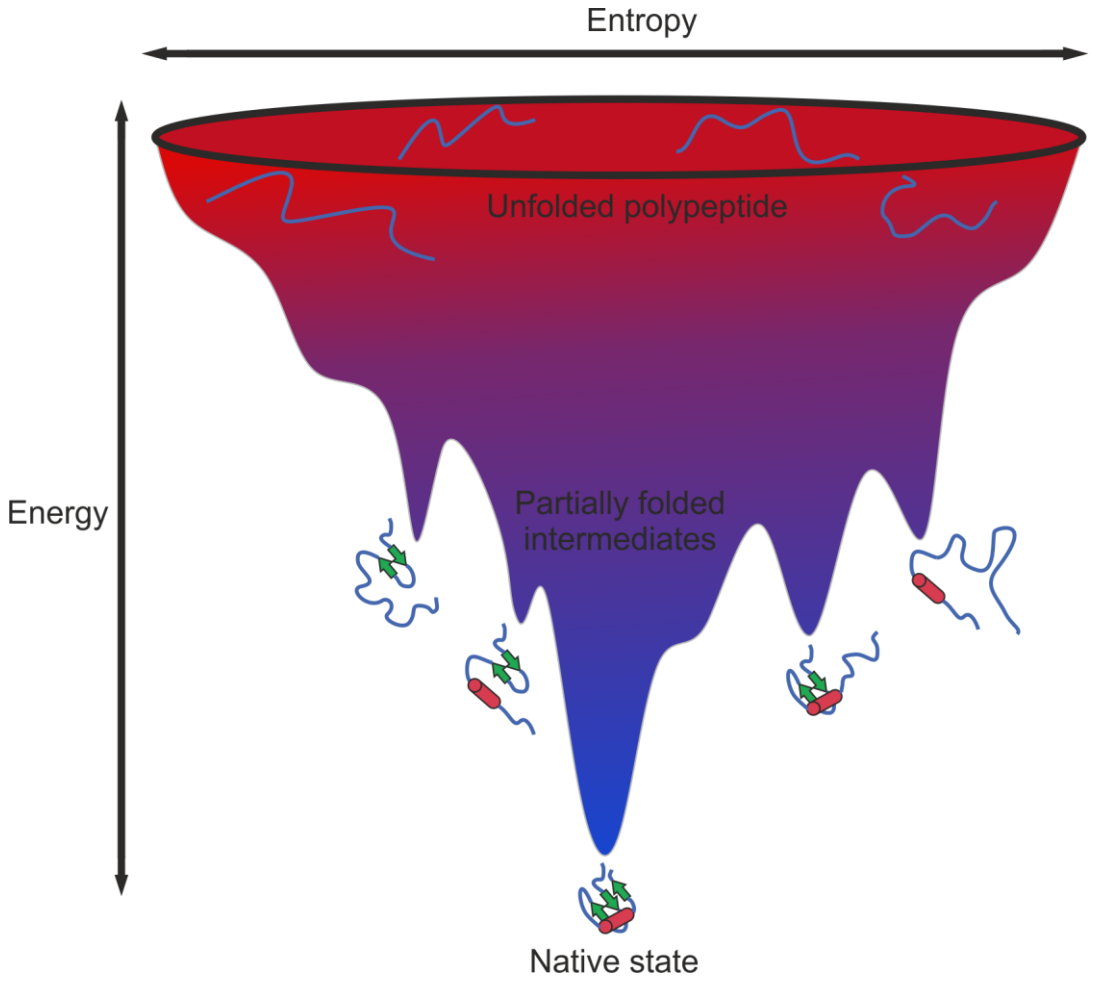

Figure 2.2 Idealised folding funnel/energy landscape for protein folding. From the unfolded polypeptide, native-like interactions are favoured in the folding process which produce partially folded conformers of lower internal free energy (y axis) and reduced conformational entropy (x axis). This process continues until the native state is reached.

2.1.2 Misfolding, aggregation and disease

Given the immense complexity of protein folding, and the sheer number of possible conformations a polypeptide chain may adopt, it would be remarkable if protein misfolding were never to occur. Frequently, protein misfolding is a result of amino acid substitutions in the polypeptide sequence, improper proteolysis, or destabilising solution conditions such as changes in temperature or pH [94]. A common, and expected, consequence of protein misfolding is the loss of biological function, and is associated with many diseases, collectively known as proteinopathies or conformational diseases [95]. Cystic fibrosis is one such example, usually caused by the deletion of a phenylalanine residue at position 508, shorthanded to ΔF508, in the polypeptide of a particular transmembrane conductance regulator protein [96].

On the other hand, some misfolded proteins experience a toxic *gain* of function. This, too, is associated with various diseases including bovine spongiform encephalopathy (BSE), commonly known as mad cow disease, where the misfolded prion protein 'replicates' by misfolding other correctly folded proteins of the same type, eventually leading to large insoluble protein aggregates [97]. Indeed, protein aggregation is a common consequence of misfolding and, although the specific sequence of events leading to aggregation is difficult to elucidate and differs from protein to protein, aggregation is generally thought to be driven, at least in part, by hydrophobic side chains, normally buried in the native fold, becoming solvent exposed in the misfolded species. These misfolded species are then proposed to aggregate into small, initially soluble, oligomers, before assembling further into larger, insoluble species sometimes containing many thousands of protein molecules (Figure 2.3).

Figure 2.3 Generalised mechanism of protein aggregation. A misfolded or partially folded species generated from the native state aggregates into oligomeric species, before proceeding to larger insoluble aggregates, such as amyloid fibrils.

The size, composition and morphology of protein aggregates can vary significantly depending on the protein involved and the nature of aggregation. For example, the bovine serum albumin (BSA) protein as well as several therapeutic antibodies have been shown to form large, amorphous aggregates when stressed under extensional flow conditions [98]. Still, a wide variety of different proteins have been shown, with an equally wide variety of different stimuli, to aggregate into highly ordered, highly stable protein aggregates with rope-like morphologies. These types of protein aggregate, collectively known as amyloid, are associated with more than 60 human diseases [99], including well known afflictions such as Alzheimer's disease [100], Parkinson's disease [101] and type 2 diabetes mellitus [102].

2.1.3 Structure and formation of amyloid

Although the different proteins and peptides that form amyloid often share little structural or sequence homology, the resulting aggregate fibril structures are strikingly similar. First described in atomic detail by William Astbury in the 1930's [103], mature amyloid fibrils are now known to consist of 2-6 protofilaments, 2-5 nm in diameter, that twist to form rope-like structures 7-13 nm wide [94]. The protofilaments are constructed from a core of stacked β-sheets running parallel to the long axis of the fibril, with the individual β-strands that make up those sheets, perpendicular to the fibril axis (Figure 2.4) [104]. This so called "cross-β" structure, named for the distinguishing "cross" pattern observed during analysis by X-ray fibre diffraction [105, 106], is a defining characteristic of amyloid fibrils. Similarly, many fibrils are known to

share common non-amyloid components as part of the overall *in vivo* structure. Long unbranched polysaccharides known as glycosaminoglycans (GAGs), various metal ions and Serum Amyloid P (SAP), a pentameric protein (each subunit ~ 25 kDa) observed to make up approximately 14% of amyloid deposits by dry mass, are all known to associate with amyloid deposits *in vivo* [94].

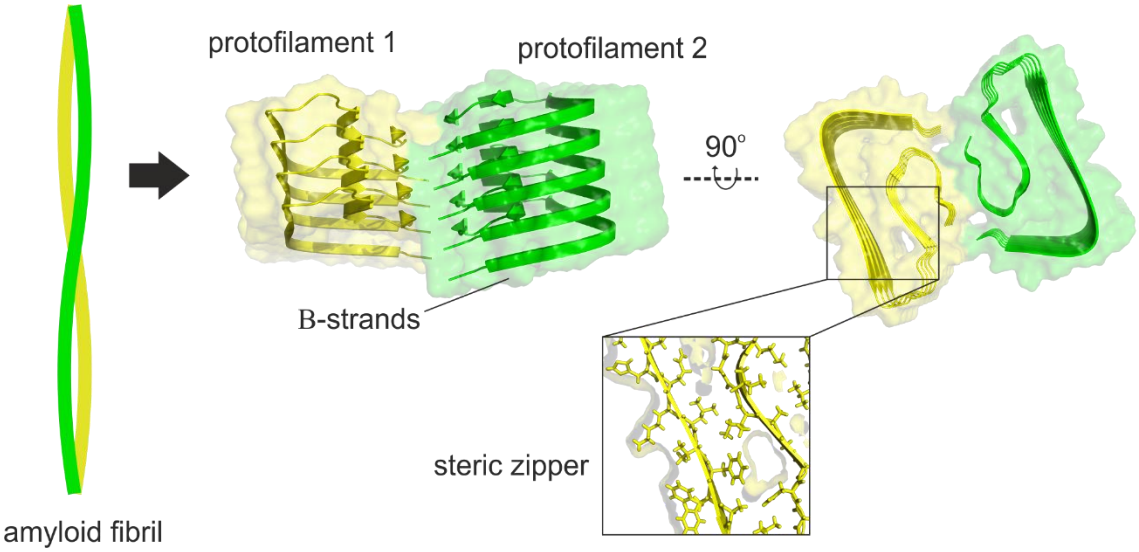

Figure 2.4 Structure of an amyloid fibril. Twisted protofilaments forming the overall amyloid fibril consist of stacked β-sheets stabilised by extensive hydrogen bonding between strands, and steric zipper interactions. PDB: 5OQV [107].

Generally, amyloid fibrils and protofilaments are extraordinarily stable structures, held together by extensive hydrogen bonding between β-strands, and interdigitated amino acid side chains in the fibril core that form solvent free 'steric zipper' interfaces [108]. Indeed, it has been suggested that the amyloid fibril state can be more thermodynamically stable than the native state under certain conditions (Figure 2.5) [109], where drastic changes in pH, or dissolution in strong organic solvents is often required to disaggregate fibril structures [110, 111].

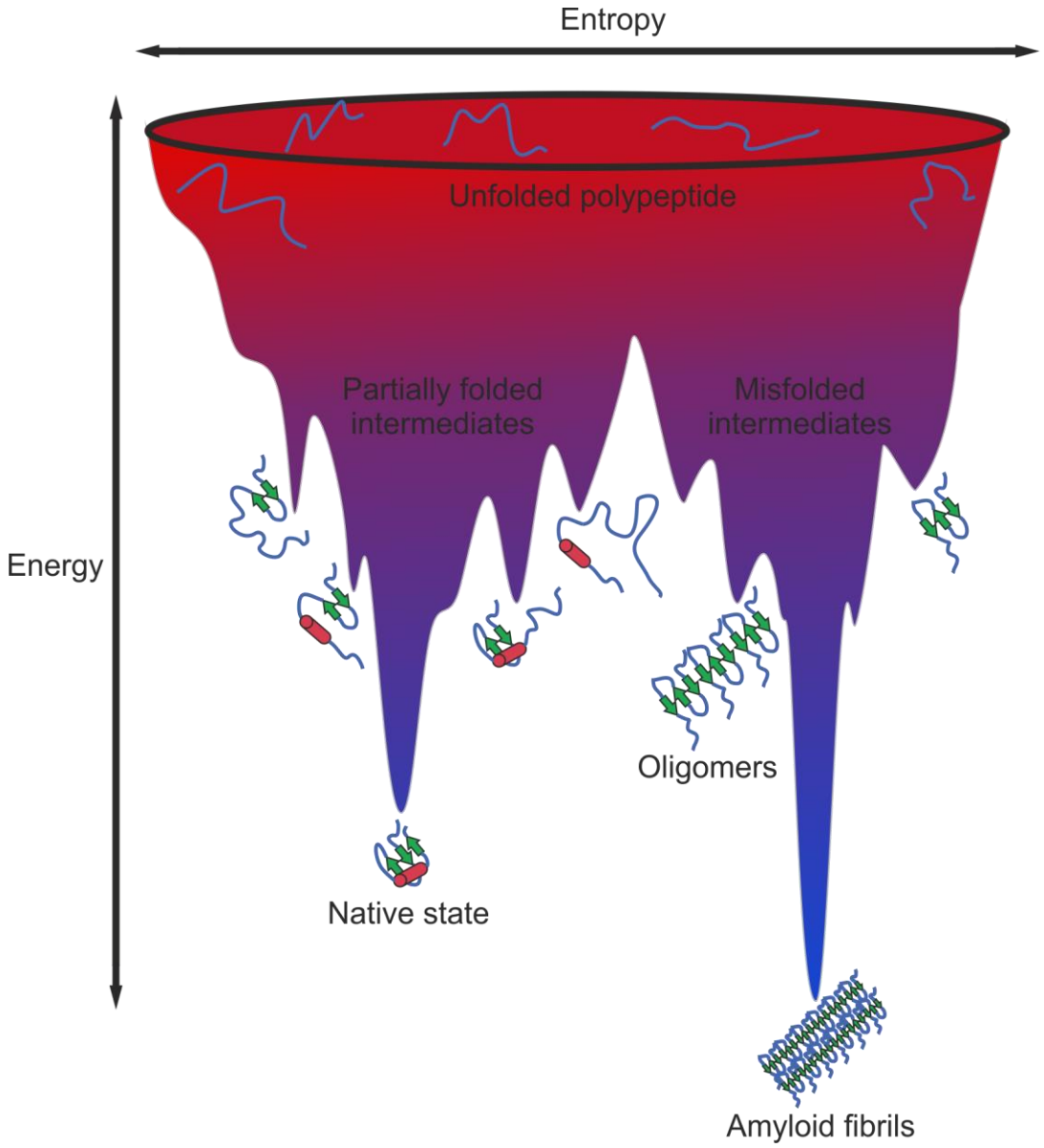

Figure 2.5 Energy landscape for protein folding, misfolding and aggregation. Protein aggregation, thought to be caused by misfolding, leads to oligomer formation and, ultimately, the formation of highly stable, rigid, amyloid fibrils.

Needless to say, understanding the conformational changes that allow proteins to form amyloid from, initially stable, soluble protein monomers, is of paramount importance to the prevention and treatment of amyloid diseases.

2.2 Beta-2 microglobulin (β_2m)

Wild-type β_2-microglobulin (β_2m) is a small, 99 residue member of the immunoglobulin (Ig) superfamily of protein structures [112, 113]. As is typical for members of this group, β_2m has a "β-sandwich" fold consisting of seven anti-parallel β strands, labelled A-G, organised into two β-sheets, where strands A, B, E and D form one sheet and strands C, F and G form the other (Figure 2.6b). These two β-sheets are stabilised by a single, central disulphide bond between strands B and F, at residues 25 and 80 [77].

2.2.1 Normal function and dialysis related amyloidosis

β_2m is part of a complex of proteins known as the class 1 major histocompatibility complex (MHC-1), formed by the non-covalent, 1:1 association of β_2m, the light chain component of the complex, with the α1 protein, the heavy chain component (Figure 2.6a) [114]. Present on the surface of all nucleated cells, the function of this complex is to bind short peptides (8-10 residues) from proteins processed in the cytosol [115]. These peptides are transported from the cytosol to an organelle in cells known as the endoplasmic reticulum, where assembly of the MHC-1 occurs. After binding, the MHC-1 is transported to the cell surface where the bound peptide is presented for recognition by T-cells [115]. These cells recognise the peptide as 'self' or 'non-self', where the identification of a 'non-self' antigen, perhaps indicative of viral infection in the cytosol, triggers pathways leading to an immune response [116]. Although not directly involved in interactions with the bound peptide, β_2m is critical for the assembly and stability of the complex [117], and is essential for efficient transport of the MHC1 to the cell surface [118]. The binding of β_2m to the α1 chain of the complex is stabilised by extensive intermolecular interactions between the two proteins including contacts made in the B-C loop (His31-Asp34), a continuous eleven residue stretch in the D-E loop and parts of the D and E strands (Ser52-Tyr63), as well as a network of hydrogen bonds in the A and B strands [115].

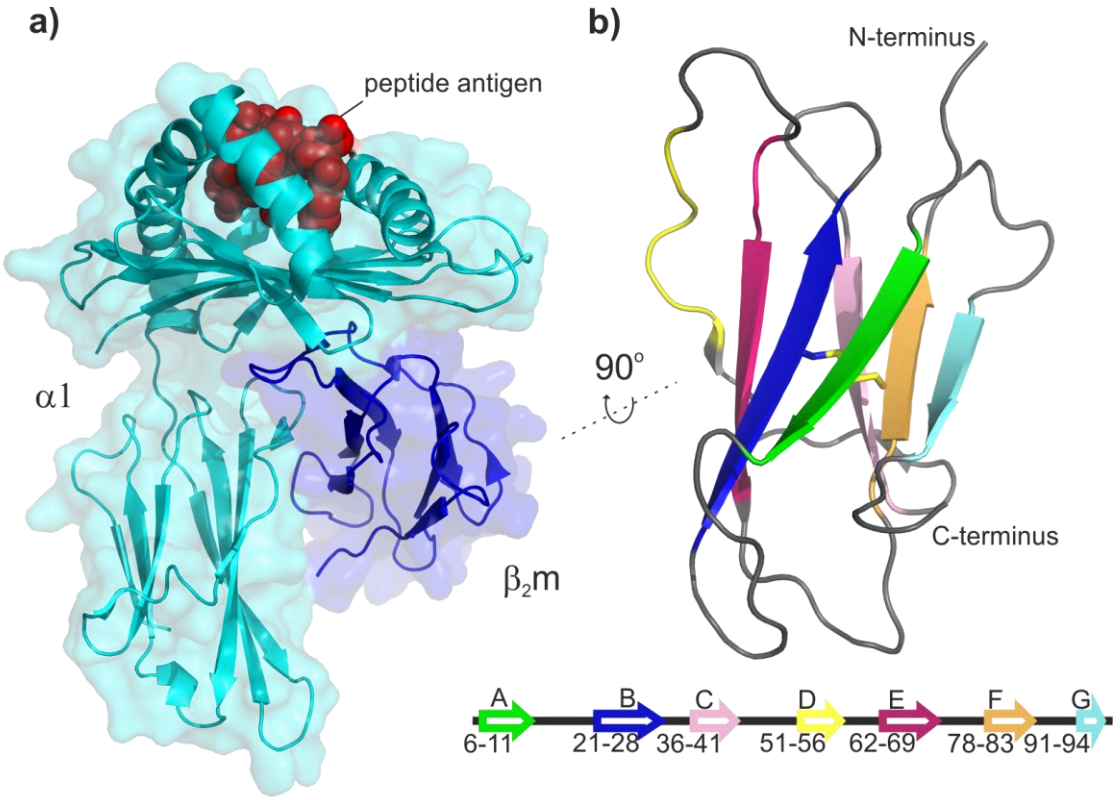

Figure 2.6 The structures of β2m and the class 1 major histocompatibility protein complex. **a)** The class 1 major histocompatibility complex (MHC1). The α1 chain (cyan) is bound to the β2m light chain component (blue) and a peptide antigen (red – shown as spheres). PDB: 2XPG [119]. **b)** NMR structure of monomeric β2m. β-strands A-G are coloured as in the sequence diagram below. The disulphide bond between residues 25 and 80 is shown as sticks. PDB: 2XKS [78].

Similar to many other proteins, β2m is being constantly turned over in the body. When the MHC-1 is degraded, the membrane bound α1 heavy chain is internalised back into the cell, leaving the non-covalently associated β2m protein to be released into the blood [120] where it is then cleared and degraded by the kidneys [115].

Patients with abnormal kidney function have a reduced rate of β2m clearance [121]. Similarly, despite recent improvements in dialysis technology [122], filtration membranes used in kidney dialysis machines are typically ineffective at filtering out β2m [123] causing a sustained increase in serum β2m concentration up to 60 times normal levels [124]. The end result is protein aggregation, and the formation of β2m amyloid fibrils, typically localised to osteoarticular tissues, such as the bones and joints (Figure

2.7) [123, 124]. Whilst β2m fibril formation has been documented in long surviving non-dialysed kidney disease patients [121], build-up of amyloid deposits typically takes years, and is usually beyond the life expectancy of most non-dialysed patients. As such, amyloid deposits of this kind are more commonly found in patients undergoing long-term hemodialysis, with an estimated incidence of >95% after 15 years of treatment [123]. Even with kidney transplantation, this condition, known as dialysis related amyloidosis (DRA), is difficult to reverse, eventually leading to pathological destruction of the bones and joints with symptoms including bone cysts, restricted movement, joint pain and carpal tunnel syndrome [115].

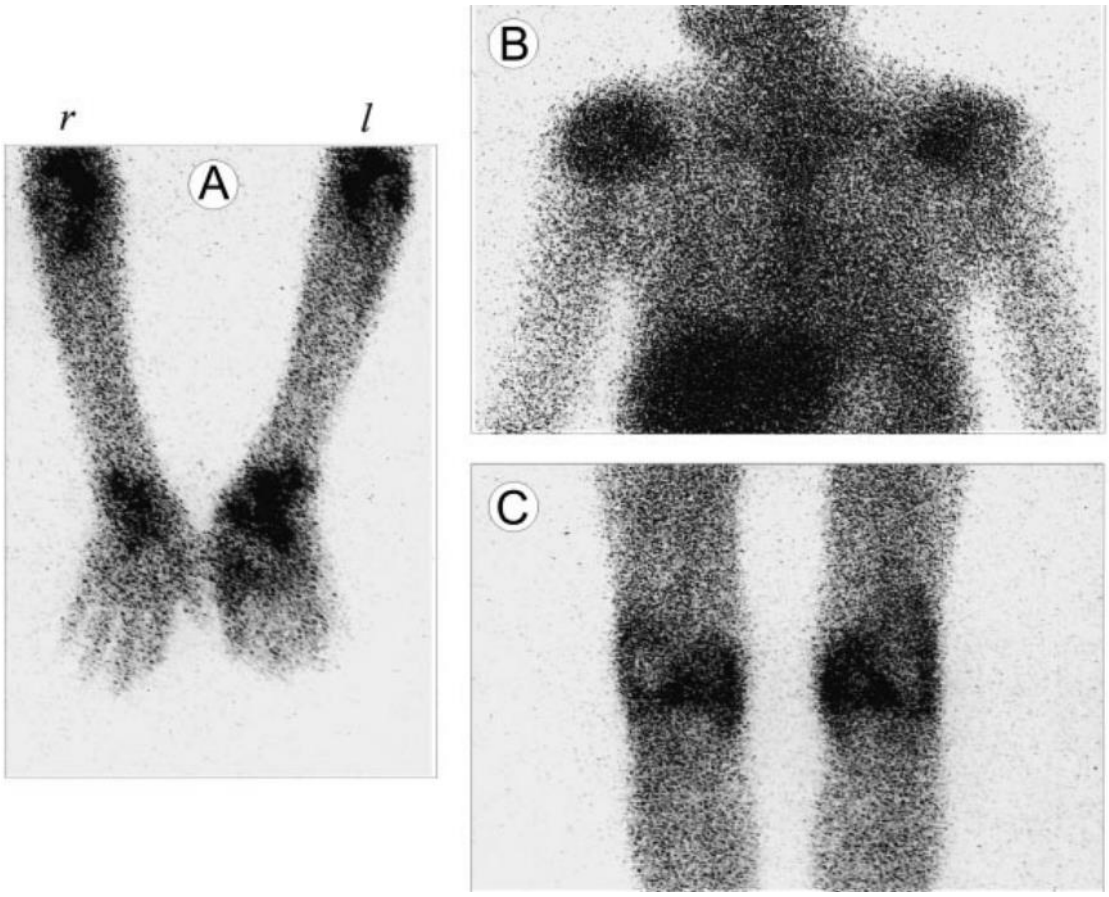

Figure 2.7 β2m amyloid deposits in dialysis related amyloidosis (DRA). Indium labelled β2m amyloid fibrils are localised to the bones and joints of DRA patients. Zoomed images are shown of the arms (**a**), chest (**b**) and knees (**c**). Taken, with permission, from [125].

2.2.2 β2m aggregation *in vitro*

In an effort to understand how amyloid fibril deposits in DRA are formed, the structure, folding pathway, and amyloidogenic properties of β2m have been studied extensively [115, 126]. Despite its fibrillogenic properties *in vivo*, however, β2m does not readily form amyloid fibrils *in vitro* under physiological conditions, even after 100 days, and when incubated at concentrations 20 times higher than those found in DRA patients [78, 113]. Whilst strongly acidic conditions (pH < 4) do permit aggregation of β2m into amyloid fibrils *in vitro*, and considerable research has been targeted at the aggregation of this acid unfolded state [127-131], unlike amyloid deposits associated with DRA, β2m fibrils generated under acidic conditions rapidly depolymerise when returned to physiological pH, highlighting the differences between *in vitro* fibrillation from the acid unfolded state, and *in vivo* fibrillation from native conditions [110]. This, combined with the observation that many dialysis patients with similarly increased levels of serum β2m do not display symptoms of DRA [132], suggests that additional factors must be important for β2m amyloid formation *in vivo*.

Several studies have shown that the addition of accessory molecules such as pre-formed amyloid fibril seeds [133-135], or molecules commonly associated with fibrils such as SAP [136] and GAGs [137], permit β2m fibril formation *in vitro* at, or near, pathophysiological conditions. In one such case, the addition of collagen was shown to cause fibrillation of β2m under neutral pH conditions *in vitro* [138]. β2m has been shown to bind collagen proteins with μM affinity [139], and *ex vivo* fibrils from DRA patients are also associated with collagen, leading to the hypothesis that this property may be responsible for the specificity of DRA amyloid deposits to the bones and joints, tissues typically high in collagen fibres [138]. Copper ions have also been implicated in the amyloidogenic properties of β2m [140]. In the presence of Cu^{2+}, β2m readily forms amyloid fibrils at neutral pH *in vitro* [141] and the symptoms of DRA patients were shown to improve after switching to Cu^{2+} free dialysis membranes [142, 143]. Binding of Cu^{2+} ions has also been shown to destabilise the native state of β2m and delay refolding [144]. Nevertheless, while understanding the solution conditions and additional factors

which favour β2m amyloid formation is useful, insights into the structure and folding pathway of β2m are essential to determine how these accessory molecules affect the protein's structure, and change its amyloidogenic properties.

2.2.3 β2m folding pathway and the I_T state

Changes in tryptophan fluorescence observed during stopped-flow refolding experiments have shown that β2m folds in two stages: a fast phase (~2.1 s^{-1}) which generates a stable partially folded intermediate, followed by a very slow folding phase (0.02 s^{-1}) into the final native state of the protein (Figure 2.8a) [136]. Further probing of this folding pathway revealed that an engineered variant in which the Pro 32 amino acid was changed to a much smaller glycine residue (P32G), was able to fold into the protein's native state without this slow folding phase [136]. Given that the native, fully folded structure of β2m is known to contain a relatively uncommon *cis* peptide bond between residues His 31 and Pro 32 (Figure 2.8b) [145], it was suggested that *trans-cis* isomerisation of this bond is responsible for the slow phase in the refolding of β2m [136].

Whilst only representing ~5% of the protein at equilibrium in wild-type β2m, the folding intermediate structure found between the fast and flow folding phases of β2m, usually referred to as the I_T state ($Intermediate_{Trans}$) due to the non-native *trans* His 31-Pro 32 peptide bond, was significantly more populated in the P32G variant (~30% at equilibrium). Interestingly, this variant was also shown to elongate existing wild-type β2m fibrils faster than the wild-type protein, with an increasing elongation rate occurring under solution conditions favouring a higher relative population of the I_T state folding intermediate[136]. Another engineered proline variant, P5G, found to populate ~60% I_T state at equilibrium, was also able to form amyloid fibrils *de novo* under physiological conditions without the addition of any accessory molecules [146].

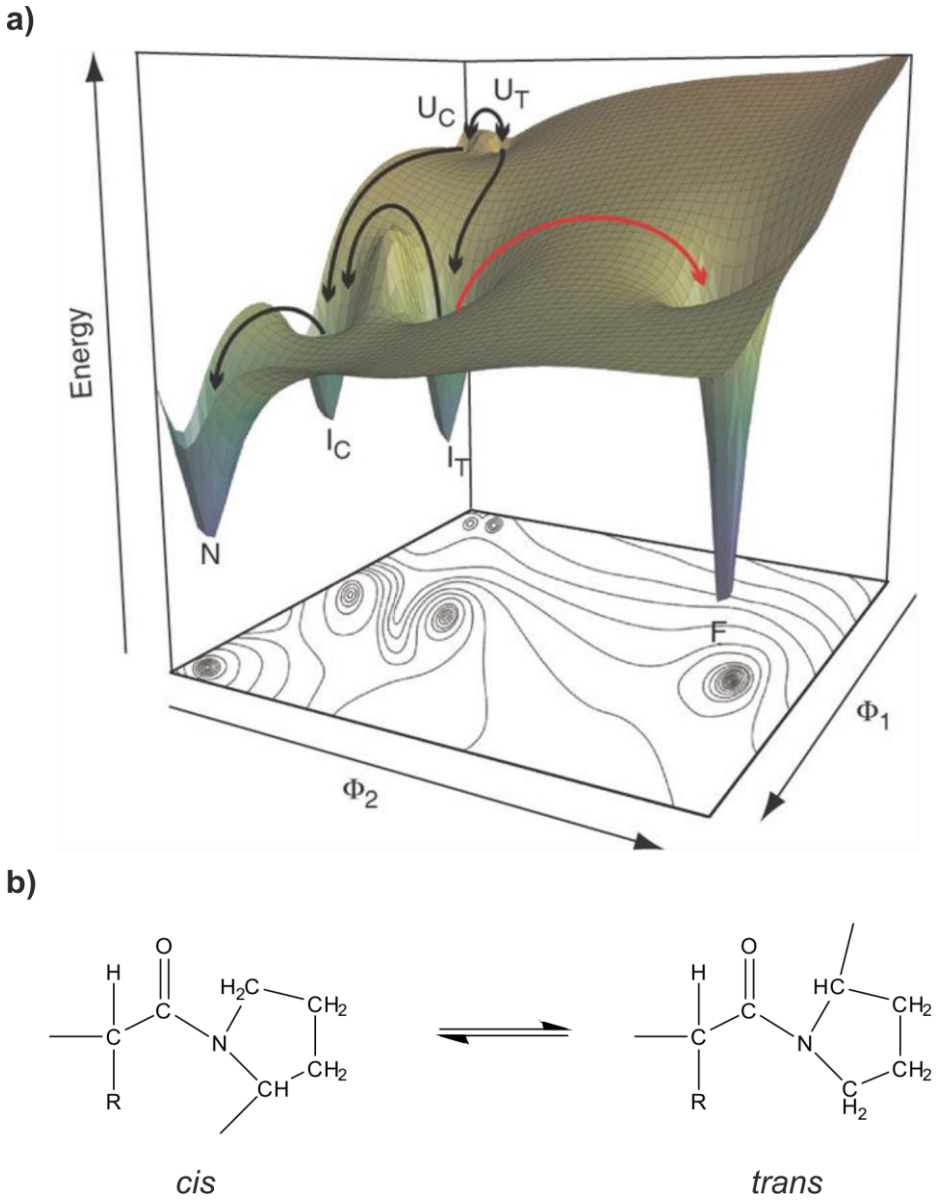

Figure 2.8 The folding pathway of β2m. **a)** Folding funnel of β2m under physiological conditions. Parallel folding pathways with (I_T), and without (I_C) a *trans* His-Pro 32 peptide bond form intermediate states (I) while folding into the native state (N) from the unfolded state (U). The folding intermediate I_T is proposed as a link between the folding and aggregation pathways. Taken from [136]. **b)** *Cis/trans* isomerisation of proline residues in a polypeptide.

With the His-Pro 32 peptide bond in the *trans* configuration, β2m has been shown to bind Cu^{2+} ions with 10,000 fold greater affinity than the native structure, and it has been suggested that Cu^{2+} binding to His 31 may induce *cis-trans* isomerisation, and generation of the I_T state folding intermediate, consistent with earlier work showing increased β2m amyloidogenicity in the presence of copper [147]. Similarly, *cis-trans*

isomerisation of proline residues has been linked to aggregation in several other Ig domains [148-150]. As a result, the I_T state folding intermediate of β_2m has been highlighted as a leading candidate for the amyloidogenic precursor of β_2m fibril formation.

2.2.4 ΔN6 β_2-microglobulin

Considered to be a structural mimic of the I_T state, ΔN6 is a proteolytically cleaved truncation variant of β_2m lacking the six N-terminal amino acids. This variant readily forms amyloid fibrils *in vitro* under physiological conditions in the absence of accessory molecules and, at equilibrium, is approximately 90% in the *trans* His-Pro 32 conformer [78, 146]. ΔN6 has a higher affinity for collagen relative to full length β_2m [139] and has been detected in the amyloid deposits of DRA patients [151, 152] constituting ~30% of protein extracted from *ex vivo* fibrils [153]. Although not detected in the blood plasma of DRA patients [154], leading to the inevitable question of whether formation of ΔN6 is a cause, or result of amyloid formation in DRA, it has been shown that ΔN6 can initiate fibrillation of full length β_2m *in vitro*, even when added at ~1% concentration relative to the full length protein [78]. This, coupled with their known association *in vivo*, led to the suggestion that that ΔN6 promotes aggregation of the wild-type protein [155]. Some have suggested a prion-like mechanism whereby a ΔN6-β_2m collision initiates amyloidogenesis by triggering *cis-trans* isomerisation of full length β_2m, causing it to adopt the non-native, I_T state precursor to amyloid formation [78]. Others suggest a secondary nucleation mechanism where formation of ΔN6 amyloid fibrils seed the growth of amyloid fibrils made from the wild-type protein [156]. In spite of recent efforts, an exact mechanism of how β_2m forms amyloid fibrils in DRA, and indeed how the I_T state is involved in amyloid formation, has yet to be elucidated.

2.2.5 D76N β2-microglobulin

In 2012, a study published in the New England Journal of Medicine reported a unique, hereditary, systemic amyloidosis discovered in several members of a French family experiencing progressive bowel dysfunction [157]. With disease onset in middle age and slow disease progression over many years, amyloid deposits were identified in various tissues of the affected family members including the spleen, heart, liver and nerves. Proteomic analysis of these amyloid deposits found them to be composed of a variant of β2m, with an aspartic acid to asparagine amino acid substitution at position 76, shown by DNA sequencing, to be caused by a single guanine to adenine base substitution at position 286 in the β2m gene [157]. Interestingly, despite affected family members being heterozygous for this mutation, indicating that wild-type β2m is also present in patients, amyloid deposits contained only the D76N variant, and were not localised to the bones and joints, as in DRA. Similarly distinct from DRA, affected individuals had normal renal function, and normal concentrations of β2m in the blood [157]. Patients were not immune-deficient, and the D76N containing MHC-1 was shown to have comparable structure, dissociation patterns and stability compared with the wild-type complex [158], suggesting the D76N variant may retain its biological function.

Structurally, the D76N variant is almost indistinguishable from the wild-type protein [78, 157] (Figure 2.9), and has been shown to fold via a similar pathway involving the I_T state [156]. Unlike wild-type β2m, however, D76N is highly amyloidogenic *in vitro* in the absence of accessory molecules and readily forms amyloid fibrils under neutral pH conditions [159]. While this amino acid substitution has been shown to significantly destabilise the native state of the protein [156], as has the N-terminal truncation in ΔN6 [146], the native state of murine β2m is also less stable than that of D76N, and yet does not form amyloid fibrils [160], suggesting that thermodynamic stability of the native state is not necessarily correlated with the propensity to form amyloid in β2m.

While some evidence suggests D76N has an increased population of I_T state at equilibrium relative to the wild-type protein (~25% compared to ~4% for the wild-

type protein) [156], others have shown no significant difference [161]. Similarly, the P32G variant of the wild-type protein, shown to populate ~30% I_T state at equilibrium, is unable to form amyloid fibrils *de novo* at physiological pH, unlike the D76N variant [146]. Numerous *in silico* studies have suggested that the I_T state in D76N is structurally different to that of the I_T state in the wild-type protein, either by comparatively more unfolding close to the N and C-termini [162] or a more disordered D-strand [163], suggesting that this may be responsible for the increased aggregation propensity of the D76N variant. However, subsequent studies using CD and NMR have shown that the I_T state structures of D76N and the wild-type protein are similar, instead suggesting there may be an alternative aggregation-prone conformation, distinct from the I_T state present in the wild-type protein or ΔN6 [161]. Interestingly, no increase in aggregation propensity was observed for other D-N variants (D34N, D38N, D53N, D59N and D98N) in Asn-scan mutagenesis studies [159] suggesting the amino acid position, rather than the residue substitution itself, is the important factor in aggregation propensity. Indeed, several other D76 variants (D76H, D76E and D76A) have all been shown to form amyloid fibrils *in vitro* in the absence of additional factors, under the same experimental conditions as D76N [164].

The D76N variant of β_2m, therefore, raises an important question:

How does a single amino acid substitution in a solvent exposed loop of the protein increase amyloidogenicity so significantly, seemingly without significantly affecting the native conformation or folding pathway?

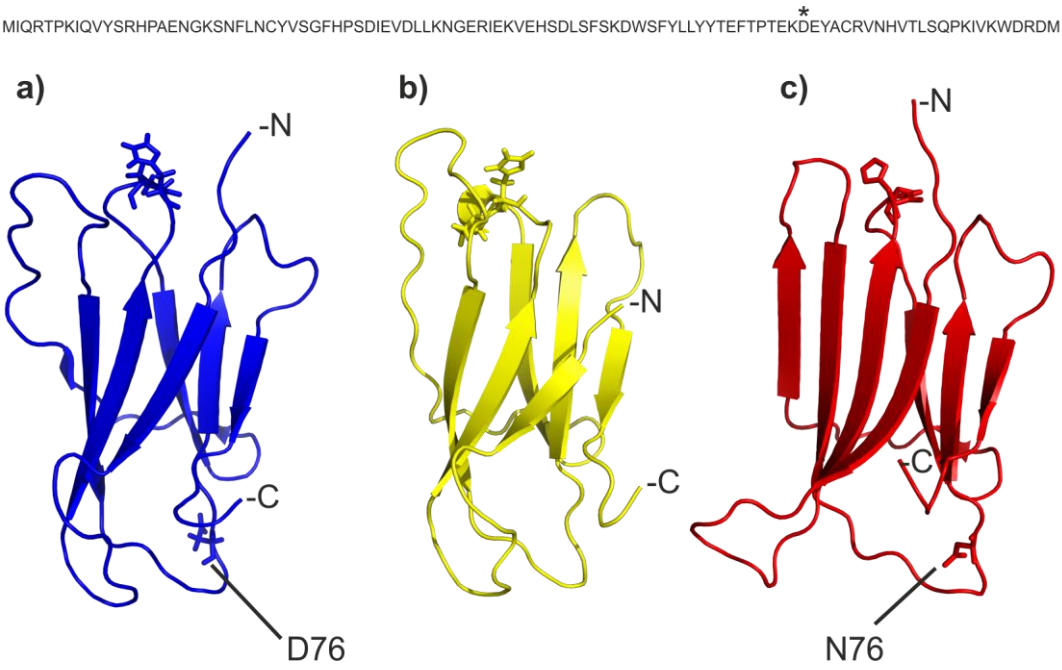

Figure 2.9 Wild-type, and aggregation-prone variants of β2m. NMR structures of **a)** wild-type (PDB: 2XKS, [78]), **b)** ΔN6 (PDB: 2XKU, [78]) and an X-ray crystallography structure of **c)** D76N (PDB: 4FXL, [157]) β2m are shown. Side chains of position 76 are highlighted in the wild-type and D76N structures. Side chains of His31 and Pro32 are shown as sticks at the top of all three structures. The N and C-termini have been annotated –N and –C respectively. The amino acid sequence of wild-type β2m is shown. The site of the D76N amino acid substitution is highlighted with an *.

2.3 Protein aggregation in biopharmaceuticals

Small molecule drugs, such as aspirin, have been used to treat diseases for more than 100 years [165]. However, a recent push for more targeted medicines, with reduced risk of off-target toxicity, often associated with small molecule treatments, has led to an increasing interest in therapies derived from biological sources, commonly referred to as biopharmaceuticals [166]. Perhaps the most striking surge in biopharmaceutical development of the last 20 years has been in therapeutic monoclonal antibodies (mAbs), where 112 therapeutic mAbs were approved in the United States and the European Union between 2015 and 2018, compared with less than 10, in the years leading up to 1989 [167].

Structurally, mAbs are ~150 kDa tetrameric proteins, made from two pairs of polypeptide chains, with each pair consisting of one heavy chain (~50 kDa each) and one light chain (~25 kDa each). This 'dimer of dimers' is arranged into a quaternary

structure with an overall 'Y' shape, characteristic of mAbs (Figure 2.10a), which can be broken down into three main sections: the F_C region, and the two Fab arms. Typically, each of these sections is made from four distinct Ig domains (of similar structure to β_2m) where each Fab arm comprises two Ig domains from the light chain and two from the heavy chain, and the F_C region comprises the remaining two domains from each copy of the heavy chain (Figure 2.10a).

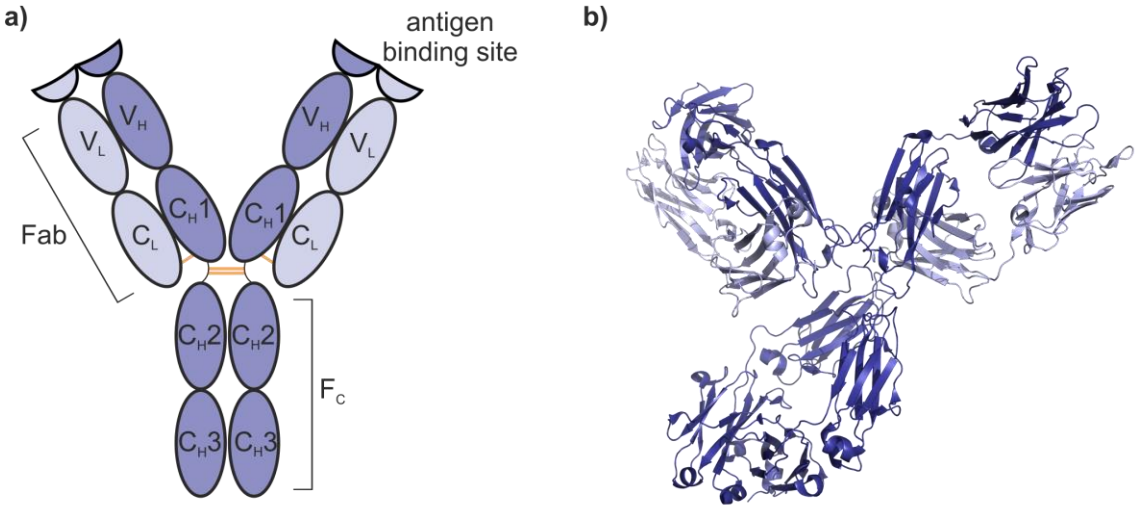

Figure 2.10 The structure of an IgG1 antibody. **a**) Schematic diagram of an antibody structure. Disulphide bonds are shown in yellow. Domains annotated V_x and C_xN show variable and constant domains, respectively. Subscripts L and H denote the light and heavy chains, respectively. The crystal structure of Pembrolizumab (PDB: 5DK3) [168] is shown in **b**). Heavy and light chains are coloured dark and light blue, respectively.

In nature, mAbs constitute an integral part of the adaptive immune system, where mAb binding to proteins on the surface of infecting bacteria or viruses, for example, can result in a variety of therapeutic outcomes, ranging from death or paralysis of the infectious agent, or complement activation; the recruitment of immune cells to the F_C binding site of the antibody [169]. Despite the typically high specificity of mAbs to their respective targets (pM-nM affinities are common [170]), usually referred to as antigens, the vast array of different and constantly evolving infectious targets requires significant adaptability of the mAb antigen binding site to remain effective. While

most of the mAb structure is comprised of constant domains (denoted C_H1-3 or C_L in Figure 2.10a), so called due to their *lack* of variability among mAb variants, the capacity for mAbs to adapt to bind a wide range of different antigens arises from hypervariable loop structures in the antigen binding site in the variable domains of the Fab arms (denoted V_L and V_H in Figure 2.10a for the variable domains of the light and heavy chains, respectively). Typically, there are twelve of these loop structures for a given mAb protein, three for each of the variable domains, where the amino acid sequences in these loops, also known as the complementarity determining regions (CDRs), are readily substituted between antibody variants, adapting the structure, conformation and microenvironment of the antigen binding site to suit a multitude of different targets.

In the development of biotherapeutic antibodies, this system is 'hijacked', and the structure and sequence of the CDR regions is purposefully changed to produce mAbs which bind a target chosen by the developer, typically one the natural immune system has failed to identify. For example, Pembrolizumab, the structure of which is shown in Figure 2.10b, is a biotherapeutic used to treat a variety of different cancers by binding to the PD-1 receptor protein on the surface of activated T cells. Cancerous cells often highly express the binding partner of this receptor, PD-L1, on their surface, such that activated immune cells recognise the tumour as 'self', hence preventing an anti-tumour immune response. Pembrolizumab binding to PD-1 receptors interferes with this interaction, allowing activated T cells and the natural immune system to attacked the tumour [171].

While the benefits of developing specifically targeted biotherapeutic antibodies are obvious, the development process for these products harbours numerous opportunities for protein aggregation. Coupled with the engineered amino acid sequence of the mAb, *itself* a possible cause of aggregation, biotherapeutics are subjected to an array of physical, chemical and mechanical stresses at various stages of production, storage or even during the administration of the drug to patients. For example, changes in pH or temperature during protein production in bioreactors [172],

or downstream purification [173], freeze-thaw cycles during storage [174], and interaction with siliconized surfaces on syringes prior to subcutaneous injection of the drug [175], are all possible causes of protein aggregation in biopharmaceuticals. Not only does protein aggregation decrease the yield of useful product, passing the increased cost on to consumers, but can also result in more insidious outcomes, such as reducing the efficacy of treatment, requiring higher doses to remain effective, or worse, the triggering of an immune response in patients, compromising patient safety. Consequently, mitigating protein aggregation in the early stages of biopharmaceutical development is of paramount importance.

2.3.1 MEDI1912 and MEDI1912_STT

Initially designed to bind the nerve growth factor (NGF) protein for the potential treatment of chronic pain, MEDI1912, developed by Medimmune (now AstraZeneca), is an IgG1 class mAb which, despite low pM affinity for its target antigen [170], displayed significant propensity to reversibly self-associate into protein aggregates during manufacture. Noting several other undesirable biophysical characteristics, such as adsorption to filter membranes during purification, resulting in decreased yield, and significant oligomerisation at low (<1 mg ml^{-1}) concentrations, three surface exposed hydrophobic amino acids in CDR loops one and two of the V_H domain were highlighted for their involvement in the reversible self-association dimer interface: W30, F31 and L57 [170]. These amino acids in MEDI1912, hereafter referred to as WFL, were substituted for three less hydrophobic groups (W30S, F31T, L57T) generating a triple substitution variant: STT. Despite these CDR substitutions, the STT variant maintained a low pM affinity for NGF, with significantly improved biophysical characteristics including significantly reduced self-association, a 2-fold improved half-life in rat *in vivo* models, and less non-specific tissue association [170]. Although WFL and STT have been shown to behave differently under flow induced stress conditions [176], the exact mechanism of aggregation and the conformational changes associated with these amino acid substitutions remain unexplored.

2.4 Mass spectrometry in structural biology

In recent years, mass spectrometry has evolved a plethora of different approaches aimed at the biophysical characterisation of proteins, revealing various different aspects of protein structure including protein dynamics, protein-protein and protein-ligand interactions, as well as differences in conformation and shape [177]. These methods can be broadly split into two groups: those that require the protein sample to remain intact, and those that require the protein to be fragmented. While a complete review of structural MS methods is beyond the scope of this thesis, an overview of some of the most common techniques used in structural MS, as well as those used in this thesis, are shown Figure 2.11, and are discussed in the next section.

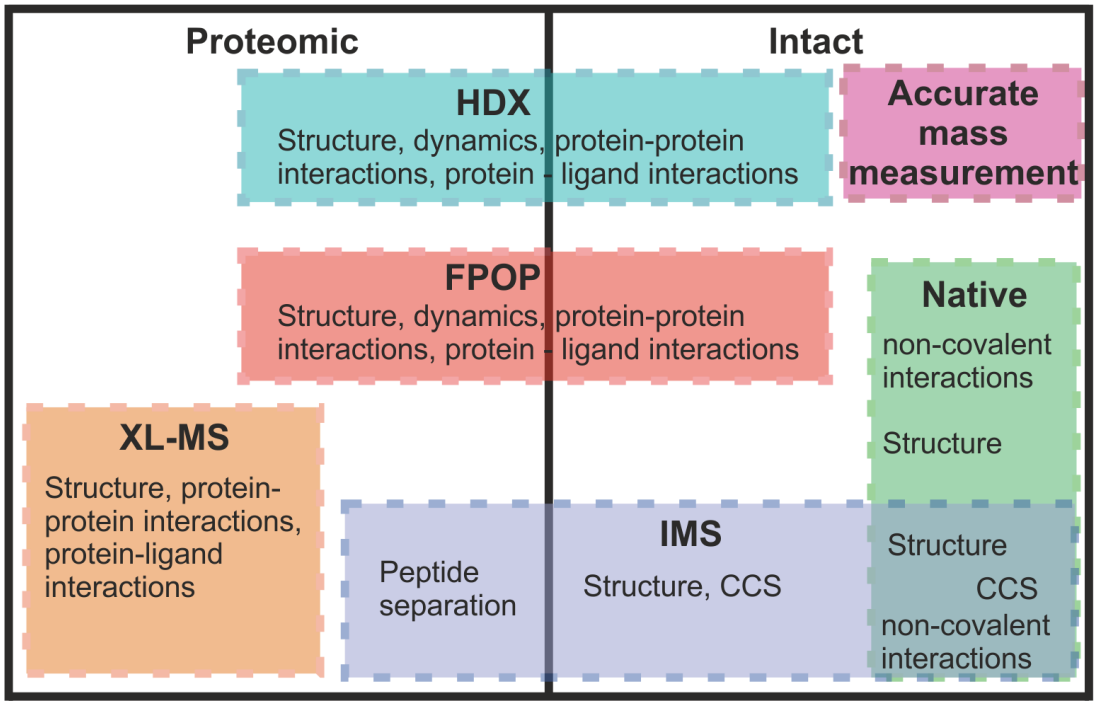

Figure 2.11 A summary of structural MS methods. Broadly, structural MS methods can be split into two categories: intact, where the polypeptide chain of the protein is analysed intact, or proteomic, where MS fragmentation and/or enzymatic digestion is used to study proteins at the peptide level.

2.4.1 Accurate mass determination, native MS and ion mobility

As discussed earlier in Section 1.2.1, the advent of ESI has allowed large molecules such as proteins to be ionised and analysed intact by use of MS. By using volatile, but non-denaturing, solution conditions, such as ammonium acetate solutions, proteins can be ionised and introduced into the instrument from their native solution phase conformation. Typically, folded proteins have a lower solvent accessible surface area (SASA) than unfolded proteins and, as such, have fewer accessible ionisable groups, resulting in native proteins adopting narrower charge state distributions, with fewer charges on average (i.e. higher *m/z*) when ionised by ESI (Figure 2.12b). Conversely, unfolded proteins, with a larger SASA and more accessible ionisable groups, adopt more charges from ESI (lower *m/z*) and have wider charge state distributions (Figure 2.12a). Thus analysis of charge state distributions can yield information on the conformation of proteins [178-180].

Typically for native MS experiments, considerable effort is made to optimise instrument conditions, aimed at striking a balance between effective transmission of high *m/z* ions, maintaining the intact molecule and any non-covalent interactions (particularly important for protein complexes), and aiding the desolvation process, usually achieved by voltage and pressure manipulation within the instrument [181-183]. That said, complete desolvation of native ions, particularly for larger complexes, remains challenging, and broader, less resolved, solvated charge state peaks are frequently observed in native MS spectra, decreasing the mass accuracy. This, coupled with the fewer charge states observed for native charge state distributions, equating to fewer data points from which to calculate a mass, means that denatured MS is the preferred technique to calculate an average mass of a protein, whilst native MS is more typically used for structural characterisation of the folded protein or native protein complex.

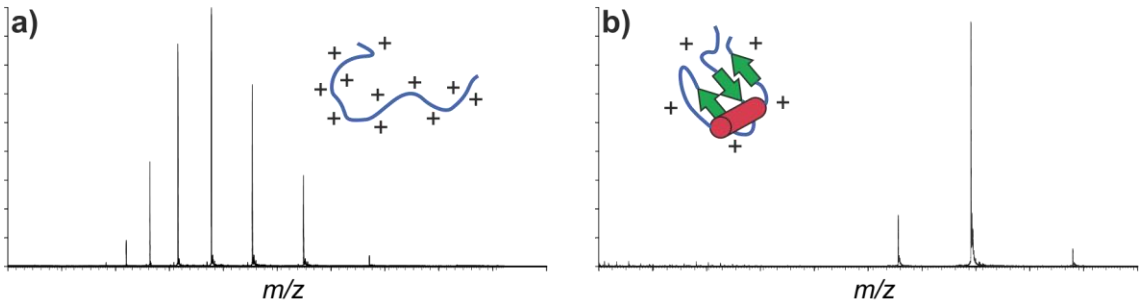

Figure 2.12 Idealised native and non-native charge state distributions. **a)** Unfolded proteins have more accessible ionisable groups, and adopt higher charge states and wider charge state distributions. **b)** Natively folded proteins have fewer exposed ionisable groups, and so adopt lower charge states and a narrow charge state distribution, the latter indicating reduced flexibility of the structure.

By introducing the protein into the instrument from its native conformation, IMS can be used as a gas phase separation technique to separate different co-populated conformations of a protein, with the same *m/z* but different sizes or shapes. This technique is now well established as a method to study the conformational distribution of proteins [184], including aggregation-prone samples [185, 186] and the early stage oligomers they form in the aggregation cascade, that would otherwise overlap in a 1D mass spectrum [187, 188]. The CCS values calculated from native IMS-MS data can then be compared with CCS values calculated *in silico*, using a variety of different algorithms [189-191], from structural data obtained from X-ray crystallography or NMR experiments. This information can be used for low resolution modelling of structures observed in IMS experiments, to determine the structure and conformation of proteins, oligomers or protein complexes [184, 192].

There is considerable debate, however, as to the extent to which proteins retain their native conformation in the gas phase. Some proteins have been shown to undergo significant gas phase collapse, where the lack of solvent, and subsequent loss of the hydrophobic effect, leads to self-solvation of side chains and conformational changes [192, 193]. Others however, have shown in ion trap-IMS experiments that, when sprayed under non-denaturing solution conditions, gas phase protein ions retain a CCS consistent with the native conformation for several hundred milliseconds [194, 195],

before adopting stable gas phase conformations. Similarly, gas phase spectroscopic approaches have shown that protein ions retain native secondary structure in the gas phase [196, 197], and that, when decelerated onto a surface and recovered after ionisation, some protein ions can retain biological activity [198]. As such, most proteins are considered to retain a native-like gas phase conformation on the timescale of an IMS experiment, providing the sample was introduced from non-denaturing solution conditions and that no collision induced unfolding has occurred, intentionally or otherwise, within the instrument.

2.4.2 Fragmentation and peptide sequencing

Many structural MS methods for protein characterisation require tandem MS experiments, and fragmentation of the protein sample. Although proteins can be introduced into the mass spectrometer intact and fragmented within the instrument, usually referred to as 'top-down' MS/MS, more commonly, proteins are first proteolytically digested into peptides using digestive enzymes, before MS/MS is used to analyse the resulting peptides, typically following prior LC separation. This is usually referred to as a 'bottom-up' approach which, in its simplest form, can be used to determine the sequence of amino acids from which the peptides are made, where multiple peptides can be used to determine the amino acid sequence of the protein. Typically, this is performed using a product ion scan and CID (Figure 2.13).

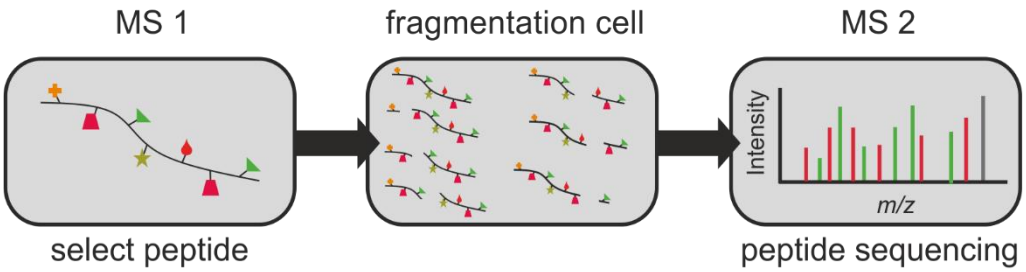

Figure 2.13 Peptide sequencing by product ion scan MS/MS. Peptides with specific *m/z* are selected in the quadrupole. Fragmentation results in multiple fragment ions with different masses, typically including some remaining intact peptide. Ions exiting the fragmentation cell are separated by their *m/z* in the second mass analyser, where differences in mass from fragment ion peaks are used to determine the amino acid sequence of the peptide.

Alternative fragmentation techniques, such as ETD and ECD, can be used for peptide and protein fragmentation in instances where maintaining non-covalent interactions is crucial. For example, mapping of non-covalent protein complexes in 'top-down MS' experiments [199], mapping post translational modifications [200] and localising sites of electrostatic interactions [201]. Importantly, these fragmentation techniques generate different fragment ions from peptides. Where CID and HCD generally cause fragmentation at the peptide bond, generating b and y ions, ETD and ECD generally cleave the N-Cα bond, resulting in the formation of c and z fragment ions (Figure 2.14) [202-204].

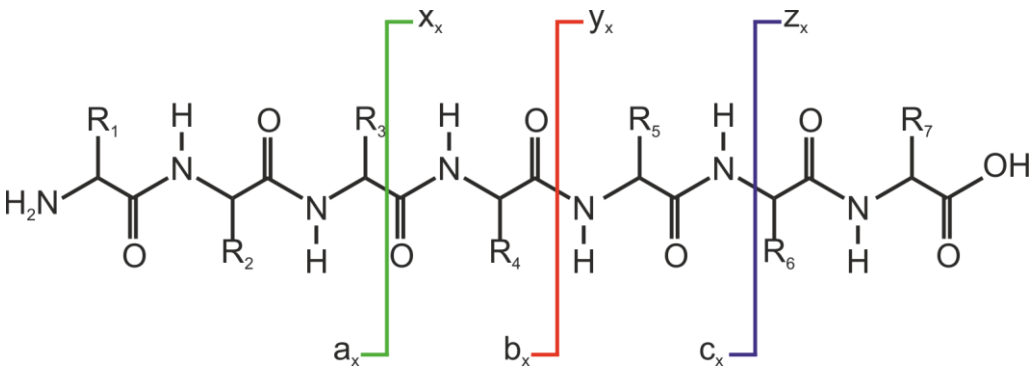

Figure 2.14 Fragment ions generated from peptide ion dissociation. Different fragmentation methods cleave peptides at different bonds. X, y and z ions are formed when the positive charge is retained at the C-terminal side of the peptide. A, b and c ions are formed when the positive charge is retained by the N-terminal side of the peptide. The subscript x defines the number of amino acids present in each ion.

2.4.3 Hydrogen deuterium exchange (HDX)

Developed at the Carlsberg laboratory in the late 1950's [205] (yes, *that* Carlsberg), hydrogen deuterium exchange (HDX) is a non-covalent labelling technique where labile protons, such as those involved in N-H, O-H or S-H bonds [206], are exchanged for deuterium, a heavy isotope of hydrogen with an additional neutron (+1 Da). Although deuterium exchange is detectable by other methods [207-209], the mass difference resulting from deuterium incorporation is readily detectable by MS, which has the advantage of lower sample requirements, and the ability to study larger proteins or protein complexes when compared with other analytical techniques used to measure HDX, such as NMR. Although many variations on this method exist, such as 'exchange-out' reactions (D→H exchange) [210], or rapid pulsed labelling techniques [211], HDX in structural MS is typically performed using the forward exchange reaction (H→D, 'exchange-in') in a continuous labelling approach, where the sample is first diluted into a deuterated buffer solution, and left to equilibrate for a fixed period of time, before quenching the reaction to limit further exchange (Figure 2.15). The deuterated protein sample is then either analysed at the intact level [212], or, more commonly, proteolytically cleaved into peptide fragments before LC-MS analysis is used to separate the labelled peptides, and localise differences in deuterium uptake to peptide level resolution [213].

Although any labile proton in a protein can exchange for deuterium, in practice, many, such as those on amino acid side chains, undergo rapid back-exchange to the protonated form when the reaction is quenched [214], typically leaving only the deuterium incorporated at the amide nitrogen on the peptide backbone. As such, HDX-MS largely only probes deuterium uptake observed at these positions on the protein – with one backbone amide group for each amino acid in the sequence, except proline residues, which have no exchangeable amide group (Table 2.1).

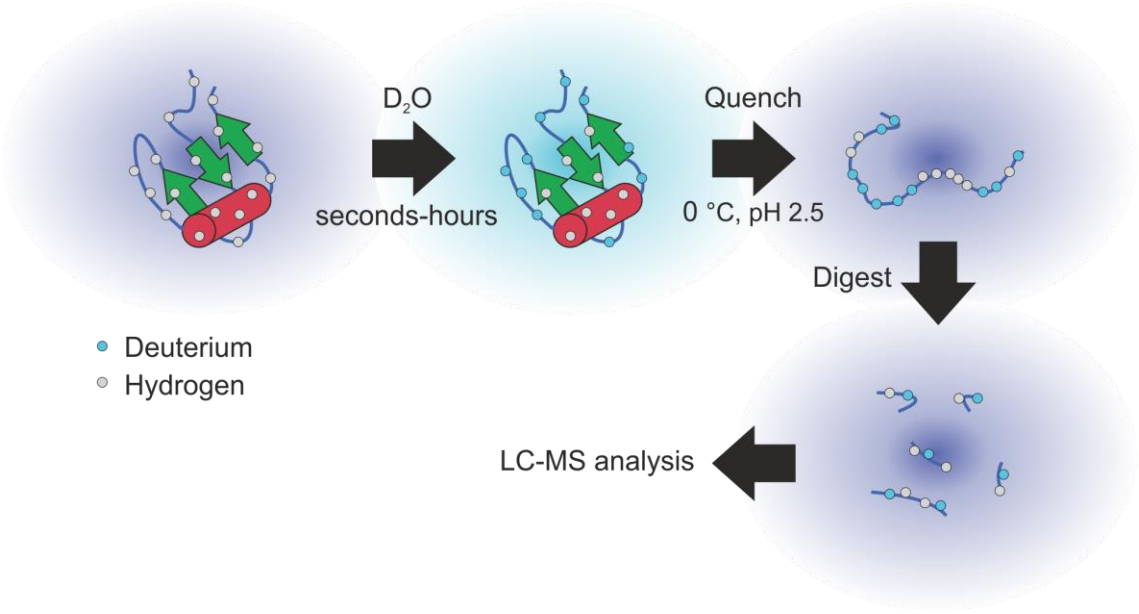

Figure 2.15 General HDX-MS experimental workflow. Protein samples are diluted into deuterated buffer solutions where solvent accessible and exchangeable (i.e. not hydrogen bonded) backbone amide hydrogens exchange for deuterium. After incubation, the reaction is quenched by dilution into low pH, low temperature protiated quench solution, which unfolds the proteins and minimises further deuterium exchange. The protein is then digested into peptides which are then analysed by LC-MS.

Primarily, the two main factors affecting the rate of deuterium exchange in a protein structure are solvent accessibility and hydrogen bonding [211, 215]. Indeed, HDX is particularly sensitive to these factors; backbone amides in folded proteins can have a decreased rate of exchange by 6-8 orders of magnitude compared with unfolded proteins [206, 211]. Increased access to the deuterium buffer solution allows faster deuterium exchange, so exposed regions of the protein increase in mass faster than more buried regions. This makes HDX a useful technique for probing changes in protein conformation [212, 216], or sites of protein-protein [217] or protein-ligand [218] interactions, where changes in solvent accessibility of certain regions of the protein often occur. Additionally, backbone amides involved in hydrogen bonding are protected from exchange [214, 219], allowing HDX to probe changes in hydrogen bonding and secondary structure. Proteins, however, are dynamic entities, where local, or even global, structural fluctuations, as well as transient hydrogen bond separation can occur, resulting in many amide groups in protein structures fluctuating between exchange competent, and non-exchangeable states. These aspects of protein dynamics

give rise to two different exchange regimes in HDX, referred to as EX1 and EX2 kinetics [211, 214].

The exchange mechanism of an amide group in equilibrium between exchange competent (exposed to solvent, not H-bonded) and non-exchangeable (buried, H-bonded) states, loosely defined as 'open' and 'closed', can be described as:

$$\text{N-H}_{\text{closed}} \underset{k_{cl}}{\overset{k_{op}}{\rightleftharpoons}} \text{N-H}_{\text{Open}} \xrightarrow{k_{ch}} \text{N-D}_{\text{Open}} \underset{k_{op}}{\overset{k_{cl}}{\rightleftharpoons}} \text{N-D}_{\text{Closed}}$$

Where k_{op} and k_{cl} are the rate constants for opening and reclosing respectively, and k_{ch} is the chemical rate constant of deuterium exchange, defined as the rate constant measured under conditions of maximal solvent exposure, for amides not involved in hydrogen bonding [206]. The EX1 and EX2 exchange regimes are the result of a kinetic competition between the reclosing of the exchangeable state (formation of a hydrogen bond or protein refolding) and the chemical deuterium exchange rate of the amide group in question. If reclosing is faster than deuterium exchange ($k_{cl} > k_{ch}$), then the probability of successful HDX during a single opening event is small, and opening must occur multiple times before deuterium exchange is likely to take place – this is known as EX2 kinetics. Alternatively, if deuterium exchange is faster than reclosing ($k_{ch} > k_{cl}$) then deuterium labelling is likely to occur on the first available opening event – this is defined as EX1 kinetics, although in practice this is not commonly seen in proteins at physiological pH [206]. During peptide level MS analysis, the two regimes can be distinguished by their distinctive isotope patterns [220, 221] although mixed EX1-EX2 kinetics are often observed [220]. Thus, HDX can be used to study changes in protein dynamics, as well as conformation, protein-protein, and protein-ligand interactions.

Solution pH is also an important factor in HDX where, at near physiological conditions, increases in pH increase the chemical exchange rate by approximately one order of magnitude per pH unit [206]. Consequently, this means that increasing pH above physiological conditions alters the limit of EX1 kinetics as k_{ch} increases [214]. However, as deuterium exchange can be catalysed under both acidic and basic conditions (Figure 2.16a), a complex relationship is observed where both the extremes of pH correlate with faster exchange rates, resulting in a 'V' shaped curve of exchange rate vs pH (Figure 2.16b). This curve has an exchange rate minima for backbone amide groups at ~pH 2.5-3.0, and, as deuterium exchange is also slower at lower temperatures, this pH, and temperatures around 0 °C, are typically used to quench the exchange reaction and minimise further deuterium exchange prior to MS analysis. This is a crucial step in the experimental workflow, not just to prevent further deuterium being incorporated on to the sample, but to reduce back exchange of deuterium from the sample into the protiated ESI solvents used in MS analysis. Although loss of *some* of the deuterium label during analysis is unavoidable, quench conditions decrease the exchange rate by ~5 orders of magnitude from typical labelling conditions (pH 7, 25 °C) [215], and increase the half-life of deuterium on peptides to between 30-120 minutes [222] (approximately 500x less than the half-life of teaspoons in an Australian research institute [223]).

The final significant factor affecting the deuterium exchange rate is the primary sequence of amino acids in the protein. The backbone amide hydrogen of each amino acid residue has a different chemical exchange rate with deuterium (except proline, which has no backbone amide group), governed by inductive and steric effects of the side chain, and side chains of adjacent residues, affecting the acidity of the amide N-H bond, and thus its propensity to exchange with deuterium by acid and base catalysed exchange [224].

Fortunately, the effects of pH, temperature and nearby side chains have been well-characterised [224, 225], and it is now possible to predict the unprotected chemical exchange rate of different amino acids under all conditions [214].

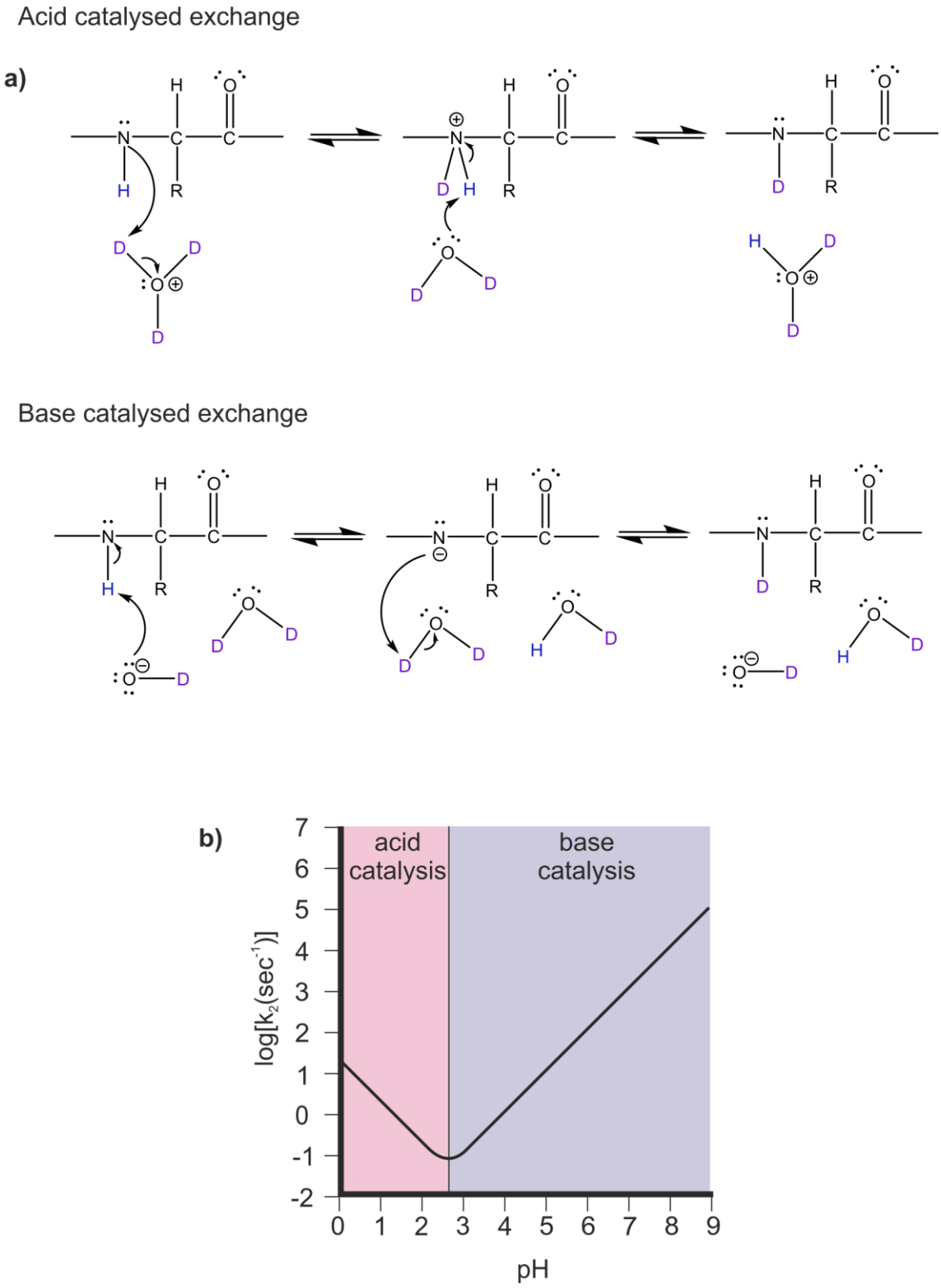

Figure 2.16 Mechanisms of acid and base catalysed deuterium exchange. **a)** Deuterium exchange onto the amide nitrogen of the peptide backbone can occur under acidic (D_3O^+) or basic (OD^-) conditions. This generates a complex relationship between pH and deuterium exchange rate **(b)**, with a 'V' shaped curve with a minimum exchange rate at approximately pH 2.5.

2.4.4 Fast photochemical oxidation of proteins (FPOP)

Developed in the early 2000's [226, 227], Fast Photochemical Oxidation of Proteins (FPOP) is a covalent labelling technique where hydroxyl radicals liberated from photolysis of hydrogen peroxide covalently label solvent accessible regions of the protein. Although hydroxyl radicals can attack almost any region of a protein, where attack on certain residues, or the α-carbon itself can result in fragmentation of the polypeptide backbone [228], more commonly, steric inaccessibility of the backbone leads to hydroxyl radical attack primarily on amino acid side chains, preferentially labelling large hydrophobic residues, or side chains containing sulfur atoms [228]. This hydroxyl radical labelling results in a variety of different covalent modifications of different masses. By far, the most common of these are +16 Da hydroxylations (addition of OH and abstraction of H), although many others are possible, including the formation of carbonyl groups (+14 Da, addition of O and abstraction of 2H), decarboxylation (-30 Da) and deguanidination (-43 Da). A summary of common oxidative modifications, and the side chains on which they are typically observed, are shown in Table 2.2.

Table 2.2 Reactivities and common mass additions in hydroxyl radical oxidation of amino acid side chains. Taken from [228].

Side chain	Reactivity rate (M^{-1} s^{-1})	Common Δmasses (Da)
Cys (most reactive)	3.5 x 10^{10}	+48, +32, -16
Trp	1.3 x 10^{10}	+16, +32, +48 etc
Tyr	1.3 x 10^{10}	+16, +32
Met	8.5 x 10^{9}	+16, +32, -32
Phe	6.9 x 10^{9}	+16, +32, +48
His	4.8 x 10^{9}	+16, -22, -10, +5
Arg	3.5 x 10^{9}	-43, +16, +14
Ile	1.8 x 10^{9}	+16, +14
Leu	1.7 x 10^{9}	+16, +14
Val	8.5 x 10^{8}	+16, +14
Pro	6.5 x 10^{8}	+16, +14
Gln	5.4 x 10^{8}	+16, +14
Thr	5.1 x 10^{8}	+16
Lys	3.5 x 10^{8}	+16, +14
Ser	3.2 x 10^{8}	+16
Glu	2.3 x 10^{8}	-30, +16, +14
Ala	7.7 x 10^{7}	+16
Asp	7.5 x 10^{7}	-30, +16
Asn	4.9 x 10^{7}	+16
Gly	1.7 x 10^{7}	-

A typical FPOP experiment involves a solution containing the protein of interest, hydrogen peroxide (typically <0.5% (*v/v*)), and a free amino acid of moderate hydroxyl radical reactivity, typically histidine or glutamine, known as the scavenger. The purpose of this scavenger amino acid is to control the degree of oxidative

modification on the protein analyte, and control the lifetime of hydroxyl radicals in solution [229]. If more labelling/longer labelling timescales are required, then a less reactive, or lower concentration of scavenger can be added to the solution, and *vice versa* [230]. This solution is irradiated with UV light, typically of 248 nm wavelength, causing photolysis of the solution hydrogen peroxide, generating the desired hydroxyl radicals [231]. Although it has been demonstrated that a considerable proportion of these radicals rapidly recombine back into hydrogen peroxide [230], the remaining radicals go on to covalently label the protein analyte and scavenger amino acid, before the reaction is quenched, typically with a mixture of catalase, an enzyme which degrades excess hydrogen peroxide, and methionine, a highly reactive free amino acid which removes any radicals left in solution (Figure 2.17) [231].

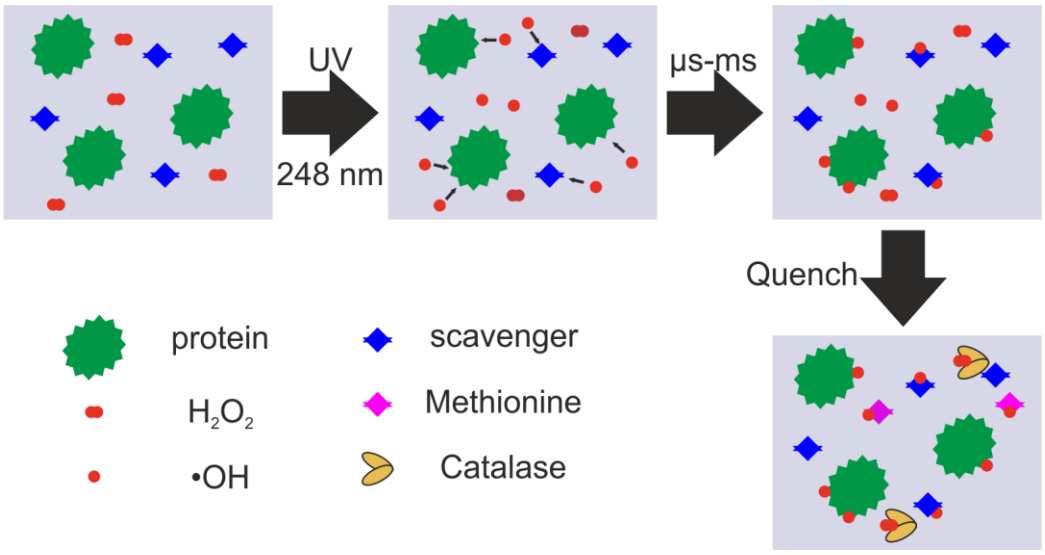

Figure 2.17 General theory of FPOP labelling. Solution containing the protein sample, hydrogen peroxide and a scavenger amino acid is irradiated with 248 nm UV light, causing photolysis of the hydrogen peroxide, generating hydroxyl radicals. These hydroxyl radicals then covalently label the protein sample, before the reaction is quenched to prevent further radical oxidation.

The rationale behind performing an FPOP experiment is that a side chain with greater access to solvent, such as those on the surface of proteins, will also have greater access to the hydroxyl radicals in solution, and will undergo more oxidative labelling than

side chains with less solvent accessible surface area. Although the target, and nature of the labelling is very different, these characteristics mean FPOP can be used to probe many of the same changes as HDX; changes in protein structure, conformation and dynamics, as well as protein-protein or protein ligand interactions, all of which can change a side chain's accessibility to solvent, and thus its degree of oxidative modification in FPOP. Again similar to HDX, changes in FPOP oxidative labelling can be observed by introducing the protein sample into the mass spectrometer intact, and quantifying the observed distributions of different mass modifications. However, unlike HDX, quenching can be performed under neutral pH conditions, and the covalent nature of the label means that no back exchange occurs during the experiment. Combined, these properties make proteolytic digestion and LC-MS/MS analysis of the oxidised peptides a more attractive option, as choice of digestive enzyme is not restricted to acid proteases as in HDX, and lengthy analytical procedures can be used to analyse the resulting peptides, without the concern of losing the label.

However, unlike the wealth of knowledge available concerning solution conditions and protein structure on deuterium labelling in HDX [224, 225], these parameters are not well understood with regards to oxidative labelling in FPOP. Work by Xie *et al.*, has shown a positive correlation between the fraction of the side chain that is exposed to solvent and the extent of modification observed, normalised for the reactivity of each side chain [232]. However, this relationship was only observed for the most reactive side chains, while the correlation was less clear or absent for less reactive residues. The authors proposed that highly reactive side chains compete for hydroxyl radicals with nearby side chains that are less reactive, highlighting possible effects of sequence or local environment on the extent of oxidative modification, in addition to solvent accessible surface area [232]. Similarly, although it is not currently disputed that the primary radical generated by FPOP, the hydroxyl radical, labels the protein sample on the timescale of μs under typical FPOP solution conditions [230], Vahidi *et al.*, have demonstrated that radicals in FPOP experiments can exist in such solutions for up to

a millisecond, suggesting that generation of secondary radicals, possibly with dissolved oxygen, can continue to label the protein long after the primary hydroxyl radicals have been exhausted [233]. Additionally, despite the covalent nature of the label making residue level assignment of modifications trivial *in principle*, *in practice* the complex, manual, and time intensive nature of the data analysis is such that FPOP oxidations are commonly quantified to peptide level resolution [231, 234].

Nevertheless, despite these shortcomings in our current understanding of the technique, FPOP holds great potential as a structural MS method of the future. Espino *et al.,* have already shown that FPOP can be performed in live cells to probe protein structure *in vivo* [235]. Others have demonstrated that generation of hydroxyl radicals can be used, not just to label the proteins themselves, but to generate other radicals with different side chain labelling preferences [236, 237]. Numerous studies have also highlighted the role of FPOP in epitope mapping and antibody structure – a crucial step in assessing the role of FPOP for industrially relevant applications in biopharma and biotechnology [238-241].

2.5 Aim of the thesis

The aims of this thesis are threefold (Figure 2.18):

1. Use the two well-characterised variants of β2m (wild-type and ΔN6) as a benchmark to develop FPOP, compare the results with existing structural MS methods, such as HDX, and gain insight on the usefulness and limitations of FPOP to study the structure of aggregation-prone proteins. This information will be used to guide the remaining two goals.
2. Using what can be learned from this method development, examine the structure of D76N β2m and compare these results with the wild-type protein, with a view to understanding how such similar structures can be associated with significantly different aggregation propensities, as well as probing any similarities in structure to the, already aggregation-prone, ΔN6 variant.

3. Test the effectiveness of FPOP to characterise the mAbs WFL and STT, determine any structural changes caused by the amino acid substitutions that may be linked to the propensity of WFL to undergo reversible self-association, and assess the utility of FPOP, more generally, in characterising large, complex biopharmaceutical molecules, such as mAbs.

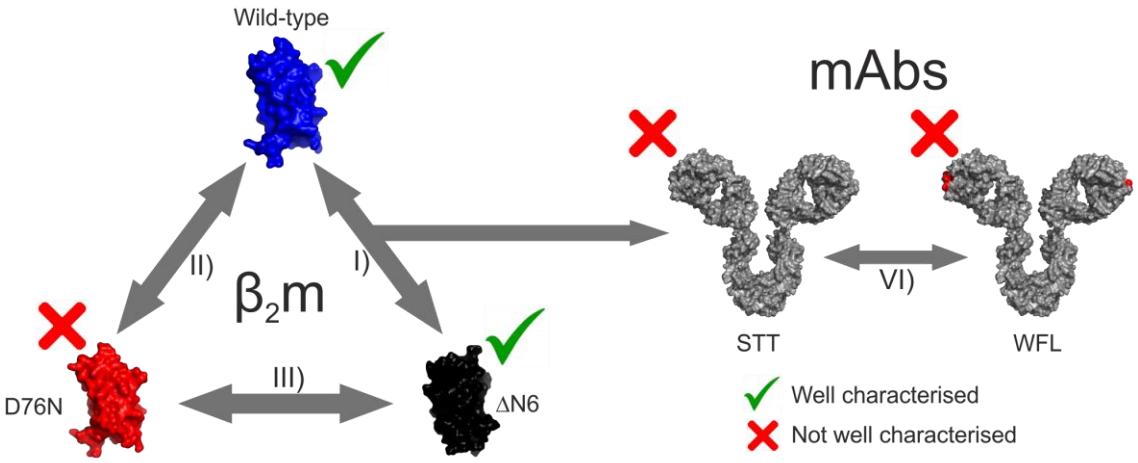

Figure 2.18 Aims of this thesis. **I**) Use two well characterised variants of β2m to develop FPOP and compare these data with more well-established structural MS methods, including HDX. These developments will be used to compare the D76N β2m variant with both the wild-type protein (**II**) and the ΔN6 variant (**III**) to assess any structural changes caused by the amino acid substitution which affect the propensity of the protein to aggregate. **VI**) The method development from FPOP will be used to assess the utility of the technique to characterise WFL and STT, and gain insight on any structural/dynamical changes linked to reversible self-association in these mAbs.

Chapter 3:

Materials and methods

3 Materials and methods

3.1 Protein preparation and purification

3.1.1 Wild-type, D76N and ΔN6

The three variants of β_2m were each overexpressed in BL21 [DE3] pLysS cells containing a pET23a plasmid containing either the wild-type β_2m gene, the D76N gene (identical to wild-type with the exception of a G→A base substitution at positions 286), or the ΔN6 gene (missing the six N terminal amino acids) (Figure 3.1).

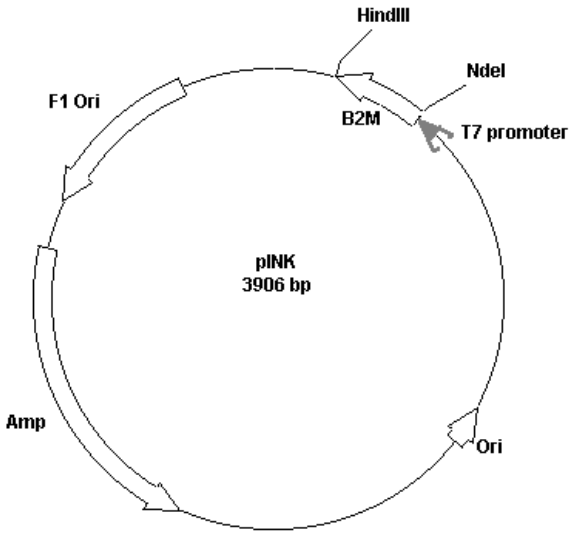

Figure 3.1 The pINK plasmid containing the gene of one of three variants of β_2m. Expression of the β_2m protein is under control of the T7 promoter, and the plasmid contains an ampicillin resistance selection marker.

Glycerol stocks (provided by Dr Hugh Smith) containing BL21 [DE3] pLysS *Escherichia coli* carrying the Pet23a plasmid with either the wild-type, D76N or ΔN6 gene were used to grow starter cultures containing 100 ml lysogeny broth (LB – Melford Laboratories, Ipswich, UK), 50 μg ml^{-1} carbenicillin and 50 μg ml^{-1} chloramphenicol. These were incubated overnight at 37 °C with aeration (200 rpm).

Large scale 1 L cultures were then set up containing 25 g LB, 5 ml of starter culture and 50 μg ml^{-1} carbenicillin. These were incubated at 37 °C with aeration (200 rpm) to an OD_{600} of 0.6 and then induced with 1 mM isopropyl β-D-1-thiogalactopyranoside (IPTG) before overnight incubation (37 °C, 200 rpm).

After 16 hours, cells were harvested by centrifugation at 15,000 rpm for 20 minutes using a Beckman JLA 16.250 rotor (approximately 33,700 G) (4 °C). The cell pellets were incubated in 200 ml lysis buffer (100 μg ml^{-1} lysozyme, 50 μg ml^{-1} phenylmethylsulfonyl fluoride (PMSF), 20 μg ml^{-1} DNase, 1 mM ethylenediaminetetraacetic acid (EDTA) in 25 mM Tris.HCl pH 8.0) for 30 min at room temperature before being further lysed using a cell disrupter (constant cell disruptor systems, Northhants, UK) at a pressure of 30 kpsi.

This cell lysate was then centrifuged as above for 30 min. The resulting pellet (containing the inclusion bodies) was then washed with 200 ml, 25 mM Tris.HCl pH 8.0 and any dark material on the pellet surface was removed. The pellet was then resuspended in 200 ml 25 mM Tris.HCl pH 8.0 and centrifuged again (as above). This process was repeated three times to remove any dark material left on the pellet surface following centrifugation.

The resulting clean pellet was then solubilised in 200 ml, 25 mM Tris.HCl pH 8.0 containing 8 M urea and incubated at room temperature overnight with gentle stirring, before a final centrifugation step (15,000 rpm for 1 hour) was used to remove any precipitate.

The protein was then allowed to refold by dialysis into 5 L, 25 mM Tris.HCl pH 8.0, using 3500 molecular weight cut off (MWCO) dialysis tubing (Thermo Scientific, Hemel Hempstead, UK). The dialysis buffer was changed a total of 6 times with a two hour equilibration period between changes.

Refolded protein was then purified by anion exchange chromatography using an XK50 fast-flow Q-Sepharose column (GE Healthcare, Buckinghamshire, UK). The column was equilibrated with 2 column volumes of buffer (25 mM Tris.HCl pH 8.0)

before the refolded protein was added. The bound protein was then eluted with a 0-125 mM NaCl gradient at room temperature in 25 mM Tris.HCl pH 8.0 buffer. Eluted fractions containing the protein were then dialysed into purite 18 MΩ water using the above dialysis protocol, before being concentrated to ≈ 1 mM using Sartorius vivaspin 2, 3,000 MWCO spin columns.

The refolded, concentrated ion exchange product was then filtered (0.22 μm filter units, Fischer Scientific) and further purified by size exclusion chromatography using a Superdex 75 prep grade XK 26/60 column (Amersham Biosciences, Buckinghamshire, UK) equilibrated with 150 mM ammonium acetate (pH 7.4) at room temperature. The eluted fractions containing monomeric protein were collected and analysed by SDS-PAGE to confirm the presence of monomeric β_2m (or D76N/ΔN6). These fractions were then pooled, and stored at ≈400 μM at -80 °C.

Protein preparation and purification of all three variants of β_2m was carried out with the help and supervision of Dr Hugh Smith (Radford research laboratory).

3.1.1.1 SDS-PAGE

Tris-tricine buffered SDS-PAGE gels were used to confirm the presence of β_2m in the eluted gel filtration fractions. Samples were diluted 1:1 with 2X loading buffer (50 mM Tris.HCl pH 6.8, 100 mM dithiotheritol (DTT), 2% *w/v* sodium dodecyl sulphate (SDS), 0.1% *w/v* bromophenol blue, 10% *v/v* glycerol) and boiled for 5 min prior to being loaded onto the gel. A 60 mA current was applied until the samples had entered the resolving gel, at which point the current was increased to 100 mA. The completed gels were then stained with Instant Blue (Expedeon protein solutions, Cambridgeshire, UK) overnight and then imaged using the Genesnap software (Syngene bioimaging). Molecular weight markers used for SDS-PAGE analysis were 2-250 kDa precision plus protein standard ladders (Bio Rad, Hertfordshire, UK). Components of the resolving and stacking gels are listed in Table 3.1. The cathode

running buffer was 100 mM Tris 100mM tricine, 0.1 % (*w/v*) SDS, pH 8.25. The anode running buffer was 200 mM Tris.HCl, pH 8.9.

Table 3.1 Solution components of Tris-tricine buffered SDS-PAGE gels used for analysis of β_2m.

Solution Component	Volume added to stacking gel (ml)	Volume added to Resolving gel (ml)
30% *w/v* acrylamide: 0.8% *w/v* bis-acrylamide	7.5	0.83
3 M Tris.HCl, 0.3% *w/v* SDS pH 8.45	5.0	1.55
H_20	0.44	3.72
Glycerol	2.0	0
10% *w/v* ammonium persulfate	0.1	0.2
TEMED	0.01	0.01

3.1.1.2 Circular dichroism spectroscopy

Circular dichroism (CD) experiments were performed in the far-UV range (wavelengths of 200 nm-260 nm with a 1 nm step size) on a Chirascan plus CD spectrometer (Applied PhotoPhysics, Surrey, UK) at 25°C. Each sample contained 20 μM protein (≈0.2 mg ml^{-1} for β_2m), in 25 mM sodium phosphate buffer (pH 7.4). The pathlength was 1 mm. Measured ellipticity at each wavelength was converted to mean residue ellipticity using Equation 3.1 [242].

$$[\theta] = \frac{\theta \times MRW}{10 \times d \times c} \quad (3.1)$$

Equation 3.1 Conversion of measured ellipticity to mean residue ellipticity. Where θ is the measured ellipticity (degrees) MRW is the mean residue weight, d is the path length (cm) and c is the protein concentration (g ml^{-1}).

CD experiments were carried out by Dr Hugh Smith (Radford research laboratory).

3.1.2 WFL and STT

The two mAb variants MEDI1912_WFL and MEDI1912_STT were provided by AstraZeneca (formerly Medimmune) in formulation buffer (125 mM L- arginine, 20 mM sodium succinate, pH 6.0).

3.2 Native MS

3.2.1 Sample preparation

Samples prepared for native MS were 2x buffer exchanged into 150 mM ammonium acetate (pH 7.4) using 7k MWCO zeba spin desalting columns (Thermo Scientific, Hemel Hempstead, UK). The final sample was diluted to a concentration of 10 μM, calculated based on the absorbance at 280 nm and the Beer-Lambert law, using an extinction coefficient of 20065 M^{-1} cm^{-1} for all β_2m variants.

Samples were then loaded into borosilicate glass capillaries pulled in-house (Sutter Intrument Company, Novato, CA, USA) and coated with palladium using a sputter coater (Polaron SC7620, Quorum Technologies Ltd, Kent, UK).

3.2.2 Waters Synapt G1 HDMS

The instrument was first calibrated using ~10 mg ml^{-1} caesium iodide clusters across the *m/z* acquisition range (usually 500-8000 *m/z*) before data were analysed using MassLynx v4.1 and Driftscope v3.0 (Waters, Wilmslow, UK), if IMS acquisition mode was active. All samples were analysed in positive ionisation mode.

Ion mobility experiments were performed under two different sets of T-wave conditions. Source and T-wave conditions for the instrument in each case are listed in Table 3.2.

Table 3.2 Summary of instrument source and IMS conditions used in native IMS-MS experiments.

Instrument Parameter	T-wave 1 (CCS calculations)	T-wave 2 (detailed ATD analysis)
Cone voltage (V)	70	70
Backing Pressure (mbar)	2.1	2.1
IMS T-wave velocity (ms^{-1})	200	300
IMS T-wave height (V)	4-20 V ramp (100% cycle)	4-10 V ramp (100% cycle)
m/z acquisition range	500-8000	500-8000
Trap CE (V)	5	5
Transfer T-wave velocity (ms^{-1})	248	248
Transfer T-wave height (V)	3	3

3.2.2.1 Calculating rotationally averaged collision cross sections

The calibration approach used here is taken from Ruotolo *et al* [66]. CCS values were calculated by manual calibration using native calibrant proteins from the Bush database of known CCS values generated from drift cell measurements [69]. These CCS values were corrected for ion mass, charge state and the buffer gas mass, according to Equation 3.2.

$$\Omega' = \frac{\Omega_{Lit}}{z\sqrt{\left(\frac{1}{m} + \frac{1}{m_g}\right)}} \quad (3.2)$$

Equation 3.2 Correcting literature CCS for mass, charge and buffer gas mass. Where Ω' is the corrected CCS, Ω_{Lit} is the published literature cross section for the calibrant protein, derived from DTIMS measurements, z is the ion charge state, m is the ion mass and m_g is the buffer gas mass. The term in brackets is equivalent to the reciprocal of the reduced mass of the ion neutral pair (μ from Equation 1.9).

Drift time measurements of calibrant proteins were then corrected for *m/z* dependent flight time between the exit of the transfer cell and the pusher region [243] according to Equation 3.3. Flight time for ions to traverse the transfer cell is also included in the measured drift time. Although this can be corrected for, knowing the length of the transfer cell and the transfer T-wave velocity [66], this correction was not applied in our experiments for simplicity, as this flight time is independent of *m/z* and only made minimal changes to measured CCS values, well below other sources of error (i.e. calibration, precise determination of peak apex) [63].

$$t'_D = t_D - \frac{C\sqrt{\frac{m}{z}}}{1000} \quad (3.3)$$

Equation 3.3 Correcting drift time for *m/z* dependent flight time. Where t'_D is the corrected drift time, t_D is the measured drift time, *m/z* is the mass to charge ratio of the ion and C is the enhanced duty cycle (EDC) delay coefficient.

Corrected drift time and corrected CCS values from calibrant proteins were then used to generate a linear calibration plot (Equation 3.4).

$$\Omega' = A\, t'_D + N \quad (3.4)$$

Equation 3.4 Linear calibration curve used to determine unknown CCS values from analyte proteins. Where Ω' is the corrected CCS of the analyte protein, A is the fit determined slope of the curve, t'_D is the corrected drift time of the analyte protein, and N is the fit determined y axis intercept.

Fit determined constants from the calibration plot were used to determine CCS values of analyte proteins, by combining Equation 3.2 and Equation 3.4 (Equation 3.5).

$$\Omega = A\, t'_D + N\, z \sqrt{\left(\frac{1}{m} + \frac{1}{m_g}\right)} \tag{3.5}$$

Equation 3.5 Calculation of CCS values for analyte proteins based on a linear calibration plot. Where Ω is the calculated CCS of the analyte protein, A and N are fit determined constants from the calibration curve (Equation 3.4), t'_D is the corrected drift time of the analyte protein, z is the charge state of the analyte protein, m is the ion mass and m_g is the buffer gas mass.

IMS data for calibrant proteins and analyte proteins were acquired on the same day under identical IMS conditions. Literature CCS values were taken from a database of published cross sections [69]. Although N_2 was used as a separation gas in the IMS cell of the Synapt instrument, CCS values acquired in He separation gas were used for calibration [69] as these allow comparison to computationally derived CCS values, where He is the most commonly used *in silico* buffer gas [190]. Annotation for CCS values in this thesis follows recommendations by Gabelica *et al.,* [244] and will be shown as: $^{TW}CCS_{N2>He}$.

Peak top times from IMS arrival time distributions (ATDs) were determined by Gaussian curves fitted to ATD data using the multiple peak fit function from Origin 2017 (Origin Lab Corporation).

3.2.3 Calculation of *in silico* CCS

To calculate CCS values from protein structures derived from X-ray crystallography or NMR data, gas phase molecular dynamics (MD) simulations (i.e. absent of solvent) were first performed on the analyte PDB structures using NAMD (v2.9) [245] and the

CHARMM force field [246]. A radial cut-off of 12 Å around each atom was used with a time-step of 2 fs. Simulations were run for 2 ps and kept at a constant temperature of 300 K.

The resulting post-MD structures were used as input data for IMPACT, a software developed by the Robinson group to determine *in silico* CCS values from protein structures [190].

3.3 Intact mass analysis

Intact mass analysis for accurate mass determination was performed using a Waters Xevo G2-XS Q-TOF MS operating in MS mode. Prior to introduction into the mass spectrometer, protein samples at a concentration of 5 µM, were loaded onto a MassPREP micro desalting column (Waters corporation, Wilmslow, Manchester, UK) before being eluted with an MeCN gradient containing 0.1% *v/v* formic acid.

3.4 Hydrogen Deuterium Exchange

3.4.1 Experimental

HDX-MS experiments were carried out using an automated sample handling robot (LEAP technologies, Fort Lauderdale, FL, USA) coupled to an M-Class Acquity LC system and HDX manager (Waters Ltd., Wilmslow, UK). 30 µl of protein stock solution containing 8 µM of either wild-type β_2m, D76N or ΔN6 in equilibration buffer (10 mM potassium phosphate, pH 7.4) was added to 135 µl of deuterated label buffer (10 mM potassium phosphate, pD 7.4). This was incubated at 4 °C for 30, 60, 120, 1800 or 7200 seconds, before 50 µl of the labelled solution was quenched by dilution into 100 µl quench buffer (10 mM potassium phosphate, 2 M guanidine HCl, 200 mM tris(2-carboxyethyl)phosphine pH 2.2) at 1 °C, giving a final quench pH ~ 2.5. 50 µl of quenched sample (~ 24 pmol) was passed through an immobilised ethylene bridged hybrid (BEH) pepsin column (Waters Ltd., Wilmslow, UK) at 20 °C at a flow rate of

500 µl min^{-1} before the resulting peptides were trapped using a VanGuard pre-column Acquity UPLC BEH C18 trap column (1.7 µm, 2.1 µm x 5 µm, Waters Ltd., Wilmslow, UK). After valve switching, the resulting peptic peptides were transferred to a C18 column (75 µm x 150 mm, Waters Ltd., Wilmslow, UK) and separated by gradient elution of 0-40% MeCN (0.1% *v/v* formic acid) in H_20 (0.3% *v/v* formic acid) over 7 minutes at 40 µl min^{-1}. Peptides were analysed using a Synapt G2Si mass spectrometer (Waters Ltd., Wilmslow, UK) operating in DIA mode. Dynamic range extension, with an $HDMS^E$ workflow (with ion mobility separation) was used to separate peptides prior to fragmentation in the transfer cell (exact details of this type of workflow are described in [247].

3.4.2 Data processing and analysis

HDX data were processed using Protein Lynx Global Server (PLGS v3.0.2) and DynamX (v3.0.0) software supplied with the mass spectrometer. Criteria for confidently identified peptides were as follows: min intensity = 1000, min products per amino acid = 0.3, max sequence length = 25, max ppm error = 5, file threshold = 4/5 replicates.

To visualise data and generate difference plots, data were further processed using an in-house developed algorithm originally written in R by the author, and later developed by Dr James Ault (MS facility manager) using R and Java. This processing method, named PAVED (positional averaging for visualising exchange data), combines the mean relative fractional uptake values per residue, along with their standard deviations from replicate measurements, per time point, for all peptides covering a given residue.

Further details on the development and functioning of this algorithm can be found in Section 4.4. The original R code developed by the author for the first version of this algorithm (not the final version in PAVED) can be found in Section 8.1.

3.5 Fast Photochemical Oxidation of Proteins

3.5.1 Experimental procedures for the analysis of β_2m

Immediately prior to UV irradiation, 1 µl of 5% *v/v* H_2O_2 was added to 100 µl of protein solution containing 10 µM of protein (either wild-type β_2m, D76N or ΔN6) and 20 mM L-histidine in 10 mM potassium phosphate pH 7.4, to give a final H_2O_2 concentration of 0.05 % *v/v*. The sample was then passed at a flowrate of 20 µl min^{-1}, through a fused silica capillary (inner diameter: 100 µm) and exposed to UV irradiation (beam width ~3 mm) using a Compex 50 Pro KrF excimer laser operating at 248 nm (Coherent Inc., Ely, UK) with a firing frequency of 15 Hz and a pulse duration of 20 ns. Laser power was kept constant at 110 mJ. The outflow from the capillary was collected in an Eppendorf tube containing 20 µl quench solution (100 mM L-methionine, 1 µM catalase in 10 mM potassium phosphate pH 7.4) and placed immediately on ice.

Following UV irradiation and quenching, the single disulphide bond in β_2m was reduced by incubation with 10 mM DTT for 1 hr at 55 °C, shaking at 500 rpm. The resulting free thiols were alkylated (incubation with 55 mM iodoacetamide for 45 min, 20 °C at 500 rpm in the dark). A 1:50 *w/w* ratio of chymotrypsin:protein was then added, and left for 18 hours at 37 °C, shaking at 500 rpm, to digest the samples into peptides.

The resulting chymotryptic peptides (1 µl at 0.5 µM peptide concentration) were injected onto a UPLC M-Class Acquity system equipped with a C18 column (75 µm x 150 mm, Waters Ltd., Wilmslow, UK) and separated by gradient elution of 1-50% MeCN in H_2O, over 60 min at 0.3 µl min^{-1}, where both mobile phases contained 0.1% *v/v* formic acid. Peptides eluting from the UPLC were analysed using a Q-Exactive Plus orbitrap mass spectrometer (ThermoFisher, Bremen, Germany) operating in DDA mode with the following acquisition parameters: TopN = 5, max injection time = 300 ms, dynamic exclusion = 3 s.

3.5.2 Experimental procedures for the analysis of WFL and STT

Immediately prior to UV irradiation, 3 µl of 5% *v/v* H_2O_2 was added to 100 µl of protein solution containing 0.1 mg ml^{-1} of either WFL or STT and 10 mM L-histidine in formulation buffer (125 mM L- arginine, 20 mM sodium succinate, pH 6.0), to give a final H_2O_2 concentration of 0.15 % *v/v*. The sample was then passed at a flowrate of 20 µl min^{-1}, through the FPOP experimental setup and quenched as described in Section 3.5.1.

Following UV irradiation and quenching, disulphide bonds were reduced by incubation with 10 mM DTT for 1 hr at 65 °C, shaking at 500 rpm. The resulting free thiols were alkylated (incubation with 55 mM iodoacetamide for 45 min, 20 °C at 500 rpm in the dark). A 1:50 *w/w* ratio of trypsin:protein was then added, and left for 18 hours at 37 °C, shaking at 500 rpm, to digest the samples in to peptides.

The resulting tryptic peptides (1 µl at 0.5 µM peptide concentration) were injected onto a UPLC M-Class Acquity system equipped with a C18 column (75 µm x 150 mm, Waters Ltd., Wilmslow, UK) and separated by gradient elution of 1-60% MeCN in H_2O, over 90 min at 0.3 µl min^{-1}, where both mobile phases contained 0.1% *v/v* formic acid. Peptides eluting from the UPLC were analysed using an Orbitrap Fusion mass spectrometer (ThermoFisher, Bremen, Germany) operating in orbitrap-iontrap mode where the orbitrap was operated at 240,000 resolution and the linear ion trap was operated in rapid mode. The following DDA acquisition parameters were used: TopN = 7, max injection time = 200 ms, dynamic exclusion = 3 s.

3.5.3 Data processing and analysis

Peptides were identified using PEAKS v8.5 (Bioinformatics Solution Inc., Waterloo, ON, Canada). Variable mass additions of +16 Da, +32 Da, +14 Da, +73 Da and +89 Da were searched to identify FPOP oxidations (the latter two being singly and doubly oxidised cys side chains following carbamidomethylation). MS/MS data were manually curated to identify and assign genuine FPOP oxidations. Data were then

quantified manually at the residue level using Xcalibur software (v4.0.27.19, ThermoFisher, Bremen, Germany) by integrating peaks in the extracted ion chromatograms (XICs) of each peptide ion, generated by extracting the *m/z* of the base peak of each peptide isotope distribution, for each charge state, for the modified and unmodified versions of each peptide using Equation 3.6.

$$\%\, Modified = \frac{\sum Modified_{Peak}}{Unmodified + \sum Modified_{All\ Peaks}} \quad (3.6)$$

Equation 3.6 Quantifying FPOP oxidations at residue level resolution. The modified peak of interest, generated from using XIC analysis, is quantified against the ion counts of all other identifiable versions of the peptide, both modified and unmodified.

3.5.4 Calculation of solvent accessible surface area

Calculation of the solvent accessible surface area of side chains in the NMR structures of wild-type and ΔN6 was performed in Pymol using the "get_area" command. Dot_solvent was set to on. Dot_density was set to 4.

3.6 Homology modelling of mAbs

Homology models of the Fab and Fc domains of MEDI19129-WFL were generated using SWISS-MODEL [248]. The homology model for the Fab domain was generated using PDB: 5WKZ [249] and the homology model for the Fc domain was generated using PDB: 5K65 [250] which had sequence identities to WFL of 95.23% and 89.81% respectively. These homology models were then roughly aligned into the canonical 'Y' shape of an IgG using PDB: 1IGY [251].

Chapter 4:

IMS-MS and HDX-LC-IMS-MS/MS comparing β_2m variants

4 IMS-MS and HDX-LC-IMS-MS/MS comparing β_2m variants

The three variants of β2m (wild-type, D76N and ΔN6, discussed in detail in Section 2.2) provide an ideal model system to study both the structural and dynamical factors which make proteins amyloidogenic, and to develop methods which can provide unique insights in the characterisation of such factors. The D76N variant, for example, differs by only a single amino acid from the wild-type protein in sequence, but exhibits a significantly increased propensity to aggregate, thus offering an opportunity to study how this amino acid substitution affects the protein structure, and why these differences modulate the aggregation propensity of this, largely unstudied, β2m variant so significantly. Similarly, both ΔN6 and the wild-type protein are well-characterised protein variants with known structures [78], and provide a useful benchmark to develop new methods or analysis techniques to study aggregation-prone proteins.

This chapter summarises the beginnings of the investigation into the structure and dynamics of the three variants of β2m with three main aims:

1. Perform an initial characterisation of the recombinantly expressed β2m variants to ensure purity and correct folding.
2. Perform a low resolution structural characterisation of the three variants using IMS, to establish any global effects of the D76N mutation, or global similarities to the ΔN6 truncation variant.
3. Analyse the three variants using HDX to identify changes in structure or dynamics caused by the D76N mutation at higher resolution, and use the well-characterised wild-type and ΔN6 variants to develop new HDX-MS analysis techniques.

Data for the wild-type protein and for the ΔN6 truncation variant shown in the HDX section of this chapter were subsequently published in Cornwell., *et al.*, JASMS, 2019 [252].

4.1 Protein preparation and initial characterisation

Wild-type, D76N, and ΔN6 β2m were expressed recombinantly and purified as described in Section 3.1. The final gel filtration purification step showed all three proteins eluting as a single peak from the size exclusion column (an example of wild-type β2m is shown in Figure 4.1). SDS-PAGE analysis of fractions collected from the gel filtration eluate show the elution peak to consist of pure protein with a band at approximately 12 kDa consistent with the mass of monomeric β2m (Figure 4.1b). For the wild-type protein, pooling fractions 4-7 (Figure 4.1b) generated a final yield of ~40 mg L^{-1} (10 L total prepared volume), which was approximately consistent across all three variants.

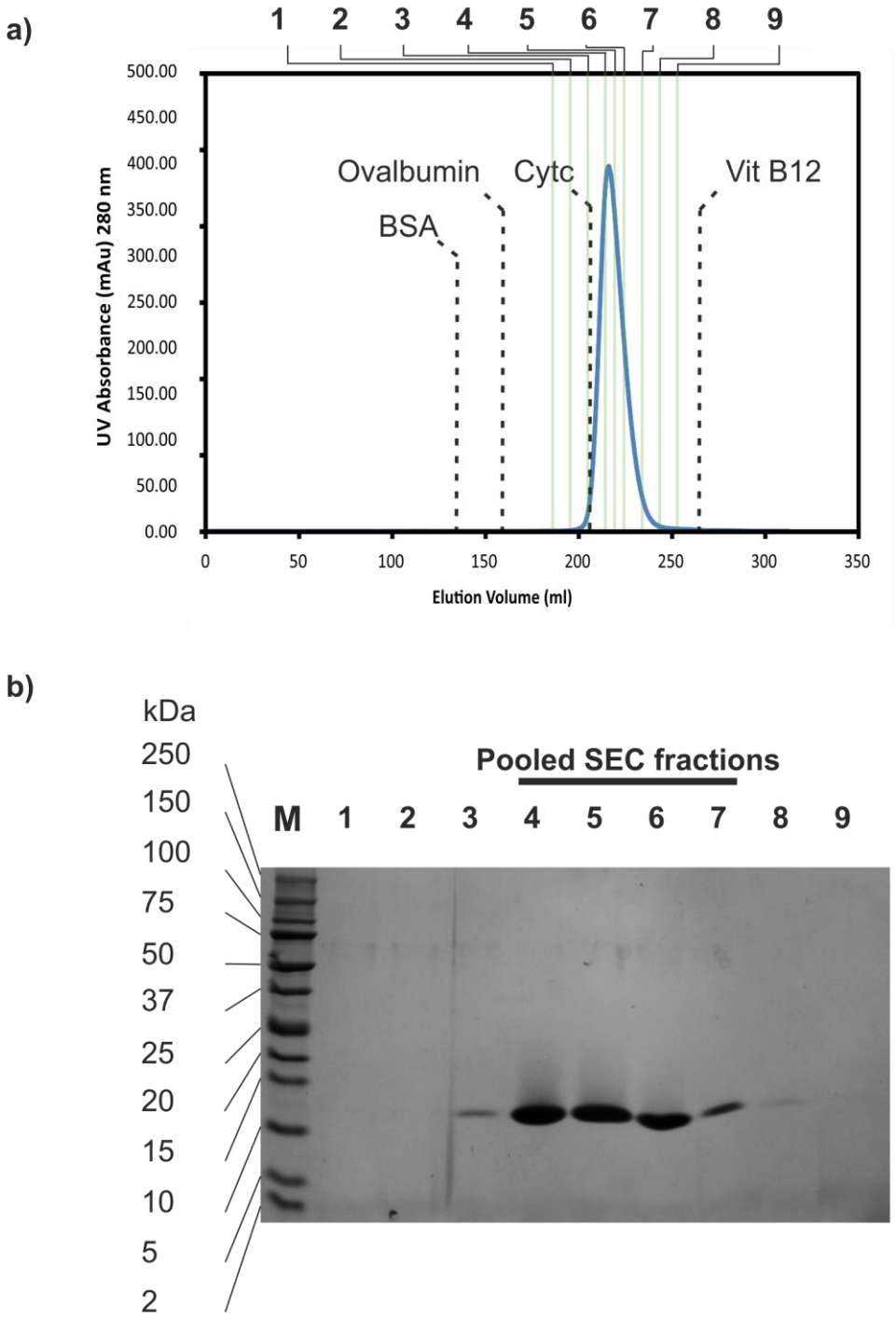

Figure 4.1 Size exclusion purification of wild-type β2m. **a**) The single peak at elution volume ~ 225 ml is found at a similar elution volume to the calibrant protein cytochrome c (dashed vertical lines) and corresponds to monomeric β2m. **b**) Fractions collected at nine different elution volumes (green vertical lines in **a**) analysed by SDS-PAGE showing a single band for each fraction at ~12 kDa corresponding to wild-type β2m.

To ensure that the protein samples had refolded correctly from the preparation process, which was initiated from a urea unfolded state (see Section 3.1 for details),

far UV-CD was used to assess bulk protein secondary structure (Figure 4.2). For both the wild-type protein and the ΔN6 truncation variant, these data are consistent with previously published CD spectra [146, 159]. The D76N variant shows a remarkably similar CD spectrum to that of the wild-type protein which consistent with the observed similarity of their folded protein structures and β-sheet content [77, 157].

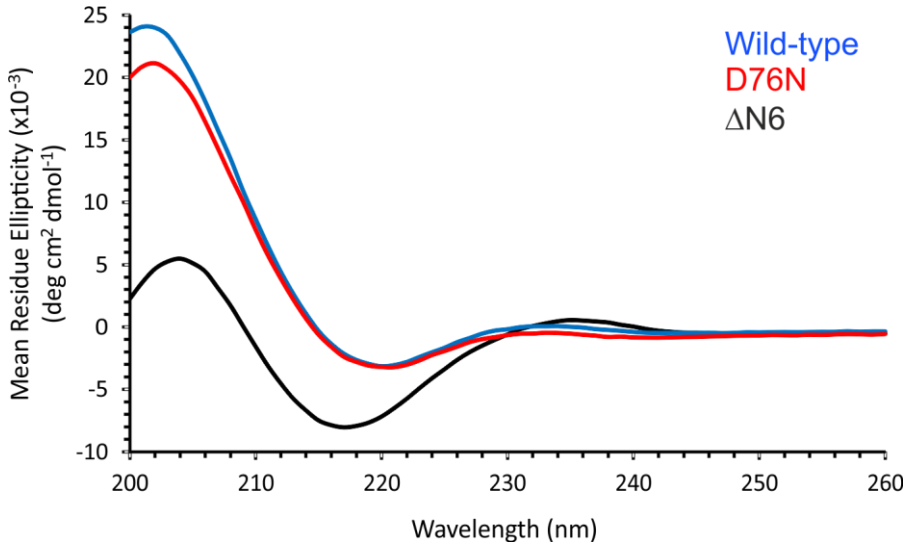

Figure 4.2 CD spectra for three variants of β2m. Traces for the wild-type protein (blue), D76N (red) and ΔN6 (black) are shown. Detailed experimental conditions can be found in Section 3.1.1.2. Dr Hugh Smith of the Radford research laboratory is gratefully acknowledged for acquiring these data.

For final characterisation of the β2m samples, accurate mass analysis was performed under denaturing conditions to determine the precise mass of each prepared protein sample (Figure 4.3). The data show masses of 11860.36 ± 0.02 Da, 11859.35 ± 0.05 Da and 11136.29 ± 0.98 Da for the wild-type protein, the D76N variant, and the ΔN6 truncation variant, respectively. These match closely the theoretical average masses for each variant (11860.4 Da, 11859.4 Da and 11136.5 Da) indicating the presence of the intact disulphide bond in all three variants, and identifying the 1 Da difference in mass between the wild-type protein and the D76N variant, associated with the D→N amino acid substitution (Figure 4.3a and b). No significant impurities could be detected in samples from any of the three variants.

Together, these data indicate that the wild-type protein, the D76N variant, and the ΔN6 truncation variant, have all been expressed as the desired species with intact disulphide bonds, no detectable impurities, with the correct mass and associated native protein fold.

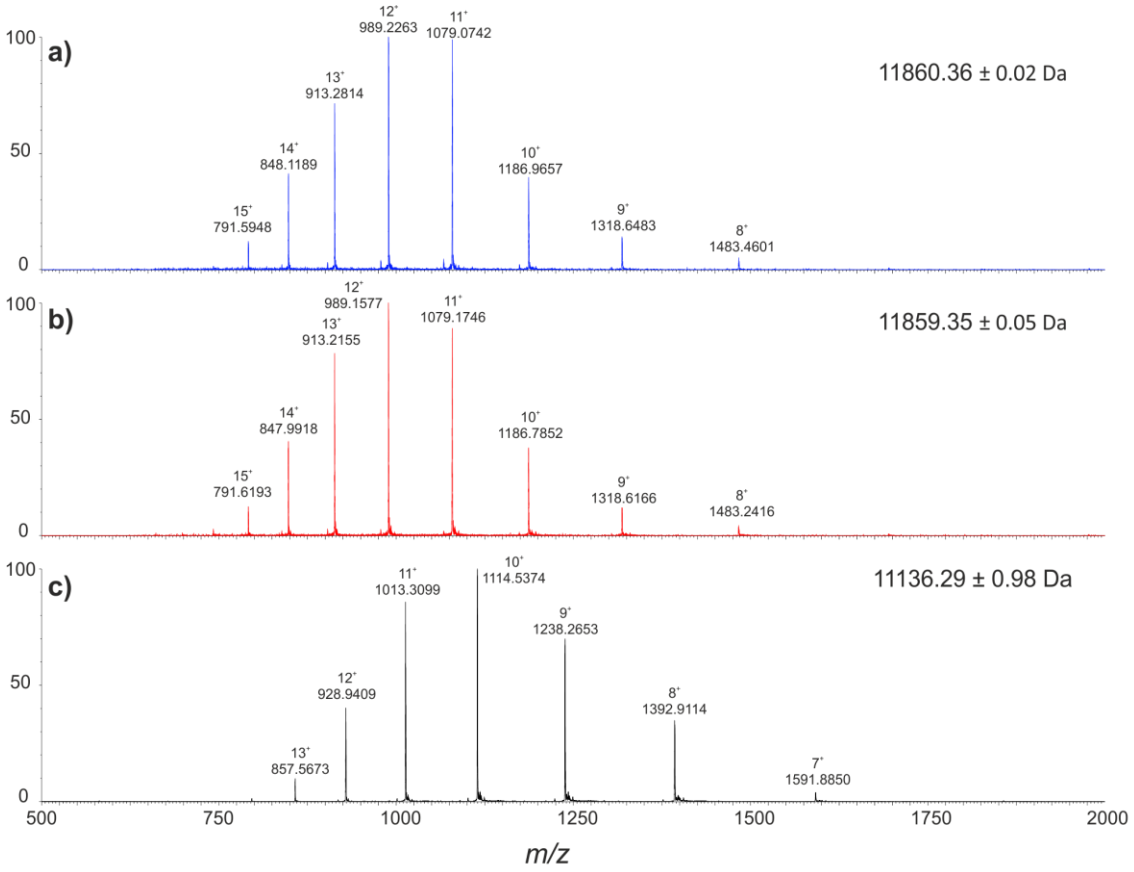

Figure 4.3 Denatured ESI-MS analysis of three variants of β2m. Wild-type (**a**), D76N (**b**) and ΔN6 β2m (**c**) analysed by ESI-MS under denaturing conditions. The intact MS method used to acquire these spectra can be found in Section 3.3. Annotations above each peak show the *m/z* and charge state. The mass and standard deviation calculated from each spectrum is shown in the top right hand corner.

4.2 Native IMS-MS

Native IMS-MS experiments were performed on the three variants of β2m for an initial, low resolution structural comparison of the three proteins to observe the effect, if any, of the D76N mutation on global protein structure by IMS-MS, and to identify any similarities to the aggregation-prone ΔN6 truncation variant.

Native ESI-MS analysis for the three variants showed narrow charge state distributions ranging from 5^+ to 8^+ charge states for the wild-type protein and the D76N variant, and 4^+ to 7^+ charge states for the truncation variant (Figure 4.4). The highest charge state observed in each spectrum (8^+) is consistent with the largest predicted charge state for native globular proteins based on simplified Rayleigh equation modelling (Equation 4.1) [253]. This model estimates, based on the mass of the protein and assuming a globular, roughly spherical fold, the maximum number of charges a solvent droplet of equivalent size to the protein could accommodate before undergoing fission due to Coulombic repulsion (similar to ESI mechanisms described in Section 1.2.1). Thus, this model serves to assess the protein charge state above which Coulombic repulsion is likely to significantly affect protein conformation or, alternatively, determine the charge state above which increased surface area (i.e. protein unfolding) would likely be required to adopt further charges.

For β2m, this model calculates ~8.5 charges would be needed to reach this threshold, consistent with the highest observable charge state (8^+) observed in the spectra, indicating that the protein conformation is likely native-like.

Other than a minor, but reproducible, reduction the in the intensity of the 6^+ charge state of the D76N variant relative to the wild-type protein (Figure 4.4a and b), the native ESI mass spectra of the wild-type and D76N variants are largely indistinguishable and remain distinct to that of the ΔN6 truncation variant (Figure 4.4c).

$$Z_R = 0.078M^{0.5} \quad (4.1)$$

Equation 4.1 Simplified Rayleigh equation to model charges on the surface of globular, natively folded proteins. In this equation, Z_R is the number of charges on the protein, and M is the average mass of the protein in Da. Equation taken from [253].

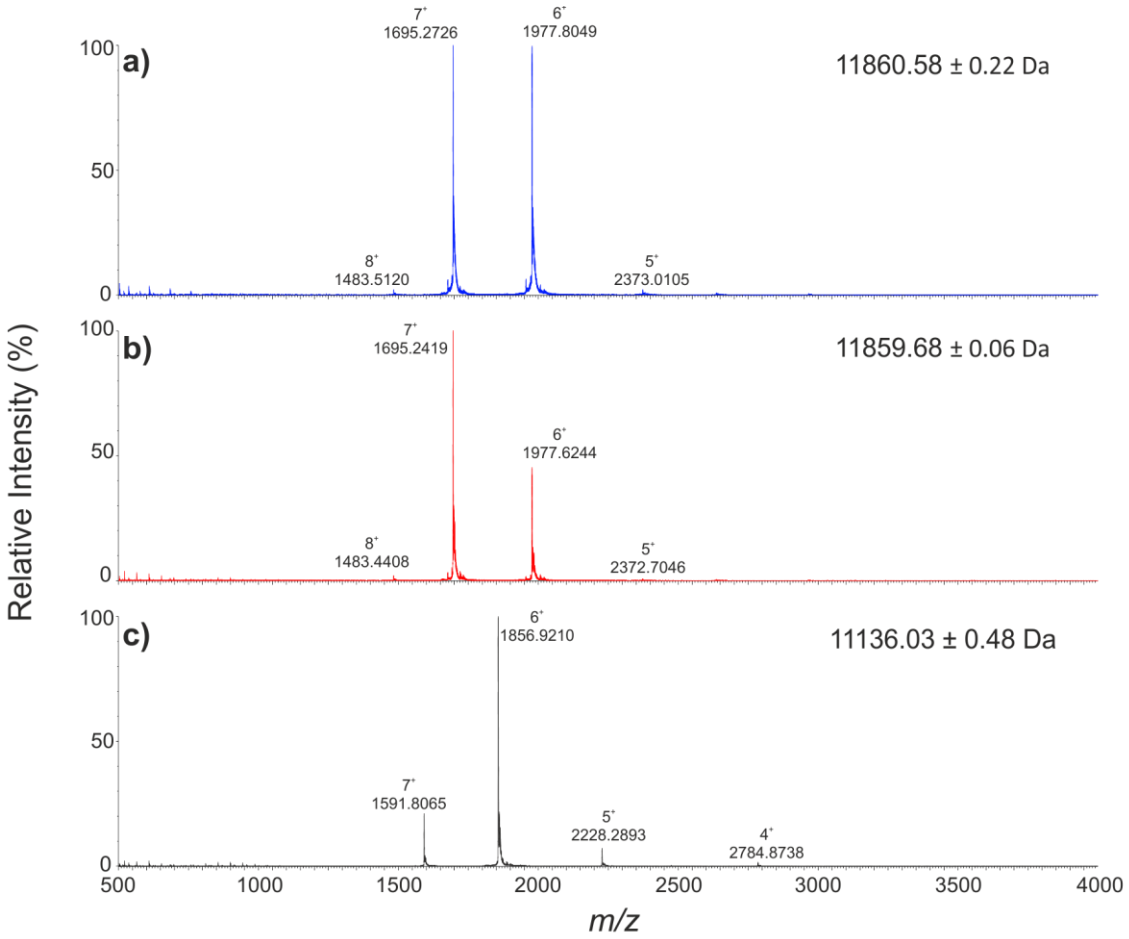

Figure 4.4 Native ESI-MS analysis of three variants of β2m. Wild-type (**a**), D76N (**b**) and ΔN6 β2m (**c**) analysed by ESI-MS under non-denaturing solution conditions, 150 mM ammonium acetate pH 7.4. Instrument conditions are listed in Section 3.2.2. Annotations above each peak show the *m/z* and charge state. The mass calculated from each spectrum is shown in the top right hand corner.

Native IMS-MS analysis of these samples identified multiple peaks within the arrival time distributions (ATDs) of different charge states for all three variants, consistent with the presence of multiple protein conformations (Figure 4.5). This was most obvious upon closer examination of the ATDs, after adjusting T-wave IMS conditions for optimal separation (Figure 4.6).

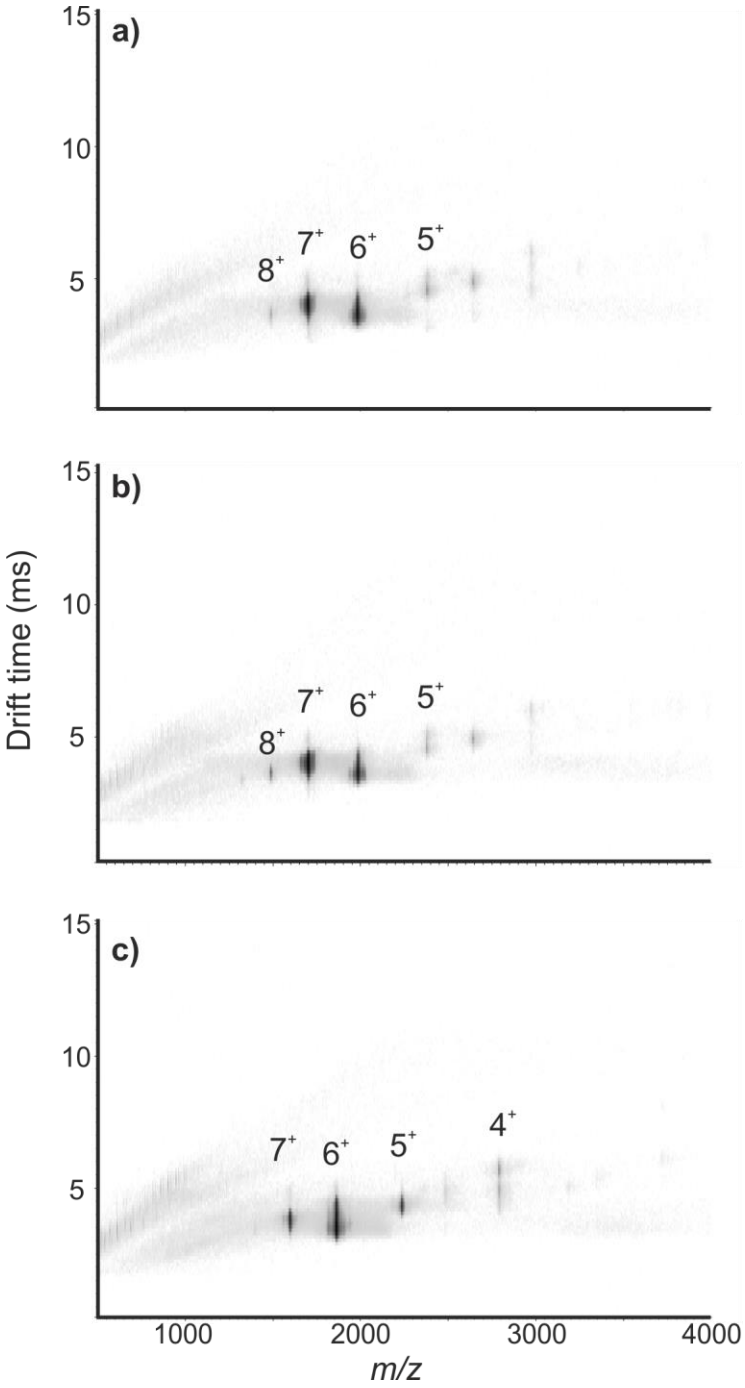

Figure 4.5 3D IMS-MS plots of three variants of β2m. Plots were exported from Driftscope v3.0 with ion intensity on a logarithmic scale. Plots are for the wild-type protein (**a**), the D76N variant (**b**) and the ΔN6 truncation variant (**c**). T-wave conditions were 'T-wave 1' as described in Table 3.2.

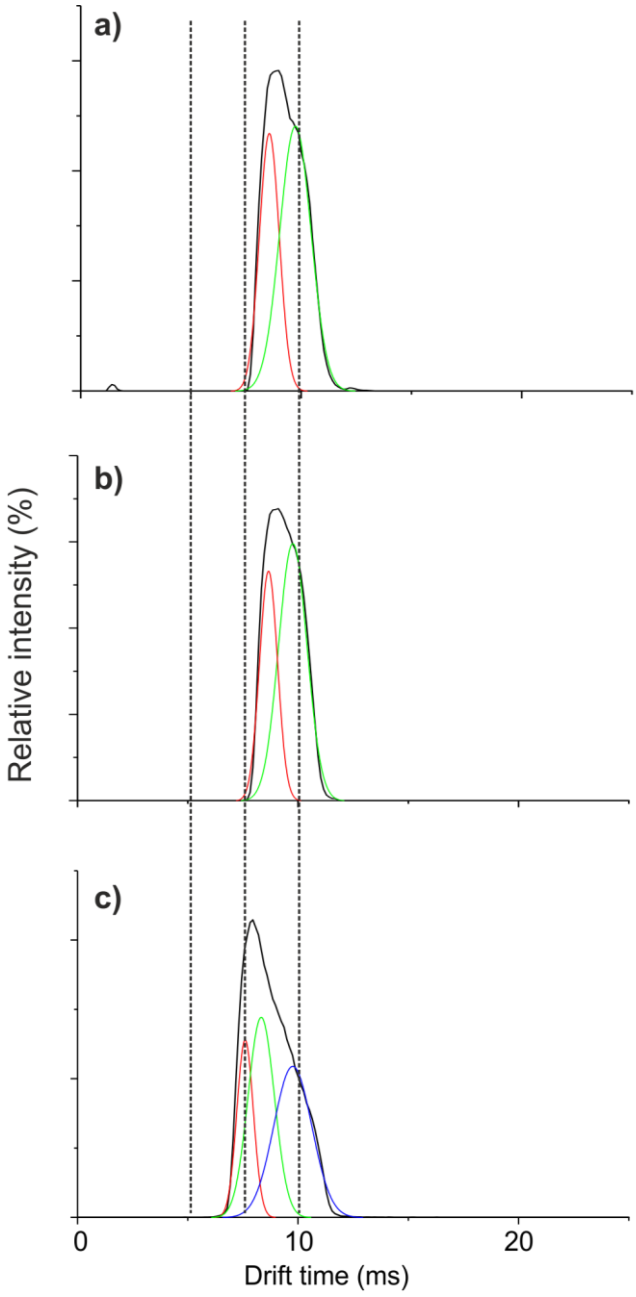

Figure 4.6 Arrival time distributions from ESI-IMS-MS analysis of the 6^+ charge state of three variants of β2m. Black trace indicates the overall arrival time distribution, where red, green and blue traces show Gaussian fitted curves to the data for wild-type (**a**), D76N (**b**) and ΔN6 (**c**). R^2 values for Gaussian fits were 0.998, 0.996 and 0.994 for wild-type, D76N and ΔN6, respectively. T wave conditions were 'T-wave 2' as described in Table 3.2. Reference lines are shown at 5.0, 7.5 and 10.0 ms.

Assuming the presence of either two or three conformers – an assumption made upon manual inspection of the ATDs, CCS values calculated for these conformers

(calibration plot shown in Figure 4.7) were similar for the wild-type protein and the D76N variant (Table 4.1) and the D76N amino acid substitution did not significantly or reproducibly affect the relative intensity of either conformer. This similarity in CCS and ATD is consistent with the known similarity between the two protein structures, when observed by X-ray crystallography (Figure 2.9) [77, 157].

Similar to the native ESI-MS data, the native ESI-IMS-MS data for the ΔN6 truncation variant was distinct from that of the wild-type protein and the D76N variant showing a significantly wider ATD and generally smaller CCS values than either of the other two variants (Table 4.1, Figure 4.6c). This is consistent with the removal of the six N-terminal amino acids, and could indicate increased conformational flexibility of ΔN6 relative to the wild-type protein and D76N.

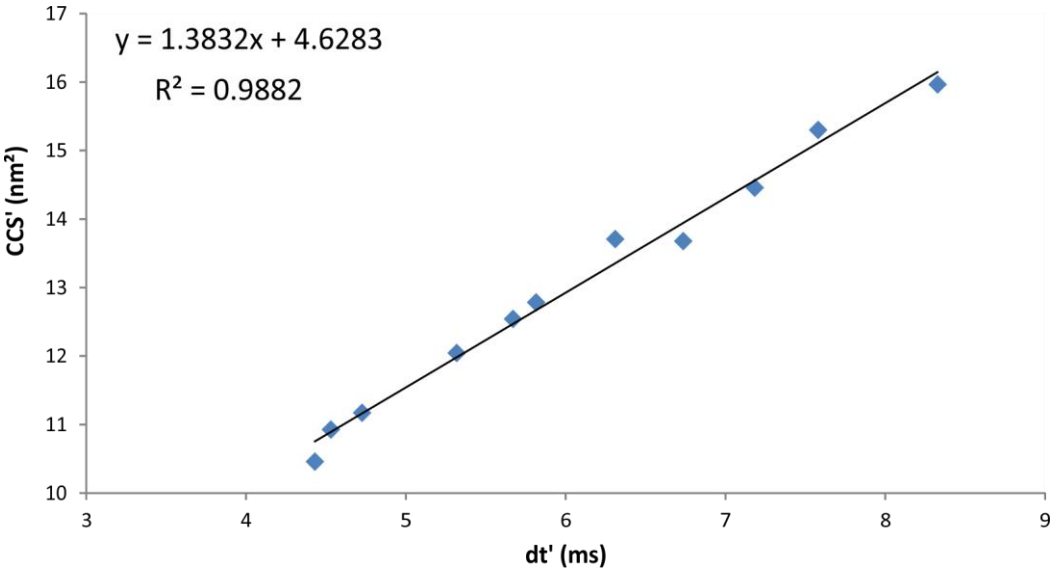

Figure 4.7 Linear calibration plot for native ESI-IMS-MS CCS values. Proteins and charge states used for calibration were: cytochrome c (6^+), β-lactoglobulin monomer (7^+, 8^+, 9^+), β-lactoglobulin dimer (11^+, 12^+, 13^+), and alcohol dehydrogenase (23^+, 24^+, 25^+, 26^+). T wave conditions were 'T-wave 1' as described in Table 3.2. R^2 value and the equation of the fitted linear trend line used for calibration are shown in the top left hand corner.

Table 4.1 Calculated CCS values for wild-type, D76N, and ΔN6 β2m.

	Rotationally averaged collision cross section (nm^2)		
Charge State	Wild-type	D76N	ΔN6
4^+	-	-	11.63
5^+	12.43 13.30	12.34 13.16	12.03
6^+	12.44 13.31	12.41 13.35	12.07 13.19 14.53
7^+	15.45 15.51	15.45 16.04	15.06 15.76
8^+	16.47	16.96	-

Calculations of *in silico* CCS values from the X-ray crystal structures of both the wild-type protein (PDB: 1LDS, Figure 4.8b) and the D76N variant (PDB: 4FXL, Figure 4.8c) showed similar calculated CCS values (14.52 nm^2 vs 14.50 nm^2 for wild-type and D76N β2m crystal structures, respectively) consistent with the known similarity in protein structure between the two variants [77, 157]. However, these CCS values, along with the *in silico* CCS values calculated for the NMR structures of the wild-type protein (PDB: 2XKS, Figure 4.8a) and the ΔN6 truncation variant (PDB: 2XKU, Figure 4.8d), were consistently larger (~15%) compared with the measured CCS values from the IMS data (Table 4.1).

In silico CCS calculations of these protein structures, following molecular dynamics simulations performed *in vacuo*, revealed slightly smaller cross sections (Figure 4.8) more consistent with those of the measured CCS values, suggesting a slight gas-phase compaction for each of the three β2m variants. The post MD structures of the wild-type protein reveal that this partial gas-phase collapse likely results from compaction of the N-terminus, and partially also from the collapse of the A-B loop protrusion in

the crystal structure, a feature absent in the NMR structure (Figure 4.8a and b). Interestingly, despite this large protrusion that is absent in the NMR structure of the wild-type protein, the NMR structure of wild-type β2m undergoes significantly more gas phase reduction in CCS than the crystal structure (~14.5 % compared to 10%), with a much lower endpoint CCS value. This likely results from the significant shift in conformation of the flexible D-strand, a rigid element in the crystal structure, the collapse of which is the likely cause of the difference in CCS between the two post-MD conformations.

Interestingly, the measured CCS values for the compact and extended conformations observed for the lowest discernible charge state of the wild-type protein (5^+) were found to be consistent with the post-MD CCS values of the NMR and crystal structures, respectively. Although curious, the data presented here are insufficient to determine the identity of the two conformations, and the CCS and relative abundance of neither is significantly affected by the D76N amino acid substitution.

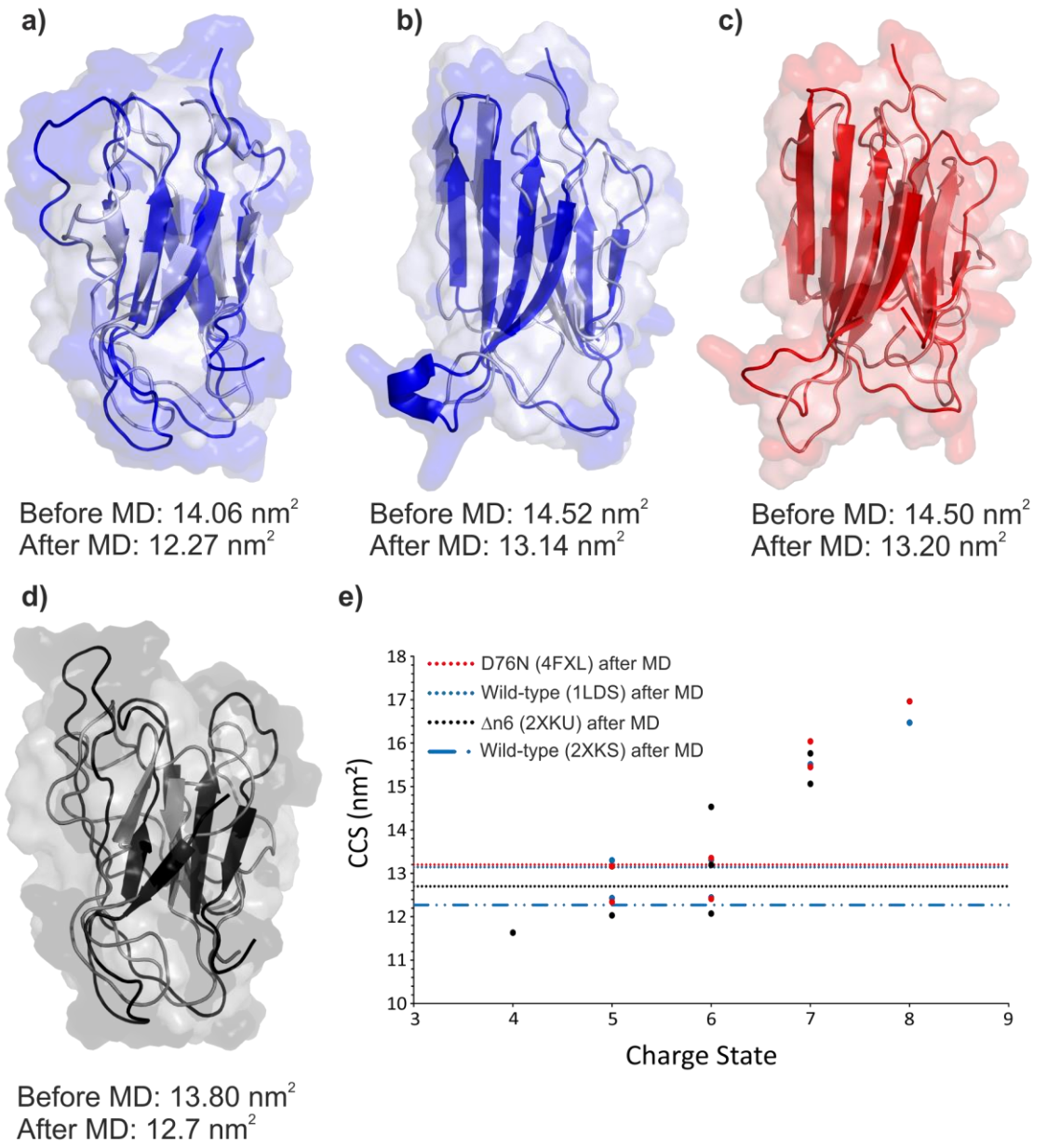

Figure 4.8 Gas-phase molecular dynamics and CCS values for three variants of β2m. Protein structures for the wild-type protein, **a** shows the NMR structure (PDB: 2XKS), **b** shows the crystal structure (PDB: 1LDS), the D76N variant (**c**, PDB: 4FXL) and the NMR structure of the truncation variant (**d**, PDB: 2XKU) before (dark colours) and after (pale colours) gas-phase molecular dynamics simulations. CCS values calculated for each structure using IMPACT (see Section 3.2.3) are shown. CCS values calculated from travelling wave ESI-IMS-MS data are shown in **e** as data points (blue = wild-type, red = D76N, black = ΔN6), and compared to the *in silico* CCS values, shown as horizontal lines.

4.3 HDX-LC-IMS-MS

Seeking alternative structural MS methods to characterise the three β2m variants further, HDX, followed by reduction of the central disulphide bond, proteolytic digestion under quench conditions, and LC-IMS-MS analysis of the resulting peptides, was used to determine whether any changes in the solvent accessibility or hydrogen bonding of backbone amide protons could be detected between the three proteins.

To determine the reproducible sequence coverage from the proteolytic digestion, all three variants were first diluted directly into the low pH quench solution, with no deuteration, prior to online digestion via an immobilised pepsin column. The resulting peptides were separated by RP-LC and analysed using a Waters Synapt G2Si using an HDMS^E workflow (Figure 4.9, detailed methods can be found in Section 3.4.1).

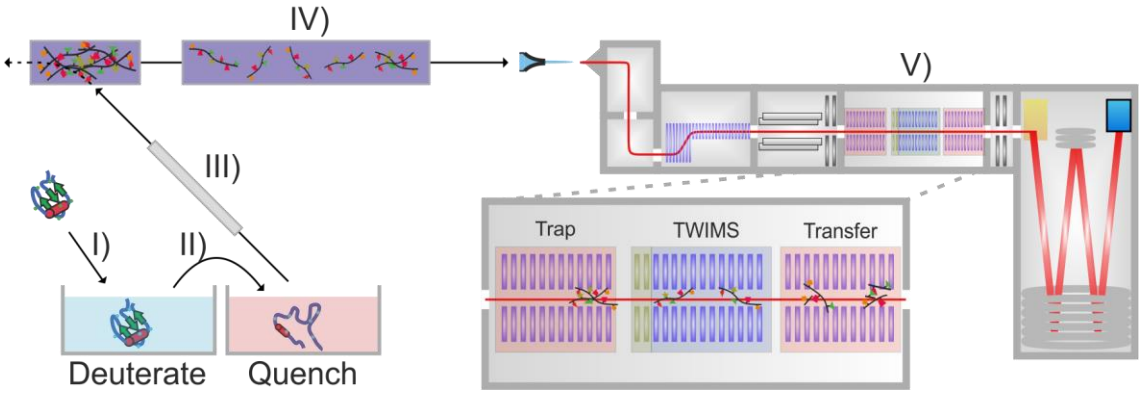

Figure 4.9 Automated HDX-LC-IMS-MS/MS workflow using a Synapt G2Si. **I**) Solution containing a low μM concentration of protein is diluted into deuterated buffer to begin deuterium exchange. **II**) After incubation periods of varying length, the deuterated sample is further diluted into a low temperature, low pH quench solution to unfold the protein and minimise further deuterium exchange. **III**) The quenched sample is passed through an immobilised protease column to digest the protein into peptides, which are subsequently passed through a trapping column for desalting and alignment prior to LC separation. **IV**) After valve switching, the trapped peptides, still under quench conditions, are separated by RP-LC, prior to ESI. **V**) Peptide ions are trapped, and separated by IMS prior to fragmentation in the transfer cell and ToF-MS analysis. Detailed methods can be found in Section 3.4.1.

A total of 51 peptides were identified that were present reproducibly in the peptic digests of both the wild-type protein and the D76N variant, achieving 100% sequence coverage. Of these, 46 were also present reproducibly in the digest of the ΔN6 truncation variant, where the missing five peptides all included the six N-terminal residues, which are absent in ΔN6 β2m (Figure 4.10).

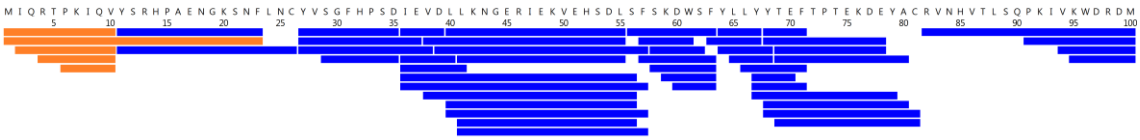

Figure 4.10 Sequence coverage of wild-type, D76N and ΔN6 β2m from online pepsin digestion. The annotated amino acid sequence is shown. Peptides coloured blue were found in all three variants. Peptides coloured orange were found in the wild-type protein and the D76N variant only. Peptide identification criteria can be found in Section 3.4.2.

All three variants were then subjected to deuterium labelling at 4 °C for 30, 60, 120, 1800 or 7200 seconds before quenching, peptic digestion and LC-IMS-MS analysis, as before. Assignment of the deuterated peptides was performed by automated alignment of their IMS drift time and LC retention time to those of the previously identified unlabelled peptides.

As the incorporation of deuterium on to a peptide increases its mass by increments of 1 Da, this overlaps with the mass differences associated with the natural abundance of ^{13}C isotopes in organic molecules. As a consequence, deuterium uptake in proteins, under the most commonly observed EX2 exchange kinetics, results in an observable shift in peptide isotope distributions towards higher *m/z* values, where this increase is quantified by subtracting the weighted average mass of the deuterated peptide isotope distribution, from that of the undeuterated peptide (Figure 4.11a-c). These data were used to generate deuterium uptake plots, where mass increase versus time can be compared between variants for each peptide identified (Figure 4.11d).

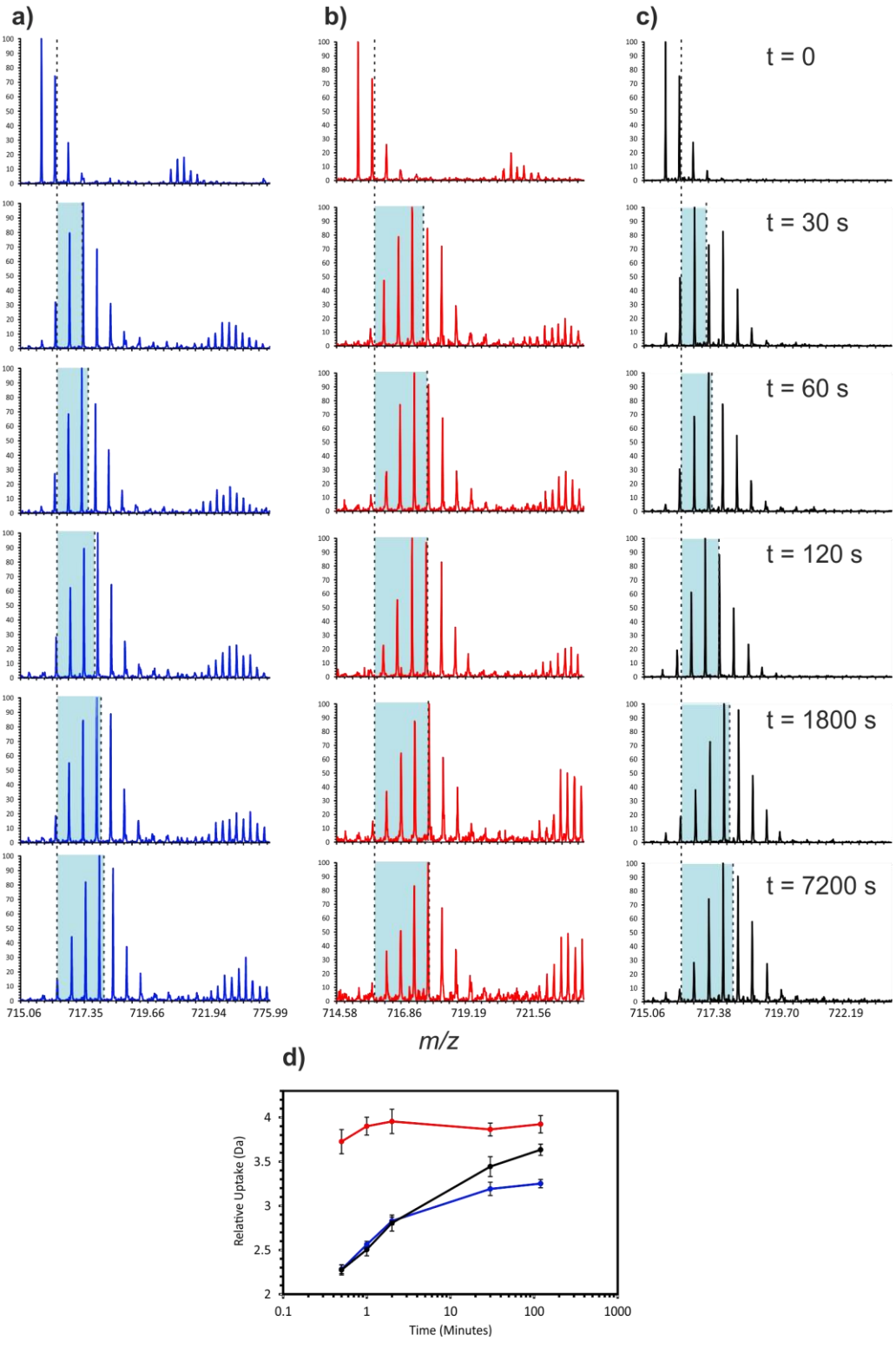

Figure 4.11 Generating deuterium uptake plots for peptides of β2m variants. Isotope distributions for the 2^+ charge state of peptide 68-79 (Sequence: TEFTPTEK(D/N)EYA) for wild-type (**a**), D76N (**b**) and ΔN6 β2m (**c**). The weighted average *m/z* (dashed line) for the undeuterated sample (top three spectra in **a**-**c**) is compared to that of the deuterated samples. The increase in *m/z* (blue shaded region) is corrected for charge state to calculate mass increase in Da. Mass increase, or deuterium uptake, is then plotted against time to generate deuterium uptake plots for each peptide (**d** – coloured as in **a**-**c**), which can be used to compare deuterium uptake for the same peptide from different proteins. Error bars show standard deviation, n = 5.

The most obvious identifiable differences between the three variants were significantly increased deuterium uptake in the ΔN6 truncation variant, relative to the wild-type protein and the D76N variant, on peptides surrounding the D-E loop (residues 56-60), B-C loop (28-34) and the C-terminus (81-99), regions where deuterium uptake in the wild-type and D76N proteins were remarkably similar to each other (Figure 4.12). Multiple overlapping peptides covering the same regions were also identified, most of which showed similar trends of increased deuterium uptake in ΔN6. However, in some instances the overlapping peptides showed differing trends. For example, although peptide 81-99, covering the C-terminus of β_2m, showed higher deuterium incorporation in the truncation variant relative to the other two proteins, peptides covering the final six residues in the C-terminus (94-99) showed no significant difference in uptake between any of the variants (Figure 4.12). Instances of this nature make data interpretation challenging, as multiple, sometimes contradictory, uptake plots of overlapping peptides covering the same region, with varying degrees of overlap, need to be interpreted simultaneously, across multiple different proteins, as well as multiple different time points, to determine the regions of most significant difference.

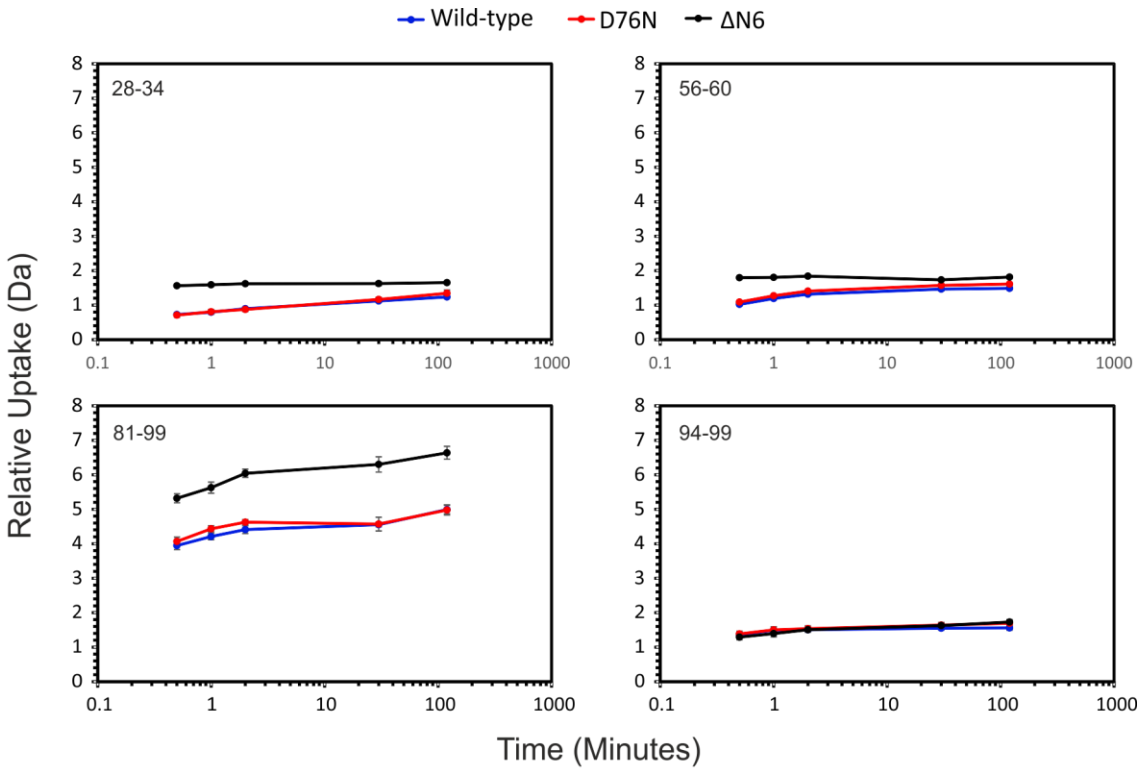

Figure 4.12 Example deuterium uptake plots highlighting increases in uptake in the ΔN6 truncation variant. Amino acid residues of β2m covered by each peptide are shown in the top left hand corner of each plot. Error bars show standard deviation, n = 5.

4.4 Development of a new HDX-MS processing algorithm

In an ideal scenario, comparisons between states in HDX-MS experiments would be between individual backbone amides of the protein structure, the highest resolution unit of the experiment, where a single deuterium uptake value per time point is obtained for each exchangeable backbone amide, in contrast to overlapping peptide level data which generates *multiple* uptake values per time point, for *groups* of backbones amides. This would allow for a simple, residue by residue comparison of deuterium uptake between states, which can be plotted readily onto protein structures for data interpretation and visualisation, avoiding the difficulties associated with developing robust data interpretation and presentation strategies for complex, overlapping peptide level data [254]. Indeed, HDX-MS experiments *can* be conducted to provide residue level resolution by fragmenting deuterated peptides using alternative fragmentation techniques, such as ETD, and quantifying deuterium

incorporation at each backbone amide by analysing the isotope distributions of the resulting fragment ions [216, 255]. However, these experiments are plagued by poor, charge dependent fragmentation efficiency, often requiring the addition of non-volatile supercharging reagents to achieve adequate peptide fragmentation [255]. Similarly, MS source conditions must be carefully tuned to avoid transferring excess internal energy to peptide ions, and minimise gas phase scrambling of the non-covalent and labile, deuterium label [216, 256]. This additional experimental complexity is such that, despite the problematic interpretation and visualisation, HDX-MS experiments are typically performed to peptide level resolution [206, 257].

Numerous efforts have been made to consolidate peptide level deuterium uptake data to attain a single uptake value per amino acid, and simplify comparisons between states. One popular approach is a subtraction analysis, whereby the deuterium content of the overlapped region between peptides is calculated from the difference in deuterium content of the two peptides which overlap [258]. In the example presented in Figure 4.12, this would mean the deuterium content, and any differences in uptake between the three variants of β2m, between residues 81-93 could be assessed by subtracting the deuterium content of peptide 94-99 from peptide 81-99. While conceptually appealing, there are several problems with this approach. Firstly, in cases where more than two peptides cover the same overlapped region, multiple subtraction analyses are possible, which can still result in multiple uptake values per exchangeable amide. For example, two additional peptides, that cover the C-terminal ~10 amino acids of β2m (other than the two listed above) were also identified (Figure 4.10), so a simple subtraction of peptides 81-99 and 94-99 would discard these, otherwise valid, data. Secondly, recent evidence suggests that, excepting cases where almost complete deuterium retention on the overlapped peptides can be achieved (i.e. no back exchange), subtraction analyses often provide unreliable results, as peptides of different lengths but similar sequence, can form different secondary structures, such as alpha helices, under quench conditions [257]. The resulting differential hydrogen bonds that form can change the back exchange behaviour of the peptide and, as such,

the deuterium uptake values for identical amide groups present on different peptides cannot be considered equivalent [257].

Many commercial HDX-MS processing methods, such as those in the Waters DynamX software used in our studies, circumvent this issue entirely by plotting data for all observed peptides, ordered by amino acid starting position, next to one another on the x axis, against change in absolute mass on the y axis, for each time point [259]. These so called 'butterfly plots', have an advantage in that they present the raw data in a minimally processed form. However, as a result, they can be challenging to interpret and visualise, as peptide lengths, and the regions of the protein each peptides covers, are not readily identifiable. Similarly, a threshold for differences in absolute mass between peptides of different states is typically set as the determinant of statistically significant difference [260, 261]. This can be misleading, however, as the biological significance of that mass change is somewhat dependent on the length of the peptide, which is not typically taken into account when measuring *only* changes in absolute mass. For instance, a difference of 0.5 Da in the weighted average mass of a 20 amino acid long peptide between two states, would appear, on a butterfly plot, to be of equal significance to the same mass difference on a five amino acid long peptide, despite being four times more concentrated, in terms of mass increase per exchangeable site, in the latter example.

One novel approach however, designed to consolidate peptide level data across multiple time points into a single plot, sums the mass increase for a given peptide across all measured time points, before correcting for the number of exchangeable sites in the peptide, generating a single, fractional mass increase value for each peptide observed [170, 262]. These values are then averaged across all peptides covering a

particular amino acid in the protein sequence, to generate a single uptake value for each residue in the protein (Equation 4.2).

$$\bar{M}_j = \frac{1}{n}\sum_{1}^{n}\frac{1}{q_i}\sum_{0}^{t}(m_i^t - m_i^0) \tag{4.2}$$

Equation 4.2 Previously published HDX-MS peptide level data consolidation approaches. Where $\bar{M}_j$ is the mean mass increase at amino acid j, summed across all measured time points, n is the number of overlapping peptides covering amino acid j, q_i is the number of exchangeable amides for peptide i, m_i^t is the weighted average mass for peptide i at time t and $m_i^0$is the weighted average mass for peptide i at time 0.

The advantage of this approach is not only that it corrects mass increase for peptide length, but it consolidates peptide level HDX-MS data into the desired, single value per amino acid, which can be easily compared between states. However, although the usefulness of this approach has been demonstrated in numerous publications [170, 262, 263], there are, perhaps, three significant limitations to this method. Firstly, statistical significance of any differences identified cannot be calculated, as there is, at present, no way of propagating errors in the deuterium uptake measurements of the peptides, to the final uptake value obtained for each residue. Similarly, without statistical analysis, robust methods of data presentation and visualisation, such as heat maps on protein structures, are challenging to develop. Lastly, the summation of uptake measurements across time points is such that minor differences observed over multiple time points accumulate, and may appear significantly larger in the processed data than the peptide deuterium uptake plot would suggest [170].

To address these issues, the following algorithm was developed to provide the desired single uptake measurement per amino acid from the overlapped peptide level data, for processing, visualising and comparing the HDX-MS data for the β2m variants, using relative fractional uptake data exported from DynamX. This simple approach not only evaluates each time point independently, but also allows statistical analysis of the

processed data to determine significant differences between states, offering robust criteria for data visualisation and presentation between datasets.

$$\overline{X}_C = \frac{\sum_{i=1}^{z} n_i \bar{X}_i}{\sum_{i=1}^{z} n_i} \tag{4.3}$$

Equation 4.3 PAVED algorithm: calculating combined mean relative fractional uptake per residue. Where $\overline{X}_C$ is the combined mean relative fractional uptake for a given residue at a given time point, n_i is the number of replicates for peptide i. $\overline{X}_i$ is the mean relative fractional uptake for peptide i at a given time point. Peptides i to z are all the peptides that cover an amino acid position, excluding the N-terminal residue of each due to back exchange.

$$S_C = \sqrt{\frac{\sum_{i=1}^{z} n_i \left[{S_i}^2 + \left(\overline{X}_i - \overline{X}_C \right)^2 \right]}{\sum_{i=1}^{z} n_i}} \tag{4.4}$$

Equation 4.4 PAVED algorithm: calculating combined standard deviation per residue. Where S_c is the combined standard deviation for a given residue at a given time point, S_i is the standard deviation of peptide i at a given time point. $\overline{X}_C$ is the combined mean relative fractional uptake for a given residue at a given time point, n_i is the number of replicates for peptide i. $\overline{X}_i$ is the mean relative fractional uptake for peptide i at a given time point. Peptides i to z are all the peptides that cover an amino acid position, excluding the N-terminal residue of each due to back exchange.

For a given time point and state, Equation 4.3 calculates the combined mean relative fractional uptake (deuterium uptake corrected for the number of exchangeable amides in the peptide) for each amino acid, by averaging the relative fractional uptake values for peptides which cover the amino acid in question. Equation 4.4 then uses this combined mean, and the standard deviations for each of the peptides, arising from replicate measurements, as well as variances between charge states from the same measurement, to calculate a combined standard deviation. This process is repeated for each residue in the sequence, for every measured time point, and all states (wild-type, ΔN6 and D76N in these experiments). Knowing the combined mean relative fractional uptake, combined standard deviation, and the total number of measurements for each residue (n = replicates x peptides covering the residue), statistical analysis can be

performed using one way ANOVA and post hoc Tukey tests, to determine significant differences, on a per residue basis, between states at equivalent time points [264].

Although the presence of multiple charge states for a given peptide provides multiple measurements of deuterium uptake, and were included in the calculation of both the combined mean relative fractional uptake and the combined standard deviation of each residue, it was decided to exclude the number of charge states from the calculation of n, as this would weight larger peptides, offering lower structural resolution, more significantly than smaller ones in the final calculation of combined relative fractional uptake. Additionally, the N-terminal amide of each peptide has been observed to undergo rapid back exchange, within 1-2 minutes, under quench conditions, leaving no deuterium on this residue [221]. It was therefore decided to exclude the N-terminal residue of each peptide from our analysis, and the calculation of relative fractional uptake.

This processing algorithm was designed to process output files from DynamX, and was initially written in R (original code can be found in Section 8.1) before being further developed by James Ault (MS facility manager) for faster processing speeds, and the inclusion of a graphical user interface (Figure 4.13). This software, named PAVED (Positional Averaging for Visualising Exchange Data) is now available for free download at:

https://biologicalsciences.leeds.ac.uk/downloads/download/28/software_download

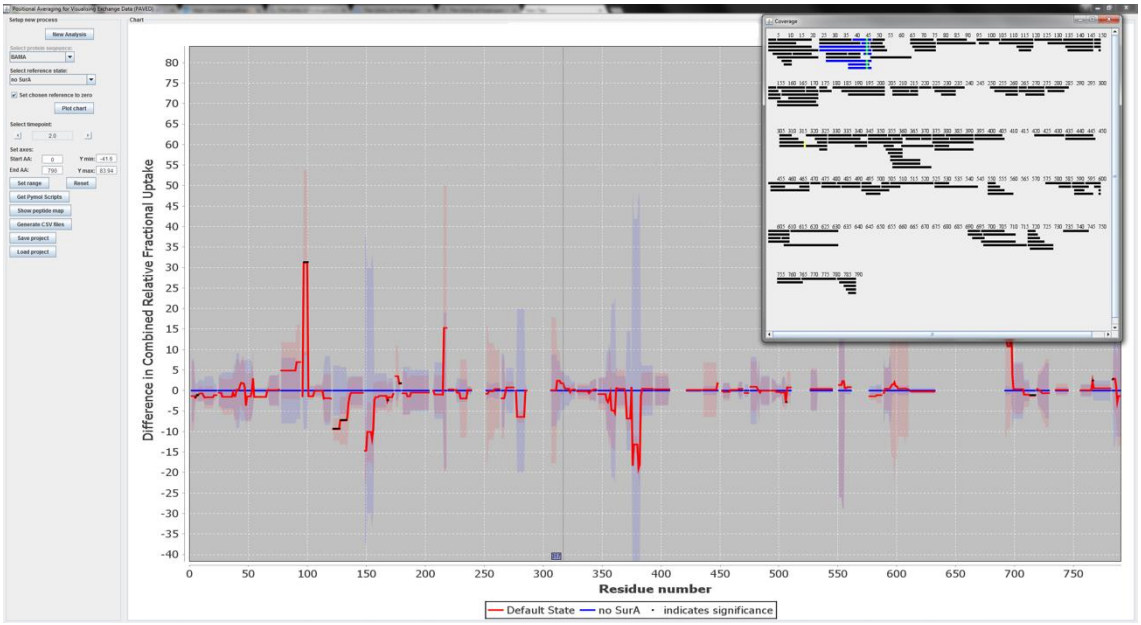

Figure 4.13 PAVED graphical user interface. PAVED software for visualising and presenting peptide level HDX-MS data. Software and GUI created by James Ault.

4.5 Evaluating the PAVED algorithm

To evaluate the utility of the PAVED algorithm, the differences in HDX behaviour of wild-β2m and the ΔN6 truncation variant, being the two well-characterised variants of β2m, were first compared with previously published studies comparing the two proteins using NMR relaxation methods [78] as well as intact HDX-MS [134].

Despite the initial 100% sequence coverage (Figure 4.10), the removal of the N-terminal residue of each peptide during processing results in the loss of coverage of two internal amides (Tyr 26 and Arg 81), as well as the N-terminal methionine (Figure 4.14b). Figure 4.14c shows the PAVED processed HDX-MS data for wild-type β2m after 30 seconds of deuteration. As deuterium incorporation is dependent on both the primary sequence and the solvent accessibility and dynamics of each amide, factors which are unique to each protein, these combined relative fractional uptake plots provide a unique protein 'fingerprint' of deuterium uptake across the protein sequence, for a given peptide list. Indeed, this 'fingerprint' deuterium uptake pattern is remarkably similar for all three β2m variants after 30 seconds of labelling, likely reflective of their similar sequences and protein structures (Figure 4.15).

After processing, significant errors in the combined mean relative fractional uptake values are observed across all three variants between residues 35-40 and 65-70 (Figure 4.14c, Figure 4.15). This is due to the positional averaging of peptides with minimal overlap, covering different regions of the protein, which have significantly different relative fractional uptake values, and accurately reflects the uncertainty of the deuterium uptake measurements in these regions (Figure 4.14a and b). The same effect is observed in ΔN6 at the C-terminal region (residues 90-99) where overlapping peptides discussed earlier (peptides 81-99 and 94-99, Figure 4.12) showed differing trends with regards to the deuterium uptake differences relative to the wild-type protein. Here, the positional averaging algorithm has reduced the combined mean relative fractional uptake at the extreme C-terminus to show no statistical significance to the wild-type protein, but significant differences *are* shown between residues 82-90 (F-G loop), accurately reflecting the complex overlapping peptide level data for this region (Figure 4.12, Figure 4.15, Figure 4.17).

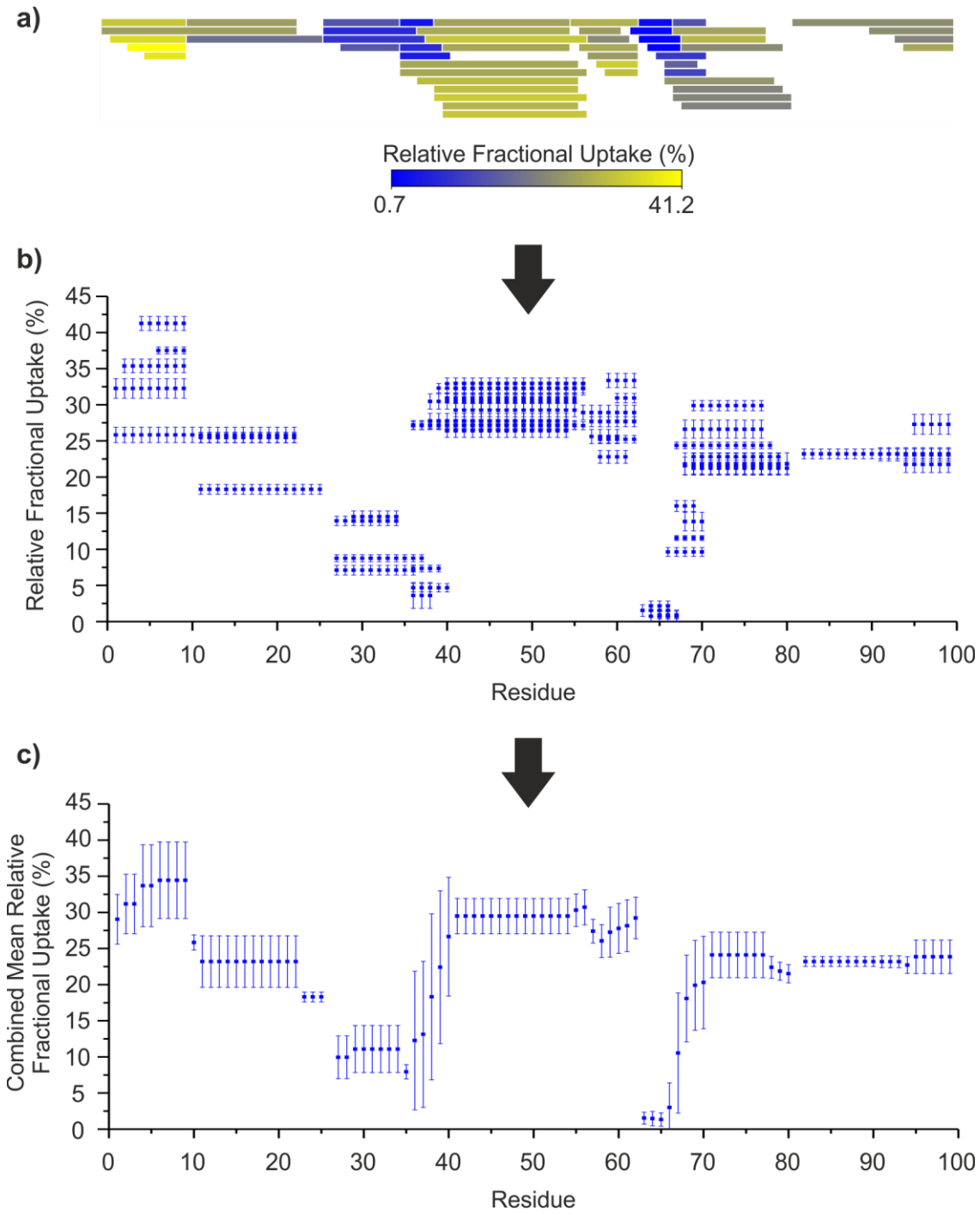

Figure 4.14 Consolidation of HDX-MS data using positional averaging. Relative fractional uptake data taken from DynamX (**a**) is processed by removing the N-terminal residue from each peptide due to back exchange. Multiple uptake measurements for each residue can then be identified by evaluating the relative fractional uptake value for each peptide, and the residues each peptide covers (**b**). Finally, Equation 4.3 and Equation 4.4 are used to combine the mean and standard deviations for multiple measurements of the same residue, from the overlapping peptides, to achieve a single uptake measurements and error value, per residue, per time point, per state (**c**). Data are shown for wild-type β2m for the 30 second time point. Error bars shown in **b)** are standard deviations associated with replicate measurements (n=5) and variances between charge states of the same replicate. Error bars shown in **c)** are combined standard deviations calculated using Equation 4.4.

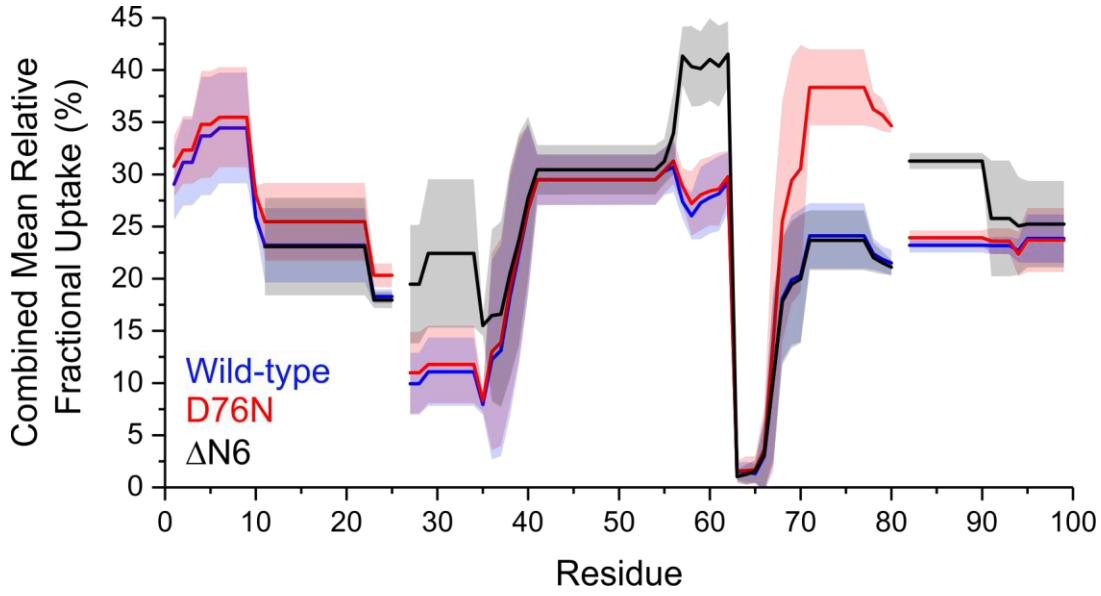

Figure 4.15 Comparing HDX-MS between three β2m variants data after 30 seconds deuteration. Combined mean relative fractional uptake per residue was calculated using the PAVED algorithm. Shaded regions show combined standard deviation.

Similarly significant differences ($p < 0.05$, based on combined standard deviation and combined mean relative fractional uptake) between ΔN6 and the wild-type protein are observed in the B-C and D-E loop regions (residues 27-35 and 57-62, respectively), consistent with NMR relaxation experiments [78]. Including significant differences identified in the F-G loop (residues 82-90), these regions highlight a total of 24 backbone amides with statistically significantly ($p < 0.05$) increased deuterium uptake in the ΔN6 truncation. This is remarkably close to the 22 ± 1 backbone amides estimated to have decreased protection in this variant from intact HDX-MS data [134]. Although these differences are largely consistent across all time points measured, at later labelling time points (1800 and 7200 seconds), both the ΔN6 truncation variant and the D76N variant show smaller increases in deuterium uptake (2-3%) relative to the wild-type protein, across the length of the β2m sequence (Figure 4.16). This is likely the result of decreased stability of the native fold in both proteins, and increased propensity of D76N and ΔN6 to populate the unfolded state, relative to the wild-type protein [146, 156], and effectively demonstrates the utility of evaluating each deuteration time point separately.

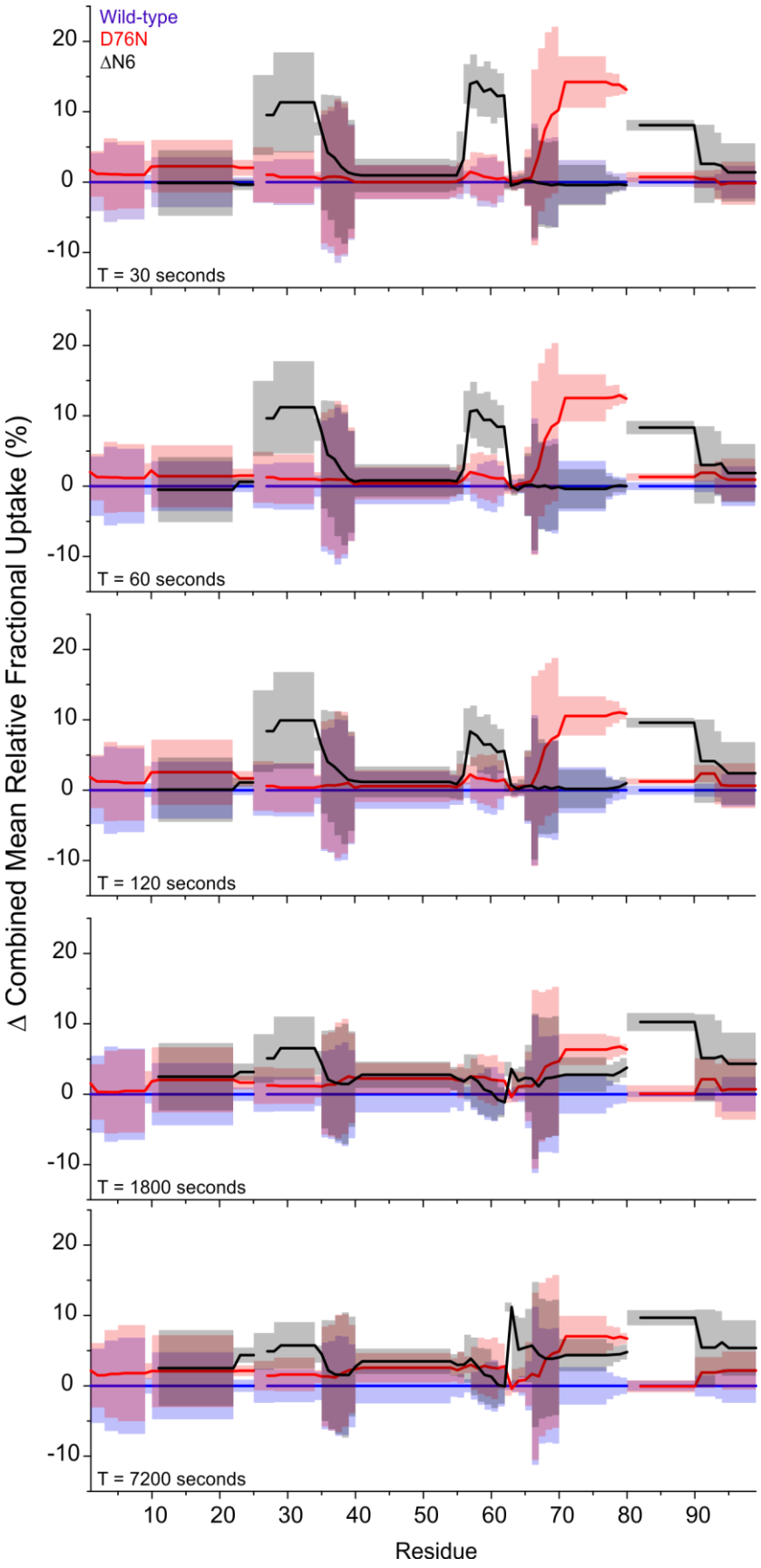

Figure 4.16 PAVED difference plots of HDX-MS data for wild-type, D76N and ΔN6 β2m. Shaded regions show combined standard deviation.Wild-type β2m has been set to zero for reference. Incubation time in deuterated buffer is shown in the bottom left hand corner of each plot.

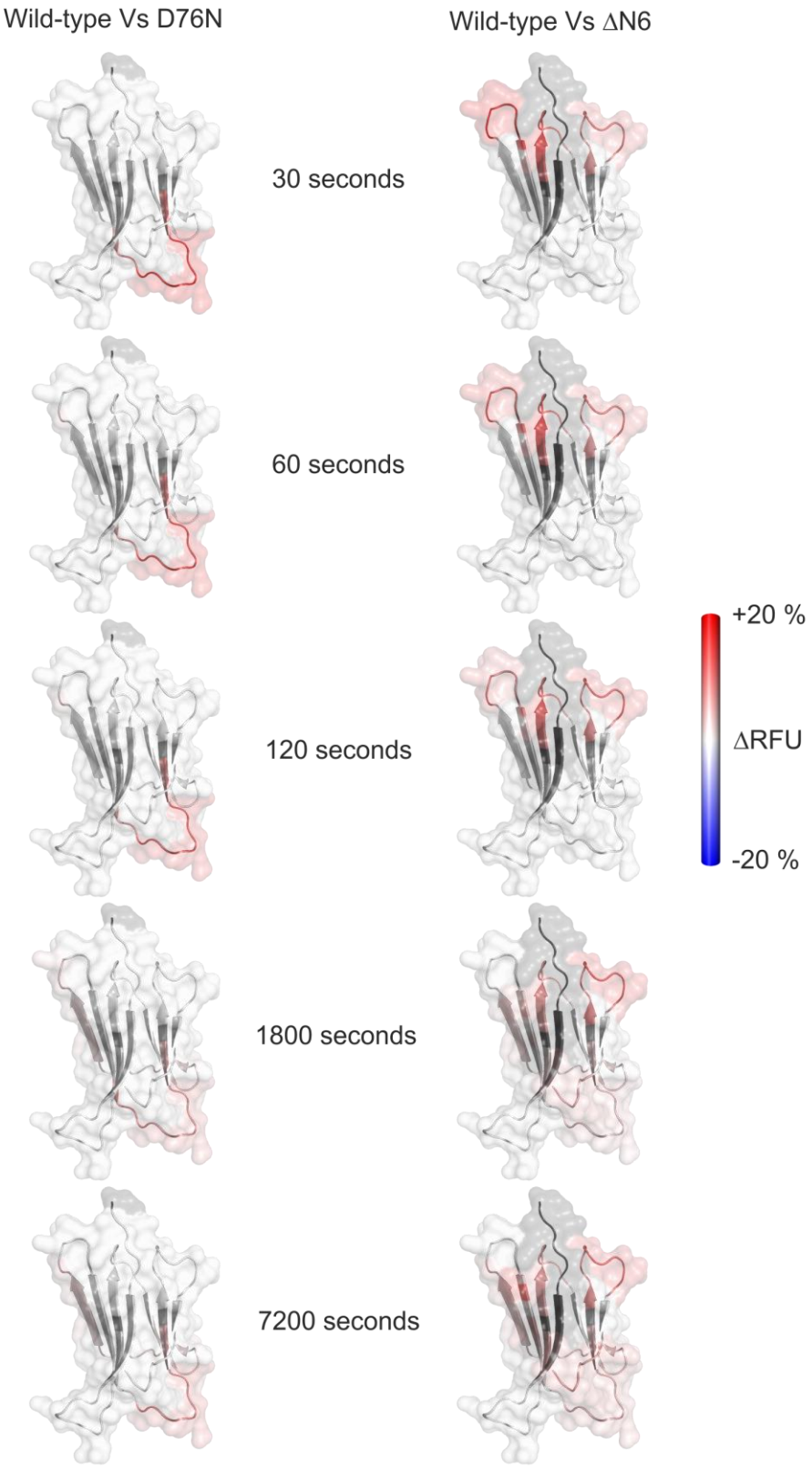

Figure 4.17 Visualising differences in deuterium uptake relative to wild-type β2m. Statistically significant differences ($p < 0.05$ based on PAVED processed data) are shown. Increases in deuterium uptake, relative to the wild-type protein, are shown in red. Decreases are shown in blue. Missing residues and the N-terminal truncation are shown in black. For reference, a detailed, annotated structure of b2m can be found in Figure 2.6 in Section 2.2. PDB: 4FXL [157].

With a deuterium uptake value for each residue, and statistical analyses determining significant differences, the PAVED processing algorithm was then used to screen data for statistical significance as a robust method of data presentation and visualisation. Residues which show statistically significant differences between states were then coloured according to the magnitude of the difference in relative fractional uptake, and plotted on the β2m structure (Figure 4.17). Structurally, the differences observed between the wild-type and the ΔN6 truncation variant at the earliest labelling time points, are located proximal to the N-terminal truncation (Figure 4.17), consistent with earlier reports [78].

4.6 Deuterium uptake behaviour of the D76N variant of β2m

Relative to both the wild-type protein, and the ΔN6 truncation variant, D76N shows remarkably increased deuterium uptake in the E-F loop (residues 65-80), directly surrounding the amino acid substitution. Indeed, uptake plots indicate that the deuterium uptake has largely plateaued from the earliest measured time point, for all peptides covering this region (Figure 4.18). However, as a consequence of the difference in amino acid sequence for these peptides between the wild-type protein and the D76N variant, it should be noted that the intrinsic deuterium exchange rate is also different.

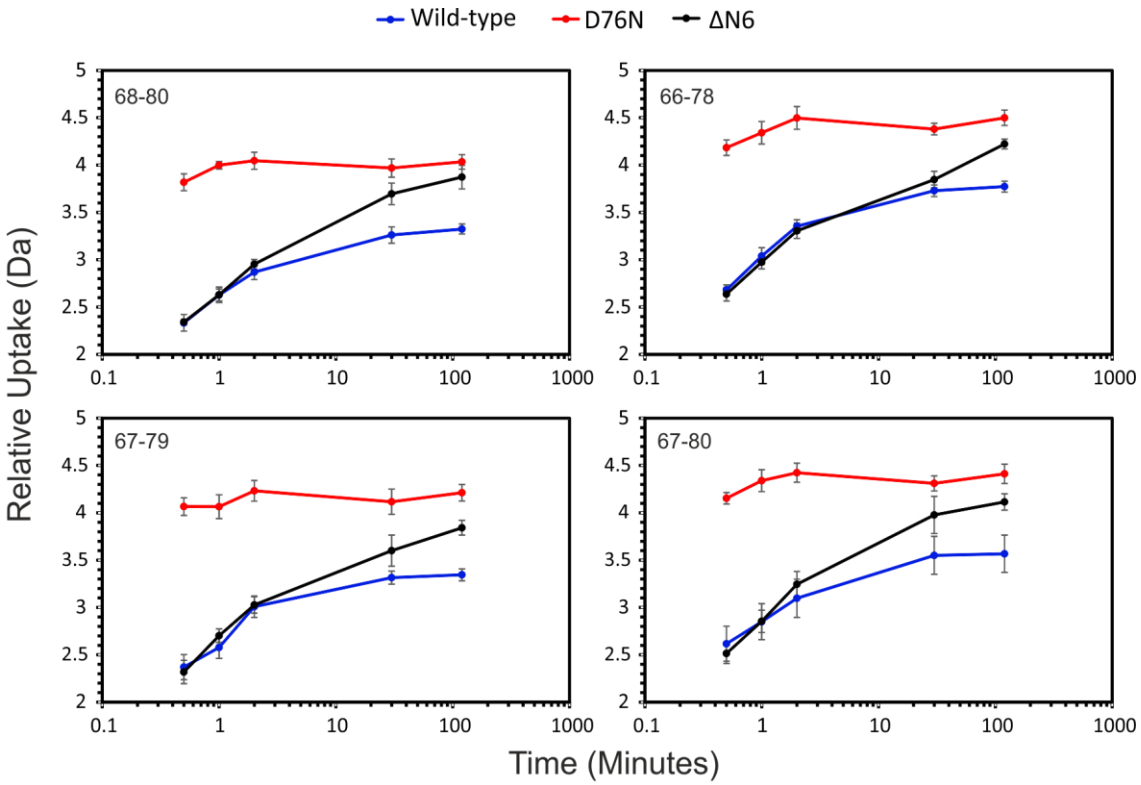

Figure 4.18 Deuterium uptake plots for peptides covering the D76N substitution. Amino acid residues of β2m covered by each peptide are shown in the top left hand corner of each plot. Error bars show standard deviation, n = 5.

To determine whether these differences were a result of structural change in the protein, or differences associated with a change in chemical exchange rate, peptides including residues 68-80 from both the wild-type protein and the D76N variant were purchased from Peptide Synthetics and fully deuterated in label buffer for 24 hours. Following labelling, the fully deuterated peptides were quenched and analysed by LC-MS, in the same fashion as peptides from the proteolytic digests. The wild-type peptide was found to have an average mass increase of 6.16 Da, compared with 6.80 Da increase of the D76N peptide. These values can be considered the effective maximum possible exchange for these peptides, on our system, after back exchange and can therefore be used as a benchmark for back exchange correction, and the determination of fractional deuterium uptake for each time point.

After back exchange correction, despite the naturally increased deuterium exchange rate of the D76N peptide relative to the wild-type peptide, the D76N variant still

shows ~20% increased deuterium uptake at the earliest labelling time points, relative to both the wild-type protein and the ΔN6 truncation variant, indicating that these changes are associated with a change in hydrogen bonding, solvent accessibility and/or dynamics in the D76N variant (Figure 4.19).

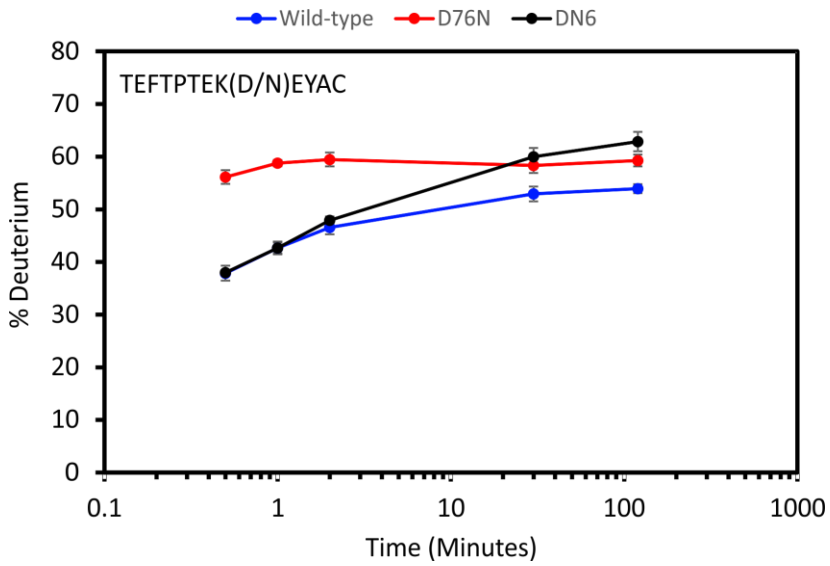

Figure 4.19 Back exchange correction for peptides covering the D76N substitution. Correction was performed using synthetic peptides purchased from Peptide Synthetics which were fully deuterated in label buffer. Peptide sequence is shown in the top left hand corner. Error bars show standard deviation, n = 5.

Minor increases in deuterium uptake for the D76N variant, relative to the wild-type protein, were also observed in the A-B loop (residues 12-22, Figure 4.15, Figure 4.16, and Figure 4.20). Although, after PAVED processing, these differences proved not to be statistically significant, structurally the A-B loop is on the same side of the protein's β-sandwich structure as the E-F loop and the D76N mutation. This proximity to the D-N substitution site, and the observed HDX differences surrounding the mutation, suggests that these minor changes in the A-B loop may be real, but insufficiently resolved by the comparatively long peptides which cover this region.

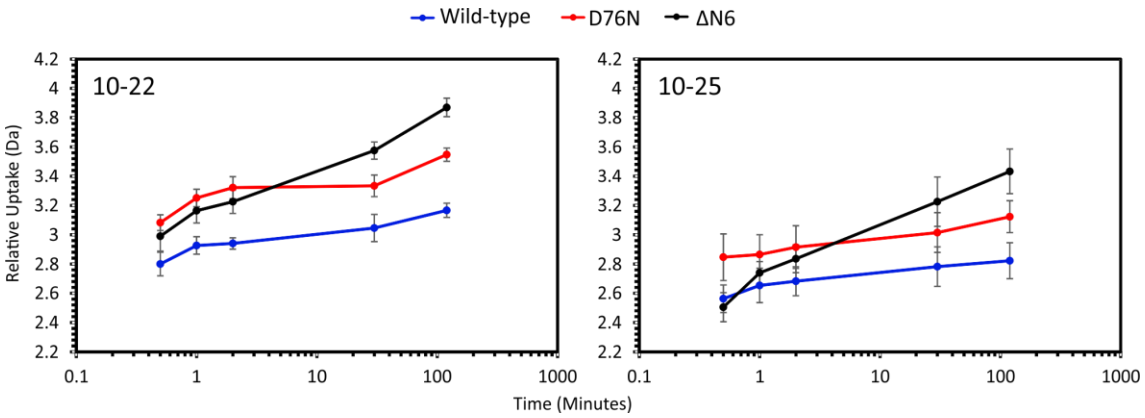

Figure 4.20 A-B loop hydrogen exchange uptake plots. Amino acid residues of β2m covered by each peptide are shown in the top left hand corner of each plot. Error bars show standard deviation, n = 5.

4.7 Discussion

4.7.1 The PAVED algorithm

The differences observed and characterised by the PAVED processing algorithm between the ΔN6 truncation variant and the wild-type protein are consistent with earlier reports [78] [134, 146] [156], and indicate changes in structure directly proximal to the N-terminal truncation, as well as a decreased stability of the native fold, relative to the wild-type protein.

Due to the correction for peptides of different lengths, and the propagation or errors in the averaging calculations, the PAVED algorithm offers a useful method of visualising peptide level HDX-MS data, highlighting both the statistical and biological significance of the data. Similarly, by using all the available peptide data, this approach avoids bias in peptide selection for data presentation, either as uptake plots or as heat maps on protein structures, instead offering a robust, statistically driven method for data visualisation.

However, the shortcomings of this approach must also be discussed. The minor differences in deuterium uptake between the wild-type protein and the ΔN6 truncation variant, between residues 90-99 in the processed data (Figure 4.15), are in contradiction with the actual peptide level data, where data points in the uptake plot

overlay (Figure 4.12). Although processing with PAVED has correctly assigned differences in this region as not statistically significant, the combined average deuterium uptake in the processed data is higher in the ΔN6 variant than in the wild-type protein in this region, as a result of a much longer, overlapping peptide where deuterium uptake in ΔN6 *is* increased relative to the wild-type protein. This 'smoothing' effect on the data is to some extent unavoidable with this approach, and is a similar issue for the alternative processing method described in Equation 4.2.

Clearly, shorter peptides provide higher structural resolution on changes in deuterium uptake, where overlap with longer peptides exacerbates the smoothing effect on the data during processing. The PAVED algorithm developed here lends itself to further development in this regard as, currently, peptides of all lengths are weighted equally in the calculation of the relative fractional uptake for each residue. In reality, the relative fractional uptake for a given residue is more likely to be represented accurately by shorter peptides than by longer peptides as, in the former case, an individual amide makes a larger relative contribution to the measured peptide level data.

As such, a modelling approach, based on the PAVED processing algorithm, could be conceived whereby shorter peptides are weighted more heavily in the calculation of relative fractional uptake:

$$\overline{X}_C = \frac{\sum_{i=1}^{z} n_i \bar{X}_i {l_i}^{-1}}{\sum_{i=1}^{z} n_i \, {l_i}^{-1}} \tag{4.5}$$

Equation 4.5 Proposed modelling of HDX data based on PAVED processing. Where $\overline{X}_C$ is the combined mean relative fractional uptake for a given residue at a given time point, n_i is the number of replicates for peptide i. $\overline{X}_i$ is the mean relative fractional uptake for peptide i at a given time point. l_i is the number of exchangeable amides in peptide i , excluding the N-terminal residue. Peptides i to z are all the peptides that cover an amino acid position, excluding the N-terminal residue of each.

Although such a modelling approach would need to be tested on control proteins with precisely known deuterium uptake behaviour, weighting shorter peptides more

heavily may mitigate the smoothing effect of the algorithm, thus further simplifying data interpretation.

4.7.2 HDX behaviour of the D76N variant

The markedly increased deuterium uptake of the E-F loop in the D76N variant, observed here for the first time, is suggestive of a significant structural or dynamical change in this region. These observations are consistent with ssNMR experiments which identified structural changes between wild-type β2m and D76N at both the E-F loop, and more minor differences at residues Arg 12 and His 13 in the A-B loop [164]. These findings could be consistent with the minor differences in deuterium exchange of the A-B loop observed by HDX-MS, where such minor differences are expectedly unresolved, both dynamically and spatially, by the comparatively long (> 11 residues) peptides identified which cover this region (Figure 4.10).

Although increased solvent accessibility in the E-F loop of the D76N variant, relative to the wild-type protein, could account for the observed relative increase in deuterium uptake, this explanation seems unlikely, as the E-F loop extends out into bulk solvent, and is largely solvent exposed in both variants (Figure 2.9). In the NMR structure of wild-type β2m, Asp 76 is involved in an extensive hydrogen bonding network in the E-F loop involving residues Tyr 78, Thr 73 and Lys 75 (Figure 4.21). Three of these contacts are main-chain hydrogen bonds involving backbone amide protons, changes in which would be visible by HDX-MS experiments (Figure 4.21). While many of these hydrogen bonds are also present in the crystal structure of the D76N variant [157], static crystallographic structures are not necessarily representative of the solution phase conformational distribution of the protein. Indeed, MD simulations of the D76N variant have indicated that the D-N substitution disrupts hydrogen bonding in the E-F loop, causing the loss of molecular contact between hydrogen bonded residues [265]. These simulations are consistent with the observed de-protection of backbone amides in the E-F loop of D76N and, given the central role

that residue 76 plays in the structure of the E-F loop in the wild-type protein, loss of hydrogen bonding in the E-F loop seems a plausible explanation for the increased deuterium uptake in this region observed here using HDX-MS.

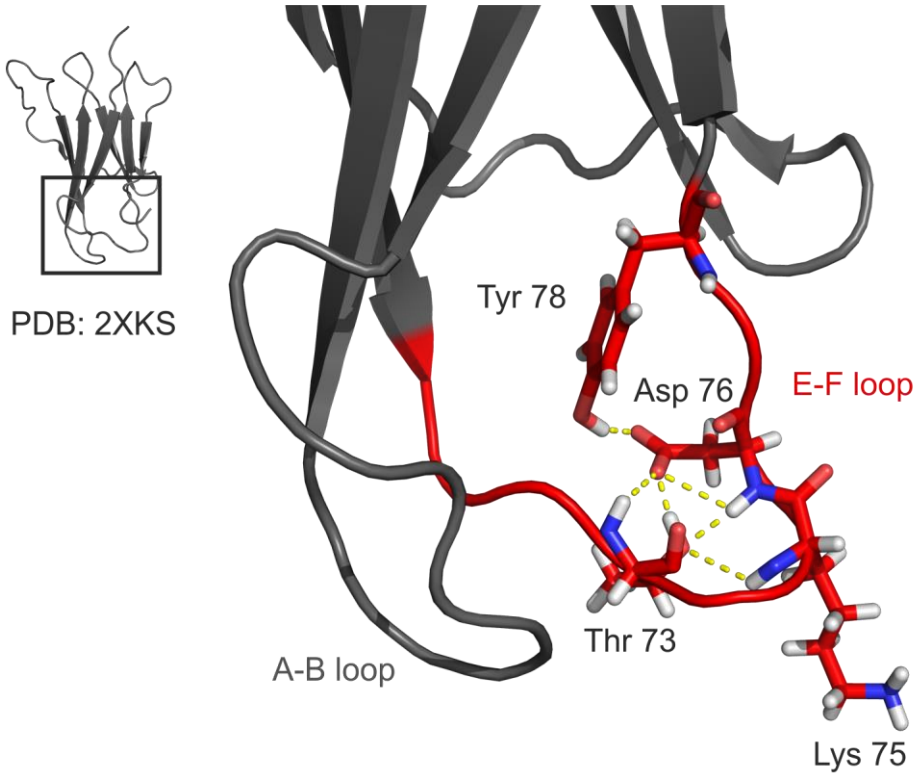

Figure 4.21 Hydrogen bonding in the E-F loop of wild-type β2m. Side chains in the E-F loop (red) involved in hydrogen bonding are shown as sticks and coloured by element: oxygen = pink, nitrogen = blue, hydrogen = white. Polar contacts between atoms are shown as dashed yellow lines. The C-terminus has been hidden for clarity. PDB: 2XKS [78].

4.7.3 Insights on the aggregation propensity of the D76N variant

Analysis of both the IMS, and HDX data demonstrate that the D76N variant is distinct, in terms of protein structure and dynamics, from the aggregation-prone ΔN6 truncation variant, with little similarity in terms of deuterium uptake behaviour or IMS ATDs. While the IMS data showed that the D76N variant was largely indistinguishable from the wild-type protein, as indeed most regions of the protein were using PAVED analysis of the HDX-MS data (Figure 4.16, Figure 4.17), the marked increase in deuterium uptake in the E-F loop of the D76N variant relative to

the wild-type protein, and hypothesised loss of hydrogen bonding, is an important observation regarding the increased aggregation propensity of this variant. The hydrogen bonding analysis in Section 4.7.2, coupled with previous studies demonstrating the critical nature of the D76 residue in preventing the aggregation of β2m [159] is highly suggestive that the structure of the E-F loop is a key factor in preventing oligomerisation and amyloid formation in β2m. Although considerably more research is needed before any firm conclusions can be drawn from these data, the clear distinction between D76N and the ΔN6 truncation variant, considered to be a structural mimic of the amyloidogenic I_T state [78, 146], shown by these data and by others [161] could indicate an alternative, or additional route, to amyloid formation in β2m, not involving the I_T state folding intermediate. If true, further analysis of the β2m model protein system could prove invaluable in studying the potential multiplicity of pathways available to amyloid formation from the native state of a protein structure.

4.7.4 Attempted HDX-ETD single residue experiments

In an effort to gain higher resolution structural information on the HDX behaviour of the E-F loop in D76N, and ascertain precisely which residues were responsible for the increased deuterium uptake in this region, single residue HDX-MS experiments using ETD peptide fragmentation were attempted. Although problems with method development meant these experiments ultimately failed to yield any useful results, the discussion of these data may help future research and, for the interested reader, are presented (briefly) in this section.

With help from Malcolm Anderson (Principal applications chemist, Waters Corporation, Wilmslow, UK) the Synapt G2Si instrument was tuned to optimise ETD fragmentation and minimise deuterium scrambling, using the peptide P1 standard similar to earlier reports [266]. Good sequence coverage was obtained (Figure 4.22), and minimal deuterium scrambling was observed after incorporation of the peptide with deuterated buffer, as evidenced by the retention of deuterium at the C-terminal end

of the peptide, where the slower exchanging isoleucine and lysine side chains are located (Figure 4.23).

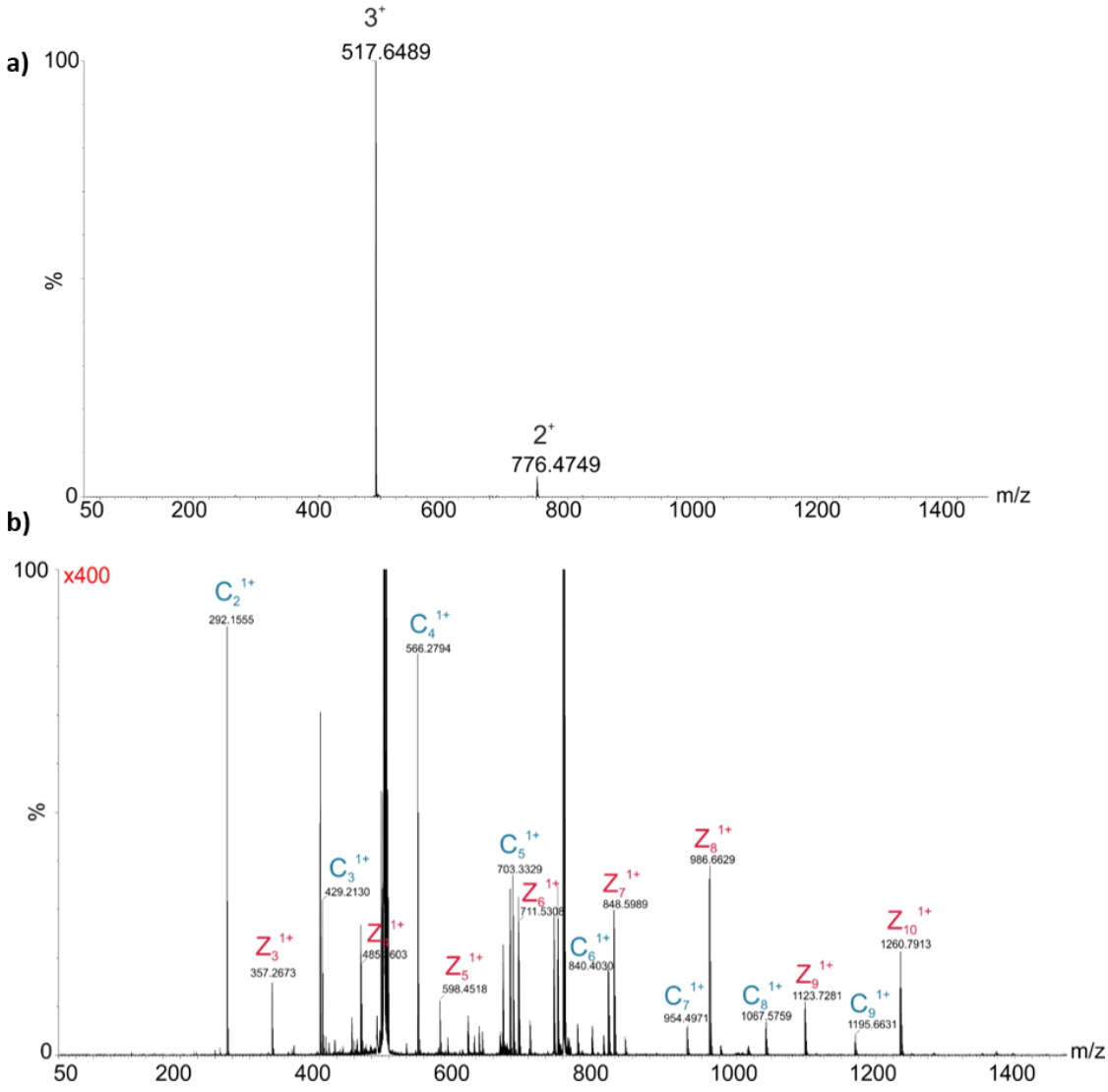

Figure 4.22 ETD fragmentation of peptide P1. **a)** Fragmentation spectrum of peptide P1 (sequence: HHHHHHIIKIIK) and a 400x y axis zoomed image **(b)**. C and Z ions are shown in blue and pink, respectively, above each peak.

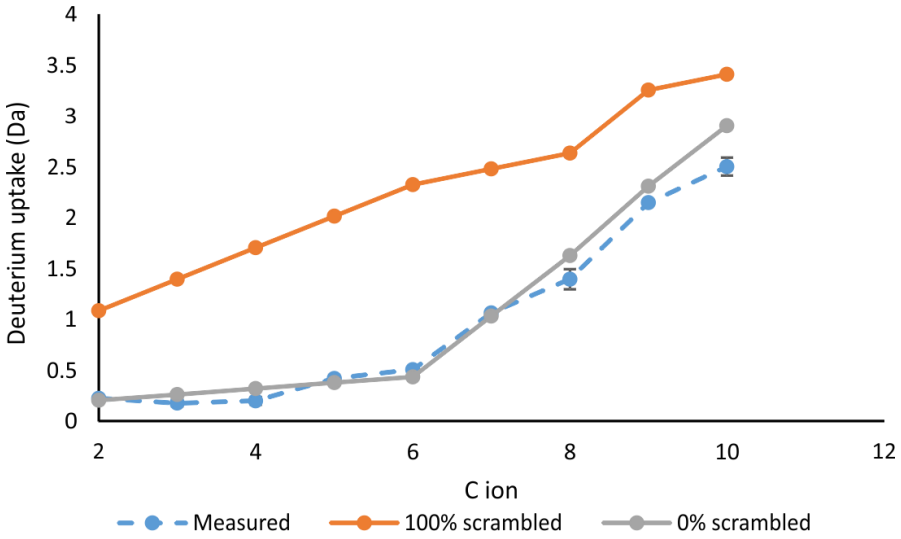

Figure 4.23 Deuterium scrambling analysis on peptide P1. Deuterium content of peptide P1, following instrument tuning, matches that of the unscrambled values obtained from modelling equations found in [266].

Although the fragmentation efficiency was low, ETD fragmentation was successfully incorporated into the online LC-IMS-MS workflow (outlined in section 3.4.1) by combining multiple acquisitions to increase the total level of signal. This was successfully tested on the 3^+ charge state of the N-terminal peptide of wild-type β2m where, after six combined LC-MS acquisitions, almost a complete fragment ion series could be observed (Figure 4.24).

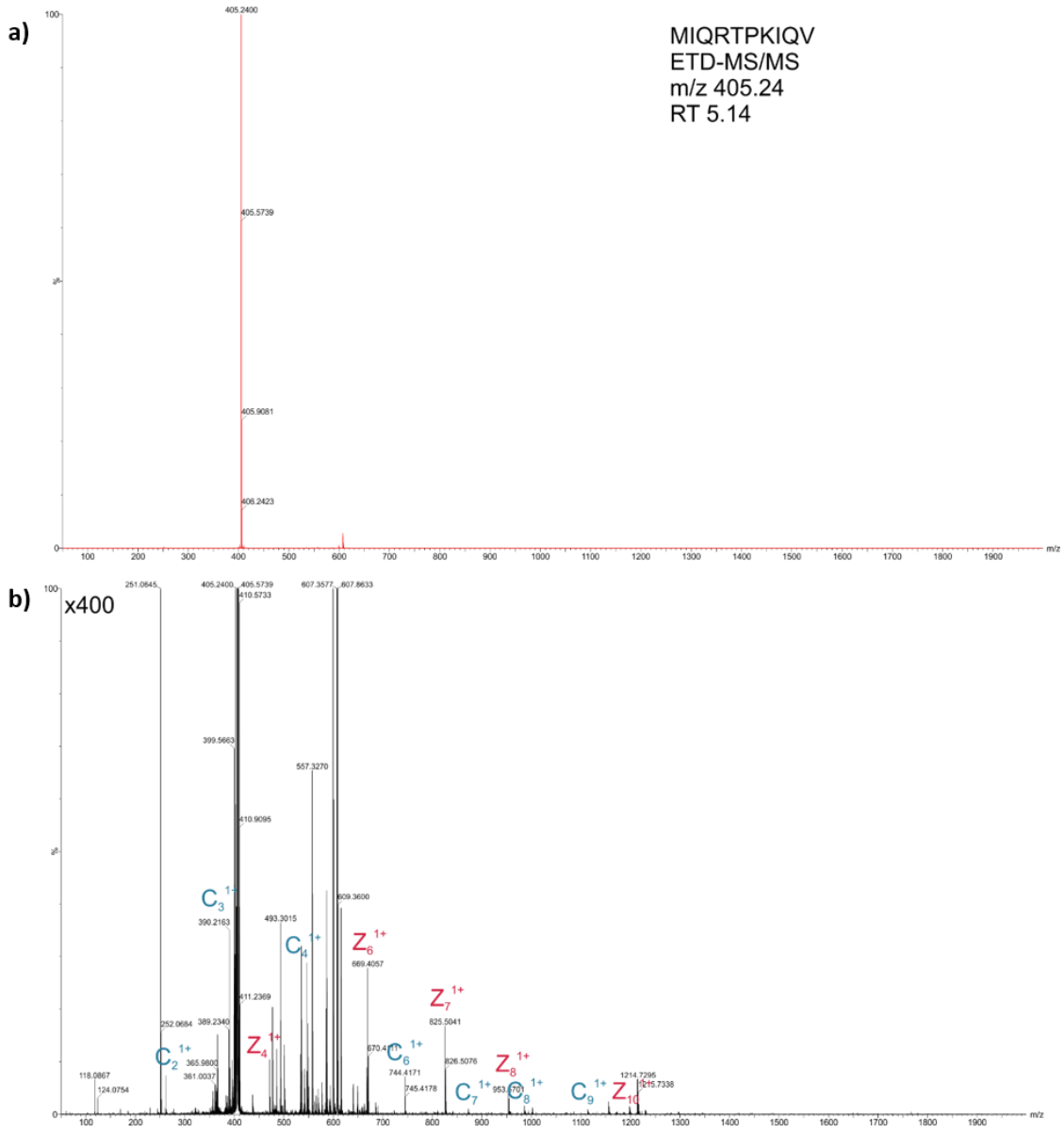

Figure 4.24 Online HDX-LC-ETD-MS of the N-terminal peptide of β2m. **a)** ETD fragmentation spectrum of peptide 0-9 of wild-type β2m (sequence : MIQRTPKIQV) from online LC-ETD-MS/MS experiments. **b)** 400x y axis zoomed image of the fragmentation spectrum. C and Z ions are annotated blue and pink, respectively.

Despite these successes however, the peptides that were identified in the region of the E-F loop were all doubly charged, and yielded no identifiable fragment ions when subjected to ETD fragmentation, even after combining multiple acquisitions. In accordance with earlier ETD methods [255], 0.05 % (*v/v*) supercharging reagent (M-NBA) was added to the LC solvents to increase the charge states of identified peptides. Whilst this did produce a 3^+ charge state of one peptide covering the desired region,

the intensity of this charge state was too low (~5e4) to identify any fragment ions following ETD, even after combining multiple acquisitions (Figure 4.25). Additionally, the added supercharging reagent, presumably due to its lack of volatility, frustrated the author (and the MS facility manager) to a great degree by fouling the front end of the mass spectrometer with brown goo.

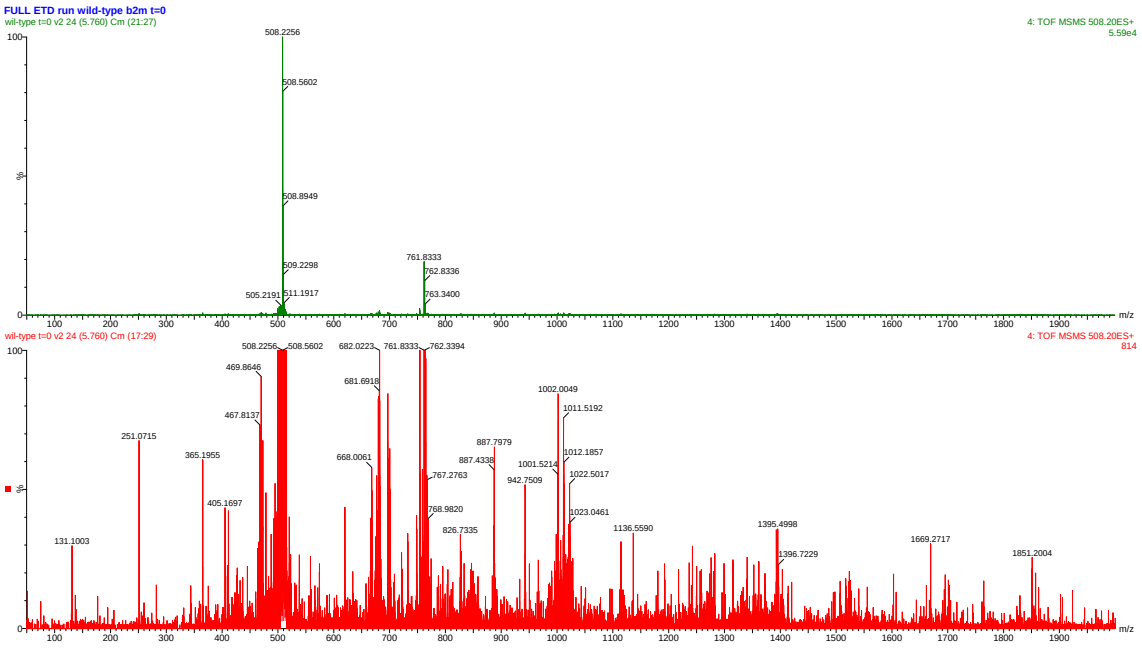

Figure 4.25 ETD fragmentation of the E-F loop of wild-type β2m. Fragmentation spectrum (top) and a 400x y axis zoom (bottom) of peptide 67-78 (sequence YTEFTPTEKDEY) of wild-type β2m after six combined acquisitions. No ETD fragment ions could be identified.

Alternative digest strategies using two different acid proteases (other than pepsin) were similarly ineffective at providing an abundant, triply charged peptide in the region of the E-F loop (Figure 4.26).

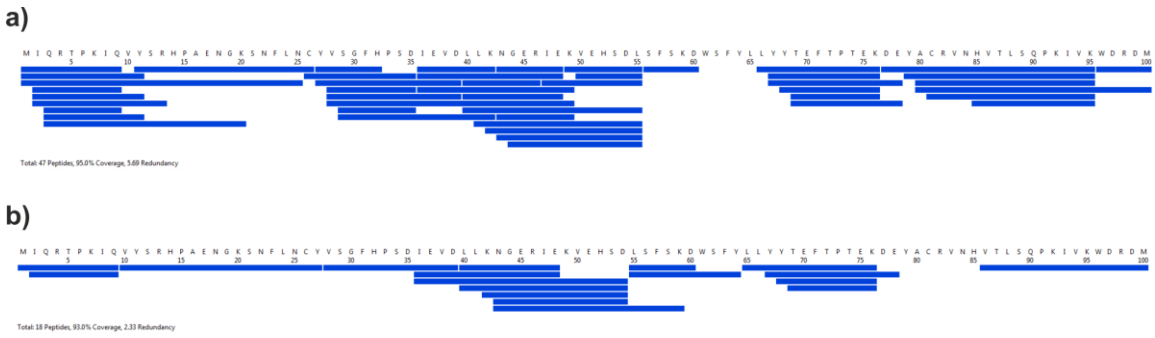

Figure 4.26 Alternative acid protease digests of wild-type β2m. Digests using Nepenthesin **(a)** and Aspergillopepsin **(b)** both failed to provide abundant, triply charged peptides in the region of the E-F loop that would be conducive to successful ETD fragmentation.

While these experiments were not successful in attaining the greater understanding of the E-F loop of D76N as desired, and certainly highlight the need for more orthogonal digestion methods, many experimental parameters were left unchanged, due to time constraints, which may have yielded better results. For example, alternative quench conditions or a re-optimisation of the digest protocol, as opposed to changing proteolytic enzyme, may provide more ETD compatible peptides in the preferred region. Alternatively, orthogonal fragmentation strategies, such as UV photodissociation, have been shown to successfully localise deuterium incorporation on peptides to residue level without adding internal energy sufficient to produce deuterium scrambling [267]. It has been proposed that this fragmentation technique also has higher fragmentation efficiency and a more limited dependence on the charge state of the peptide precursor. These characteristics could make this an ideal fragmentation method to suit the issued thus far encountered with these experiments.

Given the stark difference in deuterium uptake between the, otherwise startlingly similar, wild-type protein and the D76N variant, and the time constraints limiting the

development time that was available for the above method, the importance of the continuation and further development of this, or similar, methods to further understand the E-F loop of D76N cannot be overstated. The implications of this are discussed further in section 7.2.

Chapter 5:

FPOP-LC-MS/MS comparing β_2m variants

5 FPOP-LC-MS/MS comparing β2m variants

As discussed earlier in Section 2.4.4, fast photochemical oxidation of proteins (FPOP) is an emerging technique frequently used in conjunction with MS analysis, used for the characterisation and understanding of protein structures, although the method itself, and the intricacies of how to analyse and interpret the resulting data, are poorly understood. This chapter aims to address some of these issues, with the following aims:

1. Evaluate the current FPOP method used in our laboratory and determine the significance, and incidence, of structural artefacts created by FPOP labelling in these experiments.
2. Use the well-characterised wild-type and ΔN6 truncation variants of β2m to develop the FPOP method, and gain a greater understanding of how to interpret and analyse FPOP-LC-MS/MS data.
3. Use FPOP-LC-MS/MS to characterise the, poorly understood, D76N variant of β2m and identify any changes that may be associated with the increased propensity of this variant to aggregate.

FPOP data for wild-type β2m and the ΔN6 truncation variant from this chapter were subsequently published in Cornwell., *et al.*, JASMS, 2019 [252].

5.1 FPOP method validation

In an ideal FPOP experiment, each protein, and the solution immediately surrounding it, would be irradiated no more than once. This is because once a protein has been irradiated, it has the possibility, although not certainty, of being labelled by a nearby hydroxyl radical, and the introduction of such non-native oxidations may shift the protein structure into a non-native conformation. As a result, continued oxidative labelling of the protein increases the chance of probing non-native structures generated as artefacts of FPOP labelling, rather than the protein in its native state.

However, the experimental setup typically used in FPOP, both in the literature and our laboratory (described in detail in Section 3.5), makes the determination of exactly how many irradiation events, or 'shots', a protein has undergone quite challenging. The FPOP analyte solution is passed, at a fixed flow rate, through a capillary that intersects orthogonally the beam of a UV excimer laser, necessary to liberate hydroxyl radicals from hydrogen peroxide. Due to the nature of the laser itself, this beam is not constant and is instead pulsed at a constant frequency, for a fixed duration of 20 ns (Figure 5.1). Although this extremely short pulse duration can be assumed as instantaneous, for most practical purposes, this setup is such that many other parameters are involved in determining how many times a protein molecule is irradiated including: laser firing frequency, beam width, diffusion of the protein in solution, and time spent in the irradiation window, the latter of which is directly proportional to the flowrate of the solvent in the capillary.

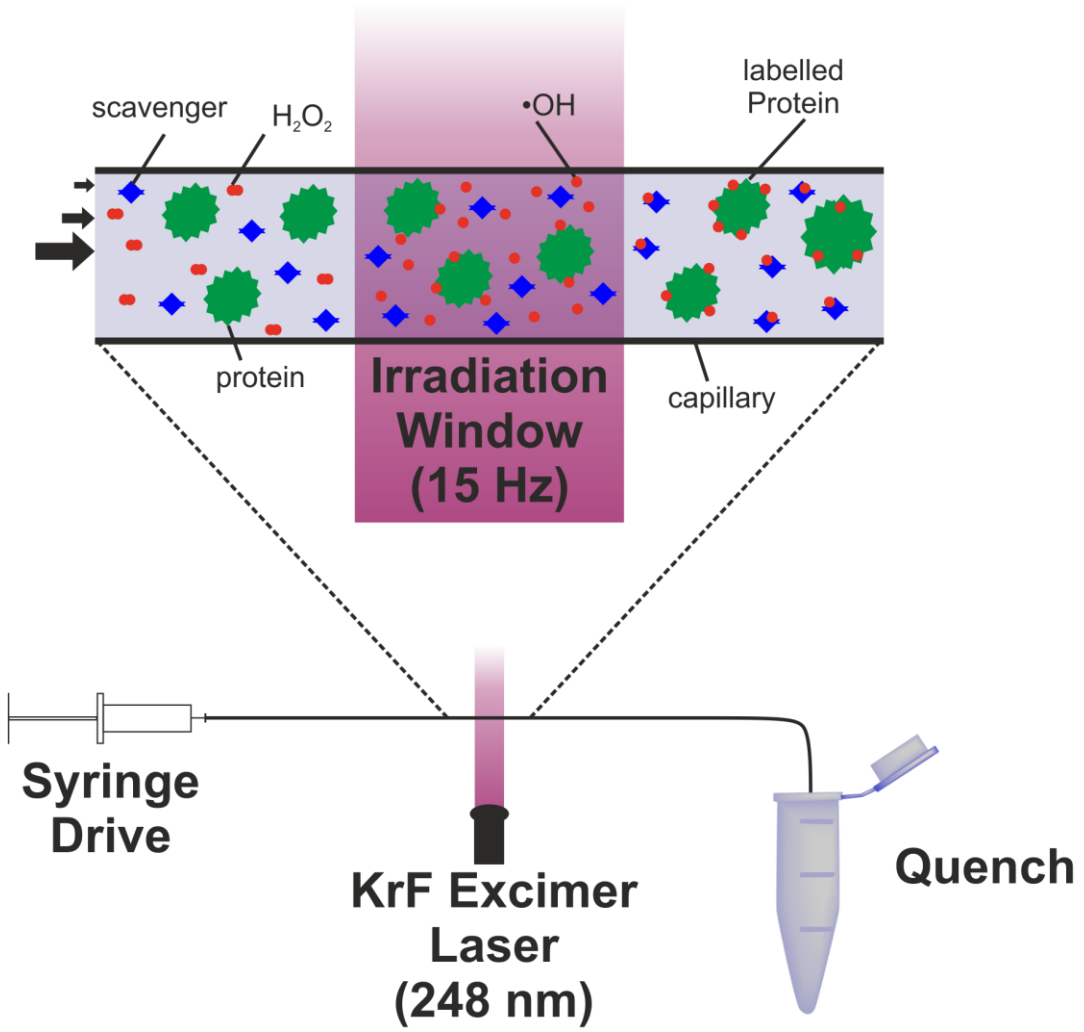

Figure 5.1 Schematic diagram of a typical FPOP experimental setup. Solution containing the protein sample, hydrogen peroxide and a scavenger amino acid is passed through a capillary intersecting an irradiation window where 248 nm UV light causes photolysis of the hydrogen peroxide, generating hydroxyl radicals. These hydroxyl radicals then covalently label the protein sample, before the sample is diverted into a quench solution to prevent further radical oxidation.

The beam width (~3 mm), firing frequency (15 Hz) and the flowrate (20 µl min^{-1}) of the analyte solution have been optimised previously in our laboratory to approximate each bolus of liquid in the capillary experiencing a single shot, which can be demonstrated, knowing the inner radius of the capillary (50 µm), by showing that the irradiated volume per second is approximately equal to the flow rate used [231].

$$Irradiated\ volume\ per\ second = \pi r^2 \times w \times f \quad (5.1)$$
$$= \pi(50 \times 10^{-6})^2 \times (3 \times 10^{-3}) \times 15$$
$$= 3.54 \times 10^{-10}\ m^3 s^{-1}$$
$$= 21\ \mu l\ min^{-1}$$

Equation 5.1 Calculating irradiation volumes in FPOP capillary experimental setups assuming a plug flow model. Area of the capillary (units = m^2) multiplied by beam width (denoted w, units = m) multiplied by laser firing frequency (denoted f, units = s^{-1}). Units of $m^3\ s^{-1}$ converted to μl min^{-1} by multiplying by 10^9 (units = μl s^{-1}) and multiplying again by 60 (μl min^{-1}).

Although others have used more conservative experimental parameters, opting for a brief exclusion volume with no irradiation between each shot [227], which has been achieved by increasing the flowrate or reducing the firing frequency, both of these calculations are flawed in that they assume a 'plug flow' model where all solvent across the radius of the capillary is flowing at the same rate. In reality, the flow regime in the capillary is more accurately described by a laminar flow model, where solvent travels faster at the centre of the capillary, and slower at the capillary walls, a scenario typically visualised as a series of concentric rings of varying flow rates around the capillary centre (Figure 5.2). The velocity of solvent at any given radius from the centre of the capillary can be calculated using Equation 5.2 [268].

$$v(r) = 2\left(\frac{V}{\pi r^2}\right)\left(1 - \frac{r^2}{R^2}\right) \quad (5.2)$$

Equation 5.2 Calculating the velocity of solvent at different radii from the capillary centre in laminar flow. Where v(r) is the velocity at a given radius (r) from the capillary centre (units = m s^{-1}), V is flow rate (units = $m^3\ s^{-1}$) and R is the capillary radius (units = m).

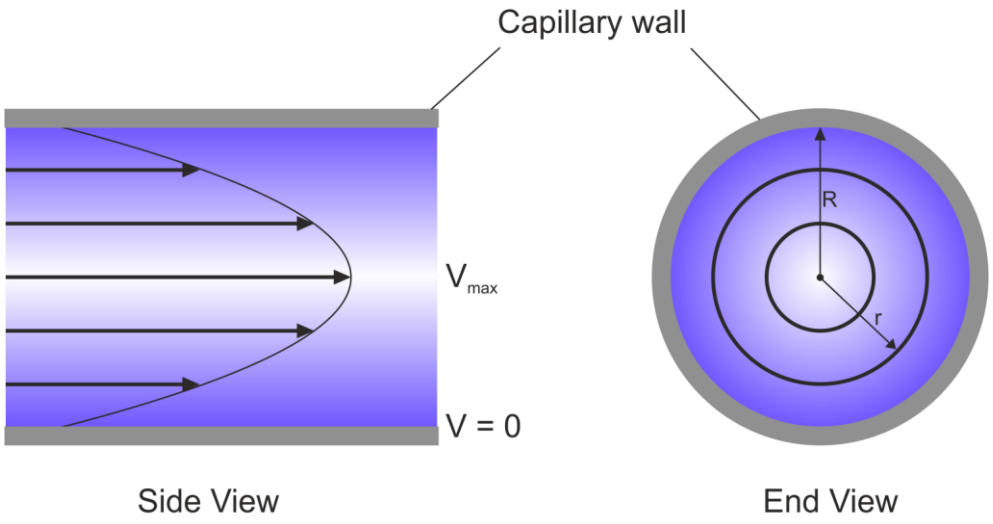

Figure 5.2 Visualising laminar flow in capillaries. Side view (left) and end view (right) of laminar flow shows solvent flows faster at the capillary centre and slower at the capillary walls. R and r are annotated as in Equation 5.2.

Laminar flow regimes have been described previously in the context of FPOP experiments by Konermann *et al.*, where the authors concluded that diffusion of the protein both axially along the capillary, and laterally between flow regimes were negligible factors in the resulting number of irradiation events experienced by protein molecules in the sample. However, the authors also concluded that due to the slower moving proteins in solvent nearer the capillary walls, multiple shots for a certain proportion of the sample, and only minimal radiation exposure for proteins in faster flow regimes in the capillary centre, are inevitable consequences of laminar flow in these experiments [268]. Nevertheless, based on these findings, the FPOP method used previously in our laboratory was re-evaluated to determine the degree to which multiple exposure events were occurring under the present experimental conditions.

Using Equation 5.2 and experimental parameters listed in Section 3.5, the velocity of solvent, and time spent inside the irradiation window, at various different radii from the capillary centre, were calculated (Figure 5.3). By assuming this velocity is consistent across short widths of the capillary, we can simplify the problem by splitting the flow in the capillary into multiple, smaller 'plug flow' models, where each

concentric ring of flow, of arbitrary width, is approximated to have the same average velocity. This approximation is most accurate closest to the capillary centre, where the dependence of velocity on radial position is the lowest (Figure 5.3). As such, the calculation was split into multiple 5 μm wide rings from the capillary centre (0-5 μm, 5-10 μm etc…) where, smaller, 1 μm intervals were used after 45 μm from the capillary centre, where radial position affects velocity most significantly.

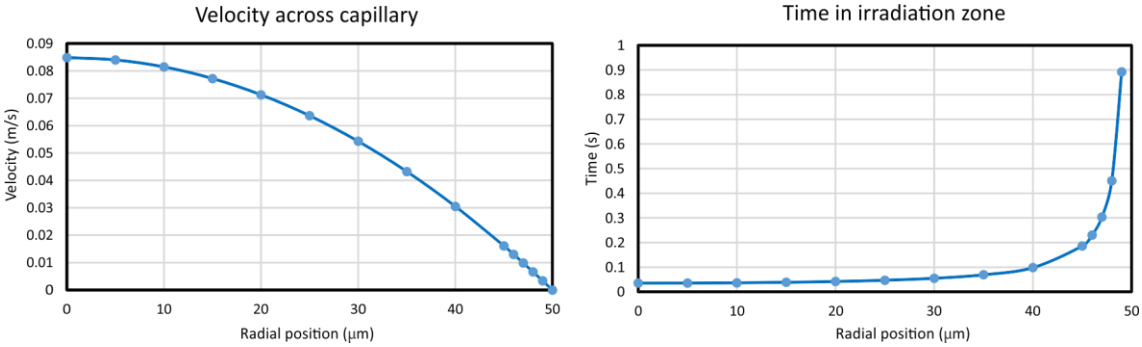

Figure 5.3 Velocities and time spent in the irradiation zone calculated for different flow regimes in the FPOP capillary. Calculated using Equation 5.2 and experimental parameters listed in Section 3.5. A radius of 0 on the x axis is the capillary centre. The work of Prof. Nik Kapur (Applied Fluid Mechanics, School of Mechanical Engineering, University of Leeds) is gratefully acknowledged for his help in these calculations.

Knowing the firing frequency of the laser (15 Hz) and the time spent in the irradiation window for each concentric ring of flow, or flow regime, we can determine the average number of shots and, consequently, the maximum and minimum number of shots, a protein could experience under each flow regime, maximum being a scenario where a protein is irradiated the instant it enters the beam width, and the minimum being a protein that follows one that was instantly irradiated (equivalent to one fewer than the maximum number of hits). As the proportion of protein receiving the maximum and minimum number of shots under each flow regime must sum to 1, we can determine the fraction of protein, under each flow regime, that receives the maximum and minimum number of shots (Equation 5.3, Table 5.1).

$$x + y = 1 \tag{5.3}$$
$$\alpha x + \beta y = average\ shots$$

Equation 5.3 Simultaneous equations calculating the maximum and minimum number of irradiation events for different flow regimes in FPOP. Where x and y are the proportions of protein receiving the maximum and minimum number of shots, and α and β are the maximum and minimum number of shots for a given flow regime.

Calculating the cross sectional area of each flow regime ring, we can determine the mean flow rate of solvent in each regime, by multiplying by the mean velocity of the solvent at this radius (Table 5.1). Dividing this by the mean flow across the whole capillary, we can estimate the fraction of the sample subjected to each flow regime. Knowing how much of the sample is in each flow regime, and how much of each flow regime experiences different numbers of irradiation events, we can determine, overall, the proportion of the sample that is under the desired single exposure conditions (Figure 5.4).

Table 5.1 Determining the number of irradiation events under different flow regimes of a laminar flow model in FPOP experiments.

Radius (μm)	Velocity (m s^{-1})	Time in zone (s)	Max hits	Average hits	Min hits fraction	Max hits fraction	Mean flow at this radius (m^3 s^{-1})	Fraction flow at this radius (%)
0	0.084883	0.035343	1	0.530144	0.469856	0.530144		
0-5	0.084034	0.0357	1	0.535499	0.464501	0.535499	6.6E-12	2.210133
5-10	0.081487	0.036816	1	0.552233	0.447767	0.552233	1.92E-11	6.429478
10-15	0.077243	0.038838	1	0.582576	0.417424	0.582576	3.03E-11	10.15768
15-20	0.071301	0.042075	1	0.631124	0.368876	0.631124	3.92E-11	13.12685
20-25	0.063662	0.047124	1	0.706858	0.293142	0.706858	4.5E-11	15.06909
25-30	0.054325	0.055223	1	0.82835	0.17165	0.82835	4.69E-11	15.7165
30-35	0.04329	0.0693	2	1.039498	0.960502	0.039498	4.42E-11	14.8012
35-40	0.030558	0.098175	2	1.472622	0.527378	0.472622	3.6E-11	12.05527
40-45	0.016128	0.186015	3	2.79023	0.20977	0.79023	2.15E-11	7.210839
45-46	0.013038	0.230097	4	3.451457	0.548543	0.451457	3.73E-12	1.248176
46-47	0.00988	0.303633	5	4.5545	0.4455	0.5545	2.89E-12	0.966672
47-48	0.006655	0.450803	7	6.762038	0.237962	0.762038	1.99E-12	0.665094
48-49	0.003361	0.892498	14	13.38747	0.612531	0.387469	1.02E-12	0.343013

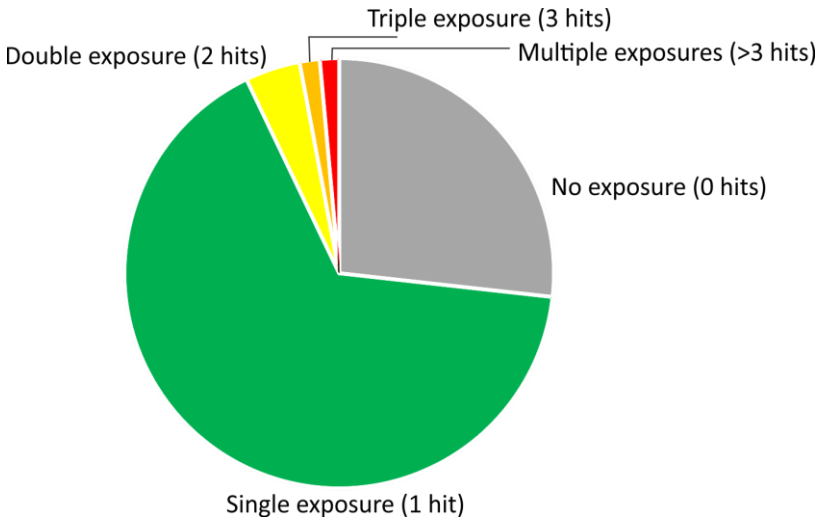

Figure 5.4 Exposure events per protein in the current FPOP experimental arrangement.

Figure 5.4 indicates that ~two thirds (66%) of the sample is under single exposure conditions using these experimental parameters, just over 25% of the sample experiences no irradiation events at all, leaving less than 8% of the sample to experience multiple exposures. This is slightly more oxidation than was suggested as optimal by Konermann *et al.*, [268] and as such, the effects of multiple exposure events on wild-type β2m were evaluated to determine the significance of these events with regards to their effect on protein conformation and downstream analysis.

Native MS experiments showed no significant change in the charge state distribution following FPOP compared with the control protein, with the most notable change being a significant decrease in signal intensity for the FPOP sample, presumably due to signal splitting between the various different oxidised species (Figure 5.5).

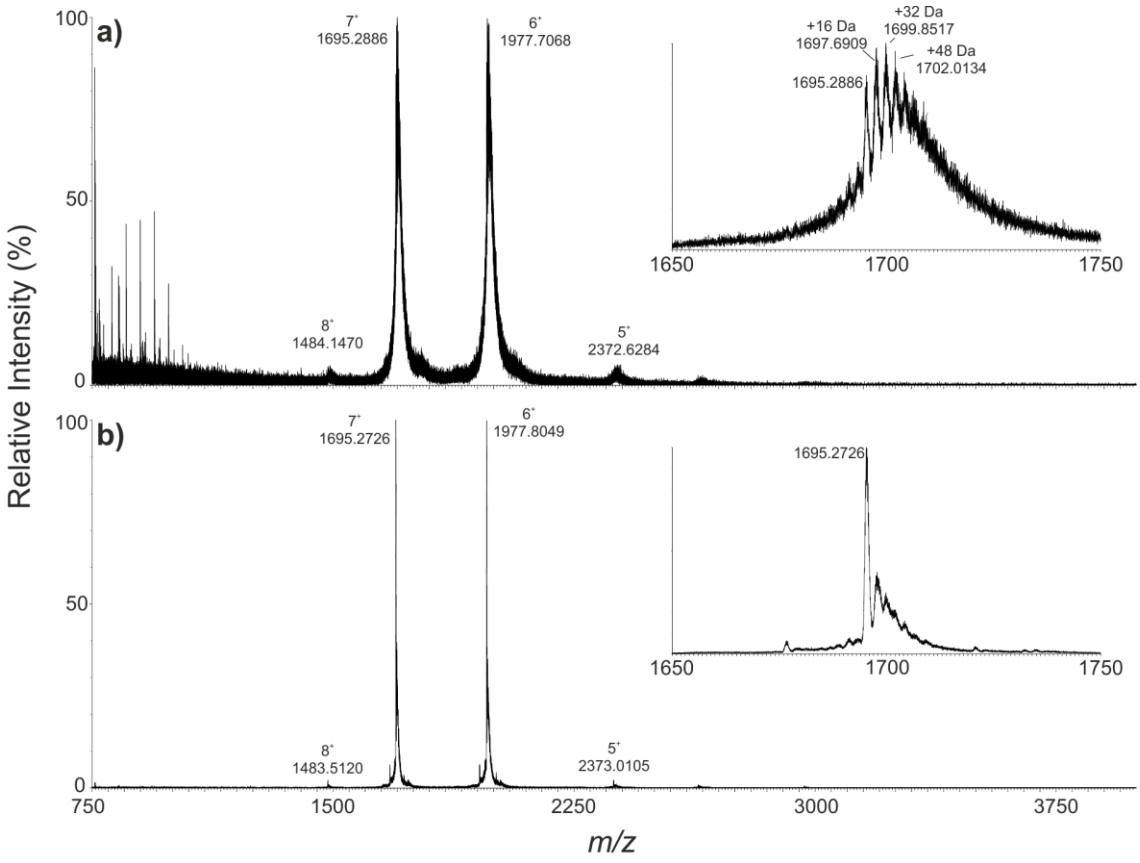

Figure 5.5 Native MS of FPOP oxidised wild-type β2m. (**a**) Wild-type β2m oxidised by FPOP (as per experimental procedures described in section 3.5.1) compared with (**b**) the control without FPOP or exposure to hydrogen peroxide. Inset shows a zoom of the 7^+ charge state ions highlighting the observable +16 Da oxidations in the oxidised sample and no oxidations, although some salt adducts, on the non-oxidised sample. The ESI-MS solution was 150 mM ammonium acetate, pH 7.4.

ESI-IMS-MS of the native protein showed identical ATDs for the unmodified and oxidised versions of the protein for up to three oxidations, which is the maximum number resolvable using native MS (Figure 5.6a), thus indicating no significant conformational changes result from FPOP oxidation for wild-type β2m under the conditions employed.

To determine the effect, if any, of multiple oxidations on proteolytic digestion of the wild-type protein, samples of wild-type β2m contained in Eppendorf tubes, rather than the typical capillary flow setup, were irradiated between one and ten times, reduced, alkylated and digested with trypsin, before the tryptic peptides were analysed by LC-MS/MS. Figure 5.6b shows that as the number of irradiation events

increases, the percentage of the protein sequence covered from the peptides identified decreases. A likely explanation for this is that multiple irradiation events cause significant oxidation which splits the peptide signal among many different oxidised species eluting at different retention times, which fall below the limit of detection.

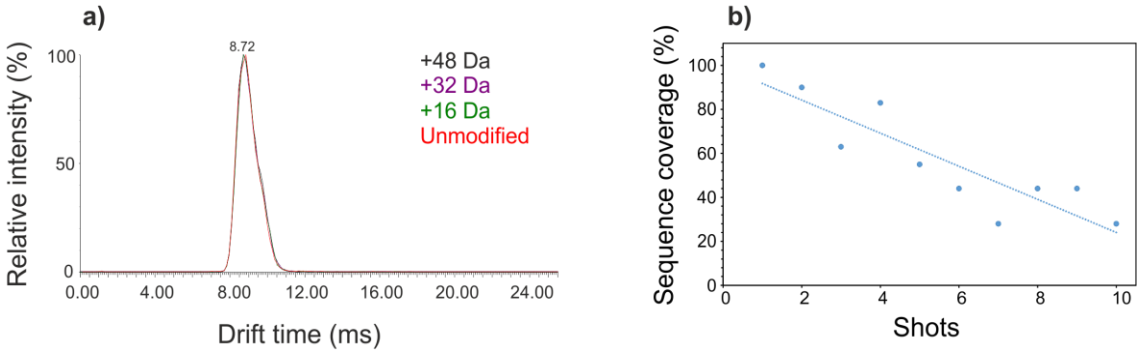

Figure 5.6 The effect of FPOP oxidation on native IMS ATDs and sequence coverage in proteolytic digests of wild-type β2m. **a**) ATD extracted from the 6^+ charge state ions of wild-type β2m for the unmodified, and up to three oxidative FPOP modifications. **b**) Sequence coverage from tryptic digests of β2m following FPOP oxidation.

Although some evidence suggests that FPOP oxidations can partially unfold proteins [269], others have found limited oxidation to be relatively benign [226, 270], with some evidence suggesting that certain enzymes can even retain activity following oxidation by FPOP [271]. This is consistent with the fact that FPOP labels primarily solvent exposed side chains, often hydrophilic structures with a high degree of conformational freedom, and thus are unlikely to be significantly structurally perturbed by the effect of a small, hydrophilic modification such as hydroxylation.

Overall, these data suggest that the current FPOP experimental setup is unlikely to generate significant detectable structural artefacts, given only ~8% of the sample experiences multiple exposure events (Figure 5.4), and such exposure has no significant effect on the native protein conformation, to the resolution of an IMS experiment. Additionally, those molecules that do experience multiple exposure events contribute less to the analysis of oxidations in LC-MS/MS data, as the higher

levels of oxidation split the peptide signal further across multiple oxidised species, increasing the likelihood that such species fall below the limit of detection.

5.2 FPOP LC-MS/MS of wild-type, D76N and ΔN6 β2m

Wild-type, D76N, and ΔN6 β2m were subjected to FPOP oxidation under native conditions, prior to intact MS analysis under denaturing conditions. All three variants showed significant oxidation, observable as a series of +16 Da mass additions that were absent in the control samples (Figure 5.7). After quantification, no significant difference in the degree of oxidation was observed between the three variants. In each case, ~65% of the total protein signal was observed to be modified.

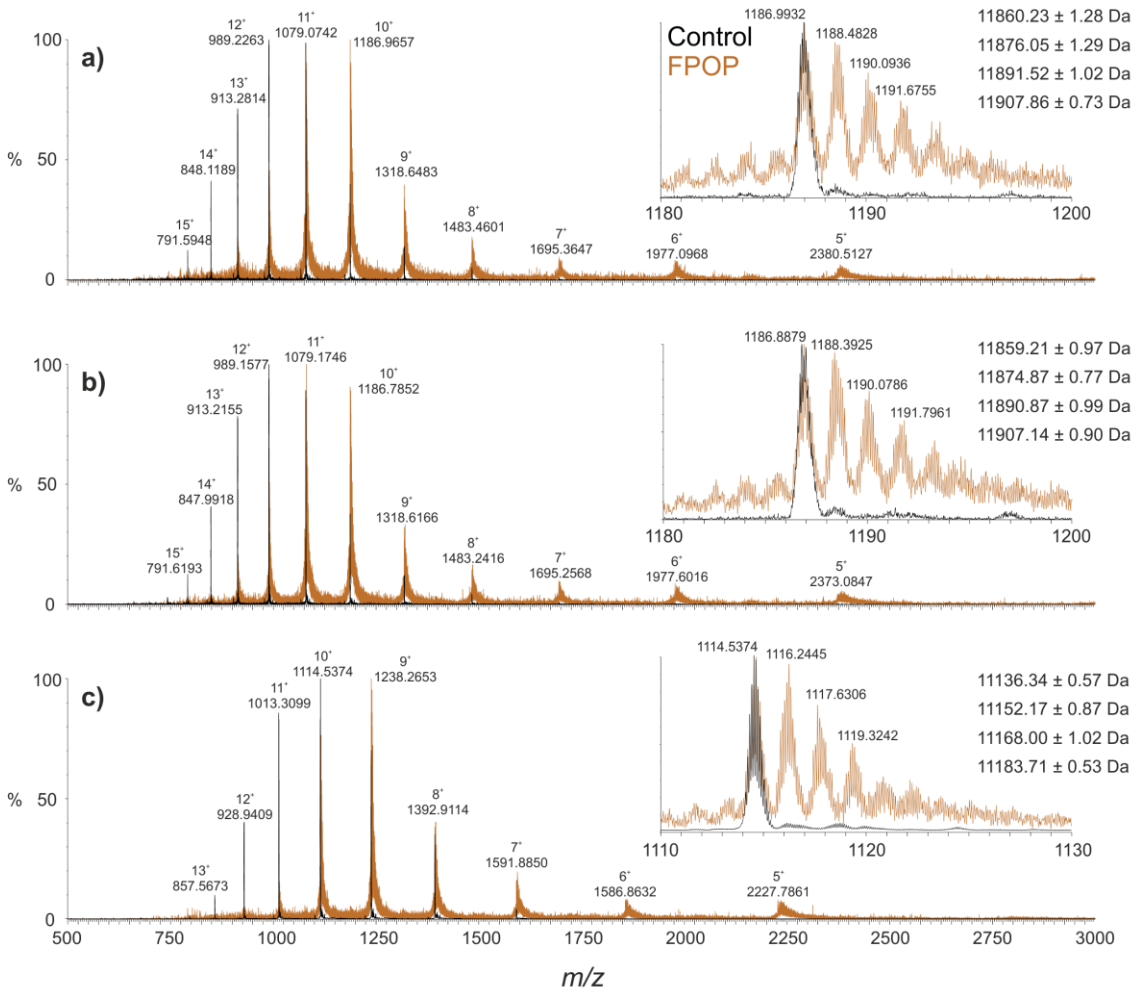

Figure 5.7 Denatured ESI-MS of three β2m variants following FPOP. (**a**) Wild-type, (**b**) D76N, and (**c**) ΔN6 before (black) and after (orange) FPOP. Annotations above each peak show *m/z* and charge state. Inset shows a zoom of the 10^+ charge state ions. Calculated masses from each species in the spectra are shown in the top right hand corner.

Although no global differences in oxidation could be detected between the three variants, to determine if any differences could be observed by FPOP at higher resolution, the three oxidised β2m variants were enzymatically digested with chymotrypsin and the resulting peptides were then analysed by LC-MS/MS using a Q-Exactive quadrupole orbitrap mass spectrometer operating in DDA mode (experimental details can be found in Section 3.5.1). The data were then searched automatically for peptide MS/MS data matching the wild-type β2m/D76N/ΔN6 amino acid sequences, along with possible variable mass additions of +16 Da, +32 Da, and +14 Da, in order to identify oxidations generated from FPOP. Greater than 95% sequence

coverage was observed reproducibly in all three variants (Figure 5.8), where manual inspection of peptide coverage maps identified seven chymotryptic peptides for which both modified and unmodified peptides were present in all replicates for all three proteins (green peptides in Figure 5.8). An additional peptide at the N-terminus (absent in ΔN6) that fit these criteria for the wild-type protein and the D76N variant (orange peptide in Figure 5.8) was also identified. Thus, these eight peptides were used to assess differences in FPOP oxidation between the three variants.

Figure 5.8 Peptide coverage of three variants of β2m following chymotrpyptic digest. Bars represent identified peptides. The D76N modified site is identified with an asterisk. Blue = irreproducible peptides or peptides for which no oxidised products could be identified that were found in this representative coverage map. Orange = reproducible peptides found in all replicates of both wild-type and D76N β2m, for which both modified and unmodified versions could be identified. Green = reproducible peptides found in all replicates of all three variants for which modified and unmodified versions could be found.

Manual inspection of tandem MS spectra for modified versions of these eight chymotryptic peptides could be used to assign 19 different modified sites (approximately 20% of the β2m sequence, summarised in Table 5.2), all but one of which could be localised to single amino acid resolution. The location of these modified sites are shown in the structure of β2m in Figure 5.9.

Table 5.2 Residues modified by FPOP in wild-type, D76N and ΔN6 β2m.

Peptide	Sequence	Modified residues
0-10 (Wild-type and D76N only)	MIQRTPKIQVY	Met 0
11-26	SRHPAENGKSNFLNCY	His 13, Lys 19, Phe 22, Tyr 26,
27-40	VSGFHPSDIEVDLL	Val 27, Phe 30, His 31, Ile 35 (wild-type and D76N only)
41-54	KNGERIEKVEHSDL	Lys 48, His 51
55-63	SFSKDWSFY	Trp 60
67-78	YTEFTPTEK(D/N)EY	Tyr 67, Phe 70, Tyr 78
79-87	ACRVNHVTL	His 84
88-95	SQPKIVKW	Lys 94, Trp 95, unknown (Pro 90 or Lys 91)

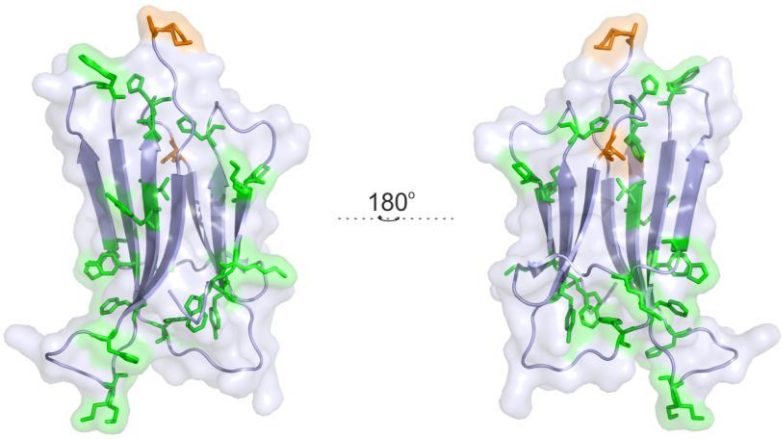

Figure 5.9 Residues modified by FPOP in wild-type, D76N and ΔN6 β2m mapped onto the β2m structure. Modified residues are shown as sticks. Green = modified in all three variants. Orange = modified in wild-type and D76N only. B-sheets are shown as ribbons and coloured blue. PDB: 4FXL [157].

To quantify and compare the degree of oxidation at each of these sites between the three variants of β2m, the LC elution profiles for *m/z* values corresponding to modified versions of each peptide were analysed individually by generating extracted ion chromatograms (XICs) (Figure 5.10). Tandem MS spectra which positively identified oxidised residues within modified peptides could then be assigned to peaks in the XIC based on the retention time (RT) at which the MS/MS data were acquired. Quantification of each modified species was then calculated by peak integration, and comparison of the peak area to that of the unmodified version of the same peptide, according to Equation 3.6 (Section 3.5.3). The results for the overall % modified for each site, for all three variants are shown in Figure 5.11.

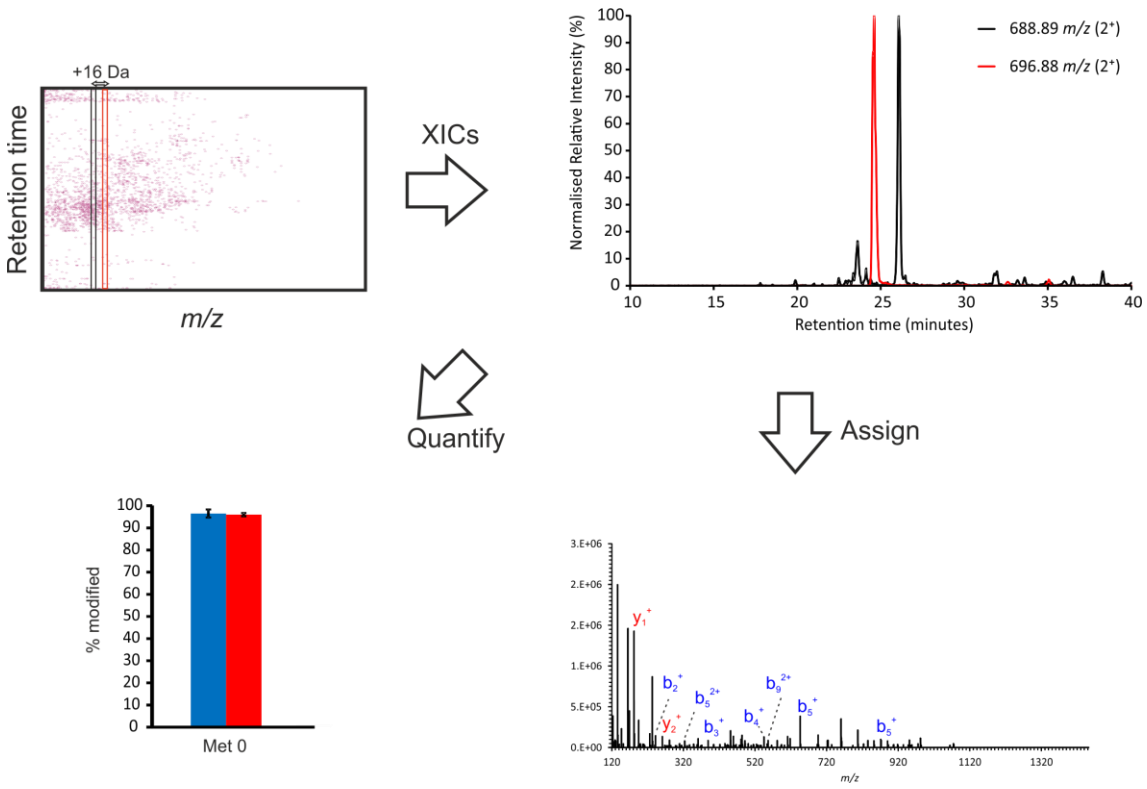

Figure 5.10 Analysis workflow for FPOP-LC-MS/MS experiments. Extracted ion chromatograms (XICs) are generated for the unmodified, and modified versions of each peptide *m/z*. The MS/MS acquired for each peak is used to identify the modification site. Integration of XICs is used to quantify levels of oxidation relative to the unmodified version of each peptide. Example shown here is that of peptide 0-10 of β2m (sequence: MIQRTPKIQVY) where Met 0 was found to be the only oxidised side chain.

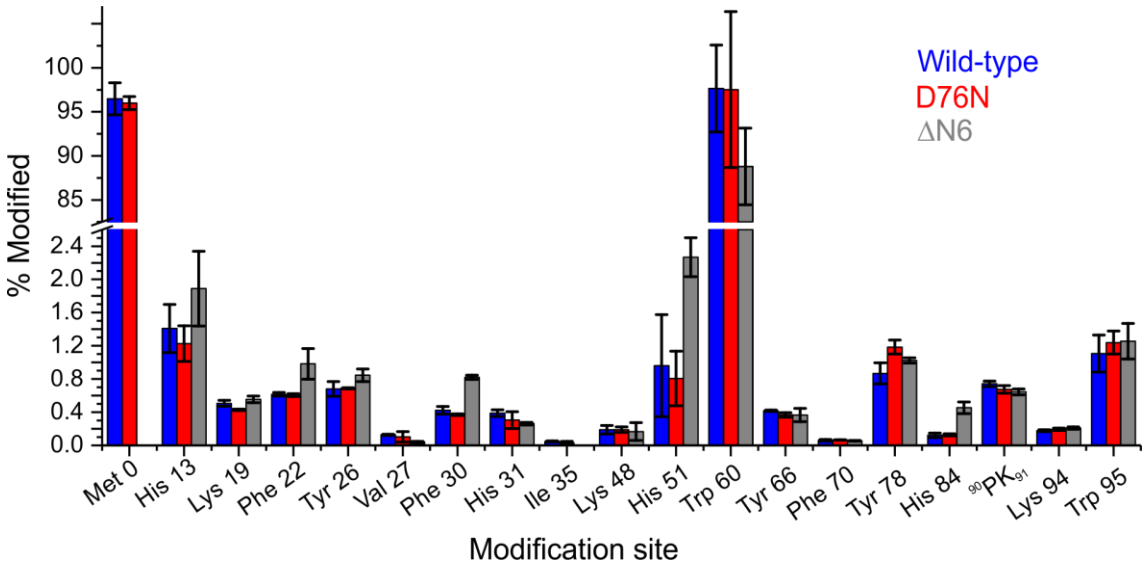

Figure 5.11 Residue level quantification of FPOP oxidations in three variants of β2m. The residue, or amino acid sequence, to which the modification could be localised is shown on the x axis. Error bars show standard deviation. N = 3.

Although methods for calculating the degree of modification at FPOP oxidised sites are established in the literature [231, 241], precisely how to interpret changes observed between states (in the case of these experiments: wild-type, D76N and ΔN6 β2m) is still poorly defined, with recent evidence suggesting that primary sequence may complicate the relationship between solvent accessible surface area (SASA) and the degree of modification [232]. Similarly, the complex, manual, and time consuming nature of data analysis is such that FPOP data are commonly quantified to peptide, rather than residue, level resolution [231, 234], thus hampering an in-depth analysis of data provided by these experiments. To that end, the differences in FPOP oxidation between the wild-type protein and the ΔN6 truncation variant, observed here at the residue level, were first compared to the differences associated with the solution phase NMR structures of the two proteins (currently no NMR structure is available for the D76N variant) [78], offering a rare opportunity to gain insight into the detailed interpretation of changes observed by FPOP, using these NMR structures as a point of reference.

5.2.1 Wild-type Vs ΔN6

Seven of the nineteen oxidised sites were observed to have statistically significant ($p < 0.05$) differences in their degree of oxidation between the wild-type protein and the ΔN6 truncation variant: Phe 22, Val 27, Phe 30, Ile35, His 31, Trp 60 and His 84. Mapping these side chains onto the wild-type NMR structure (PDB: 2XKS, [78]), it can be observed that spatially, six of these seven sites are located proximal to the N-terminal truncation in the D-E, B-C and F-G loops (Figure 5.12). This is expected given the substantial conformational changes localised to this region associated with the removal of the N-terminal hexapeptide, and is consistent with earlier reports [78, 272].

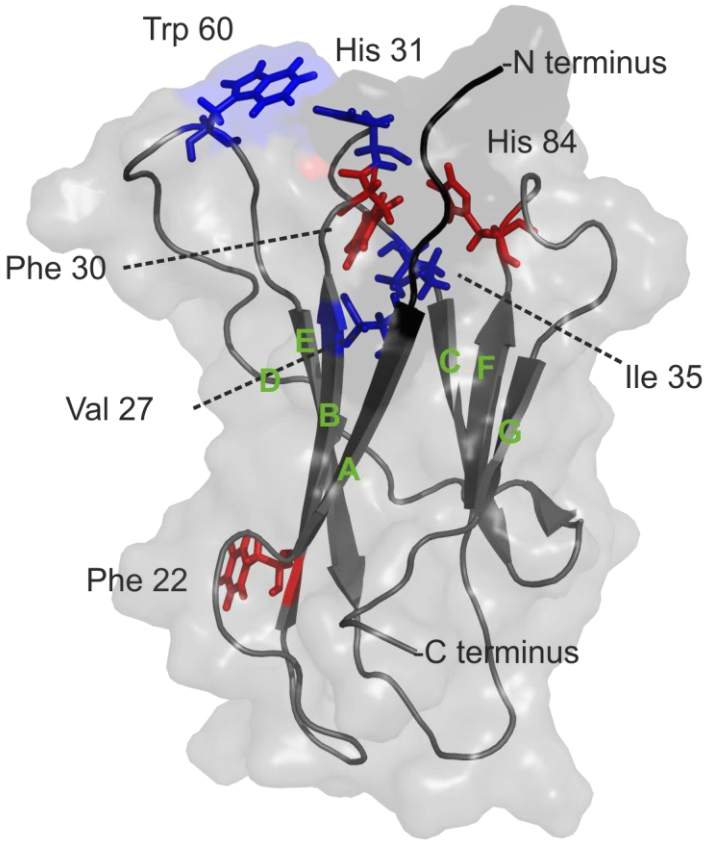

Figure 5.12 Differences in FPOP oxidation between wild-type and ΔN6 β2m. Residues with higher observed labelling in the truncation variant are shown in red. Residues with lower observed oxidation in the truncation variant are shown in blue. $P < 0.05$. PDB: 2XKS [78].

The remaining residue, Phe 22, is located at the N-terminal end of the B-strand, on the opposite end of the β-sandwich structure to the N-terminal truncation (Figure 5.12), Indeed, His 51, located at the N-terminal end of the D-strand, showed similarly increased labelling in the truncation variant (Figure 5.11). Although these changes proved not to be statistically significant ($p = 0.505$), likely caused by the considerable measurement error due to the low signal intensity of this peptide [273], Phe 22 and His 51 are somewhat proximal in the NMR structure, and face each other in the wild-type crystal structure (Figure 5.13) [77], suggesting a possible, and subtle, long range conformational change in this region caused by the removal of the N-terminal six amino acids.

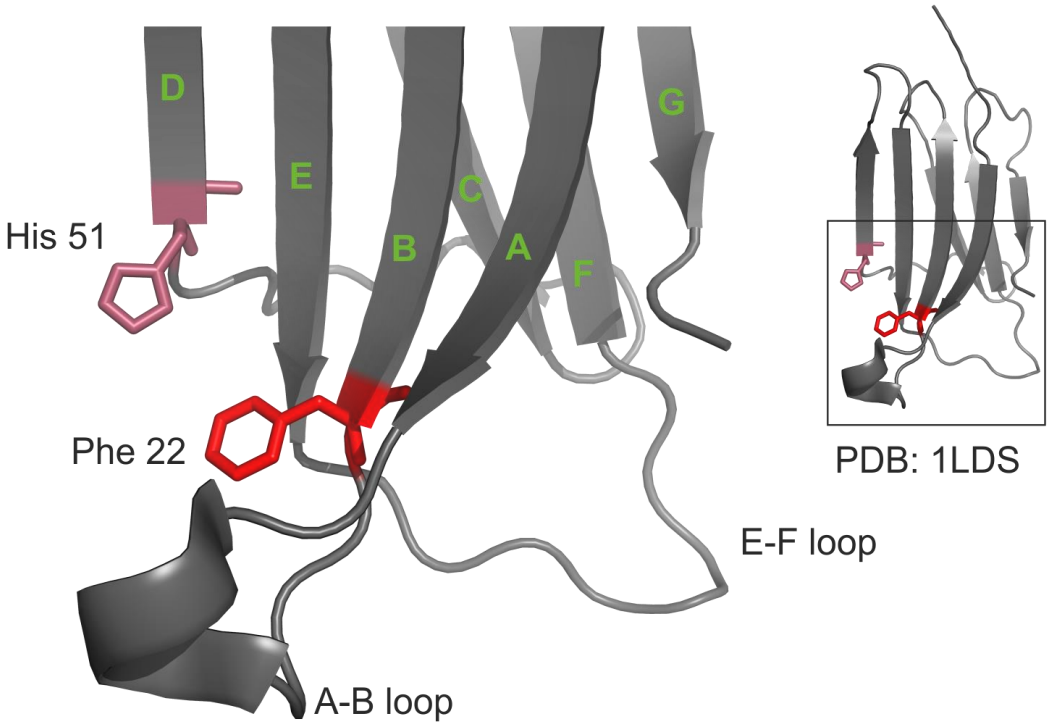

Figure 5.13 Minor side chain rearrangements detected by FPOP between wild-type and ΔN6 β2m. Side chains His 51 and Phe 22 both showed increased oxidation in the truncation variant and are annotated (red sticks). PDB: 1LDS [77].

From the NMR structures of each protein, the SASA for side chains modified by FPOP was calculated (see Section 3.5.4 for method details), and corrected for the maximal

possible solvent exposure for side chains of that type, based on their solvent accessibility in Gly-x-Gly tripeptides [274]. The fold change of these SASAs between the two proteins was then correlated with the changes in the levels of oxidation observed on these side chains. The results, shown in Figure 5.14, highlight that most of the modified side chains show minimal changes in SASA between the two variants, and minimal changes in FPOP oxidation (blue data points centred closet to the origin in Figure 5.14). Interestingly, the majority of side chains observed to have significantly different degrees of oxidation show a general positive correlation between calculated changes in SASA and measured changes in oxidation, where increases in SASA show increases in the extent of modification, and *vice versa* (Figure 5.14).

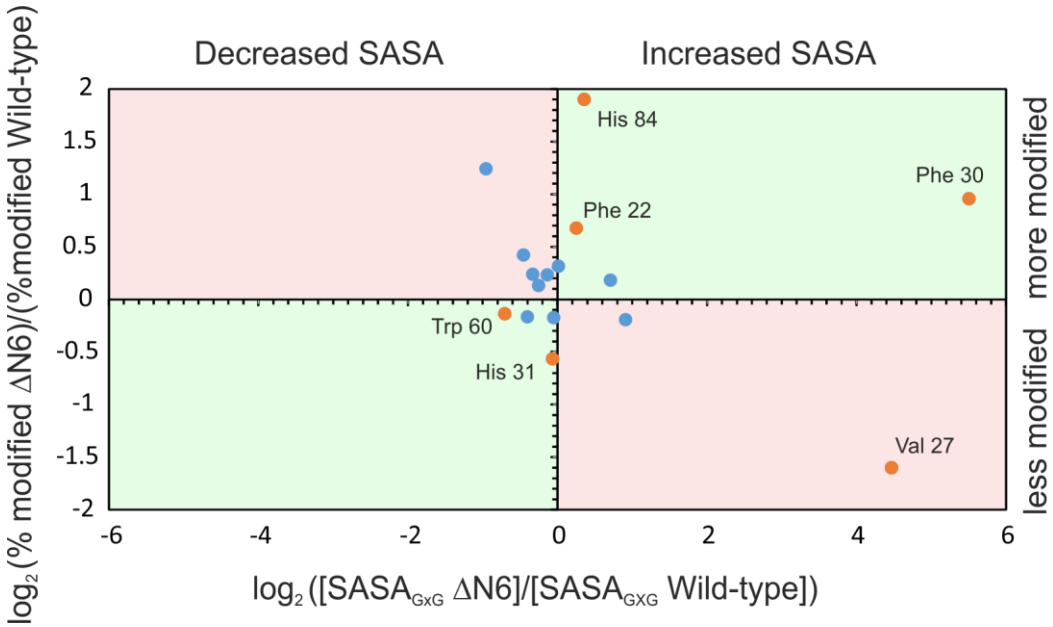

Figure 5.14 FPOP oxidation compared with SASA calculated from NMR structures. Green boxes indicate regions of positive correlation between FPOP and SASA as calculated from NMR structures (i.e. more modified in the ΔN6 variant, and more solvent exposed, or less modified and less solvent exposed). Red areas indicate regions of negative correlation between NMR and FPOP data (i.e. more solvent exposed but less labelled). Statistically significant ($p < 0.05$) changes observed by FPOP are coloured orange and annotated. Ile 35 is not included in these data as this side chain was not observed to modify in the truncation variant.

A notable and obvious exception to this is the Val 27 side chain which, despite increasing in SASA by more than 20x in the truncation variant, oxidises by FPOP less than half as much as in the wild-type protein (Figure 5.11, Figure 5.14). In both variants, Val 27 is located at the C-terminal end of the B-strand, proximal to the N-terminus of the protein. Closer inspection of this region reveals that the nearby Phe 30 side chain, rotates almost 180° between the two variants. In the wild-type structure, Phe 30 is positioned in a largely solvent inaccessible position facing the D-E loop, whereas in the truncation variant, this side chain is rotated to face bulk solvent, positioned directly adjacent to the Val 27 side chain (Figure 5.15). Given the relatively high reactivity to hydroxyl radicals of phenylalanine side chains compared with valine residues, it seems plausible that the proximity of Phe 30 to Val 27 causes increased competition for hydroxyl radicals in the region, resulting in lower labelling in the less reactive valine group, despite increased access to solvent. This is consistent with observations made by Xie *et al.*, where increased competition for hydroxyl radicals was observed in unfolded proteins in FPOP experiments [232].

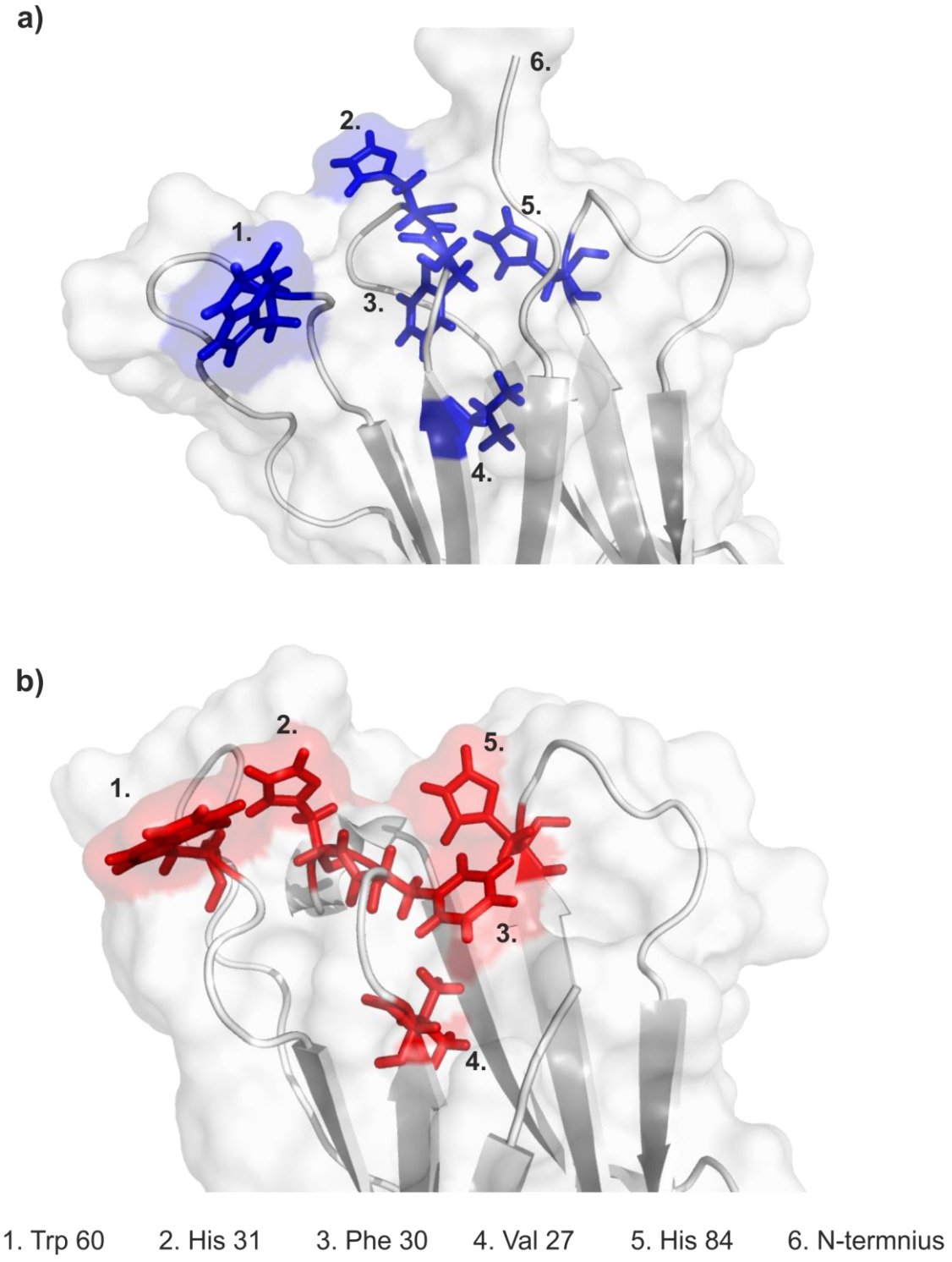

Figure 5.15 The rotation of the Phe 30 side chain in the ΔN6 truncation variant of β2m. The NMR structures of (**a**) the wild-type protein and (**b**) the truncation variant. Side chains proximal to the N-terminal truncation which showed statistically different level of oxidation between the two variants are shows as sticks and coloured red and blue, respectively. PDB: 2XKS (wild-type), 2XKU (ΔN6) [78].

5.2.2 Positional isomers in FPOP experiments

When examining the XIC profiles of modified peptides, several species of the same *m/z* are observed frequently as different peaks in the XIC. Each peak corresponds to a different version of the modified peptide, where hydroxyl radical labelling has occurred on a different side chain in the peptide sequence. An example of this is shown in Figure 5.16a, where seven differently modified species of peptide 11-26 of the β2m sequence could be identified by use of MS/MS. However, certain residue types, when modified, appeared more than once in the XIC, with multiple peaks at different retention times. In the example shown in Figure 5.16a, both Phe 22 and Tyr 26 were identified as the modified residue within the peptide, at multiple different retention times.

Across all the modified residues in the experiment, peptides containing modified Phe side chains were observed to elute at three different retention times, peptides containing modified Tyr residues were observed to elute at two different retention times, and peptides which contained modified Trp side chains, were observed to elute at up to nine different retention times (summarised in Table 5.3). These peaks correspond to positional isomers formed by hydroxyl radical attack at different positions on the same aromatic side chain, based on well-established oxidation chemistries of aromatic amino acids, such as Trp [275], Phe [276, 277] and Tyr [228].

However, despite the fact that these positional isomers are a known and expected consequence of the hydroxyl radical-mediated oxidation of aromatic side chains, these products are, to date, seldom mentioned in the FPOP literature [241, 278]. To that end, the NMR structures of wild-type and ΔN6 β2m were again used to assess the properties of positional isomers in FPOP experiments, and to determine their utility in detecting conformational changes in proteins at higher structural resolution.

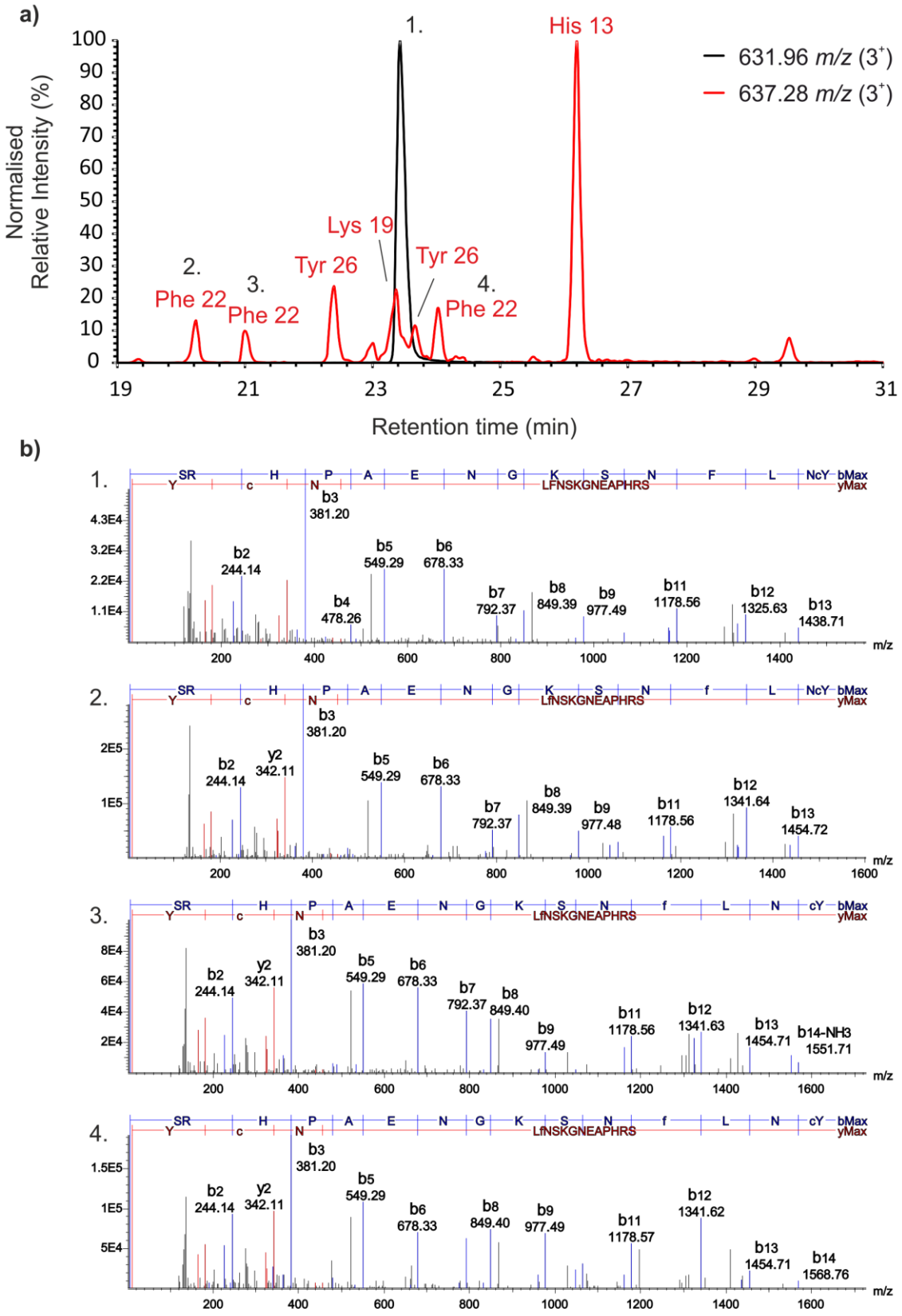

Figure 5.16 Identification of positional isomers in FPOP modified peptides. **a**) XIC of peptide 11-26 of β2m (sequence: SRHPAENGKSNFLNCY) showing unmodified (black) and +16 Da modified (red) LC-MS traces. Modified residues within the peptide are annotated above each peak. Tandem MS spectra for peaks 1, 2, 3, and 4 are shown in **b)**. "b" and "y" ions are coloured blue and red, respectively.

Table 5.3 A summary of residues to which multiple mono-oxidised XIC peaks could be assigned.

Residue	Number of XIC Peaks observed
Phe 22	3
Tyr 26	2
Phe 30	3
Trp 60	9
Tyr 67	2
Phe 70	3
Tyr 78	2
Trp 95	4

5.2.2.1 Phenylalanine isomers

The three isomers observed for each of the modified Phe side chains are consistent with the three possible positional isomers caused by net incorporation of oxygen at the *ortho*, *meta* and *para* positions of the benzene ring (Figure 5.17). Although these products have the same *m/z*, with identical fragment ion spectra, it has been widely reported that such positional isomers, when separated by RP-LC, elute in a predictable retention time order of *para* < *meta* < *ortho*, both as free amino acids, and in peptide chains [279-283]. Assigning the observed positional isomers based on this retention time order, and quantifying each peak in the XICs separately, more detailed structural information can be extracted from the available data.

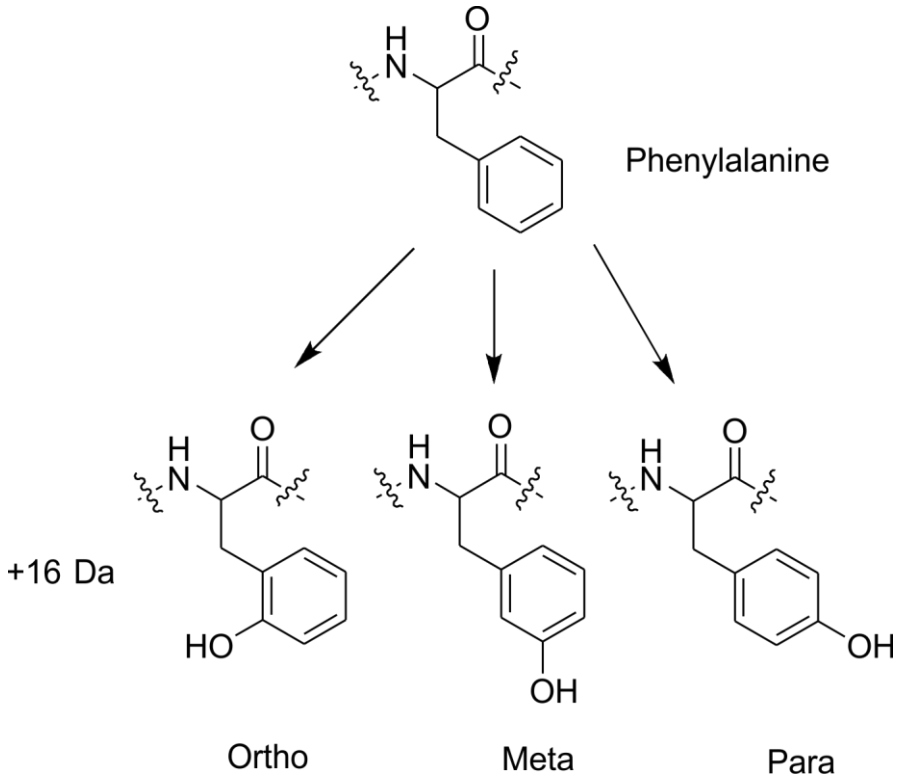

Figure 5.17 Positional isomers of +16 Da hydroxyl radical-mediated phenylalanine oxidation.

Most notably, when quantifying isomers of Phe 30, a trend of increasing difference in the degree of modification between the wild-type protein and the truncation variant is observed, where ΔN6 β2m shows increasingly more modification, relative to the wild-type protein, for isomers at shorter retention times. Indeed, the *para* isomer shows >four-fold more modification in the truncation variant than in the wild-type protein, whereas the *ortho* isomer shows only a ~1.3-fold change (Figure 5.18b). The rotation of the Phe 30 side chain discussed earlier clearly shows the *para* position as undergoing the largest structural movement of the three possible isomeric positions (Figure 5.15). Calculation of the SASA of each of the positional isomers for this side chain from the NMR structures of both variants shows an increase in SASA in the truncation variant for the *ortho*, *meta* and *para* isomers of 1.51 Å^2, 6.98 Å^2 and 12.16 Å^2, respectively. This is in good agreement with the increasing trend of modification shown in the truncation variant and supports the assignment made for each isomer.

As free amino acids, Phe side chains oxidise with known ratios of *para*:*meta*:*ortho* products, with expected isomer ratios of 1.5:1:2 or 2.1:1:2.3, depending on solution conditions [228]. These expected isomer ratios are not matched by the measured isomer ratios from FPOP oxidation for either variant, for any of the Phe residues observed to modify (Table 5.4). However, as all of these side chains are, at least partially, buried in the NMR structures of both proteins, and given the observed changes in isomer ratio in Phe 30 upon structural rearrangement, it is reasonable to conclude that changes in SASA not only affect the overall oxidation of the residue, but also the observed isomer distribution.

Table 5.4 A summary of Phenylalanine positional isomer ratios calculated from FPOP quantification data for Phe 22, Phe 30 and Phe 70 in the β2m protein sequence.

Residue	**Phe 22**		**Phe 30**		**Phe 70**	
Protein	Wild-type	ΔN6	Wild-type	ΔN6	Wild-type	ΔN6
Isomer ratio (p:m:o)	1.16:1:1.27	2.15:1:0.94	0.35:1:0.76	1.19:1:0.70	0.57:1:0.54	0.47:1:0.52
SASA (Å²)	~88.3	~105.2	~2.2	~48.8	~11.0	~5.7
% solvent exposed	~49	~58.4	~1.2	~27.1	~6.1	~3.2

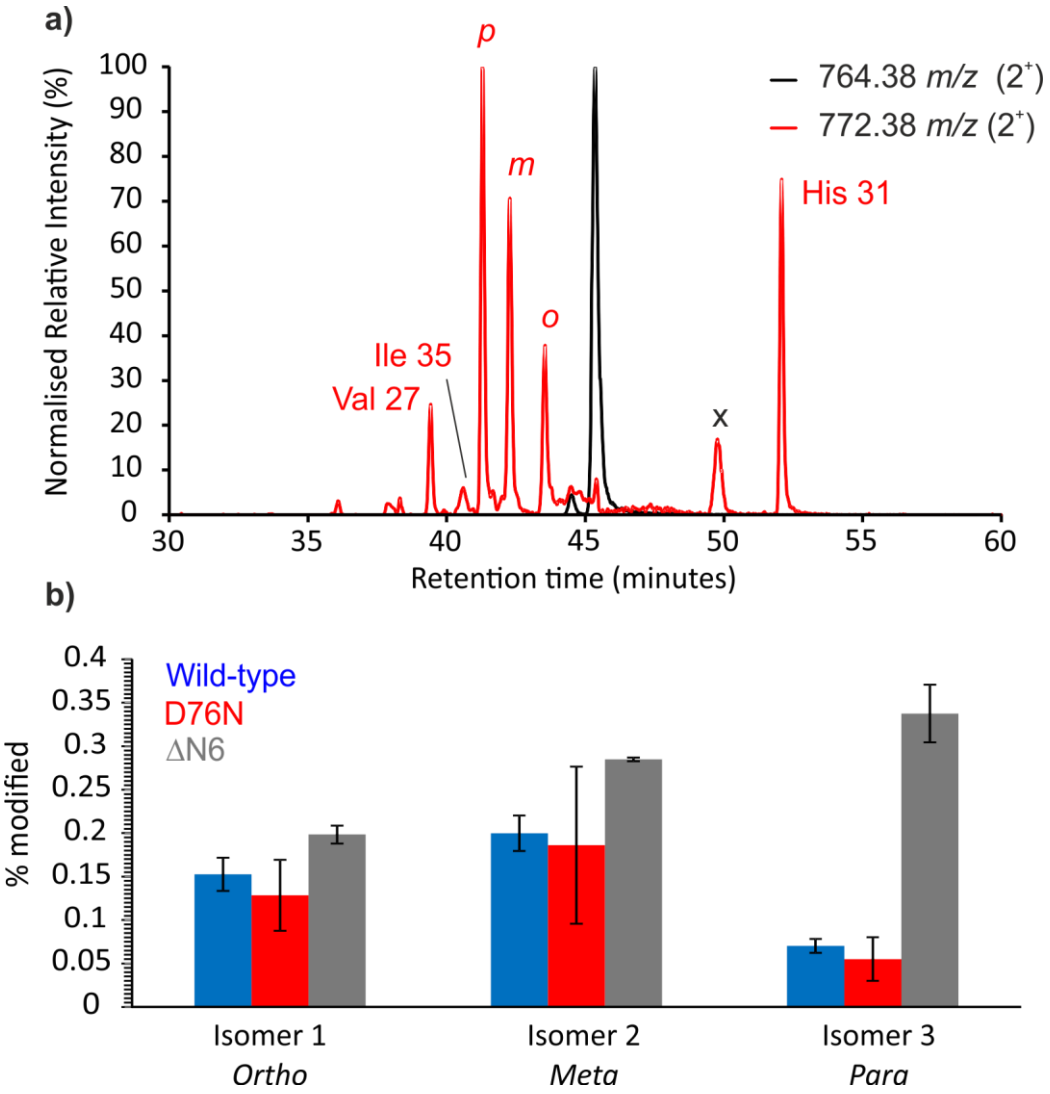

Figure 5.18 Quantification of positional isomers identified from Phe30. **a**) XIC of peptide 27-40 of β2m (sequence: VSGFHPSDIEVLL) showing unmodified (black) and +16 Da modified (red) LC traces. The *m/z* values used to generate each XIC are shown in the top right hand corner. Modified residues identified by MS/MS within each peptide are annotated above each peak. The black cross indicates an overlapping and interfering isotope distribution from another peptide. Isomers of Phe 30 are denoted p, m, and o for *para*, *meta*, and *ortho* isomers, respectively. **b**) Quantification of positional isomers. Error bars show standard deviation. n = 3.

5.2.2.2 Tryptophan isomers

Tryptophan side chains, among the most highly reactive residues to hydroxyl radical oxidation, have complex oxidation chemistry generating multiple oxidation products across several masses [228]. Indeed, the peptide containing Trp 60, which showed a small but statistically significant decrease in oxidation upon the truncation of the N-terminal six amino acids, was observed to have nine different oxidation products

present in the XIC of the modified peptide, all of which were identified by MS/MS to be present on the Trp 60 side chain (Figure 5.19a).

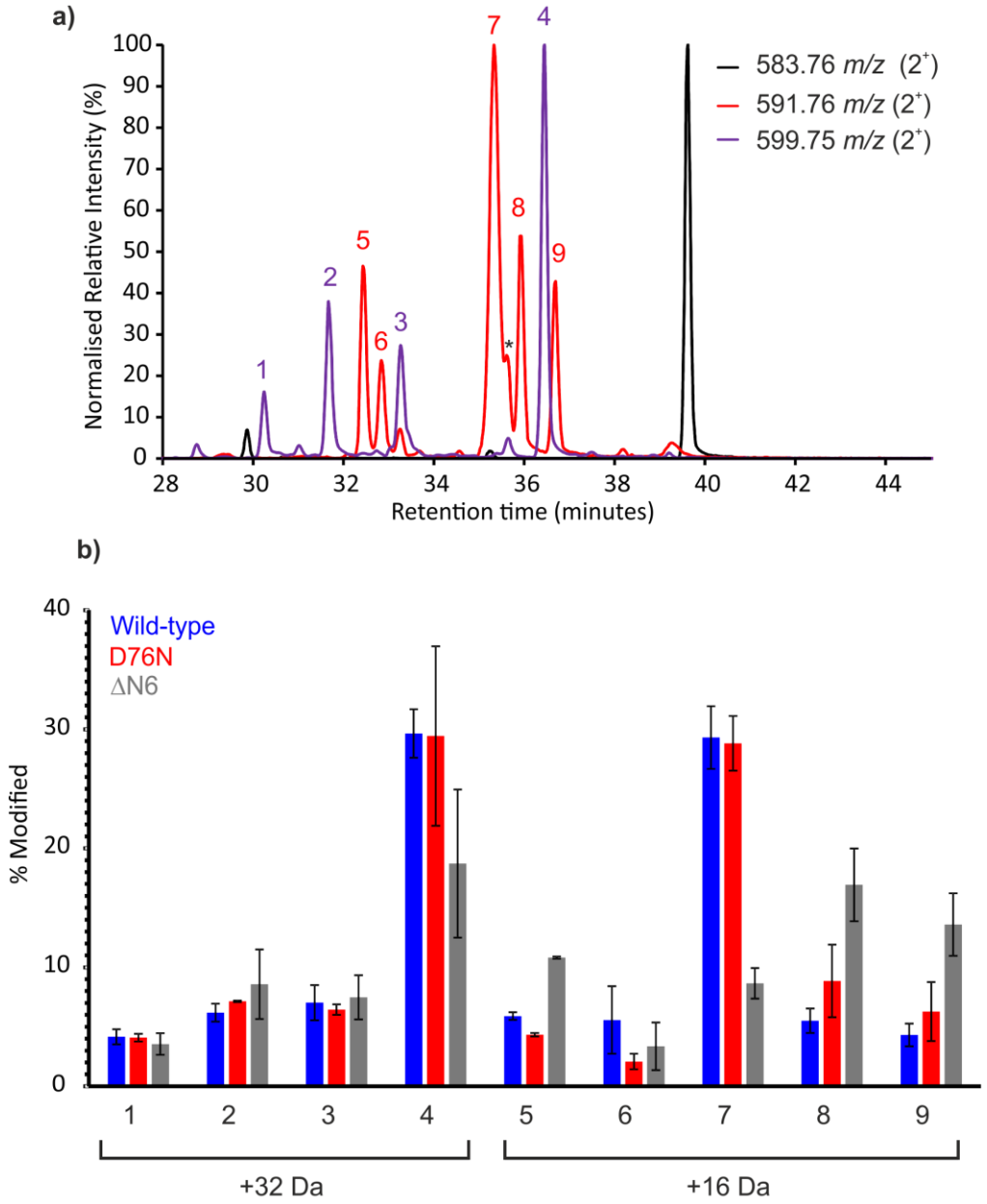

Figure 5.19 Quantification of positional isomers identified from Trp 60. **a**) XIC of peptide 55-63 of β2m (sequence: SFSKDWSFY) showing unmodified (black), +16 Da modified (red), and +32 Da modified (purple) LC traces. The *m/z* values used to generate each XIC are shown in the top right hand corner. Identified Trp 60 positional isomers are annotated above each peak in the XIC with numbers 1-9. Secondary peak identified as a possible tautomer oxidation product is highlighted with an asterisk. **b**) Quantification of isomers 1-9. Error bars show standard deviation. n = 3.

However, Trp 60, unlike Phe 30, is not well defined in the NMR structures of either variant, and occupies a variety of different positions in each state of the PDB file, likely reflective of the highly dynamic nature of the D-E loop in which Trp 60 is found (Figure 5.20). While this makes a direct comparison of the FPOP data to the NMR structure challenging, the well-established literature on tryptophan oxidation, and characteristics observed in the XIC of the modified peptides, permits some *tentative* positional isomer assignments to be made.

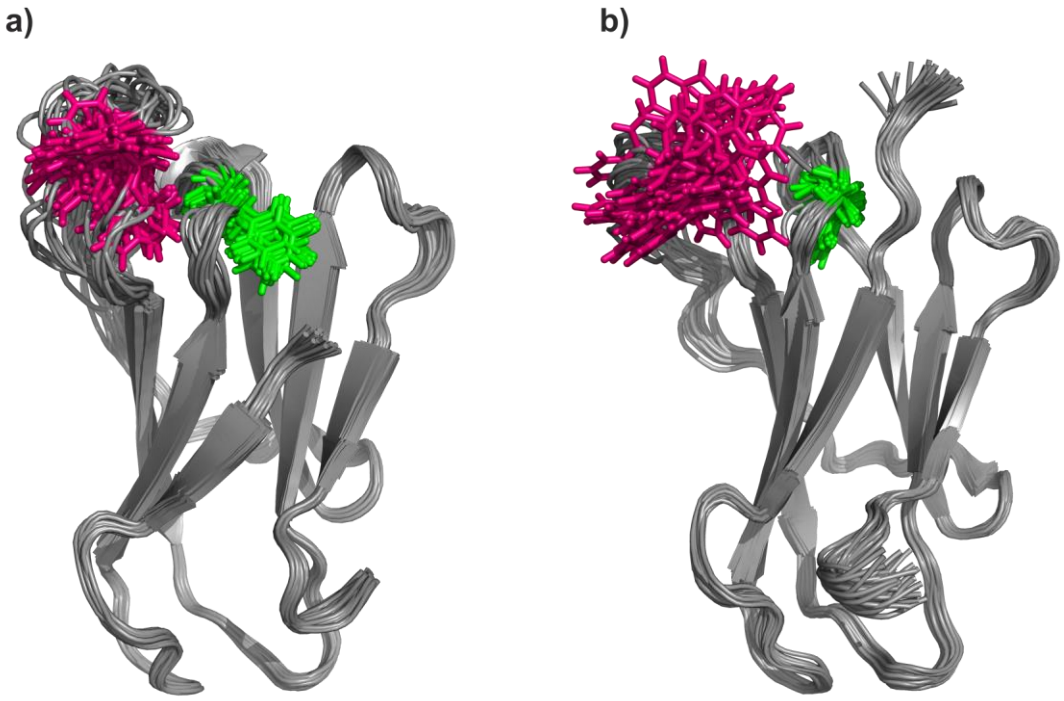

Figure 5.20 Overlaid states in the NMR structures of wild-type and ΔN6 β2m. 30 different structural models from the NMR structures of (**a**) the truncation variant and (**b**) the wild-type protein are superimposed, highlighting the side chain orientations of the Trp 60 and Phe 30 side chains, coloured pink and green, respectively. PDB: 2XKU (ΔN6), 2XKS (wild-type) [78].

In hydroxyl radical-mediated oxidation of free tryptophan, hydroxyl radicals have been reported to attack preferentially the 5-membered pyrrole moiety, compared with the 6-membered benzene moiety of the indole group, with a ratio of ~60:40 [228, 275]. Pyrrole ring oxidation of tryptophan yields two major products: the singly oxidised product, 2-hydroxytryptophan (+16 Da), and the doubly oxidised product,

N-formylkynurenine (+32 Da) (Figure 5.21). This is consistent with the two dominant oxidation products of Trp 60 for the wild-type protein (peaks 7 and 4, respectively in Figure 5.19a). Strikingly, comparing the ratio of modification for these two oxidation products with that of the remaining oxidation products observed for Trp 60, a ratio of 60.4:39.6 is observed in favour of the dominant +16 Da and +32 Da products – remarkably close to that of the expected ratio for free tryptophan in solution [228, 275]. This can be rationalised by closer inspection of the wild-type NMR structure, which shows the Trp 60 side chain is, on average, ~80% solvent exposed and thus, can be expected to behave similarly to the free amino acid in solution. Similarly, the 2-hydroxytryptophan product, tentatively assigned to peak 7 in Figure 5.19a, is known to undergo keto-enol tautomerism [284]. These tautomers interconvert during separation by RP-LC, and can be observed as a double peak [285]. A smaller shoulder peak is observed on peak 7 at ~30% relative intensity (denoted with an * in Figure 5.19a). Examination of the full MS scan for this retention time revealed no interfering isotope distributions from other peptides (Figure 5.22a). Similarly, examination of the tandem MS spectra did not show any evidence of multiple species (Figure 5.22b), indicating that the shoulder peak is the same modified residue as the main peak. As the four other possible +16 Da positional isomers, caused by oxidation on the benzene ring of the indole group, can be reasonably assigned to the four other +16 Da oxidation products observed (peaks 5, 6, 8 and 9), this shoulder peak could be the alternative tautomer for the 2-hydroxytryptophan product, reinforcing the assignment made for this XIC peak. The remaining three +32 Da oxidised species are likely dihydroxytryptophan, where both aromatic rings of the indole group are oxidised (Figure 5.21).

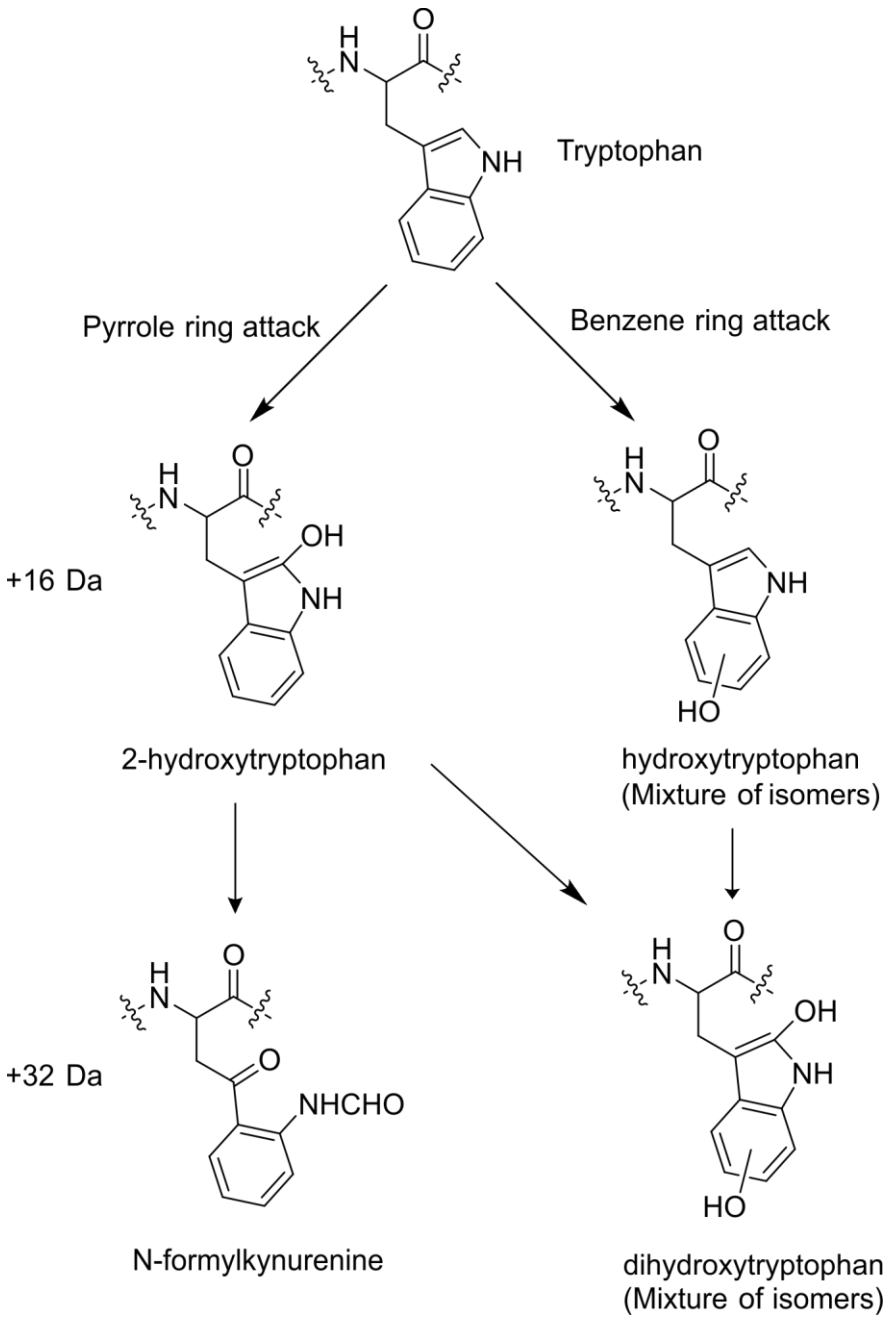

Figure 5.21 Common oxidation products of the hydroxyl radical-mediated oxidation of tryptophan.

In the case of ΔN6, peaks 7 and 4, (assigned as oxidation products resulting from hydroxyl radical attack on the pyrrole ring) both have significantly lower levels of modification than the wild-type protein, by up to 3-fold (Figure 5.19b). However, three of the four remaining +16 Da oxidation products, assigned as oxidation resulting from hydroxyl radical attack on the benzene ring, show the opposite trend, where the ΔN6 truncation variant shows increased labelling relative to the wild-type protein

(peaks 5, 8, and 9 in Figure 5.19b). Previous reports have shown that the Trp 60 side chain is less accessible to solvent in the truncation variant, as well as other amyloidogenic variants of β2m, both by partial proteolysis [134] and other covalent labelling MS methods [286]. These FPOP data, however, suggest a side chain rearrangement, rather than complete burial, where the 6-membered ring of the indole group becomes more solvent exposed in the truncation variant but the 5-membered ring becomes less solvent exposed.

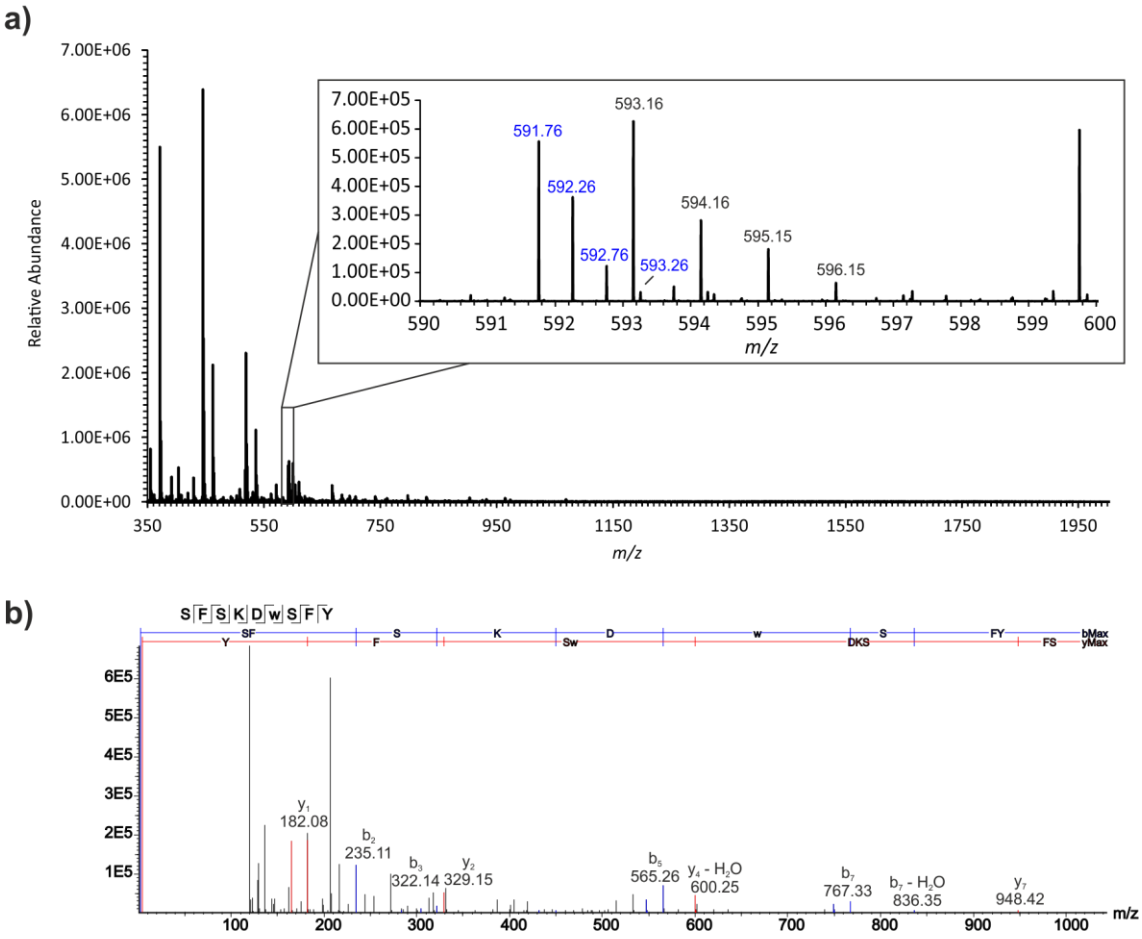

Figure 5.22 Full and tandem MS scans of the 2-hydroxytryptophan oxidation product of Trp 60. **a**) Full MS scan combined between retention times 35-36 min, encompassing the XIC peak proposed as the 2-hydroxytryptophan oxidation product of Trp 60. Inset: zoomed image between *m/z* 590-600. Isotopic distribution of the Trp 60 modified peptide species is annotated in blue and shows no interferring isotope distributions from other peptides. **b**) Tandem MS spectra of peak 7 in Figure 5.19a. B and Y ions are annotated blue and red respectively.

5.2.3 FPOP behaviour of the D76N variant of β2m

Of all the oxidations identified, only two show statistically significant differences between the wild-type and D76N variants of β2m: Lys 19, located in the A-B loop, and Tyr 78, located in the E-F loop, proximal to the D76N amino acid substitution (Figure 5.11, Figure 5.23). As both of these changes only show minimal differences in the degree of oxidation (~ 1.4 fold change), these data are largely consistent with the crystal structures of the two proteins which show minimal structural differences between the two variants [77, 157].

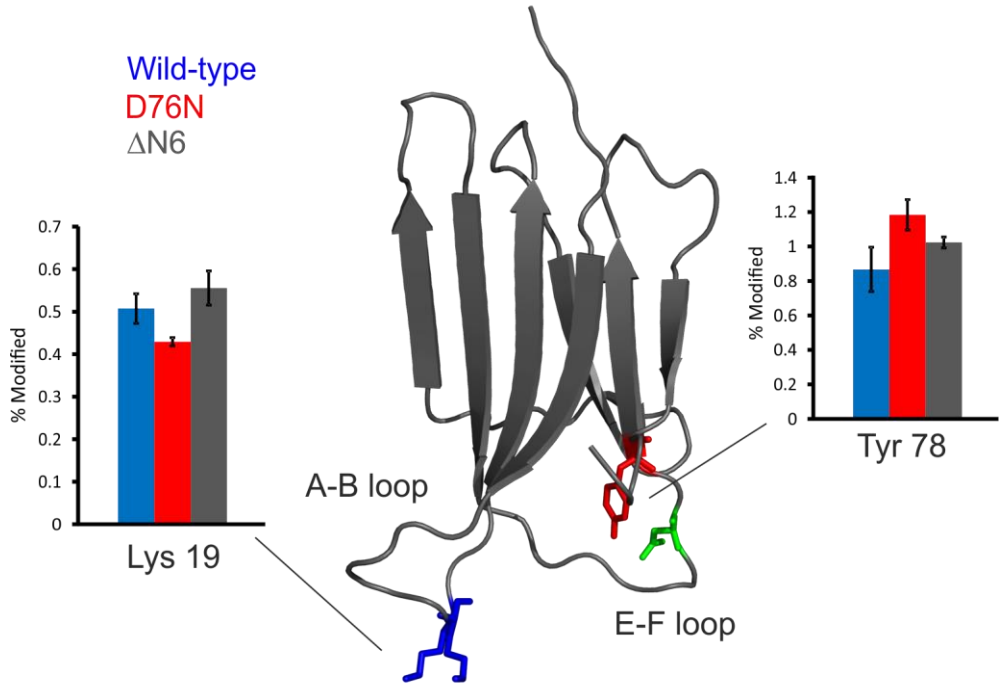

Figure 5.23 Structural differences between wild-type and D76N β2m observed by FPOP. Tyr 78 (red sticks) and Lys 19 (blue sticks) both show statistically significant ($p < 0.05$) differences between the wild-type (blue bars) and D76N (red bars) variants of β2m. Quantification of these modification sites is also included for the ΔN6 truncation variant (grey bars). The D76N amino acid substitution is shown in green on the protein structure. Error bars show standard deviation. N=3. PDB: 4FXL [157].

Closer examination of the Tyr 78 oxidation reveals two positional isomers, consistent with the two expected isomeric oxidation products of tyrosine (*ortho* and *meta*) [228], both of which show increased oxidation in the D76N variant (Figure 5.24). Although

these changes could be due to the D-N substitution itself, and the known effects of primary sequence on side chain oxidation in FPOP [232], these data could suggest a subtle rearrangement of the Tyr 78 side chain in the E-F loop, as well as Lys 19 in the nearby A-B loop, of the D76N variant.

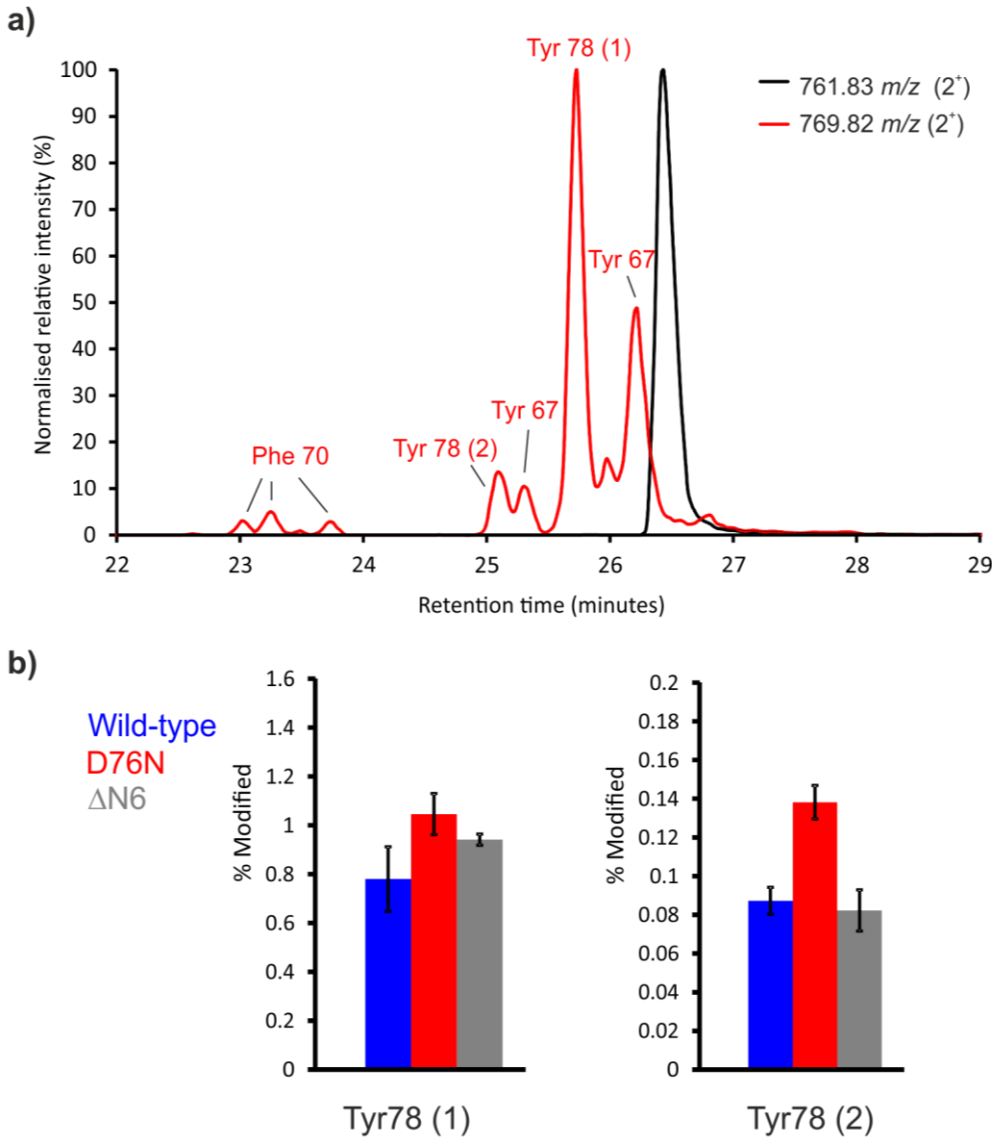

Figure 5.24 Positional isomers of oxidised Tyr 78 in three variants of β2m. **a**) XIC of the unmodified (black) and modified (red) version of peptide 67-78 of β2m (sequence: YTEFTPTEK(D/N)EY). The *m/z* values used to generate each XIC are shown in the top right hand corner. Residues modified in each peptide in the XIC, identified by MS/MS, are annotated above each peak. **b**) Quantification of the two Tyr 78 positional isomers for wild-type (blue), D76N (red) and ΔN6 (grey). Error bars show standard deviation. N = 3.

5.3 Discussion

5.3.1 Interpretation of FPOP data

The suggestion made by others [232, 287, 288] that primary sequence, and proximity to reactive side chains, affects the degree to which side chains of a protein structure label in FPOP experiments is, to some extent, supported by observations made here in comparing the FPOP oxidation levels of wild-type β2m and the truncation variant. For example, Phe residues 56 and 62, despite both being highly reactive and largely solvent accessible in the NMR structures of both proteins, were not observed to label in either variant, presumably due to increased local competition for hydroxyl radicals, due to their close proximity to the significantly more reactive, Trp 60 side chain (Figure 5.25).

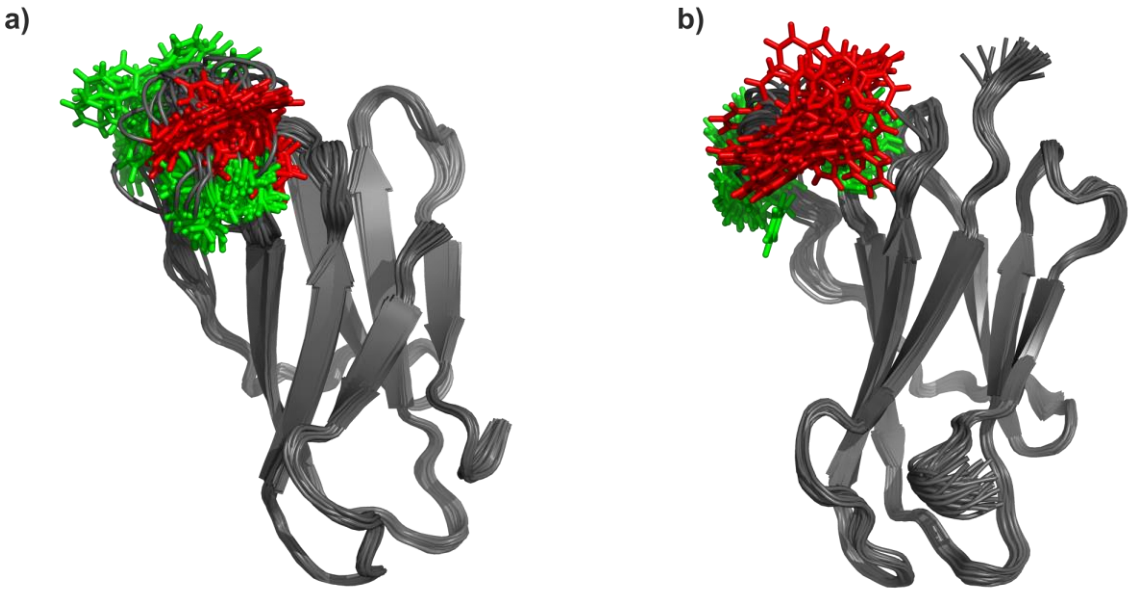

Figure 5.25 Proximity of the Trp 60 side chain to nearby Phe side chains. 30 states of the NMR structures of (**a**) the truncation variant and (**b**) the wild-type protein are shown, highlighitng the side chain orientations of the Trp 60 side chain (red) as well as the Phe 56 and Phe 62 side chains (green). PDB: 2XKU (ΔN6), 2XKS (wild-type) [78].

However, in the case of the Phe 30 rearrangement, the effects of proximity to this reactive group were only observed on the nearby Val 27 residue, when the Phe 30

side chain rotated to the solvent exposed position, in place of the truncated N-terminus. Given that, in both variants, Phe 30 and Val 27 are the same distance apart in *sequence*, these data could suggest an effect of nearby, reactive solvent accessible side chains on the degree of labelling of other groups, in *space*. Although this phenomenon requires further exploration, if true it raises a number of important questions regarding the interpretation of FPOP data:

1. Over what distance, in 3D space, are the effects of nearby reactive side chains significant?
2. Does this distance change for side chains of different reactivities?
3. Does the solvent accessibility of either group, or the presence of *multiple* reactive side chains, change the significance of this effect?

Indeed, the detailed comparison of FPOP data with calculated SASAs from the NMR structures in Figure 5.14, although finding a *general* positive correlation between SASA and the degree of oxidation for *most* of the changes which showed statistical significance, no definitive correlation was observed between the magnitude of changes in SASA and the magnitude of changes in FPOP oxidation, for equivalent side chains. This may be due to the complication of microenvironment factors discussed above, but could similarly be affected by differential sensitivity to changes in SASA for side chains of varying reactivities. That is to say, is a tryptophan side chain, for example, more or less sensitive to changes in SASA than a phenylalanine side chain? To the author's knowledge, this factor has yet to be explored in the FPOP literature but, given the known and well-established differences in reactivity to hydroxyl radical oxidation of the different side chains, is certainly a plausible scenario which requires further study, before detailed interpretations of unknown protein structures can be made from FPOP data.

That said, the examination of positional isomers following these FPOP experiments highlights the potential for achieving sub-amino acid level resolution on changes in protein structure using this technique. Although further study is required to

determine the usefulness of positional isomers in FPOP, which would no doubt benefit from a greater understanding of the effects of local microenvironment, it is important to note that side chain movements, at this level of detail, are largely invisible to other structural MS methods, such as HDX. Moreover, the propensity of FPOP to label large hydrophobic side chains, coupled with the immense detail provided by separate quantification of positional isomers, is of great significance in the study of aggregation-prone proteins, where solvent exposure of typically buried, hydrophobic groups is often implicated in the aggregation mechanism [170].

5.3.2 FPOP method development

Being a new method, multiple stages of the FPOP experiment lend themselves towards further development, including the oxidation process itself, as well as the associated LC-MS/MS workflows and data processing/analysis.

5.3.2.1 Internal standards

During sample oxidation, the inclusion of internal standards, or dosimetry experiments to assess the hydroxyl radical dose given to each sample, would be a useful tool to develop the robustness and reproducibility of the technique, and has been implemented successfully into the FPOP workflow elsewhere [289-291]. Although not used in the experiments described here due to the identical solution conditions between samples, internal standards such as leu-enkephalin have been used in FPOP to correct for changes in hydroxyl radical dose, thus allowing comparisons of samples at different concentration, or under different buffer conditions where the •OH scavenging ability of the solution may vary [291]. However, as discussed earlier, a deeper understanding of the reactivities of different side chains, and the effects of their relative solvent accessibilities, would be needed before the corrections applied from the oxidation of internal standards could be relied upon for detailed analyses. Namely, does side chain reactivity affect the sensitivity of side chains to change in •OH dose

(i.e. is a tryptophan side chain more or less sensitive to change in •OH dose than a phenylalanine?), and does the solvent accessibility of each side chain affect that sensitivity (is a buried tryptophan more or less sensitive to changes in •OH dose than an exposed tryptophan?). Considering the sensitivity to oxidation of the internal standard itself is of critical importance, such effects require further study before an optimal choice of internal standard can be made.

5.3.2.2 LC-MS/MS development

Although the assignments of FPOP isomers identified for the two β2m variants are consistent with the existing literature regarding known oxidation chemistries [228] and the affirmed elution orders of positional isomers by RP-LC [279-283], these assignments cannot be made with *certainty*, without retention time alignment of identical oxidised peptides with known, unique, positional isomers. Not only would this be prohibitively expensive, but the low throughput of this method makes this approach largely impractical. However, positional isomers of both Phe [292] and Trp [293] are distinguishable by differential UV absorbance spectra, and UV detectors are routinely implemented for online analysis in LC-MS/MS workflows. Indeed, Trp oxidation in heat stressed antibodies has been characterised previously in precisely this manner [294] and thus, make this an appealing development opportunity for the routine characterisation of positional isomers in FPOP experiments.

With regards to MS/MS procedures, the DDA approach used in our experiments and most commonly in the literature, while effective, requires instrumentation capable of fast MS/MS acquisition and, due to the oxidised products frequently having the same *m/z*, partial or incomplete LC separation of different versions of a modified peptide, results in co-selection of the different modified peptides by the quadrupole, and the generation of difficult to interpret, chimeric MS/MS data (Figure 5.26).

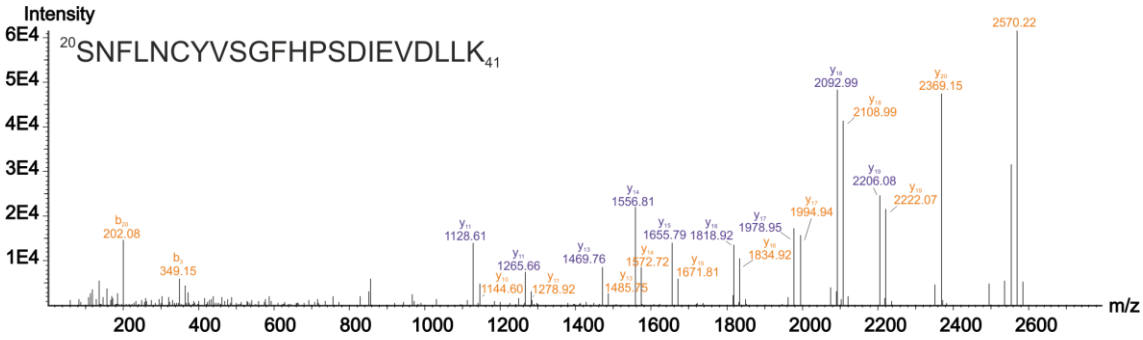

Figure 5.26 Chimeric MS/MS data from co-isolation of overlapping oxidised peptides. Example shown is peptide 20-41 (sequence: SNFLNCYVSGFHPSDIEVDLLK) resulting from tryptic digestion of β2m following FPOP. Overlapping or partially separated oxidised peptides with the same *m/z* in the XIC result in co-selection by the quadrupole during DDA, and the generation of chimeric MS/MS data. A distinct pattern of dual fragment ion peaks is observed where the two peptides, modified on different amino acids, generate a mixed spectrum of both modified (yellow), and unmodified (purple) fragment ions for each b and y ion.

A possible solution to this problem, largely unexplored in the current literature, could be to use DIA as an alternative mode of acquisition, as the assignment of fragment ions to their respective precursors is carried out by automated retention time alignment. Although control experiments would be required to ensure current DIA processing algorithms correctly assign fragment ions from co-eluting oxidised peptides with similar fragment ion spectra, this approach has the potential to allow for the identification and quantification of partially separated or overlapping modified peptides with the same *m/z* by generating XICs of unique fragment ions (Figure 5.27).

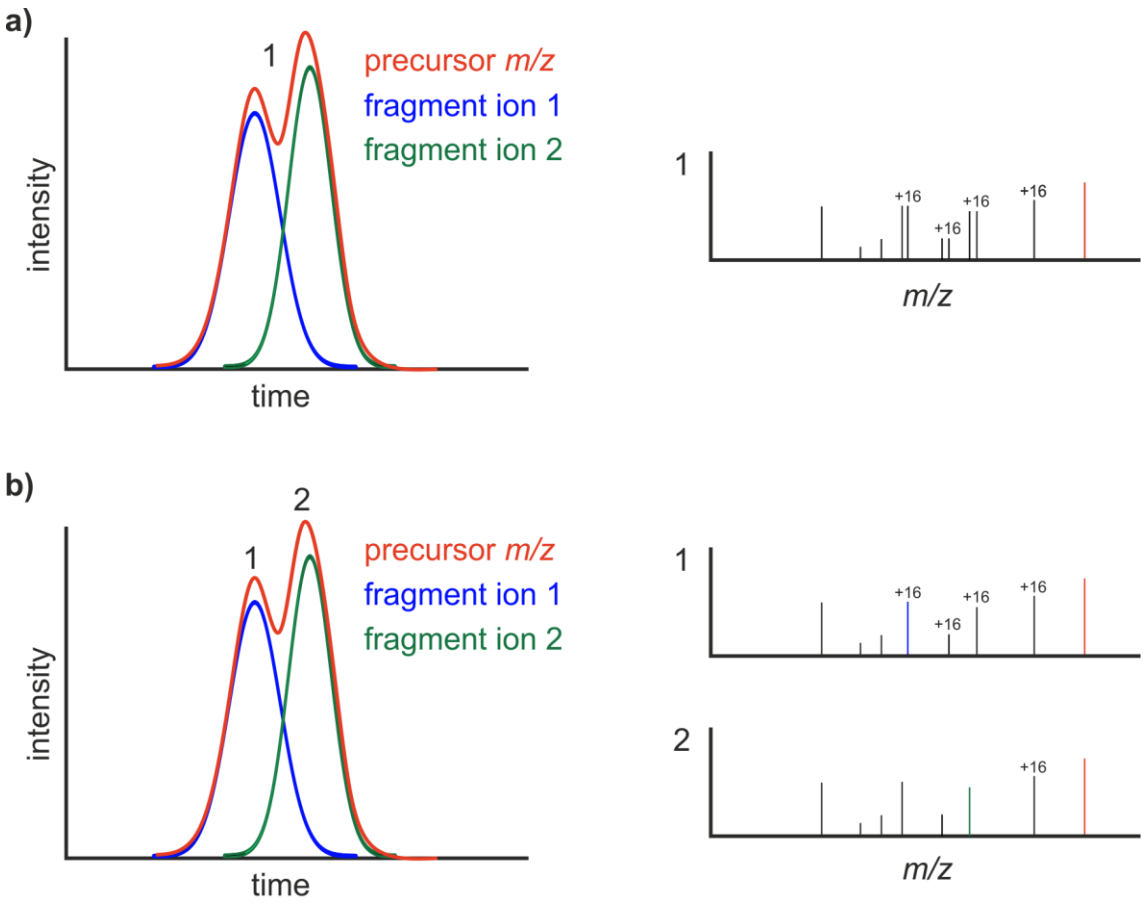

Figure 5.27 A schematic representation of DDA vs DIA MS/MS workflows for FPOP data acquisition. **a**) Acquisition of fragment ion spectra via DDA quadrupole selection of overlapping oxidised peptides with the same *m/z* can result in chimeric MS/MS with multiple fragment ion series present. **b**) By applying DIA workflows, reconstructed fragment ion spectra from retention time alignment allows deconvolution of overlapping species by examination of specific fragment ion XICs (blue and green MS/MS peaks) against the precursor *m/z* (orange).

5.3.3 FPOP of the ΔN6 truncation variant of β2m

Previous studies have observed that burial of the Trp 60 side chain is correlated with the propensity of β2m to form amyloid fibrils [134, 286]. In the truncation variant, previous reports have shown that the Trp 60 side chain is less accessible to proteases [134]. Similarly, copper ions, which have been implicated in the promotion of amyloid formation of β2m both *in vitro* and in DRA [140-144], have been shown to reduce the solvent accessibility of the Trp 60 side chain upon binding, using alternative MS based covalent labelling methods [286]. However, the covalent labelling reagent used in that study, dimethyl(2-hydroxy-5-nitrobenzyl)sulfonium bromide, usually shorthanded

to HNSB, is comparatively large, giving rise to a 151 Da mass addition upon modification of the tryptophan side chain [286]. The smaller size of the hydroxyl radical in FPOP labelling, and the identification of positional isomers has allowed experiments performed here to obtain a higher resolution analysis of Trp 60, suggesting only partial burial of this residue in the amyloidogenic truncation variant.

The minor conformational changes observed for Phe 22 and His 51 are intriguing, as these are distant from the site of the N-terminal truncation. While the significance of these changes, with regards to the aggregation propensity of the truncation variant, are difficult to ascertain from these data without further study, the conformation of the D-strand in which His 51 is located has been implicated numerous times in the aggregation of β2m [295, 296], and could provide additional insight into the aggregation of the ΔN6 truncation variant.

5.3.4 FPOP of the D76N variant of β2m

For the most part, the wild-type protein and the D76N variant were largely indistinguishable by FPOP, exhibiting only minor differences in labelling on two side chains: Tyr 76 and Lys 19. While these changes are both located nearby to the D76N substitution, indicating the amino acid change has *some* effect on the solvent accessibility of nearby side chains, these data are largely consistent with the known similarity between the crystal structures of the two variants [77, 157], and suggest only minimal changes in protein structure caused by the D76N substitution. These data are, perhaps, unsurprising, as even considerable side chain movements nearby to the D-N substitution could easily remain undetectable by FPOP, assuming the residue adopts a similarly solvent exposed position in the D76N variant, a likely scenario given the solvent exposed nature of the E-F loop in which the D76N substitution is found.

Curiously, these data are in contrast to the deuterium exchange behaviour of the E-F loop in this variant, relative to the wild-type protein, discussed earlier in Section 4.6 and 4.7.2. These differences will be discussed in detail later in Section 7.2.

Chapter 6:

FPOP-LC-MS/MS of WFL and STT

6 FPOP-LC-MS/MS of WFL and STT

As discussed earlier in Section 2.3, protein aggregation in biopharmaceutical development is of critical importance to patient safety, and the future development of biopharmaceutical products. Given the minor, triple amino acid substitution made in the heavy chain CDRs (W30S, F31T, L57T), and subsequent drastic changes in the propensity to undergo reversible self-association, the two mAbs WFL and STT developed by Medimmune (discussed in detail in Section 2.3.1), provide an ideal model system by which to study aggregation in pharmaceutically relevant mAbs. Similarly, these proteins offer an opportunity to develop further the FPOP methodology for the study of larger, more complex protein systems, and assess the potential utility of this technique for probing conformational changes associated with aggregation propensity in mAbs. As such, the two mAb variants, WFL and STT, were subjected to FPOP-LC-MS/MS analysis, with the following aims:

1. Identify differences in conformation and structure which may be associated with the propensity of WFL to undergo reversible self-association
2. Develop the FPOP-LC-MS/MS methodology for more complex protein systems, and assess the utility of FPOP in the study of biopharmaceutical protein structure.

Data in this chapter were subsequently published in Cornwell *et al.*, Analytical Chemistry, 2019 [297].

6.1 Initial characterisation and overview

Both WFL and STT were subjected to oxidation by FPOP as described in Section 3.5.2. Both proteins were oxidised in their formulation buffer (20 mM sodium succinate, 125 mM L-arginine, pH 6.0 – optimised by Medimmune) at 0.1 mg ml^{-1}, conditions at which both proteins are known to be predominantly monomeric [170]. 10 mM L-histidine was added as a scavenger amino acid, and 3 µl of 5 % *v/v* H_2O_2 was added

immediately prior to oxidation. This is 3x the hydrogen peroxide used in the FPOP experiments performed with β_2m (Section 5) and was necessary to overcome the •OH scavenging effect of the arginine excipient in the formulation buffer.

Following FPOP, reduction of disulphide bonds, alkylation and proteolytic digestion using trypsin (detailed methods described in Section 3.5.2) yielded good sequence coverage for the heavy and light chains for both WFL and STT (an example coverage map is shown in Figure 6.1). A total of 19 peptides were used for quantification of identified FPOP oxidations (green lines in Figure 6.1), as these were found to be present in all replicates of both proteins, and had both modified, and unmodified versions. Of these 19 peptides, MS/MS data were used to identify 50 different modified sites (28 identified on the heavy chain, and 22 on the light chain), the majority of which could be localised to residue level resolution, and were observed in both variants (Table 6.1, Figure 6.2).

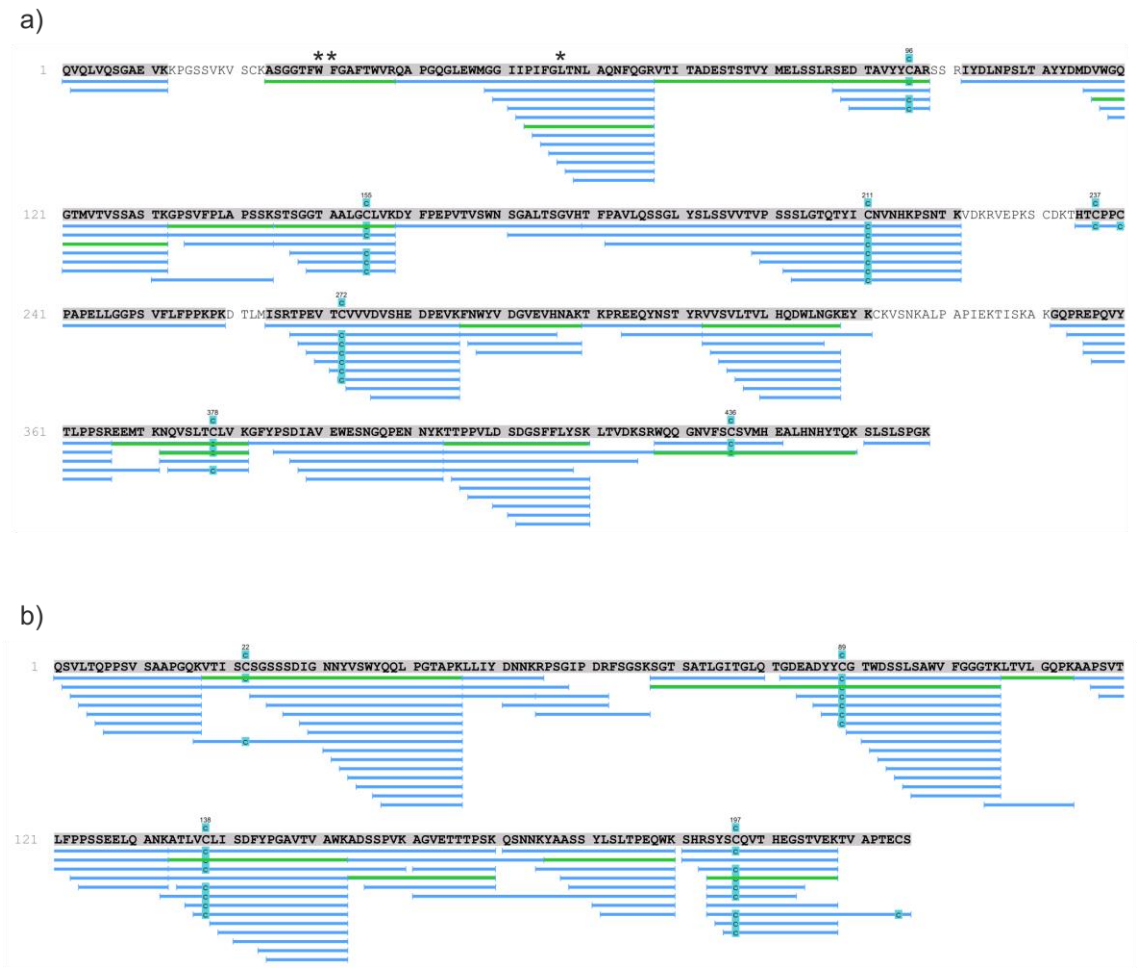

Figure 6.1 Example peptide coverage map of mAbs WFL and STT following FPOP and tryptic digestion. Coverage maps for the heavy chain (**a**) and light chain (**b**) are shown. The W30S, F31T and L57T modification sites are annotated with an *. Example shown is that of WFL. Blue bars show identified peptides. Green bars show peptides used for FPOP quantification (all were identified in all replicates of WFL and STT, and had both modified and unmodified versions).

Table 6.1 A summary of modifications observed following FPOP of the mAbs WFL and STT.

Peptide	Sequence	Modified residues
24-38 (Heavy chain)	ASGGTF(ST/WF)GAFTWVR	Trp 36 STT only: Phe 34, Phe 29 WFL only: Trp 30, Phe 31
53-67 (heavy chain)	PIFG(T/L)TNLAQNFQGR	Phe 55
68-87 (Heavy chain)	VTITADESTSTVYMELSSLR	Met 81
117-132 (Heavy chain)	VWGQGTMVTVSSASTK	Met 123
133-144 (Heavy chain)	GPSVFPLAPSSK	Pro 134, Val 136, Phe 137, Pro 138 (STT only)
145-158 (Heavy chain)	STSGGTAALGCLVK	Leu 153, Ser 147, Cys 155
286-299 (Heavy chain)	FNWYVDGVEVHNAK	286-FNW-288, His 296
313-328 (Heavy chain)	VVSVLTVLHQDWLNGK	His 321, Trp 324
367-381 (Heavy chain)	EEMTKNQVSLTCLVK	Met 369
372-381 (Heavy chain)	NQVSLTCLVK	372-NQ-373, Cys 378
404-420 (Heavy chain)	TTPPVLDSDGSFFLYSK	Leu 409, Phe 415, 413-GSF-415, 404-TTPPVLDS-411
428-450 (Heavy chain)	WQQGNVFSCSVMHEALHNHYTQK	428–WQQGNVFSCSVM-439
18-46 (Light chain)	VTISCSGSSSDIGNNYVSWYQQLPGTAPK	18–VTISCSGSSSDIGNNYV-34, Trp 36, 40-LPGTA-44
68-106 (Light chain)	SGTSATLGITGLQTGDEADYYCGTWDSSLSAWVFG GGTK	77–TGLQTGDEADYYCGTWDS-94
107-114 (Light chain)	LTVLGQPK	Leu 110, 114-PK-115
134-153 (Light chain)	ATLVCLISDFYPGAVTVAWK	Trp 152
154-170 (Light chain)	ADSSPVKAGVETTTPSK	154-ADSSP-158, Lys 160
176-190 (Light chain)	YAASSYLSLTPEQWK	Tyr 176, Leu 184, 186-PE-187, Trp 189, 186-PEQWK-190
194-208 (Light chain)	SYSCQVTHEGSTVEK	194-SYSCQ-198, His 201, Cys 197

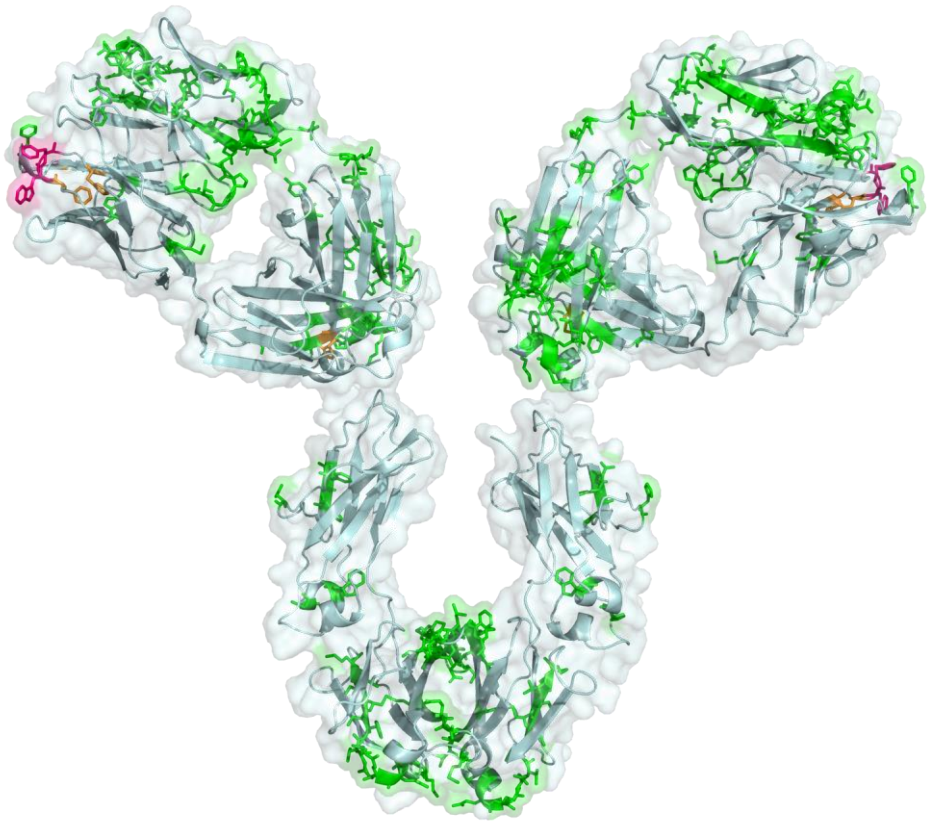

Figure 6.2 Modified residues identified following FPOP-LC-MS/MS of WFL and STT. Modifications are shown as sticks and coloured by the protein variant (i.e. WFL or STT) on which they were identified. Green shows modifications identified in both WFL and STT, orange shows modifications identified only in STT, and pink shows modifications only idenitified in WFL.

6.2 Regions surrounding the W30S and F31T mutations

Perhaps the most obvious differences between WFL and STT, with regards to the identified oxidation sites, were observed directly proximal to the W30S and F31T amino acid substitutions in the V_HCDR1 loop of the mAbs, nearby to which were four of the five modified sites *not* common to both WFL and STT (Table 6.1). XICs for the modified and unmodified versions of the peptide containing the W30 and F31 residues in WFL are shown in Figure 6.3a. Multiple modified species eluting at different retention times were observed for both W30 and F31 oxidation, corresponding to the multiple positional isomers expected from incorporation of oxygen at different positions on the aromatic groups of those side chains [228].

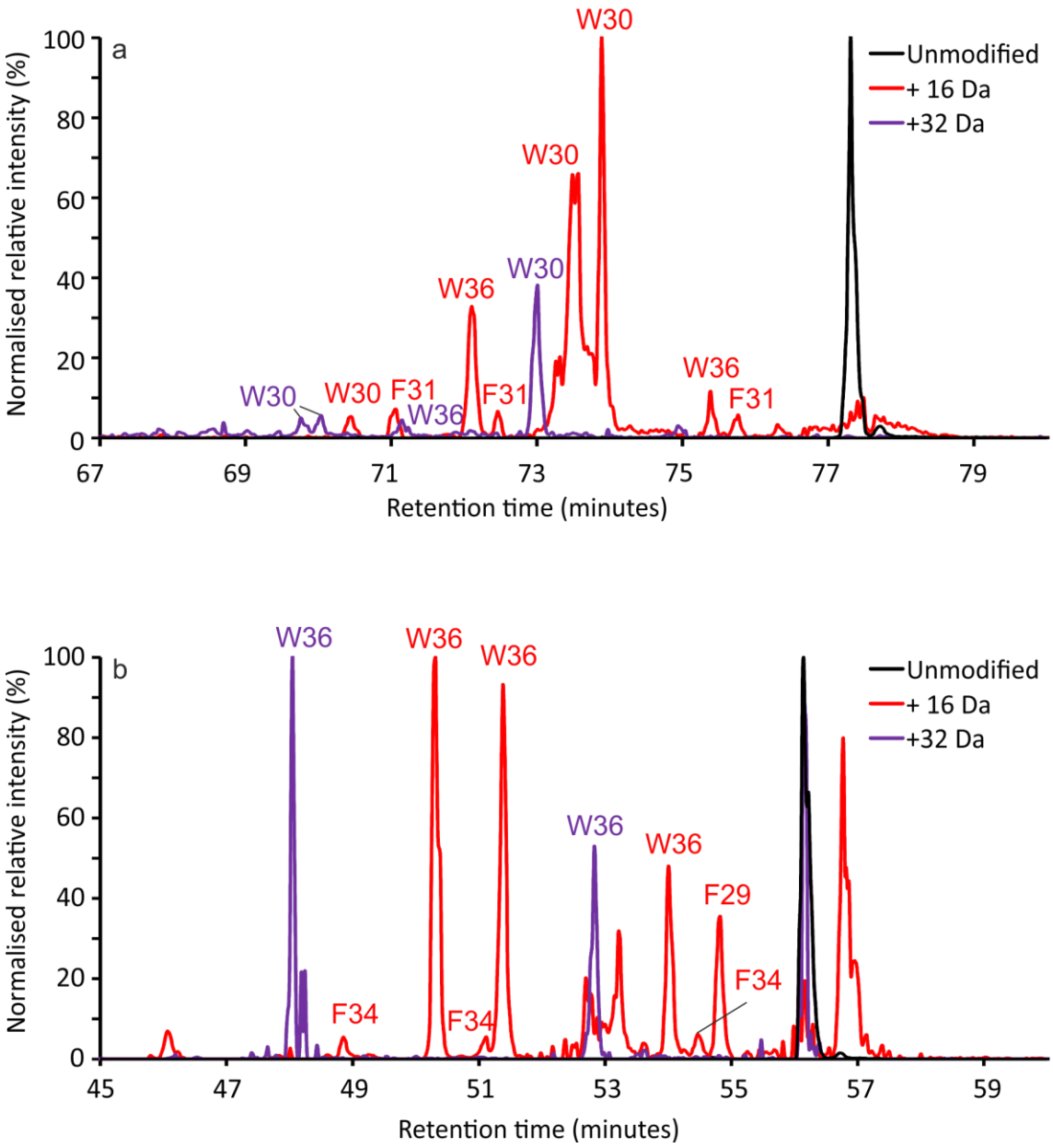

Figure 6.3 XICs for modified and unmodified peptides covering the W30S and F31T mutations. XICs for the unmodified (black), as well as +16 Da (red) and doubly oxidised +32 Da (purple) modified peptides are shown. Peaks are annotated according to which modified residue was identified for each peak using MS/MS. Peptide 24-38 of WFL (sequence: ASGGTFWFGAFTWVR) is shown in **a**). Peptide 24-38 of STT (sequence: ASGGTFWFGAFTWVR is shown in **b**).

However, despite a dominant series of y type fragment ions in the tandem MS spectra of these modified species – not uncommon for tryptic peptides, typically basic at their C-terminus [298], MS/MS data for several oxidised products, for both WFL and STT, could only localise the modification site to between residues 35 and 37 (35-TWV-37)

(Figure 6.4). This can be further narrowed down to Trp 36 or Val 37, if water loss ions are used for assignment [299]. Given the significantly higher reactivity to hydroxyl radical oxidation of tryptophan than either threonine or valine, as well as the presence of multiple oxidation products and double (+32 Da) oxidations in this region, these modifications are most likely present on the Trp 36 side chain. Although this residue is present in the core of the V_H domain, surprisingly, following quantification, Trp 36 was found to be ~6-fold more oxidised in the WFL variant than in the STT variant (Figure 6.5a). This could suggest a marked difference in the conformation and solvent accessibility of side chains in the region of the V_H domain caused by the WFL-STT substitutions.

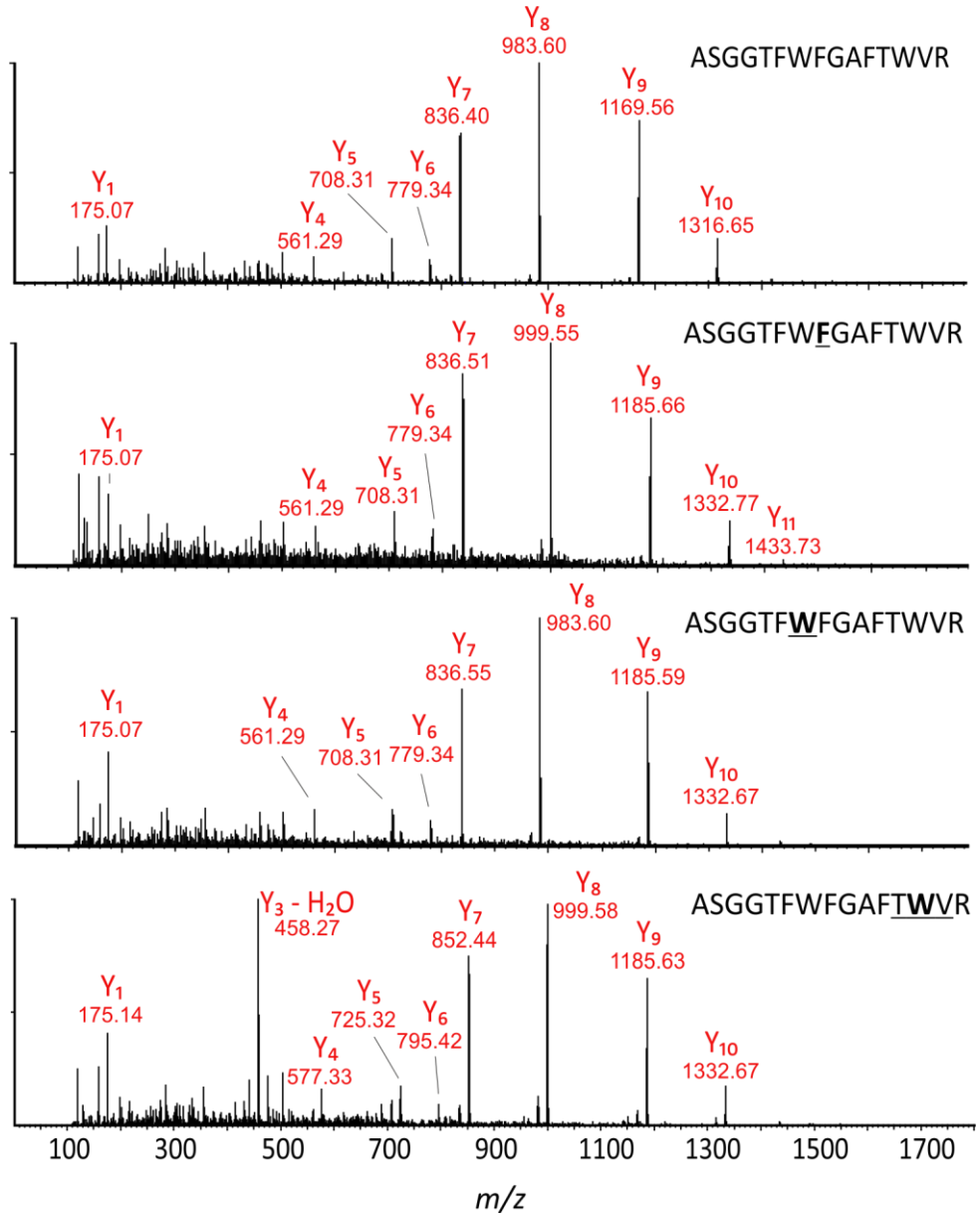

Figure 6.4 Representative MS/MS for peptide 24-38 of WFL. The region, or residue, to which MS/MS could localise the +16 Da modification are shown underlined on the sequence of each peptide, shown in the top right hand corner of each spectrum. The assignment made for the modification site is shown in bold. The top spectrum shows the unmodified version of the peptide.

This hypothesis is supported by a closer examination of other oxidised products in the region. The Phe 29 and Phe 34 side chains, located either side of the W30S and F31T substitutions, were only observed to modify in the STT variant (Figure 6.3b, Figure 6.5a). Similarly, the Phe 55 side chain in the V_HCDR2 loop, adjacent to the L57T substitution site and spatially proximal to the W30S and F31T substitutions, was

oxidised ~2x more in the STT mAb variant (Figure 6.5a). Taken together, these findings could suggest a structural rearrangement of the V_H domain, where the solvent accessibility of all four of these side chains (Trp 36, Phe 29, Phe 35 and Phe 55) has been changed by the WFL-STT triple substitution.

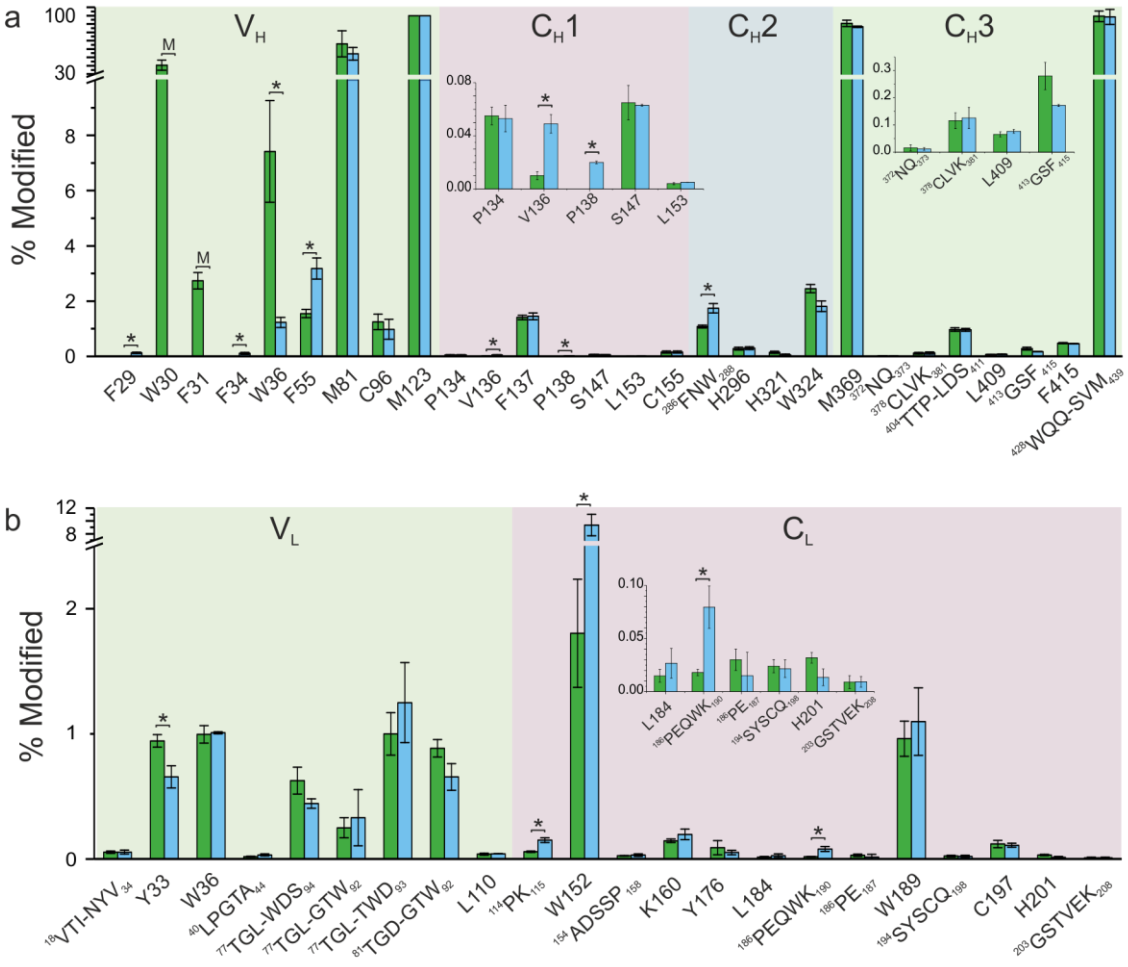

Figure 6.5 Quantification of FPOP modifications identified in WFL and STT. Modification sites for WFL (green) and STT (cyan) for the heavy chain (**a**) and the light chain (**b**) are shown along the x axis of each plot. Modifications are localised to residue level or a short sequence of amino acids. Where resolution was >6 amino acids, the first and last three residues of the sequence to which the modification could be localised are shown. Inserts show zoomed in quantification of low abundance modifications. Mutation sites that were modified in either variant are annotated with an 'M'. * = $p < 0.01$. Error bars show standard deviation (N=3).

However, although the effects of local microenvironment and sequence have yet to be fully established in FPOP experiments, these effects cannot be ruled out as a

potential cause of, or contributor to, the changes in oxidation observed in this region. For example, the W30S, F31T and L57T substitutions are expected to decrease the reactivity of these amino acid positions with regards to their susceptibility to hydroxyl radical oxidation, by factors of 40, 13 and 3, respectively [228]. While this likely explains the absence of any observed oxidation on Ser 30 and Thr 31 in STT (residue 57 labels in neither variant), the newly diminished competition for hydroxyl radicals in the region could explain the increased modification of the nearby Phe 55 side chain in STT, as well as the oxidation of Phe 29 and Phe 34 observed only in STT. All three of these side chains are proximal to the site of the amino acid substitutions (~10 Å) and, as such, the removal of highly reactive groups in the region, and subsequent reduction in competition for hydroxyl radicals, could be expected to make hydroxyl radical attack on nearby, less solvent accessible, or less reactive, groups more likely. Similar effects regarding changing competition for hydroxyl radicals have been proposed previously in the context of unfolded proteins in FPOP experiments [232]. Alternatively, recent reports have suggested that hydrogen peroxide, from which hydroxyl radicals are liberated in FPOP, preferentially interacts with certain side chains, including a favoured hydrogen bond interaction with threonine side chains over leucine side chains [300, 301]. Thus, the L57T mutation could increase the local concentration of hydrogen peroxide in the region, offering an alternative explanation for the increased oxidation of the nearby Phe 55 side chain in the STT variant.

6.3 Constant domains and the C_L-C_H1 interface

The only remaining oxidation product that was not observed to be modified in both mAb variants was Pro 138, which was labelled only in STT, and is present in the C_L domain, near to the interface of the C_L and C_H1 domains (Figure 6.5a, Figure 6.6). Remarkably, following quantification, only three other side chains across both the heavy and light chains, each with a p value < 0.01, showed a > 4-fold difference in the degree of labelling between the two variants: Val 136, Trp 152 and an unknown

modification between residues Pro 186 and Lys 190 (Figure 6.5a and b). All three of these side chains are similarly located proximal to the C_L-C_H1 interface and all show significantly lower levels of oxidation in the WFL variant (Figure 6.6). Minor (< 2-fold), although statistically significant, changes in oxidation were also observed at the top of the nearby C_H2 domain, with similarly decreased labelling in the WFL variant (Figure 6.6). These results are surprising, as these changes are a distance of > 60 Å from the WFL-STT triple substitution, and suggest a conformational change of the constant domains, or a change in orientation of the constant domains, particularly the C_L and C_H1 domains, relative to one another.

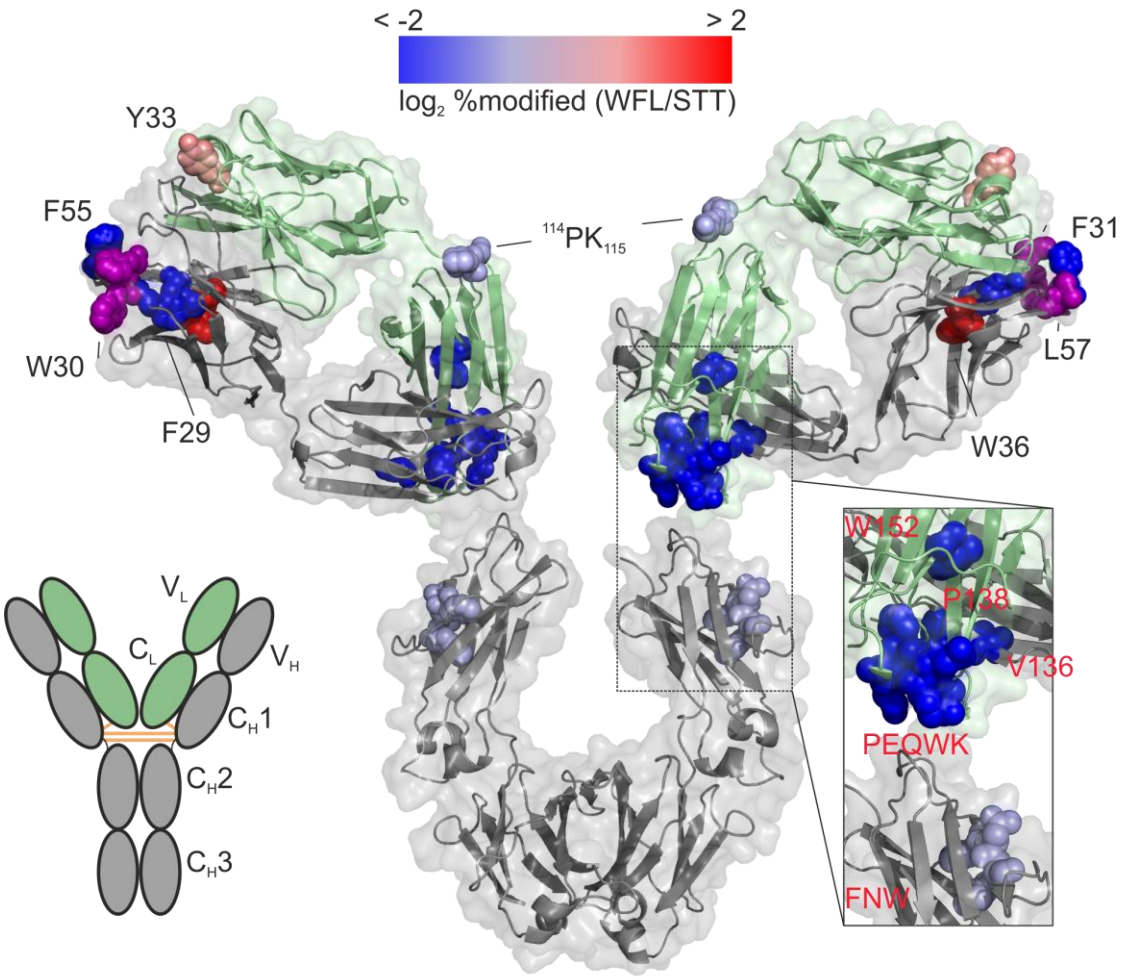

Figure 6.6 Differences in FPOP oxidation between WFL and STT. Modified sites which showed statistically significant differences ($p < 0.01$) are shown as spheres and coloured by the magnitude of the difference observed (dark red indicates ≥ 4 fold increase in labelling in WFL, dark blue indicates ≥ 4 fold decrease in labelling in WFL). Amino acid substitution sites are shown as purple spheres. Heavy and light chains are shown in grey and green respectively. A model mAb structure is shown in the bottom left hand corner for clarity. The right hand side insert shows a zoomed image of the C_L – C_H1 and C_H1 – C_H2 domain interfaces where modification sites are annotated in red showing either residue level resolution, or a short sequence of amino acids to which the modification could be localised.

Perhaps the most striking difference in the degree of oxidative labelling between the two variants surrounding the C_L-C_H1 interface is observed for Trp 152 in the light chain, located on the edge of the C_L domain (Figure 6.6). Although, at the residue level, this side chain showed ~5-fold less oxidation in WFL than in STT, examination of the XIC for peptides containing modified Trp 152 identified five different products using MS/MS, eluting at different retention times, where Trp 152 was the modified side chain in each case. These likely correspond positional isomers, four with a single

(+16 Da) oxidation and one doubly oxidised (+32 Da) species (Figure 6.7a). However, unlike the tryptophan isomers discussed earlier in Section 5.2.2.2, the data obtained here cannot feasibly be used to ascertain the precise identity of each positional isomer, and no robust, or routine, method of characterising positional isomers in FPOP has yet been developed. That said, separate quantification of these isomers can yield *some* additional information regarding the change in orientation of this side chain between the two mAb variants. Following quantification, only three isomer oxidation products showed statistically significant ($p < 0.01$) changes between the two variants, whereas two of the isomers, including the doubly oxidised product, show no significant change (Figure 6.7b).

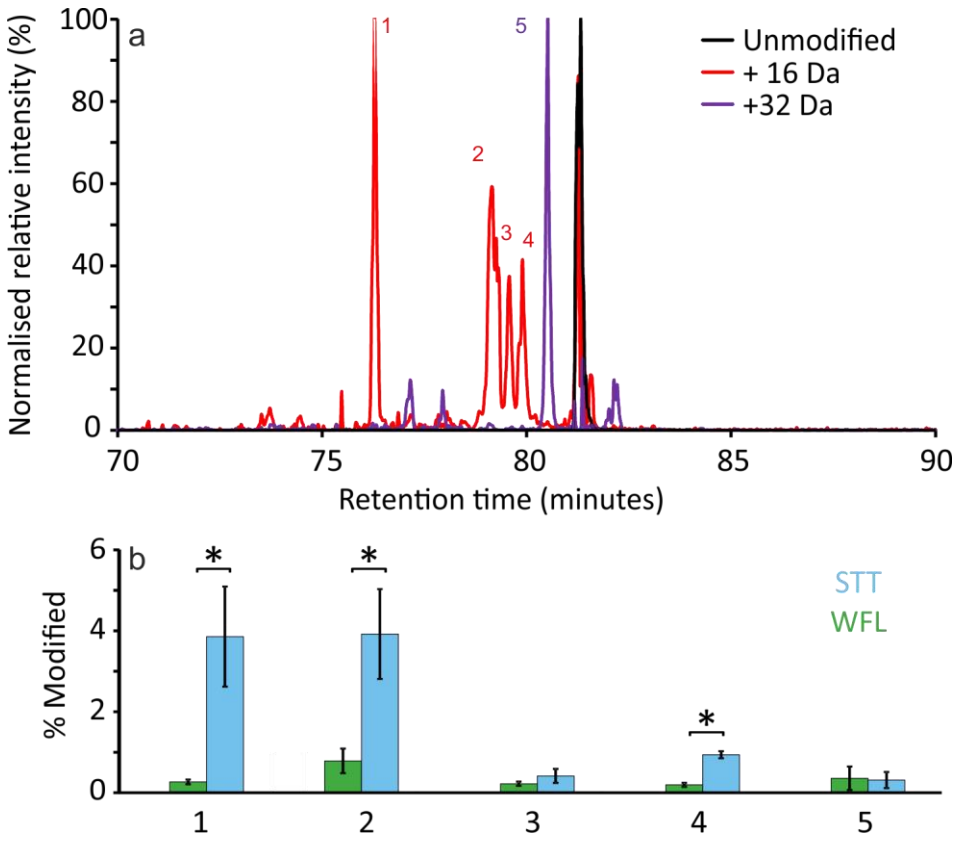

Figure 6.7 Identifying and quantifying positional isomers of oxidised Trp 152. **a**) XICs of the unmodified (black), +16 Da modified (red) and +32 Da modified (purple) versions of peptide 134-153 (sequence: ATLVCLISDFYPGAVTVAWK. Peaks are annotated 1-5 according to their quantification data shown **b**). Error bars show standard deviation (n=3).

As some of the isomer products of Trp 152 show differences in labelling by up to ~14-fold, this could be suggestive of a significant change in the solvent accessibility of this side chain. However, the relationship between changing solvent accessible surface area and changes in oxidation has not been fully established in FPOP, and is likely complicated by various factors such as the reactivity of the side chain itself, and the effects of microenvironment [232, 300]. Alternatively, the observation that some of the oxidation products show no significant change between WFL and STT could indicate that part of the Trp 152 side chain remains largely unchanged between mAb variants, indicative of a more subtle side chain movement. Although establishing the utility of positional isomers in FPOP requires further research, this alternative explanation, involving more subtle conformational change in the region, is to some extent supported by other nearby side chains, where Phe 137, Trp 189 and Lys 160 all show no significant change between the two mAb variants (Figure 6.5).

Despite the difficulty in establishing the significance of the conformational changes observed at the C_L-C_H1 interface, long range conformational changes of this type have been observed by other groups, where changes in the conformation of the C_L-C_H1 interface thought to be related to antigen binding have been reported [302]. Similarly, one report identified a change in orientation of the C_L-C_H1 domains associated with changes in CDR loop structure, thus altering the surface exposed hydrophobicity of the region [303]. Interestingly, the changes observed in WFL and STT suggest a similar trend in reverse, whereby changes in surface exposed hydrophobicity of the CDR loops, as a result of the WFL-STT substitutions, illicit changes in the orientation of the C_L-C_H1 domains. Taken together, these data could suggest a long range conformational link between the antigen binding regions and the constant domains of the Fab arm.

It has been suggested that conformational changes between the constant and variable domains of the Fab arm are mediated through the flexible 'elbow' angle between the two regions [304]. Although no modified residues were identified in the elbow region

between the V_H and C_H1 domains, one modified species was observed, localised to residues Pro 114 or Lys 115, in the elbow region linking the V_L and C_L domains (Figure 6.6). This species was observed to be statistically significantly ($p < 0.01$) less oxidised in the WFL variant, highlighting a conformational change in this region between the two variants (Figure 6.5b, Figure 6.6), possibly mediating the changes observed in the C_L-C_H1 interface, caused by the WFL-STT triple substitution in the heavy chain CDRs.

6.4 Analysis of retention time data

Given the complexity of LC-MS/MS data obtained from proteolytic digests of protein samples oxidised by FPOP, any additional information that can be mined from such data to aid in interpretation offers a clear advantage. In particular, the task of identifying oxidised residues within modified peptides, and assigning those modified species to elution peaks in the XIC trace of each peptide is often a challenge, not least because of the manual nature of the data analysis, but also because these assignments, at present, rely solely on the MS/MS data obtained – the quality of which can suffer significantly owing to the inherent low abundance of oxidised peptides in the sample, and the possibility of chimeric fragmentation spectra from co-isolation in the quadrupole.

Currently, LC separation is an essential part of the FPOP experimental workflow – used primarily to separate peptides over time, allowing more DDA cycles to occur, and the acquisition of more fragmentation spectra which can be used for assignment of oxidised residues. However, although changes in retention time for oxidised peptides, relative to the unmodified version of the peptide, is a well-established phenomenon [240], any relationship between changes in retention time and the nature of the modified peptide (i.e. which residue within the peptide is modified) has, thus far, not been explored or systematically investigated. Given the necessity of LC separation in the current FPOP workflow, these data are essentially 'free', requiring no additional experiments to be performed, or any changes to the current LC-MS/MS

experimental workflow. Using the abundance of data provided by FPOP-LC-MS/MS analysis of WFL and STT, combined with the β_2m dataset discussed in Section 5.2, we sought to explore the utility of using the separation data itself, in conjunction with MS/MS, as an aid to assign modified residues in oxidised peptides.

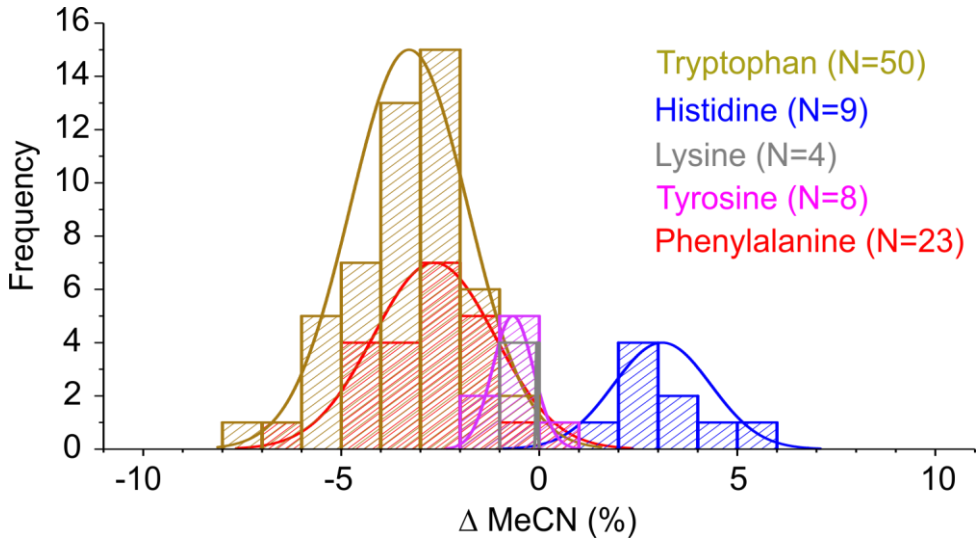

Figure 6.8 Analysis of the effect of FPOP oxidations on peptide retention time in RP-LC. Data included in this analysis consists only of modifications which could be unambiguously assigned to residue level resolution combined from the WFL/STT data set, as well as the FPOP data from Chapter 5. X axis shows change in MeCN concentration at which peptides eluted, relative to the unmodified version of the peptide (set as 0 on the x axis). Histograms binned every Δ1% are shown as shaded columns. Gaussian fits to raw data are shown as solid lines.

Figure 6.8 shows a retention time analysis of the most commonly modified residues within oxidised peptides observed in this thesis, identified by MS/MS, and their subsequent change in retention time relative to the unmodified version of that peptide, by RP-LC. Nearly all the modified peptides observed elute at a lower aqueous concentration of organic solvent (i.e. shorter retention time) than their unmodified counterparts. This is expected, given the addition of oxygen and subsequent decrease in hydrophobicity of the peptide. Interestingly, peptides where lysine was the modified residue were observed to have a remarkably reproducible effect on the

retention time of the peptide, eluting at an MeCN concentration 0.05 – 0.1 % *v/v* lower than the unmodified version of the peptide (Figure 6.8). This minimal effect on retention time is largely consistent with the marginal change in hydrophobicity caused by incorporation of oxygen to lysine side chains.

Another notable observation made from these data is that peptides where histidine was the modified residue elute reproducibly at higher MeCN concentrations (i.e. longer retention times) (Figure 6.8). The dominant +16 Da product generated from hydroxyl radical oxidation of histidine is 2-oxo histidine, the structure of which is shown in Figure 6.9. It has been reported previously that oxidation of histidine into 2-oxo histidine renders protonation of the side chain significantly less favourable, likely due to the significantly lower proton affinity of the oxidised product [305, 306]. This suggests that the 2-oxo histidine product, unlike the unmodified histidine side chain, is likely to remain un-protonated under typical LC-MS conditions, likely resulting in increased hydrophobicity of the peptide, despite the incorporation of an oxygen atom.

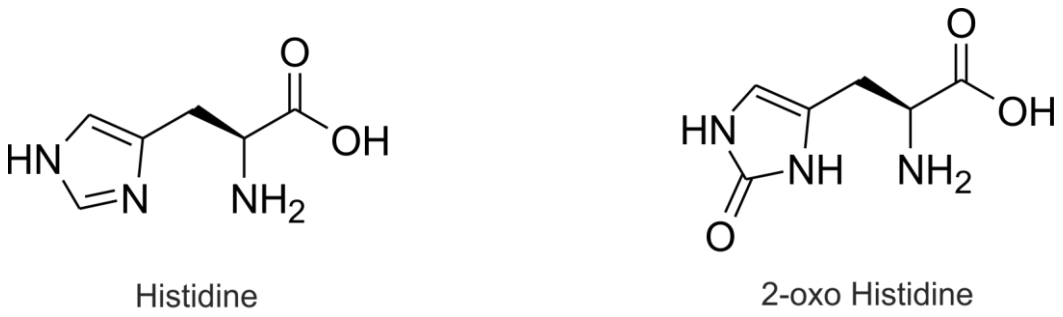

Figure 6.9 Chemical structures of histidine and 2-oxo histidine.

This hypothesis is supported by the observation that histidine modifications frequently show a significant charge state bias towards lower charge states when ionised by ESI (Figure 6.10). In the experiments presented here, this observation was unique to histidine modifications, and was not found on any other type of modified

residue. However, this charge state bias was not observed on *all* peptides where histidine was the oxidised residue, and likely depends on the presence of other protonatable groups in the peptide.

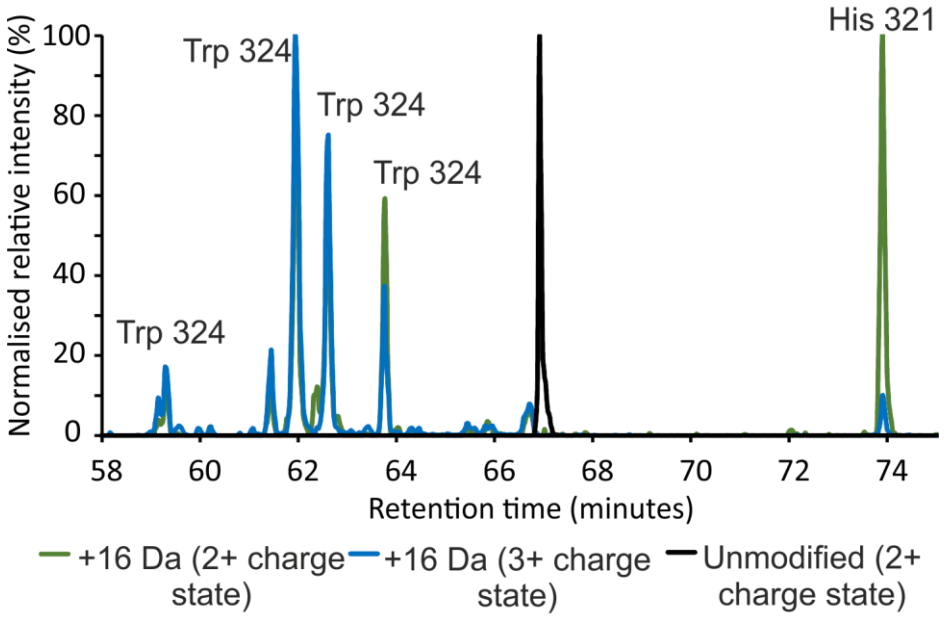

Figure 6.10 Histidine oxidations in peptides show charge state biases towards lower charge states. XIC of peptide 313-328 (sequence: VVSVLTVLHQDWLNGK) showing the unmodified version (black), and two charge states of the +16 Da modified version (2^+ = green, 3^+ = blue). Peptides where the oxidation was present on the histidine side chain show longer retention times and charge state biases towards lower charge states, whereas peptides where tryptophan was the oxidised side chain show shorter retention times and the XICs of the two charge states largely overlay.

In several instances, examination of the XICs for modified and unmodified versions of a peptide revealed similar retention time profiles, where the oxidised peptide product eluted at the same retention time as the unmodified version of the peptide. An example of this is shown in Figure 6.11a, where MS/MS could reliably identify the modified residue as Tyr 94 (Figure 6.11b). Although it cannot be ruled out that some oxidations generated from hydroxyl radical attack during FPOP do not affect the retention time of the peptide, an alternative explanation is that such oxidations occur *after* LC separation during the ESI process [228, 307, 308]. As such, suspected 'in-source' oxidations generated from ESI were excluded from analysis and not quantified. This

observation further highlights the importance of performing comprehensive analyses of FPOP data, including careful examination of retention time profiles and LC separation data.

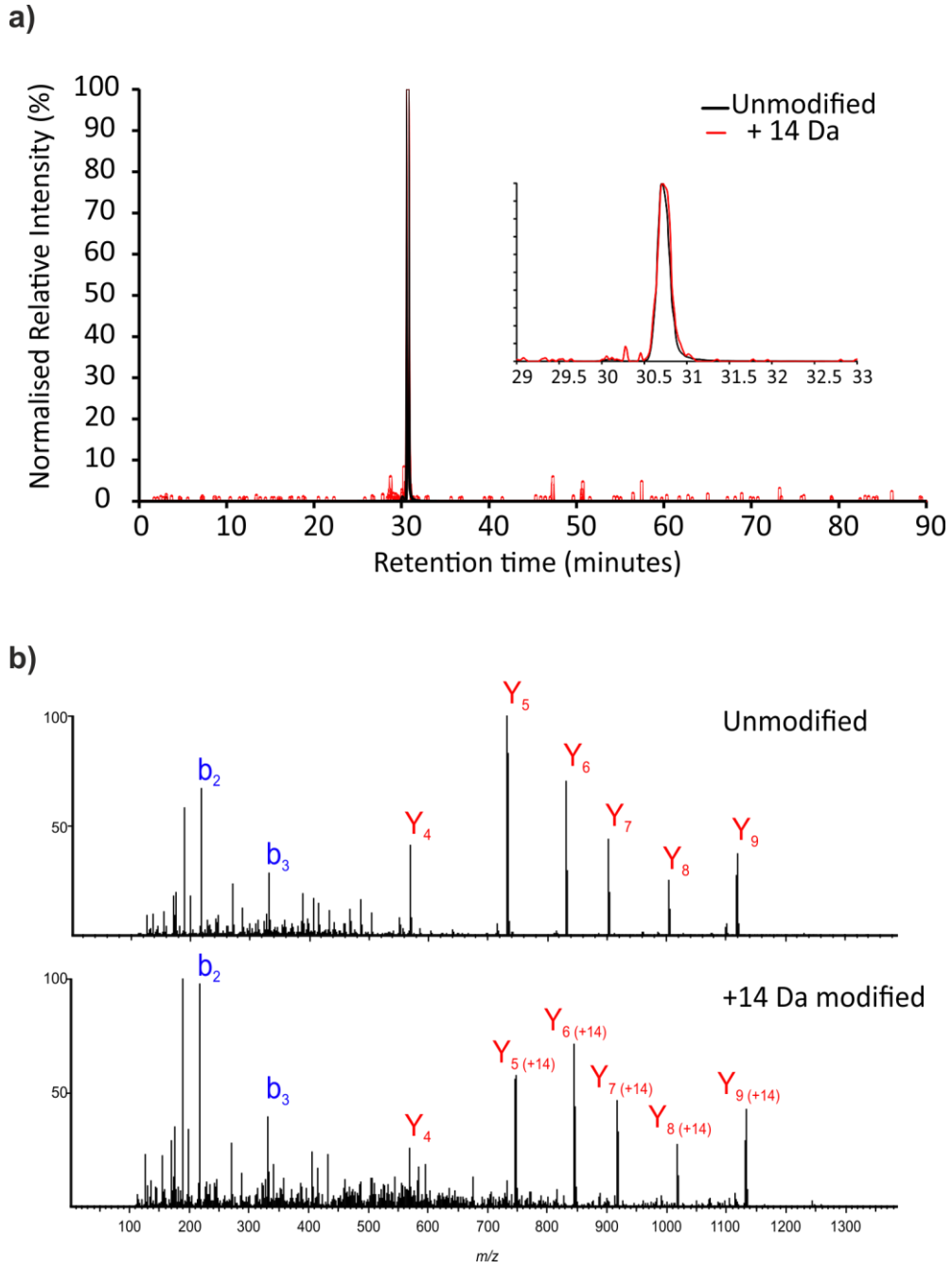

Figure 6.11 Possible in-source oxidations observed during FPOP-LC-MS/MS experiments. **a**) XIC for peptide 88-98 (sequence: SEDTAVYYCAR) in the heavy chain of WFL showing the unmodified (black) and +14 Da modified (red) LC elution traces. Insert: expansion of the XIC between 29 and 33 minutes. MS/MS for the modified (bottom) and unmodified (top) are shown in **b**.

6.5 Discussion

The changes in conformation observed between WFL and STT at the C_L-C_H1 interface support the view that long range changes in conformation can occur between the constant and variable domains of the Fab arm in mAbs. However, the significance of this conformational change, and indeed the changes in oxidation observed surrounding the WFL-STT substitutions in the CDR regions, cannot be reliably determined from these data. Interpretation of FPOP data in this regard would benefit greatly from a greater understanding of positional isomers, the effects of changing solvent accessibility for different side chains as well as changes in local microenvironment.

Similarly, the significance of the observed changes in conformation between the two mAb variants, with regards to the poor pharmacological properties of WFL [170] cannot be established from these data. However, a recent report demonstrated that, for light chain dimers, structurally similar to that of the Fab domain [309], the C_L domains were observed to modulate protein aggregation, and the interface between constant domains was suggested as a potential target for mitigating protein aggregation [310]. This could suggest a possible role of the C_L domain in the aggregation of WFL, where the conformational changes observed, caused by the WFL-STT substitution, play a role in the reversible self-association of the WFL mAb variant.

Critically, however, these data definitively show that amino acid substitutions in the variable domain of the Fab arm, can affect the conformation and positioning of side chains in the constant domains of the Fab arm. Typically, these two distinct regions are often assumed to be functionally independent [311, 312]. While the functionality of this conformational link cannot be established from these data, the observation itself may prove critical in the identification of aggregation-prone sites, or undesirable conformational changes, generated distal from the site of amino acid substitutions that may otherwise go overlooked.

6.5.1 Retention time analysis

The retention time analysis of peptides oxidised by FPOP, from both the mAb data discussed here, and the β_2m data discussed in Section 5, highlight the potential utility of using the LC separation data as an aid, not only to assign modified residues within oxidised peptides, but to avoid erroneous assignments of in-source oxidations generated from the ESI process. Undoubtedly, MS/MS remains the gold standard in determining oxidation sites in FPOP. However, as peptides in FPOP experiments often have the same *m/z*, are typically low abundance and sometimes only partially separated by LC, the resulting chimeric, or poor quality, tandem MS spectra, are such that finding alternative, or complementary methods of assignment offers a distinct advantage. Given the current necessity of using LC in FPOP experimental workflows, the LC separation data seems an obvious place to start, in looking for such alternatives. Although considerably more data would be needed to establish whether changes in retention time could be used as a predictive tool in FPOP assignments, even the small data set collated here demonstrates the potential utility of using changes in retention time to assign lysine and histidine oxidations within oxidised peptides, given their unique, and reproducible effect on the elution of the peptide. Indeed, retention time prediction tools have long been established in other peptide LC-MS workflows [313], and may prove to be a useful future tool in characterising positional isomers in FPOP.

Chapter 7:

Concluding remarks

7 Concluding remarks

The work presented here has outlined several novel findings and advances that are of crucial importance to the field of structural MS, particularly with regards to the use of FPOP and other structural MS techniques in the study of aggregation-prone proteins.

In this last section, the overall findings of this thesis are discussed in a broader scientific context, with regards to the thesis aims laid out in Section 2.5.

7.1 A new understanding of FPOP

The detailed comparison of FPOP data between wild-type β_2m and the ΔN6 truncation variant, outlined in Section 5.2.1, and subsequently published in 2018 [252], allowed for the first time a detailed characterisation of positional isomers in FPOP experiments. These data highlight the possibility, with further study, of utilising positional isomers in FPOP for more detailed analyses of protein structures. However, the well-characterised variants studied in these experiments also revealed a complex relationship between SASA, or change in SASA, and the degree to which side chains label in FPOP. While these data are in line with those of other studies [232, 287, 288], these combined observations begin to illustrate the true complexity of using FPOP to analyse protein structures, where nearby side chains in sequence or space, changing solution conditions, and the reactivity of the side chain itself, all likely play a role in the degree to which amino acid groups oxidise, and the sensitivity of the oxidation on these side chains to changes in protein structure and local microenvironment.

Efforts to understand these effects in FPOP experiments should be considered amongst the highest priority tasks for future work in this field. In the immediate future, disentanglement of these factors would allow optimal design of internal standards in FPOP experiments [289-291], greatly improving the robustness and reproducibility of the technique, but would also widen the range of possible

experiments available to FPOP users. Similarly, a greater understanding of the interplay between different side chains, SASA and amino acid reactivity on the degree to which side chains label in FPOP would also release this technique from its current limitations with regards to data interpretation.

These efforts would also likely benefit from a more detailed understanding of the precise reactivities of the different amino acids, specifically for oxidation induced by FPOP. Indeed, the general observations made from the FPOP data presented here show that tyrosine side chains modify considerably less, on average, than tryptophan side chains, even when similarly solvent exposed (section 5.2). Given that the reactivities of these two residue types are predicted to be precisely the same, from reactivity data produced by electron pulse radiolysis (Table 2.2), we must entertain the possibility that the reactivity of the amino acids in FPOP differs slightly from these data.

In much the same way that the effects of pH, temperature and sequence have been largely unravelled with regards to deuterium incorporation in HDX, in the long term, achieving a near complete understanding of the factors described above in FPOP, particularly in the age of machine learning, seems largely feasible. Although challenging, the prize for such an endeavour: a known relationship between absolute SASA and the degree of labelling for a given amino acid type, under a given set of conditions, promises the establishment of low resolution protein structural models, derived *de novo* from MS data alone. With the already recognised possibility of expanding the FPOP platform to include alternative radical based labelling reactions [236, 237], as well as *in vivo* work [235], adding FPOP to the suite of well-established structural MS techniques already available, could yet prove to be a critical step forward in the advancement of structural MS as a field.

7.1.1 How do HDX and FPOP compare?

In addition to the findings outlined above, the comparison of wild-type β_2m to the truncation variant using both FPOP and HDX highlights the similarity regarding the

identified regions of difference between the two proteins, where both techniques identified the region directly proximal to the N-terminal truncation as the site of most significant structural change. However, the closest agreement between the two methods was observed at the earliest labelling time points of the HDX experiment, prior to larger scale increases in deuterium uptake across the length of the protein, likely associated with the decreased stability of the native fold of the truncation variant, relative to the wild-type protein. These large scale changes were not observed by FPOP, and could indicate a time dependence of the agreement between the two methods, where faster HDX labelling time points show better correlation with FPOP data, than longer deuterium incubation times. Similarly, the trend in labelling between the two methods was not observed to be consistent, where, upon truncation of the N-terminus, both increased and decreased labelling of sites was observed using FPOP, but only increased labelling was observed using HDX. This is not entirely unexpected, given the different labelling targets (i.e. side chain vs backbone) of the two methods. Similarly, although the *precise* timescale of FPOP labelling is still currently disputed [233], the differing labelling timescales of the two methods, along with the broad/low resolution vs narrow/high resolution coverage of structural changes for HDX and FPOP, respectively, grant these two methods a high degree of complementarity when used together. Indeed, an increasing number of studies have utilised both HDX and FPOP in the characterisation of protein structural changes or binding events [217, 278, 314], further demonstrating the useful structural MS niche FPOP is beginning to occupy.

7.2 The D76N variant

Given its overwhelming structural similarity to the wild-type protein, the observation that the D76N variant of β_2m has significantly increased deuterium uptake in the E-F loop surrounding the D-N amino acid substitution, is of notable importance. These changes could not be described solely by the changes in intrinsic exchange rate caused

by the change in amino acid sequence, and demonstrate a significant structural change in the D76N variant, with some evidence supporting minor changes in deuterium uptake in the nearby A-B loop as well. Although the differences between the wild-type protein and D76N shown by FPOP were also in these regions, supporting both the minor changes observed by HDX in the A-B loop, and the observation that HDX and FPOP, as structural MS techniques, highlight similar regions of structural change, the differences in oxidation observed were minor, compared with the substantial differences in deuterium uptake between the two proteins.

There are several possible explanations for this observation. One is that the differences are observed more significantly at timescales appropriate for HDX (sec – hours) than for FPOP (μs-ms). However, the most significant changes in deuterium uptake were observed at the earliest labelling time points of the HDX experiment and, as such, one might expect to observe *larger* differences with faster labelling techniques such as FPOP, as opposed to the minimal changes in oxidation which these data show. Alternatively, the difference in resolution and coverage between FPOP and HDX could explain the discrepancy, whereby residues in the E-F loop which significantly change in SASA are covered by the peptide level HDX data, but were not labelled in the FPOP experiment. Lastly, both the HDX and FPOP data could be explained by the difference in the protein structural factors each technique probes. For example, a significant loss of hydrogen bonding in residues of the E-F loop, a hypothesis outlined in Section 4.7.2, would likely dramatically increase the deuterium uptake of the region, in line with the observed uptake behaviour. However, such H-bond losses would not necessarily cause significant movement of the amino acid side chains involved and, indeed, given the largely solvent accessible nature of the E-F loop in both proteins, would likely only make minimal changes to the SASA of side chains in this region. Hydrogen bonding is not currently believed to significantly affect oxidation of amino acid side chains by FPOP. Therefore, the fact that oxidation by FPOP remained largely similar between the wild-type protein and the D76N variant, could support, or at least does not contradict, the hypothesis that the D76N

substitution has disturbed hydrogen bonding in the E-F loop, as opposed to having caused a wholesale structural rearrangement of the region.

Although considerably more work is needed before a determination of how, or even if, the stability and structure of the E-F loop factor in to the increased aggregation propensity of this variant, given the stark similarity between the structure and dynamics of D76N and the wild-type protein when studied by other methods [157, 161], these large scale changes in HDX surrounding the D-N substitution are encouraging and worthy of further investigation. It would be wise for future work to be directed towards establishing precisely which residues cause the increase in deuterium uptake by, for example, continuing to develop the single residue HDX-MS experiments using ETD peptide fragmentation outlined in section 4.7.4. Additionally, utilising site directed mutagenesis to disrupt hydrogen bonding in this region by other means, will be useful to establish the significance of the E-F or A-B loops on aggregation propensity, before an aggregation mechanism can be elucidated. The observation by FPOP, HDX and IMS that the D76N variant is largely distinct from the aggregation-prone ΔN6 truncation variant, considered to be a structural mimic of the amyloidogenic I_T state folding intermediate, is consistent with the results of others [161]. Although this research is certainly in the early stages, these data could suggest an alternative, or additional, aggregation pathway for the D76N variant not involving the amyloidogenic I_T state. If true, this would offer a remarkable opportunity to study the common factors which direct both the I_T state, and the D76N variant towards amyloid formation and, more generally, gain insight into which factors lead proteins to form amyloid – an essential step in future disease prevention and treatment.

7.3 What did we learn from studying biopharmaceuticals?

The detailed characterisation of the mAbs WFL and STT by FPOP, subsequently published in 2019 [297], gave a unique insight into the effect of the triple CDR substitutions on the structure of these proteins. Although some studies have suggested

a functional allosteric link between the constant and variable domains of mAbs [315], it is generally considered that these two domains are functionally independent [311, 312]. Although the existence of a functional link between the constant and variable domains of the Fab arms in WFL/STT cannot be established from these data, the FPOP data clearly demonstrate that the structural features of the heavy chain CDR in these proteins significantly affect the structure of the interface between the C_H1 and C_L domains. Although these conformational changes are likely minor, as discussed in Section 6.3, these data highlight three key findings:

1. Long range conformational changes in mAbs *can* be transmitted between the constant and variable domains of the Fab arm.
2. FPOP, as a technique, is capable of distinguishing these minor conformational changes, which could be important for protein aggregation and reversible self-association.
3. FPOP could be a useful method for screening new biopharmaceuticals for long range interactions which may/may not be beneficial.

Indeed, despite the significantly increased complexity of the sample compared with the FPOP study of the three variants of β_2m (Section 5), sub-amino acid level resolution on *some* of the oxidised products identified was still achievable, and could be used to gain additional insight on the long range conformational changes observed.

Similarly, the large data set obtained from LC-MS/MS analysis of the oxidised mAb samples provided a useful starting point for the comprehensive analysis of RT data from oxidised peptides. Although limited, the LC RT data obtained here demonstrate, for the first time, that changes in RT may be useful as an aid in determining the oxidised site within the peptide. Given that LC separation is, at present, an essential part of the FPOP experimental workflow, the utility of analysing and compiling these data cannot be overstated, and future work should continue to compile LC RT data from FPOP experiments in an effort to expand and assess the predictability of RT changes for specific types of oxidation.

However, the limitations of this work must also be discussed. Firstly, the difficulty in the interpretation of changes surrounding the site of the amino acid substitutions would greatly benefit from an increased understanding of the effects of local microenvironment and sequence, discussed earlier in Section 7.1. Secondly, following FPOP-LC-MS/MS analysis, only ~2.5x the number of oxidised sites were identified in WFL and STT (50 in total) than in the FPOP data for the β_2m variants (19 in total), despite WFL and STT being ~12x larger. Although, the interfaces between domains of the antibody reduce the available surface area per Ig subunit, when compared with monomeric β_2m, this is considerably lower than one might expect, for a protein consisting of multiple Ig domains of similar structure to β_2m. Undoubtedly, further optimisation of the LC-MS/MS method used would yield more confidently identified modifications. However, a comprehensive analysis of such large proteins following FPOP oxidation and 'bottom-up' LC-MS sample prep, with hundreds, if not thousands, of low abundance, modified peptides with the same *m/z* and similar fragmentation spectra, may be asking too much of even the most capable MS/MS instrumentation.

Although the current experimental workflow is largely effective and provides an enormous quantity of data for each sample, with regards to optimising FPOP for larger molecules such as biopharmaceuticals, it would be unwise to rule out alternative experimental strategies to that of the traditional LC-MS/MS workflow, especially given the early stage of method development FPOP currently occupies.

For example, could a 'top-down' approach be considered? Modern orbitrap MS instruments are capable of utilising multiple ion activation techniques, and have been used successfully for top-down sequencing of mAbs previously [316]. While this may complicate quantification of oxidised sites and likely remove the possibility of characterising positional isomers, this method would subvert other issues with the traditional bottom-up LC-MS/MS approach. For example, issues with failing enzymatic digestion at oxidised lysine residues, and signal splitting from multiple

oxidised species eluting at different retention times. Alternatively, a 'Middle-down' approach could be used, using enzymatic digestion or reduction of disulphide bonds to generate smaller subunits of the protein for subsequent top-down analysis [317, 318].

Regardless, these data demonstrate that, although significantly more work is required to optimise FPOP for the study of larger, more complex molecules, this method has the potential to characterise the structure of mAbs, in great detail, and may prove to be a useful additional tool to study the reversible self-association of biotherapeutics.

7.4 Final thoughts

The study of aggregation-prone proteins, and the development of methods which make their characterisation possible, is of critical importance to the prevention and treatment of disease in the modern era. The work presented in this thesis demonstrates a modest step forward in the understanding and development of several MS based techniques ideally suited to this purpose, as well as an increased understanding of the protein systems studied.

The lessons learned during this project however, stretch much further than those outlined above. With each research project, the subtleties of each obstacle stumbled across provide a valuable insight to those involved, as to how future work might be streamlined for faster research progression. While many of the issues encountered during the course of this PhD project could easily be attributed to any eager young scientist with a limited experience pool, most others could be attributed to challenges in appropriate data interpretation, usually arising from a multitude of different, plausible explanations. Hindered by a fledgling scientific career, or perhaps because of it, the author has often resorted to searching for answers to these problems from outside of the scientific realm.

During his time in the military, the famous comic, writer and poet, Spike Milligan, was once asked by a fellow serviceman where, in the UK, he was from. Although he had been born in India, Spike responded by saying that he was from London, where he had lived from the age of twelve, having moved there with his parents in 1931.

"Which part?" remarked the serviceman - London being a rather large place.

"… Well, all of me." Said Spike.

Although likely not the intention of either man, this exchange demonstrates, quite effectively, that such difficulties in the interpretation of data can arise, even when not really asking the *wrong* question, by asking the *right* question, imprecisely.

Given that protein aggregation and FPOP are both, independently, incredibly complex, multi-faceted subjects for study, moving forward, a high degree of precision in the research questions posited will undoubtedly prove beneficial in the further implementation and development of FPOP, as well as other methods in the structural MS toolbox, to study the aggregation of amyloidogenic proteins like D76N, or biopharmaceuticals like WFL and STT. While this thesis outlines some of the questions, and suggests some new avenues of research to begin this effort, there is, unquestionably, a long way to go, where - to paraphrase the great, Douglas Adams - making progress will require us to think the unthinkable, to do the undoable, and to "grapple with the ineffable itself, and see if we may not eff it after all."

Chapter 8:

Appendices

8 Appendices

The following appendices contain raw data, figures and information relating to each chapter.

8.1 Related information for Chapter 4

Table 8.1 Raw state data (as exported from DynamX) for HDX-MS experiments.

Start	End	Sequence	MaxUptake	Protein	Exposure	Centre	Centre SD	Uptake	Uptake SD
1	10	MIQRTPKIQV	8	Wild-type	0	1214.649	0.104704	0	0
1	10	MIQRTPKIQV	8	Wild-type	0.5	1217.23	0.0247	2.580781	0.107578
1	10	MIQRTPKIQV	8	Wild-type	1	1217.36	0.045922	2.711117	0.114332
1	10	MIQRTPKIQV	8	Wild-type	2	1217.506	0.025463	2.857303	0.107756
1	10	MIQRTPKIQV	8	Wild-type	30	1217.582	0.046735	2.933384	0.114661
1	10	MIQRTPKIQV	8	Wild-type	120	1217.785	0.065008	3.136351	0.123243
1	23	MIQRTPKIQVYSRHPAENGKSNF	20	Wild-type	0	2703.133	0.167672	0	0
1	23	MIQRTPKIQVYSRHPAENGKSNF	20	Wild-type	0.5	2708.3	0.129742	5.167058	0.212006
1	23	MIQRTPKIQVYSRHPAENGKSNF	20	Wild-type	1	2708.628	0.175295	5.495531	0.242574
1	23	MIQRTPKIQVYSRHPAENGKSNF	20	Wild-type	2	2708.786	0.10498	5.652998	0.197824
1	23	MIQRTPKIQVYSRHPAENGKSNF	20	Wild-type	30	2709.109	0.202872	5.97659	0.263193
1	23	MIQRTPKIQVYSRHPAENGKSNF	20	Wild-type	120	2709.453	0.142575	6.320577	0.220094
2	10	IQRTPKIQV	7	Wild-type	0	1083.224	0.05378	0	0
2	10	IQRTPKIQV	7	Wild-type	0.5	1085.7	0.037933	2.475867	0.065812
2	10	IQRTPKIQV	7	Wild-type	1	1085.83	0.030087	2.606238	0.061624
2	10	IQRTPKIQV	7	Wild-type	2	1085.99	0.045149	2.765807	0.070219
2	10	IQRTPKIQV	7	Wild-type	30	1086.224	0.08209	2.9998	0.098138
2	10	IQRTPKIQV	7	Wild-type	120	1086.312	0.041402	3.088398	0.067871
4	10	RTPKIQV	5	Wild-type	0	841.915	0.024333	0	0
4	10	RTPKIQV	5	Wild-type	0.5	843.9773	0.041792	2.062316	0.04836
4	10	RTPKIQV	5	Wild-type	1	844.0443	0.017357	2.129315	0.029889
4	10	RTPKIQV	5	Wild-type	2	844.1681	0.044022	2.253073	0.0503
4	10	RTPKIQV	5	Wild-type	30	844.2945	0.036671	2.379467	0.04401
4	10	RTPKIQV	5	Wild-type	120	844.3475	0.04001	2.432472	0.046828
6	10	PKIQV	3	Wild-type	0	584.6948	0.007523	0	0
6	10	PKIQV	3	Wild-type	0.5	585.8201	0.012492	1.125356	0.014582
6	10	PKIQV	3	Wild-type	1	585.8903	0.007017	1.195543	0.010288
6	10	PKIQV	3	Wild-type	2	585.9739	0.013561	1.279155	0.015508
6	10	PKIQV	3	Wild-type	30	586.048	0.013962	1.353241	0.01586
6	10	PKIQV	3	Wild-type	120	586.1986	0.024513	1.503808	0.025642
11	23	YSRHPAENGKSNF	11	Wild-type	0	1507.565	0.030325	0	0
11	23	YSRHPAENGKSNF	11	Wild-type	0.5	1510.365	0.074444	2.800139	0.080383
11	23	YSRHPAENGKSNF	11	Wild-type	1	1510.492	0.051381	2.926296	0.059663
11	23	YSRHPAENGKSNF	11	Wild-type	2	1510.505	0.023414	2.940129	0.038312
11	23	YSRHPAENGKSNF	11	Wild-type	30	1510.611	0.087883	3.04557	0.092968
11	23	YSRHPAENGKSNF	11	Wild-type	120	1510.732	0.037683	3.166781	0.04837
11	26	YSRHPAENGKSNFLNC	14	Wild-type	0	1837.935	0.086961	0	0
11	26	YSRHPAENGKSNFLNC	14	Wild-type	0.5	1840.497	0.03678	2.562254	0.094419
11	26	YSRHPAENGKSNFLNC	14	Wild-type	1	1840.589	0.078763	2.653526	0.117328
11	26	YSRHPAENGKSNFLNC	14	Wild-type	2	1840.617	0.047244	2.682016	0.098966
11	26	YSRHPAENGKSNFLNC	14	Wild-type	30	1840.717	0.103526	2.782132	0.135203
11	26	YSRHPAENGKSNFLNC	14	Wild-type	120	1840.758	0.086924	2.822377	0.122955
27	35	YVSGFHPSD	7	Wild-type	0	1008.961	0.027743	0	0
27	35	YVSGFHPSD	7	Wild-type	0.5	1009.936	0.034714	0.974845	0.044438
27	35	YVSGFHPSD	7	Wild-type	1	1010.045	0.054767	1.083407	0.061393
27	35	YVSGFHPSD	7	Wild-type	2	1010.199	0.111729	1.237752	0.115122
27	35	YVSGFHPSD	7	Wild-type	30	1010.56	0.052192	1.598825	0.059107
27	35	YVSGFHPSD	7	Wild-type	120	1010.712	0.050249	1.750528	0.057399
27	37	YVSGFHPSDIE	9	Wild-type	0	1251.238	0.044765	0	0
27	37	YVSGFHPSDIE	9	Wild-type	0.5	1251.879	0.038914	0.640529	0.059314
27	37	YVSGFHPSDIE	9	Wild-type	1	1251.965	0.023498	0.726735	0.050557
27	37	YVSGFHPSDIE	9	Wild-type	2	1252.065	0.037962	0.82654	0.058694
27	37	YVSGFHPSDIE	9	Wild-type	30	1252.77	0.063106	1.532005	0.07737
27	37	YVSGFHPSDIE	9	Wild-type	120	1253.012	0.060228	1.774184	0.075042
27	38	YVSGFHPSDIEV	10	Wild-type	0	1350.069	0.015799	0	0
27	38	YVSGFHPSDIEV	10	Wild-type	0.5	1350.945	0.045757	0.876329	0.048408
27	38	YVSGFHPSDIEV	10	Wild-type	1	1351.146	0.071398	1.077086	0.073125
27	38	YVSGFHPSDIEV	10	Wild-type	2	1351.368	0.029131	1.299108	0.033139
27	38	YVSGFHPSDIEV	10	Wild-type	30	1352.07	0.055107	2.001372	0.057327
27	38	YVSGFHPSDIEV	10	Wild-type	120	1352.373	0.141616	2.304499	0.142495
29	35	SGFHPSD	5	Wild-type	0	746.7241	0.028105	0	0
29	35	SGFHPSD	5	Wild-type	0.5	747.4501	0.026492	0.725981	0.038623
29	35	SGFHPSD	5	Wild-type	1	747.5174	0.020176	0.793253	0.034597
29	35	SGFHPSD	5	Wild-type	2	747.6198	0.014116	0.895645	0.031451
29	35	SGFHPSD	5	Wild-type	30	747.8446	0.024055	1.120448	0.036993
29	35	SGFHPSD	5	Wild-type	120	747.9613	0.028167	1.237126	0.03979

36	39	IEVD	3	Wild-type	0	475.4448	0.023089	0	0
36	39	IEVD	3	Wild-type	0.5	475.553	0.048904	0.108264	0.054081
36	39	IEVD	3	Wild-type	1	475.6176	0.040733	0.172778	0.046821
36	39	IEVD	3	Wild-type	2	475.7806	0.044417	0.335846	0.050059
36	39	IEVD	3	Wild-type	30	476.0594	0.025927	0.614595	0.034717
36	39	IEVD	3	Wild-type	120	476.0687	0.054696	0.623888	0.059369
36	40	IEVDL	4	Wild-type	0	588.586	0.011613	0	0
36	40	IEVDL	4	Wild-type	0.5	588.8798	0.014841	0.293809	0.018844
36	40	IEVDL	4	Wild-type	1	588.9283	0.01735	0.342316	0.020877
36	40	IEVDL	4	Wild-type	2	588.9982	0.028759	0.412221	0.031015
36	40	IEVDL	4	Wild-type	30	589.3154	0.0204	0.729424	0.023473
36	40	IEVDL	4	Wild-type	120	589.4759	0.021141	0.889905	0.02412
36	41	IEVDLL	5	Wild-type	0	701.8437	0.018952	0	0
36	41	IEVDLL	5	Wild-type	0.5	702.0775	0.021814	0.233829	0.028897
36	41	IEVDLL	5	Wild-type	1	702.1788	0.035366	0.335057	0.040125
36	41	IEVDLL	5	Wild-type	2	702.2346	0.029955	0.390876	0.035447
36	41	IEVDLL	5	Wild-type	30	702.4983	0.020631	0.654582	0.028015
36	41	IEVDLL	5	Wild-type	120	702.6459	0.016583	0.802174	0.025183
36	56	IEVDLLKNGERIEKVEHSDLS	20	Wild-type	0	2424.7	0.080807	0	0
36	56	IEVDLLKNGERIEKVEHSDLS	20	Wild-type	0.5	2430.141	0.094319	5.44138	0.124201
36	56	IEVDLLKNGERIEKVEHSDLS	20	Wild-type	1	2430.354	0.110033	5.654528	0.136518
36	56	IEVDLLKNGERIEKVEHSDLS	20	Wild-type	2	2430.493	0.081614	5.793608	0.11485
36	56	IEVDLLKNGERIEKVEHSDLS	20	Wild-type	30	2430.79	0.069179	6.090295	0.106375
36	56	IEVDLLKNGERIEKVEHSDLS	20	Wild-type	120	2431.362	0.100432	6.662527	0.128905
36	57	IEVDLLKNGERIEKVEHSDLSF	21	Wild-type	0	2571.858	0.083893	0	0
36	57	IEVDLLKNGERIEKVEHSDLSF	21	Wild-type	0.5	2577.55	0.081021	5.692236	0.116629
36	57	IEVDLLKNGERIEKVEHSDLSF	21	Wild-type	1	2577.795	0.075574	5.937171	0.112914
36	57	IEVDLLKNGERIEKVEHSDLSF	21	Wild-type	2	2577.974	0.098131	6.115651	0.129103
36	57	IEVDLLKNGERIEKVEHSDLSF	21	Wild-type	30	2578.21	0.098929	6.351619	0.129711
36	57	IEVDLLKNGERIEKVEHSDLSF	21	Wild-type	120	2578.718	0.08745	6.859912	0.121183
38	55	VDLLKNGERIEKVEHSDL	17	Wild-type	0	2095.454	0.156101	0	0
38	55	VDLLKNGERIEKVEHSDL	17	Wild-type	0.5	2100.174	0.085673	4.720057	0.178065
38	55	VDLLKNGERIEKVEHSDL	17	Wild-type	1	2100.303	0.12088	4.849235	0.197432
38	55	VDLLKNGERIEKVEHSDL	17	Wild-type	2	2100.352	0.155914	4.898328	0.220628
38	55	VDLLKNGERIEKVEHSDL	17	Wild-type	30	2100.392	0.116166	4.938038	0.194582
38	55	VDLLKNGERIEKVEHSDL	17	Wild-type	120	2100.908	0.113463	5.453825	0.19298
38	56	VDLLKNGERIEKVEHSDLS	18	Wild-type	0	2182.409	0.107436	0	0
38	56	VDLLKNGERIEKVEHSDLS	18	Wild-type	0.5	2187.891	0.157287	5.482425	0.190477
38	56	VDLLKNGERIEKVEHSDLS	18	Wild-type	1	2188.157	0.203902	5.747961	0.230474
38	56	VDLLKNGERIEKVEHSDLS	18	Wild-type	2	2188.224	0.123916	5.815004	0.164005
38	56	VDLLKNGERIEKVEHSDLS	18	Wild-type	30	2188.234	0.151841	5.824919	0.186006
38	56	VDLLKNGERIEKVEHSDLS	18	Wild-type	120	2188.769	0.145229	6.360423	0.180648
39	57	DLLKNGERIEKVEHSDLSF	18	Wild-type	0	2230.32	0.069108	0	0
39	57	DLLKNGERIEKVEHSDLSF	18	Wild-type	0.5	2236.133	0.097198	5.813481	0.119261
39	57	DLLKNGERIEKVEHSDLSF	18	Wild-type	1	2236.223	0.072818	5.903107	0.100391
39	57	DLLKNGERIEKVEHSDLSF	18	Wild-type	2	2236.413	0.078956	6.093021	0.104928
39	57	DLLKNGERIEKVEHSDLSF	18	Wild-type	30	2236.471	0.069825	6.151945	0.098242
39	57	DLLKNGERIEKVEHSDLSF	18	Wild-type	120	2236.782	0.086729	6.462497	0.110895
40	55	LLKNGERIEKVEHSDL	15	Wild-type	0	1881.099	0.108406	0	0
40	55	LLKNGERIEKVEHSDL	15	Wild-type	0.5	1885.058	0.083856	3.95827	0.137054
40	55	LLKNGERIEKVEHSDL	15	Wild-type	1	1885.169	0.141897	4.069735	0.178569
40	55	LLKNGERIEKVEHSDL	15	Wild-type	2	1885.184	0.174013	4.084348	0.205018
40	55	LLKNGERIEKVEHSDL	15	Wild-type	30	1885.228	0.161414	4.128637	0.194438
40	55	LLKNGERIEKVEHSDL	15	Wild-type	120	1885.379	0.138553	4.279747	0.175923
40	56	LLKNGERIEKVEHSDLS	16	Wild-type	0	1968.041	0.059337	0	0
40	56	LLKNGERIEKVEHSDLS	16	Wild-type	0.5	1972.986	0.089191	4.945505	0.107126
40	56	LLKNGERIEKVEHSDLS	16	Wild-type	1	1973.224	0.123681	5.183197	0.137178
40	56	LLKNGERIEKVEHSDLS	16	Wild-type	2	1973.324	0.165952	5.282796	0.176241
40	56	LLKNGERIEKVEHSDLS	16	Wild-type	30	1973.322	0.109178	5.281705	0.12426
40	56	LLKNGERIEKVEHSDLS	16	Wild-type	120	1973.513	0.117593	5.471807	0.131716
40	57	LLKNGERIEKVEHSDLSF	17	Wild-type	0	2115.183	0.033729	0	0
40	57	LLKNGERIEKVEHSDLSF	17	Wild-type	0.5	2120.779	0.127769	5.596368	0.132146
40	57	LLKNGERIEKVEHSDLSF	17	Wild-type	1	2120.875	0.115587	5.692133	0.120407
40	57	LLKNGERIEKVEHSDLSF	17	Wild-type	2	2120.941	0.096867	5.75843	0.102571
40	57	LLKNGERIEKVEHSDLSF	17	Wild-type	30	2121.031	0.090115	5.848536	0.096221
40	57	LLKNGERIEKVEHSDLSF	17	Wild-type	120	2121.171	0.093805	5.988472	0.099684
41	55	LKNGERIEKVEHSDL	14	Wild-type	0	1767.991	0.058232	0	0
41	55	LKNGERIEKVEHSDL	14	Wild-type	0.5	1771.792	0.088348	3.800837	0.105813
41	55	LKNGERIEKVEHSDL	14	Wild-type	1	1771.816	0.117883	3.824241	0.131481
41	55	LKNGERIEKVEHSDL	14	Wild-type	2	1771.824	0.107219	3.832733	0.122012
41	55	LKNGERIEKVEHSDL	14	Wild-type	30	1771.834	0.125103	3.842438	0.137991
41	55	LKNGERIEKVEHSDL	14	Wild-type	120	1772.053	0.093791	4.061388	0.110398
41	56	LKNGERIEKVEHSDLS	15	Wild-type	0	1854.994	0.058292	0	0
41	56	LKNGERIEKVEHSDLS	15	Wild-type	0.5	1859.382	0.126264	4.387788	0.13907
41	56	LKNGERIEKVEHSDLS	15	Wild-type	1	1859.485	0.173958	4.491089	0.183465
41	56	LKNGERIEKVEHSDLS	15	Wild-type	2	1859.592	0.171771	4.597704	0.181393
41	56	LKNGERIEKVEHSDLS	15	Wild-type	30	1859.536	0.219089	4.541573	0.226711
41	56	LKNGERIEKVEHSDLS	15	Wild-type	120	1859.779	0.194701	4.784412	0.20324
41	57	LKNGERIEKVEHSDLSF	16	Wild-type	0	2002.222	0.099094	0	0
41	57	LKNGERIEKVEHSDLSF	16	Wild-type	0.5	2007.382	0.103249	5.159903	0.143108
41	57	LKNGERIEKVEHSDLSF	16	Wild-type	1	2007.552	0.079292	5.329351	0.126913
41	57	LKNGERIEKVEHSDLSF	16	Wild-type	2	2007.575	0.124392	5.352889	0.159038
41	57	LKNGERIEKVEHSDLSF	16	Wild-type	30	2007.594	0.081441	5.371251	0.128266

41	57	LKNGERIEKVEHSDLSF	16	Wild-type	120	2007.704	0.078509	5.481297	0.126425
56	63	SFSKDWSF	7	Wild-type	0	1004.179	0.040787	0	0
56	63	SFSKDWSF	7	Wild-type	0.5	1006.203	0.058805	2.024336	0.071566
56	63	SFSKDWSF	7	Wild-type	1	1006.394	0.062525	2.214566	0.074652
56	63	SFSKDWSF	7	Wild-type	2	1006.59	0.035866	2.410775	0.054313
56	63	SFSKDWSF	7	Wild-type	30	1006.803	0.026759	2.623998	0.048781
56	63	SFSKDWSF	7	Wild-type	120	1006.802	0.020354	2.623154	0.045583
57	61	FSKDW	4	Wild-type	0	682.7389	0.034363	0	0
57	61	FSKDW	4	Wild-type	0.5	683.7629	0.019432	1.023997	0.039477
57	61	FSKDW	4	Wild-type	1	683.9297	0.016582	1.190741	0.038155
57	61	FSKDW	4	Wild-type	2	684.0549	0.013217	1.31596	0.036817
57	61	FSKDW	4	Wild-type	30	684.2023	0.023405	1.463416	0.041576
57	61	FSKDW	4	Wild-type	120	684.2281	0.01184	1.489208	0.036345
57	63	FSKDWSF	6	Wild-type	0	917.0544	0.033516	0	0
57	63	FSKDWSF	6	Wild-type	0.5	918.7138	0.024238	1.659342	0.041362
57	63	FSKDWSF	6	Wild-type	1	918.8735	0.025493	1.819125	0.04211
57	63	FSKDWSF	6	Wild-type	2	919.0168	0.029862	1.962417	0.04489
57	63	FSKDWSF	6	Wild-type	30	919.2065	0.027549	2.152097	0.043385
57	63	FSKDWSF	6	Wild-type	120	919.2342	0.03474	2.179745	0.048272
58	62	SKDWS	4	Wild-type	0	622.5009	0.019386	0	0
58	62	SKDWS	4	Wild-type	0.5	623.4123	0.029885	0.911366	0.035622
58	62	SKDWS	4	Wild-type	1	623.5272	0.035785	1.026264	0.040699
58	62	SKDWS	4	Wild-type	2	623.6677	0.031186	1.166819	0.03672
58	62	SKDWS	4	Wild-type	30	623.7645	0.031362	1.263533	0.03687
58	62	SKDWS	4	Wild-type	120	623.8083	0.028379	1.3074	0.034368
58	63	SKDWSF	5	Wild-type	0	769.8156	0.016578	0	0
58	63	SKDWSF	5	Wild-type	0.5	771.0771	0.019898	1.261503	0.025899
58	63	SKDWSF	5	Wild-type	1	771.2769	0.025342	1.461355	0.030283
58	63	SKDWSF	5	Wild-type	2	771.4586	0.02425	1.643	0.029375
58	63	SKDWSF	5	Wild-type	30	771.6542	0.016102	1.838629	0.023111
58	63	SKDWSF	5	Wild-type	120	771.6739	0.03316	1.858345	0.037073
59	63	KDWSF	4	Wild-type	0	682.7111	0.036858	0	0
59	63	KDWSF	4	Wild-type	0.5	684.0453	0.014384	1.334227	0.039565
59	63	KDWSF	4	Wild-type	1	684.1448	0.027562	1.4337	0.046023
59	63	KDWSF	4	Wild-type	2	684.2457	0.021238	1.534621	0.042539
59	63	KDWSF	4	Wild-type	30	684.3661	0.037837	1.654985	0.052822
59	63	KDWSF	4	Wild-type	120	684.3644	0.01269	1.653264	0.038981
60	63	DWSF	3	Wild-type	0	554.4942	0.015262	0	0
60	63	DWSF	3	Wild-type	0.5	555.422	0.012195	0.927757	0.019536
60	63	DWSF	3	Wild-type	1	555.5664	0.030893	1.072245	0.034457
60	63	DWSF	3	Wild-type	2	555.6644	0.006733	1.170183	0.016681
60	63	DWSF	3	Wild-type	30	555.7901	0.022097	1.295879	0.026856
60	63	DWSF	3	Wild-type	120	555.8	0.029092	1.30585	0.032852
63	67	FYLLY	4	Wild-type	0	718.7383	0.021872	0	0
63	67	FYLLY	4	Wild-type	0.5	718.7994	0.024491	0.061098	0.032836
63	67	FYLLY	4	Wild-type	1	718.8011	0.021443	0.062717	0.03063
63	67	FYLLY	4	Wild-type	2	718.7885	0.023216	0.050115	0.031897
63	67	FYLLY	4	Wild-type	30	718.8295	0.014193	0.091151	0.026074
63	67	FYLLY	4	Wild-type	120	718.9046	0.011066	0.166217	0.024512
64	67	YLLY	3	Wild-type	0	571.6766	0.014298	0	0
64	67	YLLY	3	Wild-type	0.5	571.7411	0.015292	0.064561	0.020935
64	67	YLLY	3	Wild-type	1	571.7512	0.016326	0.074592	0.021702
64	67	YLLY	3	Wild-type	2	571.7374	0.018958	0.060809	0.023745
64	67	YLLY	3	Wild-type	30	571.7082	0.01982	0.031637	0.024439
64	67	YLLY	3	Wild-type	120	571.8033	0.012071	0.126712	0.018712
64	68	YLLYY	4	Wild-type	0	734.7492	0.021619	0	0
64	68	YLLYY	4	Wild-type	0.5	734.7782	0.027171	0.028983	0.034722
64	68	YLLYY	4	Wild-type	1	734.7996	0.022469	0.050381	0.03118
64	68	YLLYY	4	Wild-type	2	734.7826	0.02301	0.033351	0.031573
64	68	YLLYY	4	Wild-type	30	734.849	0.030814	0.099714	0.037641
64	68	YLLYY	4	Wild-type	120	734.9274	0.038254	0.178153	0.04394
65	68	LLYY	3	Wild-type	0	571.6098	0.005148	0	0
65	68	LLYY	3	Wild-type	0.5	571.6372	0.014922	0.027446	0.015785
65	68	LLYY	3	Wild-type	1	571.6266	0.023175	0.016771	0.023739
65	68	LLYY	3	Wild-type	2	571.6295	0.005174	0.019661	0.007299
65	68	LLYY	3	Wild-type	30	571.6238	0.008409	0.014009	0.00986
65	68	LLYY	3	Wild-type	120	571.6561	0.009061	0.046313	0.010421
66	71	LYYTEF	5	Wild-type	0	835.8	0.021728	0	0
66	71	LYYTEF	5	Wild-type	0.5	836.2815	0.020505	0.481524	0.029876
66	71	LYYTEF	5	Wild-type	1	836.3913	0.02516	0.591292	0.033243
66	71	LYYTEF	5	Wild-type	2	836.4463	0.03084	0.646286	0.037726
66	71	LYYTEF	5	Wild-type	30	836.4681	0.013879	0.668112	0.025783
66	71	LYYTEF	5	Wild-type	120	836.4616	0.008243	0.661659	0.023239
67	70	YYTE	3	Wild-type	0	575.5419	0.021735	0	0
67	70	YYTE	3	Wild-type	0.5	576.0215	0.007024	0.479649	0.022842
67	70	YYTE	3	Wild-type	1	576.1379	0.00799	0.59599	0.023158
67	70	YYTE	3	Wild-type	2	576.1921	0.017942	0.650198	0.028184
67	70	YYTE	3	Wild-type	30	576.1485	0.003639	0.60662	0.022038
67	70	YYTE	3	Wild-type	120	576.1772	0.00432	0.63529	0.022161
67	71	YYTEF	4	Wild-type	0	722.7504	0.008058	0	0
67	71	YYTEF	4	Wild-type	0.5	723.2127	0.011071	0.46227	0.013693
67	71	YYTEF	4	Wild-type	1	723.2947	0.015834	0.544315	0.017766
67	71	YYTEF	4	Wild-type	2	723.33	0.011098	0.579632	0.013715

67	71	YYTEF	4	Wild-type	30	723.2908	0.017073	0.54043	0.018879
67	71	YYTEF	4	Wild-type	120	723.3096	0.013159	0.559216	0.015431
67	79	YYTEFTPTEKDEY	11	Wild-type	0	1686.698	0.038113	0	0
67	79	YYTEFTPTEKDEY	11	Wild-type	0.5	1689.379	0.035484	2.681019	0.052074
67	79	YYTEFTPTEKDEY	11	Wild-type	1	1689.737	0.079747	3.039339	0.088386
67	79	YYTEFTPTEKDEY	11	Wild-type	2	1690.052	0.057253	3.354169	0.068779
67	79	YYTEFTPTEKDEY	11	Wild-type	30	1690.427	0.046935	3.728623	0.060461
67	79	YYTEFTPTEKDEY	11	Wild-type	120	1690.471	0.043514	3.772836	0.057845
68	71	YTEF	3	Wild-type	0	559.5784	0.015936	0	0
68	71	YTEF	3	Wild-type	0.5	559.9933	0.035481	0.414868	0.038895
68	71	YTEF	3	Wild-type	1	560.0963	0.014391	0.517897	0.021472
68	71	YTEF	3	Wild-type	2	560.1499	0.00957	0.57151	0.018588
68	71	YTEF	3	Wild-type	30	560.1157	0.011267	0.537321	0.019516
68	71	YTEF	3	Wild-type	120	560.1106	0.014284	0.53217	0.0214
68	78	YTEFTPTEKDE	9	Wild-type	0	1360.344	0.106569	0	0
68	78	YTEFTPTEKDE	9	Wild-type	0.5	1362.739	0.035781	2.395582	0.112415
68	78	YTEFTPTEKDE	9	Wild-type	1	1363.006	0.046428	2.662683	0.116243
68	78	YTEFTPTEKDE	9	Wild-type	2	1363.184	0.070815	2.840493	0.127952
68	78	YTEFTPTEKDE	9	Wild-type	30	1363.374	0.055382	3.029884	0.120101
68	78	YTEFTPTEKDE	9	Wild-type	120	1363.437	0.019504	3.093667	0.108339
68	80	YTEFTPTEKDEYA	11	Wild-type	0	1594.649	0.042436	0	0
68	80	YTEFTPTEKDEYA	11	Wild-type	0.5	1597.019	0.125935	2.370042	0.132893
68	80	YTEFTPTEKDEYA	11	Wild-type	1	1597.226	0.106183	2.576974	0.114349
68	80	YTEFTPTEKDEYA	11	Wild-type	2	1597.657	0.105206	3.007809	0.113442
68	80	YTEFTPTEKDEYA	11	Wild-type	30	1597.964	0.053511	3.315008	0.068296
68	80	YTEFTPTEKDEYA	11	Wild-type	120	1597.994	0.04661	3.344791	0.063034
68	81	YTEFTPTEKDEYAC	12	Wild-type	0	1697.844	0.169876	0	0
68	81	YTEFTPTEKDEYAC	12	Wild-type	0.5	1700.461	0.073725	2.616891	0.185185
68	81	YTEFTPTEKDEYAC	12	Wild-type	1	1700.694	0.084463	2.850218	0.189716
68	81	YTEFTPTEKDEYAC	12	Wild-type	2	1700.94	0.108224	3.096801	0.201421
68	81	YTEFTPTEKDEYAC	12	Wild-type	30	1701.394	0.107374	3.550778	0.200965
68	81	YTEFTPTEKDEYAC	12	Wild-type	120	1701.411	0.098699	3.567592	0.196468
69	78	TEFTPTEKDE	8	Wild-type	0	1196.973	0.013275	0	0
69	78	TEFTPTEKDE	8	Wild-type	0.5	1199.363	0.054871	2.39007	0.056454
69	78	TEFTPTEKDE	8	Wild-type	1	1199.643	0.053923	2.669759	0.055533
69	78	TEFTPTEKDE	8	Wild-type	2	1199.768	0.072229	2.795043	0.073439
69	78	TEFTPTEKDE	8	Wild-type	30	1199.939	0.051623	2.966071	0.053303
69	78	TEFTPTEKDE	8	Wild-type	120	1199.939	0.080987	2.965905	0.082068
69	80	TEFTPTEKDEYA	10	Wild-type	0	1431.381	0.027154	0	0
69	80	TEFTPTEKDEYA	10	Wild-type	0.5	1433.662	0.041045	2.281274	0.049214
69	80	TEFTPTEKDEYA	10	Wild-type	1	1433.942	0.025286	2.561441	0.037104
69	80	TEFTPTEKDEYA	10	Wild-type	2	1434.21	0.034059	2.829133	0.043558
69	80	TEFTPTEKDEYA	10	Wild-type	30	1434.572	0.070446	3.191361	0.075499
69	80	TEFTPTEKDEYA	10	Wild-type	120	1434.631	0.038041	3.250817	0.046738
69	81	TEFTPTEKDEYAC	11	Wild-type	0	1534.514	0.028031	0	0
69	81	TEFTPTEKDEYAC	11	Wild-type	0.5	1536.848	0.083577	2.333675	0.088152
69	81	TEFTPTEKDEYAC	11	Wild-type	1	1537.142	0.057711	2.628267	0.064158
69	81	TEFTPTEKDEYAC	11	Wild-type	2	1537.384	0.074591	2.869776	0.079684
69	81	TEFTPTEKDEYAC	11	Wild-type	30	1537.775	0.081868	3.260855	0.086534
69	81	TEFTPTEKDEYAC	11	Wild-type	120	1537.838	0.044611	3.323974	0.052687
82	100	RVNHVTLSQPKIVKWDRDM	17	Wild-type	0	2323.565	0.035898	0	0
82	100	RVNHVTLSQPKIVKWDRDM	17	Wild-type	0.5	2327.509	0.110425	3.944402	0.116114
82	100	RVNHVTLSQPKIVKWDRDM	17	Wild-type	1	2327.776	0.08834	4.211121	0.095355
82	100	RVNHVTLSQPKIVKWDRDM	17	Wild-type	2	2327.977	0.105686	4.4125	0.111616
82	100	RVNHVTLSQPKIVKWDRDM	17	Wild-type	30	2328.121	0.056432	4.555759	0.066882
82	100	RVNHVTLSQPKIVKWDRDM	17	Wild-type	120	2328.558	0.119209	4.992804	0.124497
91	100	PKIVKWDRDM	8	Wild-type	0	1288.379	0.039091	0	0
91	100	PKIVKWDRDM	8	Wild-type	0.5	1290.231	0.062899	1.852006	0.074057
91	100	PKIVKWDRDM	8	Wild-type	1	1290.339	0.076685	1.959608	0.086074
91	100	PKIVKWDRDM	8	Wild-type	2	1290.395	0.068407	2.015696	0.078788
91	100	PKIVKWDRDM	8	Wild-type	30	1290.467	0.068597	2.088125	0.078953
91	100	PKIVKWDRDM	8	Wild-type	120	1290.529	0.069089	2.150282	0.079381
94	100	VKWDRDM	6	Wild-type	0	949.9624	0.019987	0	0
94	100	VKWDRDM	6	Wild-type	0.5	951.2677	0.064491	1.305274	0.067517
94	100	VKWDRDM	6	Wild-type	1	951.3227	0.024772	1.360305	0.03183
94	100	VKWDRDM	6	Wild-type	2	951.4715	0.062699	1.509127	0.065808
94	100	VKWDRDM	6	Wild-type	30	951.4607	0.040988	1.498313	0.045601
94	100	VKWDRDM	6	Wild-type	120	951.4885	0.047423	1.526095	0.051463
95	100	KWDRDM	5	Wild-type	0	850.8711	0.039349	0	0
95	100	KWDRDM	5	Wild-type	0.5	852.2357	0.056807	1.364618	0.069104
95	100	KWDRDM	5	Wild-type	1	852.3595	0.036966	1.48835	0.053989
95	100	KWDRDM	5	Wild-type	2	852.3744	0.049272	1.50328	0.063056
95	100	KWDRDM	5	Wild-type	30	852.42	0.028675	1.548889	0.048689
95	100	KWDRDM	5	Wild-type	120	852.4299	0.048849	1.558744	0.062726
1	10	MIQRTPKIQV	8	D76N	0	1214.573	0.067792	0	0
1	10	MIQRTPKIQV	8	D76N	0.5	1217.253	0.032829	2.679976	0.075323
1	10	MIQRTPKIQV	8	D76N	1	1217.426	0.033249	2.852556	0.075507
1	10	MIQRTPKIQV	8	D76N	2	1217.525	0.053099	2.952003	0.086112
1	10	MIQRTPKIQV	8	D76N	30	1217.603	0.068468	3.02958	0.096352
1	10	MIQRTPKIQV	8	D76N	120	1217.887	0.043425	3.314023	0.080508
1	23	MIQRTPKIQVYSRHPAENGKSNF	20	D76N	0	2703.118	0.125231	0	0
1	23	MIQRTPKIQVYSRHPAENGKSNF	20	D76N	0.5	2708.725	0.121379	5.606965	0.1744
1	23	MIQRTPKIQVYSRHPAENGKSNF	20	D76N	1	2709.061	0.163565	5.94378	0.206

1	23	MIQRTPKIQVYSRHPAENGKSNF	20	D76N	2	2709.273	0.137202	6.155132	0.185761
1	23	MIQRTPKIQVYSRHPAENGKSNF	20	D76N	30	2709.46	0.261306	6.342915	0.289765
1	23	MIQRTPKIQVYSRHPAENGKSNF	20	D76N	120	2709.857	0.188388	6.739016	0.226214
2	10	IQRTPKIQV	7	D76N	0	1083.259	0.02496	0	0
2	10	IQRTPKIQV	7	D76N	0.5	1085.741	0.03257	2.482787	0.041034
2	10	IQRTPKIQV	7	D76N	1	1085.854	0.042696	2.594848	0.049457
2	10	IQRTPKIQV	7	D76N	2	1086.025	0.050398	2.766048	0.056241
2	10	IQRTPKIQV	7	D76N	30	1086.114	0.04448	2.854963	0.051005
2	10	IQRTPKIQV	7	D76N	120	1086.361	0.038038	3.102603	0.045496
4	10	RTPKIQV	5	D76N	0	841.9159	0.013515	0	0
4	10	RTPKIQV	5	D76N	0.5	844.0246	0.031648	2.108745	0.034412
4	10	RTPKIQV	5	D76N	1	844.103	0.030681	2.187142	0.033526
4	10	RTPKIQV	5	D76N	2	844.2297	0.034826	2.313846	0.037356
4	10	RTPKIQV	5	D76N	30	844.3057	0.036339	2.389851	0.038771
4	10	RTPKIQV	5	D76N	120	844.4603	0.026876	2.544403	0.030083
6	10	PKIQV	3	D76N	0	584.6648	0.014043	0	0
6	10	PKIQV	3	D76N	0.5	585.8118	0.018717	1.147042	0.0234
6	10	PKIQV	3	D76N	1	585.8841	0.010758	1.219249	0.017691
6	10	PKIQV	3	D76N	2	585.949	0.013569	1.284219	0.019528
6	10	PKIQV	3	D76N	30	586.052	0.013941	1.387178	0.019788
6	10	PKIQV	3	D76N	120	586.2373	0.024839	1.572488	0.028534
11	23	YSRHPAENGKSNF	11	D76N	0	1507.559	0.032641	0	0
11	23	YSRHPAENGKSNF	11	D76N	0.5	1510.642	0.042634	3.082214	0.053694
11	23	YSRHPAENGKSNF	11	D76N	1	1510.81	0.050408	3.250812	0.060053
11	23	YSRHPAENGKSNF	11	D76N	2	1510.881	0.068237	3.321196	0.075642
11	23	YSRHPAENGKSNF	11	D76N	30	1510.894	0.066178	3.334292	0.07379
11	23	YSRHPAENGKSNF	11	D76N	120	1511.106	0.031438	3.546851	0.045319
11	26	YSRHPAENGKSNFLNC	14	D76N	0	1837.955	0.092234	0	0
11	26	YSRHPAENGKSNFLNC	14	D76N	0.5	1840.801	0.129421	2.846175	0.158924
11	26	YSRHPAENGKSNFLNC	14	D76N	1	1840.82	0.099579	2.864586	0.135731
11	26	YSRHPAENGKSNFLNC	14	D76N	2	1840.87	0.113566	2.915365	0.146303
11	26	YSRHPAENGKSNFLNC	14	D76N	30	1840.97	0.099934	3.014697	0.135993
11	26	YSRHPAENGKSNFLNC	14	D76N	120	1841.078	0.058547	3.123201	0.109247
27	35	YVSGFHPSD	7	D76N	0	1008.939	0.064844	0	0
27	35	YVSGFHPSD	7	D76N	0.5	1010.08	0.044142	1.140295	0.078443
27	35	YVSGFHPSD	7	D76N	1	1010.167	0.05298	1.228129	0.083735
27	35	YVSGFHPSD	7	D76N	2	1010.227	0.05793	1.287529	0.086952
27	35	YVSGFHPSD	7	D76N	30	1010.645	0.034703	1.705458	0.073546
27	35	YVSGFHPSD	7	D76N	120	1010.805	0.045229	1.865792	0.079059
27	37	YVSGFHPSDIE	9	D76N	0	1251.227	0.036886	0	0
27	37	YVSGFHPSDIE	9	D76N	0.5	1251.92	0.036407	0.692901	0.051827
27	37	YVSGFHPSDIE	9	D76N	1	1252.063	0.02709	0.83658	0.045765
27	37	YVSGFHPSDIE	9	D76N	2	1252.143	0.055579	0.915842	0.066705
27	37	YVSGFHPSDIE	9	D76N	30	1252.875	0.057019	1.647859	0.067909
27	37	YVSGFHPSDIE	9	D76N	120	1253.203	0.035328	1.975954	0.051074
27	38	YVSGFHPSDIEV	10	D76N	0	1350.047	0.02207	0	0
27	38	YVSGFHPSDIEV	10	D76N	0.5	1350.944	0.106963	0.897149	0.109216
27	38	YVSGFHPSDIEV	10	D76N	1	1351.173	0.057426	1.125995	0.061521
27	38	YVSGFHPSDIEV	10	D76N	2	1351.357	0.067824	1.310359	0.071325
27	38	YVSGFHPSDIEV	10	D76N	30	1352.139	0.084097	2.092369	0.086945
27	38	YVSGFHPSDIEV	10	D76N	120	1352.391	0.048147	2.344108	0.052964
29	35	SGFHPSD	5	D76N	0	746.7026	0.053272	0	0
29	35	SGFHPSD	5	D76N	0.5	747.4112	0.031135	0.708644	0.061703
29	35	SGFHPSD	5	D76N	1	747.5083	0.039117	0.805663	0.066091
29	35	SGFHPSD	5	D76N	2	747.5792	0.028927	0.876586	0.060619
29	35	SGFHPSD	5	D76N	30	747.869	0.025569	1.166365	0.05909
29	35	SGFHPSD	5	D76N	120	748.0476	0.075141	1.345056	0.092109
36	39	IEVD	3	D76N	0	475.5109	0.045347	0	0
36	39	IEVD	3	D76N	0.5	475.7004	0.045225	0.189565	0.064044
36	39	IEVD	3	D76N	1	475.7344	0.038981	0.22358	0.059798
36	39	IEVD	3	D76N	2	475.8323	0.073035	0.321386	0.085968
36	39	IEVD	3	D76N	30	476.0918	0.025153	0.580927	0.051856
36	39	IEVD	3	D76N	120	476.1075	0.016073	0.596622	0.048111
36	40	IEVDL	4	D76N	0	588.588	0.017301	0	0
36	40	IEVDL	4	D76N	0.5	588.8683	0.013641	0.280311	0.022032
36	40	IEVDL	4	D76N	1	588.9702	0.014879	0.382186	0.022819
36	40	IEVDL	4	D76N	2	589.0569	0.024847	0.468858	0.030277
36	40	IEVDL	4	D76N	30	589.3521	0.006357	0.764118	0.018432
36	40	IEVDL	4	D76N	120	589.4953	0.01733	0.907255	0.024488
36	41	IEVDLL	5	D76N	0	701.802	0.040287	0	0
36	41	IEVDLL	5	D76N	0.5	702.0781	0.009985	0.276047	0.041506
36	41	IEVDLL	5	D76N	1	702.1281	0.028744	0.326075	0.04949
36	41	IEVDLL	5	D76N	2	702.2047	0.040219	0.40271	0.056926
36	41	IEVDLL	5	D76N	30	702.5231	0.01376	0.721072	0.042572
36	41	IEVDLL	5	D76N	120	702.6589	0.01	0.856891	0.04151
36	56	IEVDLLKNGERIEKVEHSDLS	20	D76N	0	2424.632	0.088187	0	0
36	56	IEVDLLKNGERIEKVEHSDLS	20	D76N	0.5	2430.226	0.09881	5.594392	0.13244
36	56	IEVDLLKNGERIEKVEHSDLS	20	D76N	1	2430.576	0.112375	5.943935	0.142846
36	56	IEVDLLKNGERIEKVEHSDLS	20	D76N	2	2430.781	0.084861	6.149406	0.122386
36	56	IEVDLLKNGERIEKVEHSDLS	20	D76N	30	2431.384	0.104342	6.751901	0.136617
36	56	IEVDLLKNGERIEKVEHSDLS	20	D76N	120	2431.952	0.153837	7.319607	0.177321
36	57	IEVDLLKNGERIEKVEHSDLSF	21	D76N	0	2571.86	0.103524	0	0
36	57	IEVDLLKNGERIEKVEHSDLSF	21	D76N	0.5	2577.656	0.087186	5.796469	0.135346

36	57	IEVDLLKNGERIEKVEHSDLSF	21	D76N	1	2578.041	0.114704	6.181188	0.154513
36	57	IEVDLLKNGERIEKVEHSDLSF	21	D76N	2	2578.166	0.120698	6.306813	0.159013
36	57	IEVDLLKNGERIEKVEHSDLSF	21	D76N	30	2578.833	0.095937	6.973582	0.141142
36	57	IEVDLLKNGERIEKVEHSDLSF	21	D76N	120	2579.295	0.146062	7.435163	0.179029
38	55	VDLLKNGERIEKVEHSDL	17	D76N	0	2095.42	0.13714	0	0
38	55	VDLLKNGERIEKVEHSDL	17	D76N	0.5	2100.242	0.090379	4.822237	0.164243
38	55	VDLLKNGERIEKVEHSDL	17	D76N	1	2100.459	0.083853	5.039241	0.160744
38	55	VDLLKNGERIEKVEHSDL	17	D76N	2	2100.556	0.09622	5.135591	0.167528
38	55	VDLLKNGERIEKVEHSDL	17	D76N	30	2100.916	0.097287	5.495687	0.168143
38	55	VDLLKNGERIEKVEHSDL	17	D76N	120	2101.423	0.073753	6.003079	0.155714
38	56	VDLLKNGERIEKVEHSDLS	18	D76N	0	2182.436	0.112589	0	0
38	56	VDLLKNGERIEKVEHSDLS	18	D76N	0.5	2187.918	0.104534	5.481722	0.153635
38	56	VDLLKNGERIEKVEHSDLS	18	D76N	1	2188.226	0.129085	5.789975	0.171287
38	56	VDLLKNGERIEKVEHSDLS	18	D76N	2	2188.326	0.141021	5.889302	0.180453
38	56	VDLLKNGERIEKVEHSDLS	18	D76N	30	2188.855	0.090413	6.418506	0.144398
38	56	VDLLKNGERIEKVEHSDLS	18	D76N	120	2189.269	0.084091	6.83231	0.140526
39	57	DLLKNGERIEKVEHSDLSF	18	D76N	0	2230.253	0.074887	0	0
39	57	DLLKNGERIEKVEHSDLSF	18	D76N	0.5	2236.25	0.08537	5.996274	0.113561
39	57	DLLKNGERIEKVEHSDLSF	18	D76N	1	2236.489	0.073074	6.236207	0.104632
39	57	DLLKNGERIEKVEHSDLSF	18	D76N	2	2236.558	0.082704	6.304549	0.11157
39	57	DLLKNGERIEKVEHSDLSF	18	D76N	30	2236.876	0.100226	6.623086	0.125113
39	57	DLLKNGERIEKVEHSDLSF	18	D76N	120	2237.328	0.031028	7.075112	0.08106
40	55	LLKNGERIEKVEHSDL	15	D76N	0	1881.048	0.099721	0	0
40	55	LLKNGERIEKVEHSDL	15	D76N	0.5	1885.059	0.084147	4.010852	0.13048
40	55	LLKNGERIEKVEHSDL	15	D76N	1	1885.183	0.050975	4.134851	0.111995
40	55	LLKNGERIEKVEHSDL	15	D76N	2	1885.348	0.144835	4.300298	0.175845
40	55	LLKNGERIEKVEHSDL	15	D76N	30	1885.579	0.069173	4.531026	0.121364
40	55	LLKNGERIEKVEHSDL	15	D76N	120	1885.976	0.068893	4.928047	0.121204
40	56	LLKNGERIEKVEHSDLS	16	D76N	0	1968.115	0.070604	0	0
40	56	LLKNGERIEKVEHSDLS	16	D76N	0.5	1972.882	0.146943	4.767532	0.163024
40	56	LLKNGERIEKVEHSDLS	16	D76N	1	1973.094	0.065851	4.979841	0.096547
40	56	LLKNGERIEKVEHSDLS	16	D76N	2	1973.198	0.099481	5.083375	0.121989
40	56	LLKNGERIEKVEHSDLS	16	D76N	30	1973.359	0.074173	5.244672	0.102404
40	56	LLKNGERIEKVEHSDLS	16	D76N	120	1973.688	0.119276	5.573226	0.138606
40	57	LLKNGERIEKVEHSDLSF	17	D76N	0	2115.204	0.037369	0	0
40	57	LLKNGERIEKVEHSDLSF	17	D76N	0.5	2120.762	0.091456	5.558762	0.098796
40	57	LLKNGERIEKVEHSDLSF	17	D76N	1	2120.848	0.132432	5.644276	0.137603
40	57	LLKNGERIEKVEHSDLSF	17	D76N	2	2121.039	0.09516	5.834874	0.102235
40	57	LLKNGERIEKVEHSDLSF	17	D76N	30	2121.152	0.043065	5.948531	0.057018
40	57	LLKNGERIEKVEHSDLSF	17	D76N	120	2121.4	0.039449	6.196491	0.054338
41	55	LKNGERIEKVEHSDL	14	D76N	0	1767.968	0.048341	0	0
41	55	LKNGERIEKVEHSDL	14	D76N	0.5	1771.688	0.079894	3.720359	0.09338
41	55	LKNGERIEKVEHSDL	14	D76N	1	1771.873	0.084116	3.904612	0.097017
41	55	LKNGERIEKVEHSDL	14	D76N	2	1771.931	0.101508	3.962466	0.112431
41	55	LKNGERIEKVEHSDL	14	D76N	30	1772.115	0.113608	4.14691	0.123466
41	55	LKNGERIEKVEHSDL	14	D76N	120	1772.465	0.04531	4.496725	0.066256
41	56	LKNGERIEKVEHSDLS	15	D76N	0	1854.965	0.045304	0	0
41	56	LKNGERIEKVEHSDLS	15	D76N	0.5	1859.413	0.189525	4.44759	0.194864
41	56	LKNGERIEKVEHSDLS	15	D76N	1	1859.567	0.139585	4.601586	0.146753
41	56	LKNGERIEKVEHSDLS	15	D76N	2	1859.67	0.160673	4.705046	0.166938
41	56	LKNGERIEKVEHSDLS	15	D76N	30	1859.9	0.174812	4.934937	0.180587
41	56	LKNGERIEKVEHSDLS	15	D76N	120	1860.158	0.161214	5.192442	0.167458
41	57	LKNGERIEKVEHSDLSF	16	D76N	0	2002.18	0.055875	0	0
41	57	LKNGERIEKVEHSDLSF	16	D76N	0.5	2007.367	0.073585	5.186809	0.092394
41	57	LKNGERIEKVEHSDLSF	16	D76N	1	2007.502	0.103799	5.321543	0.117883
41	57	LKNGERIEKVEHSDLSF	16	D76N	2	2007.624	0.054743	5.444177	0.078223
41	57	LKNGERIEKVEHSDLSF	16	D76N	30	2007.683	0.118471	5.50292	0.130986
41	57	LKNGERIEKVEHSDLSF	16	D76N	120	2007.958	0.136745	5.777713	0.14772
56	63	SFSKDWSF	7	D76N	0	1004.11	0.049095	0	0
56	63	SFSKDWSF	7	D76N	0.5	1006.275	0.053962	2.164997	0.072953
56	63	SFSKDWSF	7	D76N	1	1006.489	0.04302	2.378996	0.065276
56	63	SFSKDWSF	7	D76N	2	1006.71	0.051318	2.600274	0.07102
56	63	SFSKDWSF	7	D76N	30	1006.899	0.051641	2.78934	0.071254
56	63	SFSKDWSF	7	D76N	120	1006.969	0.028458	2.859684	0.056746
57	61	FSKDW	4	D76N	0	682.675	0.020621	0	0
57	61	FSKDW	4	D76N	0.5	683.7655	0.019166	1.090536	0.028152
57	61	FSKDW	4	D76N	1	683.948	0.004372	1.273035	0.021079
57	61	FSKDW	4	D76N	2	684.0808	0.014076	1.405753	0.024967
57	61	FSKDW	4	D76N	30	684.2476	0.034603	1.572547	0.040282
57	61	FSKDW	4	D76N	120	684.2878	0.014246	1.612744	0.025063
57	63	FSKDWSF	6	D76N	0	917.0146	0.035469	0	0
57	63	FSKDWSF	6	D76N	0.5	918.7162	0.019237	1.70165	0.04035
57	63	FSKDWSF	6	D76N	1	918.9272	0.045801	1.912645	0.057929
57	63	FSKDWSF	6	D76N	2	919.0802	0.026995	2.065674	0.044573
57	63	FSKDWSF	6	D76N	30	919.3166	0.031263	2.302087	0.04728
57	63	FSKDWSF	6	D76N	120	919.3376	0.033707	2.323077	0.048931
58	62	SKDWS	4	D76N	0	622.4948	0.016934	0	0
58	62	SKDWS	4	D76N	0.5	623.4009	0.037982	0.906099	0.041586
58	62	SKDWS	4	D76N	1	623.5592	0.040241	1.064395	0.043659
58	62	SKDWS	4	D76N	2	623.6663	0.036673	1.171486	0.040393
58	62	SKDWS	4	D76N	30	623.8551	0.043555	1.360279	0.046731
58	62	SKDWS	4	D76N	120	623.8362	0.052092	1.34135	0.054775
58	63	SKDWSF	5	D76N	0	769.7661	0.143677	0	0

58	63	SKDWSF	5	D76N	0.5	771.1094	0.02229	1.343312	0.145395
58	63	SKDWSF	5	D76N	1	771.3225	0.019541	1.556418	0.144999
58	63	SKDWSF	5	D76N	2	771.4906	0.034204	1.724512	0.147692
58	63	SKDWSF	5	D76N	30	771.7158	0.046722	1.949724	0.151082
58	63	SKDWSF	5	D76N	120	771.7471	0.019096	1.981024	0.14494
59	63	KDWSF	4	D76N	0	682.6851	0.036611	0	0
59	63	KDWSF	4	D76N	0.5	683.9717	0.02751	1.286639	0.045794
59	63	KDWSF	4	D76N	1	684.1382	0.014104	1.453152	0.039233
59	63	KDWSF	4	D76N	2	684.2738	0.032235	1.58874	0.048779
59	63	KDWSF	4	D76N	30	684.4337	0.047875	1.748623	0.060269
59	63	KDWSF	4	D76N	120	684.531	0.025572	1.845919	0.044657
60	63	DWSF	3	D76N	0	554.4967	0.007193	0	0
60	63	DWSF	3	D76N	0.5	555.4145	0.032827	0.917848	0.033606
60	63	DWSF	3	D76N	1	555.5461	0.016035	1.049419	0.017574
60	63	DWSF	3	D76N	2	555.6707	0.030686	1.174058	0.031518
60	63	DWSF	3	D76N	30	555.7916	0.022079	1.294924	0.023221
60	63	DWSF	3	D76N	120	555.8365	0.013391	1.339862	0.015201
63	67	FYLLY	4	D76N	0	718.7342	0.030732	0	0
63	67	FYLLY	4	D76N	0.5	718.7971	0.021714	0.062944	0.037629
63	67	FYLLY	4	D76N	1	718.7858	0.012726	0.051674	0.033263
63	67	FYLLY	4	D76N	2	718.7852	0.018822	0.051042	0.036038
63	67	FYLLY	4	D76N	30	718.8094	0.012167	0.075276	0.033053
63	67	FYLLY	4	D76N	120	718.8836	0.025436	0.149393	0.039893
64	67	YLLY	3	D76N	0	571.6159	0.027193	0	0
64	67	YLLY	3	D76N	0.5	571.6945	0.015253	0.078604	0.031179
64	67	YLLY	3	D76N	1	571.6971	0.015628	0.081246	0.031364
64	67	YLLY	3	D76N	2	571.6934	0.0254	0.077512	0.03721
64	67	YLLY	3	D76N	30	571.7246	0.016654	0.108778	0.031887
64	67	YLLY	3	D76N	120	571.7824	0.022867	0.166547	0.035529
64	68	YLLYY	4	D76N	0	734.7674	0.047698	0	0
64	68	YLLYY	4	D76N	0.5	734.7922	0.016275	0.02477	0.050398
64	68	YLLYY	4	D76N	1	734.851	0.050173	0.083661	0.069227
64	68	YLLYY	4	D76N	2	734.8304	0.063469	0.063017	0.079394
64	68	YLLYY	4	D76N	30	734.9056	0.122127	0.13825	0.131111
64	68	YLLYY	4	D76N	120	734.9946	0.062856	0.227201	0.078905
65	68	LLYY	3	D76N	0	571.5809	0.017939	0	0
65	68	LLYY	3	D76N	0.5	571.6404	0.024848	0.059453	0.030646
65	68	LLYY	3	D76N	1	571.6274	0.014384	0.046411	0.022993
65	68	LLYY	3	D76N	2	571.633	0.019115	0.052051	0.026214
65	68	LLYY	3	D76N	30	571.6414	0.018816	0.060413	0.025997
65	68	LLYY	3	D76N	120	571.6635	0.012547	0.082607	0.021892
66	71	LYYTEF	5	D76N	0	835.7851	0.020451	0	0
66	71	LYYTEF	5	D76N	0.5	836.3528	0.032404	0.567695	0.038318
66	71	LYYTEF	5	D76N	1	836.4703	0.041127	0.685143	0.045932
66	71	LYYTEF	5	D76N	2	836.4683	0.017341	0.683179	0.026813
66	71	LYYTEF	5	D76N	30	836.4964	0.02462	0.711232	0.032006
66	71	LYYTEF	5	D76N	120	836.5325	0.046764	0.747393	0.05104
67	70	YYTE	3	D76N	0	575.5297	0.022386	0	0
67	70	YYTE	3	D76N	0.5	576.0941	0.020144	0.564391	0.030115
67	70	YYTE	3	D76N	1	576.1961	0.005963	0.666453	0.023167
67	70	YYTE	3	D76N	2	576.2223	0.009666	0.692642	0.024384
67	70	YYTE	3	D76N	30	576.182	0.017427	0.652332	0.02837
67	70	YYTE	3	D76N	120	576.1926	0.013201	0.662876	0.025989
67	71	YYTEF	4	D76N	0	722.7329	0.019331	0	0
67	71	YYTEF	4	D76N	0.5	723.2749	0.003933	0.541972	0.019727
67	71	YYTEF	4	D76N	1	723.376	0.005878	0.64314	0.020205
67	71	YYTEF	4	D76N	2	723.3921	0.020415	0.659224	0.028115
67	71	YYTEF	4	D76N	30	723.3496	0.010948	0.616702	0.022216
67	71	YYTEF	4	D76N	120	723.3705	0.011296	0.637609	0.02239
67	79	YYTEFTPTEKNEY	11	D76N	0	1685.631	0.025989	0	0
67	79	YYTEFTPTEKNEY	11	D76N	0.5	1689.815	0.077915	4.184076	0.082135
67	79	YYTEFTPTEKNEY	11	D76N	1	1689.971	0.11578	4.340902	0.118661
67	79	YYTEFTPTEKNEY	11	D76N	2	1690.128	0.11722	4.497766	0.120067
67	79	YYTEFTPTEKNEY	11	D76N	30	1690.011	0.055539	4.380104	0.061319
67	79	YYTEFTPTEKNEY	11	D76N	120	1690.13	0.076695	4.499557	0.080979
68	71	YTEF	3	D76N	0	559.5725	0.022797	0	0
68	71	YTEF	3	D76N	0.5	560.0789	0.01781	0.506453	0.028929
68	71	YTEF	3	D76N	1	560.1414	0.011622	0.568951	0.025589
68	71	YTEF	3	D76N	2	560.1585	0.013741	0.586045	0.026618
68	71	YTEF	3	D76N	30	560.1404	0.01417	0.567922	0.026842
68	71	YTEF	3	D76N	120	560.1732	0.009051	0.600715	0.024528
68	78	YTEFTPTEKNE	9	D76N	0	1359.357	0.061159	0	0
68	78	YTEFTPTEKNE	9	D76N	0.5	1363.033	0.033066	3.675727	0.069526
68	78	YTEFTPTEKNE	9	D76N	1	1363.128	0.035155	3.770896	0.070543
68	78	YTEFTPTEKNE	9	D76N	2	1363.103	0.036571	3.746284	0.071259
68	78	YTEFTPTEKNE	9	D76N	30	1362.947	0.041304	3.590029	0.0738
68	78	YTEFTPTEKNE	9	D76N	120	1363.143	0.047118	3.785875	0.077205
68	80	YTEFTPTEKNEYA	11	D76N	0	1593.542	0.060625	0	0
68	80	YTEFTPTEKNEYA	11	D76N	0.5	1597.608	0.070345	4.06616	0.092865
68	80	YTEFTPTEKNEYA	11	D76N	1	1597.607	0.110306	4.064482	0.125868
68	80	YTEFTPTEKNEYA	11	D76N	2	1597.774	0.090496	4.231597	0.108926
68	80	YTEFTPTEKNEYA	11	D76N	30	1597.659	0.118325	4.117409	0.132952
68	80	YTEFTPTEKNEYA	11	D76N	120	1597.754	0.063329	4.211859	0.08767

68	81	YTEFTPTEKNEYAC	12	D76N	0	1696.717	0.030187	0	0
68	81	YTEFTPTEKNEYAC	12	D76N	0.5	1700.871	0.052499	4.154027	0.060559
68	81	YTEFTPTEKNEYAC	12	D76N	1	1701.057	0.112346	4.3396	0.116331
68	81	YTEFTPTEKNEYAC	12	D76N	2	1701.141	0.095837	4.423755	0.100479
68	81	YTEFTPTEKNEYAC	12	D76N	30	1701.028	0.073206	4.310272	0.079185
68	81	YTEFTPTEKNEYAC	12	D76N	120	1701.129	0.098385	4.411646	0.102912
69	78	TEFTPTEKNE	8	D76N	0	1196.023	0.012761	0	0
69	78	TEFTPTEKNE	8	D76N	0.5	1199.633	0.034685	3.610346	0.036958
69	78	TEFTPTEKNE	8	D76N	1	1199.663	0.037894	3.64014	0.039985
69	78	TEFTPTEKNE	8	D76N	2	1199.592	0.091284	3.569292	0.092171
69	78	TEFTPTEKNE	8	D76N	30	1199.393	0.071473	3.369751	0.072603
69	78	TEFTPTEKNE	8	D76N	120	1199.606	0.057044	3.58259	0.058454
69	80	TEFTPTEKNEYA	10	D76N	0	1430.322	0.042827	0	0
69	80	TEFTPTEKNEYA	10	D76N	0.5	1434.048	0.129707	3.726412	0.136594
69	80	TEFTPTEKNEYA	10	D76N	1	1434.223	0.091209	3.900798	0.100763
69	80	TEFTPTEKNEYA	10	D76N	2	1434.276	0.131614	3.954575	0.138407
69	80	TEFTPTEKNEYA	10	D76N	30	1434.186	0.058812	3.863939	0.072754
69	80	TEFTPTEKNEYA	10	D76N	120	1434.245	0.088715	3.923276	0.098512
69	81	TEFTPTEKNEYAC	11	D76N	0	1533.436	0.027766	0	0
69	81	TEFTPTEKNEYAC	11	D76N	0.5	1537.255	0.084483	3.819046	0.088928
69	81	TEFTPTEKNEYAC	11	D76N	1	1537.435	0.027826	3.998879	0.039309
69	81	TEFTPTEKNEYAC	11	D76N	2	1537.482	0.085727	4.045802	0.090111
69	81	TEFTPTEKNEYAC	11	D76N	30	1537.405	0.092964	3.968517	0.097022
69	81	TEFTPTEKNEYAC	11	D76N	120	1537.47	0.071504	4.033793	0.076706
82	100	RVNHVTLSQPKIVKWDRDM	17	D76N	0	2323.559	0.036512	0	0
82	100	RVNHVTLSQPKIVKWDRDM	17	D76N	0.5	2327.626	0.117442	4.066652	0.122987
82	100	RVNHVTLSQPKIVKWDRDM	17	D76N	1	2327.992	0.081892	4.432753	0.089663
82	100	RVNHVTLSQPKIVKWDRDM	17	D76N	2	2328.183	0.063839	4.62351	0.073543
82	100	RVNHVTLSQPKIVKWDRDM	17	D76N	30	2328.129	0.196082	4.56983	0.199452
82	100	RVNHVTLSQPKIVKWDRDM	17	D76N	120	2328.539	0.141636	4.98007	0.146267
91	100	PKIVKWDRDM	8	D76N	0	1288.393	0.037954	0	0
91	100	PKIVKWDRDM	8	D76N	0.5	1290.255	0.116675	1.861692	0.122693
91	100	PKIVKWDRDM	8	D76N	1	1290.558	0.115179	2.164236	0.121271
91	100	PKIVKWDRDM	8	D76N	2	1290.703	0.094827	2.309773	0.102141
91	100	PKIVKWDRDM	8	D76N	30	1290.808	0.265519	2.414757	0.268218
91	100	PKIVKWDRDM	8	D76N	120	1290.891	0.222585	2.497556	0.225797
94	100	VKWDRDM	6	D76N	0	949.958	0.029286	0	0
94	100	VKWDRDM	6	D76N	0.5	951.1507	0.066865	1.192707	0.072997
94	100	VKWDRDM	6	D76N	1	951.3044	0.067611	1.346384	0.073681
94	100	VKWDRDM	6	D76N	2	951.3407	0.095715	1.382741	0.100095
94	100	VKWDRDM	6	D76N	30	951.3046	0.019364	1.346591	0.035109
94	100	VKWDRDM	6	D76N	120	951.6492	0.023426	1.69123	0.037502
95	100	KWDRDM	5	D76N	0	850.8568	0.064341	0	0
95	100	KWDRDM	5	D76N	0.5	852.2432	0.040685	1.386415	0.076125
95	100	KWDRDM	5	D76N	1	852.3555	0.067351	1.498793	0.093145
95	100	KWDRDM	5	D76N	2	852.3943	0.04514	1.537557	0.078596
95	100	KWDRDM	5	D76N	30	852.4941	0.042827	1.637341	0.077291
95	100	KWDRDM	5	D76N	120	852.5511	0.023912	1.694373	0.068641
11	23	YSRHPAENGKSNF	11	ΔN6	0	1507.495	0.037201	0	0
11	23	YSRHPAENGKSNF	11	ΔN6	0.5	1510.484	0.095233	2.989718	0.102241
11	23	YSRHPAENGKSNF	11	ΔN6	1	1510.659	0.075175	3.164558	0.083876
11	23	YSRHPAENGKSNF	11	ΔN6	2	1510.72	0.070509	3.224995	0.079721
11	23	YSRHPAENGKSNF	11	ΔN6	30	1511.07	0.045306	3.575224	0.058622
11	23	YSRHPAENGKSNF	11	ΔN6	120	1511.364	0.05075	3.869537	0.062925
11	26	YSRHPAENGKSNFLNC	14	ΔN6	0	1837.884	0.057194	0	0
11	26	YSRHPAENGKSNFLNC	14	ΔN6	0.5	1840.399	0.094384	2.514222	0.110361
11	26	YSRHPAENGKSNFLNC	14	ΔN6	1	1840.624	0.051517	2.739648	0.076975
11	26	YSRHPAENGKSNFLNC	14	ΔN6	2	1840.72	0.075712	2.835142	0.094886
11	26	YSRHPAENGKSNFLNC	14	ΔN6	30	1841.11	0.15855	3.225593	0.16855
11	26	YSRHPAENGKSNFLNC	14	ΔN6	120	1841.317	0.14138	3.432686	0.152511
27	35	YVSGFHPSD	7	ΔN6	0	1008.995	0.058462	0	0
27	35	YVSGFHPSD	7	ΔN6	0.5	1010.913	0.032352	1.917408	0.066817
27	35	YVSGFHPSD	7	ΔN6	1	1010.978	0.062263	1.982236	0.085408
27	35	YVSGFHPSD	7	ΔN6	2	1011.081	0.042597	2.085801	0.072335
27	35	YVSGFHPSD	7	ΔN6	30	1011.075	0.005145	2.080008	0.058688
27	35	YVSGFHPSD	7	ΔN6	120	1011.144	0.087233	2.14811	0.105011
27	37	YVSGFHPSDIE	9	ΔN6	0	1251.252	0.031903	0	0
27	37	YVSGFHPSDIE	9	ΔN6	0.5	1252.663	0.030503	1.411797	0.044139
27	37	YVSGFHPSDIE	9	ΔN6	1	1252.729	0.056784	1.476987	0.065133
27	37	YVSGFHPSDIE	9	ΔN6	2	1252.821	0.039326	1.569772	0.050639
27	37	YVSGFHPSDIE	9	ΔN6	30	1253.211	0.091449	1.959106	0.096854
27	37	YVSGFHPSDIE	9	ΔN6	120	1253.527	0.045852	2.275289	0.055859
27	38	YVSGFHPSDIEV	10	ΔN6	0	1350.364	0.08177	0	0
27	38	YVSGFHPSDIEV	10	ΔN6	0.5	1351.898	0.096883	1.533954	0.126778
27	38	YVSGFHPSDIEV	10	ΔN6	1	1352.214	0.134442	1.849836	0.157357
27	38	YVSGFHPSDIEV	10	ΔN6	2	1352.145	0.086814	1.780851	0.11926
27	38	YVSGFHPSDIEV	10	ΔN6	30	1352.811	0.064228	2.447229	0.103979
27	38	YVSGFHPSDIEV	10	ΔN6	120	1353.015	0.108172	2.650374	0.1356
29	35	SGFHPSD	5	ΔN6	0	746.7365	0.027362	0	0
29	35	SGFHPSD	5	ΔN6	0.5	748.3017	0.020828	1.565132	0.034387
29	35	SGFHPSD	5	ΔN6	1	748.3254	0.033508	1.588852	0.043261
29	35	SGFHPSD	5	ΔN6	2	748.3577	0.012021	1.621219	0.029887
29	35	SGFHPSD	5	ΔN6	30	748.3617	0.048549	1.625206	0.055729

29	35	SGFHPSD	5	ΔN6	120	748.3875	0.009498	1.650938	0.028964
36	39	IEVD	3	ΔN6	0	475.4701	0.035276	0	0
36	39	IEVD	3	ΔN6	0.5	475.7984	0.040038	0.328274	0.053361
36	39	IEVD	3	ΔN6	1	475.8742	0.030837	0.40406	0.046854
36	39	IEVD	3	ΔN6	2	475.9847	0.032541	0.514582	0.047993
36	39	IEVD	3	ΔN6	30	476.1166	0.021223	0.646466	0.041168
36	39	IEVD	3	ΔN6	120	476.2061	0.037354	0.73596	0.051378
36	40	IEVDL	4	ΔN6	0	588.6323	0.020651	0	0
36	40	IEVDL	4	ΔN6	0.5	589.0045	0.012121	0.372164	0.023945
36	40	IEVDL	4	ΔN6	1	589.0805	0.019481	0.448178	0.02839
36	40	IEVDL	4	ΔN6	2	589.1649	0.023085	0.5326	0.030974
36	40	IEVDL	4	ΔN6	30	589.3289	0.023588	0.696544	0.031351
36	40	IEVDL	4	ΔN6	120	589.4364	0.029406	0.804076	0.035933
36	41	IEVDLL	5	ΔN6	0	701.8469	0.042	0	0
36	41	IEVDLL	5	ΔN6	0.5	702.1927	0.031013	0.345709	0.052209
36	41	IEVDLL	5	ΔN6	1	702.3147	0.019003	0.467714	0.046099
36	41	IEVDLL	5	ΔN6	2	702.3922	0.02093	0.545223	0.046926
36	41	IEVDLL	5	ΔN6	30	702.5182	0.014515	0.671255	0.044438
36	41	IEVDLL	5	ΔN6	120	702.5966	0.022083	0.749627	0.047452
36	56	IEVDLLKNGERIEKVEHSDLS	20	ΔN6	0	2424.69	0.103566	0	0
36	56	IEVDLLKNGERIEKVEHSDLS	20	ΔN6	0.5	2430.389	0.098329	5.698412	0.14281
36	56	IEVDLLKNGERIEKVEHSDLS	20	ΔN6	1	2430.612	0.124062	5.922076	0.161608
36	56	IEVDLLKNGERIEKVEHSDLS	20	ΔN6	2	2430.851	0.148246	6.161086	0.18084
36	56	IEVDLLKNGERIEKVEHSDLS	20	ΔN6	30	2431.245	0.166662	6.554392	0.19622
36	56	IEVDLLKNGERIEKVEHSDLS	20	ΔN6	120	2431.93	0.168612	7.239599	0.197879
36	57	IEVDLLKNGERIEKVEHSDLSF	21	ΔN6	0	2571.912	0.122433	0	0
36	57	IEVDLLKNGERIEKVEHSDLSF	21	ΔN6	0.5	2577.922	0.103046	6.009414	0.160026
36	57	IEVDLLKNGERIEKVEHSDLSF	21	ΔN6	1	2578.066	0.137453	6.154019	0.184074
36	57	IEVDLLKNGERIEKVEHSDLSF	21	ΔN6	2	2578.303	0.129946	6.390176	0.178538
36	57	IEVDLLKNGERIEKVEHSDLSF	21	ΔN6	30	2578.828	0.202865	6.915885	0.236947
36	57	IEVDLLKNGERIEKVEHSDLSF	21	ΔN6	120	2579.345	0.131415	7.432613	0.17961
38	55	VDLLKNGERIEKVEHSDL	17	ΔN6	0	2095.459	0.153392	0	0
38	55	VDLLKNGERIEKVEHSDL	17	ΔN6	0.5	2100.232	0.115158	4.772982	0.191809
38	55	VDLLKNGERIEKVEHSDL	17	ΔN6	1	2100.356	0.083879	4.896946	0.174828
38	55	VDLLKNGERIEKVEHSDL	17	ΔN6	2	2100.523	0.096812	5.063317	0.181389
38	55	VDLLKNGERIEKVEHSDL	17	ΔN6	30	2100.811	0.098702	5.351916	0.182404
38	55	VDLLKNGERIEKVEHSDL	17	ΔN6	120	2101.383	0.12286	5.923269	0.196529
38	56	VDLLKNGERIEKVEHSDLS	18	ΔN6	0	2182.43	0.131256	0	0
38	56	VDLLKNGERIEKVEHSDLS	18	ΔN6	0.5	2188.049	0.136536	5.618854	0.189394
38	56	VDLLKNGERIEKVEHSDLS	18	ΔN6	1	2188.198	0.11668	5.767554	0.17562
38	56	VDLLKNGERIEKVEHSDLS	18	ΔN6	2	2188.337	0.289046	5.907259	0.317452
38	56	VDLLKNGERIEKVEHSDLS	18	ΔN6	30	2188.658	0.227036	6.227771	0.262247
38	56	VDLLKNGERIEKVEHSDLS	18	ΔN6	120	2189.127	0.166516	6.696594	0.212028
39	57	DLLKNGERIEKVEHSDLSF	18	ΔN6	0	2230.31	0.059031	0	0
39	57	DLLKNGERIEKVEHSDLSF	18	ΔN6	0.5	2236.391	0.098665	6.080458	0.114976
39	57	DLLKNGERIEKVEHSDLSF	18	ΔN6	1	2236.473	0.036446	6.163007	0.069375
39	57	DLLKNGERIEKVEHSDLSF	18	ΔN6	2	2236.674	0.087614	6.363807	0.105644
39	57	DLLKNGERIEKVEHSDLSF	18	ΔN6	30	2236.95	0.150785	6.639726	0.161928
39	57	DLLKNGERIEKVEHSDLSF	18	ΔN6	120	2237.445	0.076215	7.134648	0.096402
40	55	LLKNGERIEKVEHSDL	15	ΔN6	0	1881.042	0.161818	0	0
40	55	LLKNGERIEKVEHSDL	15	ΔN6	0.5	1885.207	0.122782	4.164452	0.203127
40	55	LLKNGERIEKVEHSDL	15	ΔN6	1	1885.304	0.044111	4.26167	0.167723
40	55	LLKNGERIEKVEHSDL	15	ΔN6	2	1885.576	0.235433	4.533469	0.285682
40	55	LLKNGERIEKVEHSDL	15	ΔN6	30	1885.953	0.118055	4.911043	0.200305
40	55	LLKNGERIEKVEHSDL	15	ΔN6	120	1886.326	0.100349	5.283235	0.190408
40	56	LLKNGERIEKVEHSDLS	16	ΔN6	0	1968.121	0.041546	0	0
40	56	LLKNGERIEKVEHSDLS	16	ΔN6	0.5	1973.04	0.13443	4.918831	0.140704
40	56	LLKNGERIEKVEHSDLS	16	ΔN6	1	1973.04	0.1013	4.919315	0.109488
40	56	LLKNGERIEKVEHSDLS	16	ΔN6	2	1973.236	0.090027	5.114837	0.099151
40	56	LLKNGERIEKVEHSDLS	16	ΔN6	30	1973.575	0.07571	5.454575	0.086361
40	56	LLKNGERIEKVEHSDLS	16	ΔN6	120	1973.962	0.084953	5.841557	0.094568
40	57	LLKNGERIEKVEHSDLSF	17	ΔN6	0	2115.138	0.061011	0	0
40	57	LLKNGERIEKVEHSDLSF	17	ΔN6	0.5	2120.931	0.095615	5.793206	0.113422
40	57	LLKNGERIEKVEHSDLSF	17	ΔN6	1	2120.994	0.096624	5.856394	0.114274
40	57	LLKNGERIEKVEHSDLSF	17	ΔN6	2	2121.149	0.075141	6.011397	0.096791
40	57	LLKNGERIEKVEHSDLSF	17	ΔN6	30	2121.263	0.027103	6.125103	0.06676
40	57	LLKNGERIEKVEHSDLSF	17	ΔN6	120	2121.617	0.083632	6.479149	0.103521
41	55	LKNGERIEKVEHSDL	14	ΔN6	0	1767.961	0.06078	0	0
41	55	LKNGERIEKVEHSDL	14	ΔN6	0.5	1771.973	0.087124	4.012766	0.10623
41	55	LKNGERIEKVEHSDL	14	ΔN6	1	1772.065	0.069286	4.104435	0.092167
41	55	LKNGERIEKVEHSDL	14	ΔN6	2	1772.169	0.071673	4.208147	0.093975
41	55	LKNGERIEKVEHSDL	14	ΔN6	30	1772.454	0.105741	4.492958	0.121965
41	55	LKNGERIEKVEHSDL	14	ΔN6	120	1772.711	0.041097	4.749984	0.07337
41	56	LKNGERIEKVEHSDLS	15	ΔN6	0	1855.001	0.052737	0	0
41	56	LKNGERIEKVEHSDLS	15	ΔN6	0.5	1859.643	0.140975	4.641197	0.150516
41	56	LKNGERIEKVEHSDLS	15	ΔN6	1	1859.796	0.061655	4.794553	0.081132
41	56	LKNGERIEKVEHSDLS	15	ΔN6	2	1859.815	0.061743	4.813912	0.081199
41	56	LKNGERIEKVEHSDLS	15	ΔN6	30	1860.143	0.072389	5.141865	0.089562
41	56	LKNGERIEKVEHSDLS	15	ΔN6	120	1860.417	0.087071	5.415649	0.101797
41	57	LKNGERIEKVEHSDLSF	16	ΔN6	0	2002.221	0.118496	0	0
41	57	LKNGERIEKVEHSDLSF	16	ΔN6	0.5	2007.423	0.093867	5.202024	0.15117
41	57	LKNGERIEKVEHSDLSF	16	ΔN6	1	2007.601	0.136472	5.379632	0.180738
41	57	LKNGERIEKVEHSDLSF	16	ΔN6	2	2007.616	0.100131	5.394805	0.155137

41	57	LKNGERIEKVEHSDLSF	16	ΔN6	30	2007.891	0.144454	5.669797	0.186837
41	57	LKNGERIEKVEHSDLSF	16	ΔN6	120	2008.211	0.129402	5.989759	0.17546
56	63	SFSKDWSF	7	ΔN6	0	1004.145	0.040328	0	0
56	63	SFSKDWSF	7	ΔN6	0.5	1006.977	0.054058	2.831453	0.067444
56	63	SFSKDWSF	7	ΔN6	1	1006.94	0.051208	2.795049	0.065182
56	63	SFSKDWSF	7	ΔN6	2	1006.973	0.075171	2.828144	0.085306
56	63	SFSKDWSF	7	ΔN6	30	1006.806	0.058217	2.660634	0.070821
56	63	SFSKDWSF	7	ΔN6	120	1006.917	0.067924	2.771412	0.078994
57	61	FSKDW	4	ΔN6	0	682.7149	0.004597	0	0
57	61	FSKDW	4	ΔN6	0.5	684.511	0.041409	1.796157	0.041663
57	61	FSKDW	4	ΔN6	1	684.5186	0.025934	1.80376	0.026339
57	61	FSKDW	4	ΔN6	2	684.5564	0.025077	1.841538	0.025495
57	61	FSKDW	4	ΔN6	30	684.4484	0.021662	1.733552	0.022145
57	61	FSKDW	4	ΔN6	120	684.5282	0.023931	1.81332	0.024369
57	63	FSKDWSF	6	ΔN6	0	917.06	0.051501	0	0
57	63	FSKDWSF	6	ΔN6	0.5	919.3813	0.044549	2.321359	0.068095
57	63	FSKDWSF	6	ΔN6	1	919.3732	0.029473	2.313251	0.059338
57	63	FSKDWSF	6	ΔN6	2	919.3798	0.034736	2.319861	0.06212
57	63	FSKDWSF	6	ΔN6	30	919.2255	0.027314	2.165511	0.058296
57	63	FSKDWSF	6	ΔN6	120	919.3143	0.016631	2.254379	0.054119
58	62	SKDWS	4	ΔN6	0	622.5054	0.0138	0	0
58	62	SKDWS	4	ΔN6	0.5	623.8879	0.019832	1.38247	0.024161
58	62	SKDWS	4	ΔN6	1	623.867	0.022414	1.361531	0.026322
58	62	SKDWS	4	ΔN6	2	623.8597	0.023874	1.354306	0.027576
58	62	SKDWS	4	ΔN6	30	623.7683	0.039157	1.262871	0.041517
58	62	SKDWS	4	ΔN6	120	623.8018	0.032126	1.296329	0.034964
58	63	SKDWSF	5	ΔN6	0	769.8086	0.01995	0	0
58	63	SKDWSF	5	ΔN6	0.5	771.9618	0.119249	2.153236	0.120906
58	63	SKDWSF	5	ΔN6	1	771.9575	0.120859	2.148932	0.122495
58	63	SKDWSF	5	ΔN6	2	771.8986	0.15124	2.090048	0.15255
58	63	SKDWSF	5	ΔN6	30	771.6846	0.011063	1.876034	0.022812
58	63	SKDWSF	5	ΔN6	120	771.7189	0.009604	1.910388	0.022141
59	63	KDWSF	4	ΔN6	0	682.7736	0.042265	0	0
59	63	KDWSF	4	ΔN6	0.5	684.3386	0.008836	1.564963	0.043178
59	63	KDWSF	4	ΔN6	1	684.3053	0.023513	1.531719	0.048365
59	63	KDWSF	4	ΔN6	2	684.3138	0.010615	1.540193	0.043577
59	63	KDWSF	4	ΔN6	30	684.2117	0.018175	1.438044	0.046007
59	63	KDWSF	4	ΔN6	120	684.2581	0.017624	1.484498	0.045792
60	63	DWSF	3	ΔN6	0	554.5122	0.007954	0	0
60	63	DWSF	3	ΔN6	0.5	555.9015	0.022384	1.389337	0.023755
60	63	DWSF	3	ΔN6	1	555.8708	0.023179	1.358663	0.024505
60	63	DWSF	3	ΔN6	2	555.8867	0.024228	1.374465	0.0255
60	63	DWSF	3	ΔN6	30	555.7531	0.004202	1.240912	0.008996
60	63	DWSF	3	ΔN6	120	555.8124	0.041775	1.300204	0.042526
63	67	FYLLY	4	ΔN6	0	718.7455	0.016955	0	0
63	67	FYLLY	4	ΔN6	0.5	718.787	0.017806	0.041526	0.024587
63	67	FYLLY	4	ΔN6	1	718.8076	0.011743	0.062055	0.020624
63	67	FYLLY	4	ΔN6	2	718.8255	0.035517	0.079979	0.039356
63	67	FYLLY	4	ΔN6	30	718.9799	0.037351	0.234444	0.041019
63	67	FYLLY	4	ΔN6	120	719.3594	0.019683	0.613899	0.025978
64	67	YLLY	3	ΔN6	0	571.5967	0.016427	0	0
64	67	YLLY	3	ΔN6	0.5	571.6622	0.011286	0.065513	0.01993
64	67	YLLY	3	ΔN6	1	571.6436	0.008514	0.04694	0.018502
64	67	YLLY	3	ΔN6	2	571.6494	0.006526	0.052766	0.017676
64	67	YLLY	3	ΔN6	30	571.6745	0.022676	0.0778	0.028001
64	67	YLLY	3	ΔN6	120	571.7076	0.021448	0.110904	0.027016
64	68	YLLYY	4	ΔN6	0	734.7599	0.018045	0	0
64	68	YLLYY	4	ΔN6	0.5	734.7809	0.02354	0.020967	0.029661
64	68	YLLYY	4	ΔN6	1	734.7814	0.02304	0.021449	0.029266
64	68	YLLYY	4	ΔN6	2	734.7913	0.006247	0.031363	0.019096
64	68	YLLYY	4	ΔN6	30	734.8819	0.035136	0.121995	0.039499
64	68	YLLYY	4	ΔN6	120	735.1289	0.033438	0.368951	0.037997
65	68	LLYY	3	ΔN6	0	571.717	0.016407	0	0
65	68	LLYY	3	ΔN6	0.5	571.7889	0.019613	0.071858	0.025571
65	68	LLYY	3	ΔN6	1	571.7944	0.02106	0.077376	0.026697
65	68	LLYY	3	ΔN6	2	571.7845	0.02952	0.067512	0.033773
65	68	LLYY	3	ΔN6	30	571.8397	0.022066	0.12268	0.027497
65	68	LLYY	3	ΔN6	120	571.9526	0.013694	0.235568	0.02137
66	71	LYYTEF	5	ΔN6	0	835.8105	0.025642	0	0
66	71	LYYTEF	5	ΔN6	0.5	836.2956	0.008616	0.485084	0.027051
66	71	LYYTEF	5	ΔN6	1	836.4342	0.037385	0.623623	0.045333
66	71	LYYTEF	5	ΔN6	2	836.516	0.020011	0.705425	0.032526
66	71	LYYTEF	5	ΔN6	30	836.5731	0.027405	0.762518	0.03753
66	71	LYYTEF	5	ΔN6	120	836.7264	0.02282	0.915828	0.034326
67	70	YYTE	3	ΔN6	0	575.5851	0.024345	0	0
67	70	YYTE	3	ΔN6	0.5	576.0136	0.008559	0.428432	0.025806
67	70	YYTE	3	ΔN6	1	576.1114	0.017037	0.526223	0.029715
67	70	YYTE	3	ΔN6	2	576.1742	0.020636	0.589065	0.031915
67	70	YYTE	3	ΔN6	30	576.2036	0.01719	0.618418	0.029803
67	70	YYTE	3	ΔN6	120	576.2814	0.014579	0.696243	0.028377
67	71	YYTEF	4	ΔN6	0	722.7584	0.018961	0	0
67	71	YYTEF	4	ΔN6	0.5	723.2214	0.025812	0.462979	0.032027
67	71	YYTEF	4	ΔN6	1	723.3115	0.028226	0.553114	0.034003

67	71	YYTEF	4	ΔN6	2	723.3721	0.016624	0.613663	0.025217
67	71	YYTEF	4	ΔN6	30	723.4249	0.015121	0.666525	0.024252
67	71	YYTEF	4	ΔN6	120	723.5133	0.017945	0.75485	0.026106
67	79	YYTEFTPTEKDEY	11	ΔN6	0	1686.65	0.044152	0	0
67	79	YYTEFTPTEKDEY	11	ΔN6	0.5	1689.286	0.05584	2.635969	0.071186
67	79	YYTEFTPTEKDEY	11	ΔN6	1	1689.626	0.058447	2.97572	0.07325
67	79	YYTEFTPTEKDEY	11	ΔN6	2	1689.956	0.068171	3.305485	0.08122
67	79	YYTEFTPTEKDEY	11	ΔN6	30	1690.496	0.075218	3.846173	0.087219
67	79	YYTEFTPTEKDEY	11	ΔN6	120	1690.872	0.026228	4.222168	0.051355
68	71	YTEF	3	ΔN6	0	559.5779	0.035117	0	0
68	71	YTEF	3	ΔN6	0.5	559.9831	0.026257	0.40524	0.043848
68	71	YTEF	3	ΔN6	1	560.1154	0.031236	0.537525	0.046999
68	71	YTEF	3	ΔN6	2	560.1844	0.033099	0.606511	0.048257
68	71	YTEF	3	ΔN6	30	560.185	0.029289	0.60717	0.045728
68	71	YTEF	3	ΔN6	120	560.2372	0.031687	0.659286	0.0473
68	78	YTEFTPTEKDE	9	ΔN6	0	1360.345	0.037326	0	0
68	78	YTEFTPTEKDE	9	ΔN6	0.5	1362.824	0.08063	2.478761	0.08885
68	78	YTEFTPTEKDE	9	ΔN6	1	1363.115	0.053888	2.770399	0.065553
68	78	YTEFTPTEKDE	9	ΔN6	2	1363.351	0.072288	3.005703	0.081356
68	78	YTEFTPTEKDE	9	ΔN6	30	1363.799	0.091174	3.453553	0.098519
68	78	YTEFTPTEKDE	9	ΔN6	120	1363.928	0.084319	3.583091	0.092212
68	80	YTEFTPTEKDEYA	11	ΔN6	0	1594.649	0.021002	0	0
68	80	YTEFTPTEKDEYA	11	ΔN6	0.5	1596.968	0.121651	2.318666	0.12345
68	80	YTEFTPTEKDEYA	11	ΔN6	1	1597.351	0.068164	2.702078	0.071326
68	80	YTEFTPTEKDEYA	11	ΔN6	2	1597.676	0.084889	3.027049	0.087448
68	80	YTEFTPTEKDEYA	11	ΔN6	30	1598.25	0.163031	3.601	0.164378
68	80	YTEFTPTEKDEYA	11	ΔN6	120	1598.491	0.075076	3.842102	0.077958
68	81	YTEFTPTEKDEYAC	12	ΔN6	0	1697.832	0.079241	0	0
68	81	YTEFTPTEKDEYAC	12	ΔN6	0.5	1700.347	0.071951	2.514766	0.107033
68	81	YTEFTPTEKDEYAC	12	ΔN6	1	1700.686	0.086959	2.853831	0.117648
68	81	YTEFTPTEKDEYAC	12	ΔN6	2	1701.077	0.110461	3.244538	0.135944
68	81	YTEFTPTEKDEYAC	12	ΔN6	30	1701.811	0.179361	3.978263	0.196086
68	81	YTEFTPTEKDEYAC	12	ΔN6	120	1701.947	0.034483	4.114371	0.086419
69	78	TEFTPTEKDE	8	ΔN6	0	1197.22	0.068069	0	0
69	78	TEFTPTEKDE	8	ΔN6	0.5	1199.44	0.044805	2.219443	0.081492
69	78	TEFTPTEKDE	8	ΔN6	1	1199.605	0.047295	2.384024	0.082887
69	78	TEFTPTEKDE	8	ΔN6	2	1199.858	0.042894	2.637304	0.080457
69	78	TEFTPTEKDE	8	ΔN6	30	1200.269	0.03069	3.04833	0.074668
69	78	TEFTPTEKDE	8	ΔN6	120	1200.402	0.040803	3.181874	0.079362
69	80	TEFTPTEKDEYA	10	ΔN6	0	1431.369	0.04311	0	0
69	80	TEFTPTEKDEYA	10	ΔN6	0.5	1433.644	0.0381	2.274996	0.057533
69	80	TEFTPTEKDEYA	10	ΔN6	1	1433.873	0.056143	2.504343	0.070784
69	80	TEFTPTEKDEYA	10	ΔN6	2	1434.174	0.079457	2.805079	0.090398
69	80	TEFTPTEKDEYA	10	ΔN6	30	1434.813	0.103746	3.443753	0.112346
69	80	TEFTPTEKDEYA	10	ΔN6	120	1435.003	0.046748	3.633929	0.063591
69	81	TEFTPTEKDEYAC	11	ΔN6	0	1534.458	0.018855	0	0
69	81	TEFTPTEKDEYAC	11	ΔN6	0.5	1536.799	0.021758	2.341039	0.028791
69	81	TEFTPTEKDEYAC	11	ΔN6	1	1537.088	0.079899	2.629423	0.082094
69	81	TEFTPTEKDEYAC	11	ΔN6	2	1537.411	0.046283	2.952472	0.049976
69	81	TEFTPTEKDEYAC	11	ΔN6	30	1538.154	0.11245	3.69519	0.114019
69	81	TEFTPTEKDEYAC	11	ΔN6	120	1538.331	0.123583	3.873121	0.125013
82	100	RVNHVTLSQPKIVKWDRDM	17	ΔN6	0	2323.531	0.053418	0	0
82	100	RVNHVTLSQPKIVKWDRDM	17	ΔN6	0.5	2328.85	0.118535	5.3189	0.130015
82	100	RVNHVTLSQPKIVKWDRDM	17	ΔN6	1	2329.158	0.153269	5.627	0.162311
82	100	RVNHVTLSQPKIVKWDRDM	17	ΔN6	2	2329.574	0.106082	6.042988	0.118772
82	100	RVNHVTLSQPKIVKWDRDM	17	ΔN6	30	2329.83	0.21345	6.299611	0.220033
82	100	RVNHVTLSQPKIVKWDRDM	17	ΔN6	120	2330.169	0.177698	6.63818	0.185553
91	100	PKIVKWDRDM	8	ΔN6	0	1288.419	0.021031	0	0
91	100	PKIVKWDRDM	8	ΔN6	0.5	1290.04	0.043555	1.620705	0.048367
91	100	PKIVKWDRDM	8	ΔN6	1	1290.198	0.06479	1.778596	0.068117
91	100	PKIVKWDRDM	8	ΔN6	2	1290.327	0.086882	1.907464	0.089391
91	100	PKIVKWDRDM	8	ΔN6	30	1290.393	0.018091	1.973686	0.027741
91	100	PKIVKWDRDM	8	ΔN6	120	1290.687	0.035386	2.267943	0.041163
94	100	VKWDRDM	6	ΔN6	0	950.0268	0.053029	0	0
94	100	VKWDRDM	6	ΔN6	0.5	951.4433	0.038685	1.416455	0.06564
94	100	VKWDRDM	6	ΔN6	1	951.5949	0.065723	1.568028	0.084448
94	100	VKWDRDM	6	ΔN6	2	951.6546	0.043516	1.627736	0.068598
94	100	VKWDRDM	6	ΔN6	30	951.8932	0.066203	1.866411	0.084823
94	100	VKWDRDM	6	ΔN6	120	952.0252	0.005004	1.998399	0.053265
95	100	KWDRDM	5	ΔN6	0	850.9581	0.050067	0	0
95	100	KWDRDM	5	ΔN6	0.5	852.2467	0.052306	1.28858	0.072406
95	100	KWDRDM	5	ΔN6	1	852.3529	0.083326	1.394813	0.09721
95	100	KWDRDM	5	ΔN6	2	852.4617	0.048027	1.503583	0.069378
95	100	KWDRDM	5	ΔN6	30	852.5842	0.02992	1.626101	0.058326
95	100	KWDRDM	5	ΔN6	120	852.6869	0.04392	1.728786	0.066601

Table 8.2 PAVED processed data for D76N β_2m.

Residue	D76N									
	Combined relative fractional uptake (%)					Combined standard deviation				
	0.5	1	2	30	120	0.5	1	2	30	120
1	30.76726	32.68793	33.83785	34.79216	37.56018	2.879176	3.129053	3.222989	3.353562	4.010618
2	32.3343	34.14837	35.73022	36.78984	39.81442	3.248417	3.310514	3.781857	3.956762	4.58556
3	32.3343	34.14837	35.73022	36.78984	39.81442	3.248417	3.310514	3.781857	3.956762	4.58556
4	34.79445	36.54699	38.3669	39.54163	42.58283	5.117576	5.058866	5.632276	5.882978	6.233241
5	34.79445	36.54699	38.3669	39.54163	42.58283	5.117576	5.058866	5.632276	5.882978	6.233241
6	35.48251	37.36592	39.25498	40.88116	44.54952	4.792393	4.819319	5.349534	5.912012	6.8363
7	35.48251	37.36592	39.25498	40.88116	44.54952	4.792393	4.819319	5.349534	5.912012	6.8363
8	35.48251	37.36592	39.25498	40.88116	44.54952	4.792393	4.819319	5.349534	5.912012	6.8363
9	35.48251	37.36592	39.25498	40.88116	44.54952	4.792393	4.819319	5.349534	5.912012	6.8363
10	28.03483	29.7189	30.77566	31.71458	33.69508	0.872	1.03	0.928805	1.448825	1.13107
11	25.46159	26.57769	27.26413	27.85329	29.41592	3.73229	4.413142	4.647929	4.632685	5.127771
12	25.46159	26.57769	27.26413	27.85329	29.41592	3.73229	4.413142	4.647929	4.632685	5.127771
13	25.46159	26.57769	27.26413	27.85329	29.41592	3.73229	4.413142	4.647929	4.632685	5.127771
14	25.46159	26.57769	27.26413	27.85329	29.41592	3.73229	4.413142	4.647929	4.632685	5.127771
15	25.46159	26.57769	27.26413	27.85329	29.41592	3.73229	4.413142	4.647929	4.632685	5.127771
16	25.46159	26.57769	27.26413	27.85329	29.41592	3.73229	4.413142	4.647929	4.632685	5.127771
17	25.46159	26.57769	27.26413	27.85329	29.41592	3.73229	4.413142	4.647929	4.632685	5.127771
18	25.46159	26.57769	27.26413	27.85329	29.41592	3.73229	4.413142	4.647929	4.632685	5.127771
19	25.46159	26.57769	27.26413	27.85329	29.41592	3.73229	4.413142	4.647929	4.632685	5.127771
20	25.46159	26.57769	27.26413	27.85329	29.41592	3.73229	4.413142	4.647929	4.632685	5.127771
21	25.46159	26.57769	27.26413	27.85329	29.41592	3.73229	4.413142	4.647929	4.632685	5.127771
22	25.46159	26.57769	27.26413	27.85329	29.41592	3.73229	4.413142	4.647929	4.632685	5.127771
23	20.32982	20.46133	20.82404	21.53355	22.30858	1.135171	0.969507	1.045021	0.971379	0.780336
24	20.32982	20.46133	20.82404	21.53355	22.30858	1.135171	0.969507	1.045021	0.971379	0.780336
25	20.32982	20.46133	20.82404	21.53355	22.30858	1.135171	0.969507	1.045021	0.971379	0.780336
26	NA	NA	NA	NA	NA	NA	NA	NA	NA	NA
27	10.98677	12.69999	13.89096	21.19897	24.01677	3.906197	3.614997	3.525742	2.637495	2.114723
28	10.98677	12.69999	13.89096	21.19897	24.01677	3.906197	3.614997	3.525742	2.637495	2.114723
29	11.7833	13.55331	14.80115	21.73106	24.73785	3.705115	3.524542	3.489404	2.532939	2.40049
30	11.7833	13.55331	14.80115	21.73106	24.73785	3.705115	3.524542	3.489404	2.532939	2.40049
31	11.7833	13.55331	14.80115	21.73106	24.73785	3.705115	3.524542	3.489404	2.532939	2.40049
32	11.7833	13.55331	14.80115	21.73106	24.73785	3.705115	3.524542	3.489404	2.532939	2.40049
33	11.7833	13.55331	14.80115	21.73106	24.73785	3.705115	3.524542	3.489404	2.532939	2.40049
34	11.7833	13.55331	14.80115	21.73106	24.73785	3.705115	3.524542	3.489404	2.532939	2.40049
35	8.335195	10.27764	11.63981	19.61662	22.69806	1.080316	1.132898	1.634531	1.539831	0.923773
36	13.01316	14.74829	16.36394	22.72699	25.3009	9.4576	9.536167	9.080963	7.110521	7.100681
37	13.89887	15.65711	17.39526	23.46323	25.85854	9.940184	10.01349	9.416527	7.422726	7.5228
38	19.03455	20.64169	22.02796	26.83451	29.28281	11.13412	11.1991	10.44605	8.217897	8.354223
39	22.89081	24.5264	25.50116	29.32461	31.84371	10.7018	10.62898	10.08867	8.196102	7.985709
40	26.67246	27.99311	28.68518	31.57186	33.86274	7.98514	8.085498	7.863651	6.377809	6.271573
41	29.48154	30.71099	31.35221	33.33081	35.51685	2.398672	2.292757	2.261731	2.207845	2.094788
42	29.48154	30.71099	31.35221	33.33081	35.51685	2.398672	2.292757	2.261731	2.207845	2.094788
43	29.48154	30.71099	31.35221	33.33081	35.51685	2.398672	2.292757	2.261731	2.207845	2.094788
44	29.48154	30.71099	31.35221	33.33081	35.51685	2.398672	2.292757	2.261731	2.207845	2.094788
45	29.48154	30.71099	31.35221	33.33081	35.51685	2.398672	2.292757	2.261731	2.207845	2.094788
46	29.48154	30.71099	31.35221	33.33081	35.51685	2.398672	2.292757	2.261731	2.207845	2.094788
47	29.48154	30.71099	31.35221	33.33081	35.51685	2.398672	2.292757	2.261731	2.207845	2.094788
48	29.48154	30.71099	31.35221	33.33081	35.51685	2.398672	2.292757	2.261731	2.207845	2.094788

49	29.48154	30.71099	31.35221	33.33081	35.51685	2.398672	2.292757	2.261731	2.207845	2.094788
50	29.48154	30.71099	31.35221	33.33081	35.51685	2.398672	2.292757	2.261731	2.207845	2.094788
51	29.48154	30.71099	31.35221	33.33081	35.51685	2.398672	2.292757	2.261731	2.207845	2.094788
52	29.48154	30.71099	31.35221	33.33081	35.51685	2.398672	2.292757	2.261731	2.207845	2.094788
53	29.48154	30.71099	31.35221	33.33081	35.51685	2.398672	2.292757	2.261731	2.207845	2.094788
54	29.48154	30.71099	31.35221	33.33081	35.51685	2.398672	2.292757	2.261731	2.207845	2.094788
55	30.37174	31.66162	32.30711	34.31046	36.34122	2.164647	1.912229	1.856618	1.541183	1.660565
56	31.27829	32.86231	34.0844	35.84696	37.61774	2.22233	2.076128	2.629048	2.427767	2.243344
57	28.85092	32.56298	35.57283	39.1765	39.96306	1.742661	1.305983	1.407483	1.124585	1.1808
58	27.2143	31.08544	34.09918	38.10619	38.60868	3.085914	2.874018	3.017	2.657765	3.057541
59	28.03958	31.95933	35.03573	39.04109	39.86523	3.399942	3.295771	3.495534	3.261129	3.986574
60	28.40463	32.39095	35.62138	39.6301	40.55049	3.299556	3.236842	3.562135	3.358994	4.059133
61	28.59483	32.48512	35.70097	39.68283	40.58914	3.516501	3.480656	3.833318	3.602058	4.375702
62	29.7833	33.66017	36.98374	40.818	42.00022	2.479512	2.4526	2.74888	2.750478	3.264082
63	1.5736	1.29185	1.27605	1.8819	3.734825	0.940725	0.831575	0.90095	0.826325	0.997325
64	1.604328	2.030525	1.811736	2.988028	4.988806	1.360853	1.389047	1.552262	2.191351	1.69857
65	1.698688	1.909652	1.79256	2.744463	4.429996	1.294811	1.279756	1.413903	1.991788	1.798274
66	3.62973	4.268294	4.166764	5.040498	6.533569	4.046528	4.871526	4.919775	4.933847	4.527197
67	14.05905	15.03538	16.23858	16.11262	16.23131	12.49426	12.36971	13.50268	12.71575	11.91278
68	25.52424	27.40051	28.82687	27.92195	28.57057	11.59341	10.89045	11.03534	10.65014	10.92394
69	29.42225	31.11798	31.95971	30.83322	31.80893	11.79163	11.08475	10.86123	10.48613	10.80828
70	30.55089	32.06509	32.84688	31.76065	32.80006	11.8524	11.24948	11.00179	10.57348	10.86524
71	38.34272	39.47898	39.82711	38.62963	39.78363	3.660608	3.345134	2.795264	2.237637	2.897134
72	38.34272	39.47898	39.82711	38.62963	39.78363	3.660608	3.345134	2.795264	2.237637	2.897134
73	38.34272	39.47898	39.82711	38.62963	39.78363	3.660608	3.345134	2.795264	2.237637	2.897134
74	38.34272	39.47898	39.82711	38.62963	39.78363	3.660608	3.345134	2.795264	2.237637	2.897134
75	38.34272	39.47898	39.82711	38.62963	39.78363	3.660608	3.345134	2.795264	2.237637	2.897134
76	38.34272	39.47898	39.82711	38.62963	39.78363	3.660608	3.345134	2.795264	2.237637	2.897134
77	38.34272	39.47898	39.82711	38.62963	39.78363	3.660608	3.345134	2.795264	2.237637	2.897134
78	36.23243	37.56019	38.50965	37.63966	38.26688	1.722451	1.680244	1.891717	1.711794	1.7422
79	35.70166	37.13741	37.91486	37.06612	37.73924	1.560735	1.48623	1.551307	1.428499	1.365106
80	34.66775	36.25839	36.82232	35.98938	36.71728	0.675804	0.736736	0.829387	0.770629	0.782961
81	NA	NA	NA	NA	NA	NA	NA	NA	NA	NA
82	23.92148	26.07502	27.19712	26.88135	29.29453	0.723453	0.527429	0.432606	1.173247	0.860394
83	23.92148	26.07502	27.19712	26.88135	29.29453	0.723453	0.527429	0.432606	1.173247	0.860394
84	23.92148	26.07502	27.19712	26.88135	29.29453	0.723453	0.527429	0.432606	1.173247	0.860394
85	23.92148	26.07502	27.19712	26.88135	29.29453	0.723453	0.527429	0.432606	1.173247	0.860394
86	23.92148	26.07502	27.19712	26.88135	29.29453	0.723453	0.527429	0.432606	1.173247	0.860394
87	23.92148	26.07502	27.19712	26.88135	29.29453	0.723453	0.527429	0.432606	1.173247	0.860394
88	23.92148	26.07502	27.19712	26.88135	29.29453	0.723453	0.527429	0.432606	1.173247	0.860394
89	23.92148	26.07502	27.19712	26.88135	29.29453	0.723453	0.527429	0.432606	1.173247	0.860394
90	23.92148	26.07502	27.19712	26.88135	29.29453	0.723453	0.527429	0.432606	1.173247	0.860394
91	23.59632	26.56398	27.94158	28.53291	30.15005	1.242371	1.235774	1.233391	3.006039	2.206068
92	23.59632	26.56398	27.94158	28.53291	30.15005	1.242371	1.235774	1.233391	3.006039	2.206068
93	23.59632	26.56398	27.94158	28.53291	30.15005	1.242371	1.235774	1.233391	3.006039	2.206068
94	22.35703	25.18923	26.19305	26.503	29.44902	2.143373	2.302312	2.734076	3.792014	2.037826
95	23.69985	26.38589	27.39254	28.06395	30.61703	3.071566	3.023085	3.191692	4.323385	2.715836
96	23.69985	26.38589	27.39254	28.06395	30.61703	3.071566	3.023085	3.191692	4.323385	2.715836
97	23.69985	26.38589	27.39254	28.06395	30.61703	3.071566	3.023085	3.191692	4.323385	2.715836
98	23.69985	26.38589	27.39254	28.06395	30.61703	3.071566	3.023085	3.191692	4.323385	2.715836
99	23.69985	26.38589	27.39254	28.06395	30.61703	3.071566	3.023085	3.191692	4.323385	2.715836

Table 8.3 Paved processed data for wild-type β2m.

Residue	Wild-type									
	Combined relative fractional uptake (%)					Combined standard deviation				
	0.5	1	2	30	120	0.5	1	2	30	120
1	29.04753	30.68331	31.99064	33.27513	35.40364	3.432847	3.468858	3.908552	3.660581	4.029622
2	31.15486	32.8662	34.4976	36.46818	38.30908	4.127063	4.220227	4.805171	5.475362	5.293564
3	31.15486	32.8662	34.4976	36.46818	38.30908	4.127063	4.220227	4.805171	5.475362	5.293564
4	33.67773	35.29622	37.13857	39.24847	40.89417	5.665942	5.582307	6.204381	6.772623	6.425241
5	33.67773	35.29622	37.13857	39.24847	40.89417	5.665942	5.582307	6.204381	6.772623	6.425241
6	34.44455	36.20726	38.23855	40.42038	42.74072	5.299214	5.317258	5.97401	6.499551	6.841938
7	34.44455	36.20726	38.23855	40.42038	42.74072	5.299214	5.317258	5.97401	6.499551	6.841938
8	34.44455	36.20726	38.23855	40.42038	42.74072	5.299214	5.317258	5.97401	6.499551	6.841938
9	34.44455	36.20726	38.23855	40.42038	42.74072	5.299214	5.317258	5.97401	6.499551	6.841938
10	25.83529	27.47766	28.26499	29.88295	31.60289	1.06003	1.21287	0.98912	1.315965	1.10047
11	23.19764	25.17408	24.7169	25.81411	27.32845	3.565489	3.549078	4.047397	4.425161	4.763569
12	23.19764	25.17408	24.7169	25.81411	27.32845	3.565489	3.549078	4.047397	4.425161	4.763569
13	23.19764	25.17408	24.7169	25.81411	27.32845	3.565489	3.549078	4.047397	4.425161	4.763569
14	23.19764	25.17408	24.7169	25.81411	27.32845	3.565489	3.549078	4.047397	4.425161	4.763569
15	23.19764	25.17408	24.7169	25.81411	27.32845	3.565489	3.549078	4.047397	4.425161	4.763569
16	23.19764	25.17408	24.7169	25.81411	27.32845	3.565489	3.549078	4.047397	4.425161	4.763569
17	23.19764	25.17408	24.7169	25.81411	27.32845	3.565489	3.549078	4.047397	4.425161	4.763569
18	23.19764	25.17408	24.7169	25.81411	27.32845	3.565489	3.549078	4.047397	4.425161	4.763569
19	23.19764	25.17408	24.7169	25.81411	27.32845	3.565489	3.549078	4.047397	4.425161	4.763569
20	23.19764	25.17408	24.7169	25.81411	27.32845	3.565489	3.549078	4.047397	4.425161	4.763569
21	23.19764	25.17408	24.7169	25.81411	27.32845	3.565489	3.549078	4.047397	4.425161	4.763569
22	23.19764	25.17408	24.7169	25.81411	27.32845	3.565489	3.549078	4.047397	4.425161	4.763569
23	18.30181	18.95376	19.15726	19.87237	20.15984	0.674421	0.838057	0.7069	0.965736	0.87825
24	18.30181	18.95376	19.15726	19.87237	20.15984	0.674421	0.838057	0.7069	0.965736	0.87825
25	18.30181	18.95376	19.15726	19.87237	20.15984	0.674421	0.838057	0.7069	0.965736	0.87825
26	NA	NA	NA	NA	NA	NA	NA	NA	NA	NA
27	9.935545	11.44098	13.28568	19.95878	22.58856	2.961796	3.145945	3.627734	2.497345	2.430764
28	9.935545	11.44098	13.28568	19.95878	22.58856	2.961796	3.145945	3.627734	2.497345	2.430764
29	11.08156	12.547	14.44248	20.57133	23.12705	3.266256	3.348472	3.7395	2.437217	2.336599
30	11.08156	12.547	14.44248	20.57133	23.12705	3.266256	3.348472	3.7395	2.437217	2.336599
31	11.08156	12.547	14.44248	20.57133	23.12705	3.266256	3.348472	3.7395	2.437217	2.336599
32	11.08156	12.547	14.44248	20.57133	23.12705	3.266256	3.348472	3.7395	2.437217	2.336599
33	11.08156	12.547	14.44248	20.57133	23.12705	3.266256	3.348472	3.7395	2.437217	2.336599
34	11.08156	12.547	14.44248	20.57133	23.12705	3.266256	3.348472	3.7395	2.437217	2.336599
35	7.940139	9.422847	11.08743	18.518	21.37907	1.005939	1.497425	1.972676	1.664636	2.03424
36	12.26052	13.7727	15.65471	21.36386	23.97491	9.592874	9.322289	8.640776	6.1512	6.16166
37	13.11778	14.72234	16.7332	22.08746	24.68521	10.10662	9.748019	8.882229	6.352571	6.37544
38	18.30948	19.71732	21.2182	24.84557	27.49761	11.47936	11.1423	10.06689	6.975545	7.113573
39	22.40781	23.57957	24.45466	26.80142	29.65568	10.56672	10.27279	9.947914	7.376331	7.008377
40	26.64198	27.7232	28.33296	29.28526	31.47765	8.215107	7.812559	7.671941	6.256803	5.907006
41	29.48361	30.30661	30.78752	31.10297	32.94723	2.446	2.56948	2.659614	2.597978	2.502521
42	29.48361	30.30661	30.78752	31.10297	32.94723	2.446	2.56948	2.659614	2.597978	2.502521
43	29.48361	30.30661	30.78752	31.10297	32.94723	2.446	2.56948	2.659614	2.597978	2.502521
44	29.48361	30.30661	30.78752	31.10297	32.94723	2.446	2.56948	2.659614	2.597978	2.502521
45	29.48361	30.30661	30.78752	31.10297	32.94723	2.446	2.56948	2.659614	2.597978	2.502521
46	29.48361	30.30661	30.78752	31.10297	32.94723	2.446	2.56948	2.659614	2.597978	2.502521
47	29.48361	30.30661	30.78752	31.10297	32.94723	2.446	2.56948	2.659614	2.597978	2.502521
48	29.48361	30.30661	30.78752	31.10297	32.94723	2.446	2.56948	2.659614	2.597978	2.502521

49	29.48361	30.30661	30.78752	31.10297	32.94723	2.446	2.56948	2.659614	2.597978	2.502521
50	29.48361	30.30661	30.78752	31.10297	32.94723	2.446	2.56948	2.659614	2.597978	2.502521
51	29.48361	30.30661	30.78752	31.10297	32.94723	2.446	2.56948	2.659614	2.597978	2.502521
52	29.48361	30.30661	30.78752	31.10297	32.94723	2.446	2.56948	2.659614	2.597978	2.502521
53	29.48361	30.30661	30.78752	31.10297	32.94723	2.446	2.56948	2.659614	2.597978	2.502521
54	29.48361	30.30661	30.78752	31.10297	32.94723	2.446	2.56948	2.659614	2.597978	2.502521
55	30.29979	31.30002	31.90542	32.29417	34.09958	2.26057	2.204612	2.100783	1.876235	1.550401
56	30.69826	31.8991	32.94812	33.97649	35.00673	2.415168	2.068305	2.071775	2.39783	1.69422
57	27.39157	30.57464	33.34853	36.64646	36.97792	1.643933	1.208713	1.127414	1.06496	0.943649
58	26.03778	29.32153	32.41521	35.66005	36.12293	2.276212	2.187992	1.915227	2.245055	1.975759
59	27.25743	30.40836	33.40693	36.61248	37.02098	3.452302	3.180574	2.857056	3.004408	2.695451
60	27.7814	31.17023	34.20681	37.55298	37.97794	3.453059	3.513133	3.298437	3.627488	3.418315
61	28.14498	31.40385	34.42478	37.71424	38.10687	3.580952	3.723632	3.495597	3.871651	3.666626
62	29.21715	32.5533	35.47564	38.93943	39.23642	2.88652	2.916171	2.805109	2.968373	2.948054
63	1.52745	1.567925	1.252875	2.278775	4.155425	0.8209	0.76575	0.797425	0.65185	0.6128
64	1.468019	1.771283	1.371206	1.942064	4.277661	0.989693	0.918685	0.934211	1.029313	0.8206
65	1.329731	1.468221	1.192246	1.57329	3.594188	0.92801	1.03202	0.874895	1.108874	1.391622
66	2.989881	3.539745	3.538941	3.93108	4.851447	3.432893	4.255033	4.770128	4.824268	3.500029
67	10.53131	12.45816	13.5119	13.99167	14.89156	8.308508	9.63424	10.68423	11.2034	11.24521
68	18.08193	20.80416	22.80452	24.03657	24.82424	5.996327	6.109455	6.71196	8.227444	8.208621
69	19.90212	22.67675	24.74014	26.44784	27.25955	6.216411	6.468965	6.808228	8.217053	8.066016
70	20.30149	22.9695	25.05308	27.07055	27.9067	6.387902	6.725779	7.066399	8.363758	8.219997
71	24.10859	26.94094	29.27255	32.27455	32.74465	3.137593	3.580982	3.266313	2.760763	2.67572
72	24.10859	26.94094	29.27255	32.27455	32.74465	3.137593	3.580982	3.266313	2.760763	2.67572
73	24.10859	26.94094	29.27255	32.27455	32.74465	3.137593	3.580982	3.266313	2.760763	2.67572
74	24.10859	26.94094	29.27255	32.27455	32.74465	3.137593	3.580982	3.266313	2.760763	2.67572
75	24.10859	26.94094	29.27255	32.27455	32.74465	3.137593	3.580982	3.266313	2.760763	2.67572
76	24.10859	26.94094	29.27255	32.27455	32.74465	3.137593	3.580982	3.266313	2.760763	2.67572
77	24.10859	26.94094	29.27255	32.27455	32.74465	3.137593	3.580982	3.266313	2.760763	2.67572
78	22.38437	24.96802	27.61548	31.03611	31.50328	1.517789	1.878255	1.998373	1.922089	1.903374
79	21.86107	24.22848	26.85838	30.321	30.7677	1.239557	1.346343	1.47993	1.409099	1.380661
80	21.51133	23.81471	25.94777	29.61698	30.00105	1.264724	1.24287	1.300378	1.308621	1.173714
81	NA	NA	NA	NA	NA	NA	NA	NA	NA	NA
82	23.20236	24.7713	25.95588	26.79858	29.36944	0.683024	0.560912	0.656565	0.393424	0.732335
83	23.20236	24.7713	25.95588	26.79858	29.36944	0.683024	0.560912	0.656565	0.393424	0.732335
84	23.20236	24.7713	25.95588	26.79858	29.36944	0.683024	0.560912	0.656565	0.393424	0.732335
85	23.20236	24.7713	25.95588	26.79858	29.36944	0.683024	0.560912	0.656565	0.393424	0.732335
86	23.20236	24.7713	25.95588	26.79858	29.36944	0.683024	0.560912	0.656565	0.393424	0.732335
87	23.20236	24.7713	25.95588	26.79858	29.36944	0.683024	0.560912	0.656565	0.393424	0.732335
88	23.20236	24.7713	25.95588	26.79858	29.36944	0.683024	0.560912	0.656565	0.393424	0.732335
89	23.20236	24.7713	25.95588	26.79858	29.36944	0.683024	0.560912	0.656565	0.393424	0.732335
90	23.20236	24.7713	25.95588	26.79858	29.36944	0.683024	0.560912	0.656565	0.393424	0.732335
91	23.17622	24.64854	25.57604	26.41135	28.26236	0.813889	0.8415	0.919121	0.854319	1.50584
92	23.17622	24.64854	25.57604	26.41135	28.26236	0.813889	0.8415	0.919121	0.854319	1.50584
93	23.17622	24.64854	25.57604	26.41135	28.26236	0.813889	0.8415	0.919121	0.854319	1.50584
94	22.70234	23.94255	25.47821	25.96844	27.39238	1.145788	1.205368	0.979461	1.06038	1.870607
95	23.84984	25.4753	26.75249	27.35992	28.44307	2.326472	2.82055	2.314402	2.471774	2.415501
96	23.84984	25.4753	26.75249	27.35992	28.44307	2.326472	2.82055	2.314402	2.471774	2.415501
97	23.84984	25.4753	26.75249	27.35992	28.44307	2.326472	2.82055	2.314402	2.471774	2.415501
98	23.84984	25.4753	26.75249	27.35992	28.44307	2.326472	2.82055	2.314402	2.471774	2.415501
99	23.84984	25.4753	26.75249	27.35992	28.44307	2.326472	2.82055	2.314402	2.471774	2.415501

Table 8.4 Paved processed data for ΔN6 β2m.

Residue	ΔN6									
	Combined relative fractional uptake (%)					Combined standard deviation				
	0.5	1	2	30	120	0.5	1	2	30	120
1	NA	NA	NA	NA	NA	NA	NA	NA	NA	NA
2	NA	NA	NA	NA	NA	NA	NA	NA	NA	NA
3	NA	NA	NA	NA	NA	NA	NA	NA	NA	NA
4	NA	NA	NA	NA	NA	NA	NA	NA	NA	NA
5	NA	NA	NA	NA	NA	NA	NA	NA	NA	NA
6	NA	NA	NA	NA	NA	NA	NA	NA	NA	NA
7	NA	NA	NA	NA	NA	NA	NA	NA	NA	NA
8	NA	NA	NA	NA	NA	NA	NA	NA	NA	NA
9	NA	NA	NA	NA	NA	NA	NA	NA	NA	NA
10	NA	NA	NA	NA	NA	NA	NA	NA	NA	NA
11	23.08124	24.67991	24.78458	28.29666	29.8484	4.663502	4.621169	4.587535	4.786274	5.399766
12	23.08124	24.67991	24.78458	28.29666	29.8484	4.663502	4.621169	4.587535	4.786274	5.399766
13	23.08124	24.67991	24.78458	28.29666	29.8484	4.663502	4.621169	4.587535	4.786274	5.399766
14	23.08124	24.67991	24.78458	28.29666	29.8484	4.663502	4.621169	4.587535	4.786274	5.399766
15	23.08124	24.67991	24.78458	28.29666	29.8484	4.663502	4.621169	4.587535	4.786274	5.399766
16	23.08124	24.67991	24.78458	28.29666	29.8484	4.663502	4.621169	4.587535	4.786274	5.399766
17	23.08124	24.67991	24.78458	28.29666	29.8484	4.663502	4.621169	4.587535	4.786274	5.399766
18	23.08124	24.67991	24.78458	28.29666	29.8484	4.663502	4.621169	4.587535	4.786274	5.399766
19	23.08124	24.67991	24.78458	28.29666	29.8484	4.663502	4.621169	4.587535	4.786274	5.399766
20	23.08124	24.67991	24.78458	28.29666	29.8484	4.663502	4.621169	4.587535	4.786274	5.399766
21	23.08124	24.67991	24.78458	28.29666	29.8484	4.663502	4.621169	4.587535	4.786274	5.399766
22	23.08124	24.67991	24.78458	28.29666	29.8484	4.663502	4.621169	4.587535	4.786274	5.399766
23	17.95873	19.56891	20.25101	23.03995	24.51919	0.788293	0.549821	0.677757	1.203929	1.089364
24	17.95873	19.56891	20.25101	23.03995	24.51919	0.788293	0.549821	0.677757	1.203929	1.089364
25	17.95873	19.56891	20.25101	23.03995	24.51919	0.788293	0.549821	0.677757	1.203929	1.089364
26	NA	NA	NA	NA	NA	NA	NA	NA	NA	NA
27	19.47257	21.07566	21.68253	25.04508	27.49067	5.682848	5.333445	5.820789	3.45466	2.617218
28	19.47257	21.07566	21.68253	25.04508	27.49067	5.682848	5.333445	5.820789	3.45466	2.617218
29	22.43009	23.75101	24.36799	27.11703	28.87269	7.111965	6.556965	6.865541	4.486244	3.309263
30	22.43009	23.75101	24.36799	27.11703	28.87269	7.111965	6.556965	6.865541	4.486244	3.309263
31	22.43009	23.75101	24.36799	27.11703	28.87269	7.111965	6.556965	6.865541	4.486244	3.309263
32	22.43009	23.75101	24.36799	27.11703	28.87269	7.111965	6.556965	6.865541	4.486244	3.309263
33	22.43009	23.75101	24.36799	27.11703	28.87269	7.111965	6.556965	6.865541	4.486244	3.309263
34	22.43009	23.75101	24.36799	27.11703	28.87269	7.111965	6.556965	6.865541	4.486244	3.309263
35	15.51309	17.45466	17.62521	22.96982	25.89236	0.976736	1.60911	0.950282	1.711679	1.218915
36	16.47075	18.26457	19.69392	23.44676	26.14322	8.235128	7.695631	7.358809	6.951353	7.166828
37	16.60143	18.5735	20.06926	23.73623	26.28693	8.885977	8.266669	7.882799	7.4755	7.727563
38	20.50875	21.97002	23.60134	26.31041	29.0377	10.0806	9.372413	8.784167	8.086154	8.439125
39	23.77131	24.66362	25.93238	28.25499	31.19555	10.13258	9.482065	9.154093	8.55413	8.906932
40	27.74205	28.36805	29.61105	31.43904	34.21211	7.752652	7.259242	7.063117	6.794115	7.090681
41	30.43828	31.12032	31.96205	33.87885	36.43915	2.384808	2.30413	2.192405	1.87311	1.789351
42	30.43828	31.12032	31.96205	33.87885	36.43915	2.384808	2.30413	2.192405	1.87311	1.789351
43	30.43828	31.12032	31.96205	33.87885	36.43915	2.384808	2.30413	2.192405	1.87311	1.789351
44	30.43828	31.12032	31.96205	33.87885	36.43915	2.384808	2.30413	2.192405	1.87311	1.789351
45	30.43828	31.12032	31.96205	33.87885	36.43915	2.384808	2.30413	2.192405	1.87311	1.789351
46	30.43828	31.12032	31.96205	33.87885	36.43915	2.384808	2.30413	2.192405	1.87311	1.789351
47	30.43828	31.12032	31.96205	33.87885	36.43915	2.384808	2.30413	2.192405	1.87311	1.789351
48	30.43828	31.12032	31.96205	33.87885	36.43915	2.384808	2.30413	2.192405	1.87311	1.789351

49	30.43828	31.12032	31.96205	33.87885	36.43915	2.384808	2.30413	2.192405	1.87311	1.789351
50	30.43828	31.12032	31.96205	33.87885	36.43915	2.384808	2.30413	2.192405	1.87311	1.789351
51	30.43828	31.12032	31.96205	33.87885	36.43915	2.384808	2.30413	2.192405	1.87311	1.789351
52	30.43828	31.12032	31.96205	33.87885	36.43915	2.384808	2.30413	2.192405	1.87311	1.789351
53	30.43828	31.12032	31.96205	33.87885	36.43915	2.384808	2.30413	2.192405	1.87311	1.789351
54	30.43828	31.12032	31.96205	33.87885	36.43915	2.384808	2.30413	2.192405	1.87311	1.789351
55	31.26619	31.97114	32.72792	34.53208	37.07429	2.151729	2.044226	1.982977	1.626655	1.51714
56	33.94452	34.31195	35.09788	35.80695	38.03411	3.965058	3.553334	3.462061	2.013664	1.799852
57	41.34752	41.19248	41.70162	39.14657	40.83253	2.817921	2.947139	3.30077	3.187169	3.409643
58	40.33381	40.11887	40.15269	37.54538	38.88165	3.844257	4.027451	4.289778	3.757862	4.109958
59	40.13219	39.81456	39.87805	37.2705	38.57662	3.56549	3.771428	3.988749	3.503932	3.827788
60	41.01491	40.59659	40.72626	37.87245	39.27713	3.957445	3.994554	4.249376	3.547789	3.954613
61	40.36674	39.84702	39.84089	36.92997	38.23302	3.892289	3.822386	3.938517	2.943458	3.29517
62	41.52773	41.00877	41.03754	37.78728	39.16499	3.16535	3.057481	3.150784	2.132881	2.485181
63	1.03815	1.551375	1.999475	5.8611	15.34748	0.614675	0.5156	0.9839	1.025475	0.64945
64	1.248697	1.217422	1.514139	3.834769	9.422683	0.96827	0.791127	0.889112	1.747486	4.832652
65	1.53534	1.557867	1.698204	3.89841	9.030079	1.063618	1.007522	1.005668	1.585072	4.255016
66	3.168608	3.740785	4.180263	6.1688	10.57783	3.41084	4.476273	5.053336	4.768786	5.20997
67	10.40667	12.33475	13.69499	15.11014	19.34345	7.808869	8.98722	10.06079	10.33279	10.30818
68	17.82569	20.90079	23.30793	26.28205	28.68594	6.082761	6.232902	6.738303	8.690364	8.524522
69	19.45595	22.35783	24.96848	28.80873	31.11528	6.092494	6.035405	6.488383	8.514978	8.222354
70	19.984	22.85961	25.51267	29.64493	31.95647	6.149728	6.119594	6.563628	8.50005	8.206409
71	23.68515	26.55067	29.46427	35.05409	37.10456	2.870304	2.799015	2.740086	2.474581	2.308435
72	23.68515	26.55067	29.46427	35.05409	37.10456	2.870304	2.799015	2.740086	2.474581	2.308435
73	23.68515	26.55067	29.46427	35.05409	37.10456	2.870304	2.799015	2.740086	2.474581	2.308435
74	23.68515	26.55067	29.46427	35.05409	37.10456	2.870304	2.799015	2.740086	2.474581	2.308435
75	23.68515	26.55067	29.46427	35.05409	37.10456	2.870304	2.799015	2.740086	2.474581	2.308435
76	23.68515	26.55067	29.46427	35.05409	37.10456	2.870304	2.799015	2.740086	2.474581	2.308435
77	23.68515	26.55067	29.46427	35.05409	37.10456	2.870304	2.799015	2.740086	2.474581	2.308435
78	22.0363	24.92433	27.91542	33.72727	35.93577	1.415726	1.434863	1.442162	1.500272	1.641778
79	21.52917	24.33331	27.35373	33.47968	35.25588	1.089536	0.94908	0.984521	1.485746	1.1213
80	21.10118	23.83611	26.93924	33.37241	34.79963	0.706139	0.886119	0.868688	1.385915	1.076454
81	NA	NA	NA	NA	NA	NA	NA	NA	NA	NA
82	31.28765	33.1	35.54699	37.05654	39.04812	0.764794	0.954771	0.698659	1.294312	1.091488
83	31.28765	33.1	35.54699	37.05654	39.04812	0.764794	0.954771	0.698659	1.294312	1.091488
84	31.28765	33.1	35.54699	37.05654	39.04812	0.764794	0.954771	0.698659	1.294312	1.091488
85	31.28765	33.1	35.54699	37.05654	39.04812	0.764794	0.954771	0.698659	1.294312	1.091488
86	31.28765	33.1	35.54699	37.05654	39.04812	0.764794	0.954771	0.698659	1.294312	1.091488
87	31.28765	33.1	35.54699	37.05654	39.04812	0.764794	0.954771	0.698659	1.294312	1.091488
88	31.28765	33.1	35.54699	37.05654	39.04812	0.764794	0.954771	0.698659	1.294312	1.091488
89	31.28765	33.1	35.54699	37.05654	39.04812	0.764794	0.954771	0.698659	1.294312	1.091488
90	31.28765	33.1	35.54699	37.05654	39.04812	0.764794	0.954771	0.698659	1.294312	1.091488
91	25.77323	27.66623	29.69514	31.55189	33.6987	5.557339	5.508557	5.925573	6.233826	5.417037
92	25.77323	27.66623	29.69514	31.55189	33.6987	5.557339	5.508557	5.925573	6.233826	5.417037
93	25.77323	27.66623	29.69514	31.55189	33.6987	5.557339	5.508557	5.925573	6.233826	5.417037
94	25.05135	27.15542	28.83974	31.39294	33.56802	4.693668	4.627271	5.030648	5.073565	4.456424
95	25.23141	27.34063	29.14772	31.69007	33.81994	4.140582	4.136014	4.443698	4.424069	3.940654
96	25.23141	27.34063	29.14772	31.69007	33.81994	4.140582	4.136014	4.443698	4.424069	3.940654
97	25.23141	27.34063	29.14772	31.69007	33.81994	4.140582	4.136014	4.443698	4.424069	3.940654
98	25.23141	27.34063	29.14772	31.69007	33.81994	4.140582	4.136014	4.443698	4.424069	3.940654
99	25.23141	27.34063	29.14772	31.69007	33.81994	4.140582	4.136014	4.443698	4.424069	3.940654

Figure 8.1 R code for the original PAVED algorithm.

```
desired_p_value<- 0.05
Residue_number <- 100
pdb_file<- "4fxl"
## Hi Nick! i've annotated this code as best i can, the Packages you need are: datasets,
graphics, grDevices, methods, plyr, readr, stats and utils.
##All of the following are just lines to set up how the progress bars work - they're basically
just tick counters which count up every time a loop is passed
plot.progress <- function(...)       {
  vectOfBar <- c(...)*100
  numOfBar <- length(vectOfBar)
  plot(c(0,100), c(0,numOfBar), type='n', xlab='', ylab='', yaxt='n', mar=c(3,3,3,3))
  for(i in 1:numOfBar) {
    rect(0, 0.1+i-1, vectOfBar[i], 0.9+i-1, col=rainbow(numOfBar)[i])
    text(0.5, 0.5+i-1, paste('Status ', i, ': ', round(vectOfBar[i],2), '%', sep=''), adj=0)
  }
  title('Calculating Mean Relative Fractional Uptake per residue')
}
plot.progress2 <- function(...)      {
  vectOfBar <- c(...)*100
  numOfBar <- length(vectOfBar)
  plot(c(0,100), c(0,numOfBar), type='n', xlab='', ylab='', yaxt='n', mar=c(3,3,3,3))
  for(i in 1:numOfBar) {
    rect(0, 0.1+i-1, vectOfBar[i], 0.9+i-1, col=rainbow(numOfBar)[i])
    text(0.5, 0.5+i-1, paste('Status ', i, ': ', round(vectOfBar[i],2), '%', sep=''), adj=0)
  }
  title('Calculating N per residue')
}
plot.progress3 <- function(...)      {
  vectOfBar <- c(...)*100
  numOfBar <- length(vectOfBar)
  plot(c(0,100), c(0,numOfBar), type='n', xlab='', ylab='', yaxt='n', mar=c(3,3,3,3))
  for(i in 1:numOfBar) {
    rect(0, 0.1+i-1, vectOfBar[i], 0.9+i-1, col=rainbow(numOfBar)[i])
    text(0.5, 0.5+i-1, paste('Status ', i, ': ', round(vectOfBar[i],2), '%', sep=''), adj=0)
  }
  title('Calculating Standard Deviation per residue')
}
plot.progress4 <- function(...)      {
  vectOfBar <- c(...)*100
  numOfBar <- length(vectOfBar)
  plot(c(0,100), c(0,numOfBar), type='n', xlab='', ylab='', yaxt='n', mar=c(3,3,3,3))
  for(i in 1:numOfBar) {
    rect(0, 0.1+i-1, vectOfBar[i], 0.9+i-1, col=rainbow(numOfBar)[i])
    text(0.5, 0.5+i-1, paste('Status ', i, ': ', round(vectOfBar[i],2), '%', sep=''), adj=0)
```

```
  }
  title('Calculating N per peptide')
}
plot.progress5 <- function(...)      {
  vectOfBar <- c(...)*100
  numOfBar <- length(vectOfBar)
  plot(c(0,100), c(0,numOfBar), type='n', xlab='', ylab='', yaxt='n', mar=c(3,3,3,3))
  for(i in 1:numOfBar) {
    rect(0, 0.1+i-1, vectOfBar[i], 0.9+i-1, col=rainbow(numOfBar)[i])
    text(0.5, 0.5+i-1, paste('Status ', i, ': ', round(vectOfBar[i],2), '%', sep=''), adj=0)
  }
  title('Assigning N values to main data frame')
}
#Read in the data from Dynamx - requires state data.csv and cluster data.csv
# After reading in data - bottom two lines of code re-arrange that data accoridng to State (eg:
Wild-type, D76N etc..)
library(readr)
main_data_frame <- read.csv("state data.csv", header=TRUE)
main_data_frame2<- read.csv("cluster data.csv", header=TRUE)
main_data_frame <- arrange(main_data_frame, State)
main_data_frame2 <- arrange(main_data_frame2, State)
#The block of code below creates lots of vectors that are needed later - a list of unique
peptides and uniqe timepoints, caluclating the
#relative fractional uptake from the imported data etc... nothing complicated here.
Sequence <- c(1:Residue_number)
Unique_peptides <- (as.character(unique(paste(main_data_frame[,2],main_data_frame[,3],sep =
','))))
Unique_timepoints <-unique(main_data_frame[,10])
Number_of_timepoints <- length(unique(main_data_frame[,10]))
Number_of_states <- length(unique(main_data_frame[,9]))
Unique_states <- (as.character(unique(main_data_frame[,9])))
Relative_fractional_uptake <- (main_data_frame$Uptake/main_data_frame$MaxUptake)*100
RFU_SD<-(main_data_frame$Uptake.SD/main_data_frame$MaxUptake)*100
All_Peptides<-(paste(main_data_frame[,2],main_data_frame[,3],sep = ','))
All_Peptides_MDF2 <- (paste(main_data_frame2[,2],main_data_frame2[,3],sep = ','))
main_data_frame2$Unique_start_and_end <-All_Peptides_MDF2
#The Nested loop below calculated the number of rows in cluster data that every unique peptide
appears, separately, for every time point and every state.
## this is essentially N for each peptide per TP per state (including charge states) because
the cluster data is almost the raw data
## when the base loop (for v in 1:..) finishes it bins the data to a vector (n_for_peptides).
This is a single column with each row corresponding to n at that timepoint at that state for
each peptides (nrow = n unqiue peptides)
## outside the base loop ive then column bound this vector to a new empty vector
(n_for_peptides_timepoints). The second loop up then changes the timepoint and the base loop
```

```
runs again. This occurs until all the tps for the first state have been run, then that whole
vector gets binned out to
## another vector (n_for_peptides_timepoints_and_states) the top loop switches to the next
state and the base loop runs again. This happens until all the tps for all the states are
finished.
## i have made all my nested loops this way - i didn't know how else to do it - but i suspect
this is why everything goes so slowly... any adivce?
n_for_peptides_timepoints_and_states<-c()
n_for_peptides_timepoints<-c()
n_for_peptdies<-c()
for (x in 1:(length(Unique_states))) {
for (w in 1:(length(Unique_timepoints))) {
for (v in 1:(length(Unique_peptides))) {n_for_peptdies[v] <- sum(All_Peptides_MDF2 ==
Unique_peptides[v] & main_data_frame2$Exposure == Unique_timepoints[w] & main_data_frame2$State
== Unique_states[x])}
n_for_peptides_timepoints<-cbind(n_for_peptides_timepoints, n_for_peptdies)}
n_for_peptides_timepoints_and_states<-cbind(n_for_peptides_timepoints_and_states,
n_for_peptides_timepoints)
n_for_peptides_timepoints<-c()}
## the next block finds the number of unique charge states for each peptide at each tp at each
state and uses it to find the actual value of n (closest integer) for each peptide
charge_states<- ddply(main_data_frame2,c("State", "Unique_start_and_end",
"Exposure"),summarise,charge_states_per_peptide=length(unique(z)))
n_for_peptides_timepoints_and_states_without_charge_states <- c()
n_for_peptides_timepoints_and_states_without_charge_states2 <- c()
n_for_peptides_timepoints_and_states_without_charge_states3 <- c()
for(K in 1:(length(Unique_states))){
for(J in 1:(length(Unique_timepoints))){
for(I in 1:(length(Unique_peptides))){
for(H in 1: (nrow(charge_states))){
if (charge_states[H,1] == Unique_states[K] & charge_states[H,2] == Unique_peptides[I] &
charge_states[H,3] == Unique_timepoints[J])
n_for_peptides_timepoints_and_states_without_charge_states[I] =
(n_for_peptides_timepoints_and_states[I,(J+((K-
1)*(length(Unique_timepoints))))]/charge_states[H,4])}
  plot.progress4((I/(length(Unique_peptides))), ((J-1)/(length(Unique_timepoints))), ((K-
1)/length(Unique_states)))}
  for(L in
((nrow(as.matrix(n_for_peptides_timepoints_and_states_without_charge_states))+1):((length(Uniqu
e_peptides))+1))){
    n_for_peptides_timepoints_and_states_without_charge_states[L] = NA}

  n_for_peptides_timepoints_and_states_without_charge_states2<-
cbind(n_for_peptides_timepoints_and_states_without_charge_states2,
n_for_peptides_timepoints_and_states_without_charge_states)
  n_for_peptides_timepoints_and_states_without_charge_states<-c()}
```

```
  n_for_peptides_timepoints_and_states_without_charge_states3<-
cbind(n_for_peptides_timepoints_and_states_without_charge_states3,
n_for_peptides_timepoints_and_states_without_charge_states2)
  n_for_peptides_timepoints_and_states_without_charge_states2<-c()}
n_for_peptides_timepoints_and_states_without_charge_states3<-
head(n_for_peptides_timepoints_and_states_without_charge_states3,-1)
n_for_peptides_timepoints_and_states_without_charge_states3<-
round(n_for_peptides_timepoints_and_states_without_charge_states3,digits=0)
main_matrix_frame <-(main_data_frame[,2])
main_matrix_frame <-cbind(main_matrix_frame, main_data_frame[,3])
main_matrix_frame <-cbind(main_matrix_frame, main_data_frame[,10])
main_matrix_frame<- as.matrix(main_matrix_frame)
main_data_frame_subset_peptides<-main_data_frame[,4]
main_data_frame_subset_states <-main_data_frame[,9]
#to save the script running through every single row of each data frame when processing each
state, i wrote the next block of code to calcuate how many rows there were in the dataframe for
each state and created start and end points for the script to start and finish dat, based on
which state it was processing at the time.
##this alonse makes the script run 3X faster
main_data_frame_subset_nrow_states <-c()
main_data_frame_subset_nrow_states2 <-c()
for(M in 1:(length(Unique_states))){
main_data_frame_subset_nrow_states<- nrow(subset(main_data_frame,State == (Unique_states[M])))
main_data_frame_subset_nrow_states2<- rbind(main_data_frame_subset_nrow_states2,
main_data_frame_subset_nrow_states)}
startpositions<-c()
for (N in 1: (length(Unique_states))){startpositions[N]<- nrow(main_data_frame) -
(sum(main_data_frame_subset_nrow_states2[N:(length(main_data_frame_subset_nrow_states2))]))+1}
endpositions<-c()
for (P in 1:(length(Unique_states))){endpositions[P]<- nrow(main_data_frame) -
((sum(main_data_frame_subset_nrow_states2[P:(length(main_data_frame_subset_nrow_states2))])))+m
ain_data_frame_subset_nrow_states2[P]}
#This nested loop works as before - but now it calculated n for each residue based on each tp,
state and the whole peptide list


n.total5<-c()
n.total4<-c()
n.total3<-c()
n.total2<-c()
n.total<-c()
for (C in 1:(length(Unique_states))){
for (B in 1:(length(Unique_timepoints))){
for (A in 1:Residue_number){
for (z in 1:(length(Unique_peptides))) {
for (y in (startpositions[C]):(endpositions[C])){
```

```
if (Sequence[A] >= (main_matrix_frame[y,1]+1) & Sequence[A] <= main_matrix_frame[y,2] &
main_matrix_frame[y,3] == Unique_timepoints[B] & main_data_frame_subset_states[y] ==
Unique_states[C] & All_Peptides[y] == Unique_peptides[z]) n.total[z] =
n_for_peptides_timepoints_and_states_without_charge_states3[z,(B+(C-
1)*(length(Unique_timepoints)))]}}
n.total2<-sum(n.total, na.rm=TRUE)
n.total3<-rbind(n.total3,n.total2)
n.total<-c()
n.total2<-c()
plot.progress2((A/Residue_number), ((B-1)/(length(Unique_timepoints))), ((C-
1)/length(Unique_states)))
Sys.sleep(0.05)}
n.total4<-cbind(n.total4, n.total3)
n.total3<-c()}
n.total5<-cbind(n.total5, n.total4)
n.total4<-c()}
#add n for each residue to main dataframe (makes later scripting easier)
n_main_data_frame<-c()
for (G in 1:(length(Unique_states))){
for (F in 1:(length(Unique_peptides))){
for (E in 1:(length(Unique_timepoints))) {
for (D in (startpositions[G]):(endpositions[G])) {
if(All_Peptides[D] == Unique_peptides[F] & main_matrix_frame[D,3] == Unique_timepoints[E] &
main_data_frame[D,9] == Unique_states[G]) n_main_data_frame[D] =
n_for_peptides_timepoints_and_states_without_charge_states3[F,(E+((G-
1)*(length(Unique_timepoints))))]}
  plot.progress5((E/(length(Unique_timepoints))), ((F-1)/(length(Unique_peptides))), ((G-
1)/length(Unique_states)))
  Sys.sleep(0.05)  }}}
main_data_frame$n<-n_main_data_frame
#calculate mean RFU for each residue
uptake.total<-c()
data.out<-c()
Timepoints.out <- c()
alldata.out<-c()
for (q in 1:Number_of_states){
  for (p in 1:Number_of_timepoints){
    for (m in 1:Residue_number){
      for (n in (startpositions[q]):(endpositions[q])){ if (Sequence[m] >=
(main_matrix_frame[n,1]+1) & Sequence[m] <= main_matrix_frame[n,2] & main_matrix_frame[n,3] ==
Unique_timepoints[p] & main_data_frame[n,9] == Unique_states[q]) uptake.total[n] =
(Relative_fractional_uptake[n]*main_data_frame[n,17])}
      subset<- sum(uptake.total, na.rm=TRUE)/(n.total5[m,(p+((q-
1)*(length(Unique_timepoints))))])
      data.out<-rbind(data.out,subset)
      uptake.total<-c()
```

```
      plot.progress((m/Residue_number), ((p-1)/Number_of_timepoints), ((q-1)/Number_of_states))
      Sys.sleep(0.05)}
    Timepoints.out<-cbind(Timepoints.out,data.out)
    data.out<-c()}
  alldata.out<-cbind(alldata.out,Timepoints.out)
  Timepoints.out<-c()}
#Calculate SD for every residue
stdev.total<-c()
data.out2<-c()
Timepoints.out2 <- c()
alldata.out2<-c()
for (u in 1:Number_of_states){
  for (t in 1:Number_of_timepoints){
    for (s in 1:Residue_number){
      for (r in (startpositions[u]):(endpositions[u])){ if (Sequence[s] >=
(main_matrix_frame[r,1]+1) & Sequence[s] <= main_matrix_frame[r,2] & main_matrix_frame[r,3] ==
Unique_timepoints[t] & main_data_frame[r,9] == Unique_states[u]) stdev.total[r] =
main_data_frame[r,17]*((RFU_SD[r]^2)+((Relative_fractional_uptake[r]-alldata.out[s,(t+(u-
1)*(length(Unique_timepoints)))])^2))}
      subset2<- sqrt(sum(stdev.total, na.rm=TRUE)/(n.total5[s,(t+((u-
1)*(length(Unique_timepoints))))]))
      data.out2<-rbind(data.out2,subset2)
      stdev.total<-c()
      plot.progress3((s/Residue_number), ((t-1)/Number_of_timepoints), ((u-
1)/Number_of_states))
      Sys.sleep(0.05)}
    Timepoints.out2<-cbind(Timepoints.out2,data.out2)
    data.out2<-c()}
  alldata.out2<-cbind(alldata.out2,Timepoints.out2)
  Timepoints.out2<-c()}
#p values iterate by: 1 vs 2, 1 vs 3, 1vs 4 etc... then 2vs3, 2vs4 etc...
all_p_values4<-c()
all_p_values3<-c()
all_p_values2 <-c()
all_p_values<-c()
for (T in 0:(((length(Unique_states)))-2)){
  for (S in (T+1):(((length(Unique_states)))-1)){
    for (R in 1:(length(Unique_timepoints))){
      for (Q in 1:Residue_number){
        all_p_values[Q] <-
(tsum.test(alldata.out[Q,(R+((length(Unique_timepoints))*T))],alldata.out2[Q,(R+((length(Unique
_timepoints))*T))],
n.total5[Q,(R+((length(Unique_timepoints))*T))],alldata.out[Q,(R+((length(Unique_timepoints))*S
))],alldata.out2[Q,(R+((length(Unique_timepoints))*S))],
n.total5[Q,((R+(length(Unique_timepoints))*S))],alternative="two.sided", mu=0,
var.equal=FALSE,conf.level = (1-(desired_p_value))))$p.value}
```

```
      all_p_values2<-cbind(all_p_values2,all_p_values)
      all_p_values<-c()}
    all_p_values3<-cbind(all_p_values3,all_p_values2)
    all_p_values2<-c()}
  all_p_values4<-cbind(all_p_values4, all_p_values3)
  all_p_values3<-c()
}
#Difference plot calculations
difference_plot3<-c()
difference_plot2<-c()
difference_plot<-c()
for(V in 1:((length(Unique_states))-1)){
for(U in 1:(length(Unique_timepoints))){
difference_plot<- alldata.out[,(U+(V*(length(Unique_timepoints))))]-alldata.out[,U]
difference_plot2<-cbind(difference_plot2,difference_plot)
difference_plot<-c()}
  difference_plot3<-cbind(difference_plot3,difference_plot2)
  difference_plot2<-c()}
write.csv(alldata.out, "RFU.csv")
write.csv(alldata.out2, "SD.csv")
write.csv(all_p_values4, "p values.csv")
write.csv(difference_plot3, "differenceplot.csv")
```

8.2 Related information for Chapter 5

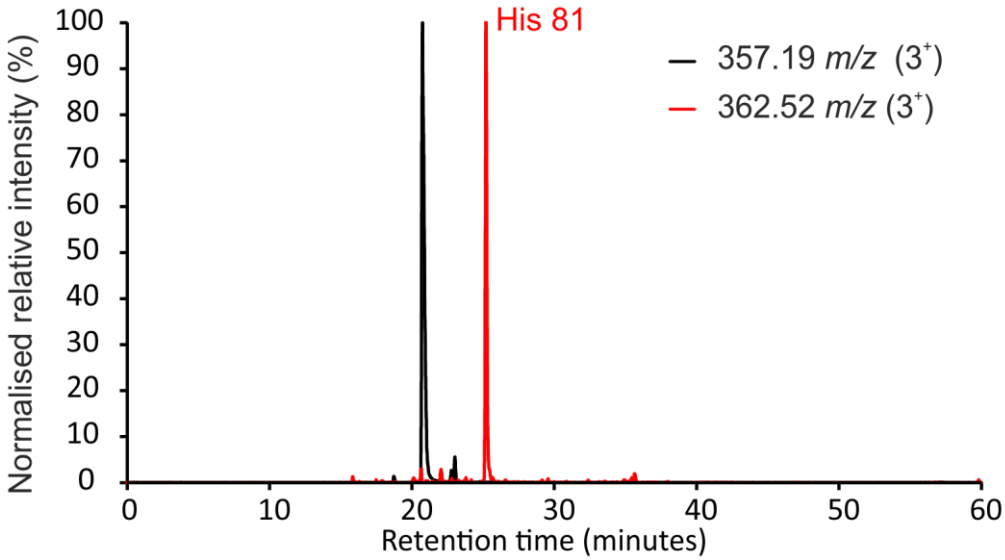

Figure 8.2 XIC of peptide 79-87. Sequence: ACRVNHVTL. Unmodified = black. Modified (+16 Da) = red. Modified residues are annotated above each peak in the XIC.

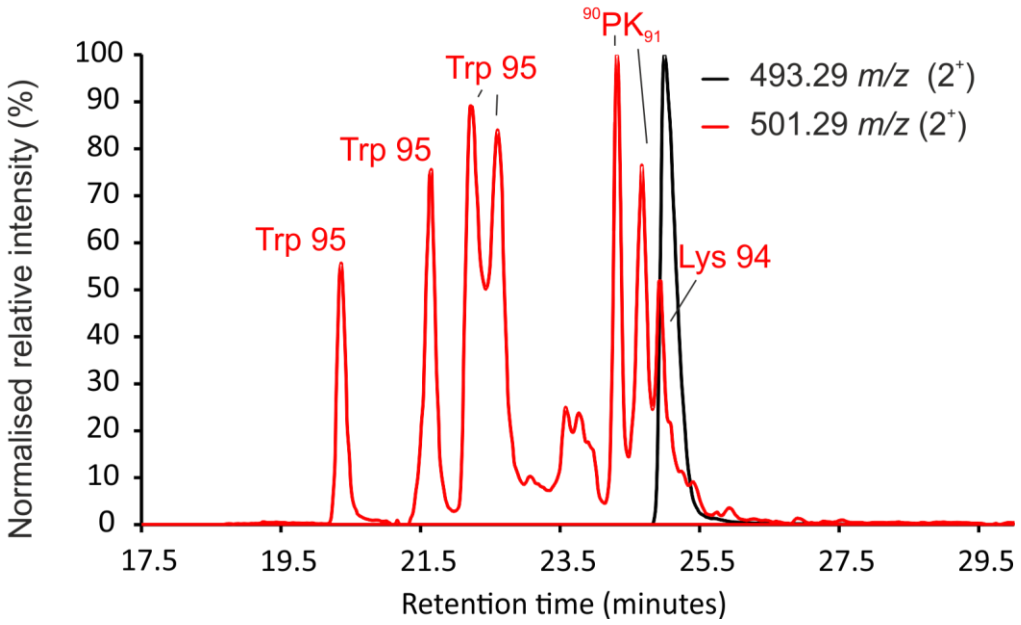

Figure 8.3 XIC of peptide 88-95. Sequence: SQPKIVKW. Unmodified = black. Modified (+16 Da) = red. Modified residues are annotated above each peak in the XIC.

Table 8.5 Quantification and assignment data for FPOP of wild-type, D76N and ΔN6 β2m.

Unmodified		Modified							
Peptide	***m/z***	**Δmass (Da)**	***m/z***	**ΔRT (± S.D) (min)**	**Wild-type (% Modified ± S.D)**	**D76N (% Modified ± S.D)**	**ΔN6 (% Modified ±S.D)**	**Assignment**	**Assignment Criteria**
MIQRTPKIQVY (0-10	688.89 (2+) 459.59 (3+)	+16	696.88 (2+) 464.93 (3+)	-1.48 ± 0.04	96.48 ± 1.81	95.99 ± 0.75	N/A	Met 0	MS/MS
SRHPAENGKSNFLNCY (11-26)	947.43 (2+) 631.96 (3+) 474.22 (4+)	+16	478.21 (4+)	+2.67 ± 0.08	1.41 ± 0.29	1.23 ± 0.22	1.89 ± 0.45	His 13	MS/MS
		+16	478.21 (4+) 637.28 (3+)	+0.65 ± 0.04	0.23 ± 0.04	0.19 ± 0.08	0.23 ± 0.02	Phe 22	MS/MS
		+16	478.21 (4+) 637.28 (3+)	+0.24 ± 0.07	0.21 ± 0.04	0.16 ± 0.05	0.18 ±0.05	Tyr 26	MS/MS
		+16	478.21 (4+) 637.28 (3+)	-0.064 ± 0.04	0.51 ± 0.04	0.43 ± 0.01	0.56 ± 0.04	Lys 19	MS/MS
		+16	478.21 (4+) 637.28 (3+)	-1.06 ± 0.06	0.47 ± 0.08	0.53 ± 0.07	0.66 ± 0.05	Tyr 26	MS/MS
		+16	478.21 (4+) 637.28 (3+)	-2.46 ± 0.07	0.18 ± 0.00	0.16 ± 0.04	0.24 ± 0.04	Phe 22	MS/MS
		+16	478.21 (4+) 637.28 (3+)	-3.27 ± 0.06	0.21 ± 0.02	0.25 ± 0.09	0.52 ± 0.14	Phe 22	MS/MS
VSGFHPSDIEVDLL (27-40)	764.38 (2+)	+ 16	772.38 (2+)	+6.55 ± 0.26	0.39 ± 0.04	0.31 ± 0.10	0.26 ± 0.02	His 31	MS/MS
		+16	772.38 (2+)	-1.98 ± 0.18	0.15 ± 0.02	0.13 ± 0.04	0.20 ± 0.01	Phe 30	MS/MS
		+16	772.38 (2+)	-3.26 ± 0.28	0.20 ± 0.02	0.19 ± 0.09	0.28 ± 0.00	Phe 30	1. MS/MS narrows modification site to GFH 2. Phe is >405X more reactive than Gly 3. Although His and Phe have similar reactivities – His on this peptide was already assigned and has only ever observed here as one +16 Da peak 4. All other +16 Da His modifications identified have retention times *longer* than the unmodified peak
		+16	772.38 (2+)	-4.20 ± 0.29	0.07 ± 0.01	0.06 ± 0.03	0.34 ± 0.03	Phe 30	MS/MS
		+16	772.38 (2+)	-5.06 ± 0.46	0.05 ± 0.01	0.03 ± 0.02	Not detected	Ile 35	MS/MS

		+16	772.38 (2+)	-6.14 ± 0.32	0.13 ± 0.01	0.10 ± 0.06	0.06 ± 0.02	Val 27	MS/MS
KNGERIEKVEHSDL (41-54)	827.43 (2+) 551.96 (3+) 414.22 (4)	+16	557.29 (3+)	+1.86 ± 0.05	0.96 ± 0.62	0.81 ± 0.33	2.27 ± 0.23	His 51	MS/MS
		+16	557.29 (3+)	- 0.06 ± 0.04	0.19 ± 0.05	0.19 ± 0.03	0.17 ± 0.11	Lys 48	MS/MS
SFSKDWSFY (55-63)	583.76 (2+)	+16	591.76 (2+)	-2.74 ± 0.05	4.32 ± 0.95	6.29 ± 2.49	13.58 ± 2.63	Trp 60	MS/MS
		+16	591.76 (2+)	-3.58 ± 0.15	5.51 ± 1.02	8.86 ± 3.05	16.93 ± 3.05	Trp 60	MS/MS
		+16	591.76 (2+)	-4.08 ± 0.11	29.31 ± 2.63	28.83 ± 2.30	8.65 ± 1.29	Trp 60	MS/MS
		+16	591.76 (2+)	-6.61 ± 0.07	5.57 ± 2.83	2.08 ± 0.65	3.36 ± 2.01	Trp 60	MS/MS
		+16	591.76 (2+)	-7.02 ± 0.06	5.90 ± 0.32	4.33 ± 0.15	10.82 ± 0.09	Trp 60	MS/MS
		+32	599.75 (2+)	-2.99 ± 0.05	29.65 ± 2.04	29.44 ± 7.54	18.71 ± 6.23	Trp 60	MS/MS
		+32	599.75 (2+)	-6.20 ± 0.05	7.03 ± 1.48	6.44 ± 0.44	7.48 ± 1.85	Trp 60	MS/MS
		+32	599.75 (2+)	-7.77 ± 0.08	6.20 ± 0.75	7.14 ± 0.07	8.58 ± 2.92	Trp 60	MS/MS
		+32	599.75 (2+)	-9.21 ± 0.09	4.16 ± 0.64	4.09 ± 0.32	3.55 ± 0.91	Trp 60	1. MS/MS identifies modification site to WSFY 2. Trp is the most reactive residue on the peptide 3. All 8 other modified peaks in the XIC were Trp 60
YTEFTPTEKDEY (67-78)	761.83 (2+)	+16	769.82 (2+)	-0.26 ± 0.04	0.35 ± 0.01	0.31 ± 0.02	0.30 ± 0.07	Tyr 67	1. MS/MS narrows modification site to YTE 2. Tyr is >25X more reactive than Thr and > 56X more reactive than Glu
		+16	769.82 (2+)	-0.74 ± 0.04	0.78 ± 0.13	1.04 ± 0.08	0.94 ± 0.02	Tyr 78	MS/MS
		+16	769.82 (2+)	-1.16 ± 0.04	0.06 ± 0.01	0.06 ± 0.02	0.06 ± 0.01	Tyr 67	1. MS/MS narrows modification site to YT 2. Tyr is 25X more reactive than Thr
		+16	769.82 (2+)	-1.34 ± 0.05	0.09 ± 0.01	0.14 ± 0.01	0.08 ± 0.01	Tyr 78	1. MS/MS narrows modification site to KDEY 2. Tyr is >34X more reactive than Lys, 56X more reactive than Glu and >173X more reactive than Asp
		+16	769.82 (2+)	-2.65 ± 0.06	0.02 ± 0.00	0.02 ± 0.00	0.02 ± 0.00	Phe 70	MS/MS
		+16	769.82 (2+)	-3.17 ± 0.06	0.03 ± 0.00	0.03 ± 0.00	0.03 ± 0.00	Phe 70	MS/MS
		+16	769.82 (2+)	-3.36 ± 0.07	0.02 ± 0.00	0.02 ± 0.00	0.02 ± 0.00	Phe 70	MS/MS
ACRVNHVTL (79-87)	535.28 (2+) 357.19 (3+)	+16	362.52 (3+)	+4.37 ± 0.07	0.12 ± 0.03	0.13 ± 0.01	0.45 ± 0.07	His 84	MS/MS
SQPKIVKW (88-95)	493.29 (2+)	+16	501.29 (2+)	-0.07 ± 0.07	0.18 ± 0.01	0.19 ± 0.01	0.21 ± 0.01	Lys 94	MS/MS

		+16	501.29 (2+)	-0.44 ± 0.12	0.39 ± 0.01	0.37 ± 0.04	0.32 ± 0.03	Unassigned	1. MS/MS narrows modification to Pro 90 or Lys 91 2. Both have similar reactivities (approx. 2 fold difference) 3. Pro can have >1 structural isomer
		+16	501.29 (2+)	-0.79 ± 0.11	0.35 ± 0.03	0.31 ± 0.02	0.32 ± 0.01	Unassigned	1. MS/MS narrows modification to Pro 90 or Lys 91 2. Both have similar reactivities (approx. 2 fold difference) 3. Pro can have >1 structural isomer
		+16	501.29 (2+)	-2.54 ± 0.14	0.35 ± 0.01	0.40 ± 0.04	0.35 ± 0.11	Trp 95	MS/MS
		+16	501.29 (2+)	-2.94 ± 0.14	0.43 ± 0.07	0.44 ± 0.12	0.39 ± 0.08	Trp 95	MS/MS
		+16	501.29 (2+)	-3.46 ± 0.14	0.17 ± 0.07	0.25 ± 0.05	0.36 ± 0.02	Trp 95	MS/MS
		+16	501.29 (2+)	-4.73 ± 0.13	0.15 ± 0.08	0.15 ± 0.03	0.16 ± 0.04	Trp 95	MS/MS

8.3 Related information for Chapter 6

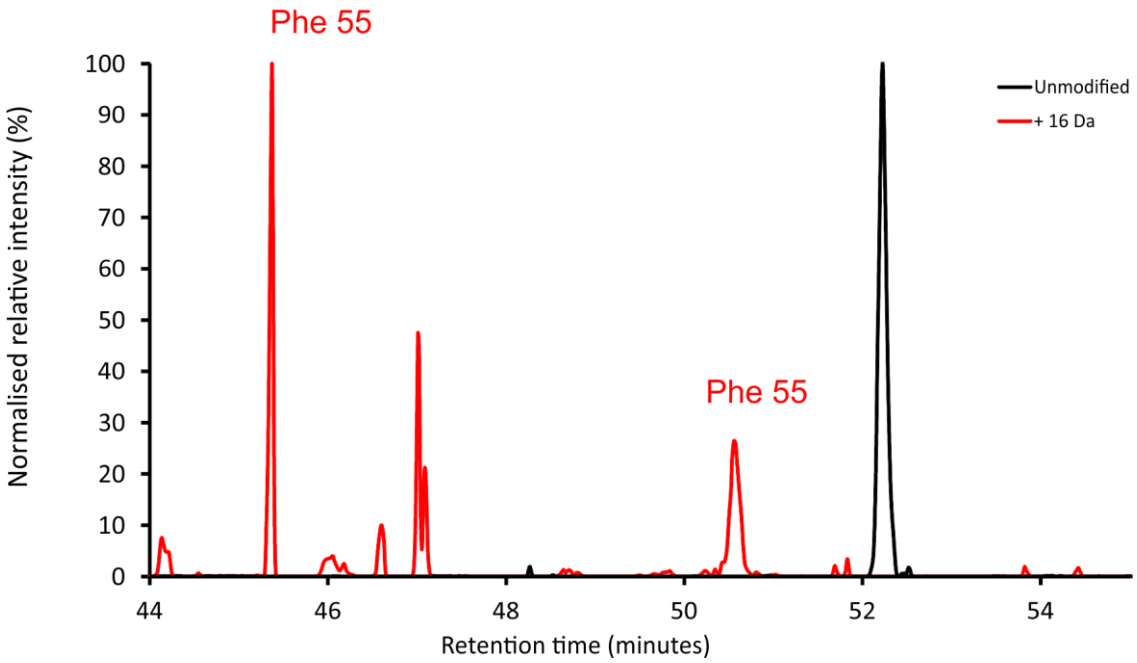

Figure 8.4 XIC of peptide 53-67 from the heavy chain of STT. Sequence: PIFGTTNLAQNFQGR. Unmodified = black. Modified (+16 Da) = red. Modified residues are annotated above each peak in the XIC.

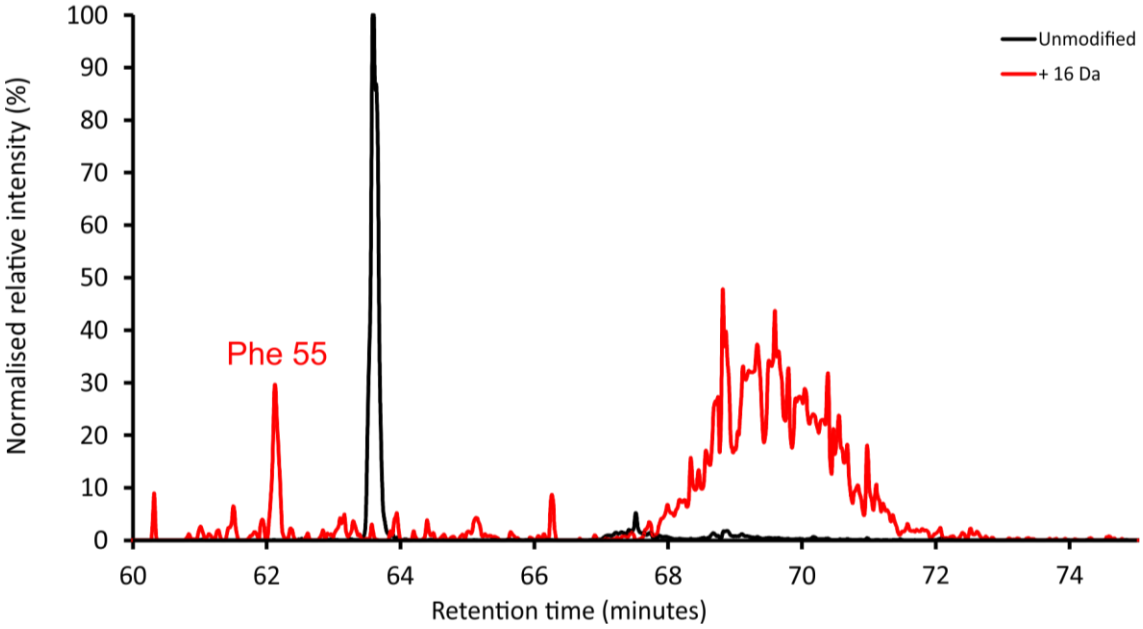

Figure 8.5 XIC of peptide 53-67 from the heavy chain of WFL. Sequence: PIFGLTNLAQNFQGR. Unmodified = black. Modified (+16 Da) = red. Modified residues are annotated above each peak in the XIC.

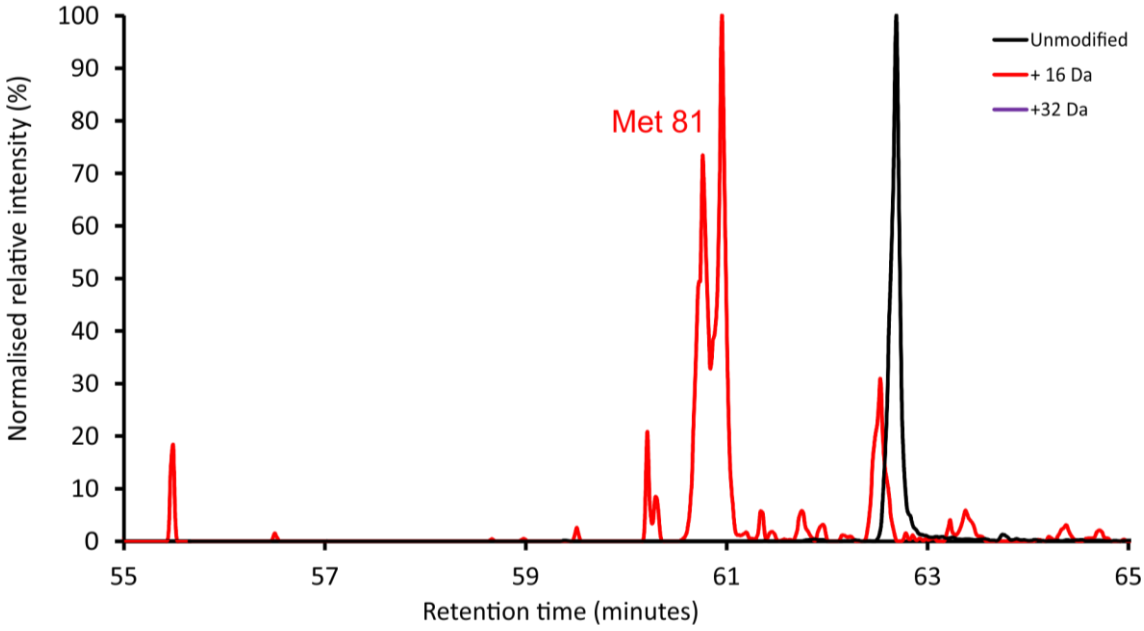

Figure 8.6 XIC of peptide 68-87 from the heavy chain.Sequence: VTITADESTSTVYMELSSLR. Unmodified = black. Modified (+16 Da) = red. Modified residues are annotated above each peak in the XIC.

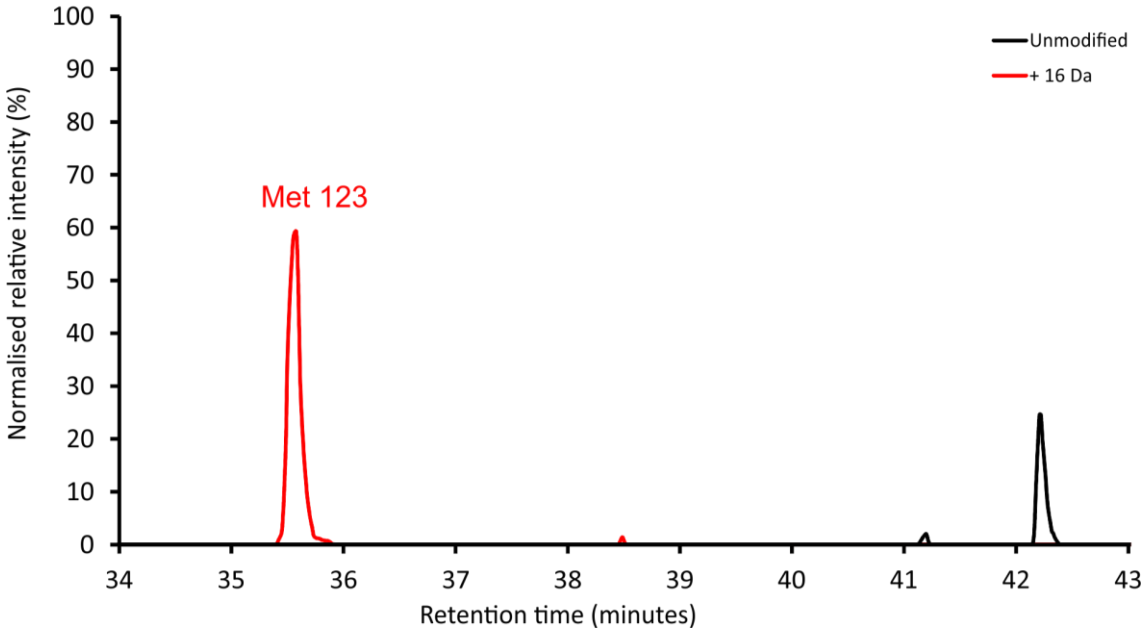

Figure 8.7 XIC of peptide 117-132 from the heavy chain.Sequence: VWGQGTMVTVSSASTK. Unmodified = black. Modified (+16 Da) = red. Modified residues are annotated above each peak in the XIC.

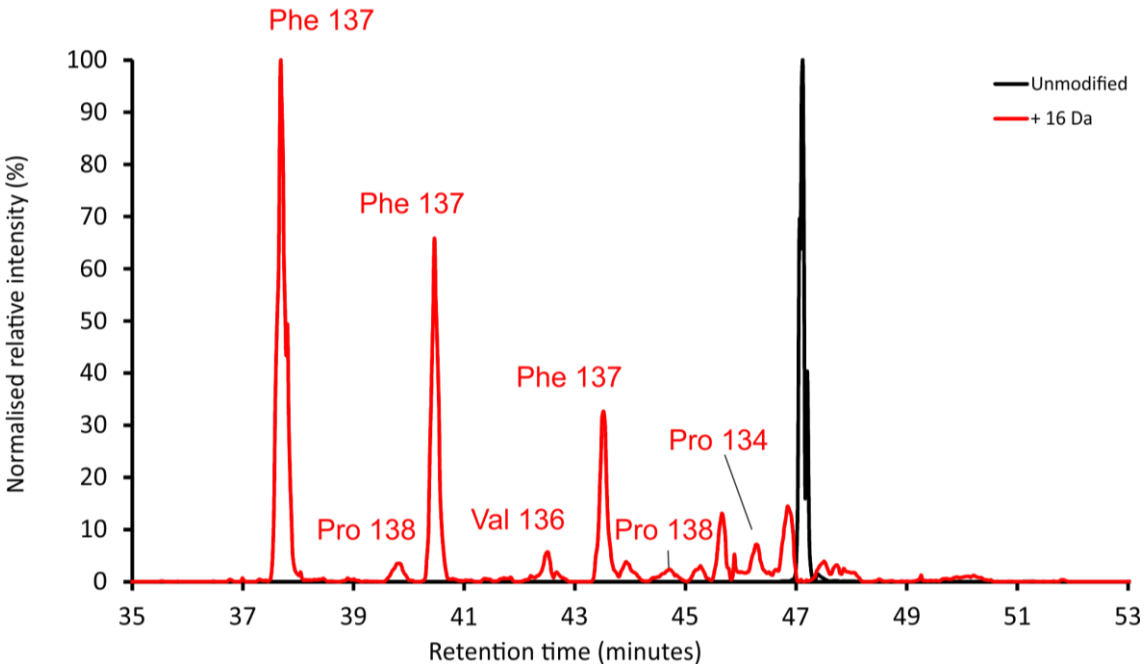

Figure 8.8 XIC of peptide 133-144 from the heavy chain. Sequence: GPSVFPLAPSSK. Unmodified = black. Modified (+16 Da) = red. Modified residues are annotated above each peak in the XIC.

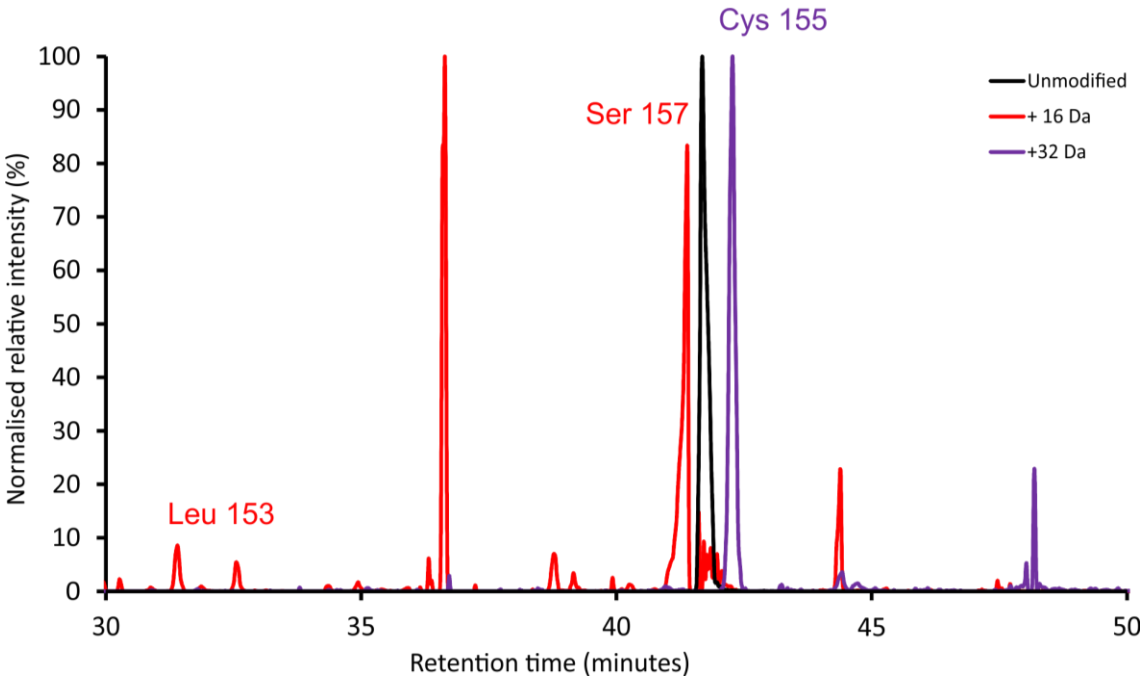

Figure 8.9 XIC of peptide 145-158 from the heavy chain. Sequence: STSGGTAALGCLVK. Unmodified = black. Modified (+16 Da) = red. Modified (+32 Da) purple. Modified residues are annotated above each peak in the XIC.

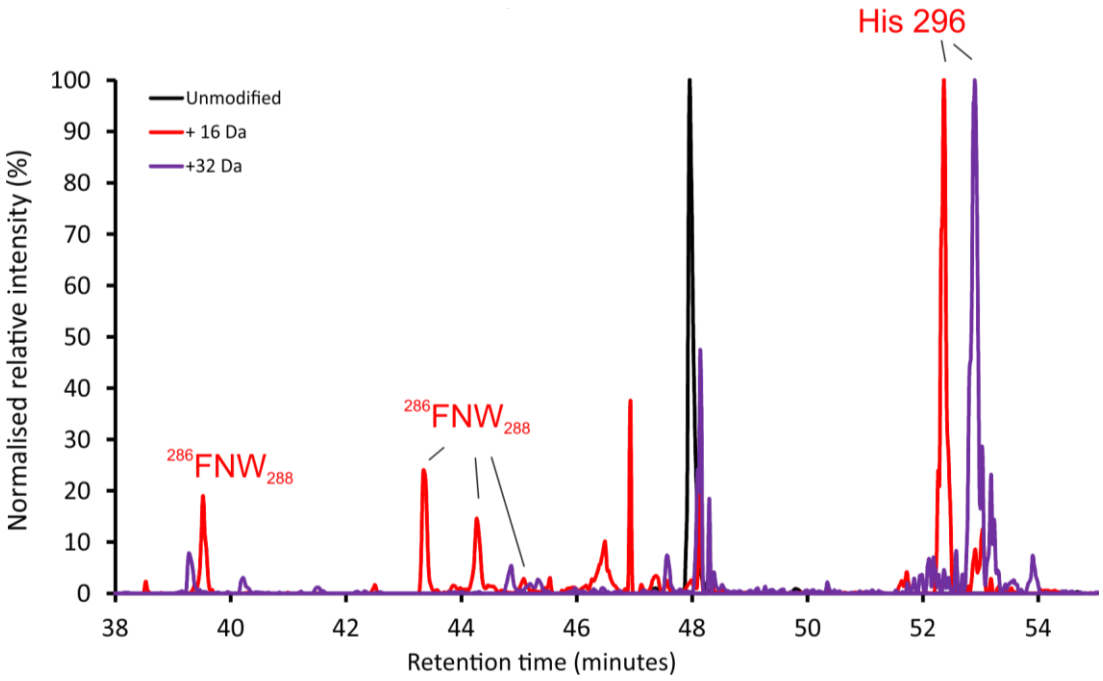

Figure 8.10 XIC of peptide 286-289 from the heavy chain. Sequence: FNWYVDGVEVHNAK. Unmodified = black. Modified (+16 Da) = red. Modified (+32 Da) = purple. Modified residues are annotated above each peak in the XIC.

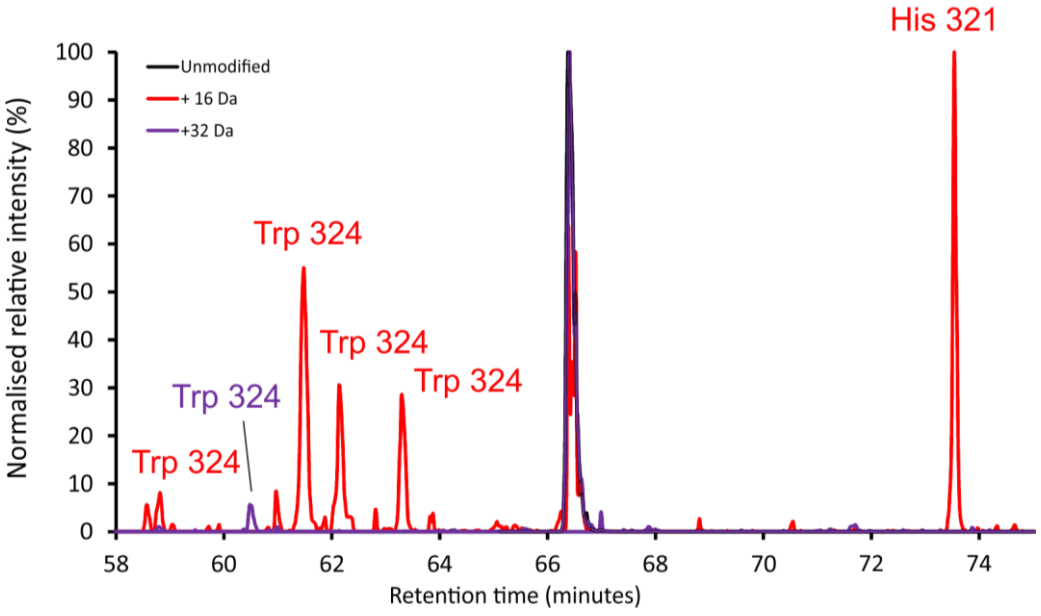

Figure 8.11 XIC of peptide 313-328 from the heavy chain.Sequence: VVSVLTVLHQDWLNGK. Unmodified = black. Modified (+16 Da) = red. Modified (+32 Da) = purple. Modified residues are annotated above each peak in the XIC.

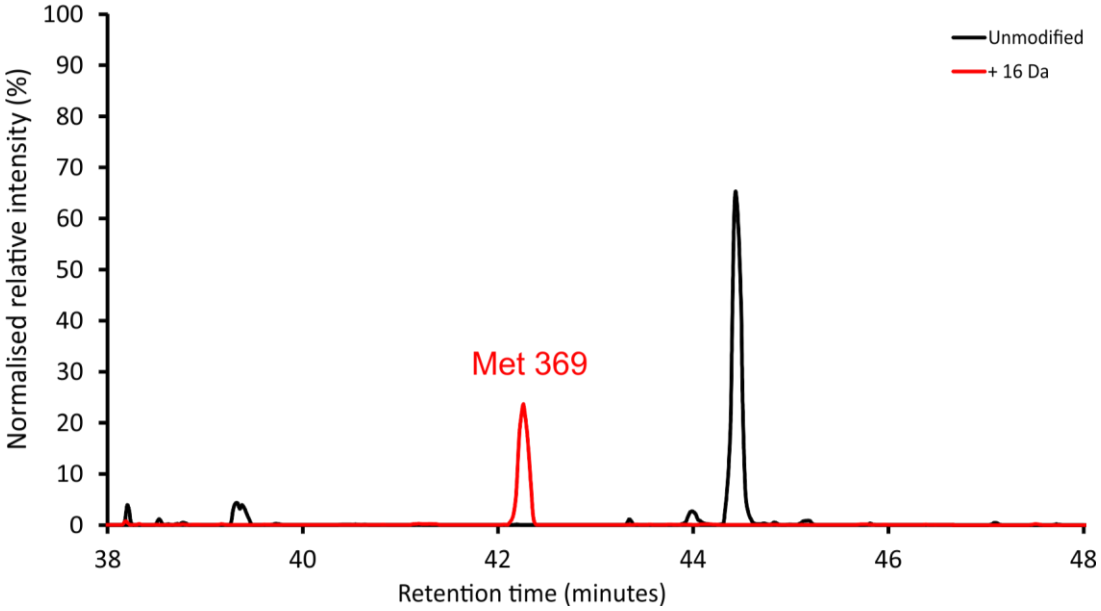

Figure 8.12 XIC of peptide 367-381 from the heavy chain. Sequence: EEMTKNQVSLTCLVK. Unmodified = black. Modified (+16 Da) = red. Modified residues are annotated above each peak in the XIC.

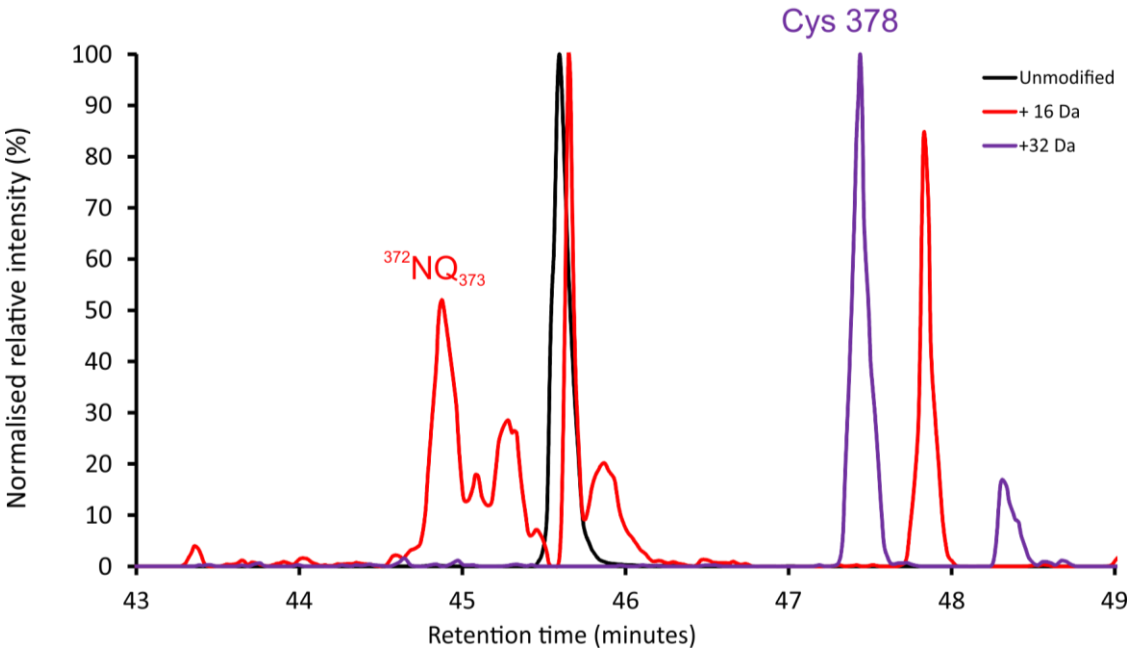

Figure 8.13 XIC of peptide 372-381 from the heavy chain. Sequence: NQVSLTCLVK. Unmodified = black. Modified (+16 Da) = red. Modified (+32 Da = purple). Modified residues are annotated above each peak in the XIC.

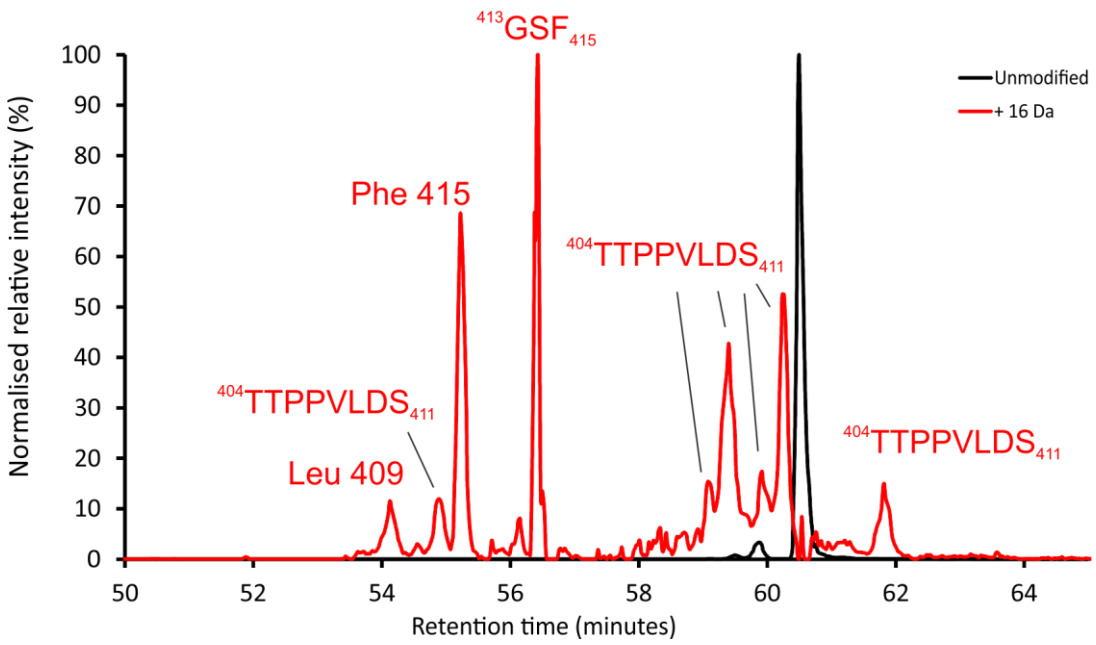

Figure 8.14 XIC of peptide 404-420 from the heavy chain. Sequence: TTPPVLDSDGSFFLYSK. Unmodified = black. Modified (+16 Da) = red. Modified residues are annotated above each peak in the XIC.

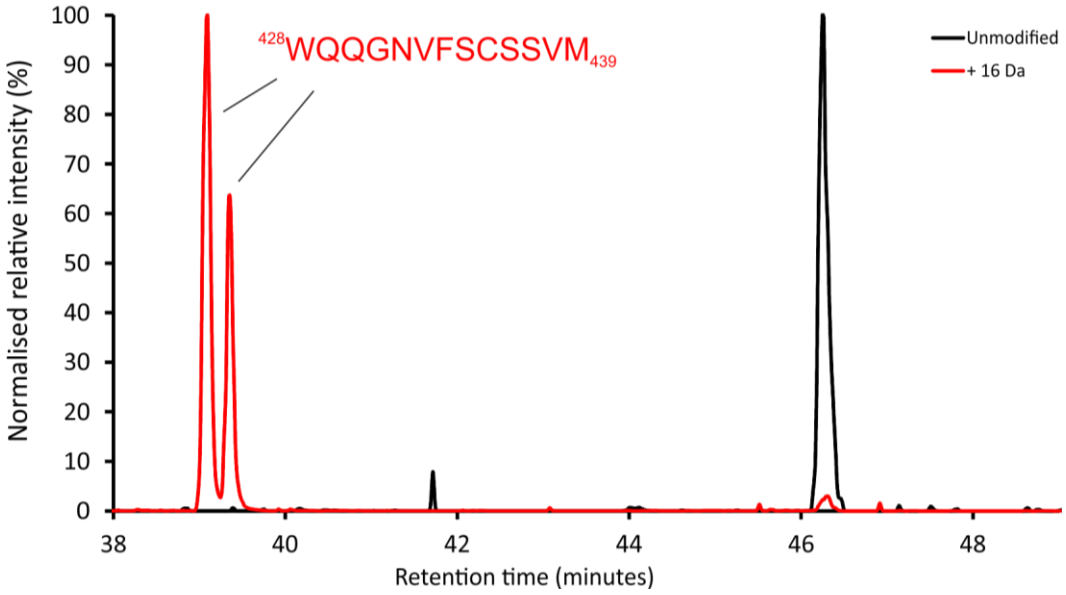

Figure 8.15 XIC of peptide 428-450 from the heavy chain.Sequence: WQQGNVFSCSSVMHEALHNHYTQK. Unmodified = black. Modified (+16 Da) = red. Modified residues are annotated above each peak in the XIC.

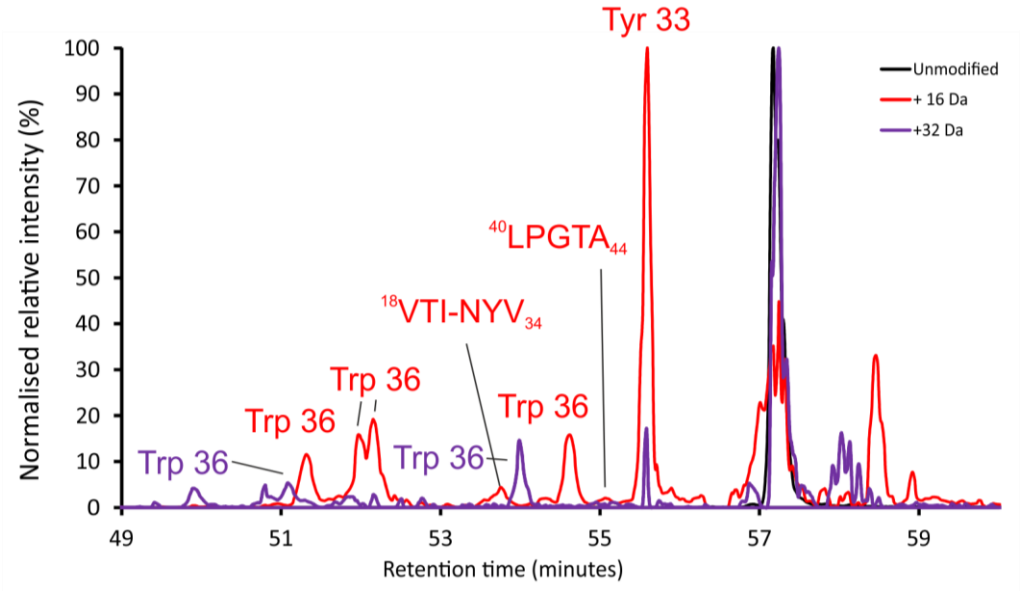

Figure 8.16 XIC of peptide 18-46 from the light chain. Sequence: VTISCSGSSSDIGNNYVSWYQQLPGTAPK. Unmodified = black. Modified (+16 Da) = red. Modified (+32 Da) = purple. Modified residues are annotated above each peak in the XIC.

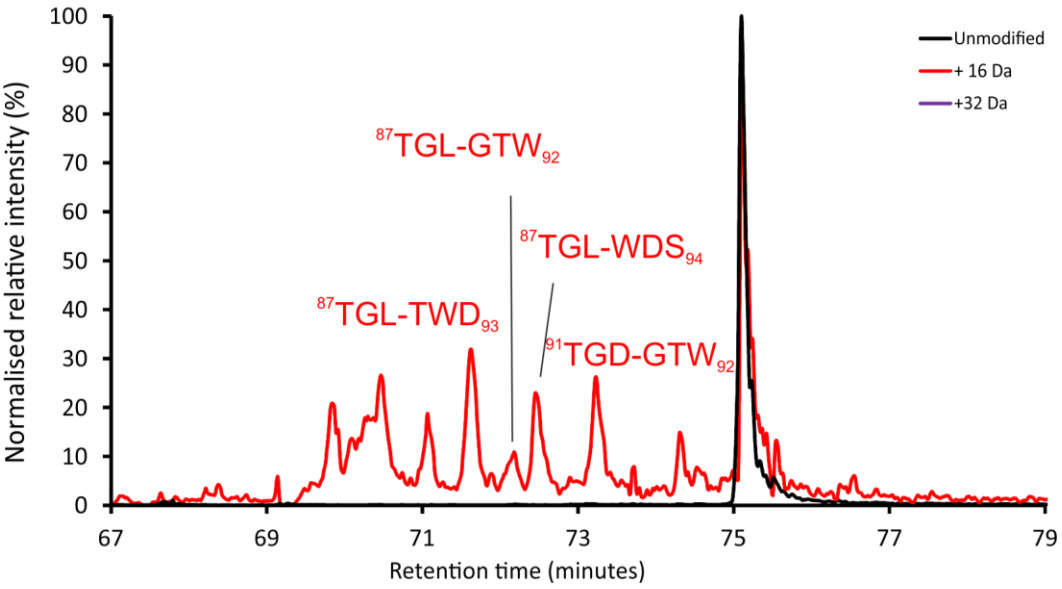

Figure 8.17 XIC of peptide 68-106 from the light chain. Sequence: SGTSATLGITGLQTGDEADYYCGTWDSSLSAWVFGGGTK. Unmodified = black. Modified (+16 Da) = red. Modified residues are annotated above each peak in the XIC.

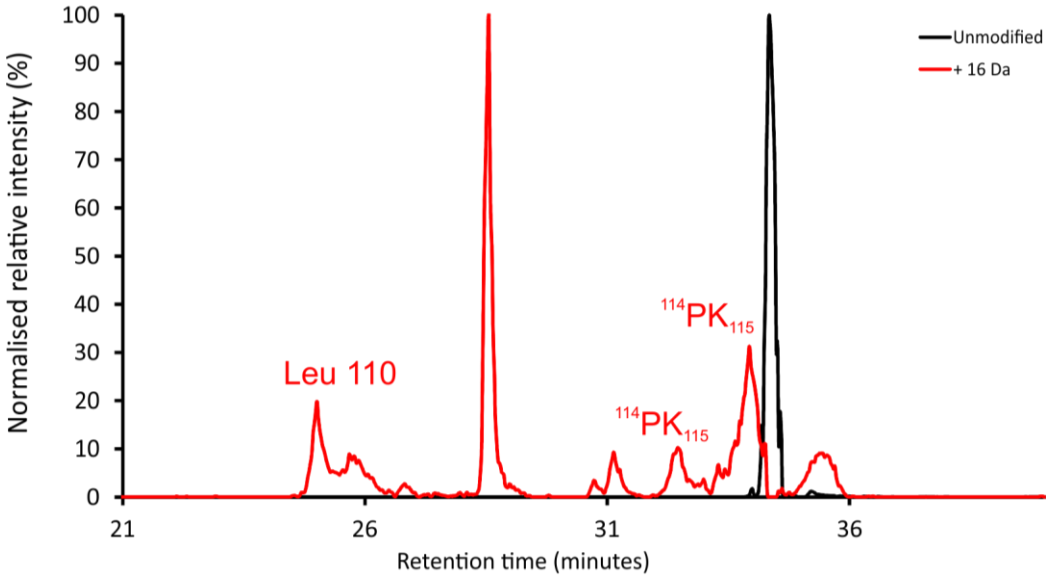

Figure 8.18 XIC for peptide 107-114 from the light chain. Sequence: LTVLGQPK. Unmodified = black. Modified (+16 Da) = red. Modified residues are annotated above each peak in the XIC.

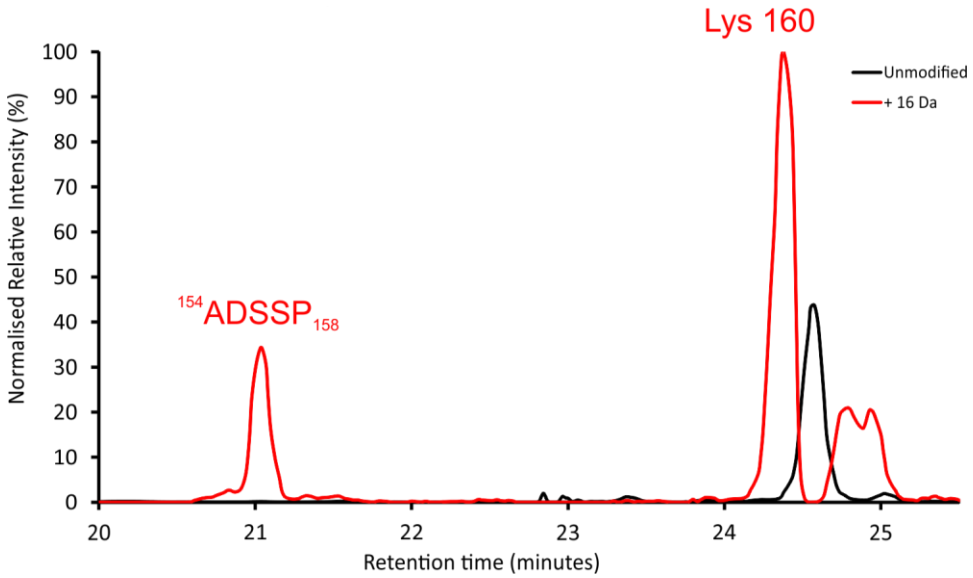

Figure 8.19 XIC for peptide 154-170 from the light chain. Sequence: ADSSPVKAGVETTTPSK. Unmodified = black. Modified (+16 Da) = red. Modified residues are annotated above each peak in the XIC.

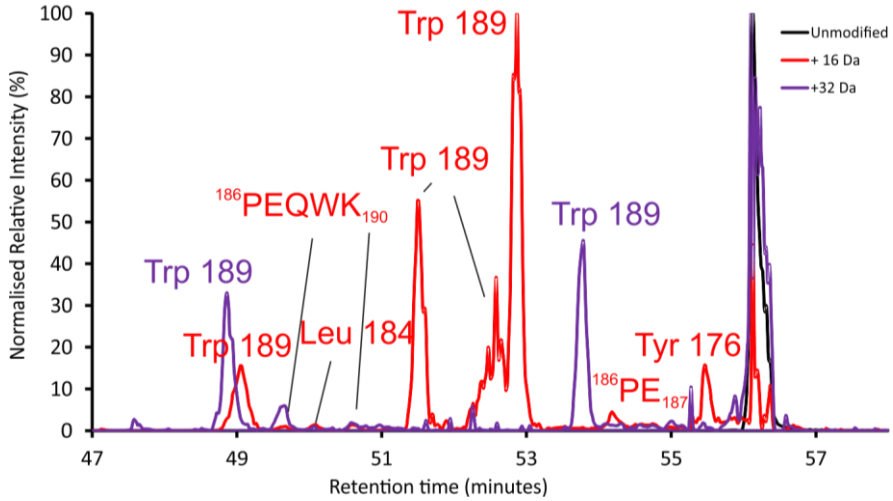

Figure 8.20 XIC for peptide 176-190 from the light chain. Sequence: YAASSYLSLTPEQWK. Unmodified = black. Modified (+16 Da) = red. Modified (+32 Da) = purple. Modified residues are annotated above each peak in the XIC.

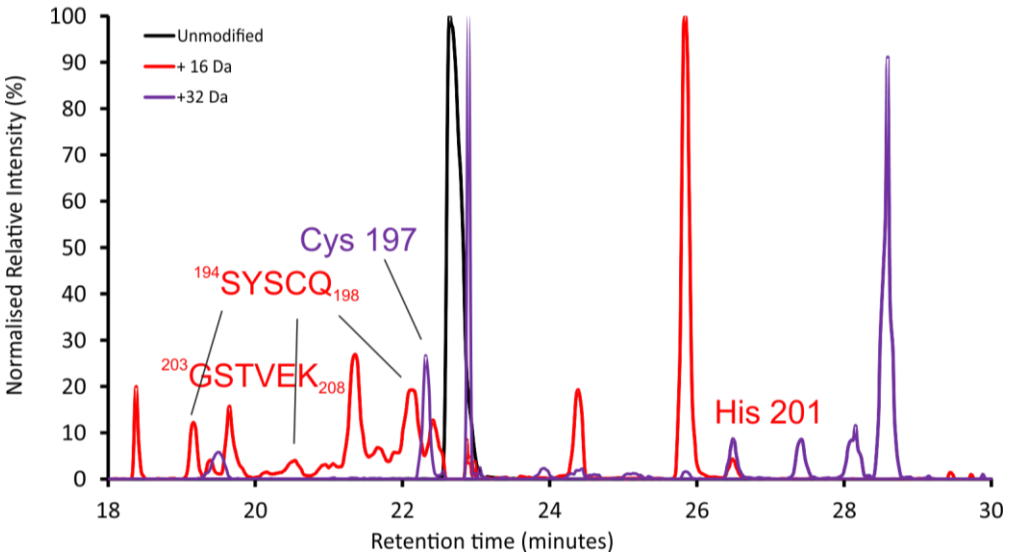

Figure 8.21 XIC for peptide 194-208 from the light chain. Sequence: SYSCQVTHEGSTVEK. Unmodified = black. Modified (+16 Da) = red. Modified (+32 Da) = purple. Modified residues are annotated above each peak in the XIC.

Table 8.6 Raw data table for WFL and STT FPOP data.

Peptide	*m/z*	Δmass (Da)	*m/z*	ΔRT (± S.D) (min)	MEDI1912_STT (% Modified ± S.D)	MEDI1912_WFL (% Modified ± S.D)	Assignment
ASGGTFSTGAFTWVR (24-38) (Heavy chain)	772.88 (2^+)	+16	780.88 (2^+)	-7.47 ± 0.12	0.04 ± 0.00		Phe 34
		+16	780.88 (2^+)	-6.07 ± 0.17	0.35 ± 0.16		Trp 36
		+16	780.88 (2^+)	-5.3 ± 0.18	0.03 ± 0.01		Phe 34
		+16	780.88 (2^+)	-4.97 ± 0.15	0.43 ± 0.06		Trp 36
		+16	780.88 (2^+)	-2.34 ± 0.15	0.26 ± 0.04		Trp 36
		+16	780.88 (2^+)	-1.89 ± 0.16	0.04 ± 0.03		Phe 34
		+16	780.88 (2^+)	-1.52 ± 0.17	0.13 ± 0.03		Phe 29
		+32	788.87 (2^+)	-8.32 ± 0.13	0.06 ± 0.01		Trp 36
		+32	788.87 (2^+)	-3.55 ± 0.16	0.13 ± 0.03		Trp 36
ASGGTFWFGAFTWVR (24-38) (Heavy chain)	845.41 (2^+)	+16	853.41 (2^+)	-6.83 ± 0.02		1.05 ± 0.16	Trp 30
		+16	853.41 (2^+)	-6.22 ± 0.02		1.13 ± 0.24	Phe 31
		+16	853.41 (2^+)	-5.19 ± 0.02		5.42 ± 1.16	Trp 36
		+16	853.41 (2^+)	-4.84 ± 0.03		0.70 ± 0.13	Phe 31
		+16	853.41 (2^+)	-3.79 ± 0.03		18.52 ± 1.34	Trp 30
		+16	853.41 (2^+)	-3.40 ± 0.03		14.46 ± 5.81	Trp 30
		+16	853.41 (2^+)	-1.91 ± 0.03		1.22 ± 0.17	Trp 36
		+16	853.41 (2^+)	-1.56 ± 0.02		0.92 ± 0.15	Phe 31
		+32	861.41 (2^+)	-7.50 ± 0.04		1.08 ± 0.32	Trp 30
		+32	861.41 (2^+)	-7.24 ± 0.03		0.86 ± 0.11	Trp 30
		+32	861.41 (2^+)	-6.13 ± 0.02		0.83 ± 0.20	Trp 36
		+32	861.41 (2^+)	-4.29 ± 0.01		4.61 ± 0.86	Trp 30
PIFGTTNLAQNFQGR (53-67) (Heavy chain)	832.43 (2^+)	+16	840.43 (2^+)	-6.80 ± 0.03	1.7 ± 0.26		Phe 55
		+16	840.43 (2^+)	-1.7 ± 0.07	1.47 ± 0.28		Phe 55
PIFGLTNLAQNFQGR (53-67) (Heavy chain)	838.45 (2^+)	+16	846.45 (2^+)	-1.48 ± 0.02		1.56 ± 0.16	Phe 55
VTITADESTSTVYMELSSLR (68-87) (Heavy chain)	1102.05 (2^+) 735.04 (3^+)	+16	1110.04 (2^+) 740.36 (3^+)	-1.91 ± 0.02	54.36 ± 7.53	66.23 ± 15.79	Met 81
VWGQGTMVTVSSASTK (117-132) (Heavy chain)	819.92 (2^+)	+16	827.91 (2^+)	-6.68 ± 0.04	100 ± 0.00	100.0 ± 0.00	Met 123
GPSVFPLAPSSK (133-144) (Heavy chain)	593.83 (2^+)	+16	601.83 (2^+)	-9.34 ± 0.15	0.97 ± 0.04	0.84 ± 0.07	Phe 137
			601.83 (2^+)	-7.20 ± 0.16	0.02 ± 0.00	0.00 ± 0.00	Pro 138

			601.83 (2^+)	-6.58 ± 0.17	0.27 ± 0.10	0.38 ± 0.02	Phe 137
			601.83 (2^+)	-4.55 ± 0.09	0.05 ± 0.01	0.01 ± 0.00	Val 136
			601.83 (2^+)	-3.61 ± 0.19	0.22 ± 0.08	0.20 ± 0.04	Phe 137
			601.83 (2^+)	-2.23 ± 0.09	0.00 ± 0.00	0.00 ± 0.00	Pro 138
			601.83 (2^+)	-0.80 ± 0.09	0.05 ± 0.01	0.06 ± 0.00	Pro 134
STSGGTAALGCLVK (145-158) (Heavy chain)	661.35 (2^+)	+16	669.34 (2^+)	-9.63 ± 0.51	0.01 ± 0.00	0.00 ± 0.00	Leu 153
		+16	669.34 (2^+)	-0.16 ± 0.09	0.06 ± 0.00	0.07 ± 0.01	Ser 147
		+32	677.34 (2^+)	0.63 ± 0.12	0.16 ± 0.04	0.16 ± 0.04	Cys 155
FNWYVDGVEVHNAK (286-299) (Heavy chain)	839.41 (2^+) 559.94 (3^+)	+16	847.41 (2^+) 565.27 (3^+)	-8.60 ± 0.09	0.50 ± 0.11	0.36 ± 0.03	286 – FNW - 288
		+16	847.41 (2^+) 565.27 (3^+)	-4.75 ± 0.06	0.48 ± 0.06	0.25 ± 0.02	286 – FNW - 288
		+16	847.41 (2^+) 565.27 (3^+)	-3.81 ± 0.06	0.71 ± 0.13	0.43 ± 0.05	286 – FNW - 288
		+16	847.41 (2^+) 565.27 (3^+)	-2.99 ± 0.08	0.07 ± 0.02	0.05 ± 0.01	286 – FNW - 288
		+16	847.41 (2^+)	4.23 ± 0.09	0.14 ± 0.04	0.19 ± 0.05	His 296
		+32	855.40 (2^+)	4.81 ± 0.08	0.16 ± 0.03	0.08 ± 0.02	His 296
VVSVLTVLHQDWLNGK (313-328) (Heavy chain)	904.51 (2^+) 603.34 (3^+)	+16	912.51 (2^+) 608.68 (3^+)	-7.68 ± 0.09	0.08 ± 0.01	0.14 ± 0.06	Trp 324
		+16	912.51 (2^+) 608.68 (3^+)	-5.02 ± 0.07	0.97 ± 0.16	1.26 ± 0.14	Trp 324
		+16	912.51 (2^+) 608.68 (3^+)	-4.35 ± 0.07	0.51 ± 0.02	0.76 ± 0.05	Trp 324
		+16	912.51 (2^+) 608.68 (3^+)	-3.22 ± 0.07	0.23 ± 0.11	0.31 ± 0.04	Trp 324
		+16	912.51 (2^+)	7.01 ± 0.09	0.05 ± 0.03	0.15 ± 0.04	His 321
		+32	920.51 (2^+) 614.00 (3^+)	-6.01 ± 0.55	0.02 ± 0.01	0.00 ± 0.00	Trp 324
EEMTKNQVSLTCLVK (367-381) (Heavy chain)	593.97 (3^+)	+16	599.31 (3^+)	-2.09 ± 0.55	86.65 ± 0.98	90.66 ± 3.90	Met 369
NQVSLTCLVK (372-381) (Heavy chain)	581.32 (2^+)	+16	589.32 (2^+)	-0.65 ± 0.11	0.01 ± 0.00	0.02 ± 0.01	372 – NQ - 373
		+32	597.31 (2^+)	1.91 ± 0.13	0.13 ± 0.04	0.12 ± 0.03	Cys 378
TTPPVLDSDGSFFLYSK (404-420) (Heavy chain)	937.47 (2^+)	+16	945.46 (2^+)	-6.33 ± 0.09	0.08 ± 0.01	0.07 ± 0.01	Leu 409

	625.32 (3^+)						
		+16	945.46 (2^+)	-5.58 ± 0.09	0.11 ± 0.01	0.08 ± 0.01	404 – TTPPVLDS - 411
		+16	945.46 (2^+)	-5.25 ± 0.08	0.46 ± 0.01	0.48 ± 0.02	Phe 415
		+16	945.46 (2^+)	-4.05 ± 0.08	0.17 ± 0.01	0.28 ± 0.05	413 – GSF - 415
		+16	945.46 (2^+)	-1.42 ± 0.07	0.08 ± 0.00	0.06 ± 0.01	404 – TTPPVLDS - 411
		+16	945.46 (2^+)	-1.12 ± 0.08	0.31 ± 0.02	0.32 ± 0.02	404 – TTPPVLDS - 411
		+16	945.46 (2^+)	-0.48 ± 0.06	0.04 ± 0.01	0.06 ± 0.02	404 – TTPPVLDS - 411
		+16	945.46 (2^+)	-0.25 ± 0.05	0.32 ± 0.05	0.35 ± 0.06	404 – TTPPVLDS - 411
		+16	945.46 (2^+)	1.36 ± 0.09	0.10 ± 0.01	0.12 ± 0.01	404 – TTPPVLDS - 411
WQQGNVFSCSVMHEALHNHYTQK (428-450) (Heavy chain)	701.08 (4^+)	+16	705.07 (4^+)	-7.28 ± 0.11	60.62 ± 6.54	67.85 ± 4.60	428 – WQQGNVFSCSVM - 439
			705.07 (4^+)	-7.02 ± 0.11	37.79 ± 6.01	31.34 ± 4.20	428 – WQQGNVFSCSVM - 439
VTISCSGSSSDIGNNYVSWYQQLPGTAPK (18-46) (Light chain)	1558.74 (2^+) 1039.50 (3^+) 779.88 (4^+)	+16	1044.83 (3^+)	-5.82 ± 0.08	0.23 ± 0.09	0.20 ± 0.03	Trp 36
		+16	1044.83 (3^+)	-5.14 ± 0.09	0.15 ± 0.05	0.17 ± 0.05	Trp 36
		+16	1044.83 (3^+)	-4.96 ± 0.09	0.22 ± 0.01	0.33 ± 0.05	Trp 36
		+16	1044.83 (3^+)	-3.39 ± 0.10	0.06 ± 0.02	0.06 ± 0.01	18 – VTISCSGSSSDIGNNYV - 34
		+16	1044.83 (3^+)	-2.53 ± 0.09	0.30 ± 0.12	0.20 ± 0.02	Trp 36
		+16	1044.83 (3^+)	-2.04 ± 0.08	0.03 ± 0.01	0.02 ± 0.00	40 – LPGTA – 44
		+16	1044.83 (3^+)	-1.58 ± 0.09	0.66 ± 0.09	0.94 ± 0.05	Tyr 33
		+32	1050.17 (3^+)	-7.16 ± 0.09	0.02 ± 0.01	0.02 ± 0.01	Trp 36
		+32	1050.17 (3^+)	-6.00 ± 0.11	0.05 ± 0.01	0.04 ± 0.00	Trp 36
		+32	1050.17 (3^+)	-3.13 ± 0.09	0.05 ± 0.02	0.05 ± 0.01	Trp 36
SGTSATLGITGLQTGDEADYYCGTWDSSLSAWVFGGGTK (68-106) (Light chain)	1339.62 (3^+) 1004.96 (4^+)	+16	1344.95 (3^+) 1008.96 (4^+)	-3.49 ± 0.04	1.26 ± 0.33	1.00 ± 0.17	87 – TGLQTGDEADYYCGTWD - 93
		+16	1344.95 (3^+) 1008.96 (4^+)	-2.96 ± 0.06	0.33 ± 0.22	0.25 ± 0.08	87 – TGLQTGDEADYYCGTW - 92
		+16	1344.95 (3^+) 1008.96 (4^+)	-2.63 ± 0.05	0.44 ± 0.04	0.63 ± 0.11	87 – TGLQTGDEADYYCGTWDS - 94
		+16	1344.95 (3^+) 1008.96 (4^+)	-1.88 ± 0.07	0.66 ± 0.11	0.89 ± 0.07	91 – TGDEADYYCGTW - 92
LTVLGQPK (107-114) (Light chain)	428.27 (2^+)	+16	436.27 (2^+)	-9.53 ± 0.18	0.04 ± 0.00	0.04 ± 0.01	Leu 110
			436.27 (2^+)	-1.88 ± 0.09	0.04 ± 0.00	0.04 ± 0.00	114 – PK - 115

			436.27 (2^+)	-0.55 ± 0.29	0.11 ± 0.02	0.02 ± 0.01	114 – PK - 115
ATLVCLISDFYPGAVTVAWK (134-153) (Light chain)	1106.09 (2^+) 737.73 (3^+)	+16	1114.08 (2^+) 743.06 (3^+)	-5.06 ± 0.03	3.86 ± 1.24	0.27 ± 0.06	Trp 152
		+16	1114.08 (2^+) 743.06 (3^+)	-2.20 ± 0.06	3.92 ± 1.11	0.79 ± 0.30	Trp 152
		+16	1114.08 (2^+) 743.06 (3^+)	-1.80 ± 0.05	0.39 ± 0.16	0.21 ± 0.05	Trp 152
		+16	1114.08 (2^+) 743.06 (3^+)	-1.47 ± 0.05	0.87 ± 0.08	0.18 ± 0.05	Trp 152
		+32	1122.08 (2^+) 748.39 (3^+)	-0.87 ± 0.08	0.32 ± 0.20	0.36 ± 0.29	Trp 152
ADSSPVKAGVETTTPSK (154-170) (Light chain)	837.94 (2^+) 558.96 (3^+)	+16	845.94 (2^+) 564.29 (3^+)	-3.59 ± 0.09	0.03 ± 0.01	0.03 ± 0.00	154 – ADSSP - 158
		+16	845.94 (2^+) 564.29 (3^+)	-0.14 ± 0.07	0.20 ± 0.04	0.15 ± 0.01	Lys 160
YAASSYLSLTPEQWK (176-190) (Light chain)	872.44 (2^+) 581.96 (3^+)	+16	800.43 (2^+)	-7.07 ± 0.20	0.11 ± 0.08	0.13 ± 0.02	Trp 189
		+16	800.43 (2^+)	-6.27 ± 0.14	0.04 ± 0.01	0.02 ± 0.00	186 – PEQWK - 190
		+16	800.43 (2^+)	-5.79 ± 0.16	0.03 ± 0.01	0.02 ± 0.01	Leu 184
		+16	800.43 (2^+)	-5.30 ± 0.15	0.04 ± 0.02	0.00 ± 0.00	186 – PEQWK - 190
		+16	800.43 (2^+)	-4.61 ± 0.17	0.36 ± 0.08	0.23 ± 0.02	Trp 189
		+16	800.43 (2^+)	-3.58 ± 0.19	0.21 ± 0.12	0.23 ± 0.14	Trp 189
		+16	800.43 (2^+)	-3.23 ± 0.16	0.31 ± 0.24	0.24 ± 0.03	Trp 189
		+16	800.43 (2^+)	-1.87 ± 0.16	0.02 ± 0.02	0.03 ± 0.01	186 – PE - 187
		+16	800.43 (2^+)	-0.61 ± 0.15	0.05 ± 0.02	0.09 ± 0.06	Tyr 176
		+32	888.43 (2^+)	-6.43 ± 2.72	0.04 ± 0.01	0.04 ± 0.01	Trp 189
		+32	888.43 (2^+)	-2.33 ± 0.17	0.07 ± 0.01	0.10 ± 0.01	Trp 189
SYSCQVTHEGSTVEK (194-208)	856.38 (2^+) 571.26 (3^+)	+16	576.59 (3^+)	-3.40 ± 0.16	0.01 ± 0.00	0.01 ± 0.00	194 – SYSCQ - 198
		+16	576.59 (3^+)	-2.94 ± 0.15	0.01 ± 0.01	0.01 ± 0.01	203 - GSTVEK - 208
		+16	576.59 (3^+)	-2.18 ± 0.06	0.00 ± 0.00	0.00 ± 0.00	194 – SYSCQ - 198
		+16	576.59 (3^+)	-0.58 ± 0.08	0.01 ± 0.01	0.02 ± 0.00	194 – SYSCQ - 198
		+16	864.38 (2^+)	3.90 ± 0.13	0.01 ± 0.01	0.03 ± 0.01	His 201

			576.59 (3^{+})				
		+32	872.38 (2^{+}) 581.92 (3^{+})	-0.38 ± 0.08	0.11 ± 0.02	0.12 ± 0.04	Cys 197

9 References

1. Thomson, J.J., *Rays of positive electricity and their application to chemical analyses*. Vol. 1. 1921: Longmans, Green and Company.
2. Thomson, J.J., *XL. Cathode Rays.* The London, Edinburgh, and Dublin Philosophical Magazine and Journal of Science, 1897. **44**(269): p. 293-316.
3. Thomson, J.J., *Bakerian Lecture:—rays of positive electricity.* Proc. R. Soc. Lond. A, 1913. **89**(607): p. 1-20.
4. Bleakney, W., *A New Method of Positive Ray Analysis and Its Application to the Measurement of Ionization Potentials in Mercury Vapor.* Physical Review, 1929. **34**(1): p. 157-160.
5. Harrison, A.G., *Chemical ionization mass spectrometry*. 2018: Routledge.
6. Fenn, J., M. Mann, C. Meng, S. Wong, and C. Whitehouse, *Electrospray ionization for mass spectrometry of large biomolecules.* Science, 1989. **246**(4926): p. 64-71.
7. Yamashita, M. and J.B. Fenn, *Electrospray ion source. Another variation on the free-jet theme.* The Journal of Physical Chemistry, 1984. **88**(20): p. 4451-4459.
8. Sir Geoffrey Taylor, F.R.S., *Disintegration of water drops in an electric field.* Proceedings of the Royal Society of London. Series A. Mathematical and Physical Sciences, 1964. **280**(1382): p. 383.
9. Kebarle, P. and L. Tang, *From ions in solution to ions in the gas phase - the mechanism of electrospray mass spectrometry.* Analytical Chemistry, 1993. **65**(22): p. 972A-986A.
10. Rayleigh, L., *XX. On the equilibrium of liquid conducting masses charged with electricity.* The London, Edinburgh, and Dublin Philosophical Magazine and Journal of Science, 1882. **14**(87): p. 184-186.
11. Dole, M., L.L. Mack, R.L. Hines, R.C. Mobley, L.D. Ferguson, and M.B. Alice, *Molecular Beams of Macroions.* The Journal of Chemical Physics, 1968. **49**(5): p. 2240-2249.
12. Iribarne, J.V. and B.A. Thomson, *On the evaporation of small ions from charged droplets.* The Journal of Chemical Physics, 1976. **64**(6): p. 2287-2294.
13. Konermann, L., E. Ahadi, A.D. Rodriguez, and S. Vahidi, *Unraveling the Mechanism of Electrospray Ionization.* Analytical Chemistry, 2013. **85**(1): p. 2-9.
14. Kebarle, P. and U.H. Verkerk, *Electrospray: from ions in solution to ions in the gas phase, what we know now.* Mass Spectrometry Reviews, 2009. **28**(6): p. 898-917.
15. Wilm, M. and M. Mann, *Analytical Properties of the Nanoelectrospray Ion Source.* Analytical Chemistry, 1996. **68**(1): p. 1-8.
16. Nemes, P., A.A. Barton, and A. Vertes, *Three-dimensional imaging of metabolites in tissues under ambient conditions by laser ablation electrospray ionization mass spectrometry.* Analytical Chemistry, 2009. **81**(16): p. 6668-6675.
17. García-Gómez, D., L. Bregy, C. Barrios-Collado, G. Vidal-de-Miguel, and R. Zenobi, *Real-Time High-Resolution Tandem Mass Spectrometry Identifies Furan Derivatives in Exhaled Breath.* Analytical Chemistry, 2015. **87**(13): p. 6919-6924.
18. Guenther, S., K.-C. Schäfer, J. Balog, J. Dénes, T. Majoros, K. Albrecht, M. Tóth, B. Spengler, and Z. Takáts, *Electrospray Post-Ionization Mass Spectrometry of Electrosurgical Aerosols.* Journal of The American Society for Mass Spectrometry, 2011. **22**(11): p. 2082.

19. Chang, D.-Y., C.-C. Lee, and J. Shiea, *Detecting Large Biomolecules from High-Salt Solutions by Fused-Droplet Electrospray Ionization Mass Spectrometry.* Analytical Chemistry, 2002. **74**(11): p. 2465-2469.
20. Cheng, S.-C., T.-L. Cheng, H.-C. Chang, and J. Shiea, *Using Laser-Induced Acoustic Desorption/Electrospray Ionization Mass Spectrometry To Characterize Small Organic and Large Biological Compounds in the Solid State and in Solution Under Ambient Conditions.* Analytical Chemistry, 2009. **81**(3): p. 868-874.
21. Shiea, J., M.-Z. Huang, H.S. Hsiu-Jung, C.-Y. Lee, C.-H. Yuan, I. Beech, and J. Sunner, *Electrospray-assisted laser desorption/ionization mass spectrometry for direct ambient analysis of solids.* Rapid Communications in Mass Spectrometry, 2005. **19**(24): p. 3701-3704.
22. Gong, X., Y. Zhao, S. Cai, S. Fu, C. Yang, S. Zhang, and X. Zhang, *Single Cell Analysis with Probe ESI-Mass Spectrometry: Detection of Metabolites at Cellular and Subcellular Levels.* Analytical Chemistry, 2014. **86**(8): p. 3809-3816.
23. Loo, J.A., *Electrospray ionization mass spectrometry: a technology for studying noncovalent macromolecular complexes.* International Journal of Mass Spectrometry, 2000. **200**(1–3): p. 175-186.
24. Sparkman, O.D., *Mass Spec Desk Reference.* Global View, Pittsburgh, 2000.
25. Marshall, A.G., C.L. Hendrickson, and S.D.H. Shi, *Scaling MS plateaus with high-resolution FT-ICRMS*. 2002, ACS Publications.
26. Paul, W. and H. Steinwedel, *Quadrupole mass filter.* Z. Naturforsch. A, 1953. **8**: p. 448.
27. Miller, P.E. and M.B. Denton, *The quadrupole mass filter: Basic operating concepts.* Journal of Chemical Education, 1986. **63**(7): p. 617.
28. Savaryn, J.P., T.K. Toby, and N.L. Kelleher, *A Researcher's Guide to Mass Spectrometry-Based Proteomics.* Proteomics, 2016. **16**(18): p. 2435-2443.
29. Hoffmann, E.d. and V. Stroobant, *Mass Spectrometry; Principles and applications, Third edition.* 2007.
30. Mathieu, É., *Mémoire sur le mouvement vibratoire d'une membrane de forme elliptique.* Journal de Mathématiques Pures et Appliquées, 1868. **13**: p. 137.
31. Collings, B.A. and D.J. Douglas, *An extended mass range quadrupole for electrospray mass spectrometry.* International Journal of Mass Spectrometry and Ion Processes, 1997. **162**(1): p. 121-127.
32. Schwartz, J.C., M.W. Senko, and J.E.P. Syka, *A two-dimensional quadrupole ion trap mass spectrometer.* Journal of the American Society for Mass Spectrometry, 2002. **13**(6): p. 659-669.
33. Douglas, D.J., A.J. Frank, and D. Mao, *Linear ion traps in mass spectrometry.* Mass Spectrometry Reviews, 2005. **24**(1): p. 1-29.
34. Makarov, A., E. Denisov, A. Kholomeev, W. Balschun, O. Lange, K. Strupat, and S. Horning, *Performance Evaluation of a Hybrid Linear Ion Trap/Orbitrap Mass Spectrometer.* Analytical Chemistry, 2006. **78**(7): p. 2113-2120.
35. Stephens, W.E., *A Pulsed Mass Spectrometer with Time Dispersion.* Phys. Rev., 1946. **69**: p. 691.
36. Cameron, A.E. and D.F. Eggers Jr, *An Ion ``Velocitron''.* Review of Scientific Instruments, 1948. **19**(9): p. 605-607.
37. Snijder, J., R.J. Rose, D. Veesler, J.E. Johnson, and A.J.R. Heck, *Studying 18 Mega Dalton Virus Assemblies with Native Mass Spectrometry().* Angewandte Chemie (International ed. in English), 2013. **52**(14): p. 4020-4023.

38. Dawson, J.H.J. and M. Guilhaus, *Orthogonal-acceleration time-of-flight mass spectrometer.* Rapid Communications in Mass Spectrometry, 1989. **3**(5): p. 155-159.
39. Mamyrin, B.A., V.I. Karataev, D.V. Shmikk, and V.A. Zagulin, *The massreflectron, a new non-magnetic time-of-flight mass spectrometer with high resolution.* Zh. Eksp. Teor. Fiz, 1973. **64**: p. 82-89.
40. Helm, D., J.P.C. Vissers, C.J. Hughes, H. Hahne, B. Ruprecht, F. Pachl, A. Grzyb, K. Richardson, J. Wildgoose, S.K. Maier, H. Marx, M. Wilhelm, I. Becher, S. Lemeer, M. Bantscheff, J.I. Langridge, and B. Kuster, *Ion Mobility Tandem Mass Spectrometry Enhances Performance of Bottom-up Proteomics.* Molecular & Cellular Proteomics, 2014. **13**(12): p. 3709.
41. Kingdon, K.H., *A Method for the Neutralization of Electron Space Charge by Positive Ionization at Very Low Gas Pressures.* Physical Review, 1923. **21**(4): p. 408-418.
42. Knight, R.D., *Storage of ions from laser-produced plasmas.* Applied Physics Letters, 1981. **38**(4): p. 221-223.
43. Gillig, K.J., B.K. Bluhm, and D.H. Russell, *Ion motion in a Fourier transform ion cyclotron resonance wire ion guide cell.* International Journal of Mass Spectrometry and Ion Processes, 1996. **157-158**: p. 129-147.
44. Makarov, A., *Electrostatic Axially Harmonic Orbital Trapping: A High-Performance Technique of Mass Analysis.* Analytical Chemistry, 2000. **72**(6): p. 1156-1162.
45. Olsen, J.V., J.C. Schwartz, J. Griep-Raming, M.L. Nielsen, E. Damoc, E. Denisov, O. Lange, P. Remes, D. Taylor, M. Splendore, E.R. Wouters, M. Senko, A. Makarov, M. Mann, and S. Horning, *A Dual Pressure Linear Ion Trap Orbitrap Instrument with Very High Sequencing Speed.* Molecular & Cellular Proteomics, 2009. **8**(12): p. 2759.
46. Perry, R.H., R.G. Cooks, and R.J. Noll, *Orbitrap mass spectrometry: instrumentation, ion motion and applications.* Mass spectrometry Reviews, 2008. **27**(6): p. 661-699.
47. Schmidt, E.M., M.A. Pudenzi, J.M. Santos, C.F.F. Angolini, R.C.L. Pereira, Y.S. Rocha, E. Denisov, E. Damoc, A. Makarov, and M.N. Eberlin, *Petroleomics via Orbitrap mass spectrometry with resolving power above 1000000 at m/z 200.* RSC Advances, 2018. **8**(11): p. 6183-6191.
48. Hu, Q., R.J. Noll, H. Li, A. Makarov, M. Hardman, and R. Graham Cooks, *The Orbitrap: a new mass spectrometer.* Journal of Mass Spectrometry, 2005. **40**(4): p. 430-443.
49. Fort, K.L., M. van de Waterbeemd, D. Boll, M. Reinhardt-Szyba, M.E. Belov, E. Sasaki, R. Zschoche, D. Hilvert, A.A. Makarov, and A.J.R. Heck, *Expanding the structural analysis capabilities on an Orbitrap-based mass spectrometer for large macromolecular complexes.* Analyst, 2018. **143**(1): p. 100-105.
50. Bracewell, R.N. and R.N. Bracewell, *The Fourier transform and its applications*. Vol. 31999. 1986: McGraw-Hill New York, USA.
51. Brenton, A.G. and A.R. Godfrey, *Accurate mass measurement: Terminology and treatment of data.* Journal of the American Society for Mass Spectrometry, 2010. **21**(11): p. 1821-1835.
52. Jennings, K.R., *Collision-induced decompositions of aromatic molecular ions.* International Journal of Mass Spectrometry and Ion Physics, 1968. **1**(3): p. 227-235.
53. Olsen, J.V., B. Macek, O. Lange, A. Makarov, S. Horning, and M. Mann, *Higher-energy C-trap dissociation for peptide modification analysis.* Nature Methods, 2007. **4**: p. 709.

54. Molnar, I. and C. Horváth, *Reverse-phase chromatography of polar biological substances: separation of catechol compounds by high-performance liquid chromatography.* Clinical chemistry, 1976. **22**(9): p. 1497-1502.
55. Swartz, M.E., *UPLC™: An Introduction and Review.* Journal of Liquid Chromatography & Related Technologies, 2005. **28**(7-8): p. 1253-1263.
56. Plumb, R.S., K.A. Johnson, P. Rainville, B.W. Smith, I.D. Wilson, J.M. Castro-Perez, and J.K. Nicholson, *UPLC/MSE; a new approach for generating molecular fragment information for biomarker structure elucidation.* Rapid Communications in Mass Spectrometry, 2006. **20**(13): p. 1989-1994.
57. Cohen, M.J. and F.W. Karasek, *Plasma chromatography™—a new dimension for gas chromatography and mass spectrometry.* Journal of Chromatographic Science, 1970. **8**(6): p. 330-337.
58. Kanu, A.B., P. Dwivedi, M. Tam, L. Matz, and H.H. Hill, Jr., *Ion mobility-mass spectrometry.* J Mass Spectrom, 2008. **43**(1): p. 1-22.
59. Ewing, R.G., D.A. Atkinson, G.A. Eiceman, and G.J. Ewing, *A critical review of ion mobility spectrometry for the detection of explosives and explosive related compounds.* Talanta, 2001. **54**(3): p. 515-529.
60. Uetrecht, C., R.J. Rose, E. van Duijn, K. Lorenzen, and A.J. Heck, *Ion mobility mass spectrometry of proteins and protein assemblies.* Chemical Society Reviews, 2010. **39**(5): p. 1633-55.
61. Mason, E.A. and H.W. Schamp, *Mobility of gaseous Ions in weak electric fields.* Annals of Physics, 1958. **4**(3): p. 233-270.
62. Mordehai, A., L. Howard, M.H. Werlich, R.T. Kurulugama, and T.A. Knotts, *Ion mobility spectrometry-mass spectrometry (IMS-MS) with improved ion transmission and IMS resolution*. 2016.
63. Smith, D.P., T.W. Knapman, I. Campuzano, R.W. Malham, J.T. Berryman, S.E. Radforda, and A.E. Ashcrofta, *Deciphering drift time measurements from travelling wave ion mobility spectrometry-mass spectrometry studies.* European Journal of Mass Spectrometry, 2009. **12**(13): p. 13.
64. Pringle, S.D., K. Giles, J.L. Wildgoose, J.P. Williams, S.E. Slade, K. Thalassinos, R.H. Bateman, M.T. Bowers, and J.H. Scrivens, *An investigation of the mobility separation of some peptide and protein ions using a new hybrid quadrupole/travelling wave IMS/oa-ToF instrument.* International Journal of Mass Spectrometry, 2007. **261**(1): p. 1-12.
65. Giles, K., S.D. Pringle, K.R. Worthington, D. Little, J.L. Wildgoose, and R.H. Bateman, *Applications of a travelling wave-based radio-frequency-only stacked ring ion guide.* Rapid Commun Mass Spectrom, 2004. **18**(20): p. 2401-14.
66. Ruotolo, B.T., J.L.P. Benesch, A.M. Sandercock, S.-J. Hyung, and C.V. Robinson, *Ion mobility-mass spectrometry analysis of large protein complexes.* Nat. Protocols, 2008. **3**(7): p. 1139-1152.
67. Giles, K., J.L. Wildgoose, D.J. Langridge, and I. Campuzano, *A method for direct measurement of ion mobilities using a travelling wave ion guide.* International Journal of Mass Spectrometry, 2010. **298**(1–3): p. 10-16.
68. Shvartsburg, A.A. and R.D. Smith, *Fundamentals of Traveling Wave Ion Mobility Spectrometry.* Analytical Chemistry, 2008. **80**(24): p. 9689-9699.
69. Bush, M.F., Z. Hall, K. Giles, J. Hoyes, C.V. Robinson, and B.T. Ruotolo, *Collision cross sections of proteins and their complexes: A calibration framework and*

database for gas-phase structural biology. Analytical Chemistry, 2010. **82**(22): p. 9557-9565.

70. Michalski, A., E. Damoc, J.-P. Hauschild, O. Lange, A. Wieghaus, A. Makarov, N. Nagaraj, J. Cox, M. Mann, and S. Horning, *Mass Spectrometry-based Proteomics Using Q Exactive, a High-performance Benchtop Quadrupole Orbitrap Mass Spectrometer.* Molecular & Cellular Proteomics, 2011. **10**(9): p. M111.011015.
71. Senko, M.W., P.M. Remes, J.D. Canterbury, R. Mathur, Q. Song, S.M. Eliuk, C. Mullen, L. Earley, M. Hardman, J.D. Blethrow, H. Bui, A. Specht, O. Lange, E. Denisov, A. Makarov, S. Horning, and V. Zabrouskov, *Novel Parallelized Quadrupole/Linear Ion Trap/Orbitrap Tribrid Mass Spectrometer Improving Proteome Coverage and Peptide Identification Rates.* Analytical Chemistry, 2013. **85**(24): p. 11710-11714.
72. Crick, F.H.C. *On protein Synthesis*. in *Symposia for the Society of Experimental Biology*. 1958.
73. Björn, L.O., *Photobiology: The science of light and life*. 2015: Springer.
74. Hirokawa, N. and Y. Tanaka, *Kinesin superfamily proteins (KIFs): Various functions and their relevance for important phenomena in life and diseases.* Experimental Cell Research, 2015. **334**(1): p. 16-25.
75. Anfinsen, C.B., E. Haber, M. Sela, and F.H. White, *The kinetics of formation of native ribonuclease during oxidation of the reduced polypeptide chain.* Proceedings of the National Academy of Sciences of the United States of America, 1961. **47**(9): p. 1309-1314.
76. Witze, E.S., W.M. Old, K.A. Resing, and N.G. Ahn, *Mapping protein post-translational modifications with mass spectrometry.* Nature Methods, 2007. **4**(10): p. 798-806.
77. Trinh, C.H., D.P. Smith, A.P. Kalverda, S.E.V. Phillips, and S.E. Radford, *Crystal structure of monomeric human β-2-microglobulin reveals clues to its amyloidogenic properties.* Proceedings of the National Academy of Sciences of the USA, 2002. **99**(15): p. 9771-9776.
78. Eichner, T., A.P. Kalverda, G.S. Thompson, S.W. Homans, and S.E. Radford, *Conformational Conversion during Amyloid Formation at Atomic Resolution.* Molecular Cell, 2011. **41**(2): p. 161-172.
79. Frauenfeld, J., J. Gumbart, E.O. Van Der Sluis, S. Funes, M. Gartmann, B. Beatrix, T. Mielke, O. Berninghausen, T. Becker, and K. Schulten, *Cryo-EM structure of the ribosome–SecYE complex in the membrane environment.* Nature Structural & Molecular Biology, 2011. **18**(5): p. 614.
80. Dill, K.A. and J.L. MacCallum, *The Protein-Folding Problem, 50 Years On.* Science, 2012. **338**(6110): p. 1042.
81. Dill, K.A. and H.S. Chan, *From Levinthal to pathways to funnels.* Nature Structural and Molecular Biology, 1997. **4**(1): p. 10.
82. Zwanzig, R., A. Szabo, and B. Bagchi, *Levinthal's paradox.* Proceedings of the National Academy of Sciences of the United States of America, 1992. **89**(1): p. 20-22.
83. Levinthal, C., *Are there pathways for protein folding?* Journal de Chimie Physique, 1968. **65**: p. 44-45.
84. Kim, P.S. and R.L. Baldwin, *Specific Intermediates in the Folding Reactions of Small Proteins and the Mechanism of Protein Folding.* Annual Review of Biochemistry, 1982. **51**(1): p. 459-489.

85. Ptitsyn, O.B., *Protein folding: Hypotheses and experiments.* Journal of Protein Chemistry, 1987. **6**(4): p. 273-293.
86. Ptitsyn, O.B. and A.A. Rashin, *A model of myoglobin self-organization.* Biophysical Chemistry, 1975. **3**(1): p. 1-20.
87. Kim, P.S. and R.L. Baldwin, *Intermediates in the Folding Reactions of Small Proteins.* Annual Review of Biochemistry, 1990. **59**(1): p. 631-660.
88. Baldwin, R.L., *How does protein folding get started?* Trends in Biochemical Sciences, 1989. **14**(7): p. 291-294.
89. Tanford, C., *Contribution of Hydrophobic Interactions to the Stability of the Globular Conformation of Proteins.* Journal of the American Chemical Society, 1962. **84**(22): p. 4240-4247.
90. Daggett, V. and A.R. Fersht, *Is there a unifying mechanism for protein folding?* Trends in Biochemical Sciences, 2003. **28**(1): p. 18-25.
91. Dobson, C.M., A. Šali, and M. Karplus, *Protein folding: a perspective from theory and experiment.* Angewandte Chemie International Edition, 1998. **37**(7): p. 868-893.
92. Dawkins, R., *The blind watchmaker: Why the evidence of evolution reveals a universe without design*. 1996: WW Norton & Company, New York, USA.
93. Tsytlonok, M. and L.S. Itzhaki, *The how's and why's of protein folding intermediates.* Archives of Biochemistry and Biophysics, 2013. **531**(1): p. 14-23.
94. Chiti, F. and C.M. Dobson, *Protein misfolding, functional amyloid, and human disease.* Annual review of Biochemistry, 2006. **75**(0066-4154): p. 333-366.
95. Carrell, R.W. and D.A. Lomas, *Conformational disease.* The Lancet, 1997. **350**(9071): p. 134-138.
96. Davies, J.C., E.W.F.W. Alton, and A. Bush, *Cystic fibrosis.* BMJ : British Medical Journal, 2007. **335**(7632): p. 1255-1259.
97. Zanusso, G. and S. Monaco, *Bovine Spongiform Encephalopathy*, in *Prions and diseases*. 2013, Springer: New York, USA. p. 1-13.
98. Dobson, J., A. Kumar, L.F. Willis, R. Tuma, D.R. Higazi, R. Turner, D.C. Lowe, A.E. Ashcroft, S.E. Radford, N. Kapur, and D.J. Brockwell, *Inducing protein aggregation by extensional flow.* Proceedings of the National Academy of Sciences of the USA, 2017.
99. Chiti, F. and C.M. Dobson, *Protein Misfolding, Amyloid Formation, and Human Disease: A Summary of Progress Over the Last Decade.* Annual Review of Biochemistry, 2017. **86**(1): p. 27-68.
100. Takata, K. and Y. Kitamura, *Molecular Approaches to the Treatment, Prophylaxis, and Diagnosis of Alzheimer's Disease: Tangle Formation, Amyloid-β, and Microglia in Alzheimer's Disease.* Journal of Pharmacological Sciences, 2012. **118**(3): p. 331-337.
101. Jain, S., Nicholas W. Wood, and Daniel G. Healy, *Molecular genetic pathways in Parkinson's disease: a review.* Clinical Science, 2005. **109**(4): p. 355-364.
102. Westermark, P., A. Andersson, and G.T. Westermark, *Islet Amyloid Polypeptide, Islet Amyloid, and Diabetes Mellitus.* Physiological Reviews, 2011. **91**(3): p. 795-826.
103. Astbury, W.T., S. Dickinson, and K. Bailey, *The X-ray interpretation of denaturation and the structure of the seed globulins.* The Biochemical Journal, 1935. **29**(10): p. 2351-2360.1.
104. Sunde, M., L.C. Serpell, M. Bartlam, P.E. Fraser, M.B. Pepys, and C.C.F. Blake, *Common core structure of amyloid fibrils by synchrotron X-ray diffraction1.* Journal of Molecular Biology, 1997. **273**(3): p. 729-739.

105. Eanes, E.D. and G.G. Glenner, *X-Ray Diffraction studies on amyloid filaments.* Journal of Histochemistry & Cytochemistry, 1968. **16**(11): p. 673-677.
106. Geddes, A.J., K.D. Parker, E.D.T. Atkins, and E. Beighton, *"Cross-β" conformation in proteins.* Journal of Molecular Biology, 1968. **32**(2): p. 343-358.
107. Gremer, L., D. Schölzel, C. Schenk, E. Reinartz, J. Labahn, R.B.G. Ravelli, M. Tusche, C. Lopez-Iglesias, W. Hoyer, H. Heise, D. Willbold, and G.F. Schröder, *Fibril structure of amyloid-β(1–42) by cryo–electron microscopy.* Science, 2017. **358**(6359): p. 116.
108. Schmidt, A., K. Annamalai, M. Schmidt, N. Grigorieff, and M. Fändrich, *Cryo-EM reveals the steric zipper structure of a light chain-derived amyloid fibril.* Proceedings of the National Academy of Sciences of the United States of America, 2016. **113**(22): p. 6200-6205.
109. Shammas, S.L., T.P.J. Knowles, A.J. Baldwin, C.E. Macphee, M.E. Welland, C.M. Dobson, and G.L. Devlin, *Perturbation of the stability of amyloid fibrils through alteration of electrostatic interactions.* Biophysical Journal, 2011. **100**(11): p. 2783-2791.
110. Myers, S.L., S. Jones, T.R. Jahn, I.J. Morten, G.A. Tennent, E.W. Hewitt, and S.E. Radford, *A Systematic Study of the Effect of Physiological Factors on β2-Microglobulin Amyloid Formation at Neutral pH.* Biochemistry, 2006. **45**(7): p. 2311-2321.
111. Yanagi, K., M. Ashizaki, H. Yagi, K. Sakurai, Y.-H. Lee, and Y. Goto, *Hexafluoroisopropanol induces amyloid fibrils of islet amyloid polypeptide by enhancing both hydrophobic and electrostatic interactions.* The Journal of Biological Chemistry, 2011. **286**(27): p. 23959-23966.
112. Becker, J.W. and G.N. Reeke, *Three-dimensional structure of beta 2-microglobulin.* Proceedings of the National Academy of Sciences of the United States of America, 1985. **82**(12): p. 4225-4229.
113. Eichner, T. and S.E. Radford, *Understanding the complex mechanisms of β(2)-microglobulin amyloid assembly.* The Febs Journal, 2011. **278**(20): p. 3868-3883.
114. Androlewicz, M.J., B. Ortmann, P.M. van Endert, T. Spies, and P. Cresswell, *Characteristics of peptide and major histocompatibility complex class I/beta 2-microglobulin binding to the transporters associated with antigen processing (TAP1 and TAP2).* Proceedings of the National Academy of Sciences of the United States of America, 1994. **91**(26): p. 12716-12720.
115. Heegaard, N.H.H., *β2-microglobulin: from physiology to amyloidosis.* Amyloid, 2009. **16**(3): p. 151-173.
116. Campbell, E.C., A.N. Antoniou, and S.J. Powis, *The multi-faceted nature of HLA class I dimer molecules.* Immunology, 2012. **136**(4): p. 380-384.
117. Otten, G.R., E. Bikoff, R.K. Ribaudo, S. Kozlowski, D.H. Margulies, and R.N. Germain, *Peptide and beta 2-microglobulin regulation of cell surface MHC class I conformation and expression.* The Journal of Immunology, 1992. **148**(12): p. 3723.
118. Williams, D.B., B.H. Barber, R.A. Flavell, and H. Allen, *Role of beta 2-microglobulin in the intracellular transport and surface expression of murine class I histocompatibility molecules.* The Journal of Immunology, 1989. **142**(8): p. 2796.
119. McMahon, R.M., L. Friis, C. Siebold, M.A. Friese, L. Fugger, and E.Y. Jones, *Structure of HLA-A*0301 in complex with a peptide of proteolipid protein: insights into the role of HLA-A alleles in susceptibility to multiple sclerosis.* Acta Crystallographica Section D, 2011. **67**(5): p. 447-454.

120. Cresswell, P., T. Springer, J.L. Strominger, M.J. Turner, H.M. Grey, and R.T. Kubo, *Immunological Identity of the Small Subunit of HL-A Antigens and β(2)-Microglobulin and Its Turnover on the Cell Membrane.* Proceedings of the National Academy of Sciences of the United States of America, 1974. **71**(5): p. 2123-2127.
121. Moriniere, P., A. Marie, N. El Esper, P. Fardellone, H. Deramond, A. Remond, J. Sebert, and A. Fournier, *Destructive spondyloarthropathy with β2-microglobulin amyloid deposits in a uremic patient before chronic hemodialysis.* Nephron, 1991. **59**(4): p. 654-657.
122. Lonnemann, G. and K.M. Koch, *β2-microglobulin amyloidosis: effects of ultrapure dialysate and type of dialyzer membrane.* Journal of the American Society of Nephrology, 2002. **13**(suppl 1): p. S72-S77.
123. Scarpioni, R., M. Ricardi, V. Albertazzi, S. De Amicis, F. Rastelli, and L. Zerbini, *Dialysis-related amyloidosis: challenges and solutions.* International Journal of Nephrology and Renovascular Disease, 2016. **9**: p. 319-328.
124. Koch, K.M., *Dialysis-related amyloidosis.* Kidney International, 1992. **41**(5): p. 1416-1429.
125. Linke, R.P., J. Schäeffer, P. Gielow, P. Lindner, F. Lottspeich, A. Plückthun, and E.H. Weiss, *Production of recombinant human β2-microglobulin for scintigraphic diagnosis of amyloidosis in uremia and hemodialysis.* European Journal of Biochemistry, 2000. **267**(3): p. 627-633.
126. Kameda, A., M. Hoshino, T. Higurashi, S. Takahashi, H. Naiki, and Y. Goto, *Nuclear Magnetic Resonance Characterization of the Refolding Intermediate of β2-Microglobulin Trapped by Non-native Prolyl Peptide Bond.* Journal of Molecular Biology, 2005. **348**(2): p. 383-397.
127. Iadanza, M.G., R. Silvers, J. Boardman, H.I. Smith, T.K. Karamanos, G.T. Debelouchina, Y. Su, R.G. Griffin, N.A. Ranson, and S.E. Radford, *The structure of a β2-microglobulin fibril suggests a molecular basis for its amyloid polymorphism.* Nature Communications, 2018. **9**(1): p. 4517.
128. McParland, V.J., N.M. Kad, A.P. Kalverda, A. Brown, P. Kirwin-Jones, M.G. Hunter, M. Sunde, and S.E. Radford, *Partially Unfolded States of β2-Microglobulin and Amyloid Formation in Vitro.* Biochemistry, 2000. **39**(30): p. 8735-8746.
129. Gosal, W.S., I.J. Morten, E.W. Hewitt, D.A. Smith, N.H. Thomson, and S.E. Radford, *Competing pathways determine fibril morphology in the self-assembly of beta2-microglobulin into amyloid.* Journal of Molecular Biology, 2005. **351**(4): p. 850-864.
130. Smith, D.P., S. Jones, L.C. Serpell, M. Sunde, and S.E. Radford, *A systematic investigation into the effect of protein destabilisation on beta 2-microglobulin amyloid formation.* Journal of Molecular Biology, 2003. **330**(5): p. 943-954.
131. Platt, G.W., K.E. Routledge, S.W. Homans, and S.E. Radford, *Fibril Growth Kinetics Reveal a Region of β(2)-microglobulin Important for Nucleation and Elongation of Aggregation.* Journal of Molecular Biology, 2008. **378**(1): p. 251-263.
132. Gejyo, F., S. Odani, T. Yamada, N. Honma, H. Saito, Y. Suzuki, Y. Nakagawa, H. Kobayashi, Y. Maruyama, Y. Hirasawa, M. Suzuki, and M. Arakawa, *β2-microglobulin: A new form of amyloid protein associated with chronic hemodialysis.* Kidney International, 1986. **30**(3): p. 385-390.
133. Naiki, H., N. Hashimoto, S. Suzuki, H. Kimura, K. Nakakuki, and F. Gejyo, *Establishment of a kinetic model of dialysis-related amyloid fibril extension in vitro.* Amyloid, 1997. **4**(4): p. 223-232.

134. Esposito, G., R. Michelutti, G. Verdone, P. Viglino, H. Hernández, C.V. Robinson, A. Amoresano, F. Dal Piaz, M. Monti, P. Pucci, P. Mangione, M. Stoppini, G. Merlini, G. Ferri, and V. Bellotti, *Removal of the N-terminal hexapeptide from human beta2-microglobulin facilitates protein aggregation and fibril formation.* Protein Science, 2000. **9**(5): p. 831-845.
135. Chiti, F., E. De Lorenzi, S. Grossi, P. Mangione, S. Giorgetti, G. Caccialanza, C.M. Dobson, G. Merlini, G. Ramponi, and V. Bellotti, *A Partially Structured Species of β2-Microglobulin Is Significantly Populated under Physiological Conditions and Involved in Fibrillogenesis.* Journal of Biological Chemistry, 2001. **276**(50): p. 46714-46721.
136. Jahn, T.R., M.J. Parker, S.W. Homans, and S.E. Radford, *Amyloid formation under physiological conditions proceeds via a native-like folding intermediate.* Nature Structural and Molecular Biology, 2006. **13**(3): p. 195-201.
137. Borysik, A.J., I.J. Morten, S.E. Radford, and E.W. Hewitt, *Specific glycosaminoglycans promote unseeded amyloid formation from beta2-microglobulin under physiological conditions.* Kidney Int, 2007. **72**(2): p. 174-81.
138. Relini, A., C. Canale, S. De Stefano, R. Rolandi, S. Giorgetti, M. Stoppini, A. Rossi, F. Fogolari, A. Corazza, G. Esposito, A. Gliozzi, and V. Bellotti, *Collagen Plays an Active Role in the Aggregation of β2-Microglobulin under Physiopathological Conditions of Dialysis-related Amyloidosis.* Journal of Biological Chemistry, 2006. **281**(24): p. 16521-16529.
139. Giorgetti, S., A. Rossi, P. Mangione, S. Raimondi, S. Marini, M. Stoppini, A. Corazza, P. Viglino, G. Esposito, G. Cetta, G. Merlini, and V. Bellotti, *β2-Microglobulin isoforms display an heterogeneous affinity for type I collagen.* Protein Science, 2005. **14**(3): p. 696-702.
140. Morgan, C.J., M. Gelfand, C. Atreya, and A.D. Miranker, *Kidney dialysis-associated amyloidosis: a molecular role for copper in fiber formation1.* Journal of Molecular Biology, 2001. **309**(2): p. 339-345.
141. Eakin, C.M., F.J. Attenello, C.J. Morgan, and A.D. Miranker, *Oligomeric assembly of native-like precursors precedes amyloid formation by β-2 microglobulin.* Biochemistry, 2004. **43**(24): p. 7808-7815.
142. Barbour, B.H., M. Bischel, and D.E. Abrams, *Copper accumulation in patients undergoing chronic hemodialysis. The role of cuprophan.* Nephron, 1971. **8**(5): p. 455-462.
143. Hardouin, P., R.M. Flipo, P. Foissac-Gegoux, A. Dumont, B. Duquesnoy, and B. Delcambre, *Dialysis—relatedβ2 microglobulin—Amyloid arthropathy Improvement of clinical symptoms after a switch of dialysis membranes.* Clinical Rheumatology, 1988. **7**(1): p. 41-45.
144. De Lorenzi, E., R. Colombo, S. Sabella, D.B. Corlin, and N.H.H. Heegaard, *The influence of Cu2+ on the unfolding and refolding of intact and proteolytically processed β2-microglobulin.* Electrophoresis, 2008. **29**(8): p. 1734-1740.
145. Verdone, G., A. Corazza, P. Viglino, F. Pettirossi, S. Giorgetti, P. Mangione, A. Andreola, M. Stoppini, V. Bellotti, and G. Esposito, *The solution structure of human β2-microglobulin reveals the prodromes of its amyloid transition.* Protein Science, 2002. **11**(3): p. 487-499.
146. Eichner, T. and S.E. Radford, *A generic mechanism of beta2-microglobulin amyloid assembly at neutral pH involving a specific proline switch.* Journal of Molecular Biology, 2009. **386**(5): p. 1312-1326.

147. Eakin, C.M., A.J. Berman, and A.D. Miranker, *A native to amyloidogenic transition regulated by a backbone trigger.* Nature Structural and Molecular Biology, 2006. **13**: p. 202.
148. Feige, M.J., F. Hagn, J. Esser, H. Kessler, and J. Buchner, *Influence of the Internal Disulfide Bridge on the Folding Pathway of the CL Antibody Domain.* Journal of Molecular Biology, 2007. **365**(4): p. 1232-1244.
149. Feige, M.J., S. Walter, and J. Buchner, *Folding Mechanism of the CH2 Antibody Domain.* Journal of Molecular Biology, 2004. **344**(1): p. 107-118.
150. Thies, M.J.W., J. Mayer, J.G. Augustine, C.A. Frederick, H. Lilie, and J. Buchner, *Folding and association of the antibody domain CH3: prolyl isomerization preceeds dimerization11Edited by A. R. Fersht.* Journal of Molecular Biology, 1999. **293**(1): p. 67-79.
151. Linke, R.P., H. Hampl, H. Lobeck, E. Ritz, J. Bommer, R. Waldherr, and M. Eulitz, *Lysine-specific cleavage of β₂-microglobulin in amyloid deposits associated with hemodialysis.* Kidney International, 1989. **36**(4): p. 675-681.
152. Stoppini, M., P. Arcidiaco, P. Mangione, S. Giorgetti, D. Brancaccio, and V. Bellotti, *Detection of fragments of β₂-microglobulin in amyloid fibrils.* Kidney International, 2000. **57**(1): p. 349-350.
153. Bellotti, V., M. Stoppini, P. Mangione, M. Sunde, C. Robinson, L. Asti, D. Brancaccio, and G. Ferri, *β 2-microglobulin can be refolded into a native state from ex vivo amyloid fibrils.* European Journal of Biochemistry, 1998. **258**(1): p. 61-67.
154. Stoppini, M., P. Mangione, M. Monti, S. Giorgetti, L. Marchese, P. Arcidiaco, L. Verga, S. Segagni, P. Pucci, G. Merlini, and V. Bellotti, *Proteomics of β2-microglobulin amyloid fibrils.* Biochimica et Biophysica Acta (BBA) - Proteins and Proteomics, 2005. **1753**(1): p. 23-33.
155. Piazza, R., M. Pierno, S. Iacopini, P. Mangione, G. Esposito, and V. Bellotti, *Micro-heterogeneity and aggregation in β 2-microglobulin solutions: effects of temperature, pH, and conformational variant addition.* European Biophysics Journal, 2006. **35**(5): p. 439.
156. Mangione, P.P., G. Esposito, A. Relini, S. Raimondi, R. Porcari, S. Giorgetti, A. Corazza, F. Fogolari, A. Penco, Y. Goto, Y.-H. Lee, H. Yagi, C. Cecconi, M.M. Naqvi, J.D. Gillmore, P.N. Hawkins, F. Chiti, R. Rolandi, G.W. Taylor, M.B. Pepys, M. Stoppini, and V. Bellotti, *Structure, Folding Dynamics, and Amyloidogenesis of D76N β(2)-Microglobulin: Roles of shear flow, hydrophobic surfaces, and α-crystallin.* The Journal of Biological Chemistry, 2013. **288**(43): p. 30917-30930.
157. Valleix, S., J.D. Gillmore, F. Bridoux, P.P. Mangione, A. Dogan, B. Nedelec, M. Boimard, G. Touchard, J.-M. Goujon, C. Lacombe, P. Lozeron, D. Adams, C. Lacroix, T. Maisonobe, V. Planté-Bordeneuve, J.A. Vrana, J.D. Theis, S. Giorgetti, R. Porcari, S. Ricagno, M. Bolognesi, M. Stoppini, M. Delpech, M.B. Pepys, P.N. Hawkins, and V. Bellotti, *Hereditary Systemic Amyloidosis Due to Asp76Asn Variant β2-Microglobulin.* New England Journal of Medicine, 2012. **366**(24): p. 2276-2283.
158. Halabelian, L., S. Ricagno, S. Giorgetti, C. Santambrogio, A. Barbiroli, S. Pellegrino, A. Achour, R. Grandori, L. Marchese, S. Raimondi, P.P. Mangione, G. Esposito, R. Al-Shawi, J.P. Simons, I. Speck, M. Stoppini, M. Bolognesi, and V. Bellotti, *Class I Major Histocompatibility Complex, the Trojan Horse for Secretion of Amyloidogenic β2-Microglobulin.* Journal of Biological Chemistry, 2014. **289**(6): p. 3318-3327.

159. de Rosa, M., A. Barbiroli, S. Giorgetti, P.P. Mangione, M. Bolognesi, and S. Ricagno, *Decoding the Structural Bases of D76N ß2-Microglobulin High Amyloidogenicity through Crystallography and Asn-Scan Mutagenesis.* PLoS ONE, 2015. **10**(12): p. e0144061.
160. Karamanos, T.K., C.L. Pashley, A.P. Kalverda, G.S. Thompson, M. Mayzel, V.Y. Orekhov, and S.E. Radford, *A Population Shift between Sparsely Populated Folding Intermediates Determines Amyloidogenicity.* Journal of the American Chemical Society, 2016. **138**(19): p. 6271-6280.
161. Smith, H.I., *Dynamic structures of rare conformations involved in amyloid formation*, in *School of Molecular and Cellular Biology*. 2018, University of Leeds.
162. Loureiro Rui, J.S., D. Vila-Viçosa, M. Machuqueiro, I. Shakhnovich Eugene, and F.N. Faísca Patricia, *A tale of two tails: The importance of unstructured termini in the aggregation pathway of β2-microglobulin.* Proteins: Structure, Function, and Bioinformatics, 2017. **85**(11): p. 2045-2057.
163. Chong, S.-H., J. Hong, S. Lim, S. Cho, J. Lee, and S. Ham, *Structural and Thermodynamic Characteristics of Amyloidogenic Intermediates of β-2-Microglobulin.* Scientific Reports, 2015. **5**: p. 13631.
164. Le Marchand, T., M. de Rosa, N. Salvi, B.M. Sala, L.B. Andreas, E. Barbet-Massin, P. Sormanni, A. Barbiroli, R. Porcari, C. Sousa Mota, D. de Sanctis, M. Bolognesi, L. Emsley, V. Bellotti, M. Blackledge, C. Camilloni, G. Pintacuda, and S. Ricagno, *Conformational dynamics in crystals reveal the molecular bases for D76N beta-2 microglobulin aggregation propensity.* Nature Communications, 2018. **9**(1): p. 1658.
165. Sneader, W., *The discovery of aspirin: a reappraisal.* British Medical Journal, 2000. **321**(7276): p. 1591-1594.
166. Jozala, A.F., D.C. Geraldes, L.L. Tundisi, V.d.A. Feitosa, C.A. Breyer, S.L. Cardoso, P.G. Mazzola, L.d. Oliveira-Nascimento, C.d.O. Rangel-Yagui, P.d.O. Magalhães, M.A.d. Oliveira, and A. Pessoa, Jr., *Biopharmaceuticals from microorganisms: from production to purification.* Brazilian journal of microbiology, 2016. **47 Suppl 1**(Suppl 1): p. 51-63.
167. Walsh, G., *Biopharmaceutical benchmarks 2018.* Nat. Biotechnol, 2018. **36**: p. 1136-1145.
168. Scapin, G., X. Yang, W.W. Prosise, M. McCoy, P. Reichert, J.M. Johnston, R.S. Kashi, and C. Strickland, *Structure of full-length human anti-PD1 therapeutic IgG4 antibody pembrolizumab.* Nature Structural and Molecular Biology, 2015. **22**(12): p. 953.
169. Forthal, D.N., *Functions of Antibodies.* Microbiology Spectrum, 2014. **2**(4): p. 1-17.
170. Dobson, C.L., P.W.A. Devine, J.J. Phillips, D.R. Higazi, C. Lloyd, B. Popovic, J. Arnold, A. Buchanan, A. Lewis, J. Goodman, C.F. van der Walle, P. Thornton, L. Vinall, D. Lowne, A. Aagaard, L.-L. Olsson, A. Ridderstad Wollberg, F. Welsh, T.K. Karamanos, C.L. Pashley, M.G. Iadanza, N.A. Ranson, A.E. Ashcroft, A.D. Kippen, T.J. Vaughan, S.E. Radford, and D.C. Lowe, *Engineering the surface properties of a human monoclonal antibody prevents self-association and rapid clearance in vivo.* Scientific Reports, 2016. **6**: p. 38644.
171. Garon, E.B., N.A. Rizvi, R. Hui, N. Leighl, A.S. Balmanoukian, J.P. Eder, A. Patnaik, C. Aggarwal, M. Gubens, L. Horn, E. Carcereny, M.-J. Ahn, E. Felip, J.-S. Lee, M.D. Hellmann, O. Hamid, J.W. Goldman, J.-C. Soria, M. Dolled-Filhart, R.Z. Rutledge, J. Zhang, J.K. Lunceford, R. Rangwala, G.M. Lubiniecki, C. Roach, K. Emancipator,

and L. Gandhi, *Pembrolizumab for the Treatment of Non–Small-Cell Lung Cancer.* New England Journal of Medicine, 2015. **372**(21): p. 2018-2028.

172. Jing, Y., M. Borys, S. Nayak, S. Egan, Y. Qian, S.-H. Pan, and Z.J. Li, *Identification of cell culture conditions to control protein aggregation of IgG fusion proteins expressed in Chinese hamster ovary cells.* Process Biochemistry, 2012. **47**(1): p. 69-75.
173. Mazzer, A.R., X. Perraud, J. Halley, J. O'Hara, and D.G. Bracewell, *Protein A chromatography increases monoclonal antibody aggregation rate during subsequent low pH virus inactivation hold.* Journal of Chromatography A, 2015. **1415**: p. 83-90.
174. Hawe, A., J.C. Kasper, W. Friess, and W. Jiskoot, *Structural properties of monoclonal antibody aggregates induced by freeze–thawing and thermal stress.* European journal of Pharmaceutical Sciences, 2009. **38**(2): p. 79-87.
175. Teska, B.M., J.M. Brake, G.S. Tronto, and J.F. Carpenter, *Aggregation and Particle Formation of Therapeutic Proteins in Contact With a Novel Fluoropolymer Surface Versus Siliconized Surfaces: Effects of Agitation in Vials and in Prefilled Syringes.* Journal of Pharmaceutical Sciences, 2016. **105**(7): p. 2053-2065.
176. Willis, L.F., A. Kumar, J. Dobson, N.J. Bond, D. Lowe, R. Turner, S.E. Radford, N. Kapur, and D.J. Brockwell, *Using extensional flow to reveal diverse aggregation landscapes for three IgG1 molecules.* Biotechnology and Bioengineering, 2018. **115**(5): p. 1216-1225.
177. Tian, Y. and B.T. Ruotolo, *The growing role of structural mass spectrometry in the discovery and development of therapeutic antibodies.* Analyst, 2018. **143**(11): p. 2459-2468.
178. Chowdhury, S.K., V. Katta, and B.T. Chait, *Probing conformational changes in proteins by mass spectrometry.* Journal of the American Chemical Society, 1990. **112**(24): p. 9012-9013.
179. Mirza, U.A. and B.T. Chait, *Do proteins denature during droplet evolution in electrospray ionization?* International Journal of Mass Spectrometry and Ion Processes, 1997. **162**(1–3): p. 173-181.
180. Li, J., C. Santambrogio, S. Brocca, G. Rossetti, P. Carloni, and R. Grandori, *Conformational effects in protein electrospray-ionization mass spectrometry.* Mass Spectrometry Reviews, 2016. **35**(1): p. 111-122.
181. Chernushevich, I.V. and B.A. Thomson, *Collisional Cooling of Large Ions in Electrospray Mass Spectrometry.* Analytical Chemistry, 2004. **76**(6): p. 1754-1760.
182. Douglas, D.J. and J.B. French, *Collisional focusing effects in radio frequency quadrupoles.* Journal of the American Society for Mass Spectrometry, 1992. **3**(4): p. 398-408.
183. Kirshenbaum, N., I. Michaelevski, and M. Sharon, *Analyzing Large Protein Complexes by Structural Mass Spectrometry.* Journal of Visualized Experiments : JoVE, 2010(40): p. 1954.
184. Wyttenbach, T., M. Grabenauer, K. Thalassinos, J.H. Scrivens, and M.T. Bowers, *The Effect of Calcium Ions and Peptide Ligands on the Relative Stabilities of the Calmodulin Dumbbell and Compact Structures.* The Journal of Physical Chemistry, 2009. **114**(1): p. 437-447.
185. Bernstein, S.L., D. Liu, T. Wyttenbach, M.T. Bowers, J.C. Lee, H.B. Gray, and J.R. Winkler, *α-Synuclein: Stable compact and extended monomeric structures and pH dependence of dimer formation.* Journal of the American Society for Mass Spectrometry, 2004. **15**(10): p. 1435-1443.

186. Woods, L.A., G.W. Platt, A.L. Hellewell, E.W. Hewitt, S.W. Homans, A.E. Ashcroft, and S.E. Radford, *Ligand binding to distinct states diverts aggregation of an amyloid-forming protein.* Nature Chemical Biology, 2011. **7**(10): p. 730-739.
187. Bernstein, S.L., N.F. Dupuis, N.D. Lazo, T. Wyttenbach, M.M. Condron, G. Bitan, D.B. Teplow, J.-E. Shea, B.T. Ruotolo, C.V. Robinson, and M.T. Bowers, *Amyloid-β protein oligomerization and the importance of tetramers and dodecamers in the aetiology of Alzheimer's disease.* Nat Chem, 2009. **1**(4): p. 326-331.
188. Smith, D.P., S.E. Radford, and A.E. Ashcroft, *Elongated oligomers in β(2)-microglobulin amyloid assembly revealed by ion mobility spectrometry-mass spectrometry.* Proceedings of the National Academy of Sciences of the United States of America, 2010. **107**(15): p. 6794-6798.
189. Mesleh, M.F., J.M. Hunter, A.A. Shvartsburg, G.C. Schatz, and M.F. Jarrold, *Structural Information from Ion Mobility Measurements: Effects of the Long-Range Potential.* The Journal of Physical Chemistry, 1996. **100**(40): p. 16082-16086.
190. Marklund, E.G., M.T. Degiacomi, C.V. Robinson, A.J. Baldwin, and J.L. Benesch, *Collision cross sections for structural proteomics.* Structure, 2015(1878-4186): p. 791-9.
191. Ewing, S.A., M.T. Donor, J.W. Wilson, and J.S. Prell, *Collidoscope: An Improved Tool for Computing Collisional Cross-Sections with the Trajectory Method.* Journal of The American Society for Mass Spectrometry, 2017: p. 1-10.
192. Devine, P.W.A., H.C. Fisher, A.N. Calabrese, F. Whelan, D.R. Higazi, J.R. Potts, D.C. Lowe, S.E. Radford, and A.E. Ashcroft, *Investigating the Structural Compaction of Biomolecules Upon Transition to the Gas-Phase Using ESI-TWIMS-MS.* Journal of The American Society for Mass Spectrometry, 2017. **28**(9): p. 1855-1862.
193. Hogan, C.J., B.T. Ruotolo, C.V. Robinson, and J. Fernandez de la Mora, *Tandem Differential Mobility Analysis-Mass Spectrometry Reveals Partial Gas-Phase Collapse of the GroEL Complex.* The Journal of Physical Chemistry B, 2011. **115**(13): p. 3614-3621.
194. Myung, S., E.R. Badman, Y.J. Lee, and D.E. Clemmer, *Structural Transitions of Electrosprayed Ubiquitin Ions Stored in an Ion Trap over ~10 ms to 30 s.* The Journal of Physical Chemistry A, 2002. **106**(42): p. 9976-9982.
195. Badman, E.R., C.S. Hoaglund-Hyzer, and D.E. Clemmer, *Monitoring Structural Changes of Proteins in an Ion Trap over ~10–200 ms: Unfolding Transitions in Cytochrome c Ions.* Analytical Chemistry, 2001. **73**(24): p. 6000-6007.
196. Seo, J., W. Hoffmann, S. Warnke, M.T. Bowers, K. Pagel, and G. von Helden, *Retention of Native Protein Structures in the Absence of Solvent: A Coupled Ion Mobility and Spectroscopic Study.* Angewandte Chemie International Edition, 2016. **55**(45): p. 14173-14176.
197. Ruotolo, B.T. and C.V. Robinson, *Aspects of native proteins are retained in vacuum.* Curr Opin Chem Biol, 2006. **10**(5): p. 402-8.
198. Ouyang, Z., Z. Takáts, T.A. Blake, B. Gologan, A.J. Guymon, J.M. Wiseman, J.C. Oliver, V.J. Davisson, and R.G. Cooks, *Preparing Protein Microarrays by Soft-Landing of Mass-Selected Ions.* Science, 2003. **301**(5638): p. 1351.
199. Lermyte, F., A. Konijnenberg, J.P. Williams, J.M. Brown, D. Valkenborg, and F. Sobott, *ETD Allows for Native Surface Mapping of a 150 kDa Noncovalent Complex on a Commercial Q-TWIMS-TOF Instrument.* Journal of The American Society for Mass Spectrometry, 2014. **25**(3): p. 343-350.

200. Chi, A., C. Huttenhower, L.Y. Geer, J.J. Coon, J.E.P. Syka, D.L. Bai, J. Shabanowitz, D.J. Burke, O.G. Troyanskaya, and D.F. Hunt, *Analysis of phosphorylation sites on proteins from Saccharomyces cerevisiae by electron transfer dissociation (ETD) mass spectrometry.* Proceedings of the National Academy of Sciences of the USA, 2007. **104**(7): p. 2193.
201. Jackson, S.N., S. Dutta, and A.S. Woods, *The Use of ECD/ETD to Identify the Site of Electrostatic Interaction in Noncovalent Complexes.* Journal of the American Society for Mass Spectrometry, 2009. **20**(2): p. 176-179.
202. Simons, J., *Mechanisms for S–S and N–Cα bond cleavage in peptide ECD and ETD mass spectrometry.* Chemical Physics Letters, 2010. **484**(4): p. 81-95.
203. Syrstad, E.A. and F. Turecček, *Toward a general mechanism of electron capture dissociation.* Journal of the American Society for Mass Spectrometry, 2005. **16**(2): p. 208-224.
204. Roepstorff, P. and J. Fohlman, *Proposal for a common nomenclature for sequence ions in mass spectra of peptides.* Biomedical mass spectrometry, 1984. **11**(11): p. 601-601.
205. Schellman, J.A. and C.G. Schellman, *Kaj Ulrik Linderstrøm-Lang (1896–1959).* Protein Science, 1997. **6**(5): p. 1092-1100.
206. Konermann, L., J. Pan, and Y.-H. Liu, *Hydrogen exchange mass spectrometry for studying protein structure and dynamics.* Chemical Society Reviews, 2011. **40**(3): p. 1224-1234.
207. Englander, S.W., T.R. Sosnick, J.J. Englander, and L. Mayne, *Mechanisms and uses of hydrogen exchange.* Current Opinion in Structural Biology, 1996. **6**(1): p. 18-23.
208. Kossiakoff, A.A., *Protein dynamics investigated by the neutron diffraction–hydrogen exchange technique.* Nature, 1982. **296**(5859): p. 713.
209. Englander, J.J., D.B. Calhoun, and S.W. Englander, *Measurement and calibration of peptide group hydrogen-deuterium exchange by ultraviolet spectrophotometry.* Analytical Biochemistry, 1979. **92**(2): p. 517-524.
210. Xiao, H., J.K. Hoerner, S.J. Eyles, A. Dobo, E. Voigtman, A.I. Mel'čuk, and I.A. Kaltashov, *Mapping protein energy landscapes with amide hydrogen exchange and mass spectrometry: I. A generalized model for a two-state protein and comparison with experiment.* Protein Science, 2005. **14**(2): p. 543-557.
211. Wales, T.E. and J.R. Engen, *Hydrogen exchange mass spectrometry for the analysis of protein dynamics.* Mass Spectrometry Reviews, 2006. **25**(1): p. 158-170.
212. Hodkinson, J.P., T.R. Jahn, S.E. Radford, and A.E. Ashcroft, *HDX-ESI-MS Reveals Enhanced Conformational Dynamics of the Amyloidogenic Protein β(2)-Microglobulin upon Release from the MHC-1.* Journal of the American Society for Mass Spectrometry, 2009. **20**(2): p. 278-286.
213. Kan, Z.-Y., B.T. Walters, L. Mayne, and S.W. Englander, *Protein hydrogen exchange at residue resolution by proteolytic fragmentation mass spectrometry analysis.* Proceedings of the National Academy of Sciences of the USA, 2013. **110**(41): p. 16438-16443.
214. Englander, S.W., *Hydrogen exchange and mass spectrometry: A historical perspective.* Journal of The American Society for Mass Spectrometry, 2006. **17**(11): p. 1481-1489.
215. Zhang, Z. and D.L. Smith, *Determination of amide hydrogen exchange by mass spectrometry: a new tool for protein structure elucidation.* Protein science : a publication of the Protein Society, 1993. **2**(4): p. 522-531.

216. Phillips, J.J., A. Buchanan, J. Andrews, M. Chodorge, S. Sridharan, L. Mitchell, N. Burmeister, A.D. Kippen, T.J. Vaughan, D.R. Higazi, and D. Lowe, *Rate of Asparagine Deamidation in a Monoclonal Antibody Correlating with Hydrogen Exchange Rate at Adjacent Downstream Residues.* Analytical Chemistry, 2017. **89**: p. 2361-2368.
217. Li, J., H. Wei, S.R. Krystek, D. Bond, T.M. Brender, D. Cohen, J. Feiner, N. Hamacher, J. Harshman, R.Y.C. Huang, S.H. Julien, Z. Lin, K. Moore, L. Mueller, C. Noriega, P. Sejwal, P. Sheppard, B. Stevens, G. Chen, A.A. Tymiak, M.L. Gross, and L.A. Schneeweis, *Mapping the Energetic Epitope of an Antibody/Interleukin-23 Interaction with Hydrogen/Deuterium Exchange, Fast Photochemical Oxidation of Proteins Mass Spectrometry, and Alanine Shave Mutagenesis.* Analytical Chemistry, 2017. **89**(4): p. 2250-2258.
218. Chalmers, M.J., S.A. Busby, B.D. Pascal, G.M. West, and P.R. Griffin, *Differential hydrogen/deuterium exchange mass spectrometry analysis of protein–ligand interactions.* Expert Review of Proteomics, 2011. **8**(1): p. 43-59.
219. Trabjerg, E., Z.E. Nazari, and K.D. Rand, *Conformational analysis of complex protein states by hydrogen/deuterium exchange mass spectrometry (HDX-MS): Challenges and emerging solutions.* TrAC Trends in Analytical Chemistry, 2018. **106**: p. 125-138.
220. Duc, N.M., Y. Du, T.S. Thorsen, S.Y. Lee, C. Zhang, H. Kato, B.K. Kobilka, and K.Y. Chung, *Effective Application of Bicelles for Conformational Analysis of G Protein-Coupled Receptors by Hydrogen/Deuterium Exchange Mass Spectrometry.* Journal of The American Society for Mass Spectrometry, 2015. **26**(5): p. 808-817.
221. Hentze, N. and M.P. Mayer, *Analyzing Protein Dynamics Using Hydrogen Exchange Mass Spectrometry.* Journal of Visualized Experiments : JoVE, 2013(81): p. 50839.
222. Wales, T.E., K.E. Fadgen, G.C. Gerhardt, and J.R. Engen, *High-Speed and High-Resolution UPLC Separation at Zero Degrees Celsius.* Analytical Chemistry, 2008. **80**(17): p. 6815-6820.
223. Lim, M.S.C., M.E. Hellard, and C.K. Aitken, *The case of the disappearing teaspoons: longitudinal cohort study of the displacement of teaspoons in an Australian research institute.* BMJ, 2005. **331**(7531): p. 1498-1500.
224. Bai, Y., S. Milne John, L. Mayne, and S.W. Englander, *Primary structure effects on peptide group hydrogen exchange.* Proteins: Structure, Function, and Bioinformatics, 1993. **17**(1): p. 75-86.
225. Molday, R.S., S.W. Englander, and R.G. Kallen, *Primary structure effects on peptide group hydrogen exchange.* Biochemistry, 1972. **11**(2): p. 150-158.
226. Aye, T.T., T.Y. Low, and S.K. Sze, *Nanosecond Laser-Induced Photochemical Oxidation Method for Protein Surface Mapping with Mass Spectrometry.* Analytical Chemistry, 2005. **77**(18): p. 5814-5822.
227. Hambly, D.M. and M.L. Gross, *Laser Flash Photolysis of Hydrogen Peroxide to Oxidize Protein Solvent-Accessible Residues on the Microsecond Timescale.* Journal of the American Society for Mass Spectrometry, 2005. **16**(12): p. 2057-2063.
228. Xu, G. and M.R. Chance, *Hydroxyl Radical-Mediated Modification of Proteins as Probes for Structural Proteomics.* Chemical Reviews, 2007. **107**(8): p. 3514-3543.
229. Zhang, B., M. Cheng, D. Rempel, and M.L. Gross, *Implementing fast photochemical oxidation of proteins (FPOP) as a footprinting approach to solve diverse problems in structural biology.* Methods, 2018. **144**: p. 94-103.

230. Niu, B., H. Zhang, D. Giblin, D.L. Rempel, and M.L. Gross, *Dosimetry Determines the Initial OH Radical Concentration in Fast Photochemical Oxidation of Proteins (FPOP).* Journal of The American Society for Mass Spectrometry, 2015. **26**(5): p. 843-846.
231. Calabrese, A.N., J.R. Ault, S.E. Radford, and A.E. Ashcroft, *Using hydroxyl radical footprinting to explore the free energy landscape of protein folding.* Methods, 2015. **89**: p. 38-44.
232. Xie, B., A. Sood, R.J. Woods, and J.S. Sharp, *Quantitative Protein Topography Measurements by High Resolution Hydroxyl Radical Protein Footprinting Enable Accurate Molecular Model Selection.* Scientific Reports, 2017. **7**(1): p. 4552.
233. Vahidi, S. and L. Konermann, *Probing the Time Scale of FPOP (Fast Photochemical Oxidation of Proteins): Radical Reactions Extend Over Tens of Milliseconds.* Journal of The American Society for Mass Spectrometry, 2016. **27**(7): p. 1156-1164.
234. Watkinson, T.G., A.N. Calabrese, J.R. Ault, S.E. Radford, and A.E. Ashcroft, *FPOP-LC-MS/MS Suggests Differences in Interaction Sites of Amphipols and Detergents with Outer Membrane Proteins.* Journal of The American Society for Mass Spectrometry, 2017. **28**(1): p. 50-55.
235. Espino, J.A., V.S. Mali, and L.M. Jones, *In Cell Footprinting Coupled with Mass Spectrometry for the Structural Analysis of Proteins in Live Cells.* Analytical Chemistry, 2015. **87**(15): p. 7971-7978.
236. Gau, B.C., H. Chen, Y. Zhang, and M.L. Gross, *Sulfate Radical Anion as a New Reagent for Fast Photochemical Oxidation of Proteins.* Analytical Chemistry, 2010. **82**(18): p. 7821-7827.
237. Cheng, M., B. Zhang, W. Cui, and M.L. Gross, *Laser-Initiated Radical Trifluoromethylation of Peptides and Proteins: Application to Mass-Spectrometry-Based Protein Footprinting.* Angewandte Chemie International Edition, 2017. **56**(45): p. 14007-14010.
238. Shi, L.R., T. Liu, M.L. Gross, and Y. Huang, *Recognition of Human IgG1 by Fcγ Receptors: Structural Insights from Hydrogen-Deuterium Exchange and Fast Photochemical Oxidation of Proteins Coupled with Mass Spectrometry.* Biochemistry, 2019. **58**: p. 1074-1080.
239. Jones, L.M., J. B. Sperry, J. A. Carroll, and M.L. Gross, *Fast Photochemical Oxidation of Proteins for Epitope Mapping.* Analytical Chemistry, 2011. **83**(20): p. 7657-7661.
240. Zhang, Y., A.T. Wecksler, P. Molina, G. Deperalta, and M.L. Gross, *Mapping the Binding Interface of VEGF and a Monoclonal Antibody Fab-1 Fragment with Fast Photochemical Oxidation of Proteins (FPOP) and Mass Spectrometry.* Journal of The American Society for Mass Spectrometry, 2017: p. 1-9.
241. Yan, Y., G. Chen, H. Wei, R.Y.C. Huang, J. Mo, D.L. Rempel, A.A. Tymiak, and M.L. Gross, *Fast Photochemical Oxidation of Proteins (FPOP) Maps the Epitope of EGFR Binding to Adnectin.* Journal of The American Society for Mass Spectrometry, 2014. **25**(12): p. 2084-2092.
242. Adler, A.J., N.J. Greenfield, and G.D. Fasman, *[27] Circular dichroism and optical rotatory dispersion of proteins and polypeptides*, in *Methods in Enzymology*. 1973, Academic Press. p. 675-735.
243. Michaelevski, I., N. Kirshenbaum, and M. Sharon, *T-wave ion mobility-mass spectrometry: basic experimental procedures for protein complex analysis.* J Vis Exp, 2010(41).

244. Gabelica, V., A.A. Shvartsburg, C. Afonso, P. Barran, J.L.P. Benesch, C. Bleiholder, M.T. Bowers, A. Bilbao, M.F. Bush, J.L. Campbell, I.D.G. Campuzano, T. Causon, B.H. Clowers, C.S. Creaser, E. De Pauw, J. Far, F. Fernandez-Lima, J.C. Fjeldsted, K. Giles, M. Groessl, C.J. Hogan Jr, S. Hann, H.I. Kim, R.T. Kurulugama, J.C. May, J.A. McLean, K. Pagel, K. Richardson, M.E. Ridgeway, F. Rosu, F. Sobott, K. Thalassinos, S.J. Valentine, and T. Wyttenbach, *Recommendations for reporting ion mobility Mass Spectrometry measurements.* Mass Spectrometry Reviews, 2019. **38**(3): p. 291-320.
245. Phillips, J.C., R. Braun, W. Wang, J. Gumbart, E. Tajkhorshid, E. Villa, C. Chipot, R.D. Skeel, L. Kalé, and K. Schulten, *Scalable molecular dynamics with NAMD.* Journal of Computational Chemistry, 2005. **26**(16): p. 1781-1802.
246. Brooks, B.R., R.E. Bruccoleri, B.D. Olafson, D.J. States, S. Swaminathan, and M. Karplus, *CHARMM: A program for macromolecular energy, minimization, and dynamics calculations.* Journal of Computational Chemistry, 1983. **4**(2): p. 187-217.
247. Cryar, A., K. Groves, and M. Quaglia, *Online Hydrogen-Deuterium Exchange Traveling Wave Ion Mobility Mass Spectrometry (HDX-IM-MS): a Systematic Evaluation.* Journal of the American Society for Mass Spectrometry, 2017. **28**(6): p. 1192-1202.
248. Waterhouse, A., M. Bertoni, S. Bienert, G. Studer, G. Tauriello, R. Gumienny, F.T. Heer, T.A P. de Beer, C. Rempfer, L. Bordoli, R. Lepore, and T. Schwede, *SWISS-MODEL: homology modelling of protein structures and complexes.* Nucleic Acids Research, 2018. **46**(W1): p. W296-W303.
249. Wilson, I.A., Lang, S., Kurosawa, Y., Ohshima, N., Ota, T., Abadejos, J., Lee, P.S., Nemazee, D., *VH1-69 germline antibody predicted from CR6261.* 2017.
250. Lobner, E., A.-S. Humm, G. Mlynek, K. Kubinger, M. Kitzmüller, M.W. Traxlmayr, K. Djinović-Carugo, and C. Obinger. *Two-faced Fcab prevents polymerization with VEGF and reveals thermodynamics and the 2.15 Å crystal structure of the complex*. Taylor & Francis.
251. Harris, L.J., E. Skaletsky, and A. McPherson, *Crystallographic structure of an intact IgG1 monoclonal antibody.* Journal of Molecular Biology, 1998. **275**(5): p. 861-872.
252. Cornwell, O., S.E. Radford, A.E. Ashcroft, and J.R. Ault, *Comparing Hydrogen Deuterium Exchange and Fast Photochemical Oxidation of Proteins: a Structural Characterisation of Wild-Type and ΔN6 β2-Microglobulin.* Journal of The American Society for Mass Spectrometry, 2018. **29**(12): p. 2413-2426.
253. Heck, A.J.R. and R.H.H. van den Heuvel, *Investigation of intact protein complexes by mass spectrometry.* Mass Spectrometry Reviews, 2004. **23**(5): p. 368-389.
254. Masson, G.R., J.E. Burke, N.G. Ahn, G.S. Anand, C. Borchers, S. Brier, G.M. Bou-Assaf, J.R. Engen, S.W. Englander, J. Faber, R. Garlish, P.R. Griffin, M.L. Gross, M. Guttman, Y. Hamuro, A.J.R. Heck, D. Houde, R.E. Iacob, T.J.D. Jørgensen, I.A. Kaltashov, J.P. Klinman, L. Konermann, P. Man, L. Mayne, B.D. Pascal, D. Reichmann, M. Skehel, J. Snijder, T.S. Strutzenberg, E.S. Underbakke, C. Wagner, T.E. Wales, B.T. Walters, D.D. Weis, D.J. Wilson, P.L. Wintrode, Z. Zhang, J. Zheng, D.C. Schriemer, and K.D. Rand, *Recommendations for performing, interpreting and reporting hydrogen deuterium exchange mass spectrometry (HDX-MS) experiments.* Nature Methods, 2019. **16**(7): p. 595-602.
255. Rand, K.D., M. Zehl, O.N. Jensen, and T.J.D. Jørgensen, *Protein Hydrogen Exchange Measured at Single-Residue Resolution by Electron Transfer Dissociation Mass Spectrometry.* Analytical Chemistry, 2009. **81**(14): p. 5577-5584.

256. Rand, K.D., M. Zehl, and T.J.D. Jørgensen, *Measuring the Hydrogen/Deuterium Exchange of Proteins at High Spatial Resolution by Mass Spectrometry: Overcoming Gas-Phase Hydrogen/Deuterium Scrambling.* Accounts of Chemical Research, 2014. **47**(10): p. 3018-3027.
257. Sheff, J.G., M. Rey, and D.C. Schriemer, *Peptide–Column Interactions and Their Influence on Back Exchange Rates in Hydrogen/Deuterium Exchange-MS.* Journal of the American Society for Mass Spectrometry, 2013. **24**(7): p. 1006-1015.
258. Pascal, B.D., M.J. Chalmers, S.A. Busby, and P.R. Griffin, *HD Desktop: An Integrated Platform for the Analysis and Visualization of H/D Exchange Data.* Journal of the American Society for Mass Spectrometry, 2009. **20**(4): p. 601-610.
259. Wei, H., J. Ahn, Y.Q. Yu, A. Tymiak, J.R. Engen, and G. Chen, *Using hydrogen/deuterium exchange mass spectrometry to study conformational changes in granulocyte colony stimulating factor upon PEGylation.* Journal of the American Society for Mass Spectrometry, 2012. **23**(3): p. 498-504.
260. Lim, X.-X., A. Chandramohan, X.-Y.E. Lim, J.E. Crowe Jr, S.-M. Lok, and G.S. Anand, *Epitope and paratope mapping reveals temperature-dependent alterations in the dengue-antibody interface.* Structure, 2017. **25**(9): p. 1391-1402.
261. Houde, D., S.A. Berkowitz, and J.R. Engen, *The Utility of Hydrogen/Deuterium Exchange Mass Spectrometry in Biopharmaceutical Comparability Studies.* Journal of Pharmaceutical Sciences, 2011. **100**(6): p. 2071-2086.
262. Stephens, A.D., N. Nespovitaya, M. Zacharopoulou, C.F. Kaminski, J.J. Phillips, and G.S. Kaminski Schierle, *Different Structural Conformers of Monomeric α-Synuclein Identified after Lyophilizing and Freezing.* Analytical Chemistry, 2018. **90**(11): p. 6975-6983.
263. Klein, T., N. Vajpai, J.J. Phillips, G. Davies, G.A. Holdgate, C. Phillips, J.A. Tucker, R.A. Norman, A.D. Scott, D.R. Higazi, D. Lowe, G.S. Thompson, and A.L. Breeze, *Structural and dynamic insights into the energetics of activation loop rearrangement in FGFR1 kinase.* Nature Communications, 2015. **6**: p. 7877.
264. Tukey, J.W., *Comparing Individual Means in the Analysis of Variance.* Biometrics, 1949. **5**(2): p. 99-114.
265. P, C. and R. R, *A systematic molecular dynamics approach to the structural characterization of amyloid aggregation propensity of [small beta]2-microglobulin mutant D76N.* Molecular BioSystems, 2016. **12**(3): p. 850-859.
266. Zehl, M., K.D. Rand, O.N. Jensen, and T.J.D. Jørgensen, *Electron Transfer Dissociation Facilitates the Measurement of Deuterium Incorporation into Selectively Labeled Peptides with Single Residue Resolution.* Journal of the American Chemical Society, 2008. **130**(51): p. 17453-17459.
267. Mistarz, U.H., B. Bellina, P.F. Jensen, J.M. Brown, P.E. Barran, and K.D. Rand, *UV Photodissociation Mass Spectrometry Accurately Localize Sites of Backbone Deuteration in Peptides.* Analytical Chemistry, 2018. **90**(2): p. 1077-1080.
268. Konermann, L., B.B. Stocks, and T. Czarny, *Laminar Flow Effects During Laser-Induced Oxidative Labeling for Protein Structural Studies by Mass Spectrometry.* Analytical Chemistry, 2010. **82**(15): p. 6667-6674.
269. Gau, B.C., J.S. Sharp, D.L. Rempel, and M.L. Gross, *Fast Photochemical Oxidation of Protein Footprints Faster than Protein Unfolding.* Analytical Chemistry, 2009. **81**(16): p. 6563-6571.

270. Maleknia, S.D. and K.M. Downard, *Radical approaches to probe protein structure, folding, and interactions by mass spectrometry.* Mass Spectrometry Reviews, 2001. **20**(6): p. 388-401.
271. Chea Emily, E. and M. Jones Lisa, *Modifications generated by fast photochemical oxidation of proteins reflect the native conformations of proteins.* Protein Science, 2018. **27**(6): p. 1047-1056.
272. Rennella, E., T. Cutuil, P. Schanda, I. Ayala, V. Forge, and B. Brutscher, *Real-Time NMR Characterization of Structure and Dynamics in a Transiently Populated Protein Folding Intermediate.* Journal of the American Chemical Society, 2012. **134**(19): p. 8066-8069.
273. Abolhasani Khaje, N., C.K. Mobley, S.K. Misra, L. Miller, Z. Li, E. Nudler, and J.S. Sharp, *Variation in FPOP Measurements Is Primarily Caused by Poor Peptide Signal Intensity.* Journal of The American Society for Mass Spectrometry, 2018.
274. Miller, S., J. Janin, A.M. Lesk, and C. Chothia, *Interior and surface of monomeric proteins.* Journal of Molecular Biology, 1987. **196**(3): p. 641-656.
275. Solar, S., W. Solar, and N. Getoff, *Resolved multisite OH-attack on aqueous tryptophan studied by pulse radiolysis.* Radiation Physics and Chemistry (1977), 1984. **23**(4): p. 371-376.
276. Solar, S., *Reaction of OH with phenylalanine in neutral aqueous solution.* Radiation Physics and Chemistry (1977), 1985. **26**(1): p. 103-108.
277. Fonseca, C., P. Domingues, A. Reis, and M.R.M. Domingues, *Identification of leucine-enkephalin radical oxidation products by liquid chromatography tandem mass spectrometry.* Biomedical Chromatography, 2008. **22**(9): p. 947-959.
278. Li, K.S., G. Chen, J. Mo, R.Y.C. Huang, E.G. Deyanova, B.R. Beno, S.R. O'Neil, A.A. Tymiak, and M.L. Gross, *Orthogonal Mass Spectrometry-Based Footprinting for Epitope Mapping and Structural Characterization: The IL-6 Receptor upon Binding of Protein Therapeutics.* Analytical Chemistry, 2017. **89**(14): p. 7742-7749.
279. Du, M., W. Wu, N. Ercal, and Y. Ma, *Simultaneous determination of 3-nitro tyrosine, o-, m-, and p-tyrosine in urine samples by liquid chromatography–ultraviolet absorbance detection with pre-column cloud point extraction.* Journal of Chromatography B, 2004. **803**(2): p. 321-329.
280. Hensley, K., S. Williamson Kelly, L. Maidt Michael, S. Prasad Gabbita, P. Grammas, and A. Floyd Robert, *Determination of Biological Oxidative Stress Using High Performance Liquid Chromatography with Electrochemical Detection (HPLC-ECD).* Journal of High Resolution Chromatography, 1999. **22**(8): p. 429-437.
281. Ishimitsu, S., S. Fujimoto, and A. Ohara, *Tyrosine Formation from Phenylalanine by Ultraviolet Irradiation.* Chemical & Pharmaceutical Bulletin, 1990. **38**(5): p. 1417-1418.
282. van der Vliet, A., A. O'Neill Charles, B. Halliwell, E. Cross Carroll, and H. Kaur, *Aromatic hydroxylation and nitration of phenylalanine and tyrosine by peroxynitrite.* FEBS Letters, 2001. **339**(1-2): p. 89-92.
283. Greifenhagen, U., A. Frolov, and R. Hoffmann, *Oxidative degradation of N ε-fructosylamine-substituted peptides in heated aqueous systems.* Amino Acids, 2015. **47**(5): p. 1065-1076.
284. Labroo, R.B. and L.A. Cohen, *Preparative separation of the diastereoisomers of dioxindolyl-L-alanine and assignment of stereochemistry at C-3.* The Journal of Organic Chemistry, 1990. **55**(16): p. 4901-4904.

285. Simat, T.J. and H. Steinhart, *Oxidation of Free Tryptophan and Tryptophan Residues in Peptides and Proteins.* Journal of Agricultural and Food Chemistry, 1998. **46**(2): p. 490-498.
286. Borotto, N.B., Z. Zhang, J. Dong, B. Burant, and R.W. Vachet, *Increased β-Sheet Dynamics and D–E Loop Repositioning Are Necessary for Cu(II)-Induced Amyloid Formation by β-2-Microglobulin.* Biochemistry, 2017. **56**(8): p. 1095-1104.
287. Sharp, J.S. and K.B. Tomer, *Effects of anion proximity in peptide primary sequence on the rate and mechanism of leucine oxidation.* Analytical Chemistry, 2006. **78**(14): p. 4885-4893.
288. Reis, A., C. Fonseca, E. Maciel, P. Domingues, and M.R.M. Domingues, *Influence of amino acid relative position on the oxidative modification of histidine and glycine peptides.* Analytical and Bioanalytical Chemistry, 2011. **399**(8): p. 2779-2794.
289. Misra, S.K., R. Orlando, S.R. Weinberger, and J.S. Sharp, *Compensated Hydroxyl Radical Protein Footprinting Measures Buffer and Excipient Effects on Conformation and Aggregation in an Adalimumab Biosimilar.* The AAPS Journal, 2019. **21**(5): p. 87.
290. Sharp, J.S., S.K. Misra, J.J. Persoff, R.W. Egan, and S.R. Weinberger, *Real Time Normalization of Fast Photochemical Oxidation of Proteins Experiments by Inline Adenine Radical Dosimetry.* Analytical Chemistry, 2018.
291. Niu, B., B.C. Mackness, D.L. Rempel, H. Zhang, W. Cui, C.R. Matthews, J.A. Zitzewitz, and M.L. Gross, *Incorporation of a Reporter Peptide in FPOP Compensates for Adventitious Scavengers and Permits Time-Dependent Measurements.* Journal of The American Society for Mass Spectrometry, 2017. **28**(2): p. 389-392.
292. Hallwell, B. and H. Kaur, *Hydroxylation of Salicylate and Phenylalanine as Assays for Hydroxyl Radicals: a Cautionary Note Visited for the Third Time.* Free Radical Research, 1997. **27**(3): p. 239-244.
293. Maskos, Z., J.D. Rush, and W.H. Koppenol, *The hydroxylation of tryptophan.* Archives of Biochemistry and Biophysics, 1992. **296**(2): p. 514-520.
294. Li, Y., A. Polozova, F. Gruia, and J. Feng, *Characterization of the Degradation Products of a Color-Changed Monoclonal Antibody: Tryptophan-Derived Chromophores.* Analytical Chemistry, 2014. **86**(14): p. 6850-6857.
295. Leney, A.C., C.L. Pashley, C.A. Scarff, S.E. Radford, and A.E. Ashcroft, *Insights into the role of the beta-2 microglobulin D-strand in amyloid propensity revealed by mass spectrometry.* Molecular BioSystems, 2014. **10**(3): p. 412-420.
296. Azinas, S., M. Colombo, A. Barbiroli, C. Santambrogio, S. Giorgetti, S. Raimondi, F. Bonomi, R. Grandori, V. Bellotti, S. Ricagno, and M. Bolognesi, *D-strand perturbation and amyloid propensity in beta-2 microglobulin.* The FEBS Journal, 2011. **278**(13): p. 2349-2358.
297. Cornwell, O., N.J. Bond, S.E. Radford, and A.E. Ashcroft, *Long-Range Conformational Changes in Monoclonal Antibodies Revealed Using FPOP-LC-MS/MS.* Analytical Chemistry, 2019. **91**(23): p. 15163-15170.
298. Brodbelt, J.S., *Ion Activation Methods for Peptides and Proteins.* Analytical chemistry, 2016. **88**(1): p. 30-51.
299. Ballard, K.D. and S.J. Gaskell, *Dehydration of peptide [M + H]+ ions in the gas phase.* Journal of the American Society for Mass Spectrometry, 1993. **4**(6): p. 477-481.

300. Liu, X.R., M.M. Zhang, B. Zhang, D.L. Rempel, and M.L. Gross, *Hydroxyl-Radical Reaction Pathways for the Fast Photochemical Oxidation of Proteins Platform As Revealed by 18O Isotopic Labeling.* Analytical Chemistry, 2019. **91**(14): p. 9238-9245.
301. Karmakar, T. and S. Balasubramanian, *Elucidating the interaction of H2O2 with polar amino acids – Quantum chemical calculations.* Chemical Physics Letters, 2014. **613**: p. 5-9.
302. Sela-Culang, I., S. Alon, and Y. Ofran, *A systematic comparison of free and bound antibodies reveals binding-related conformational changes.* The Journal of Immunology, 2012. **189**(10): p. 4890-4899.
303. Ponomarenko, N., S.D. Chatziefthimiou, I. Kurkova, Y. Mokrushina, Y. Mokrushina, A. Stepanova, I. Smirnov, M. Avakyan, T. Bobik, and A. Mamedov, *Role of κ→ λ light-chain constant-domain switch in the structure and functionality of A17 reactibody.* Acta Crystallographica Section D: Biological Crystallography, 2014. **70**(3): p. 708-719.
304. Pritsch, O., C. Magnac, G. Dumas, J.-P. Bouvet, P. Alzari, and G. Dighiero, *Can isotype switch modulate antigen-binding affinity and influence clonal selection?* European Journal of Immunology, 2000. **30**(12): p. 3387-3395.
305. Bridgewater, J.D., R. Srikanth, J. Lim, and R.W. Vachet, *The Effect of Histidine Oxidation on the Dissociation Patterns of Peptide Ions.* Journal of the American Society for Mass Spectrometry, 2007. **18**(3): p. 553-562.
306. Perrin, D.D., *Dissociation constants of organic acids and bases*. 1965, Butterworths: London.
307. Boys, B.L., M.C. Kuprowski, J.J. Noël, and L. Konermann, *Protein Oxidative Modifications During Electrospray Ionization: Solution Phase Electrochemistry or Corona Discharge-Induced Radical Attack?* Analytical Chemistry, 2009. **81**(10): p. 4027-4034.
308. Maleknia, S.D., M.R. Chance, and K.M. Downard, *Electrospray-assisted modification of proteins: a radical probe of protein structure.* Rapid Communications in Mass Spectrometry, 1999. **13**(23): p. 2352-2358.
309. Brumshtein, B., S.R. Esswein, M. Landau, C.M. Ryan, J.P. Whitelegge, M.L. Phillips, D. Cascio, M.R. Sawaya, and D.S. Eisenberg, *Formation of amyloid fibers by monomeric light chain variable domains.* The Journal of Biological Chemistry, 2014. **289**(40): p. 27513-27525.
310. Rennella, E., G.J. Morgan, J.W. Kelly, and L.E. Kay, *Role of domain interactions in the aggregation of full-length immunoglobulin light chains.* PNAS, 2019. **116**(3): p. 854.
311. Kiyoshi, M., J.M.M. Caaveiro, T. Kawai, S. Tashiro, T. Ide, Y. Asaoka, K. Hatayama, and K. Tsumoto, *Structural basis for binding of human IgG1 to its high-affinity human receptor FcγRI.* Nature Communications, 2015. **6**: p. 6866.
312. Wright, J.K. and J. Engel, *Independence of the binding of domain-specific ligands to Fab and Fc suggests that antigen-induced effects in IgG antibodies are not allosteric.* FEBS letters, 1978. **90**(1): p. 79-83.
313. Petritis, K., L.J. Kangas, B. Yan, M.E. Monroe, E.F. Strittmatter, W.-J. Qian, J.N. Adkins, R.J. Moore, Y. Xu, M.S. Lipton, D.G. Camp, and R.D. Smith, *Improved Peptide Elution Time Prediction for Reversed-Phase Liquid Chromatography-MS by Incorporating Peptide Sequence Information.* Analytical Chemistry, 2006. **78**(14): p. 5026-5039.

314. Li, K.S., L. Shi, and M.L. Gross, *Mass Spectrometry-Based Fast Photochemical Oxidation of Proteins (FPOP) for Higher Order Structure Characterization.* Accounts of Chemical Research, 2018. **51**(3): p. 736-744.
315. Bowen, A. and A. Casadevall, *Revisiting the immunoglobulin intramolecular signaling hypothesis.* Trends in Immunology, 2016. **37**(11): p. 721-723.
316. Fornelli, L., K. Srzentić, R. Huguet, C. Mullen, S. Sharma, V. Zabrouskov, R.T. Fellers, K.R. Durbin, P.D. Compton, and N.L. Kelleher, *Accurate Sequence Analysis of a Monoclonal Antibody by Top-Down and Middle-Down Orbitrap Mass Spectrometry Applying Multiple Ion Activation Techniques.* Analytical Chemistry, 2018. **90**(14): p. 8421-8429.
317. Wu, C., J.C. Tran, L. Zamdborg, K.R. Durbin, M. Li, D.R. Ahlf, B.P. Early, P.M. Thomas, J.V. Sweedler, and N.L. Kelleher, *A protease for 'middle-down' proteomics.* Nature Methods, 2012. **9**(8): p. 822-824.
318. Zhao, Y., L. Sun, M.D. Knierman, and N.J. Dovichi, *Fast separation and analysis of reduced monoclonal antibodies with capillary zone electrophoresis coupled to mass spectrometry.* Talanta, 2016. **148**: p. 529-533.